Advances in Experimental Medicine and Biology 1097

Bingmei M. Fu · Neil T. Wright *Editors*

Molecular, Cellular, and Tissue Engineering of the Vascular System

Springer

Advances in Experimental Medicine and Biology

Volume 1097

More information about this series at http://www.springer.com/series/5584

Bingmei M. Fu • Neil T. Wright
Editors

Molecular, Cellular, and Tissue Engineering of the Vascular System

Springer

Editors
Bingmei M. Fu
Department of Biomedical Engineering
The City College of the City University
of New York
New York, NY, USA

Neil T. Wright
Department of Mechanical Engineering
Michigan State University
East Lansing, MI, USA

ISSN 0065-2598 ISSN 2214-8019 (electronic)
Advances in Experimental Medicine and Biology
ISBN 978-3-319-96444-7 ISBN 978-3-319-96445-4 (eBook)
https://doi.org/10.1007/978-3-319-96445-4

Library of Congress Control Number: 2018956138

This Springer imprint is published by the registered company Springer Nature Switzerland AG
The registered company address is: Gewerbestrasse 11, 6330 Cham, Switzerland

Preface

Multidisciplinary teams of medical scientists and biomedical engineers, using recent advances in molecular biology, new imaging tools for cell and tissue observations, and modern computational methods and techniques, have made many discoveries and proposed new avenues of exploration in physiology and pathology of mammalian vascular systems. Although these results are routinely presented in the various journals of specific fields, they are seldom systematically introduced to the general audience in the medical and biomedical engineering community. The purpose of this collection is to introduce the recent progress in molecular, cellular, and tissue engineering in the vascular system.

The vascular system is composed of the vessels that carry blood and lymph throughout the body. Arteries, veins, and capillaries circulate blood throughout the body, delivering oxygen and nutrients to the body tissues and removing metabolic waste. This transport function of the vascular system is governed and regulated by the molecular, subcellular, and cellular components forming the vascular wall and the surrounding tissue. Due to its unique location at the interface of the circulating blood and the vascular wall, endothelial surface glycocalyx (ESG) plays important roles as a mechano-sensor and transducer for the blood flow, as a modulator of trans-vascular exchange, and as a barrier to the circulating cells (such as leukocytes) and endothelium adhesion. These roles of ESG are reviewed sequentially in Chaps. 1, 2, and 3. Information received at the vascular surface must be transduced into endothelial cell nucleus for further processing and subsequent use in regulating cellular functions. Chapters 4 and 5 examine the roles of nuclear envelope proteins and nuclear lamina in this process under blood flow-induced shear stress and cyclic stretch. The smooth muscle cells and elastic lamina in the wall of large arteries regulate the blood perfusion rate. Chapter 6 summarizes the regional heterogeneity of these components in the regulation of vasoconstriction in arteries. Following discussion of this basic research, Chaps. 7 and 8 discuss the formation and mechanisms of fibrous cap rupture and vulnerable plaque, and abdominal aortic aneurysm. Chapter 9 presents nonsurgical vascular interventions for coronary artery diseases. After presenting progress in large vessel research, Chap. 10 elucidates the driving force for the movement of red blood cells in narrow capillaries. Chapters 11 and 12 review the experimental studies and mathematical models for tumor metastasis in the microvascular system. Then, Chaps. 13 and 14

discuss transport across a special microvascular wall, the blood-brain barrier, and its role in the clearance of amyloid-β; accumulation of amyloid-β in the brain is one of the factors responsible for Alzheimer's disease. In addition to regulating material transport, our vascular system assists the body temperature control, and the cells of the vascular system also react actively to the temperature change. Chapter 15 reviews the mathematical models of cell response following heating, while Chap. 16 demonstrates applications of hypothermia in enhancing the treatment efficiency in brain and spinal cord injuries. Finally, the biomechanical changes of eardrums to blast waves are described in Chap. 17. Although the eardrum, a multilayer soft tissue membrane, is not in the vascular system, the mechanism for its damage due to the sudden sound pressure may be applicable to the damage of heart valves due to sudden blood pressure changes in the heart.

Last but not least, we sincerely thank our authors for their great contributions to this book. We would also like to thank Dr. Jie Fan, at Rensselaer Polytechnic Institute, and Dr. Yuliya Vengrenyuk, at the Icahn School of Medicine at Mount Sinai, for their help in reviewing some of the chapters in this book. Finally, we would like to thank Ms. Merry Stuber, Editor of Biomedical Engineering at Springer Nature, for her invitation and strong support, and Mr. Sindhuraj Thulasingam, Project Coordinator at Springer Nature, for his tireless assistance. We hope that this book, although covering only limited aspects of the current advances in the vascular system, will bring more collaboration among different disciplines and stimulate more innovative ideas for dealing with the health issues in the vascular system, which include many of the top killers worldwide.

New York, NY, USA Bingmei M. Fu
East Lansing, MI, USA Neil T. Wright

Contents

The Role of Endothelial Surface Glycocalyx in Mechanosensing and Transduction 1
Ye Zeng, X. Frank Zhang, Bingmei M. Fu, and John M. Tarbell

The Molecular Structure of the Endothelial Glycocalyx Layer (EGL) and Surface Layers (ESL) Modulation of Transvascular Exchange 29
Fitz-Roy E. Curry

Role of the Glycocalyx as a Barrier to Leukocyte-Endothelium Adhesion 51
Herbert H. Lipowsky

Mechanobiology and Vascular Remodeling: From Membrane to Nucleus 69
Ying-Xin Qi, Yue Han, and Zong-Lai Jiang

Endothelial Nuclear Lamina in Mechanotransduction Under Shear Stress 83
Julie Y. Ji

Regional Heterogeneity in the Regulation of Vasoconstriction in Arteries and Its Role in Vascular Mechanics 105
Sae-Il Murtada and Jay D. Humphrey

Microcalcifications, Their Genesis, Growth, and Biomechanical Stability in Fibrous Cap Rupture 129
Luis Cardoso and Sheldon Weinbaum

Abdominal Aortic Aneurysm Pathomechanics: Current Understanding and Future Directions 157
Erica M. C. Kemmerling and Robert A. Peattie

Vascular Intervention: From Angioplasty to Bioresorbable Vascular Scaffold 181
Fengyi Du and Jiangbing Zhou

On the Physics Underlying Longitudinal Capillary Recruitment . . . 191
Jacques M. Huyghe

Tumor Metastasis in the Microcirculation 201
Bingmei M. Fu

Modeling Cell Adhesion and Extravasation in Microvascular System 219
L. L. Xiao, W. W. Yan, Y. Liu, S. Chen, and B. M. Fu

Transport Across the Blood-Brain Barrier 235
Bingmei M. Fu

Blood-Brain Barrier Integrity and Clearance of Amyloid-β from the BBB 261
Irsalan Cockerill, Joy-Anne Oliver, Huaxi Xu, Bingmei M. Fu, and Donghui Zhu

Mathematical Models of Cell Response Following Heating 279
Neil T. Wright

Hypothermia Used in Medical Applications for Brain and Spinal Cord Injury Patients 295
Liang Zhu

Biomechanical Changes of Tympanic Membrane to Blast Waves . . 321
Rong Z. Gan

The Role of Endothelial Surface Glycocalyx in Mechanosensing and Transduction

Ye Zeng, X. Frank Zhang, Bingmei M. Fu, and John M. Tarbell

Abstract

The endothelial cells (ECs) forming the inner wall of every blood vessel are constantly exposed to the mechanical forces generated by blood flow. The EC responses to these hemodynamic forces play a critical role in the homeostasis of the circulatory system. A variety of mechanosensors and transducers, locating on the EC surface, intra- and trans-EC membrane, and within the EC cytoskeleton, have thus been identified to ensure proper functions of ECs. Among them, the most recent candidate is the endothelial surface glycocalyx (ESG), which is a matrix-like thin layer covering the luminal surface of the EC. It consists of various proteoglycans, glycosaminoglycans, and plasma proteins and is close to other prominent EC mechanosensors and transducers. This chapter summarizes the ESG composition, thickness, and structure observed by different labeling and visualization techniques and in different types of vessels. It also presents the literature in determining the ESG mechanical properties by atomic force microscopy and optical tweezers. The molecular mechanisms by which the ESG plays the role in EC mechanosensing and transduction are described as well as the ESG remodeling by shear stress, the actin cytoskeleton, the membrane rafts, the angiogenic factors, and the sphingosine-1-phosphate.

Y. Zeng (✉)
Institute of Biomedical Engineering, West China School of Basic Medical Sciences and Forensic Medicine, Sichuan University, Chengdu, China
e-mail: ye@scu.edu.cn

X. F. Zhang
Department of Mechanical Engineering and Mechanics, Lehigh University, Bethlehem, PA, USA

B. M. Fu · J. M. Tarbell
Department of Biomedical Engineering, The City College of the City University of New York, New York, NY, USA

1 Introduction

The inner wall of every blood vessel in our body is formed by endothelial cells (ECs). Besides biochemical stimuli, blood flow-induced (hemodynamic) mechanical stimuli modulate EC morphology and function by activating mechanosensors, signaling pathways, and gene and protein expressions (Mammoto et al. 2012). EC responses to the hemodynamic forces (mechanosensing and transduction) are critical to maintaining normal vascular functions (Davies et al. 1984; Chien 2007). Failure in mechanosensing and transduction contributes to

B. M. Fu, N. T. Wright (eds.), *Molecular, Cellular, and Tissue Engineering of the Vascular System*, Advances in Experimental Medicine and Biology 1097,
https://doi.org/10.1007/978-3-319-96445-4_1

serious vascular diseases including hypertension, atherosclerosis, aneurysms, stroke, thrombosis, and cancer, to name a few (Ingber 2003; Cai et al. 2012; Fu and Tarbell 2013; Tarbell and Cancel 2016).

The hemodynamic forces that ECs experience include pressure, shear, and circumferential stretch. The force (per unit surface area) perpendicular to the EC (the vessel wall) is the pressure due to the hydrodynamic force generated by the heart. The human circulatory system is ~100,000 miles long, and the magnitude of blood pressure is not uniform in all the blood vessels in the human body. The blood pressure ranges from almost zero to ~120 mmHg for a healthy adult human under resting conditions (Fung 1997). Another type of force (per unit surface area) which is tangential to the EC surface is called shear or shear stress. The shear is due to the friction between the circulating blood and the vessel wall and ranges 10–40 dyn/cm^2 for arterial ECs and 1–6 dyn/cm^2 for venous ECs (Yamamoto and Ando 2011). The third force that acts along the circumference of the vessel wall is named circumferential stretch (or wall tension), also due to the blood pressure. Like the pressure and shear, the stretch varies in different types of vessels and under resting and exercising conditions. These hemodynamic forces vary spatially in different organs (10^{-1}–1 m length scale) and tissues (10^{-2}–10^{-1} m) due to vascular sizes and patterns (e.g., branches and turns), and temporally due to the pulsatile and oscillatory nature of the blood flow in large vessels. Even at the cellular level (10^{-3} m), there is a spatial distribution of these forces (Muller et al. 2004). To sense and transmit the constantly varying hemodynamic forces from the EC surface to its cytoplasm and further into the nucleus, a variety of mechanosensors and transducers (with size in the range from 10^{-9} to 10^{-4} m) are required. So far, at least ten candidates have been identified as mechanosensors and transducers, including cell adhesion proteins (e.g., VE-cadherin, PECAM-1) (Schwartz and DeSimone 2008; Stevens et al. 2008), ion channels (Gojova and Barakat 2005; Gautam et al. 2006), tyrosine kinase receptors (e.g., vascular endothelial growth factor receptor 2) (Schwartz and DeSimone 2008), G-protein-coupled receptors and G-proteins (Yamamoto and Ando 2011), caveolae (Tabouillot et al. 2011), primary cilia (Egorova et al. 2012), actin filaments (Matsui et al. 2011), nesprins (Morgan et al. 2011), integrins (Wang et al. 2009), and endothelial surface glycocalyx (ESG) (Tarbell and Pahakis 2006; Weinbaum et al. 2007; Tarbell and Ebong 2008; Fu and Tarbell 2013).

Endothelial cells are covered by a matrix-like layer called the endothelial surface glycocalyx (ESG) in the present chapter. More generally it may be referred to as the endothelial surface layer (ESL) to emphasize the complexity of the layer and its many components as in F. E. Curry's Chap. 2. Or, for simplicity, it is perhaps most often called the "glycocalyx" to emphasize that proteoglycans, glycoproteins, and glycosaminoglycans are the central components of the surface layer. Due to its unique location, composition, and structure, in addition to serving as a selective permeability, anti-inflammatory, and anti-adhesive barrier at the luminal side of the endothelium, the ESG plays a critical role in EC mechanosensing and transduction to regulate circulation functions (Fig. 1) (Reitsma et al. 2007; Tarbell and Ebong 2008; Curry and Adamson 2012). Because of its proteoglycan and glycosaminoglycan composition, the ESG may cover the entire surface of the EC as shown in Fig. 1 and thus can interact with other EC sensors and transducers to play a role in sensing and transmitting hemodynamic forces.

This chapter only summarizes the literature for the role of ESG as a mechanosensor and transducer. Other roles are presented in Chaps. 2 and 3. The composition, structure, and organization of the ESG are first introduced in the chapter, followed by its mechanical properties. Then the mechanism by which the ESG plays its role in mechanosensing/transduction is elucidated. Finally, the remodeling of ESG by shear stress, the actin cytoskeleton, the membrane rafts, the angiogenic factors, and the S1P is described.

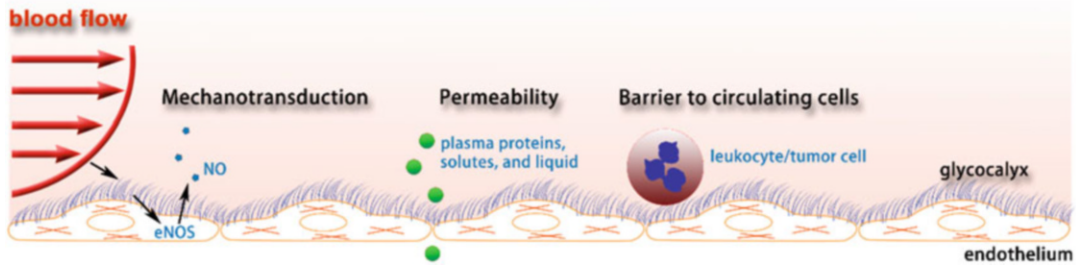

Fig. 1 Roles of endothelial surface glycocalyx (ESG) in regulating circulation functions. The ESG plays at least three roles in maintaining the normal functions of the vascular system, being a mechanosensor and transducer, a molecular sieve, and a barrier between circulating cells such as leukocytes and tumor cells and endothelial cells forming the inner wall of blood vessels

2 Composition, Organization, and Structure of ESG

2.1 Molecular Composition

The roles of mechanosensing and transduction of ESG are based on its molecular composition and organization, which are cartooned in Fig. 2 (Tarbell and Pahakis 2006; Zeng 2017). The components of the ESG have been investigated in depth (Zeng et al. 2012; Tarbell and Cancel 2016). The ESG is mainly composed of glycoproteins bearing short acidic oligosaccharides and terminal sialic acids (SA) and proteoglycans (PG) like heparan sulfate PGs (HSPG) including syndecan and glypican core proteins with long glycosaminoglycan (GAG) side chains. The negatively charged GAGs bind proteins, growth factors, cations, and other plasma components. The predominant GAGs in ECs are heparan sulfate (HS), chondroitin sulfate (CS), and hyaluronic acid (HA). Of the three, the most abundant is HS, accounting for 50–90% of the total GAGs, the rest being comprised of CS and HA (Sarrazin et al. 2011). HS and CS are covalently bound to PGs, whereas HA does not bind to a PG core protein. HA is a non-sulfated GAG, which binds with its surface receptors CD44 and receptor for HA-mediated motility (RHAMM).

The HSPG syndecan family has four members: syndecan-1, syndecan-2, syndecan-3, and syndecan-4. Syndecan-1 contains five potential GAG attachment sites, three near its NH_2-terminal ectodomain and two adjacent to the transmembrane domain near its COOH terminus. CS is only found near the COOH terminus of syndecan-1 (Tarbell and Pahakis 2006). Syndecan-3 contains eight potential GAG attachment sites, five near its NH_2-terminal ectodomain and three adjacent to the transmembrane domain near its COOH terminus. Both syndecan-2 and syndecan-4 contain three potential GAG attachment sites near their NH_2-terminal ectodomain (Bernfield et al. 1999; Lopes et al. 2006). Syndecan-4 can also contain CS and is often located on the basal side of the cell (Deepa et al. 2004). In the HSPG glypican family, only glypican-1 is expressed in ECs. Glypican-1 is a membrane glycosylphosphatidylinositol (GPI)-anchored protein, which only binds with HS. GPI-anchored protein is localized in both lipid rafts and caveolae (Lisanti et al. 1994; Schnitzer et al. 1995a). The formation and function of caveolae is dependent on phosphorylation of caveolin-1 which is induced in a HA-dependent manner (Long et al. 2012). Some fractions of HA bound to CD44 are internalized into caveolae (McGuire et al. 1987; Tarbell and Pahakis 2006). The internalized caveolae might fuse with caveosomes, thus playing an important role in transcytosis of its contents such as albumin (Schubert et al. 2001; Nichols 2003). Sphingosine-1-phosphate (S1P) protects glycocalyx that is required for

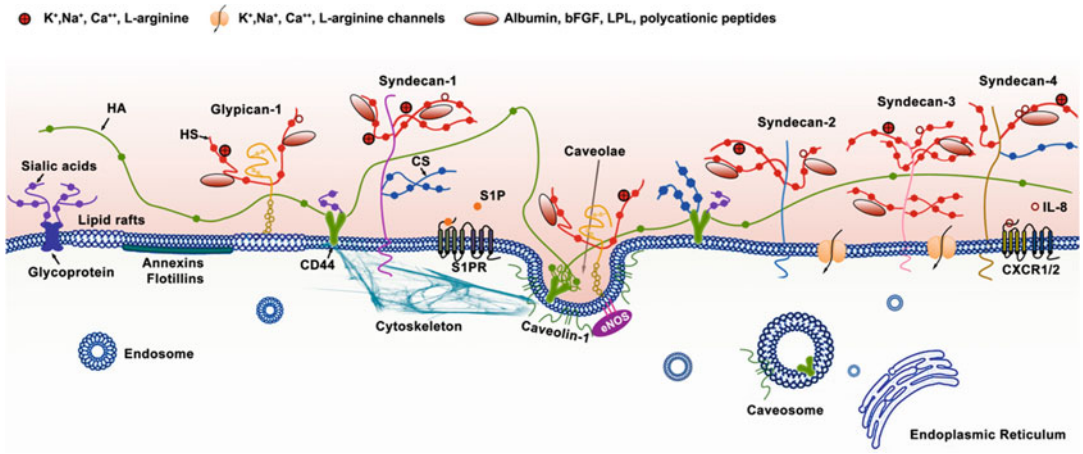

Fig. 2 Structural components of the endothelial glycocalyx. The ESG is mainly located at the luminal side of vascular ECs although syndecan-4 is dominantly basal. The apical GAGs and associated proteins and ions are directly in contact with the bloodstream, and they transfer flow forces to the core proteins that transmit them to the cell. In addition to bound plasma components, the ESG is mainly composed of glycoproteins bearing acidic oligosaccharides and terminal sialic acids (SA); proteoglycans (PG), such as heparan sulfate proteoglycans (HSPGs, syndecan family and glypican-1); and GAG side chains. The predominant GAGs in ECs are heparan sulfate (HS), chondroitin sulfate (CS), and hyaluronic acid (hyaluronan, HA). HS and CS are attached to PGs. HA binds with receptor CD44. Syndecans (including syndecan-1, syndecan-2, syndecan-3, and syndecan-4) are single transmembrane domain proteins. Glypican-1 is a membrane glycosylphosphatidylinositol (GPI)-anchored protein, which is localized in lipid rafts, as well as caveolae. Lipid rafts are characterized by high translational mobility. Integrity of the actin cytoskeleton is essential for the immobility of caveolae. Syndecan-1 and CD44 interact with the cytoskeleton. Annexins and flotillins might be involved in the formation and function of caveolae. Some fraction of HA bound to CD44 are internalized into caveolae. The phosphorylation of caveolin-1, a protein responsible for maintaining the shape of caveolae, is induced in a HA-dependent manner, which might be involved in CD44-caveolae-mediated endocytosis. It has been assumed that internalized caveolae fuse with caveosomes. Caveosomes play an important role in transcytosis of its contents such as albumin to other subcellular (non-lysosomal) compartments including the endoplasmic reticulum in ECs. Sphingosine-1-phosphate (S1P) protects the shedding of glycocalyx and induces the synthesis of glycocalyx that is required for mechanotransduction and cytokine response (i.e., IL-8/CXCR1/2-induced EC migration) (Revised from Tarbell and Pahakis (2006); Zeng (2017))

mechanotransduction and cytokine response (i.e., IL-8/CXCR1-/CXCR2-induced EC migration (Tarbell and Pahakis 2006; Weinbaum et al. 2007; Tarbell and Ebong 2008; Fu and Tarbell 2013; Zeng et al. 2013; Zeng et al. 2014; Zeng and Tarbell 2014; Zeng et al. 2015; Yan et al. 2016).

In resting conditions, syndecans and glypican-1 mRNAs in human umbilical vein endothelial cells (HUVECs) are expressed in the order: syndecan-1 > syndecan-4 > syndecan-3 > syndecan-2 > glypican-1 (Liu et al. 2016). The ESG is modified under several conditions including disturbed flow exposure in large vessels (Brands et al. 2007), protease degradation (Huxley and Williams 2000; Brands et al. 2007; Lipowsky 2012), and removal of plasma components, particularly albumin (Michel et al. 1985).

2.2 Organization

It is widely believed that the negatively charged GAGs in the ESG capture circulating plasma proteins and cations and form an interconnected gel-like structure in an aqueous environment (Ohlson et al. 2001; Sorensson et al. 2001; Weinbaum et al. 2007) and that the ESG would collapse if a GAG component was significantly reduced. However, a recent study by Zeng et al. (2012) observed that specific enzymatic removal of HS or HA did not result in cleavage or collapse of

any of the remaining components. Simultaneous removal of CS and HA by chondroitinase did not affect HS. Their results suggest that all GAGs and adsorbed proteins are well intermixed within the structure of the ESG but the GAG components do not interact with one another.

2.3 Thickness and Structure

In addition to its biochemical composition, the thickness and ultrastructure of the ESG determine its function as a mechanosensor and transducer. The first visualization of the ESG by electron microscopy (EM) used the cationic dye ruthenium red that binds to acidic mucopolysaccharides and generates electron density in the presence of osmium tetroxide (Luft 1966). Subsequent studies (Baldwin and Winlove 1984; Sims and Horne 1993) used gold colloids and immunoperoxidase labeling. Adamson and Clough (1992) then demonstrated using a large charged marker protein (unable to penetrate the ESG), cationized ferritin (molecular weight ~450 kDa), that in the absence of plasma proteins, the ESG would collapse, presumably due to elimination of intramolecular interactions with plasma proteins, and that its undisturbed thickness was several times greater than the 20 nm observed with ruthenium red (Luft 1966). All of these methods may suffer from dehydration artifacts associated with aqueous fixatives that likely dissolve all but the protein cores of proteoglycans and collapse the inherently hydrated structures. A method developed to preserve water-soluble structures using fluorocarbons as nonaqueous carriers of osmium tetroxide was applied to microvessels to obviate some of these limitations by Sims and Horne (1993). Further elaborations of the fluorocarbon-glutaraldehyde fixation methods by Rostgaard and Qvortrup (1997) revealed a filamentous brush-like surface coating on capillary walls, but a layer thickness of less than 50 nm, suggesting a cleavage of more superficial matrix structures. All of the foregoing EM studies revealed an ESG with a thickness less than 100 nm. Recently, van den Berg et al. (2003) used a new approach to stabilize the anionic carbohydrate structure on the ESG by Alcian Blue 8GX (Fig. 3). They found that the ESG thickness was 0.2–0.5 μm on rat left ventricular myocardial capillaries.

To overcome the artifact by EM, the amount of ESG was estimated based on the biophysical principles from in vivo observations (Klitzman and Duling 1979). A direct in vivo measurement of the ESG thickness with the dye-exclusion technique was developed by Vink and Duling (1996). Using a 70 kD FITC-dextran plasma tracer, which they showed was sterically excluded by the ESG, they were able to provide the first estimate of the in vivo thickness of the ESG in capillaries of hamster cremaster muscle to be ~0.4–0.5 μm. Most recently, the ESG thickness was also estimated as ~0.5 μm in rat mesenteric postcapillary venules by FITC-dextran labeling with intravital microscopy (Long et al. 2004). This estimate of the in vivo thickness of the ESG is four to five times greater than previous estimates derived from EM studies. This discrepancy was a catalyst for much of the work that has followed on the estimation of ESG thickness and its function as a barrier in cellular interactions as well as a mechanosensor and transducer of ECs. Using high-resolution, near-wall, intravital fluorescent microparticle image velocimetry (μ-PIV) to examine the velocity profile near the vessel wall in postcapillary venules of the mouse cremaster muscle, Long et al. (2004) and Smith et al. (2003) produced estimates of glycocalyx thickness of order 0.5 μm.

The poor spatial resolution of an intravital optical microscope limits the accurate measurement of the ESG thickness (Pries et al. 2000). New imaging methods have thus been developed by employing laser scanning confocal microscopy and multi-photon microscopy, and fluorescently tagged antibodies to HS or HA binding protein, or wheat germ agglutinin to label major components of the ESG. Application of these new methods has revealed a much thicker ESG in large blood vessels: 4.3–4.5 μm in the mouse common carotid artery (van den Berg et al. 2009), 2.2 μm in the mouse internal carotid artery (Reitsma et al. 2011), and 2.5 μm in the external carotid

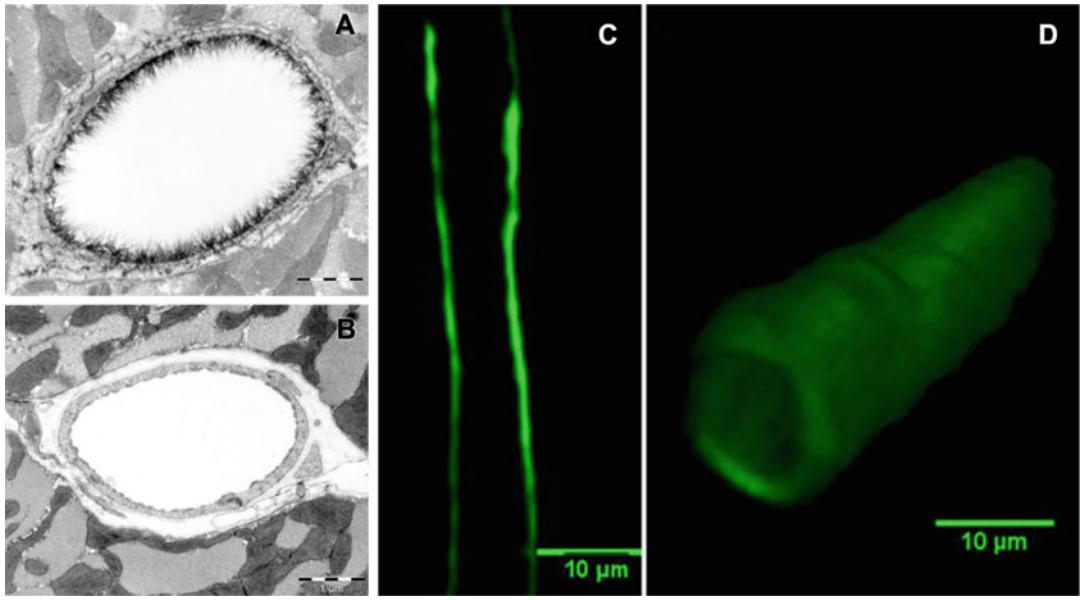

Fig. 3 The ESG at the microvessel wall observed by different visualization techniques. Left, electron microscopic view of an Alcian Blue 8GX-stained ESG on rat left ventricular myocardial capillary (**a**) after enzyme treatment to remove the ESsG (**b**). Scale bar is 1 μm. From Van den Berg et al. (2003). Right, confocal microscopic view of anti-HS labeled ESG on rat mesenteric capillaries. Midplane view (**c**) and 3D view (**d**). From Yen et al. (2012)

artery (Megens et al. 2007). Ebong et al. (2011) presented the first cryo-EM images of in vitro ESG that avoided the dehydration artifacts of conventional EM and observed structures greater than 5 μm in thickness (up to ~11 μm). Most recently, using high-sensitivity and high-resolution confocal microscopy and in situ/in vivo single microvessel and ex vivo aorta immunostaining, Yen et al. (2012) revealed that the thickness of the ESG on rat mesenteric and mouse cremaster capillaries and postcapillary venules is 1–1.5 μm. Surprisingly, there was no detectable ESG in arterioles by using fluorescence labeled anti-HS. The ESG thickness is 2–2.5 μm on rat and mouse aorta. They also observed that the ESG is continuously and evenly distributed on the aorta wall but not on the microvessel wall if looking at a vessel segment of length ~100 μm. By comparing the distance between the plasma membrane labeling and the labeling of ESG (SA residues) by wheat germ agglutinin (WGA) in a single microvessel in vivo, Betteridge et al. (2017) found that the ESG thickness is 0.17–3.02 μm in the same type of microvessels as in Yen et al., (2012), depending on the labeling and analyzing methods. However, the thickness of ESG at the same portion of the vessel is only ~0.08 μm observed by the EM through Alcian Blue labeling.

The ultrastructural organization of the ESG and its relation to the cytoskeleton components (e.g., F-actin) of ECs was first investigated by Squire (2001). Using computed autocorrelation functions and Fourier transforms of EM images of frog mesenteric microvessels, they identified a quasi-periodic substructure in the ESG, which is a 3D fibrous meshwork with characteristic spacing ~20 nm. The fiber diameter was observed as 10–12 nm. They also showed that the fibrous elements may occur in clusters with a common intercluster spacing of ~100 nm and may be linked to the underlying actin cortical cytoskeleton. The recent study by Arkill et al. (2011) observed similar ESG structures in mammalian microvessels of choroid, renal tubules, glomerulus, and psoas muscle and was confirmed by a 3D reconstruction using electron tomography by employing a tannic acid staining method

and a novel staining technique of lanthanum dysprosium glycosaminoglycan adhesion (the LaDy GAGa method) (Arkill et al. 2012). The thickness of the ESG observed by their EM method is ~100 nm, similar to what was previously found on frog mesenteric microvessels (Adamson and Clough 1992). The approximately 100 nm thick structure may form an inner core of the ESG which determines the filtration and molecular sieve function of the microvessel wall to water and solutes while a micron scale outer structure may generate a buffer region for the lubrication of RBC movement and a barrier for WBC adhesion to the ECs forming the vessel wall. But how this structure plays a role in mechanosensing and transduction remains to be elucidated. The two-layer model is discussed further in reference to permeability properties in the chapter by Curry.

The recent development of ultra-resolution stochastic optical reconstruction microscopy (STORM) has made it possible to visualize the ESG structure at high resolution (Zullo et al. 2016; Song et al. 2017). STORM employs organic dyes and fluorescent proteins as photo-switchable emitters to trade temporal resolution for a super spatial resolution (20 nm lateral and 50 nm axial at present due to the size of antibodies used to identify the ESG components), which is an order of magnitude greater than conventional confocal microscopy (Rust et al. 2006). Future studies by using STORM along with much smaller peptides instead of antibodies to identify the ESG components should elucidate the ultrastructure and molecular composition of ESG in fresh cell and tissue samples. Another method of combining lanthanum dysprosium glycosaminoglycan adhesion staining and electron tomography (Arkill et al. 2012) can also reveal the ultrastructure at high resolution.

3 Mechanical Properties of Glycocalyx

To sense and transmit the blood flow-induced forces from the ESG surface to the EC cell body and nucleus, it is necessary for the ESG fibers (core proteins and attached GAGs) to have a structural integrity, which is characterized by the flexural rigidity, EI. Applying a linear elasto-hydrodynamic model, Weinbaum et al. (2003) predicted that EI of the ESG fibers is 700 pN nm^2 by matching the time-dependent restoration of the ESG after being crushed by the passage of a WBC in a tightly fitting capillary (Vink and Duling 1996). Later, Han et al. (2016) developed a more sophisticated nonlinear elastohydrodynamic model that uses large deformation theory for elastica and a modified Brinkman equation to describe the local relative motion of the fibers and the fluid. Their prediction for the EI of the ESG fibers is 490 pN nm^2, comparable to the result predicted by the earlier linear model (Weinbaum et al. 2003). Nijenhuis et al. (2009) used optically trapped submicron probe particles to measure the viscoelastic properties of an in vitro ESG model, which consists of a 2.5 mg/mL bulk solution of hyaluronan (HA) and other components of the ESG, including CS, HS, aggrecan, albumin, and plasma. They found that CS and aggrecan, which directly interact with HA, modify the viscoelastic properties of the HA solution, while HS, plasma, and albumin have no effects.

Applying atomic force microscopy (AFM) microindentation method, the elastic modulus of the ESG on bovine lung microvascular EC (BLMVEC) monolayer was measured as ~0.3 kPa after enzyme treatment for HS and HA (O'Callaghan et al. 2011). By using an AFM nanoindentation method, a more recent study by Bai and Wang (2012) determined Young's modulus of the ESG on HUVEC monolayer to be 0.39 kPa. Due to its loose structural network and high water content, the ESG is approximately one order of magnitude softer than the plasma membrane. Oberleithner et al. (2011) were able to quantify the stiffness and thickness of ESG from AFM force-indentation curves. This method is shown in Fig. 4. Light microscopy was used to ensure that the AFM tip was located neither at the nuclear, nor at the junctional region of cultured ECs (Fig. 4a). In some experiments, the cells were stained with wheat germ agglutinin-FITC to simultaneously monitor the intactness of ESG (Fig. 4b, insets). During the indentation scan, the AFM tip travels vertically

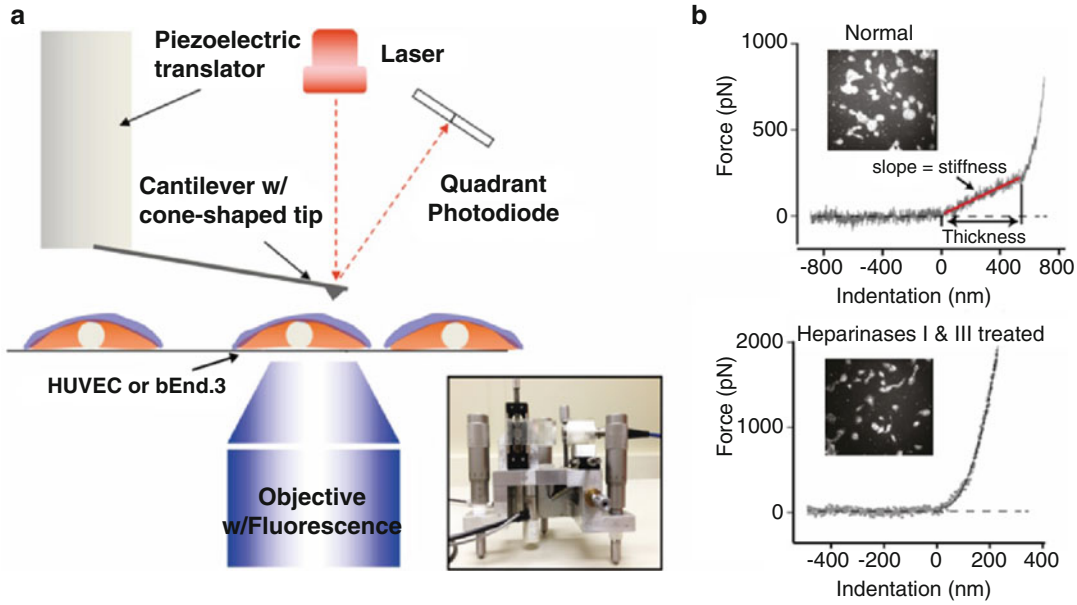

Fig. 4 AFM nanoindentation. (**a**) A schematic diagram of the AFM assay. Insert: a picture of the AFM head used for nanoindentation. The blue layer on cell surface indicates the ESG. (**b**) Quantification of thickness and stiffness of ESG by AFM nanoindentation. Cited from Song et al. (2017)

toward the HUVEC surface. Upon indentation of the ESG, the AFM cantilever, serving as a soft spring, is deflected (boxed region in Fig. 4b upper panel). The cantilever deflection is measured and plotted as a function of sample position along the *z*-axis. The resulting curve is transformed into a force-versus-indentation curve using the cantilever's spring constant and the light lever sensitivity. The slope of a force-indentation curve directly reflects the stiffness (expressed in pN/nm), which is necessary to indent the ESG for a certain distance. The first slope indicates the stiffness (in this trace 0.30 pN/nm) of the very first layer, which is the ESG. The second nonlinear region indicates the stiffness of the plasma membrane. The distance between the starting point of ESG indentation and the starting point of the second slope (projected to the *x*-axis) corresponds to the thickness of the EG (in this trace ~550 nm). In average, ESG on HUVECs has an averaged thickness of 651 ± 54 nm and stiffness of 0.25 ± 0.07 pN/nm. Treatment of HUVECs with heparinases I and III eliminated the linear spring region of the force-indentation curve, indicating that the EG was degraded by enzymatic digestion. Using this method, Oberleithner et al. (2011) further showed that sodium overload led to stiffened and thinner (i.e., collapsed) ESG, whereas treatment of ECs with thrombin, lipopolysaccharides, or tumor necrosis factor-α reduced both EG stiffness and thickness (Fels et al. 2014). Instead of simply treating the ESG force-indentation curve as a linear slope, a two-layer Hertzian model has been used by Marsh and Waugh (2013) to fit the nanoindentation curves, yielding ESG elastic modulus of 0.7 ± 0.5 kPa and thickness of 380 ± 50 nm.

4 Mechanotransduction and ESG

An important function of the ESG is to serve as a mechanosensor and transducer (Tarbell and Pahakis 2006; Weinbaum et al. 2007; Tarbell and Ebong 2008; Fu and Tarbell 2013; Haeren et al. 2016; Tarbell and Cancel 2016). It is well known that a dysfunctional endothelium is an early manifestation of atherosclerosis (AS) (Yurdagul Jr.

et al. 2016). Vascular endothelial injury in AS-susceptible locations is a prerequisite for AS formation (McAlpine and Swirski 2016; Sorci-Thomas and Thomas 2016; Taleb 2016).

In AS-susceptible locations such as branches, bifurcation, and curvatures (e.g., the aortic arch) of the arterial tree, the blood stream undergoes tremendous interference, and the flow departs from pulsatile, unidirectional shear stress to create flow separation zones that include flow reversal, oscillatory and multi-directional shear stress, and sometimes turbulence (chaotic flow) (Davies 2009; Zhou et al. 2014; Dabagh et al. 2017). In contrast, flow in adjacent undisturbed flow regions of the arteries is pulsatile and has unidirectional flow direction with minimal reversal. It has been speculated that low shear stress induces the initial lesion, and high shear stress promotes the formation of calcified vulnerable plaques (Wang et al. 2016; Eshtehardi et al. 2017).

The ESG plays an important role in EC mechanotransduction of shear stress. Weinbaum et al. (2003) pointed out that the existence of the ESG could reduce the fluid shear stress on the vascular EC surface to a negligible level by theoretical analysis, while Secomb et al. (2001) described the transfer of fluid mechanical shear stress at the interface between the fluid and the outer regions of the ESG to solid mechanical stress within the matrix. Thi et al. (2004) further showed that the ESG is required for the EC cytoskeleton to respond to shear stress.

Florian et al. (2003) showed that enzymatic removal of HS from the surface of BAECs in vitro completely blocked shear-induced NO production in both steady flow (15 dyn/cm^2) and reversing oscillatory flow (10 ± 15 dyn/cm^2) out to 3 h exposure including both the early phase (seconds to minutes after a step increase in shear) that is calcium and G-protein dependent as well as the later phase (minutes to hours) that is independent of calcium and G-protein (Kuchan et al. 1994). Yen et al. (2015) demonstrated that degradation of HS in the rat mesentery greatly inhibited NO production in response to an increase in flow. Pahakis et al. (2007) showed that shear-induced NO production was blocked by enzymes removing HS and HA, but not CS and that these treatments had no effect on the shear-induced production of the important vasodilator and antiplatelet agent, prostacyclin (PGI_2). Because the proteoglycan core protein glypican-1 only binds HS and not CS and the dominant apical syndecan (syndecan-1) binds both HS and CS, it was hypothesized that glypican-1 is the core protein that transmits the fluid shear force sensed by the GAG (HS) to the cell surface where it is ultimately transduced via the phosphorylation of eNOS into NO. This hypothesis was tested by Ebong et al. (2014) who showed that knockdown of glypican-1 using shRNA completely blocked shear-induced phosphorylation of eNOS, whereas knockdown of syndecan-1 had no effect. Because knockdown of genes by shRNA can have off-target effects, the hypothesis was further tested using atomic force microscopy (AFM) with cantilevers coated with specific antibodies to HS, glypican-1, and syndecan-1 (Bartosch et al. 2017). Force applied to HS or glypican-1 resulted in NO production, whereas force applied to syndecan-1 did not. These experiments were carried out at 10 and 30 min and did not specifically interrogate the early G-protein-dependent phase of activation.

Zeng and Liu (2016) found that shear stress has a dual role in eNOS activation: 4 dyn/cm^2 shear stress inhibited the activation of eNOS, and 15 dyn/cm^2 shear stress induced it. Removal of glypican-1 by phosphatidylinositol phospholipase C (PI-PLC) significantly suppressed the 15 dyn/cm^2 shear stress-induced eNOS activity and further reduced the 4 dyn/cm^2-inhibited eNOS activity (Zeng and Liu 2016). Therefore, eNOS activation depends on shear stress magnitudes and is mediated by glypican-1.

To follow-up on the observation that GAG removal by enzymes did not block shear-induced PGI_2 production (Pahakis et al. 2007), Russell-Puleri et al. (2017) investigated primary cilia, syndecan-4, and platelet endothelial cell adhesion molecule 1 (PECAM-1), as potential mechanosensors for PGI_2 production. Primary cilia are localized to the apical surface of EC and syndecan-4 to the basal surface and in confluent ECs PECAM-1 localizes at intercellular junctions where it regulates homophilic binding between cells. Separate knockdown of the

three putative mechanosensors in cultured cells revealed that only PECAM-1 deletion blocked shear-induced PGI_2 production and upregulation of the enzyme cyclooxygenase 2 (COX-2) by a mechanism involving inside-out activation $\alpha_5\beta_1$ integrin. The role of PECAM-1 in shear-induced PGI_2 was further confirmed in a PECAM-1 knockout mouse model (Russell-Puleri et al. 2017). Conway et al. (2013) using a fluorescence resonance energy transfer (FRET) tension sensor, showed that shear stress increased tension across PECAM-1 at intercellular junctions. Weber et al. (2017) applied tension to the extracellular domain of PECAM-1 using AFM and observed upregulation of COX-2, the precursor to PGI_2 production.

In related studies, it has been shown that PECAM-1 is also an upstream mediator of shear stress-induced NO production. Fleming et al. (2005) and Wang et al. (2015) observed that shear stress-induced tyrosine phosphorylation of PECAM-1 as well as the serine phosphorylation of Akt and eNOS was abolished by pretreatment of cells with a tyrosine kinase inhibitor. A comparable attenuation of Akt and eNOS phosphorylation and NO production was also observed in endothelial cells generated from PECAM-1-deficient mice. Xu et al. (2016) found that flow-mediated eNOS phosphorylation in vivo induced by voluntary wheel running was reduced in PECAM-1 knockout mice. However, when the extracellular domain of PECAM-1 was put under tension by AFM with the same specific antibody that led to COX-2 upregulation, there was no effect on NO production (Bartosch et al. 2017).

How can we reconcile the observations that the proteoglycan core protein glypican-1 mediates shear-induced eNOS phosphorylation and NO production (Ebong et al. 2014; Bartosch et al. 2017) with similar findings for PECAM-1 (Fleming et al. 2005; Xu et al. 2016)? Our working hypothesis is that the upstream shear stress sensor is glypican-1 that activates intracellular signaling pathways leading to tyrosine phosphorylation of PECAM-1 and downstream serine phosphorylation of eNOS and NO production. This most likely corresponds to the later phase of NO production since all of the supporting experiments were conducted in a time frame of minutes to hours.

The glycocalyx might also play an important role in early-phase mechanotransduction in response to a step change in shear stress through the interaction between the G-protein Gαq/11 and PECAM-1 (dela Paz et al. 2014). It has been shown that PECAM-1 and Gαq/11 form a mechanosensitive complex that contains an endogenous HSPG with HS chains that is critical for junctional complex assembly and regulation of the flow response. In experiments that used heparinase to cleave HS, such as Florian et al. (2003), Pahakis et al. (2007), and others, the PECAM-1/Gαq/11 complex bound by HS would have been disrupted thus altering the early-phase induction of NO production. This would be consistent with the observation by Florian et al. (2003) that heparinase treatment blocked both the early and later phase response of NO production to a step change in shear stress.

Synthesizing the above discussion of mechanisms for shear-PECAM-1-COX-2-PGI_2, the early phase shear- Gαq/11/PECAM-1-NO, and the sustained phase shear-Glypican-1-PECAM-1-NO, we arrive at the overall hypothesis summarized in Fig. 5. It should be noted that the cartoons of Figs. 5, 6, and 8 emphasize the central components of the mechanisms. They do not, for example, include the detailed components of the surface layer that may be involved in transmitting fluid shear stress to the proteoglycan core proteins glypican-1 and syndecan-1. These were shown in greater detail in Fig. 2 and discussed earlier in this section.

5 Remodeling of ESG

5.1 Shear Stress and ESG

Several studies have detected a substantial glycocalyx on cultured rat fat pad EC (RFPECs) (Thi et al. 2004; Ebong et al. 2011; Zeng et al. 2012). In a recent study using fluorescence confocal microscopy (Zeng et al. 2012), it was shown that the coverages of HS and CS on RFPECs under

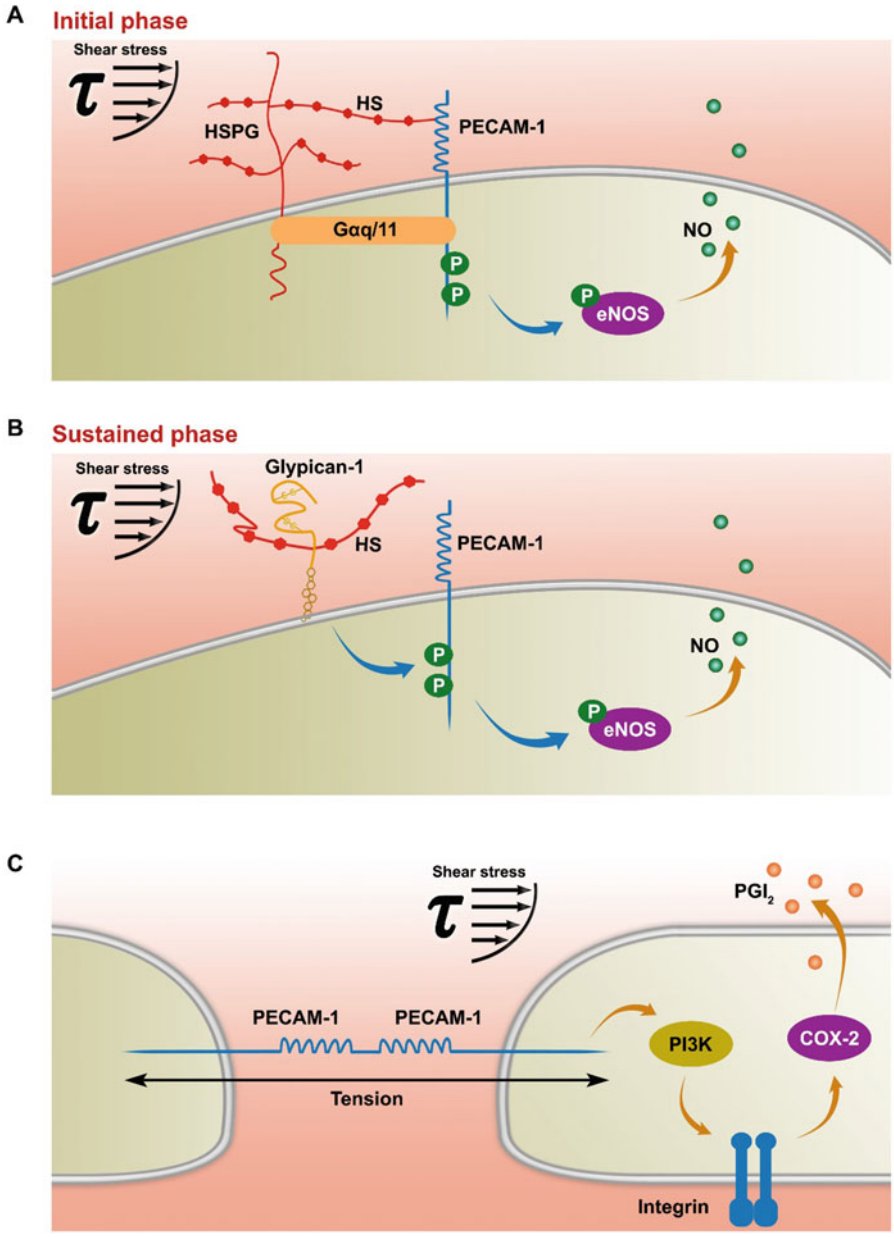

Fig. 5 Proposed mechanism of shear stress-induced NO and PGI_2. (**a**) Gαq/11/PECAM-1 bound by HS is the early phase mechanosensor for NO. (**b**) Glypican-1 is the sustained-phase shear stress sensor that leads to intracellular activation of PECAM-1 and downstream NO production. (**c**) Shear stress-induced tension on PECAM-1 induces PGI_2 production through a PI3K-Integrin-COX-2 signaling pathway

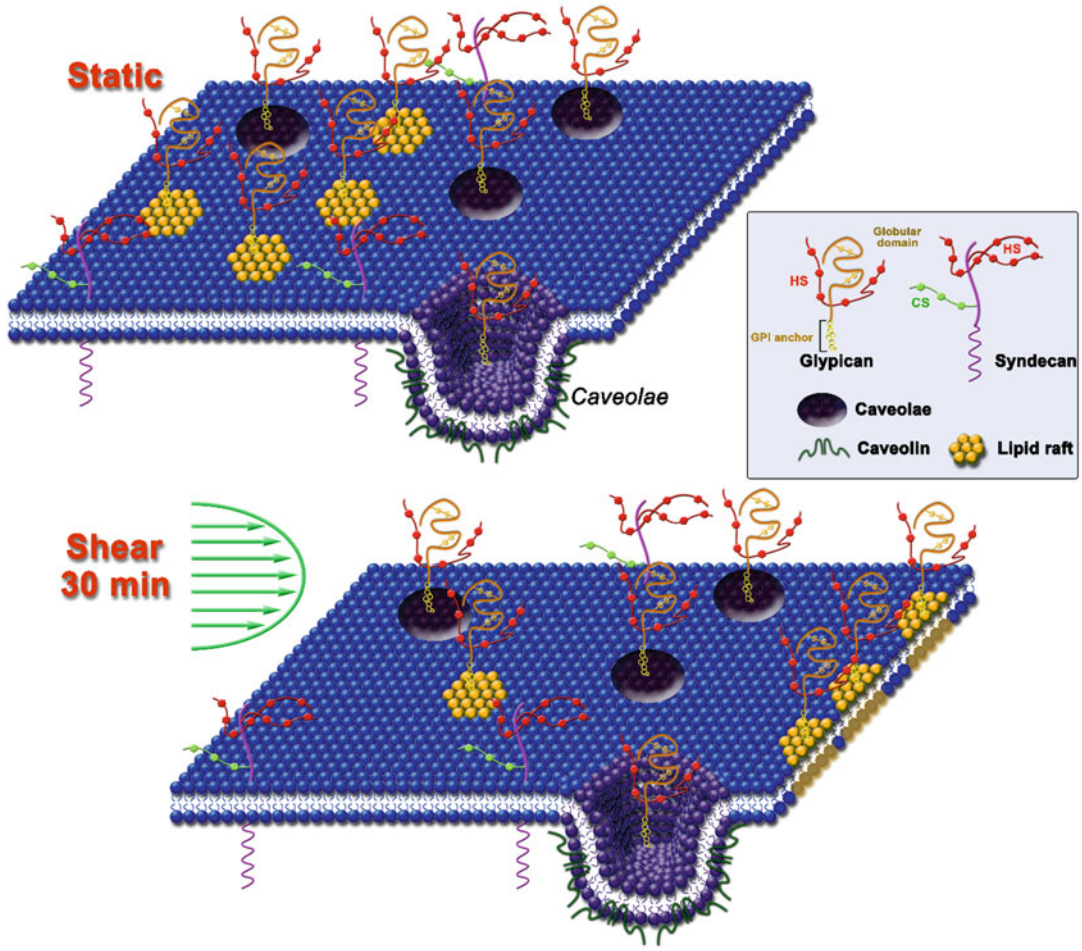

Fig. 6 Early responses of glycocalyx: fluid shear stress induces the clustering of HS via mobility of glypican-1 in lipid rafts. Under static conditions, syndecan-1 is localized outside of caveolae, while GPI-anchored glypican-1 is localized in membrane rafts including both lipid rafts and caveolae. Glypican-1 exclusively carries HS, and syndecan-1 contains CS and HS. After the initial 30 min of exposure to shear stress, lipid rafts with their anchored glypican-1 and associated HS move toward the cell junction. In contrast, the transmembrane syndecan-1 with attached HS and CS, and albumin, seem to be fixed in position, as well as the glypican-1 in caveolae. Cited from Zeng et al. (2013)

static condition are similar, but they cannot infer from this that the relative abundances (masses) are the same or similar. It must be noted that the fluorescent antibody technique can be used to map the location of target antigens, but it cannot be used to compare masses of different molecules because the specific antibody-antigen affinities may differ greatly (Thomas J. Kindt et al. 2007).

Recall that glypican-1 carries HS exclusively, and syndecan-1 carries both CS and HS. Using fluorescence confocal microscopy, it was shown that, in response to 30 min shear stress, glypican-1 was reduced in coverage and appeared to cluster near the cell boundary without expression reduction, but syndecan-1 did not appear to move (Zeng et al. 2013). In addition, by examining MFI data, there was no evidence that HS and CS or glypican-1 and syndecan-1 increased or decreased under shear stress for 30 min. These observations based on fluorescent antibody technique further confirmed that glypican-1, but not syndecan-1, redistributes in response to shear

(Zeng et al. 2013). These results combined with the observation of clustering of HS, but not CS, strongly suggest that glypican-1 carried the HS that moved and aggregated in the cell junction. Notably, glypican-1 is bound directly to the plasma membrane through a GPI anchor and localized to membrane rafts (MRs) (Tarbell and Pahakis 2006).

The MRs consist of dynamic assemblies of cholesterol and sphingolipids, in the exoplasmic leaflet of the bilayer (Lindner and Naim 2009). MRs are classified into two types: protein-based membrane domains (i.e., caveolae) and lipid-based domains (i.e., lipid rafts) (Lindner and Naim 2009; Zeng et al. 2013). Caveolae and lipid rafts exist separately on the cell surface (Schnitzer et al. 1995b); both are greatly enriched in cholesterol and exoplasmic sphingolipids. GPI-anchored proteins are localized in both caveolae and lipid rafts—with nearly half of GPI-anchored proteins localized outside of caveolae on ECs (Lisanti et al. 1994; Schnitzer et al. 1995a). The cholera toxin B subunit (CTx-B), which binds specifically to a component of the plasma membrane—glycosphingolipid, ganglioside GM_1—has been used as a MR marker in many studies (Parton 1994; De Haan and Hirst 2004). GM1 is present over the entire cell surface and enriched in caveolae (Parton 1994). Caveolin-1, which anchors caveolae to the actin cytoskeleton (Navarro et al. 2004), attaches to the cytosolic face of plasma membrane via a hydrophobic hairpin loop and provides a scaffold for caveolae formation (Razani et al. 2002). Caveolin-1 has emerged as a vital plasma membrane mechanosensor (Parton and del Pozo 2013). Meanwhile integrity of the actin cytoskeleton is essential for the immobility of caveolae (Thomsen et al. 2002). In contrast, lipid rafts are held together by specific lipid-lipid interactions (Lingwood and Simons 2010), organized in a liquid-order phase, and characterized by limited acyl chain order but high translational mobility (Lindner and Naim 2009; Simons and Sampaio 2011).

A recent study has demonstrated the changes in distribution of MRs (caveolin-1 and GM_1) after exposing statically cultured RFPECs to shear stress, focusing on the first 30 min after initiation of shear (Zeng et al. 2013). Under shear stress for 30 min, the expression and distribution of caveolin-1 did not change, indicating that caveolae are stabilized sufficiently to resist shear stress during the first 30 min of exposure. In a previous study (Rizzo et al. 2003), it was shown that the caveolae density at the plasma membrane increased sixfold after 10 dyn/cm^2 of shear stress exposure for 6 h—a much longer shear exposure than the 30 min. Although almost all caveolin-1 is localized in caveolae, nearly half of the GPI-anchored proteins reside outside caveolae on ECs (Lisanti et al. 1994; Schnitzer et al. 1995a). A large fraction of glypican-1 was likely associated with caveolae and thus was not mobilized during the 30 min of shear exposure (Zeng et al. 2013), which resulted in the smaller changes in the distribution of glypican-1 compared to HS. Thus, Zeng et al. (2013) concluded that the mobile HS is bound to glypican-1 that is outside the caveolar fraction of membrane rafts. This leads to the conclusion that lipid rafts carry the mobile glypican-1 and HS. The observation of movement of a membrane raft marker—GM_1—has further reinforced this conclusion (Zeng et al. 2013). This mechanism is summarized in Fig. 6.

The dramatic change in HS distribution was confirmed on often studied BAECs (Fig. 7) (Zeng and Tarbell 2014). After 24 h of exposure, BAECs were remodeled into an elongated (fusiform) shape whereas RFPECs retained their cobblestone morphology at 24 h (Zeng and Tarbell 2014). Other EC types as well do not elongate in response to sustained shear stress. For example, during exposure to 40 dyn/cm^2 for 24 h, pig aortic ECs did not align along the flow direction (Arisaka et al. 1995). The BAECs did maintain cobblestone morphology after 30 min of shear exposure. (Zeng and Tarbell 2014).

Similar phenomena occurred on RFPECs and BAECs showing consistent changes in the synthesis and reorganization of HS. The distributions of HS and glypican-1 became nonuniform after 30 min of shear exposure (clustering at the cell boundary) and then returned to a nearly uniform distribution between 30 min and 24 h (Zeng and Tarbell 2014). The distributions of CS

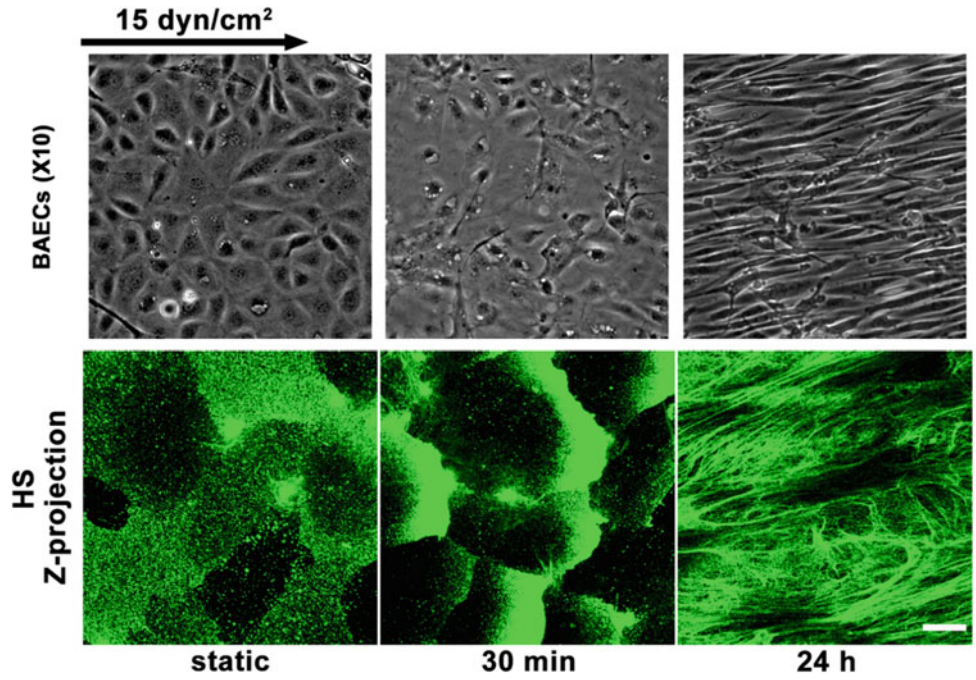

Fig. 7 Validation of the clustering and subsequent restoration of HS under shear stress using bovine aortic endothelial cells. Top: phase contrast micrographs of confluent BAEC monolayer reveal a typical dynamic change in cell morphology from cobblestone (static control) to the elongated (fusiform) and oriented in the direction of flow. Bottom: representative immunofluorescent images of HS under static and shear stress conditions. Figure adapted with permission from (Zeng and Tarbell 2014)

and syndecan-1 were not altered throughout the duration of shear exposure. The in vivo state was examined in Yen et al. (2012) where it was shown that the fully adapted state in the aorta of rats and mice shows a highly uniform coverage of HS that is similar to the 24 h state (Zeng and Tarbell 2014) (Fig. 7). Other glycocalyx components have not yet been examined in vivo.

The adaptation of the glycocalyx to fluid shear stress involves a balance between the synthesis of glycocalyx components including both GAGs and core proteins and their degradation that is modulated by enzymes such as heparanase and metalloproteases (Lipowsky 2011; Curry and Adamson 2012). Zeng and Tarbell (2014) concluded that glycocalyx components were synthesized in RFPECs and BAECs during shear exposure for 24 h, which is consistent with other studies in pig aortic EC (Arisaka et al. 1995) and human EC-RF24 cells (Gouverneur et al. 2006) showing that shear stress induces new synthesis of HS and CS. Recently, Koo et al. (2013) examined the effect of pulsatile flow on glycocalyx formation in cultured HUVECs. They reported that their atheroprotective waveform (high mean shear, no reversal) induced increases in HS and syndecan-1, a decrease in glypican-1, and no alteration of CS after 7 days of exposure. Another study showed that glypican-1 did not change on HUVECs exposed to the atheroprotective waveform for 3 days (Koo et al. 2011).

Notably, the mechanisms underlying the shear stress-induced increase in GAG synthesis are still not known. GAG synthesis induced by shear stress was concomitant with a decrease in DNA synthesis and an increase in protein synthesis (Arisaka et al. 1995). The mRNA expressions of exostosin glycosyltransferase-1 and glycosyltransferase-2 (EXT1 and EXT2), two genes encoding glycosyltransferases involved in the chain elongation step of HS

biosynthesis, did not change under shear stress (Koo et al. 2013). The disruption of actin cytoskeleton by cytochalasin D (CD) abolished the additional synthesis of HS on ECs exposed to shear stress for 24 h, indicating that the actin cytoskeleton plays a role in shear-induced HS biosynthesis.

In a recent study, Liu et al. (2016) detected that transcriptional expression of HSPGs (syndecan family and glypican-1) in HUVECs responded to the distinct magnitudes of shear stress. During the initial 0.5 h of exposure, syndecan-1 mRNA was the most upregulated, by 4 dyn/cm^2 of shear stress, and syndecan-4 mRNA was significantly upregulated, by 10 and 15 dyn/cm^2. After 24 h of exposure, the greatest increase in mRNA was syndecan-4 under 4 dyn/cm^2, and syndecan-3 under 15 dyn/cm^2. All the three magnitudes of shear stress (4, 10, and 15 dyn/cm^2) resulted in a significant increase in glypican-1 mRNA after 24 h exposure. Compared with static control, there was a 1.7-, 3.4-, and 4.1-fold increase in glypican-1 mRNA at 24 h under 4, 10, and 15 dyn/cm^2, respectively, but was not significantly changed at 0.5 h (Liu et al. 2016). These molecular changes that may be responsible for dynamic remodeling of the glycocalyx and associated with vascular homeostasis and endothelial dysfunction revealed the potential candidate components of the glycocalyx in response to cardiovascular diseases.

Moreover, increases in sulfated GAGs in the circulation media were detected after 24 h of shear exposure in an earlier study (Arisaka et al. 1995). Although researchers did not observe enhanced sulfated GAGs in the circulation media after 30 min of shear exposure (Zeng et al. 2013), they have not examined this issue at 24 h due to loss of cells from the edges of the cover slide artificially elevating the media concentration of sulfated GAG (Zeng and Tarbell 2014).

5.2 Cytoskeleton and ESG

Many studies of mechanotransduction in endothelial cells are based on the initial exposure of statically cultured cells to a step change in shear stress (Haidekker et al. 2000; Rizzo et al. 2003; Chien 2007; Pahakis et al. 2007; Yao et al. 2007). Shear stress induces EC responses via cytoskeleton-dependent and cytoskeleton - independent pathways (Silver and Siperko 2003; Wang et al. 2008) including the glycocalyx which is an important mechanosensing element on the plasma membrane surface (Tarbell and Pahakis 2006; Wang et al. 2008).

Longer-term adaptation of the endothelium to fluid shear stress is dominated by transformation in the actin cytoskeleton resulting in rearrangement of filamentous actin (F-actin) into bundles of stress fibers aligned in the direction of flow and into a diffuse network of short microfilaments including lamellipodia and filopodia (Gotlieb 1990; Malek and Izumo 1996; Li et al. 2005).The stress fiber bundles are composed of actin filaments in parallel alignment that function as cellular cytoskeletal-contractile elements (Sanger and Sanger 1980; Gotlieb 1990).

In static conditions (no shear stress), prominent microfilament bundles, the dense peripheral bands, are present at the cell periphery of confluent EC monolayers (Sanger and Sanger 1980; Satcher et al. 1997). Shear-induced increases in caveolin-1/caveolae and actin are predominantly distributed in the apical regions of the cell where a sustained clustering of lipid rafts occurs (Zeng and Tarbell 2014). Stress fibers are believed to support caveolae in the apical membrane by their association with caveolin-1 (Thomsen et al. 2002; Navarro et al. 2004). Thus, it appears that the distribution of F-actin over the cell surface, including that which has been newly synthesized, provides a supporting scaffold for new caveolae and their associated glypican/HS. It has been demonstrated that caveolae and caveolin-1 are crucial for both short- and long-term mechanotransduction in blood vessels of mice (Yu et al. 2006). Newly synthesized syndecan supported by actin provides a platform for additional HS and CS that have been synthesized as well. This is summarized in Fig. 8.

The associations of syndecan-1 with stress fiber and lamellipodia protrusion have been indicated in several studies (Carey et al. 1996; Chakravarti et al. 2005; Couchman 2010). In ad-

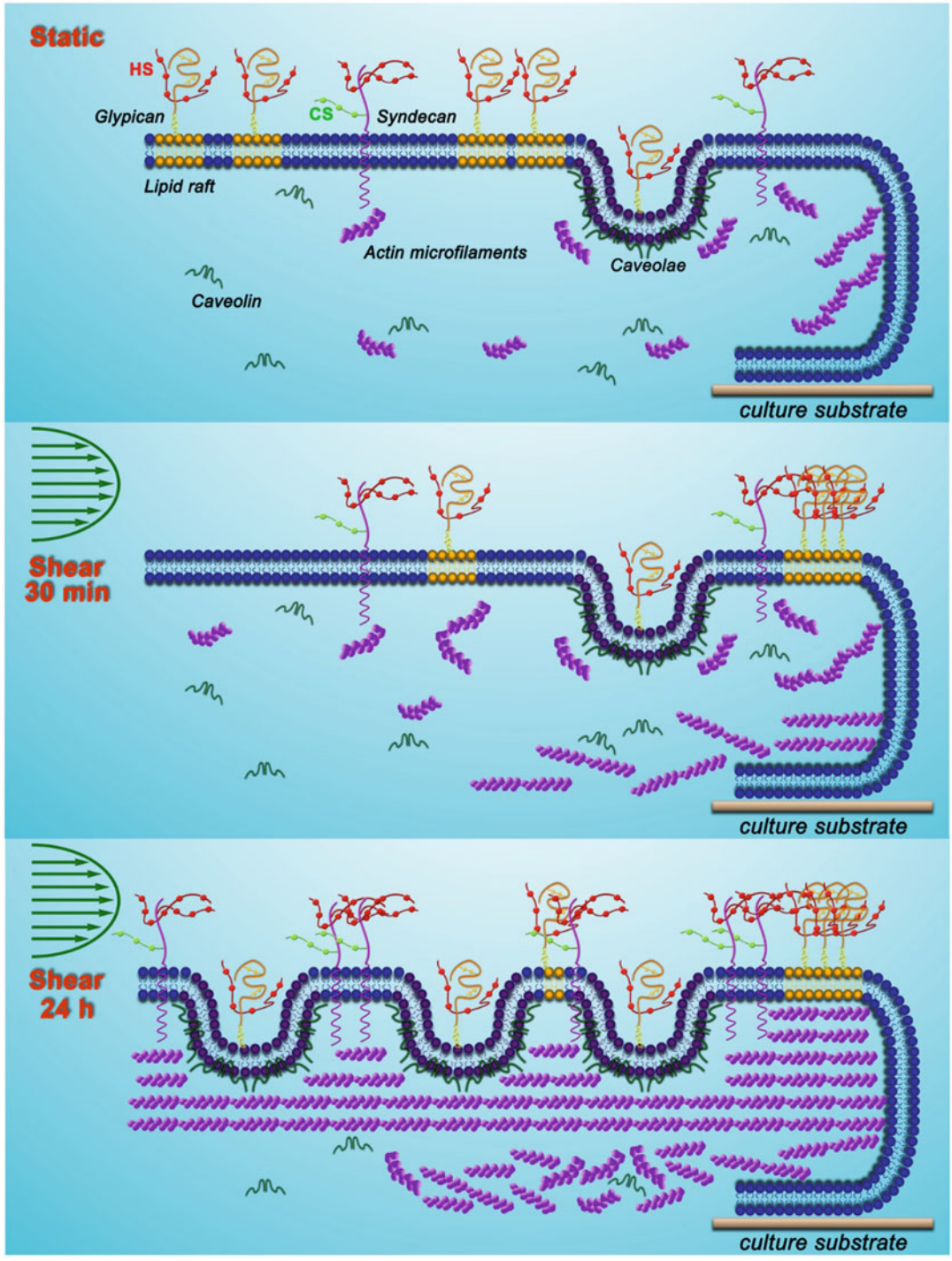

Fig. 8 Adaptive remodeling of glycocalyx with membrane rafts and actin cytoskeleton. Under static conditions, glypican-1 carrying only HS is localized on the dispersed lipid rafts and caveolae on the membrane. The actin cytoskeleton interacts with the transmembrane protein syndecan-1 and the caveolar structural protein caveolin-1 for stabilization. After 30 min of shear exposure, lipid rafts have carried glypican-1 with anchored HS to the cell boundary (clustering), while syndecan-1 carrying HS and CS and caveolae with localized

dition, HS plays a central role in mediating fluid shear stress-induced cell motility and proliferative response (Yao et al. 2007) and change of the actin cytoskeleton (Thi et al. 2004; Moon et al. 2005). To test whether actin cytoskeleton responsible the dynamic remodeling of the glycocalyx, actin cytoskeleton was disrupted by CD (Zeng and Tarbell 2014; Li and Wang 2017). At static conditions (without flow), the glycocalyx was not disrupted after CD treatment. Interestingly, the administration of CD (40 nM) did not prevent the clustering of HS on RFPECs in response to shear stress at 30 min, but abolished the recoverage of HS at 24 h (Zeng and Tarbell 2014). The phenomena at 24 h were also shown on HUVCEs and human aortic endothelial cells (HAECs) by Li and Wang (2017). These results suggested that the shear stress-induced clustering of HS at 30 min is actin cytoskeleton-independent and that the actin cytoskeleton plays an important role in the reorganization of the glycocalyx at 24 h. The dynamic modeling of the glycocalyx might contribute in both cytoskeleton-dependent and cytoskeleton -independent pathways.

5.3 S1P and ESG

S1P is emerging as a potent modulator of endothelial function in response to injury (Sanchez 2016). S1P exerts a variety of biological actions through binding with the specific G-protein-coupled receptors ($S1P_{1–5}$) on the cell surface to activate signaling cascades or serve as a second messenger (Meyer zu Heringdorf and Jakobs 2007). Receptors $S1P_{1–3}$ are expressed in many tissues in the cardiovascular system (Kimura et al. 2000; Kono et al. 2004) and have been widely investigated. S1P and its receptor, $S1P_1$, were required for embryonic angiogenesis and vascular stabilization (Kono et al. 2004). S1P can promote the formation of an actin ring around vascular ECs and strengthen cell-cell and cell-matrix interactions through $S1P_1$, maintaining the low permeability of the vascular wall (Curry and Adamson 2013). The specific agonist of $S1P_1$ (KRP-203) significantly inhibits the formation and development of AS but does not influence the S1P level in plasma (Poti et al. 2013). When mice were fed a high-fat diet, the development of an abnormal vascular phenotype and development of plaque were obvious in the descending aorta in the $Apoe^{-/-}$ and EC-specific $S1P_1$ null mice ($S1P_1^{f/f}$ VE-cadherin-Cre-ER^{T2}), but were not evident in the $Apoe^{-/-}$ and $S1P_1$ wild-type mice (Jung et al. 2012), showing that S1P could maintain the vascular homeostasis and prevent the development of AS through $S1P_1$.

How might the above observations be related to the glycocalyx? The EC glycocalyx was modified/degraded after removal of plasma components, particularly albumin, from the bathing media (Michel et al. 1985). In a recent study, it was demonstrated that S1P carried by albumin inhibits shedding of the syndecan-1 ectodomain on EC via activation of $S1P_1$ receptor (Zeng and Tarbell 2014), and thus maintains the normal vascular permeability in intact microvessels (Sha et al. 2016). The depletion of plasma protein induces syndecan-1 shedding through MMP-mediated proteolytic cleavage close to the plasma membrane on the external face (Zeng and Tarbell 2014). The shedding of the syndecan-1 ectodomain also takes away the attached HS and CS (Zeng and Tarbell 2014). After complete shedding of glycocalyx components (including syndecan-1 with attached HS and CS) by depletion of

Fig. 8 (continued) glypican-1 and anchored HS do not move. Actin microfilaments increase in both apical and basal aspects of the cell. After 24 h of exposure, new caveolae are assembled on the apical surface, which may associate with newly synthesized glypican-1. Syndecan-1 (HS/CS) and glypican-1(HS) that are bound to anchored caveolae and mobile lipid rafts are synthesized and result in nearly uniform distributions of HS and CS. Numerous long stress fibers form and most distribute in the apical part of the cell, where they stabilize new caveolae and syndecan-1. In the basal part of the cell, actin microfilaments increase, scatter, and arrange in a disorderly fashion. Our findings portray a dynamic reorganization of the EC glycocalyx (Cited from Zeng and Tarbell (2014))

plasma protein, the addition of S1P induced the recovery of endothelial glycocalyx via a PI3K pathway (Zeng et al. 2015). It was suggested that the stability of glycocalyx conferred by S1P is at least partially due to the synthesis of glycocalyx components. It can be concluded that S1P maintains the stability of glycocalyx through inhibiting the shedding and promoting the synthesis of glycocalyx components thereby contributing to the maintenance of normal vascular permeability (Sha et al. 2016) and controlling cardiovascular and immune functions (Curry and Adamson 2013). The intracellular signaling pathway involved in the S1P preserved/induced glycocalyx is still not completely understood. The activation of MMPs by inhibition of $S1P_1$ phosphorylation might be mediated by a pathway involving phosphatidylinositide 3-kinase (PI3K)/Akt and Rac1. It was demonstrated that Akt-mediated phosphorylation of $S1P_1$ (T236) is indispensable for S1P-induced Rac activation, endothelial migration, and morphogenesis (Lee et al. 2001). In addition, activation of $S1P_1$ promotes endothelial barrier integrity, migration, and survival through PI3k/Akt, eNOS, and Rac (Dudek et al. 2004; Adyshev et al. 2011). However, the activation of endothelial $S1P_3$ and $S1P_2$ could counteract the anti-inflammatory actions mediated by the $S1P_1$-PI3K/Akt-eNOS pathway.

Furthermore, vascular endothelial $S1P_1$ can respond to hemodynamic force and transduce the signals into a response that promotes the stabilization of newly formed vascular networks (Jung et al. 2012). Knockout of $S1P_1$ gene in mouse manifests as injured vessel maturation and embryonic mortality. In areas of laminar flow with high shear stress, $S1P_1$ is present on the membrane, whereas it is internalized in areas of disturbed flow with low shear stress. $S1P_1$ regulates the directional migration of lymphatic endothelial cells in response to fluid shear stress, which requires plasma or S1P (Surya et al. 2016). The change in $S1P_1$ might be associated with remodeling of the glycocalyx, and this could in turn alter mechanotransduction by the glycocalyx as discussed earlier in this section.

Cantalupo et al. (2017) identified S1P-$S1P_1$-NO signaling as a new regulatory pathway in vivo of vascular relaxation to flow and blood pressure homeostasis, providing a novel therapeutic target for the treatment of hypertension. Further investigations into the mechanoglycobiological mechanisms underlying the remodeling of the glycocalyx could bridge the effects of shear stress and S1P on atherosclerosis.

6 Angiogenesis and ESG

The term "angiogenesis" is commonly used to reference the process of vessel growth but in the strictest sense denotes vessels sprouting from pre-existing ones (Potente et al. 2011). Inadequate angiogenesis causes ischemia in myocardial infarction, stroke, and neurodegenerative or obesity-associated disorders, whereas excessive angiogenesis promotes many ailments including cancer, inflammatory disorders such as atherosclerosis, and eye diseases (Folkman 2007; Potente et al. 2011). The angiogenetic process is rather complex involving localized breakdown of the basement membrane and ECM of a pre-existing vessel, proliferation and migration of capillary EC into surrounding tissue, and new vessel formation. Stimulated by the proangiogenic signals including cytokines and associated receptors, ECs become motile and invasive.

Glycocalyx plays important roles in angiogenesis through its involvement in EC migration, proliferation, and differentiation (Alexopoulou et al. 2007; Tarbell and Cancel 2016). Through HS chains, HSPGs interact with growth factors such as vascular endothelial growth factor (VEGF) and fibroblast growth factors (FGFs) involved in vascular development and repair, extracellular matrix (ECM) components such as fibronectin and vitronectin, and many collagens. It is generally believed that HSPGs act as co-receptors working in concert with other cell surface receptors leading to high affinity binding. Examples are FGF receptors (FGFRs) interacting with FGFs and $\alpha_5\beta_1$ integrin interacting with fi-

bronectin (Steinfeld et al. 1996). Specific HSPGs carry out the functions of co-receptors in angiogenesis as well (Qiao et al. 2003).

VEGFs are mitogens for endothelial cells. There are seven VEGF isoforms which are generated via an alternative splicing mechanism from a unique gene (Achen and Stacker 1998; Neufeld et al. 1999). Among them, $VEGF_{165}$ is a major angiogenic factor that is inactivated by oxidizing agents and free radicals to inhibit angiogenesis (Gitay-Goren et al. 1996). KDR (kinase insert domain-containing receptor)/Flk-1 receptor (VEGFR2) and Flt-1 (VEGFR1) are type III tyrosine kinase receptors that bind to $VEGF_{165}$. Flt-1 with a tenfold higher affinity to VEGF than Flk-1. Flk-1 plays important roles in proliferation, migration, and permeability (Waltenberger et al. 1994; Bernatchez et al. 1999), whereas Flt-1 is responsible for the stabilization of new vascular channel (Fong et al. 1995; Chappell et al. 2016). EC also express $VEGF_{165}$-specific receptors ($VEGF_{165}$Rs, neuropilin-1 and neuropilin-2) via their exon 7 (amino acids 116–159 of $VEGF_{165}$)-encoded domains (Soker et al. 1997). HS is required to bind $VEGF_{165}$ to Flk-1 resulting in retention of $VEGF_{165}$ on the cell surface or in the ECM and for the mitogenic activity of $VEGF_{165}$ (Gitay-Goren et al. 1992; Ono et al. 1999; Stringer 2006; Teran and Nugent 2015). Glypican-1 on EC can interact with $VEGF_{165}$ mediated by the HS chains of glypican-1 and could recuperate the biological activity of $VEGF_{165}$ that was damaged by oxidation (Gengrinovitch et al. 1999). This may be important under conditions including wound repair, hypoxia-induced angiogenesis, or inflammation in which oxidants or free radicals are produced and may damage VEGFs (Gengrinovitch et al. 1999). In recent years, it was shown heparanase derived from myeloma cells activates Flk-1 through shedding of syndecan-1 in human microvascular EC (HMEC-1) thus promoting angiogenesis (Haddad et al. 2015; Jung et al. 2016). Heparanase also regulates syndecan-4 expression (Haddad et al. 2015). However, syndecan-1 coupled insulin-like growth factor-1 receptor (IGF1R) and $\alpha_V\beta_3$ integrin are required for Flk-1 and $\alpha_V\beta_3$-integrin activation during angiogenesis (Rapraeger et al. 2013). The increase in syndecan-1 and decrease in syndecan-4 in HUVECs were involved in low molecular weight fucoidan-induced angiogenesis (Haddad et al. 2015). Syndecan-1 is required in the local tissue environment for angiogenesis (Andersen et al. 2015; Tang and Weitz 2015). Moreover, in glomerular ECs, downregulation of syndecan-1 increased cell permeability, decreased cell viability, and inhibited tube formation through inhibiting VEGF-Flk-1 signaling by recruiting Flk-1 to the caveolin-dependent endocytosis route (Jing et al. 2016). How both shedding of syndecan-1 and upregulation of syndecan-1 could induce angiogenesis has not been completely clarified.

Syndecan-2 and syndecan-3 might also regulate angiogenesis in pathological conditions. Shedding of syndecans occurs in response to stimuli such as inflammatory mediators and growth factors. Shed syndecan-2 regulates angiogenesis by inhibiting EC migration via CD148 (PTPRJ) signaling (De Rossi et al. 2014). Shed syndecan-3 also inhibits angiogenesis by reducing the migratory abilities of ECs (De Rossi and Whiteford 2013).

Basic FGFs (bFGFs) are also potent endothelial growth factors that are capable of inducing angiogenesis (Joseph-Silverstein and Rifkin 1987). Glypican-1 stimulates the biological activity of bFGFs when released by PI-PLC from the surface of endothelial cells (Bashkin et al. 1992). In bovine capillary ECs, bFGF-bound GAGs were degraded by heparinase but not by chondroitinase ABC, suggesting HS bound with bGFG (Saksela and Rifkin 1990). The inclusion of bFGF (10 ng/mL for 16 h) in the culture medium increased release of HSPGs from bovine capillary ECs through increasing plasminogen activity. Pretreatment of cells with TGF-β (4 ng/mL for 6 h) before addition of bFGF inhibited the release of HSPG (Saksela and Rifkin 1990). Overexpression of glypican-1 in normal brain EC enhanced cell growth and sensitized cells to FGF2-induced mitogenesis, while overexpression of syndecan-1 had no effect (Qiao et al. 2003).

In cell recruitment, it is believed that both chemokine oligomerization and binding to GAGs are required. Chemokine interactions with GAGs facilitate the formation of chemokine gradients which provide directional cues for migrating cells (Dyer et al. 2016). A recent study demonstrated that HS is essential for interleukin (IL)-8-induced cell migration (Yan et al. 2016). After enzymatic removal of HS, they observed significant suppression of the IL-8-upregulated Rho GTPases including Cdc42, Rac1, and RhoA (Yan et al. 2016). IL-8-increased Rac1/Rho activity, as well as IL-8-induced polymerization and polarization of actin cytoskeleton and an increase in stress fibers were also suppressed. However, the interplay between the IL-8 receptors and syndecan co-receptors is still not well understood.

In addition, both HS-ligand binding and interactions of PG core proteins with cytoskeletal and/or signaling molecules are required for cell adhesion and migration. Depletion of syndecan-1 (Ebong et al. 2014) and syndecan-4 (Baeyens et al. 2014) have been shown to cause a failure to sense flow direction and inhibition of flow-induced alignment in vitro.

7 Conclusions

In the course of this review, many unanswered questions were raised, and future directions for research were suggested. In this final section, we will highlight several critical areas for future research.

Section 2 discussed composition, organization, and structure of the ESG. It is clear from this section that different methods of observation have produced a model of the ESG consisting of a more rigid inner region on the order of 500 nm in thickness that is detected by biophysical methods including red cell and large tracer molecule exclusion as well as direct physical probing with AFM and a more extended outer region of micron scale that is detected by various forms of light microscopy and cryo-SEM. The inner layer is thought to contain the proteoglycan core proteins and GAGs, while the outer layer is diffuse containing absorbed proteins, charged ions, and additional GAGs. This model requires direct validation by advanced imaging techniques such as STORM and SEM with immuno-labeled nanoparticles.

Section 3 focused on mechanical properties of the ESG. There appears to be consistency in measurements and calculations of the elastic modulus of the inner region of the ESG in the range $E = 0.3–0.7$ kPa that is an order of magnitude lower than the underlying plasma membrane. These measurements should be extended to additional cell types, and the structural components (proteoglycans and GAGs) of the ESG that control this mechanical property should be determined in order to provide a more direct understanding of how mechanical forces are transmitted to cells. It seems unlikely that AFM measurements will be capable of dissecting out the contributions of individual components directly since AFM only has resolution to treat the ESG as a homogeneous layer. Rather, knockdown of individual components followed AFM measurements may be informative. Because the ESG remodels dramatically after exposure to shear stress (Sect. 5), it will be important to extend ESG mechanical property measurements to fully flow adapted cells (after 24 h of shear).

Section 4 considered mechanotransduction and the ESG. In a variety of studies including enzyme treatments, gene knockdown, and direct force application (AFM), glypican-1 has emerged as the proteoglycan core protein that delivers shear force to the cell body for transduction into NO in the sustained phase of production. This is a somewhat controversial conclusion that should be validated in an animal model such as the glypican-1 knockout mouse. The detailed interface between the inner and outer layers of the two-layer model of the ESG that allows fluid shear forces in the outer layer to be transmitted to the proteoglycan core proteins in the inner layer remain to be determined. The intracellular signaling pathway by which mechanical activation of glypican-1 leads to the phosphorylation of PECAM-1 has not been elucidated, and the role of HSPG in the

early phase of NO production requires further investigation.

Section 5 described remodeling of the ESG. Transient remodeling after initial exposure to shear stress involves dramatic movement of glypican-1 toward cell boundaries in lipid rafts before the onset of new synthesis or cytoskeletal remodeling. This early remodeling may be involved in the association of HSPG with Gαq/11-PECAM-1 which mediates early phase mechanotransduction to produce NO, but this has not been determined. Long-term remodeling (24 h) establishes a more uniform distribution of ESG components resembling the in vivo state as a result of new HSPG synthesis and cytoskeletal remodeling. Glypican-1 is distributed in caveolae and at cell junctions in lipid rafts. It is tempting to conclude that mechanotransduction to produce NO is initiated in the lipid rafts, but currently this is not known. In addition, the intracellular signaling mechanisms that mediate new synthesis of ESG components are not established.

Section 6 reviewed angiogenesis and the ESG. The ESG is involved in many mechanisms that contribute to angiogenesis, most notably binding of growth factors on the EC surface and in the ECM which contribute to EC migration, proliferation, and differentiation. The ESG also senses interstitial flow that is known to enhance angiogenesis. However, a coherent picture of ESG involvement in angiogenesis remains to be elucidated.

Finally, we note that recent advances in our understanding of the many roles that the ESG plays in normal physiology and pathophysiology suggest that the structural integrity of ESG that is regulated by physical forces is absolutely central for mechanotransduction, cell proliferation, cell adhesion, and cell migration. Future research in mechanoglycobiology should focus on determining the mechanisms by which physical forces regulate the structure and composition of the ESG with particular emphasis on synthesis and regeneration in the face of pathological changes in structure and function. Such understanding of mechanoglycobiology may facilitate the treatment of many diseases including atherosclerosis, stroke, sepsis, diabetes, hypertension, pulmonary edema, fibrosis, and cancer.

Acknowledgments We would like to acknowledge the support from the National Natural Science Foundation of China [Grant no. 11402153(YZ)], National Institutes of Health [grant nos. SC1CA153325 (BF), RO1HL094889 (JT, BF), and RO1CA204949 (JT)].

References

Achen MG, Stacker SA (1998) The vascular endothelial growth factor family; proteins which guide the development of the vasculature. Int J Exp Pathol 79(5):255–265

Adamson RH, Clough G (1992) Plasma proteins modify the endothelial cell glycocalyx of frog mesenteric microvessels. J Physiol 445:473–486

Adyshev DM, Moldobaeva NK, Elangovan VR, Garcia JG, Dudek SM (2011) Differential involvement of ezrin/radixin/moesin proteins in sphingosine 1-phosphate-induced human pulmonary endothelial cell barrier enhancement. Cell Signal 23(12):2086–2096

Alexopoulou AN, Multhaupt HA, Couchman JR (2007) Syndecans in wound healing, inflammation and vascular biology. Int J Biochem Cell Biol 39(3):505–528

Andersen NF, Kristensen IB, Preiss BS, Christensen JH, Abildgaard N (2015) Upregulation of Syndecan-1 in the bone marrow microenvironment in multiple myeloma is associated with angiogenesis. Eur J Haematol 95(3):211–217

Arisaka T, Mitsumata M, Kawasumi M, Tohjima T, Hirose S, Yoshida Y (1995) Effects of shear stress on glycosaminoglycan synthesis in vascular endothelial cells. Ann N Y Acad Sci 748:543–554

Arkill KP, Knupp C, Michel CC, Neal CR, Qvortrup K, Rostgaard J, Squire JM (2011) Similar endothelial glycocalyx structures in microvessels from a range of mammalian tissues: evidence for a common filtering mechanism? Biophys J 101(5):1046–1056

Arkill KP, Neal CR, Mantell JM, Michel CC, Qvortrup K, Rostgaard J, Bates DO, Knupp C, Squire JM (2012) 3D reconstruction of the glycocalyx structure in mammalian capillaries using electron tomography. Microcirculation 19(4):343–351

Baeyens N, Mulligan-Kehoe MJ, Corti F, Simon DD, Ross TD, Rhodes JM, Wang TZ, Mejean CO, Simons M, Humphrey J, Schwartz MA (2014) Syndecan 4 is required for endothelial alignment in flow and atheroprotective signaling. Proc Natl Acad Sci U S A 111(48):17308–17313

Bai K, Wang W (2012) Spatio-temporal development of the endothelial glycocalyx layer and its mechanical property in vitro. J R Soc Interface 9(74):2290–2298

Baldwin AL, Winlove CP (1984) Effects of perfusate composition on binding of ruthenium red and gold colloid to glycocalyx of rabbit aortic endothelium. The

journal of histochemistry and cytochemistry: official journal of the. Hist Soc 32(3):259–266
Bartosch AMW, Mathews R, Tarbell JM (2017) Endothelial glycocalyx-mediated nitric oxide production in response to selective AFM pulling. Biophys J 113(1):101–108
Bashkin P, Neufeld G, Gitay-Goren H, Vlodavsky I (1992) Release of cell surface-associated basic fibroblast growth factor by glycosylphosphatidylinositol-specific phospholipase C. J Cell Physiol 151(1):126–137
Bernatchez PN, Soker S, Sirois MG (1999) Vascular endothelial growth factor effect on endothelial cell proliferation, migration, and platelet-activating factor synthesis is Flk-1-dependent. J Biol Chem 274(43):31047–31054
Bernfield M, Gotte M, Park PW, Reizes O, Fitzgerald ML, Lincecum J, Zako M (1999) Functions of cell surface heparan sulfate proteoglycans. Annu Rev Biochem 68:729–777
Betteridge KB, Arkill KP, Neal CR, Harper SJ, Foster RR, Satchell SC, Bates DO, Salmon AHJ (2017) Sialic acids regulate microvessel permeability, revealed by novel in vivo studies of endothelial glycocalyx structure and function. J Physiol 595(15):5015–5035
Brands J, Van Teeffelen JWGE, Van den Berg BM, Vink H (2007) Role for glycocalyx perturbation in atherosclerosis development and associated microvascular dysfunction. Futur Lipidol 2(5):527–534
Cai B, Fan J, Zeng M, Zhang L, Fu BM (2012) Adhesion of malignant mammary tumor cells MDA-MB-231 to microvessel wall increases microvascular permeability via degradation of endothelial surface glycocalyx. J Appl Physiol (1985) 113(7):1141–1153
Cantalupo A, Gargiulo A, Dautaj E, Liu C, Zhang Y, Hla T, Di Lorenzo A (2017) S1PR1 (Sphingosine-1-Phosphate Receptor 1) signaling regulates blood flow and pressure. Hypertension 70(2):426–434
Carey DJ, Bendt KM, Stahl RC (1996) The cytoplasmic domain of syndecan-1 is required for cytoskeleton association but not detergent insolubility. Identification of essential cytoplasmic domain residues. J Biol Chem 271(25):15253–15260
Chakravarti R, Sapountzi V, Adams JC (2005) Functional role of syndecan-1 cytoplasmic V region in lamellipodial spreading, actin bundling, and cell migration. Mol Biol Cell 16(8):3678–3691
Chappell JC, Cluceru JG, Nesmith JE, Mouillesseaux KP, Bradley VB, Hartland CM, Hashambhoy-Ramsay YL, Walpole J, Peirce SM, Mac Gabhann F, Bautch VL (2016) Flt-1 (VEGFR-1) coordinates discrete stages of blood vessel formation. Cardiovasc Res 111(1):84–93
Chien S (2007) Mechanotransduction and endothelial cell homeostasis: the wisdom of the cell. Am J Physiol Heart Circ Physiol 292(3):H1209–H1224
Conway DE, Breckenridge MT, Hinde E, Gratton E, Chen CS, Schwartz MA (2013) Fluid shear stress on endothelial cells modulates mechanical tension across VE-cadherin and PECAM-1. Curr Biol 23(11):1024–1030
Couchman JR (2010) Transmembrane signaling proteoglycans. Annu Rev Cell Dev Biol 26:89–114
Curry FE, Adamson RH (2012) Endothelial glycocalyx: permeability barrier and mechanosensor. Ann Biomed Eng 40(4):828–839
Curry FR, Adamson RH (2013) Tonic regulation of vascular permeability. Acta Physiol (Oxf) 207(4):628–649
Dabagh M, Jalali P, Butler PJ, Randles A, Tarbell JM (2017) Mechanotransmission in endothelial cells subjected to oscillatory and multi-directional shear flow. J R Soc Interface 14(130):pii: 20170185
Davies PF (2009) Hemodynamic shear stress and the endothelium in cardiovascular pathophysiology. Nat Clin Pract Cardiovasc Med 6(1):16–26
Davies PF, Dewey CF Jr, Bussolari SR, Gordon EJ, Gimbrone MA Jr (1984) Influence of hemodynamic forces on vascular endothelial function. In vitro studies of shear stress and pinocytosis in bovine aortic cells. J Clin Invest 73(4):1121–1129
De Haan L, Hirst TR (2004) Cholera toxin: a paradigm for multi-functional engagement of cellular mechanisms (review). Mol Membr Biol 21(2):77–92
De Rossi G, Whiteford JR (2013) A novel role for syndecan-3 in angiogenesis. F1000 Res 2:270
De Rossi G, Evans AR, Kay E, Woodfin A, McKay TR, Nourshargh S, Whiteford JR (2014) Shed syndecan-2 inhibits angiogenesis. J Cell Sci 127(Pt 21):4788–4799
Deepa SS, Yamada S, Zako M, Goldberger O, Sugahara K (2004) Chondroitin sulfate chains on syndecan-1 and syndecan-4 from normal murine mammary gland epithelial cells are structurally and functionally distinct and cooperate with heparan sulfate chains to bind growth factors. A novel function to control binding of midkine, pleiotrophin, and basic fibroblast growth factor. J Biol Chem 279(36):37368–37376
van den Berg BM, Vink H, Spaan JA (2003) The endothelial glycocalyx protects against myocardial edema. Circ Res 92(6):592–594
van den Berg BM, Spaan JA, Vink H (2009) Impaired glycocalyx barrier properties contribute to enhanced intimal low-density lipoprotein accumulation at the carotid artery bifurcation in mice. Pflugers Arch 457(6):1199–1206
Dudek SM, Jacobson JR, Chiang ET, Birukov KG, Wang P, Zhan X, Garcia JG (2004) Pulmonary endothelial cell barrier enhancement by sphingosine 1-phosphate: roles for cortactin and myosin light chain kinase. J Biol Chem 279(23):24692–24700
Dyer DP, Salanga CL, Volkman BF, Kawamura T, Handel TM (2016) The dependence of chemokine-glycosaminoglycan interactions on chemokine oligomerization. Glycobiology 26(3):312–326
Ebong EE, Macaluso FP, Spray DC, Tarbell JM (2011) Imaging the endothelial glycocalyx in vitro by rapid freezing/freeze substitution transmission electron microscopy. Arterioscler Thromb Vasc Biol 31(8):1908–1915
Ebong EE, Lopez-Quintero SV, Rizzo V, Spray DC, Tarbell JM (2014) Shear-induced endothelial NOS acti-

vation and remodeling via heparan sulfate, glypican-1, and syndecan-1. Integr Biol 6(3):338–347

Egorova AD, van der Heiden K, Poelmann RE, Hierck BP (2012) Primary cilia as biomechanical sensors in regulating endothelial function. Differentiation 83(2):S56–S61

Eshtehardi P, Brown AJ, Bhargava A, Costopoulos C, Hung OY, Corban MT, Hosseini H, Gogas BD, Giddens DP, Samady H (2017) High wall shear stress and high-risk plaque: an emerging concept. Int J Cardiovasc Imaging 33(7):1089–1099

Fels J, Jeggle P, Liashkovich I, Peters W, Oberleithner H (2014) Nanomechanics of vascular endothelium. Cell Tissue Res 355(3):727–737

Fleming I, Fisslthaler B, Dixit M, Busse R (2005) Role of PECAM-1 in the shear-stress-induced activation of Akt and the endothelial nitric oxide synthase (eNOS) in endothelial cells. J Cell Sci 118(Pt 18):4103–4111

Florian JA, Kosky JR, Ainslie K, Pang Z, Dull RO, Tarbell JM (2003) Heparan sulfate proteoglycan is a mechanosensor on endothelial cells. Circ Res 93(10):e136–e142

Folkman J (2007) Angiogenesis: an organizing principle for drug discovery? Nat Rev Drug Discov 6(4):273–286

Fong GH, Rossant J, Gertsenstein M, Breitman ML (1995) Role of the Flt-1 receptor tyrosine kinase in regulating the assembly of vascular endothelium. Nature 376(6535):66–70

Fu BM, Tarbell JM (2013) Mechano-sensing and transduction by endothelial surface glycocalyx: composition, structure, and function. Wiley Interdiscip Rev Syst Biol Med 5(3):381–390

Fung YC (1997) Biomechanics: circulation. Springer, New York, p 571

Gautam M, Shen Y, Thirkill TL, Douglas GC, Barakat AI (2006) Flow-activated chloride channels in vascular endothelium. Shear stress sensitivity, desensitization dynamics, and physiological implications. J Biol Chem 281(48):36492–36500

Gengrinovitch S, Berman B, David G, Witte L, Neufeld G, Ron D (1999) Glypican-1 is a VEGF165 binding proteoglycan that acts as an extracellular chaperone for VEGF165. J Biol Chem 274(16):10816–10822

Gitay-Goren H, Soker S, Vlodavsky I, Neufeld G (1992) The binding of vascular endothelial growth factor to its receptors is dependent on cell surface-associated heparin-like molecules. J Biol Chem 267(9):6093–6098

Gitay-Goren H, Cohen T, Tessler S, Soker S, Gengrinovitch S, Rockwell P, Klagsbrun M, Levi BZ, Neufeld G (1996) Selective binding of VEGF121 to one of the three vascular endothelial growth factor receptors of vascular endothelial cells. J Biol Chem 271(10):5519–5523

Gojova A, Barakat AI (2005) Vascular endothelial wound closure under shear stress: role of membrane fluidity and flow-sensitive ion channels. J Appl Physiol 98(6):2355–2362

Gotlieb AI (1990) The endothelial cytoskeleton: organization in normal and regenerating endothelium. Toxicol Pathol 18(4 Pt 1):603–617

Gouverneur M, Spaan JA, Pannekoek H, Fontijn RD, Vink H (2006) Fluid shear stress stimulates incorporation of hyaluronan into endothelial cell glycocalyx. Am J Physiol Heart Circ Physiol 290(1):H458–H452

Haddad O, Guyot E, Marinval N, Chevalier F, Maillard L, Gadi L, Laguillier-Morizot C, Oudar O, Sutton A, Charnaux N, Hlawaty H (2015) Heparanase and Syndecan-4 are involved in low molecular weight Fucoidan-induced angiogenesis. Mar Drugs 13(11):6588–6608

Haeren RH, van de Ven SE, van Zandvoort MA, Vink H, van Overbeeke JJ, Hoogland G, Rijkers K (2016) Assessment and imaging of the cerebrovascular Glycocalyx. Curr Neurovasc Res 13(3):249–260

Haidekker MA, L'Heureux N, Frangos JA (2000) Fluid shear stress increases membrane fluidity in endothelial cells: a study with DCVJ fluorescence. Am J Physiol Heart Circ Physiol 278(4):H1401–H1406

Han Y, Weinbaum S, Spaan JAE, Vink H (2016) Large deformation analysis of the elastic recoil of fiber layers in a brinkman medium with application to the endothelial glycocalyx. J Fluid Mech 554:217–235

Huxley VH, Williams DA (2000) Role of a glycocalyx on coronary arteriole permeability to proteins: evidence from enzyme treatments. Am J Physiol Heart Circ Physiol 278(4):H1177–H1185

Ingber DE (2003) Mechanobiology and diseases of mechanotransduction. Ann Med 35(8):564–577

Jing Z, Wei-Jie Y, Yi-Feng ZG, Jing H (2016) Downregulation of Syndecan-1 induce glomerular endothelial cell dysfunction through modulating internalization of VEGFR-2. Cell Signal 28(8):826–837

Joseph-Silverstein J, Rifkin DB (1987) Endothelial cell growth factors and the vessel wall. Semin Thromb Hemost 13(4):504–513

Jung B, Obinata H, Galvani S, Mendelson K, Ding BS, Skoura A, Kinzel B, Brinkmann V, Rafii S, Evans T, Hla T (2012) Flow-regulated endothelial S1P receptor-1 signaling sustains vascular development. Dev Cell 23(3):600–610

Jung O, Trapp-Stamborski V, Purushothaman A, Jin H, Wang H, Sanderson RD, Rapraeger AC (2016) Heparanase-induced shedding of syndecan-1/CD138 in myeloma and endothelial cells activates VEGFR2 and an invasive phenotype: prevention by novel synstatins. Oncogene 5:e202

Kimura T, Watanabe T, Sato K, Kon J, Tomura H, Tamama K, Kuwabara A, Kanda T, Kobayashi I, Ohta H, Ui M, Okajima F (2000) Sphingosine 1-phosphate stimulates proliferation and migration of human endothelial cells possibly through the lipid receptors, Edg-1 and Edg-3. Biochem J 348(Pt 1):71–76

Kindt TJ, Osborne BA, Goldsby RA (2007) Kuby immunology, 6th edn. W. H. Freeman & Company, New York

Klitzman B, Duling BR (1979) Microvascular hematocrit and red cell flow in resting and contracting striated muscle. Am J Phys 237(4):H481–H490

Kono M, Mi Y, Liu Y, Sasaki T, Allende ML, Wu YP, Yamashita T, Proia RL (2004) The sphingosine-1-phosphate receptors S1P1, S1P2, and S1P3 function coordinately during embryonic angiogenesis. J Biol Chem 279(28):29367–29373

Koo A, García-Cardeña G, Dewey CF Jr (2011) Flow regulated endothelial glycocalyx expression and its function as a protective barrier against leukocyte adhesion. In: Annual meeting of Biomedical Engineering Society. Connecticut, Harford

Koo A, Dewey CF Jr, Garcia-Cardena G (2013) Hemodynamic shear stress characteristic of atherosclerosis-resistant regions promotes glycocalyx formation in cultured endothelial cells. Am J Physiol Cell Physiol 304(2):C137–C146

Kuchan MJ, Jo H, Frangos JA (1994) Role of G proteins in shear stress-mediated nitric oxide production by endothelial cells. Am J Phys 267(3 Pt 1):C753–C758

dela Paz NG, Melchior B, Shayo FY, Frangos JA (2014) Heparan sulfates mediate the interaction between platelet endothelial cell adhesion molecule-1 (PECAM-1) and the Galphaq/11 subunits of heterotrimeric G proteins. J Biol Chem 289(11): 7413–7424

Lee MJ, Thangada S, Paik JH, Sapkota GP, Ancellin N, Chae SS, Wu M, Morales-Ruiz M, Sessa WC, Alessi DR, Hla T (2001) Akt-mediated phosphorylation of the G protein-coupled receptor EDG-1 is required for endothelial cell chemotaxis. Mol Cell 8(3):693–704

Li W, Wang W (2018) Structural alteration of the endothelial glycocalyx: contribution of the actin cytoskeleton. Biomech Model Mechanobiol 17(1): 147–158

Li YS, Haga JH, Chien S (2005) Molecular basis of the effects of shear stress on vascular endothelial cells. J Biomech 38(10):1949–1971

Lindner R, Naim HY (2009) Domains in biological membranes. Exp Cell Res 315(17):2871–2878

Lingwood D, Simons K (2010) Lipid rafts as a membrane-organizing principle. Science 327(5961):46–50

Lipowsky HH (2011) Protease activity and the role of the endothelial glycocalyx in inflammation. Drug Discov Today Dis Models 8(1):57–62

Lipowsky HH (2012) The endothelial glycocalyx as a barrier to leukocyte adhesion and its mediation by extracellular proteases. Ann Biomed Eng 40(4): 840–848

Lisanti MP, Scherer PE, Vidugiriene J, Tang Z, Hermanowski-Vosatka A, Tu YH, Cook RF, Sargiacomo M (1994) Characterization of caveolin-rich membrane domains isolated from an endothelial-rich source: implications for human disease. J Cell Biol 126(1):111–126

Liu JX, Yan ZP, Zhang YY, Wu J, Liu XH, Zeng Y (2016) Hemodynamic shear stress regulates the transcriptional expression of heparan sulfate proteoglycans in human umbilical vein endothelial cell. Cell Mol Biol (Noisy-le-Grand) 62(8):28–34

Long DS, Smith ML, Pries AR, Ley K, Damiano ER (2004) Microviscometry reveals reduced blood viscosity and altered shear rate and shear stress profiles in microvessels after hemodilution. Proc Natl Acad Sci U S A 101(27):10060–10065

Long M, Huang SH, Wu CH, Shackleford GM, Jong A (2012) Lipid raft/caveolae signaling is required for Cryptococcus neoformans invasion into human brain microvascular endothelial cells. J Biomed Sci 19:19

Lopes CC, Dietrich CP, Nader HB (2006) Specific structural features of syndecans and heparan sulfate chains are needed for cell signaling. Braz J Med Biol Res 39(2):157–167

Luft JH (1966) Fine structures of capillary and endocapillary layer as revealed by ruthenium red. Fed Proc 25(6):1773–1783

Malek AM, Izumo S (1996) Mechanism of endothelial cell shape change and cytoskeletal remodeling in response to fluid shear stress. J Cell Sci 109(Pt 4): 713–726

Mammoto A, Mammoto T, Ingber DE (2012) Mechanosensitive mechanisms in transcriptional regulation. J Cell Sci 125(Pt 13):3061–3073

Marsh G, Waugh RE (2013) Quantifying the mechanical properties of the endothelial glycocalyx with atomic force microscopy. J Vis Exp 72:e50163

Matsui TS, Kaunas R, Kanzaki M, Sato M, Deguchi S (2011) Non-muscle myosin II induces disassembly of actin stress fibres independently of myosin light chain dephosphorylation. Interface focus 1(5):754–766

McAlpine CS, Swirski FK (2016) Circadian influence on metabolism and inflammation in atherosclerosis. Circ Res 119(1):131–141

McGuire PG, Castellot JJ Jr, Orkin RW (1987) Size-dependent hyaluronate degradation by cultured cells. J Cell Physiol 133(2):267–276

Megens RT, Reitsma S, Schiffers PH, Hilgers RH, De Mey JG, Slaaf DW, oude Egbrink MG, van Zandvoort MA (2007) Two-photon microscopy of vital murine elastic and muscular arteries. Combined structural and functional imaging with subcellular resolution. J Vasc Res 44(2):87–98

Meyer zu Heringdorf D, Jakobs KH (2007) Lysophospholipid receptors: signalling, pharmacology and regulation by lysophospholipid metabolism. Biochim Biophys Acta 1768(4):923–940

Michel CC, Phillips ME, Turner MR (1985) The effects of native and modified bovine serum albumin on the permeability of frog mesenteric capillaries. J Physiol 360:333–346

Moon JJ, Matsumoto M, Patel S, Lee L, Guan JL, Li S (2005) Role of cell surface heparan sulfate proteoglycans in endothelial cell migration and mechanotransduction. J Cell Physiol 203(1):166–176

Morgan JT, Pfeiffer ER, Thirkill TL, Kumar P, Peng G, Fridolfsson HN, Douglas GC, Starr DA, Barakat AI (2011) Nesprin-3 regulates endothelial cell morphol-

ogy, perinuclear cytoskeletal architecture, and flow-induced polarization. Mol Biol Cell 22(22):4324–4334
Muller S, Labrador V, Da Isla N, Dumas D, Sun R, Wang X, Wei L, Fawzi-Grancher S, Yang W, Traore M, Boura C, Bensoussan D, Eljaafari A, Stoltz JF (2004) From hemorheology to vascular mechanobiology: an overview. Clin Hemorheol Microcirc 30(3–4):185–200
Navarro A, Anand-Apte B, Parat MO (2004) A role for caveolae in cell migration. FASEB J 18(15):1801–1811
Neufeld G, Cohen T, Gengrinovitch S, Poltorak Z (1999) Vascular endothelial growth factor (VEGF) and its receptors. FASEB J 13(1):9–22
Nichols B (2003) Caveosomes and endocytosis of lipid rafts. J Cell Sci 116(Pt 23):4707–4714
Nijenhuis N, Mizuno D, Spaan JA, Schmidt CF (2009) Viscoelastic response of a model endothelial glycocalyx. Phys Biol 6(2):025014
Oberleithner H, Peters W, Kusche-Vihrog K, Korte S, Schillers H, Kliche K, Oberleithner K (2011) Salt overload damages the glycocalyx sodium barrier of vascular endothelium. Pflugers Arch 462(4):519–528
O'Callaghan R, Job KM, Dull RO, Hlady V (2011) Stiffness and heterogeneity of the pulmonary endothelial glycocalyx measured by atomic force microscopy. Am J Physiol Lung Cell Mol Physiol 301(3):L353–L360
Ohlson M, Sorensson J, Haraldsson B (2001) A gel-membrane model of glomerular charge and size selectivity in series. Am J Physiol Renal Physiol 280(3):F396–F405
Ono K, Hattori H, Takeshita S, Kurita A, Ishihara M (1999) Structural features in heparin that interact with VEGF165 and modulate its biological activity. Glycobiology 9(7):705–711
Pahakis MY, Kosky JR, Dull RO, Tarbell JM (2007) The role of endothelial glycocalyx components in mechanotransduction of fluid shear stress. Biochem Biophys Res Commun 355(1):228–233
Parton RG (1994) Ultrastructural localization of gangliosides; GM1 is concentrated in caveolae. J Histochem Cytochem 42(2):155–166
Parton RG, del Pozo MA (2013) Caveolae as plasma membrane sensors, protectors and organizers. Nat Rev Mol Cell Biol 14(2):98–112
Potente M, Gerhardt H, Carmeliet P (2011) Basic and therapeutic aspects of angiogenesis. Cell 146(6):873–887
Poti F, Gualtieri F, Sacchi S, Weissen-Plenz G, Varga G, Brodde M, Weber C, Simoni M, Nofer JR (2013) KRP-203, sphingosine 1-phosphate receptor type 1 agonist, ameliorates atherosclerosis in LDL-R−/− mice. Arterioscler Thromb Vasc Biol 33(7):1505–1512
Pries AR, Secomb TW, Gaehtgens P (2000) The endothelial surface layer. Pflugers Arch 440(5):653–666
Qiao D, Meyer K, Mundhenke C, Drew SA, Friedl A (2003) Heparan sulfate proteoglycans as regulators of fibroblast growth factor-2 signaling in brain endothelial cells. Specific role for glypican-1 in glioma angiogenesis. J Biol Chem 278(18):16045–16053
Rapraeger AC, Ell BJ, Roy M, Li X, Morrison OR, Thomas GM, Beauvais DM (2013) Vascular endothelial-cadherin stimulates syndecan-1-coupled insulin-like growth factor-1 receptor and cross-talk between alphaVbeta3 integrin and vascular endothelial growth factor receptor 2 at the onset of endothelial cell dissemination during angiogenesis. FEBS J 280(10):2194–2206
Razani B, Woodman SE, Lisanti MP (2002) Caveolae: from cell biology to animal physiology. Pharmacol Rev 54(3):431–467
Reitsma S, Slaaf DW, Vink H, van Zandvoort MA, oude Egbrink MG (2007) The endothelial glycocalyx: composition, functions, and visualization. Pflugers Arch 454(3):345–359
Reitsma S, oude Egbrink MG, Vink H, van den Berg BM, Passos VL, Engels W, Slaaf DW, van Zandvoort MA (2011) Endothelial glycocalyx structure in the intact carotid artery: a two-photon laser scanning microscopy study. J Vasc Res 48(4):297–306
Rizzo V, Morton C, DePaola N, Schnitzer JE, Davies PF (2003) Recruitment of endothelial caveolae into mechanotransduction pathways by flow conditioning in vitro. Am J Physiol Heart Circ Physiol 285(4):H1720–H1729
Rostgaard J, Qvortrup K (1997) Electron microscopic demonstrations of filamentous molecular sieve plugs in capillary fenestrae. Microvasc Res 53(1):1–13
Russell-Puleri S, Dela Paz NG, Adams D, Chattopadhyay M, Cancel L, Ebong E, Orr AW, Frangos JA, Tarbell JM (2017) Fluid shear stress induces upregulation of COX-2 and PGI2 release in endothelial cells via a pathway involving PECAM-1, PI3K, FAK, and p38. Am J Physiol Heart Circ Physiol 312(3):H485–H500
Rust MJ, Bates M, Zhuang X (2006) Sub-diffraction-limit imaging by stochastic optical reconstruction microscopy (STORM). Nat Methods 3(10):793–795
Saksela O, Rifkin DB (1990) Release of basic fibroblast growth factor-heparan sulfate complexes from endothelial cells by plasminogen activator-mediated proteolytic activity. J Cell Biol 110(3):767–775
Sanchez T (2016) Sphingosine-1-phosphate signaling in endothelial disorders. Curr Atheroscler Rep 18(6):31
Sanger JM, Sanger JW (1980) Banding and polarity of actin filaments in interphase and cleaving cells. J Cell Biol 86(2):568–575
Sarrazin S, Lamanna WC, Esko JD (2011) Heparan sulfate proteoglycans. Cold Spring Harb Perspect Biol 3(7):pii: a004952
Satcher R, Dewey CF Jr, Hartwig JH (1997) Mechanical remodeling of the endothelial surface and actin cytoskeleton induced by fluid flow. Microcirculation 4(4):439–453
Schnitzer JE, McIntosh DP, Dvorak AM, Liu J, Oh P (1995a) Separation of caveolae from associated microdomains of GPI-anchored proteins. Science 269(5229):1435–1439
Schnitzer JE, Oh P, Jacobson BS, Dvorak AM (1995b) Caveolae from luminal plasmalemma of rat lung endothelium: microdomains enriched in caveolin, Ca(2+)-ATPase, and inositol trisphosphate receptor. Proc Natl Acad Sci U S A 92(5):1759–1763

Schubert W, Frank PG, Razani B, Park DS, Chow CW, Lisanti MP (2001) Caveolae-deficient endothelial cells show defects in the uptake and transport of albumin in vivo. J Biol Chem 276(52):48619–48622

Schwartz MA, DeSimone DW (2008) Cell adhesion receptors in mechanotransduction. Curr Opin Cell Biol 20(5):551–556

Secomb TW, Hsu R, Pries AR (2001) Motion of red blood cells in a capillary with an endothelial surface layer: effect of flow velocity. Am J Physiol Heart Circ Physiol 281(2):H629–H636

Sha T, Qi C, Fu W, Hao JI, Gong L, Wu H, Zhang Q (2016) Experimental study of USPIO-enhanced MRI in the detection of atherosclerotic plaque and the intervention of atorvastatin. Exp Ther Med 12(1):141–146

Silver FH, Siperko LM (2003) Mechanosensing and mechanochemical transduction: how is mechanical energy sensed and converted into chemical energy in an extracellular matrix? Crit Rev Biomed Eng 31(4): 255–331

Simons K, Sampaio JL (2011) Membrane organization and lipid rafts. Cold Spring Harb Perspect Biol 3(10):a004697

Sims DE, Horne MM (1993) Non-aqueous fixative preserves macromolecules on the endothelial cell surface: an in situ study. Eur J Morphol 31(4):251–255

Smith ML, Long DS, Damiano ER, Ley K (2003) Near-wall micro-PIV reveals a hydrodynamically relevant endothelial surface layer in venules in vivo. Biophys J 85(1):637–645

Soker S, Gollamudi-Payne S, Fidder H, Charmahelli H, Klagsbrun M (1997) Inhibition of vascular endothelial growth factor (VEGF)-induced endothelial cell proliferation by a peptide corresponding to the exon 7-encoded domain of VEGF165. J Biol Chem 272(50):31582–31588

Song JW, Zullo J, Lipphardt M, Dragovich M, Zhang FX, Fu B, Goligorsky MS (2018) Endothelial glycocalyx-the battleground for complications of sepsis and kidney injury. Nephrol Dial Transplant 33(2):203–211

Sorci-Thomas MG, Thomas MJ (2016) Microdomains, inflammation, and atherosclerosis. Circ Res 118(4): 679–691

Sorensson J, Ohlson M, Haraldsson B (2001) A quantitative analysis of the glomerular charge barrier in the rat. Am J Physiol Renal Physiol 280(4):F646–F656

Squire S (2001) A chance to grow. Prof Nurse 16(8 Suppl):S2

Steinfeld R, Van Den Berghe H, David G (1996) Stimulation of fibroblast growth factor receptor-1 occupancy and signaling by cell surface-associated syndecans and glypican. J Cell Biol 133(2):405–416

Stevens HY, Melchior B, Bell KS, Yun S, Yeh JC, Frangos JA (2008) PECAM-1 is a critical mediator of atherosclerosis. Dis Model Mech 1(2–3):175–181

Stringer SE (2006) The role of heparan sulphate proteoglycans in angiogenesis. Biochem Soc Trans 34(Pt 3):451–453

Surya VN, Michalaki E, Huang EY, Fuller GG, Dunn AR (2016) Sphingosine 1-phosphate receptor 1 regulates the directional migration of lymphatic endothelial cells in response to fluid shear stress. J R Soc Interface 13(125):pii:20160823

Tabouillot T, Muddana HS, Butler PJ (2011) Endothelial cell membrane sensitivity to shear stress is lipid domain dependent. Cell Mol Bioeng 4(2):169–181

Taleb S (2016) Inflammation in atherosclerosis. Arch Cardiovasc Dis 109(12):708–715

Tang GL, Weitz K (2015) Impaired arteriogenesis in syndecan-1(−/−) mice. J Surg Res 193(1):22–27

Tarbell JM, Cancel LM (2016) The glycocalyx and its significance in human medicine. J Intern Med 280(1): 97–113

Tarbell JM, Ebong EE (2008) The endothelial glycocalyx: a mechano-sensor and -transducer. Sci Signal 1(40):pt8

Tarbell JM, Pahakis MY (2006) Mechanotransduction and the glycocalyx. J Intern Med 259(4):339–350

Teran M, Nugent MA (2015) Synergistic binding of vascular endothelial growth factor-a and its receptors to heparin selectively modulates complex affinity. J Biol Chem 290(26):16451–16462

Thi MM, Tarbell JM, Weinbaum S, Spray DC (2004) The role of the glycocalyx in reorganization of the actin cytoskeleton under fluid shear stress: a "bumper-car" model. Proc Natl Acad Sci U S A 101(47):16483–16488

Thomsen P, Roepstorff K, Stahlhut M, van Deurs B (2002) Caveolae are highly immobile plasma membrane microdomains, which are not involved in constitutive endocytic trafficking. Mol Biol Cell 13(1):238–250

Vink H, Duling BR (1996) Identification of distinct luminal domains for macromolecules, erythrocytes, and leukocytes within mammalian capillaries. Circ Res 79(3):581–589

Waltenberger J, Claesson-Welsh L, Siegbahn A, Shibuya M, Heldin CH (1994) Different signal transduction properties of KDR and Flt1, two receptors for vascular endothelial growth factor. J Biol Chem 269(43):26988–26995

Wang Y, Shyy JY, Chien S (2008) Fluorescence proteins, live-cell imaging, and mechanobiology: seeing is believing. Annu Rev Biomed Eng 10:1–38

Wang N, Tytell JD, Ingber DE (2009) Mechanotransduction at a distance: mechanically coupling the extracellular matrix with the nucleus. Nat Rev Mol Cell Biol 10(1):75–82

Wang S, Iring A, Strilic B, Albarran Juarez J, Kaur H, Troidl K, Tonack S, Burbiel JC, Muller CE, Fleming I, Lundberg JO, Wettschureck N, Offermanns S (2015) P2Y(2) and Gq/G(1)(1) control blood pressure by mediating endothelial mechanotransduction. J Clin Invest 125(8):3077–3086

Wang Y, Qiu J, Luo S, Xie X, Zheng Y, Zhang K, Ye Z, Liu W, Gregersen H, Wang G (2016) High shear stress induces atherosclerotic vulnerable plaque formation through angiogenesis. Regen Biomater 3(4):257–267

Weber AMT, Mathews R, Haq Z, Cancel LM, Tarbell JM (2017) The short term response of PECAM-1 to mechanical loading: Cyclooxygenase-2 and nitric oxide

production with AFM pulling and shear stress. Biophys J 112(3):311a–311a

Weinbaum S, Zhang X, Han Y, Vink H, Cowin SC (2003) Mechanotransduction and flow across the endothelial glycocalyx. Proc Natl Acad Sci U S A 100(13):7988–7995

Weinbaum S, Tarbell JM, Damiano ER (2007) The structure and function of the endothelial glycocalyx layer. Annu Rev Biomed Eng 9:121–167

Xu S, Ha CH, Wang W, Xu X, Yin M, Jin FQ, Mastrangelo M, Koroleva M, Fujiwara K, Jin ZG (2016) PECAM1 regulates flow-mediated Gab1 tyrosine phosphorylation and signaling. Cell Signal 28(3):117–124

Yamamoto K, Ando J (2011) New molecular mechanisms for cardiovascular disease: blood flow sensing mechanism in vascular endothelial cells. J Pharmacol Sci 116(4):323–331

Yan Z, Liu J, Xie L, Liu X, Zeng Y (2016) Role of heparan sulfate in mediating CXCL8-induced endothelial cell migration. Peer J 4:e1669

Yao Y, Rabodzey A, Dewey CF Jr (2007) Glycocalyx modulates the motility and proliferative response of vascular endothelium to fluid shear stress. Am J Physiol Heart Circ Physiol 293(2):H1023–H1030

Yen WY, Cai B, Zeng M, Tarbell JM, Fu BM (2012) Quantification of the endothelial surface glycocalyx on rat and mouse blood vessels. Microvasc Res 83(3): 337–346

Yen W, Cai B, Yang J, Zhang L, Zeng M, Tarbell JM, Fu BM (2015) Endothelial surface glycocalyx can regulate flow-induced nitric oxide production in microvessels in vivo. PLoS One 10(1):e0117133

Yu J, Bergaya S, Murata T, Alp IF, Bauer MP, Lin MI, Drab M, Kurzchalia TV, Stan RV, Sessa WC (2006) Direct evidence for the role of caveolin-1 and caveolae in mechanotransduction and remodeling of blood vessels. J Clin Invest 116(5):1284–1291

Yurdagul A Jr, Finney AC, Woolard MD, Orr AW (2016) The arterial microenvironment: the where and why of atherosclerosis. Biochem J 473(10):1281–1295

Zeng Y (2017) Endothelial glycocalyx as a critical signalling platform integrating the extracellular haemodynamic forces and chemical signalling. J Cell Mol Med 21(8):1457–1462

Zeng Y, Liu J (2016) Role of glypican-1 in endothelial NOS activation under various steady shear stress magnitudes. Exp Cell Res 348(2):184–189

Zeng Y, Tarbell JM (2014) The adaptive remodeling of endothelial glycocalyx in response to fluid shear stress. PLoS One 9(1):e86249

Zeng Y, Ebong EE, Fu BM, Tarbell JM (2012) The structural stability of the endothelial glycocalyx after enzymatic removal of glycosaminoglycans. PLoS One 7(8):e43168

Zeng Y, Waters M, Andrews A, Honarmandi P, Ebong E, Rizzo V, Tarbell JM (2013) Fluid shear stress induces the clustering of Heparan sulfate via mobility of Glypican-1 in lipid rafts. Am J Physiol Heart Circ Physiol 305(6):H811–H820

Zeng Y, Adamson RH, Curry FR, Tarbell JM (2014) Sphingosine-1-phosphate protects endothelial glycocalyx by inhibiting syndecan-1 shedding. Am J Physiol Heart Circ Physiol 306(3):H363–H372

Zeng Y, Liu XH, Tarbell J, Fu B (2015) Sphingosine 1-phosphate induced synthesis of glycocalyx on endothelial cells. Exp Cell Res 339(1):90–95

Zhou J, Li YS, Chien S (2014) Shear stress-initiated signaling and its regulation of endothelial function. Arterioscler Thromb Vasc Biol 34(10): 2191–2198

Zullo JA, Fan J, Azar TT, Yen W, Zeng M, Chen J, Ratliff BB, Song J, Tarbell JM, Goligorsky MS, Fu BM (2016) Exocytosis of endothelial lysosome-related organelles hair-triggers a patchy loss of Glycocalyx at the onset of Sepsis. Am J Pathol 186(2):248–258

The Molecular Structure of the Endothelial Glycocalyx Layer (EGL) and Surface Layers (ESL) Modulation of Transvascular Exchange

Fitz-Roy E. Curry

Abstract

There has been rapid progress over the past decade to extend the concept that a quasiperiodic inner endothelial glycocalyx layer (EGL, <300 nm thick, with key components associated with the endothelial cell membrane) forms the primary molecular filter between circulating blood and the body tissues. The EGL is common to both continuous and fenestrated microvessels. The revised Starling Principle describing steady-state fluid exchange across the EGL describes new ways to understand transvascular exchange of water and plasma proteins in microvessels in both normal and disturbed states such as hemorrhage and fluid replacement during surgery. At the same time, direct optical observations describe endothelial surface layers (ESLs) with porous outer layers that extend 1–2 μm beyond the EGL. Preliminary analyses of water and plasma protein transport through barriers formed by a thick ESL in series with the EGL indicate that such two-layer structures can have permeability properties that are not consistent with measured water and plasma exchange in microvessels. Such multilayer models provide a basis for future detailed evaluations of both transports across endothelial surface layers and the methods to image components of both the EGL and the ESL. Furthermore changes in the thickness and distribution of thick ESLs in vessels with diameters larger than 50 μm may not reflect functional changes in the inner glycocalyx layer.

F.-R. E. Curry (✉)
Departments of Physiology and Membrane Biology, Biomedical Engineering, School of Medicine, University of California Davis, Davis, CA, USA
e-mail: fecurry@ucdavis.edu

1 Introduction

Our knowledge about the structure on the luminal surface layer of endothelial cells has evolved from its recognition as a thin layer observed after specialized staining in electron micrographs to the current view as a complex three-dimensional layered structure which regulates a wide range of vascular functions. These include forming a lubricating layer for red cell passage through blood vessels, sensing the magnitude and direction of plasma flows, protecting the endothelial surface from the attachment of circulating inflammatory and metastatic cancer cells, and modulating the movement of plasma proteins and water across the endothelial barrier. Several of

B. M. Fu, N. T. Wright (eds.), *Molecular, Cellular, and Tissue Engineering of the Vascular System*, Advances in Experimental Medicine and Biology 1097,
https://doi.org/10.1007/978-3-319-96445-4_2

these topics are covered in the accompanying chapters. Here the focus is on the growing understanding of the endothelial cell membrane-associated glycoprotein/proteoglycan layers as the primary molecular filter at the blood-tissue interface (Curry and Adamson 2012; Curry et al. 2016; Levick and Michel 2010; Michel et al. 2016; Van Teeffelen et al. 2007; Weinbaum et al. 2007).

Although our knowledge of the composition and structure of the endothelial surface layer is far from complete, new methods to stain, visualize, and analyze the inner layer (the true glycocalyx, also designated the endothelial glycocalyx layer, EGL) have strengthened the idea that they form a quasiperiodic array that has common features in many microvascular beds (Arkill et al. 2011, 2012). The structure is stabilized by linkage to the cell cytoskeleton and by binding of plasma proteins and other plasma constituents (Michel 1988; Michel et al. 1985; Adamson et al. 2014) and by mechanisms that inhibit the action of degrading enzymes such as matrix metalloproteinases (Zeng et al. 2014; Zhang et al. 2016). Further there have been steps to understanding the importance of the glycocalyx-junction model of transvascular fluid exchange as it applies to fluid replacement therapy (Michel et al. 2016; Woodcock and Woodcock 2012). The guiding principle is the revised Starling Principle that takes into account the colloid osmotic pressure difference across the glycocalyx, not the colloid osmotic pressure difference between plasma and the bulk interstitial fluid (Levick and Michel 2010; Michel et al. 2016). Further, some of the most important areas for future research are highlighted when current ideas about the structure and composition the glycocalyx forming the molecular filter are compared with the structure and function of the endothelial cell surface layer (ESL) formed when additional plasma and cell-derived components bind to the true glycocalyx to form a more extended layer that is generally assumed to be the primary modulator of both red cell and inflammatory cell micromechanics near the vessel wall and to form part of the mechanosensing mechanisms at the vascular wall (Lipowsky and Lescanic 2017; Reitsma et al. 2007; Tarbell et al. 2014a; b). There is growing awareness that the ESL is heterogeneous as suggested by variation in thickness and distribution across the endothelial surface in different vessels and in disease and evidence that the outer layers are more porous than the inner glycocalyx layers (Bai and Wang 2012, 2014; Gao and Lipowsky 2010; Zeng et al. 2012).

The functional consequences of known and some less well-understood structures of the EGL and ESL are examined in this review which is divided into two main sections: The first (and major section, parts 2–6) evaluates both the inner glycocalyx structure and conditions where the ESL extends beyond the inner glycocalyx by not more than 200–300 nm (total combined thickness <500 nm) and functions as both a molecular sieve and a lubricating or protective layer. The second section (parts 7–9) examines recent observations that optical measurements of the thickness of ESL layer vary by as much as an order of magnitude and evaluates ways in which the function as a molecular filter of such a thick ESL would be compromised. Overall these issues point to the need to further understand the molecular structure and composition of the EGL and ESL and the methods used to visualize the glycocalyx layers; the factors that control synthesis, degradation, and distribution of glycocalyx components; and the way the structure of the layers modulate the exchange functions of the endothelial barrier in both microvessels and vessels larger than 50 μm diameter.

2 Asymmetry in the Effectiveness of Plasma and Tissue Oncotic Pressures

The classical Starling Principle for transvascular fluid exchange was based on the demonstration that lymph was formed by ultrafiltration of plasma and not as active secretions from vascular cells as suggested by Heidenhain in the 1880s (Michel 1997; Michel et al. 2016). Specifically, plasma proteins are restricted at the endothelial barrier relative to water and small

water-soluble nutrients and metabolites so that the differences in plasma protein concentration across the selective barrier results in an oncotic pressure difference sufficient to oppose the hydrostatic pressure drop across the microvessel wall. Much of the new understanding of transvascular fluid exchange during the past century focused on quantification of transvascular fluid exchange using this classical Starling Principle (Michel 1984; Renkin 1986). This required measurement of the driving forces for exchange (the hydrostatic (Pc and Pi) and oncotic (Πc and Πi) pressures in plasma (p) and bulk interstitial (i) fluids acting across an endothelial barrier) as well as the hydraulic conductivity (Lp) and protein osmotic reflection coefficients (σ) of the barrier to macromolecules. The common form of the relation describing the transvascular ultrafiltrate flow rate per unit total area of vasculature (Jv/*A*) is

$$\mathrm{Jv}/A = \mathrm{Lp}\left[(\mathrm{Pc} - \mathrm{Pi}) - \sigma\,(\Pi\mathrm{p} - \Pi\mathrm{i})\right] \quad (1)$$

When models of fluid distribution in tissue and the whole body were constructed to describe short-term and long-term fluid exchange using this classical Starling Principle, a key assumption in the use of Eq. (1) was always that protein oncotic forces in plasma and bulk interstitial fluid were equally effective to modulate transvascular flows. In the classical experiments that demonstrated the linear relation between Jv and capillary pressure described by Eq. (1) (Landis 1927; Pappenheimer and Soto-Rivera 1948), this assumption was not specifically tested because interstitial plasma protein concentrations were deliberately maintained low. However starting in the 1980s, several key reviews and experiments led to a fundamental rethinking of the determinants of the effective colloid osmotic pressure opposing filtration (Michel 1984; Michel and Levick 2010; Michel et al. 2016). The full consequences of these revisions are still being investigated today, and an important goal should be to incorporate these concepts into new models of whole-body fluid and protein exchange. These future efforts must build on the development of the so-called revised Starling Principle and the growing understanding of how properties of both EGL and ESL constrain the application of the revised Starling Principle in different microvascular beds.

Michel (1984) noted that, in the steady state, the difference in protein concentrations between plasma and the ultrafiltrate leaving the vascular wall determines the oncotic pressure difference in Eq. (1), not the difference between plasma and the bulk interstitial fluid composition (Πi). Because the bulk interstitial composition reflected the coupling of all the protein fluxes with transvascular water flows into the interstitial, the difference in plasma protein osmotic pressure between plasma and the ultrafiltrate could be significantly larger than (Πp − Πi) in Eq. (1). To quantify the consequences of this observation, Michel derived a revised form of Eq. (1) in which the plasma protein concentration of the ultrafiltrate varied with Jv/*A*. This resulted in a nonlinear relation between Jv/*A* and capillary pressure which showed that in the steady state, there was never reabsorption. This was because, as capillary pressure was reduced, the ultrafiltrate composition approached plasma composition, and a new balance that always resulted in slow filtration was established. As discussed in more detail in Sect. 3, these theoretical ideas were first confirmed in experiments by Michel and Phillips (1987) in individually perfused capillaries of frog mesentery where steady-state filtration was established at a series of microvessel pressures under condition where the primary determinants of the oncotic pressure difference could be assumed to be the water and solute fluxes across the main water pathway.

The experiments of Michel and Philips also highlighted the need to understand the relation between the composition of fluid crossing the water pathway and the bulk interstitial composition. This difference should be small if the ultrafiltrate flows directly into a well-mixed interstitial space. This was not the case. The review by Levick (1991) demonstrated that the colloid osmotic pressure difference estimated from plasma protein concentrations and bulk interstitial fluid samples (measured with wicks or fine needles) was never sufficient to oppose filtration at the venous end of capillary bed of most mammalian

organs (fenestrated and continuous). The only exceptions were the microvessels in intestine and peritubular capillaries of the kidney (where the addition of protein free fluid from a nearby reabsorbing epithelial transport process dilutes the whole interstitial space, see below). Further the predicted filtration rates based on measured oncotic pressure differences between plasma and bulk interstitial fluid were far too high to be consistent with known rates of lymph flow and fluid accumulation in these organs and normal humans.

An understanding of the mechanisms that maintained the colloid osmotic pressure difference across the primary ultrafiltration pathway different from ($\Pi p - \Pi i$) required quantification of the water and solute fluxes across the water pathway and in the interstitial space. Levick and McDonald (1994) demonstrated that, in the fenestrated capillaries of the synovium, changes in bulk interstitial Πi (produced by injection of albumin solutions into the synovial fluid) had approximately one-third as much effect on transvascular fluid exchange as intra-arterial infusions of albumin. Figure 1, adapted from numerical results in a model of fluid and protein exchange across fenestrae and the interstitial space in the synovial microvessels (Levick (1994)), demonstrates that in the special case where there are high rates of localized filtration across fenestrae, plasma protein concentration in the interstitial fluid just beneath the fenestrae is significantly lower than the bulk protein concentration. This was the result of ultrafiltrate with low protein concentration emerging beneath the fenestrae (which occupy only 1–2% of the vascular surface) and diluting the local interstitial fluid. Plasma protein diffusion and solvent drag within the interstitial space were not sufficient to overwhelm this dilution effect so that, during filtration, the stable oncotic pressure difference across the fenestrae was always larger than the difference between a plasma and bulk tissue fluids.

Based on the idea that the glycocalyx was the primary molecular filter in the main water pathway for both fenestrated and continuous capillaries, Michel (1997) and Weinbaum (1998) independently suggested that the plasma protein

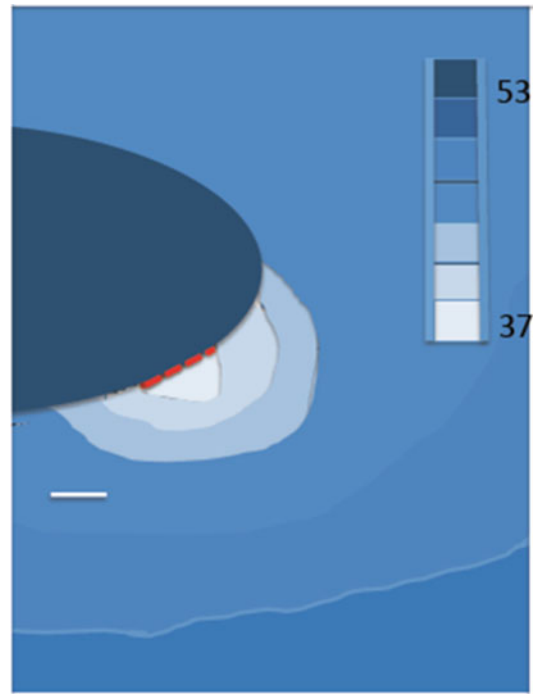

Fig. 1 Profiles of albumin concentration across a fenestrated site in a capillary where the plasma albumin concentration is 53 mg/mL (g/L) and the concentration of albumin in the bulk fluid surrounding the capillary is 44 mg/mL. There is steady filtration from the lumen into the interstitial space through the fenestrae. The profiles are constructed from the table of results (Fig. 5 of Levick 1994) from numerical solutions of the equations describing coupled water and albumin fluxes from the capillary lumen into the interstitial space. The profiles demonstrate substantial dilution of the albumin interstitial concentration under the fenestrae (to 37 mg/mL) so that this plasma protein concentration does not equal interstitial concentration and the difference in colloid osmotic pressure across the fenestrae is greater than the difference in colloid osmotic pressure between plasma and the bulk interstitial fluid. Scale bar is 0.5 μm

concentration in the space beneath the glycocalyx in both fenestrated and continuous endothelium was determined by the coupling of water and protein flows across the glycocalyx. As indicated above, this was in contrast to the plasma protein concentration in the bulk interstitial space being determined by all the fluxes of plasma protein across the vascular wall (across the glycocalyx pathway and other parallel pathways including less selective large pores and specialized transcellular pathways dependent on vesicle uptake. Then even when tissue protein concentration lev-

els approached that in the circulating plasma, plasma protein concentration of the fluid beneath the glycocalyx could be significantly lower from that in the bulk interstitial fluid. Figure 1 illustrated this idea for the special case where the protein concentration of the interstitial space is raised experimentally close to plasma concentration level (44 mg/mL in tissue vs. 53 mg/mL in plasma) and there is a localized site with diffusive and convective transport of protein into the interstitial space. The extension of this concept in continuous capillaries is described below as a step toward further integration of the revised Starling Principle into the complex whole-body models of fluid exchange.

3 The Glycocalyx and the Revised Starling Principle of Fluid Exchange

Figure 2a is a schematic describing the revised Starling Principle (Levick and Michel 2010) and Fig. 2b a specific case where the geometry of the glycocalyx and detailed investigations of the endothelial junction in rat venular microvessels are used for quantitative evaluation of the new principle based on directly measured ultrastructure and permeability data (Adamson et al. 2004). An important insight into the molecular organization of the EGL was the description of bush-like structures within the glycocalyx of fenestrated microvessels fixed using a perfluorocarbon-based perfusate (Rostgaard and Qvortrup 1997). Data from this study, as well as additional samples

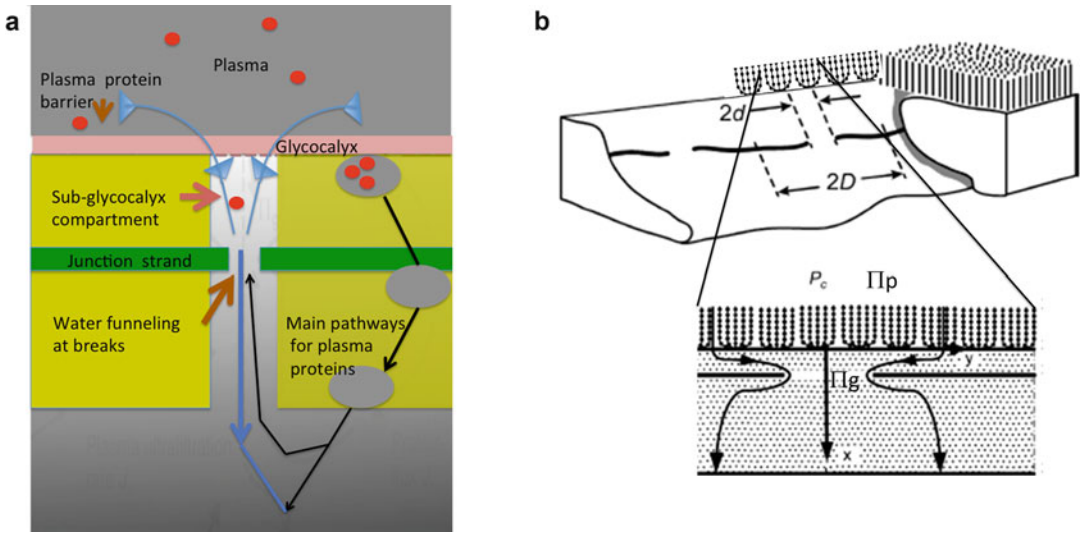

Fig. 2 The glycocalyx-cleft model of the endothelial barrier. (**a**) The EGL (pink layer overlying the endothelial cells) is identified as the primary barrier (molecular filter) to plasma proteins such as albumin. The colloid osmotic pressure that opposes filtration is between plasma and the fluid on the underside of the glycocalyx, i.e., inside the intercellular cleft and close to the glycocalyx. After crossing the glycocalyx, the plasma ultrafiltrate is funneled through infrequent breaks in the junctional strands (green band). During steady-state filtration, the difference in colloid osmotic pressure across the glycocalyx is always larger than the difference between plasma and the bulk interstitial fluid. The composition of the bulk interstitial fluid reflects the contributions from other pathways for plasma protein exchange across the endothelial barrier (vesicles, large pores, etc.) (Modified from Levick and Michel 2010). (**b**) The diagram illustrates a specific example of the glycocalyx-junction model in (**a**). It shows a view of the cleft segment reconstructed from serial sections of rat mesentery microvessels to enable the position of junction strands in the endothelial cleft and distance between gaps in the junction strands to be measured. The exploded view is an idealized diagram representing the mathematical model used to evaluate fluxes of water and albumin across the glycocalyx-junction segments using values of junction geometry, junction gap frequency, and glycocalyx thickness characteristic of rat mesenteric microvessels. From Adamson et al. (2004) with permission

supplied by Qvortrup and rapidly frozen frog mesentery microvessels, were analyzed using autocorrelation methods to reveal the quasiperiodic structure (Squire et al. 2001). Subsequent refinements in both fixative compositions, glycocalyx staining in microvessels of rat mesentery and the measurements of glycocalyx structure in microvessels of known permeability to water and plasma proteins, have enabled a detailed quantitative evaluation of the role of these bush-like structures as the primary molecular filter (Arkill et al. 2011, 2012; Curry et al. 2016) in both frog and rat mesenteric microvessels. Three key concepts have been extensively examined: (1) the molecular structure of the primary molecular filter, (2) the nonlinear shape of the steady-state curve describing filtration rate as a function of capillary pressure using the revised Starling Principle, and (3) the modeling of transport in the space beneath the glycocalyx in both the intercellular junction of the endothelial barrier and pathways in the interstitial space between the endothelial cells and surrounding pericytes. Some of the current questions related to each of these ideas are discussed below in Sects. 3.1–3.4.

3.1 The Structure of the Inner Glycocalyx (EGL) as a Molecular Filter

There is no current method that is generally agreed to preserve the integrity of the glycocalyx, and it is likely that all EM methods fail to preserve components of the ESL attached to the glycocalyx. Likewise all methods that attempt to label components of the ESL and glycocalyx in situ and observe their thickness and distribution using optical techniques have serious limitations with respect to chemical specificity, optical resolution, and the extent to which labeling conditions preserve structure (see second section of review below). Further development of high-resolution imaging and image analyses will be required to advance this area. What is agreed is that the membrane attached glycocalyx preserved by a range of fixation techniques (perfluorocarbon perfusates, specialized staining, and controlled cryo-fixation) extends no more than about 100–150 nm from the endothelium cell membrane. This structure includes proteoglycans from the syndecan and glypican families that reside close to endothelial membrane surface and whose core proteins are associated with the endothelial cell membrane (Betteridge et al. 2017; Hegermann et al. 2016; Tarbell et al. 2014a, b). The core proteins carry attachment sites for heparan sulfate and chondroitin sulfate and binding sites for other glycosaminoglycans including hyaluronic acid. The heparan sulfate and chondroitin sulfate appear to form part of the structures observed as bush-like arrays. Autocorrelation analyses of images and 3D image reconstruction techniques revealed the quasiperiodic structure of the inner glycocalyx on both continuous and fenestrated microvessels. Much remains to be understood about the relation between the images as bushes attached to the endothelial membrane viewed after specialized fixation or fast-freeze methods and the structure of the glycoproteins and proteoglycans in their native (i.e., aqueous) environment. The working hypothesis is that these structure form part of the primary molecular filter.

Further analyses indicate that these bush-like structures are themselves arranged in quasiperiodic arrays on the endothelial cell surface (assumed hexagonal in the model in Fig. 2b, but other configurations are suggested in recent observation on the glomerulus Arkill et al. 2014). On the basis of these assumptions, the model describes the exclusion of plasma proteins from the spaces between the core proteins as the primary mechanism lowering the chemical potential of water within the glycocalyx. Thus a difference in the concentration of plasma proteins across the EGL results in a difference in chemical potential of water on the two sides of the inner glycocalyx that is expressed as a difference in oncotic pressure. It should also be noted that electron micrographs examined for these analyses are sampled randomly from the endothelial cell surface and are assumed to represent the glycocalyx at the principal sites for water pathways that occupy less that 1–2% of the surface (in fenestrated vessels) and significantly smaller

fractions of the surface in continuous capillaries where the main water pathways are formed by the intercellular junction. While the structure of the glycocalyx has been observed directly at fenestrae, sampling the glycocalyx at specific sites on the endothelial surface of continuous endothelium (near junctions, caveolae) requires further investigation.

The description above also ignores other properties of the inner glycocalyx including its deformability, the osmotic effects of side chains attached to the core proteins, and both electrochemical and mechanical forces (Bhalla and Deen 2009; Damiano and Stace 2002; Secomb et al. 2001; Weinbaum et al. 2003). It is known that the passage of leukocytes deforms the EGL, but the effect of such deformation on the transport has not been described. It is assumed that, when leukocytes are not activated (when they do not release agents to degrade glycocalyx components), such transient deformations may be insignificant in terms of steady filtration in normal vessels. The role of other forces within the ESL is less well understood, but analyses of transport properties in terms of observed glycocalyx structure as developed below are made assuming that swelling due the osmotic effects of side chains, electroosmotic forces, and applied shear forces is in separate equilibrium states and independent of transvascular hydrostatic and oncotic pressure differences.

3.2 The Structure of ESL Layers Beyond the Membrane-Bound Glycocalyx up to About 500 Nm

It should be noted that the full effectiveness of circulating plasma proteins as oncotic agents requires they directly contact the interface forming primary molecular filter. At present only the innermost layers that are anchored to the endothelial cell are known to have an organized structure. Any ESL layer that extends beyond the inner layer must maintain a structure that significantly excludes albumin if it is to be part of the primary molecular barrier responsible for oncotic pressure differences. If this is not the case, the function of the surface layer as the primary oncotic barrier is compromised. Yet it is known that ESL layers can extend many hundreds of nanometers beyond the inner glycocalyx. An understanding of the structure of these ESLs must be a primary focus for future research.

The simplest way for an extended ESL to form part of the primary molecular filter for plasma proteins is for the quasiperiodic structure of the EGL to be retained for several hundred additional nanometers. One possible mechanism is the action of albumin itself to bind to the glycocalyx and form cross-linked structures with heparan sulfate, chondroitin sulfate, hyaluronic acid, and other adsorbed plasma components. It is well known that albumin is required to maintain the normal permeability and selectivity of the vessels wall. Furthermore, shielding of the positive charges from arginine or lysine on albumin blocks this protective effect (Michel et al. 1985). Thus as suggested by Fig. 3a, an ordered structure with interfiber dimensions established by the distance between the positively charged arginine groups in albumin may effectively "self-assemble" on top of the membrane-associated glycoproteins and proteoglycans to extend the molecular filter. Superresolution microscopy may enable investigations of such assemblages. In addition, albumin is one of the two circulating plasma proteins that carry sphingosine-1-phosphate (S1P) to receptors on the endothelial surface (the other is HDL). S1P released from red cells and endothelial cells protects the membrane-bound glycocalyx by stabilizing the peripheral actin band beneath the endothelial membrane and blocking the release of matrix metalloproteinases (MMP 9 and 13) that cleave syndecan core protein (Curry et al. 2012; Adamson et al. 2014; Zeng et al. 2014). These structures are illustrated in Fig. 3b.

The above picture is reasonably consistent with the series of observation by Duling and his colleagues describing red cell flows and ESL penetration by macromolecules in small (5 μm diameter) microvessels of the hamster cremaster muscle (Vink and Duling 2000). In these mi-

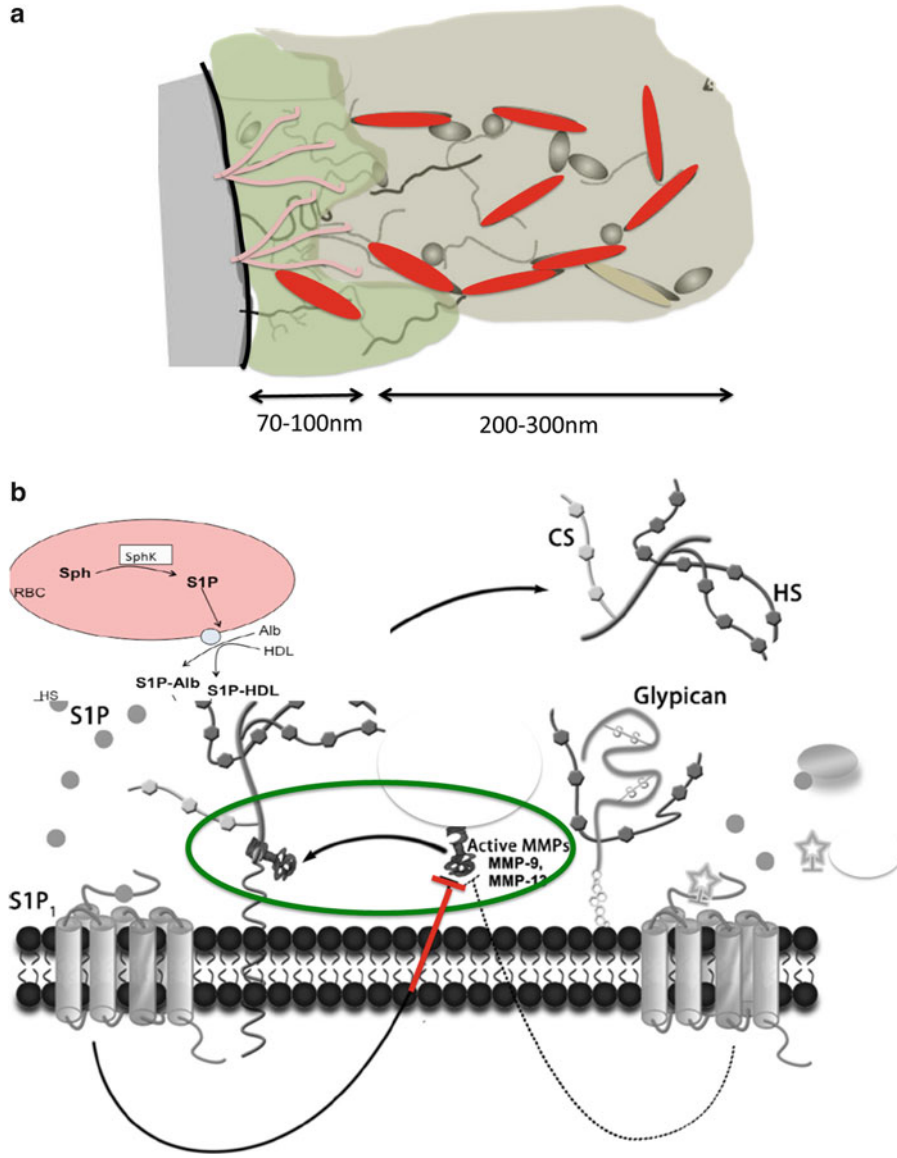

Fig. 3 The two parts illustrate mechanisms that organize and stabilize the membrane attached glycocalyx and may extend the ordered structure of the inner glycocalyx. Part (**a**) shows glycoproteins and proteoglycans associated with the endothelial cell membrane that form a quasiperiodic array by attachments to the cell cytoskeleton. The outer layer shows albumin molecules electrostatically bound to the glycoprotein side chains. Shielding of the positive arginine and lysine on albumin results in loss of the effectiveness of the glycocalyx as a molecular filter suggesting that albumin contributes to ordering structures close to the membrane-associated glycocalyx. Part (**b**) describes the role of sphingosine-1-phosphate which is bound to albumin and HDL to protect the glycocalyx. S1P (secreted from vascular cells, including red cells) activates receptors leading to the stabilization of peripheral actin band and endothelial cell cytoskeleton and inhibition of the activity of matrix metalloproteinases (MMP9 and 13) that induce the shedding of syndecan-1 from the glycocalyx by cleaving its ectodomain (Modified from Zeng et al. 2010)

crovessels both high-molecular-weight dextran (D70) and red cells were excluded from a region 400–500 nm from the endothelial cell membrane. This exclusion of both red cells and Dextran 70 was lost after exposure to free radicals after light irradiation (free radical generation) to degrade the surface layers. Dextran exclusion was also reduced by exposure to enzymes including heparinase and hyaluronidase. A mixture of hyaluronic acid and chondroitin sulfate restored the exclusion effect. Additional experiments demonstrated that macromolecules smaller than D70 including albumin slowly penetrated the ESL layer (Henry and Duling 1999; Desjardins and Duling 1990).

In addition, by at least one criterion, a layer with the permeability properties described above would also support red cell flows. Feng and Weinbaum (2000) demonstrated that a stable lubricating layer for red cell movement was established when $l/Kw^{0.5} > 100$ where l is the ESL thickness and Kw is the hydraulic conductance of the layer. This criterion is met for layers as thin as 0.3 μm when the Kw is as small as 10^{-13} to 10^{-14} cm^2. This is within the range characteristic of organized structures suggested in Figs. 2b and 3. Thus at least for microvessels, ESL structures that extend up to 200 nm beyond the EGL account for both observed permeability and hydrodynamic properties. The structure of the EGL layer in larger vessels has not been established. This is an important area for further research because, as explained in Sect. 8 below, models of possible structures of glycocalyx-endothelial surface layers that extend more than 500 nm from the endothelial surface have too high resistance to water flows if they maintain the selective and hydrodynamic properties of the inner glycocalyx. Furthermore, ESL structure extending up to 1 μm from the endothelial surface fails to account for measured colloid osmotic pressure differences if they have more porous structures with reduced resistance to plasma protein and water flows. These observations suggest that the assumption that thick ESLs that exclude plasma proteins are common throughout the vasculature must be critically reexamined. This is a key message of the current review.

3.3 Nonlinear Steady-State Pressure-Flow Relations Across the Endothelial Barrier

The form of the Starling relation that describes fluid exchange across the glycocalyx differs from that in Eq. (1) because of the substitution of the hydrostatic pressure (Pg) and colloid osmotic pressure of the plasma proteins (Πg) beneath the glycocalyx for the bulk interstitial fluid values and the hydraulic conductivity of the glycocalyx (Lp_{gcx}):

$$Jv/A = Lp_{gcx}\left[(Pc - Pg) - \sigma\,(\Pi p - \Pi g)\right] \quad (2)$$

For the revised Starling Principle, this relation is linear only when Πg is constant. Πg is constant at capillary pressures well above the colloid osmotic pressure of the plasma proteins when filtration rates are high (see Eq. (7) below). It is approximately constant for a brief period following a rapid decrease in capillary pressure from such high capillary pressures and before the composition of the fluid beneath the glycocalyx changes significantly. Thereafter a new steady-state value of Πg is established as described below.

The plasma protein concentration in the space below the glycocalyx (Cg) when water and solute are coupled is determined by the steady-state relation:

$$Cg = Js/Jv \quad (3)$$

Here Jv is given by Eq. (2), and the protein flux through the glycocalyx (Js) is given by the convective-diffusion flux equation (Curry 1984):

$$Js/A_{gcx} = (Jv/A)\;(1-\sigma)\;Cp + Ps\;(Cp - Cg) * \left[Pe/\left((\exp -Pe) - 1\right)\right] \quad (4)$$

Here Ps is the permeability coefficient to albumin, and Pe is the Peclet number $[(Jv/A)(1-\sigma)/Ps]$.

Combining Eqs. (3) and (4) gives the relation for the concentration difference across the glycocalyx:

$$\mathrm{Cp} - \mathrm{Cg} = \mathrm{Cp} * (1 - \exp\ (-\mathrm{Pe}) / (1 - \sigma \exp\ (-\mathrm{Pe})) \quad (5)$$

and the new steady-state filtration rate is (Michel 1984):

$$\mathrm{Jv}/A = \mathrm{Lp}\left[(\mathrm{Pc} - \mathrm{Pg}) - \sigma^2 \Pi \mathrm{p} * \{(1 - \exp -\mathrm{Pe}) / (1 - \sigma \exp -\mathrm{Pe})\}\right] (6)$$

At microvessel pressures well above the plasma oncotic pressure in microvessels with low permeability coefficient to plasma proteins, Pe >>1 and plasma protein concentration in the ultrafiltrate exiting the glycocalyx is $\mathrm{Cp}(1 - \sigma)$. Then Cp − Cg equals σCp, and Eq. (6) reduces to:

$$\mathrm{Jv}/A = \mathrm{Lp}_{\mathrm{gcx}}\left[(\mathrm{Pc} - \mathrm{Pg}) - \sigma^2 \Pi \mathrm{p}\right] \quad (7)$$

In summary, Eq. (6) describes the nonlinear relation between filtration rate and capillary pressure. At capillary pressures well above the osmotic pressure of the plasma proteins, the relation approaches the linear form in Eq. (7) because Cp − Cg approaches the high Peclet Number limit of σCp. The relation has a slope equal to the hydraulic conductivity of the glycocalyx and an intercept on the pressure axis of σ^2 Πp. In contrast, for pressures below the osmotic pressure exerted by the plasma protein, a fall in capillary pressure will result in transient reabsorption, but this cannot be sustained because plasma proteins accumulate beneath the glycocalyx. Reabsorption reverts to slow filtration over a short period with the filtration pressure (Pc − Pg) closely balanced by the osmotic pressure difference determined by Cp − Cg and Eq. (5). As a result, the slope of the relation between Jv/*A* and Pc is significantly less than expected from the value of Lp and becomes close to zero at low pressure (Fig. 4a). As shown in Fig. 4a, the shape of the nonlinear pressure-flow relation has been compared to that of a hockey stick.

Although Eq. (6) has not been tested under conditions where Cp − Cg is directly measured, experimental observations in individually perfused microvessels (Fig. 4b, from Michel and Phillips 1987) demonstrate that the characteristic hockey-stick shape in Fig. 4a is preserved even when there is additional resistance to albumin and water flows in the junction pathways beneath the glycocalyx (so that Lp represents of the total barrier to water flow) and Pg is small compared to Pc. Fig. 4c shows a family of hockey-stick curves characterized by successively smaller albumin permeability coefficients constructed using the values of Lp and σ measured from the slope and intercept of the linear portion of steady-state experimental results. The result that Eq. (6) can be used to describe experimental measurements in intact microvessels conforms to the hypothesis that the glycocalyx barrier is the primary determinant of the steady-state filtration rates in these microvessels. It is noted that Fig. 4d also illustrates this point in mammalian vessels as will be discussed in Sect. 3.4. Equation (6) also describes steady-state measurements of flows from lumen to abluminal sides of a cultured monolayer of bovine aortic endothelial cells (Pang and Tarbell 2003).

A further extension of the model is to take into account resistance to water flows in spaces between the cells surrounding the microvessels (pericytes) and in the interstitial space surrounding the tissue cells (muscle, skin) and the action of the lymphatic system. This is important to understand the kinetics of the approach toward a new steady state after a change in pressure. Weinbaum and colleagues demonstrated that the resistance to water and solute flows between pericyte layers surrounding rat venular microvessels accounted for the observation that a new steady state takes up to 2 min to be established after a change of pressure in rat mesentery microvessels (Zhang et al. 2008). For microvessels with continuous endothelium, an obvious extension of this approach would be to take into account further resistances to water and protein flows in the interstitium using approaches described for (Fig. 1).

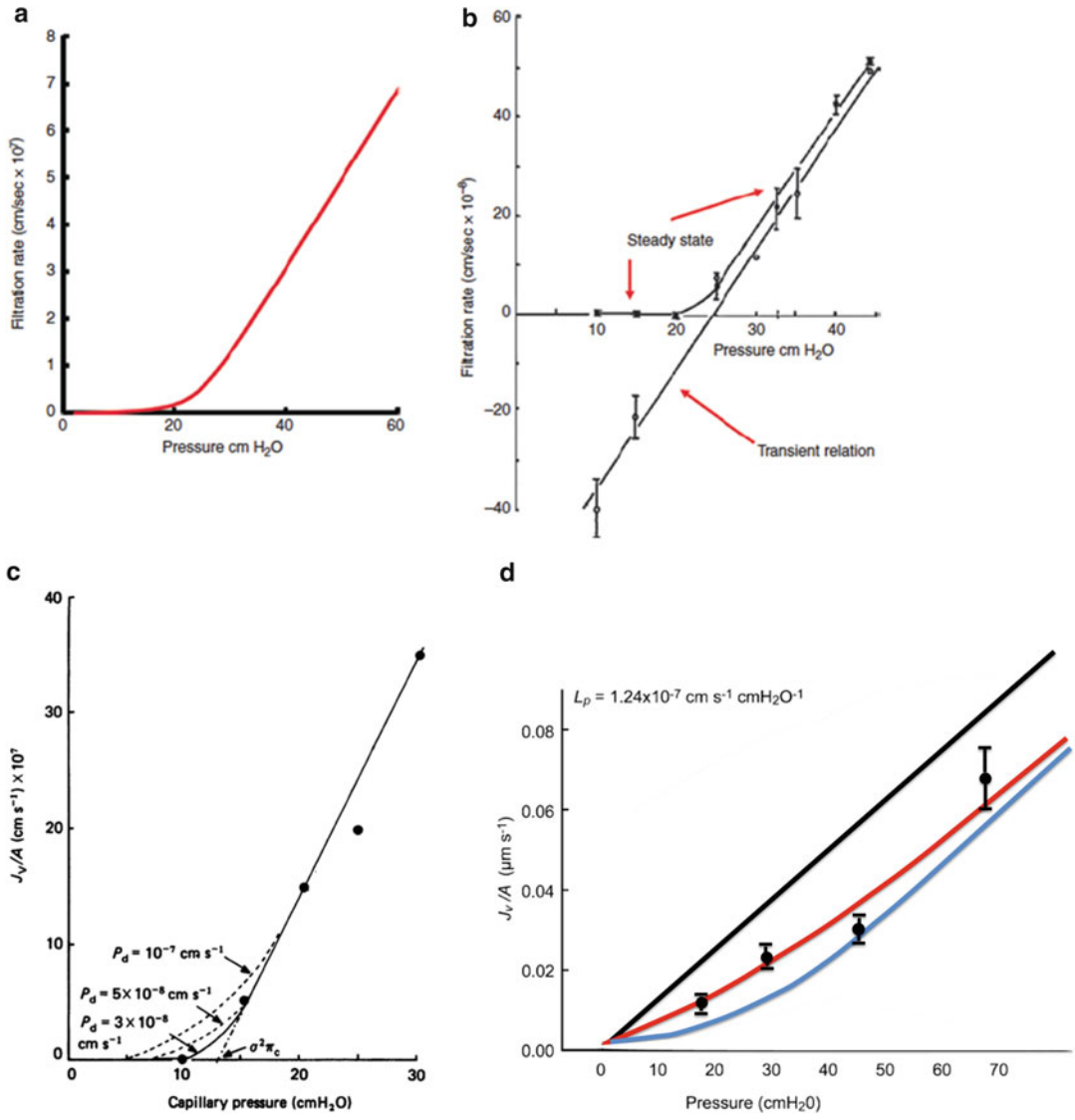

Fig. 4 The hockey-stick shape for the steady-state relation between fluid filtration rates and hydrostatic pressure difference is shown in four examples. (**a**) The curve described by text Eq. (6) shows that at low pressures, steady filtration increases only slightly as pressure increases. However as pressure approaches the effective colloid osmotic pressure of the plasma proteins, filtration increases significantly and then increases linearly with pressure. Part (**b**) shows an experiment on an individually perfused mesenteric microvessel. The vessel was initially perfused at high capillary pressure (40 cm H_2O) and filtration rate measured at this pressure. When the pressure was reduced rapidly from this level and initial transvascular fluid flow measured, the linear relation between Jv/*S* and pressure was observed with an intercept on the pressure axis of σΠp. These are the results expected when transient changes in filtration rate are measured and the colloid osmotic pressure difference is approximately constant and close to σΠp for measurements at all pressures. In contrast, when steady-state filtration was established at a series of lower capillary pressures by perfusing the vessel at each pressure for 5–10 min, the relation between Jv/S and pressure was the hockey-shaped curve. Part (**c**) shows that reasonable values of the albumin permeability coefficient can be used in Eq. (6) to describe the whole-hockey-stick-shaped curve observed experimentally. Albumin permeability coefficient is the only unknown variable used to construct the curves as the value of Lp is obtained from the slope of the linear region of the relation, and σ albumin is obtained from the intercept of the linear relation with the pressure axis. Part (**d**) shows a similar experiment to that in part (**b**) but with the interstitial fluid surrounding rat mesenteric microvessels loaded with albumin at

This would form the basis for the detailed analyses of whole-body fluid and protein distributions, updating the earlier models by Taylor, Guyton, and Bert and colleagues (Bert et al. 1988; Chen et al. 1976; Guyton et al. 1976). Another extension of the model would be a description of flows through the glycocalyx on glomerular capillaries (now recognized as the primary molecular filter) and the underlying mesangial cells and foot processes (Fridén et al. 2011; Arkill et al. 2014).

3.4 Reduced Back Diffusion of Tissue Proteins and the Funneling of Water Flows through Infrequent Breaks in the Junctional Strands

An additional mechanism must be taken into account when plasma protein is present in the tissue (typically close to 40% of plasma concentration). As described above, high tissue protein concentrations are established by plasma protein transport into the interstitial space via other pathways (large pore, vesicles, others). Because these interstitial concentrations of plasma proteins in the interstitial fluid can be higher than the concentrations in the protected region beneath the glycocalyx, the average composition of the fluid in this protected space below the glycocalyx is determined by a race between protein diffusion back into junctions from the bulk interstitial fluid and the flow of ultrafiltrate exiting the glycocalyx which is opposing such diffusion. A key mechanism that ensures the maintenance of a larger oncotic pressure difference cross the glycocalyx is the funneling of the ultrafiltrate through discontinuities in the junction strands forming the adhesion sites between adjacent endothelial cells (see Fig. 2b). Most of the junction strands have high resistance to water and all solutes larger than about 500 Daltons; thus water flow occurs through these infrequent breaks in the zipper-like seals formed by the claudin/VE-cadherin complex between adjacent endothelial cells. The result is water velocity at the discontinuities more than ten times that across the glycocalyx and a significant convective component of protein transport that opposes back diffusion so that the concentration of plasma proteins below the glycocalyx is expected to be lower than tissue concentration and $(\Pi c - \Pi g) > (\Pi c - \Pi i)$ even at low capillary pressures.

In a manner that parallels the experiment of McDonald and Levick in Fig. 1, Adamson et al. (2014) tested the effectiveness of this funneling in experiments in which the interstitial fluid surrounding a cannulated venular microvessel in rat mesentery was equilibrated with plasma proteins to make the interstitial plasma protein concentration the same concentration as that in the perfusate. According to the classical Starling Principle, there should be no oncotic pressure difference across the microvessel wall, and the filtration rates should only reflect the pressure-driven flows (straight black line in Fig. 4d). This was not the case. After establishing filtration at capillary pressures well above the colloid osmotic pressure of the perfusate, plasma proteins in the perfusate were found to exert close to 70% of their full osmotic pressure even in the presence of this large tissue protein concentration. The results showed that the high filtration limit described by Eq. (7) would account for the colloid osmotic pressure difference across the glycoca-

Fig. 4 (continued) the same concentration as in the lumen (50 mg/mL). The solid black line shows the predicted filtration rates expected when Πp and Πi were set equal so that there was no colloid osmotic pressure difference between the lumen and the tissue to oppose filtration. The measured filtration rates fall significantly below this line, indicating that a colloid osmotic pressure difference was established across the glycocalyx. The red line shows the expected curve when albumin is loaded into the peri-capillary fluid. The line indicated only slightly increased filtration rates in the low pressure range relative to the blue line which describes filtration across the glycocalyx alone in the absence of tissue albumin loading. Directly measured filtration rates in the presence of albumin loading are given as mean ± sem. (parts (**a**) and (**b**) from Michel et al. (2016) with permission, part (**c**) from Michel and Phillips (1987) with permission, and part (**d**) modified from Adamson et al. (2004)

lyx even when there was a larger plasma protein concentration in the bulk interstitial fluid. The experiment was then extended to evaluate filtration rates at a series of lower microvascular pressures where the effects of back diffusion of plasma protein from the bulk interstitial space might be more apparent. The blue curve in Fig. 4d shows the relation between steady-state filtration rates and microvessel pressure from numerical solutions for the coupled water and protein fluxes in the model in Fig. 2b with no added interstitial proteins, and the red curve shows the predicted relation when the interstitial fluid composition is fixed at the level of the perfusate. The blue curve is close to the curve described by Eq. (6). The red curve is slightly displaced upward reflecting a small amount of additional back diffusion when the interstitial protein concentrations are as high as normal plasma concentrations.

4 Reabsorption in Intestine and Kidney

A particularly interesting case of interactions of water and protein fluxes in the interstitial space close to microvessels is the role of protein free fluid that enters this space as the result of water transport across an adjacent epithelial membrane (Michel et al. 2016). At low microvessel pressures, the buildup of plasma protein concentration beneath the glycocalyx described by Eq. (5) that would stop reabsorption in the steady state is prevented by the dilution of the interstitial fluid adjacent to the microvessel by the protein free fluid transported across the epithelial barrier. In contrast to the case in Fig. 2a, the constant additional supply of protein free fluid dilutes all interstitial protein concentrations and maintains ($\Pi c - \Pi g$) close to ($\Pi c - \Pi i$) during reabsorption. It is the energy from epithelial transport of electrolytes and resultant additional osmotic water flows established by electrolyte concentrations into the bulk interstitial fluid that maintains such an oncotic pressure differences across the fenestrated endothelium of intestine and peritubular capillaries of the kidney. In the absence of this extra energy, ion gradients would collapse, and the passive coupling between water and plasma protein transport described by Eq. (6) would abolish sustained reabsorption. Although these basic concepts are now well understood, further investigations of the coupling between transepithelial and transvascular transport mechanisms to maintain tissue to plasma reabsorption in the kidney and intestinal fluid in the GI systems are areas for further quantitative evaluation.

5 Clinical Observations

It is well known that crystalloid solutions that do not contain colloids are lost relatively quickly from the plasma space when infused into normal individuals. This observation can be understood in terms of both the classical Starling Principle and the revised Starling Principle. For example, in normal individuals (lying flat with average capillary pressures close to 22 mmHg), infusion of a crystalloid solution will dilute plasma proteins. An example is shown Fig. 5a where the shift from the blue curve to the red curve represents a reduction in plasma colloid osmotic pressure from 25 to 15 mmHg (Michel et al. 2016). The hockey-stick curve in this pressure range indicates that there is a significantly increased filtration (points A–B) that would continue until much of the infused fluid was distributed into the interstitial space. The result would the same for the linear relation describing filtration using the classical Starling Principle. However if the same crystalloid solution is infused into an individual where there is a significant reduction in microvessel pressure (e.g., due to strong vasoconstriction after blood loss), the increase in the rate of filtration due to dilution of the plasma proteins (moving from the normal blue curve to the red curve is small (C to D). This is because the close balance between microvasculature pressure and the plasma protein oncotic pressure difference maintained across the glycocalyx as described by the revised Starling Principle causes the slope of the relation between filtration rates and pressure to be quite flat when microvessel pressures are low. As shown in Fig. 5b, the result is a greater

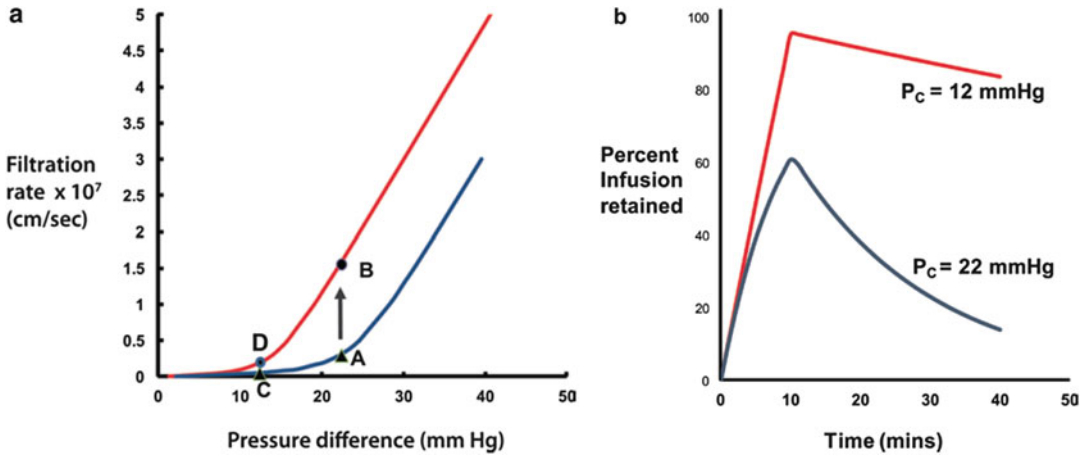

Fig. 5 (**a**) Results of modeling the effects of the infusion of a crystalloid solution in the plasma space of a normal human subject with a normal average capillary pressure of 22 mmHg (lying down) and a human with significantly reduced capillary pressure (severe vasoconstriction of skin and muscle vasculature). Part (**a**) shows the steady-state hockey-stick curves when plasma osmotic pressure is in the normal range (blue curve) and after dilution of the plasma proteins by crystalloid infusions to reduce colloid osmotic pressure by 10 mmHg (red curve). Point A represents the position in a healthy subject at rest with average mean microvascular pressure of 22 mmHg, and point B shows the filtration rate at the same microvascular pressure when the plasma proteins have been diluted by crystalloids. Point C represents steady-state filtration rate in a tissue such as the muscle and skin when the microvascular pressure has been reduced by intense vasoconstriction (e.g., following blood loss). Whereas dilution of the plasma proteins by crystalloid infusion leads to a substantial increase in fluid filtration at normal Pc, when Πc in reduced (point C), dilution of the plasma proteins raises filtration rate only marginally to point D. (**b**) Predictions of the fraction of a crystalloid infusion that is retained in the circulation in a tissue such as muscle at normal and reduced Pc (From Michel et al. (2016) with permission)

retention of the crystalloid in the plasma space (and ignoring other compensatory mechanisms such as reduced renal water loss). This may account for the observation that in the early period following fluid loss, crystalloid solutions are more effective to maintain plasma volume than expected from the results in normal subjects (see Jabaley and Dudaryk 2014 for review.) The importance of these observations in clinical fluid management is an area of active investigations (Michel et al. 2016; Woodcock and Woodcock 2012)

6 Summary of Part 1

There has been rapid progress over the past decade to extend the concept of the inner glycocalyx layer as the primary molecular filter in both continuous and fenestrated microvessels and to apply the revised Starling Principle to understand disturbance in transvascular fluid exchange in both normal and disturbed states such as hemorrhage and fluid replacement during surgery. At the same time, there is a pressing need to understand the molecular composition of the inner glycocalyx and the distribution of these components on the endothelial surface (particularly at sites of exchange such as the intercellular junction). Equally important will be insight into the ways changes in the composition and distribution of the EGL layer modulate the permeability and selectivity of the microvessel wall.

7 Imaging Thick Endothelial Surface Layers: Limitations to Current Methods

One of the most poorly understood issues is the relation between the glycocalyx-ESL functions described above and the ESL layers that are

labeled using fluorescent molecules that bind to ESL components (binding sites for wheat germ agglutinin (WGA) and antibodies to HS or CS). The resulting fluorescent images suggest structures extending 1 μm or more into the vessel lumen. Labeling methods are not the only approach that yields estimates of ESL layers having dimension of 1 μm or more, but here the focus is intravital confocal microscopy observations. Detailed evaluations of the other techniques that suggest thicker ESL layers (e.g., those based on the difference between the distribution volume of red cells and the distribution volume of tracers that are assumed to equilibrate into the ESL) have been evaluated recently (Curry et al. 2016; Michel and Curry 2009). The overall conclusion is that many of the assumptions on which the methods are based are not correct. This applies for method based on whole-body distribution volumes and observations in sublingual microvessels visualized by specialized optical methods (Curry et al. 2016).

With respect to fluorescent labeling methods, two recent papers provide key insights into the problems that complicate investigations of the relation between labeled ESL thickness and changes in vascular permeability. Betteridge et al. (2017) evaluate the binding to the ESL of WGA labeled with either FITC or TRITC in venular microvessels in which permeability coefficients (albumin permeability coefficient and albumin reflection coefficient and Lp) are also measured. Results are given before and after enzyme treatment of the same rat mesenteric venular microvessels used to develop the model in Fig. 2b. In the control state, images of the labeled ESL collected by confocal microscopy showed a Gaussian-type distribution of fluorescence intensity around a peak that was displaced from the image of a separate fluorescent marker of the endothelial cell membrane. The authors quantified the distance between the peak intensities of the ESL layer and the membrane label (P − P distance) as well as the distance between sites in the fluorescent intensity profile of the labeled ESL that are half the maximum fluorescent intensity (the so-called full-width-half-maximum estimate, FWHM). The striking result is that ESL thickness measured by different methods using different labels varied by an order of magnitude. The discrepancies were largest for FITC-WGA. The FWHM estimate was 1500 ± 140 nm compared with the P − P estimates of 243 ± 22.4 nm. The P − P TRITC-WGA estimate was 662 ± 67 nm compared with FWHM close to 1265 ± 150 nm for controls. All values were much larger than the inner glycocalyx labeled with Alcian Blue and imaged by EM (80 nm). The fractional coverage of endothelial surface by label (percent of surface with label intensity greater than zero) was between 75 and 80% in control perfusates.

After treated with neuraminidase to remove sialic acid groups, the P-P estimate was reduced for both FITC-WGA (290 ± 29 vs. 185 ± 33 nm) and TRITC (663 ± 67 to 386 ± 11). Under the same conditions, albumin permeability coefficient increased 6.9-fold. A particularly striking result was that the fractional coverage estimated using FITC-WGA was not significantly reduced by neuraminidase treatment. The fractional coverage with TRITC-WGA was reduced (from 0.79 to 0.57). Neuraminidase treatment reduced EM labeling from 80 to 40 nm. It is likely that the variability reflects the heterogeneity of label within the ESL both as a function of penetration into the ESL and distribution of binding across the surface. In addition, factors such as the composition of the perfusate (the presence of S1P and the temperature at which labeling occurs as documented by Fu and colleagues Zhang et al. 2016) in these vessels are important variables. These observations by Betteridge and colleagues indicate that measures of the ESL thickness using fluorescence methods present unsolved technical difficulties. They do not rule out the presence of thicker layers, but they reduce confidence in observations published using these methods, especially for FITC-labeled tracers. There is no clear explanation why neither FITC-labeled WGA nor TRITC-labeled WGA showed significant reduction for FWHM values after enzyme treatment. Further the striking failure of FITC-WGA to show differences in the extent of surface covered after enzyme treatment suggest that non-specific

labeling effects can be a major problem with these tracers.

The second paper by Zhang et al. (2016) also measured both solute permeability coefficients (to albumin and sodium fluorescein (MW 376)) and the distribution and fluorescent intensity of an FITC-conjugated antibody to heparan sulfate, a major component of the glycocalyx/ESL. Measurements were made first when the glycocalyx/ESL was stabilized by the presence of sphingosine-1-phosphate and albumin in the perfusate, and then when S1P was not present, lipid-free albumin remained. The images presented in the paper were not analyzed with sophistication of the methods used by Betteridge et al. (2017), but under control condition, they show ESL-antibody layers more than 1 μm in overall dimensions on the walls of a venular microvessel in the rat mesentery. In the absence of S1P, labeling of the ESL is significantly reduced. This is quantified as a reduction in fluorescent intensity of the ESL label to 10% of control values. The increase in the permeability of albumin after S1P removal was 6.5-fold, while the permeability to small solute sodium fluorescein increased 2.5-fold. While these results demonstrate a correlation between reduced ESL layer and increased permeability, the more important result was the interpretation of these observations using a form of the model in Fig. 2. Specifically, the only combination of model parameters that accounted for the observed changes in albumin permeability (6.5-fold), sodium fluorescein permeability (2.5-fold), and previous observation of a twofold increase in Lp was for the inner glycocalyx thickness to be reduced from a mean value of 250 nm to 10% of this value in the absence of S1P. While the measured fractional reduction in ESL fluorescence intensity was also 10% of its initial value, the striking discrepancy is between the initial measured thickness of the ESL measured using the fluorescent method in these vessels (1–3 μm) and the initial thickness of the inner glycocalyx which formed the principal barrier in the model (250 nm or 0.25 μm).

Taken together the results from these two recent papers indicate that much more refined methods are needed to enable reliable interpretation of changes in the thickness and distribution of various labels currently in use to probe the ESL and changes in the microvascular permeability properties.

8 Transport in Thick ESL Layers

As a step toward the development of approaches that may improve our understanding of the properties of ESL layers that extent more than 0.5 or 1 μm from the endothelial surface, the following section uses available theory and experimental data describing the permeability properties of fiber matrices (such as hyaluronic acid) to distinguish between the role of thick ESL to modulate red cell fluxes and their function as a regulator of trans-endothelial exchange of water and plasma proteins. This is important as efforts in clinical medicine to measure changes in the thickness of ESL layers as indicators of early changes in microvascular function are being developed (reviewed in Curry et al. 2016). It would be useful to know where such measurement can provide information about the function of the glycocalyx as a permeability barrier as well as change in its modulation of red cell flux and leukocyte/endothelial interactions.

8.1 Resistance to Water Flow in a Thick Matrix

The hydraulic conductance (Kw) of a matrix that significantly excludes albumin (albumin reflection coefficient of 0.9 or greater) falls in the range of 10^{-13}–10^{-14} cm^2. For example, the value of Kw calculated for the model in Fig. 2b is 9.2×10^{-14} cm^2 (Zhang et al. 2008). If a 1 μm thick ESL having Kw values in this range was in series with breaks in the junction strand (such as those in Fig. 2b that occupy less than 0.1% of the cell surface), the resistance to water movement through the combined ESL/junctional pathway would be equivalent to a series resistor with a hydraulic conductivity of $0.02–0.2 \times 10^{-7}$ cm/s cm H_2O. These values are from 5 to 50 times lower than the Lp of the rat mesenteric microvessel

in which this junction geometry is directly measured. Thus ESLs extending more than 1 μm from the endothelial surface and excluding albumin by steric effects have too large a resistance to water flows to be consistent with measured Lps in intact microvessels. This simple series model conclusion is confirmed by the more sophisticated 3D modeling result described in Fig. 9 of Adamson et al. (2004). Extrapolation of results for a combined glycocalyx-junction pathway (with appropriate resistance from some crossbridges in the junction) shows estimated Lp values approaching zero when surface layers are more than 600 nm thick.

8.2 A More Porous ESL but a Compromised Molecular Filter

ESL layers 0.5–1 μm thick meet the criterion for red cell flow on a lubricating layer ($L/Kw^{0.5}$ >100, Feng and Weinbaum 2000) with values of water conductivity (Kw) of 0.25–1 $\times$ 10^{-12} cm^2. These values are at least an order of magnitude larger than the values of Kw used to account for water resistance in the inner glycocalyx (Fig. 4) and as discussed in Sect. 8.1. They are consistent with the idea that outer layers are more porous than the inner glycocalyx layer and that ESL composition differs from the inner layers. One likely component of the outer layer is hyaluronic acid (HA) which forms a gel-like layer whose porosity depends on the concentration on HA. Figure 6 is a cartoon depicting a HA layer up to ten times the thickness on the inner glycocalyx (Curry 2017).

The concentrations of HA that corresponds to the above Kw values fall in the range of 3–10 mg/mL (Preston et al. 1965) or 10–20 mg/mL (based on measurement reported by Adamson and Curry (1982). For the purpose of the following analysis, it is convenient to note that the midrange HA concentration used by Ogston et al. (1973) to investigate partitioning of macromolecules in HA solution was 14.5 mg/mL. This concentration is used below to evaluate macromolecule transport in a gel layer such as that

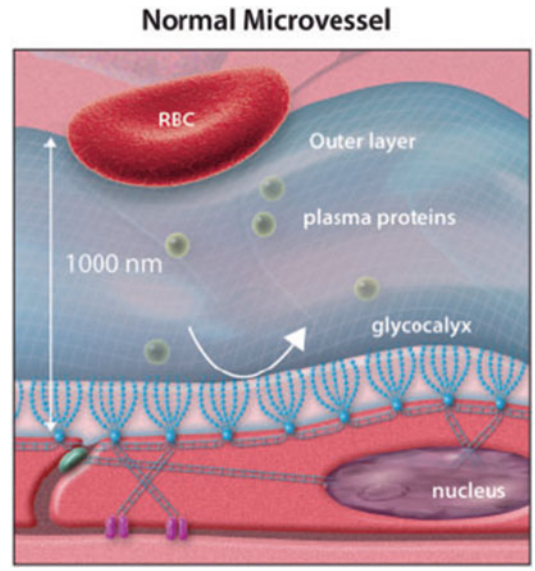

Fig. 6 A cartoon of a two-layered glycocalyx structure formed by an inner endothelial glycocalyx layer (EGL) and an outer endothelial surface layer (ESL). The figure shows dense bush-like inner layer (blue bushes) formed by proteoglycans associated with the endothelial cell membrane which forms the primary molecular barrier to plasma proteins (plasma protein exclusion represented by curved arrow) and an outer gel-like layer, which is more porous. The outer layer (1 μm or more in thickness) contains glycosaminoglycans such as hyaluronic acid and is up to ten times thicker than the inner layer (contrast with Fig. 2). Red cell and endothelial cell dimensions are not to scale. The figure suggests that structures and functions of the ESL can differ significantly from those of the inner layer (true glycocalyx) (from Curry (2017) with permission)

in Fig. 6. Specifically, albumin concentration in the HA gel is close to 50% plasma concentration (partition coefficient $\phi = 0.5$), and the gel concentration of a molecule with a Stokes radius corresponding to the diffusion coefficient of Dextran 70 would be close to 10% of its plasma concentration (Ogston et al. 1973) (the actual concentration of Dextran 70 is expected to be even lower when the elongated nature of large dextrans is taken into account). These observations are consistent with in vivo observations that fluorescent molecules as large as D70 are excluded from the extended ESL layers and that albumin can penetrate into the ESL. These preliminary calculations do not take into account many factors that may modify these preliminary

conclusions such as the contribution of other plasma-derived components within the outer layers of the ESL and electrostatic and chemical interaction that likely exist. Nevertheless they do highlight an important problem: While a porous outer ESL may form a layer that determines red cell movement and likely restricts access of nanoparticles, large dextrans, and inflammatory cells to the surface, the relatively high partition coefficients for albumin may compromise its role as a determinant of the oncotic pressure difference across the inner glycocalyx layer. Some preliminary calculations that illustrate this issue are described below.

Whereas the albumin osmotic reflection coefficient of the inner glycocalyx is estimated to be greater than 0.9, the reflection coefficient of albumin in the HA layer of the ESL with $\phi = 0.5$ is estimated to be close to 0.25 [assumes $\sigma = (1 - \phi)^2$]. If albumin transport across the combined ESL/glycocalyx layer was mainly diffusive, the relative contributions of the ESL and inner glycocalyx layer to overall osmotic reflection coefficient are weighted in proportion to their permeability coefficients (see Appendix). Thus the theory for barriers in series predicts that the combined effect of a diffusion gradient for albumin within the ESL and its lower albumin reflection coefficient would reduce the effective osmotic pressure difference exerted by albumin across the whole layer by 20–25% (series barrier reflection coefficients close to 0.75). This is far less than the experimentally measured values of the albumin osmotic reflection coefficients measured in intact microvascular beds including the muscle, skin, lung, and individually perfused microvessels (σ albumin greater than 0.9; Michel 1984). According to the series barrier relation in the Appendix, the refection coefficient of the combined ESL-EGL series barrier (which contains an ESL with an albumin partition coefficient of 0.5) would approach the measured experimental values greater than 0.9 only when the EGL layer was even more restrictive than in Fig. 2 (reflection coefficients close to 0.98 instead of 0.94 and albumin permeability coefficient of the EGL less than 10% of the ESL even though the later was up to ten times the thickness of the EGL. The observation suggests several possibilities for further investigation: (1) factors in addition to steric exclusion by the bush-like structures in Fig. 2 modulate albumin exclusion from the EGL, (2) that thicker and more porous ESL layers are either not present (or very thin) in exchange microvessels, (3) that the properties of HA solutions are not representative of the permeability properties of thick ESL layers (e.g., in arterioles and larger vessels) and new models are needed, and (4) when unstirred layer effects compromise the balance of hydrostatic and colloid osmotic forces, endothelial barriers can be protected from excess transvascular fluid exchange when the endothelial junctions and perivascular cells have a very high resistance to water flows. These are all areas for further research.

Another issue is the possibility that during filtration solvent drag through a more porous ESL would lead to albumin accumulates at an ESL/EGL boundary (concentration polarization), offsetting at least some steric exclusion with the ESL. Such concentration polarization effects would be expected to be most prominent at high capillary pressures and corresponding high filtration rates. This is because the accumulation of protein at the interface between the ESL and EGL would increase the concentration difference of albumin across the EGL. It would also increase resistance to water flow through the accumulated protein at the interface. Both mechanisms would tend to reduce the slope of the relation between Jv/*A* and pressure as pressure increased. The linearity of the relation between Jv/*A* and pressure at capillary pressures above the plasma osmotic pressure in single microvessels and whole-organ studies is evidence against significant concentration polarization. Particular examples include those in Fig. 4 and others described in detail in Michel et al. (1974) and the review by Landis and Pappenheimer (1963).

9 Summary of Part 2

On the basis of the arguments presented above, it seems reasonable to conclude that extended ESLs with porous outer layers would compromise

normal water and plasma protein functions of the primary exchange vessels on the microvasculature. Thus in vessels where thicker ESL is present, exchange of water and plasma proteins is likely limited. The primary function of such thick ESLs is likely modulation of red cell flux and the access of leukocytes to the endothelial surface. These observations also suggest that attempts to understand functions of the inner glycocalyx in microvessels by observing changes in the thickness and distribution of the ESLs in vessel with larger diameters are likely to be compromised because changes in the outer layers may not reflect changes in the inner glycocalyx layer. It remains to be seen whether alternate markers of ESL and glycocalyx change such as increased plasma levels of their components (heparin sulfate, chondroitin sulfate, and HA or the enzymes that digest these components) are more useful biomarkers of glycocalyx function (Schmidt et al. 2014). A similar conclusion applies for other approaches of such measurement of the so-called glycocalyx volumes based on estimates of the difference between circulation red cell distribution volume and the distribution volume of markers of ESL penetration by tracer molecules. For more detailed critiques of such methods, see Michel and Curry (2009) and Curry et al. (2016).

A.1 Appendix: Estimates of Reflection Coefficient of Series Barrier

The reflection coefficient for a series barrier (σ_{total}) formed by an ESL layer with a reflection coefficient of 0.25 (σ_{ESL}) and an inner glycocalyx layer (σ_{EGL}) with a reflection coefficient of 0.94 is given by the relation:

$$\sigma_{\text{total}} = \sigma_{\text{EGL}}{}^{*} P_{\text{ESL}} / (P_{\text{ESL}+} P_{\text{EGL}}) + \sigma_{\text{ESL}}{}^{*} [(P_{\text{EGL}} / (P_{\text{ESL}+} P_{\text{EGL}})]$$

where P_{ESL} and P_{EGL} are the permeability coefficients of the ESL and EGL, respectively. The relation reduces to $\sigma_{\text{total}} = \sigma_{\text{EGL}}$ when $P_{\text{ESL}} >> P_{\text{EGL}}$. The relation can also be written as:

$\sigma_{\text{total}} = \sigma_{\text{EGL}}{}^{*}(P_{\text{total}}/(P_{\text{EGL}}) + \sigma_{\text{ESL}}{}^{*}(P_{\text{total}}/(P_{\text{ESL}})$ where $1/P_{\text{total}} = 1/P_{\text{EGL}} + 1/P_{\text{ESL}}$ (Kedem and Katchalsky 1963).

The relative permeability coefficients are determine by the values of $(D\ \phi)/L$ for each layer where D is the diffusion coefficient, ϕ is the partition coefficient, and L is the thickness for each layer. Ogston et al. (1973) measured the fractional reduction in the free diffusion coefficient for albumin in HA solution of 14.5 mg/mL to be 0.75, close to two times larger the estimate for D in the inner matrix in the model in Fig. 2b (Adamson et al. 2004). The partition coefficient for album in the same HA is 0.5, while that in the inner matrix is close to 0.03 (reflection coefficient of 0.94). Thus if the ESL is ten times the thickness of the inner glycocalyx as in Fig. 6, the inner glycocalyx matrix accounts for close to 75% of the total diffusive resistance, and the effective reflection coefficient of the series barrier would be 0.78 which is 20% less than the value of the inner glycocalyx barrier 0.94.

References

Adamson RH, Curry FE (1982) Water flow through a fiber matrix of hyaluronic acid. Microvasc Res 23:239

Adamson RH, Lenz JF, Zhang X, Adamson GN, Weinbaum S, Curry FE (2004) Oncotic pressures opposing fi ltration across non-fenestrated rat microvessels. J Physiol 557:889–907

Adamson RH, Clark JF, Radeva M, Kheirolomoom A, Ferrara KW, Curry FE (2014) Albumin modulates S1P delivery from red blood cells in perfused microvessels: mechanism of the protein effect. Am J Physiol Heart Circ Physiol 306:H1011–H1017

Arkill KP, Knupp C, Michel CC, Neal CR, Qvortrup K, Rostgaard J et al (2011) Similar endothelial glycocalyx structures in microvessels from a range of mammalian tissues: evidence for a common filtering mechanism? Biophys J 101:1046–1056

Arkill KP, Neal CR, Mantell JM, Michel CC, Qvortrup K, Rostgaard J et al (2012) 3D reconstruction of the glycocalyx structure in mammalian capillaries using electron tomography. Microcirculation 19:343–351

Bai K, Wang W (2012) Spatio-temporal development of the endothelial glycocalyx layer and its mechanical property in vitro. J R Soc Interface 9:2290–2288

Bai K, Wang W (2014) Shear stress-induced redistribution of the glycocalyx on endothelial cells in vitro. Biomech Model Mechanobiol 13:303–311

Bert JL, Bowen BD, Reed RK (1988) Microvascular exchange and interstitial volume regulation in the rat: model validation. Am J Phys 254:H384–H399

Betteridge KB, Arkill KP, Neal CR, Harper SJ, Foster RR, Satchell SC, Bates DO, Salmon AHJ (2017) Sialic acids regulate microvessel permeability, revealed by novel in vivo studies of endothelial glycocalyx structure and function. J Physiol (London) 595:5015–5035

Bhalla G, Deen WM (2009) Effects of charge on osmotic reflection coefficients of macromolecules in fibrous membranes. Biophys J 97:1595–1605

Chen HI, Granger HG, Taylor AE (1976) Interaction of capillary, interstitial and lymphatic forces in the canine hind paw. Circ Res 39:245–254

Curry FE (1984) Mechanics and thermodynamics of transcapillary exchange. In: Renkin EM, Michel CC (eds) Handbook of physiology: microcirculation. American Physiological Society., Section 2, Vol. IV, Part 1, pp 309–374

Curry FE (2017) Layer upon layer: the functional consequences of disrupting the glycocalyx-endothelial barrier in vivo and in vitro. Cardiovasc Res 113:559–561

Curry FE, Adamson RH (2012) Endothelial glycocalyx: permeability barrier and mechanosensor. Ann Biomed Eng 40:828–839

Curry FE, Clark JF, Adamson RH (2012) Erythrocyte-derived sphingosine-1-phosphate stabilizes basal hydraulic conductivity and solute permeability in rat microvessels. Am J Physiol Heart Circ Physiol 303:H825–H834

Curry FE, Arkill KP, Michel CC (2016) The functions of endothelial glycocalyx and their effects on patient's outcomes during the perioperative period. A review of current methods to evaluate structure-function relations in the glycocalyx in both basic research and clinical settings. In: Farag E, Kunz A (eds) Perioperative fluid management, Chapter 3. Springer, Cham, pp 75–116

Damiano ER, Stace TM (2002) A mechano-electrochemical model of radial deformation of the capillary glycocalyx. Biophys J 82:1153–1175

Desjardins C, Duling BR (1990) Heparinase treatment suggests a role for the endothelial cell glycocalyx in regulation of capillary hematocrit. Am J Phys 258:H647–H654

Feng J, Weinbaum S (2000) Lubrication theory in highly compressible porous media: the mechanics of skiing, from red cells to humans. J Fluid Mech 422:281–317

Fridén V, Oveland E, Tenstad O, Ebefors K, Nyström J, Nilsson UA, Haraldsson B (2011) The glomerular endothelial cell coat is essential for glomerular filtration. Kidney Int 79:1322–1330

Gao L, Lipowsky HH (2010) Composition of the endothelial glycocalyx and its relation to its thickness and diffusion of small solutes. Microvasc Res 80:394–401

Guyton AC, Taylor AE, Brace RA (1976) A synthesis of interstitial fluid regulation and lymph formation. Fed Proc (8):1881–1885

Hegermann J, Lunsdorf H, Ochs M, Haller H (2016) Visualization of the glomerular endothelial glycocalyx by electron microscopy using cationic colloidal thorium dioxide. Histochem Cell Biol 145:41–51

Jabaley C, Dudaryk R (2014) Fluid resuscitation for trauma patients: crystalloids versus colloids. Curr Anesthesiol Rep 4:216–224

Kedem O, Katchalsky A (1963) Permeability of composite membranes. Trans Faraday Soc 59:1931–1953

Landis EM (1927) Microinjection studies of capillary permeability. II. The relation between capillary pressure and the rate of which fluid passes through the walls of single capillaries. Am J Phys 82:217–238

Landis EM, Pappenheimer JR (1963) Exchange of substances through the capillary walls, Chap. 29. In: Hamilton WF, Dow P (eds) Handbook of physiology, sect. 2, vol. 2. Circulation. Washington, DC: American Physiological Society, pp 961–1034

Levick JR (1991) Capillary filtration-absorption balance reconsidered in light of dynamic extravascular factors. Exp Physiol 76:825–857

Levick JR (1994) An analysis of the interaction between interstitial plasma protein, interstitial flow, and fenestral filtration and its application to synovium. Microvasc Res 47:90–125

Levick JR, McDonald JN (1994) Viscous and osmotically mediated changes in fluid movement across synovium in response to intraarticular albumin. Microvasc Res 47:68–89

Levick JR, Michel CC (2010) Microvascular fluid exchange and the revised starling principle. Cardiovasc Res 87:198–210

Lipowsky HH, Lescanic A (2017) Inhibition of inflammation induced shedding of the endothelial glycocalyx with low molecular weight heparin. Microvasc Res 112:72–78

Michel CC (1984) Fluid movements through capillary walls. In: Renkin EM, Michel CC (eds) Handbook of physiology. The cardiovascular system, vol. 4, microcirculation, part 1. Bethesda: American Physiological Society, pp 375–409

Michel CC (1988) Capillary permeability and how it may change. J Physiol 404:1–29

Michel CC (1997) Starling: the formulation of his hypothesis of microvascular fluid exchange and its significance after 100 years. Exp Physiol 82(1):1–30

Michel CC, Curry FR (2009) Glycocalyx volume: a critical review of tracer dilution methods for its measurement. Microcirculation 16:213–219

Michel CC, Phillips ME (1987) Steady-state fluid filtration at different capillary pressures in perfused frog mesenteric capillaries. J Physiol 388:421–435

Michel CC, Mason JC, Curry FE, Tooke JE, Hunter PJ (1974) A development of the Landis technique for measuring the filtration coefficient of individual capillaries in the frog mesentery. Q J Exp Physiol Cogn Med Sci 59:283–309

Michel CC, Phillips ME, Turner MR (1985) The effects of native and modified bovine serum albumin on the permeability of frog mesenteric capillaries. J Physiol 360:333–346

Michel CC, Arkill KP, Curry FE (2016) The revised Starling principle and its relevance to peri-operative fluid management. In: Farag E, Kunz A (eds) Perioperative fluid management springer (Cham, Switzerland) Chapter 2, pp 31–74

Ogston AG, Preston BN, Wells JD (1973) On the transport of compact particles through solutions of chain-polymers. Proc R, Soc London Ser A 333:297–316

Pang Z, Tarbell JM (2003) In vitro study of Starling's hypothesis in a cultured monolayer of bovine aortic endothelial cells. J Vasc Res 40:351–358

Pappenheimer JR, Soto-Rivera A (1948) Effective osmotic pressure of the plasma proteins and other quantities associated with the capillary circulation in the hind limbs of cats and dogs. Am J Physiol 152:471–491

Preston BN, Davies M, Ogston AG (1965) The composition and physicochemical properties of hyaluronic acids prepared from ox synovial fluid and from a case of mesothelioma. Biochem J 96:449–474

Reitsma S, Slaaf DW, Vink H, van Zandvoort MA, Oude Egbrink MG (2007) The endothelial glycocalyx: composition, functions, and visualization. Pflugers Arch 454:345–359

Renkin EM (1986) Some consequences of capillary permeability to macromolecules; Starling's hypothesis reconsidered. Am J Phys 250:H706–H710

Rostgaard J, Qvortrup K (1997) Electron microscopic demonstrations of filamentous molecular sieve plugs in capillary fenestrae. Microvasc Res 53:1–13

Schmidt EP, Li G, Li L, Fu L, Yang Y, Overdier KH et al (2014) The circulating glycosaminoglycan signature of respiratory failure in critically ill adults. J Biol Chem 289:8194–8202

Secomb TW, Hsu R, Pries AR (2001) Motion of red blood cells in a capillary with an endothelial surface layer: effect of flow velocity. Am J Physiol Heart Circ Physiol 281:H629–H636

Squire JM, Chew M, Nneji G, Neal C, Barry J, Michel C (2001) Quasi-periodic substructure in themicrovessel endothelial glycocalyx: a possible explanation for molecular filtering? J Struct Biol 136:239–355

Tarbell JM, Shi ZD, Dunn J, Jo H (2014a) Fluid mechanics, arterial disease, and gene expression. Annu Rev Fluid Mech 46:591–614

Tarbell JM, Simon SI, Curry FR (2014b) Mechanosensing at the vascular interface. Annu Rev Biomed Eng 16:505–532

Van Teeffelen JW, Brands J, Stroes ES, Vink H (2007) Endothelial glycocalyx: sweet shield of bloodvessels. Trends Cardiovasc Med 17:101–105

Vink H, Duling BR (2000) Capillary endothelial surface layer selectively reduces plasma solute distribution volume. Am J Physiol Heart Circ Physiol 278:H285–289

Weinbaum S (1998) Distinguished Lecture Models to solve the mysteries of biomechanics at cellular level. A new view of fiber-matrix layers. Ann Biomed Eng 26:627–643

Weinbaum S, Zhang X, Han Y, Vink H, Cowin SC (2003) Mechanotransduction and flow across the endothelial glycocalyx. Proc Natl Acad Sci U S A 100:7988–7995

Weinbaum S, Tarbell JM, Damiano ER (2007) The structure and function of the endothelial glycocalyx layer. Annu Rev Biomed Eng 9:121–167

Woodcock TE, Woodcock TM (2012) Revised Starling equation and the glycocalyx model of transvascular fluid exchange: an improved paradigm for prescribing intravenous fluid therapy. Br J Anaesth 108: 384–394

Zeng Y, Ebong EE, Fu BM, Tarbell JM (2012) The structural stability of the endothelial glycocalyx after enzymatic removal of glycosaminoglycans. PLoS One 7(8):e43168

Zeng Y, Adamson RH, Curry FE (2014) And Tarbell JM Sphingosine-1- phosphate protects endothelial glycocalyx by inhibiting syndecan-1 shedding. Am J Physiol Heart Circ Physiol 306:H363–H372

Zhang X, Adamson RH, Curry FE, Weinbaum S (2008) Transient regulation of transport by pericytes in venular microvessels via trapped microdomains. Proc Natl Acad Sci U S A 105:1374–1379

Zhang L, Zeng M, Fan J, Tarbell JM, Curry FE, Fu BM (2016) Sphingosine-1-phosphate maintains normal vascular permeability by preserving endothelial surface Glycocalyx in intact microvessels. Microcirculation 23:301–310

Role of the Glycocalyx as a Barrier to Leukocyte-Endothelium Adhesion

Herbert H. Lipowsky

Abstract

Leukocyte (WBC) to endothelial cell (EC) adhesion is a receptor-mediated process governed by the avidity and affinity of selectins, which modulate adhesive forces during WBC rolling, and integrins, which determine the strength of firm adhesion. Adhesion receptors on the EC surface lie below an endothelial surface layer (ESL) comprised of the EC glycocalyx and adsorbed proteins which, in vivo, have a thickness on the order 500 nm. The glycocalyx consists of a matrix of the glycosaminoglycans heparan sulfate and chondroitin sulfate, bound to proteoglycans and encased in hyaluronan. Together, these carbohydrates form a layer that varies in glycan content along the length of post-capillary venules where WBC-EC adhesion occurs. Thickness and porosity of the glycocalyx can vary dramatically during the inflammatory response as observed by increased infiltration and diffusion of macromolecules within the layer following activation of the EC by cytokines and chemoattractants. In models of inflammation in the living animal, the shedding of glycans and diminished thickness of the glycocalyx rapidly occur to facilitate penetration by the WBCs and adhesion to the EC. The primary effectors of glycan shedding appear to be metalloproteases and heparanase released by the EC. Retardation of glycan shedding and WBC-EC adhesion has been demonstrated in vivo using MMP inhibitors and low-molecular-weight heparin (LMWH), where the latter competitively binds to heparanase liberated by the EC. Together, these agents may serve to stabilize the ESL and provide a useful strategy for treatment of inflammatory disorders.

1 Introduction

The inflammatory process revolves around a sequence of events that leads to emigration of leukocytes (WBCs) through the microvascular wall into the tissue space. Convective transport of WBCs to the microvasculature leads to their radial migration to the microvessel wall (margination), rolling along the endothelium and firm adhesion to the endothelium (EC) prior to diapedesis (Atherton and Born 1972, 1973; Grant 1973), as depicted in Fig. 1. As blood traverses the arteriolar network, hemodynamic

H. H. Lipowsky (✉)
Department of Biomedical Engineering, Penn State University, University Park, PA, USA
e-mail: hhlbio@engr.psu.edu

B. M. Fu, N. T. Wright (eds.), *Molecular, Cellular, and Tissue Engineering of the Vascular System*, Advances in Experimental Medicine and Biology 1097,
https://doi.org/10.1007/978-3-319-96445-4_3

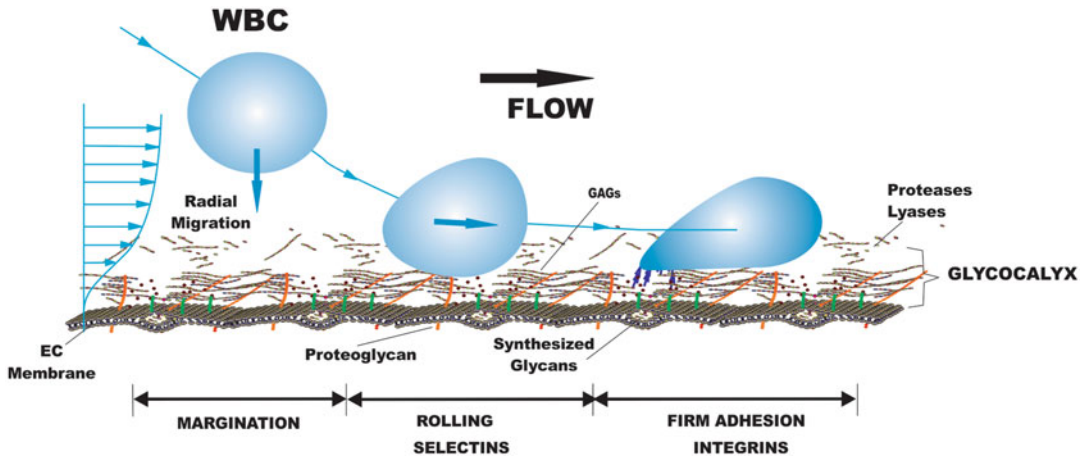

Fig. 1 Leukocyte-endothelium adhesion in post-capillary venules is an essential step in the inflammatory process. As WBCs exit the capillaries, hemodynamic forces and interactions with red cells cause the radial migration of WBCs to the EC surface (margination) with subsequent rolling along and firm adhesion to the EC. WBC rolling is facilitated by the selectin family of adhesion molecules that maintains WBC contact with the EC surface. Arrest and firm adhesion follow due to the strong adhesion mediated by integrins on the WBC and their receptors on the EC. The selectins and integrin receptors are buried within the endothelial surface layer (ESL) that consists of the EC glycocalyx and adsorbed proteins. The ESL is typically about 500 nm thick and shields selectins and integrin receptors that protrude from 20 to 40 nm above the EC membrane

and topographical features promote WBC-EC interaction (Bagge and Karlsson 1980; Braide et al. 1984; Goldsmith and Spain 1984; Schmid-Schonbein et al. 1980). As blood exits from capillaries to post-capillary venules, WBC radial migration to the EC occurs due to hemodynamic forces and red blood cell (RBC) interactions (Schmid-Schonbein et al. 1980). Rolling of WBCs on the EC is then promoted by adhesive interactions with the molecular surface layer on the EC and receptor-mediated adhesion with the selectin family of carbohydrates (Springer and Lasky 1991). Subsequent firm adhesion of WBCs ensues due to receptor-mediated adhesion of integrins on the WBC surface to counter receptors on the EC (Zarbock and Ley 2009; Springer 1990). Successful completion of the adhesion process hinges on the availability of ligands in the EC surface layer (ESL) formed by the EC glycocalyx and adsorbed proteins (Pries et al. 2000; Reitsma et al. 2007; Weinbaum et al. 2007).

The interface between blood and endothelium has been of interest for decades in light of its role in inflammation, permeability to macromolecules, and thrombosis. Early studies on the structural makeup of the capillary wall drew attention to the surface of the endothelium as an essential part of the "hematoparenchymal barrier" (Zweifach 1955). The observations of microvascular function recognized that endothelial cells continuously secrete substances that form an "intercellular cement" and the basement membrane. With advances in intravital microscopy, direct visualization of the dynamics of blood-endothelial cell (EC) interactions in the microcirculation led to hypotheses to explain the basis for blood cell to EC adhesion, the clotting of blood, and the transvascular exchange of fluid and macromolecules. It is now recognized that the surface of the endothelium is coated with a layer of polysaccharides and transmembrane proteins, as described in Chap. 1, that was subsequently visualized by electron microscopy by Bennett and others (Bennett et al. 1959; Luft 1966). In view of its predominant polysaccharide constituents, Bennett (Bennett et al. 1959) termed it the "glycocalyx," as derived from the Latin for "sweet husk." Initially viewed as an extension of the endothelial cell basement membrane onto the luminal surface of the EC, the fine structure of the glycocalyx has been described as a network

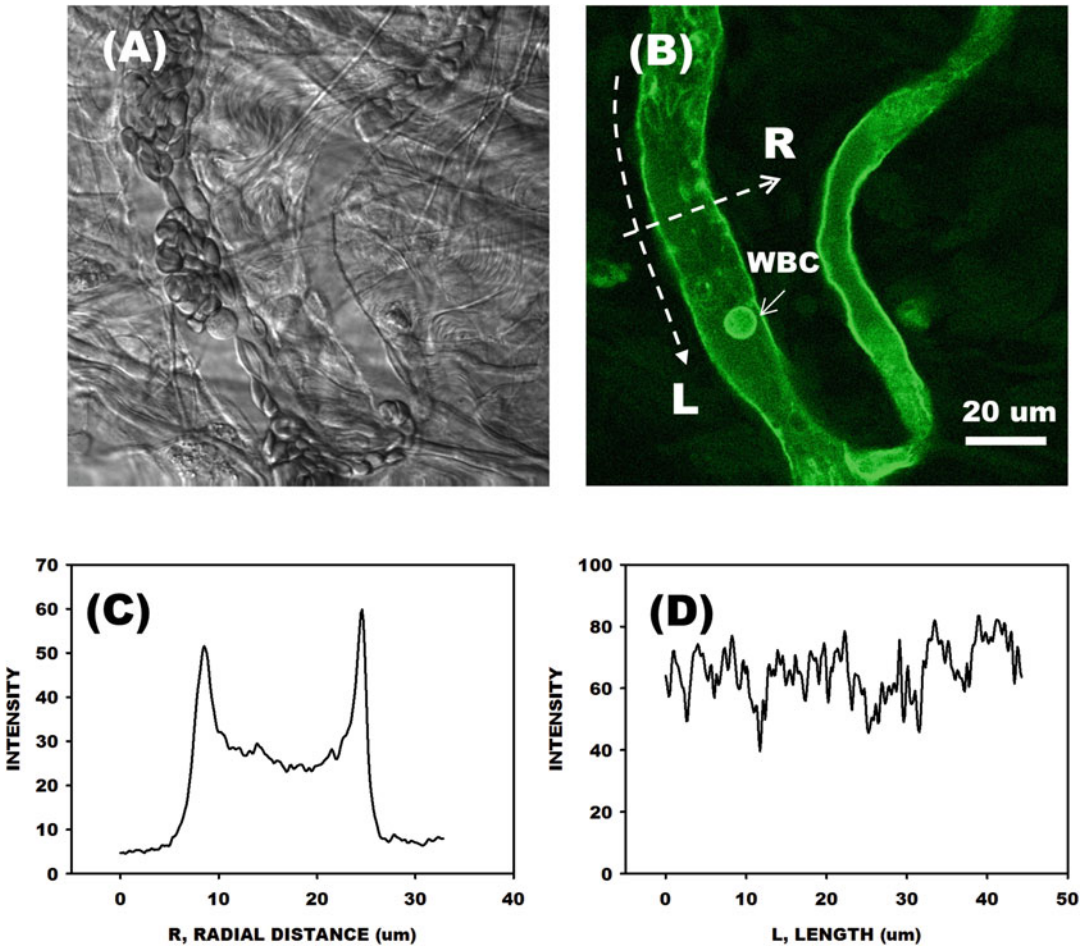

Fig. 2 Visualization of the endothelial glycocalyx. (**a**) Bright-field view of post-capillary venules in mesentery of the rat. (**b**) Fluorescence microscopy of the glycocalyx labeled with the fluorescently labeled lectin BS-1. (**c**) The average radial profile of fluorescence along the measurement line R shows a peak value at each wall with intensity proportional to the concentration of lectins bound to the EC surface. Reductions in peak fluorescence were taken as a measure of the shedding of glycans from the EC surface. (**d**) Variation of fluorescence intensity with length L along a wall varies ±50% as shown for the wall next to the dashed line

of glycoproteins on the order of 50–100 nm thick, with a characteristic spacing of 20 nm that accounts for the resistance to filtration of small molecules (Squire et al. 2001). Recognition that the EC surface contains an abundance of negatively charged carbohydrates (Simionescu et al. 1982) led to the use of lectins to visualize the endothelial surface layer (Schnitzer et al. 1990a). Visualization of the glycocalyx with lectin staining is illustrated in Fig. 2, where the surface of post-capillary venules is stained with the fluorescently labeled lectin BS-1 (*Bandeiraea simplicifolia*) (Mulivor and Lipowsky 2004). Lectins are carbohydrate-binding proteins that may be used to loosely identify specific glycoproteins in the EC surface layer (Schnitzer et al. 1990b). As shown in Fig. 2a, staining of the glycocalyx reaches a maximum at the vessel walls. The average radial profile of fluorescence along the length of a microvessel reveals a peak intensity that is proportional to concentration of lectin-binding sites on the EC surface. Peak staining along the length of one wall (Fig. 2d) illustrates the variability of glycans on the surface, which

may vary ±50% about the mean. As shown in the following, peak intensity of glycan staining may be used to quantify the shedding of glycans during the inflammatory process and changes in glycan concentration with hemodynamic (shear) conditions.

2 Microvascular Hemodynamics

Historically, the role of the glycocalyx in affecting microvascular hemodynamics arose from the seminal studies of Klitzman and Duling (1979) and Desjardin and Duling (1990) in their studies of the basis for the anomalous levels of capillary hematocrit observed in most tissues by intravital microscopy. At that time, studies subsequent to the pioneering observations of reduced small vessel hematocrit by Poiseuille (1835) and Fahraeus (1929) noted reductions in capillary hematocrit that were well below 50% of systemic values (Pries et al. 1990; House and Lipowsky 1987a). Average values of capillary hematocrit on the order of 10–20% of systemic hematocrit far exceeded the hypothetical maximum reduction of 50%, based upon red cell velocity profiles in small tubes (Sutera et al. 1970) where, for a parabolic velocity profile, peak velocity along the vessel center line may reach a maximum of twice the mean velocity. Klitzman and Duling (1979) hypothesized that the low capillary hematocrits arose from retardation of fluid on the endothelial cell surface. To validate this hypothesis and explore the role of the glycocalyx in contributing to the anomalous low capillary hematocrits, Desjardin and Duling (1990) inserted finely drawn micropipettes into feeding vessels and perfused individual capillaries with heparinase to strip off the glycocalyx. Their results showed a twofold rise in capillary hematocrit, presumably due to the resultant increase in the effective capillary diameter with degradation of the glycocalyx. Subsequent studies have shown increases in capillary hematocrit in response to its removal by perfusion with hyaluronidase (Cabrales et al. 2007) or degradation due to the presence of reactive oxygen species derived from oxidized LDL (Constantinescu et al. 2001).

To delineate the hemodynamic significance of the glycocalyx insofar as it affects the resistance to blood flow, studies have explored the effects of its enzymatic removal by direct intravital microscopy. Measurements by Pries et al. of regional pressure drops and flows in the mesenteric microvasculature following enzymatic removal of the glycocalyx, by perfusion with heparinase, suggested a 14–20% decrease in the resistance to flow (Pries et al. 1997). Their analysis of this diminished resistance suggested that removal of the glycocalyx theoretically increased microvessel diameter throughout the network by about 1 μm. Consistent with these findings, a hydrodynamically significant glycocalyx has been explicitly shown by analysis of the velocity profiles of small fluorescent microspheres in the in vivo microcirculation using techniques of particle image velocimetry (PIV) (Potter and Damiano 2008; Smith et al. 2003). Within small venules in the exteriorized cremaster muscle, these studies revealed a glycocalyx thickness on the order of about 0.3–0.4 μm which displaces blood flow from the surface of the endothelium. In contrast, similar applications of PIV to analysis of particle flow over cultured human umbilical vein and bovine aortic endothelial cells revealed hydrodynamically significant thicknesses of only 0.03 and 0.02 μm, respectively (Smith et al. 2003). Thus, in vitro models clearly fail to replicate the in vivo structure of the glycocalyx.

3 Structure of the Glycocalyx

As discussed in Chap. 1, several studies to date have reviewed the structure of the endothelial glycocalyx (Pries et al. 2000; Reitsma et al. 2007; Weinbaum et al. 2007; Chappell et al. 2009a; Gotte 2003). Salient features relevant to WBC adhesion may be summarized as follows. The most prominent components of the glycocalyx are the glycosaminoglycans (GAGs) heparan sulfate (HS), chondroitin sulfate (CS), and hyaluronan (HA). The GAGs HS and CS are covalently

linked to membrane-bound proteoglycans (PGs). Sulfate groups on HS and CS confer a negative charge to these GAGs. The density of GAGs on PGs and glycoproteins varies considerably (Reitsma et al. 2007), and each PG may carry multiple chains of HS and CS, with a ratio of HS/CS of about 4:1 (Rapraeger 1989), and their sulfation level may change depending on the physiological microenvironment (Rapraeger 1989; Vogl-Willis and Edwards 2004). HA does not possess sulfate groups and is not covalently linked to a proteoglycan core protein but is held in place by specific hyaluronan-binding proteins (Laurent and Fraser 1992). In addition to GAG-carrying proteoglycans, adsorbed blood-borne soluble proteins comprise substantial components of the glycocalyx and may be decreased by removing plasma proteins (Adamson and Clough 1992; Huxley and Curry 1991). Under normal physiological conditions, the structure of the glycocalyx layer is stable, and its molecular composition represents a dynamic balance between continued biosynthesis of new glycans and shear-dependent alterations.

Studies of the dimensions and structure of the endothelial glycocalyx have been confounded by the methods of fixation and source of the cells studied (Pries et al. 2000; Reitsma et al. 2007). In vivo observations by direct microscopy have revealed an apparent thickness of the glycocalyx, estimated by the exclusion of erythrocytes and macromolecules (Vink and Duling 1996), on the order of 400–500 nm, which significantly exceeds the dimensions obtained in either fixed specimens or cultured cells. In vitro models with cultured ECs fail to express a glycocalyx of thickness comparable to that found ex vivo (Chappell et al. 2009a). As shown therein, electron microscopy studies of fixed umbilical vein EC revealed a glycocalyx with an average thickness of 878 nm, whereas cultured HUVECs revealed a glycocalyx thickness ranging from only 29 to 118 nm.

Direct measurement of glycocalyx thickness in post-capillary venules by intravital microscopy is technically challenging. In the case of capillaries with single-file motion of RBCs, the width of the red cell column can be easily distinguished from the anatomical capillary diameter (Vink and Duling 1996) to reveal a distance to the EC surface of about 500 μm. As shown therein, infusion of fluorescently labeled 70 kDa dextran (Dx70) revealed a lesser gap between the edge of the fluorescent column and the EC on the order of 400 nm. With cessation of flow, RBCs could be observed to infiltrate the dextran exclusion space completely with zero gap. Mathematical modeling of fluid flow in the glycocalyx suggests that fluid dynamical pressures generated within the glycocalyx can lead to variations of red cell shape and gap width with flow velocity (Feng and Weinbaum 2000; Secomb et al. 2001) that are consistent with in vivo observations (Vink and Duling 1996). Studies of the width of the molecular exclusion zone in capillaries (Vink and Duling 2000) revealed that the edge of the dye column is both charge and molecule size dependent. However, anionic and neutral Dx70 maintained a discrete distance from the EC surface. Application of such techniques has been applied to measure the thickness of the glycocalyx in venules, where WBC-EC adhesion occurs (Gao and Lipowsky 2010). As shown in Fig. 3a for a 35 μm venule, the RBC column is surrounded by a plasma layer that extends to the outer edge of a dark refractive band on the EC surface. Following the infusion of fluorescently labeled Dx70 (Fig. 3b), the edge of the dye column becomes diffuse due to the relatively large diameter and path length along the optical axis. To objectively demarcate the dye exclusion zone, a sigmoidal fit of the radial intensity distribution was made (Fig. 3c) and the edge of the glycocalyx taken as the location of its inflection point. The thickness of the glycocalyx was calculated as the distance between the inflection point and the outer edge of the dark refractive band.

Shown in Fig. 3d are measurements of the thickness of this barrier to infiltration of Dx70 under controlled conditions and following infusion of enzymes to remove specific GAGs from the EC surface. Individually, all three major enzymes significantly reduced the layer thickness below its normal 500 μm level, with heparinase having the greatest effect. A mixture of all three enzymes reduced the layer thickness

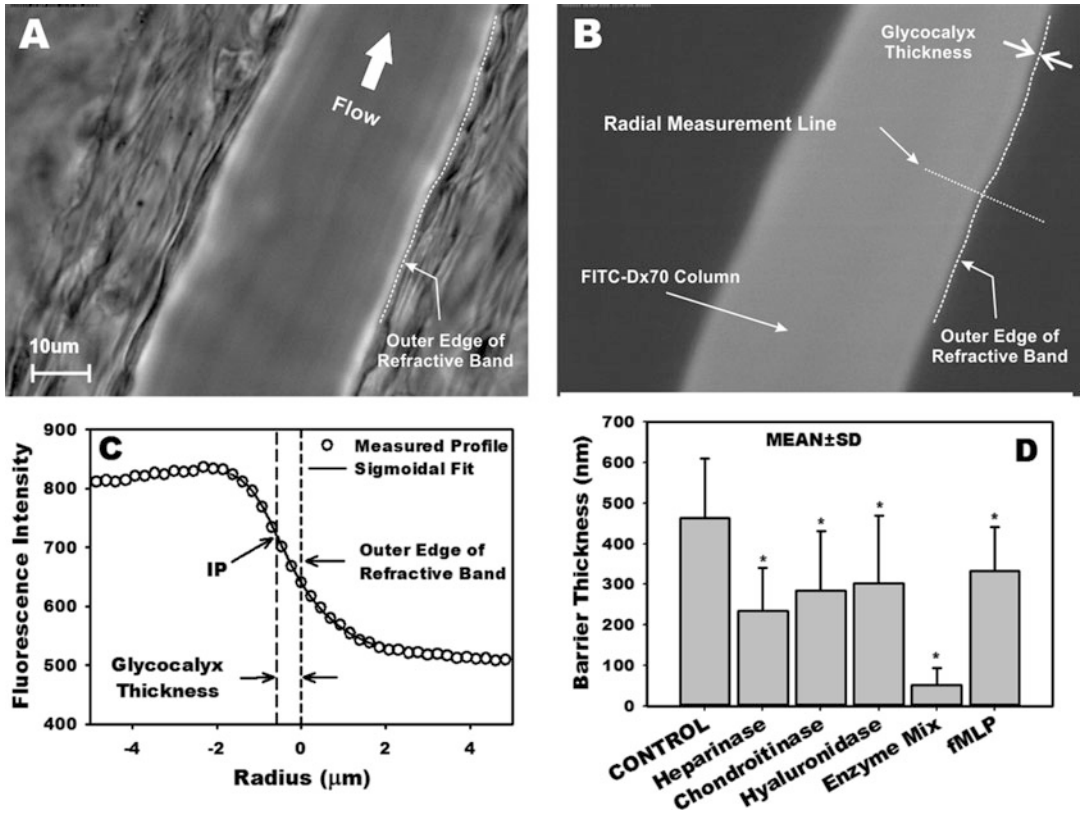

Fig. 3 Measurement of the thickness of the glycocalyx in a 35 μm diameter venule. (**a**) Bright-field view reveals the plasma layer that surrounds the red cell (RBC) core. A dark refractive band can be seen near the EC surface. The outer edge of this band is at the EC surface. (**b**) Circulating fluorescently labeled 70 kDa dextran is shown under fluorescence microscopy and infiltrates the gap between the RBC core and EC surface. (**c**) Radial distribution of dextran fluorescence intensity exhibits a sigmoidal distribution between the RBC column and EC surface (outer edge of the dark refractive band) due to the varying path length along the optical axis. An objective measure of the thickness of the glycocalyx was taken as the distance between the intensity inflection point (IP) and outer edge of the refractive band. (**d**) Thickness was observed to be significantly ($*p < 0.05$) reduced following infusion (by micropipette) with either heparanase, chondroitinase, or hyaluronidase and reduced by 90% with a mixture of all three enzymes. Activation of the endothelium with fMLP significantly reduced thickness due to shedding of glycans. Reproduced from Gao and Lipowsky (2010), with permission

by almost 90%. Accounting for cross-reactivity of the enzymes resulted in (by solving the simultaneous algebraic equations for each GAG) contributions to the thicknesses of the barrier of 43.3, 34.1, and 12.3%, for HS, CS, and HA, respectively. Thus, heparan sulfate appears to represent the major component of the glycocalyx. To simulate changes in the structure of the glycocalyx anticipated in the inflammatory response, the chemoattractant fMLP was topically applied (Fig. 3d) and revealed a significant 28% reduction in glycocalyx thickness that was not significantly different from the losses due to enzymatic cleavage.

Reductions in intensity of lectin staining of the glycocalyx due to fMLP have been correlated with the shedding of glycans (Mulivor and Lipowsky 2004). Loss of glycans has been correlated with increased infiltration of macromolecules in the surface layer in response to the cytokine TNF-α (Henry and Duling 1999, 2000). Quantitative estimates of changes in the

porosity of the ESL have been made by calculation of the diffusion coefficients (D) of the small fluorescent molecule fluorescein isothiocyanate (FITC, 350 Da) by applying a 1-D diffusion model to measurements of radial concentration gradients in the ESL (Gao and Lipowsky 2010). By comparison of measured transients in radial intensity of a bolus of FITC with that of a computational model, a diffusion coefficient D was obtained. Values of D were obtained corresponding to the thickness of the layer demarcated by Dx70 (D_{Dx70}), and a smaller sublayer 173 nm above the EC surface (D_{173}), prior to and following enzyme infusion and superfusion with fMLP. The magnitude of D_{Dx70} was twice that of D_{173} suggesting that the glycocalyx is more compact near the EC surface. Chondroitinase and hyaluronidase significantly increased both D_{Dx70} and D_{173}. However, heparinase decreased D_{Dx70} and did not induce any significant change for the D_{173}. These observations suggest that the three GAGs are not evenly distributed throughout the glycocalyx and that they each contribute to permeability of the glycocalyx to a differing extent.

4 Shedding of the Glycocalyx

Functional changes in the barrier formed by the ESL have been observed in response to a broad spectrum of agents. Topical stimulation of the endothelium for prolonged periods (20–120 min) with the cytokine TNF-α results in an increased porosity of the glycocalyx in the absence of WBC-EC adhesion (Henry and Duling 2000). Significant shedding of components of the glycocalyx in coronary vessels has been observed following perfusion of isolated hearts for 20 min with TNF-α, which was lessened by the serine protease inhibitor antithrombin III (Chappell et al. 2009b). Acute activation of the endothelium in post-capillary venules with the chemoattractant fMLP induced a rapid (<5 min) shedding of glycans from the EC surface as evidenced by a loss of lectin-laden microspheres bound to the EC surface (Mulivor and Lipowsky 2004). Shedding of proteoglycans and GAGs from cultured endothelial cells, or their analogs, occurs in response to a broad spectrum of agonists (Park et al. 2000; Colburn et al. 1994; Fux et al. 2009; Ihrcke et al. 1993; Platt et al. 1990, 1991; Fitzgerald et al. 2000). Shedding of heparan sulfate proteoglycans (namely, the ectodomain of syndecans 1–4) occurs in response to endotoxin (Colburn et al. 1994), serine and/or cysteine proteinases (Ihrcke and Platt 1996), complement activation (Platt et al. 1991), thrombin and growth factors (Subramanian et al. 1997), and activation of protein tyrosine kinase by phorbol ester (Fitzgerald et al. 2000). Using hydroxamic acid inhibitors of matrix metalloproteinases, it has been shown that proteolytic cleavage of the syndecan ectodomain results from the convergence of multiple intracellular pathways that activate a cell surface metalloproteinase (Fitzgerald et al. 2000).

In vivo, shedding of the endothelial glycocalyx has been found in response to inflammation (Mulivor and Lipowsky 2004; Henry and Duling 2000), hyperglycemia (Zuurbier et al. 2005), endotoxemia and septic shock (Hofmann-Kiefer et al. 2009), presence of oxidized LDL (Constantinescu et al. 2001), TNFα (Chappell et al. 2009b), atrial natriuretic peptide (Bruegger et al. 2005), abnormal blood shear stress (Gouverneur et al. 2006; Haldenby et al. 1994), ischemia-reperfusion injury (Mulivor and Lipowsky 2004), light-induced production of free radicals (Vink and Duling 1996), and bypass surgery (Rehm et al. 2007; Svennevig et al. 2008). These observations have led to an underlying connection between integrity of the glycocalyx and vascular homeostasis (Mulivor and Lipowsky 2004; Zuurbier et al. 2005).

Shedding of the glycocalyx in response to cytokines and chemoattractants occurs in all three principal divisions of the microvasculature: arterioles (Henry and Duling 2000), capillaries (Constantinescu et al. 2001; Henry and Duling 2000), and venules (Mulivor and Lipowsky 2004; Henry and Duling 2000). To illustrate, shown in Fig. 4 is the intensity of glycans in the ESL stained with a fluorescently labeled lectin (BS-1) in the three principal divisions of the mesenteric microvasculature (rat) (Lipowsky et al. 2011).

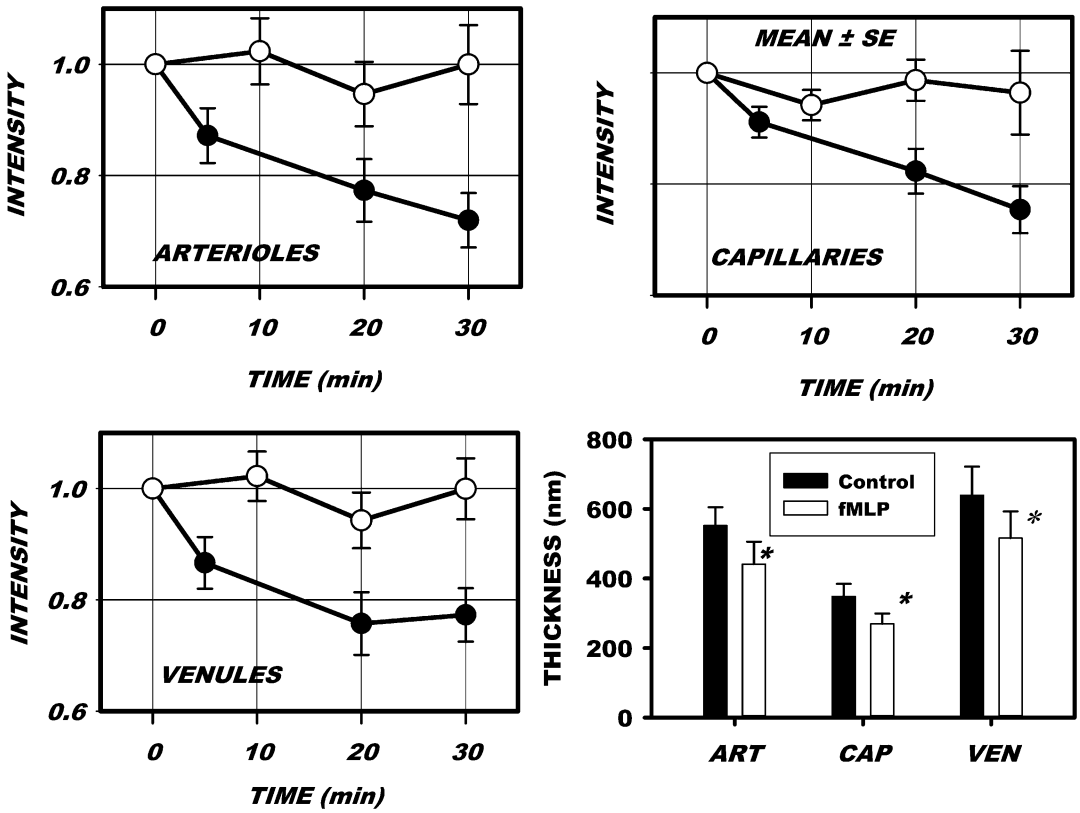

Fig. 4 Shedding of glycans on the EC surface of post-capillary venules in mesentery (rat) in response to topical application of the chemoattractant fMLP (10^{-7} M) compared to control values obtained with superfusion of the tissue with Ringer's solution. Glycan concentration was assumed proportional to the intensity of fluorescently labeled lectin (BS-1) on the EC surface and normalized to initial values. Shown are mean values ± SE for arterioles, capillaries, and venules. Intensity of the lectin stain falls rapidly within the first 5 min of onset of the fMLP and steadily decreases during the entire observation period. After 30 min exposure to fMLP, thickness of the glycocalyx decreased significantly ($*p < 0.05$). Data are mean ± SE. From Lipowsky et al. (2011), with permission

The normalized intensity is shown under resting conditions and following topical application of the chemoattractant fMLP (10^{-7} M). About 30% of all lectin-stained glycans were shed from the EC during a 30 min exposure to fMLP. This shedding appears to be accompanied by a significant reduction in thickness in each division (Fig. 4d). Although it has been postulated that such reductions in thickness are insufficient to expose WBC adhesion receptors (Marki et al. 2015), concomitant increases in porosity (Henry and Duling 1999, 2000) and deformability (Padberg et al. 2014; Wiesinger et al. 2013) of the ESL may promote WBC infiltration and adhesion during inflammation.

5 Enzymatic Cleavage of the Glycocalyx

With the majority of WBC adhesion receptors situated in post-capillary venules, as, for example, in the case of ICAM-1 (Iigo et al. 1997), shedding of the venular glycocalyx may play an important role in the inflammatory process. The cellular signaling cascades resulting from pathological conditions and initiating shedding of the glycocalyx are not fully understood. However, direct in situ observations of shedding in post-capillary venules suggest that several key enzymes may be responsible for shedding of the glycocalyx components (Mulivor and Lipowsky

2009). Matrix metalloproteases (MMPs) on the surface of the venular endothelium are rapidly activated by superfusion of the mesenteric tissue with fMLP and may be inhibited by superfusion with subantimicrobial doses (0.5 μM) of the antibiotic doxycycline (Mulivor and Lipowsky 2009). The inhibitory activity of doxycycline on shedding results from its direct effect on MMP activation and not by its ability to chelate divalent cations (Lipowsky et al. 2011), as evidenced by inhibition of MMP activation by the zinc-chelating hydroxamic acid inhibitor GM6001, and lack of inhibition by chelation of cations with EDTA. The possible role of doxycycline as a scavenger of reactive oxygen species (ROS) has been raised (Golub et al. 1998). However, direct evidence that ROS cause shedding in response to chemoattractants or cytokines remains to be obtained. In addition, MMP inhibition has been shown to have no effect on ROS-induced shedding (Lipowsky and Lescanic 2013).

Fluid shear stresses acting on the EC surface may affect the structure of the glycocalyx by either disrupting molecular constituents, affecting biosynthesis of new components, or activating proteases and lyases synthesized by the endothelium (Mulivor and Lipowsky 2004; Arisaka et al. 1995). Increased synthesis of GAGs by cultured monolayers of ECs occurs with prolonged exposure to high shear stresses of 15 or 40 dyn/cm^2 (Arisaka et al. 1995). These results were in contrast to prior studies that revealed a decrease in proteoglycan synthesis when ECs were cultured under low levels of shear stress (Grimm et al. 1988). In vivo studies of the accumulation of glycans on the surface of post-capillary venules during a 1 h period of ischemia demonstrated a 15–40% increase in glycan content on the surface of the EC (Mulivor and Lipowsky 2004). Upon reperfusion of these venules, this excess of surface glycans was washed out, and glycan levels (indicated by accumulation of lectins on the EC surface) momentarily fell below pre-ischemic (control) conditions before returning to normal levels. This postischemic fall below pre-ischemic levels was inhibited by superfusion of the tissue with pertussis toxin, thus suggesting a G-protein-mediated activation of enzymatic cleavage of GAGs and/or proteoglycans on the EC surface.

The hypothesis that matrix metalloproteinases (MMPs) may alter the endothelial glycocalyx and thus facilitate shedding under pathological conditions is well supported. Matrix metalloproteinases represent a family of over two dozen zinc-dependent proteases that play a role in normal tissue remodeling during bone growth, wound healing, reproduction, cancer, inflammation, and cardiovascular disease (Spinale 2007). MMPs (−1 and − 9) serve to cleave the endothelial insulin receptor and CD18 on leukocytes in the spontaneously hypertensive rat (DeLano and Schmid-Schonbein 2008). Oxidative stress in the diabetic heart may activate MMP-2 and lead to the development of diabetic cardiomyopathy (Yaras et al. 2008). Modification of the extracellular matrix by MMPs has been shown to be a critical step in angiogenesis (Haas et al. 2000) and atherosclerosis (Li et al. 1996). MMP-2, MMP-7, and MMP-9 were shown to be capable of directly cleaving chondroitin sulfate (Gronski et al. 1997). In addition, MMP-1 was shown to cleave the heparan sulfate proteoglycan syndecan-1 (Endo et al. 2003). MMPs can be stored within and released by the endothelium. It has been shown (Taraboletti et al. 2002) that both the active and proactive forms of MMP-2 and MMP-9 are stored in vesicles within the EC and both forms of MMP-7 have a high affinity for and bind to heparan sulfate (Yu and Woessner Jr 2000). Therefore, mechanisms exist by which MMP's may be rapidly released by endothelial cells. Innate inhibition of MMPs is derived from tissue inhibitors of metalloproteinases (TIMPs), a family of four different molecules made unique by their expression, localization, and inhibitory activity. Much like the MMPs, TIMPs are capable of binding heparan sulfate and chondroitin sulfate in the glycocalyx (Yu and Woessner Jr 2000).

The putative role of MMPs in cleaving glycans from the EC surface is supported by studies of in situ microzymography to quantify MMP activation on the surface of post-capillary venules (Mulivor and Lipowsky 2009). Hence,

it is likely that cleavage of GAG-bearing proteoglycans by either membrane-bound or cytosolic MMPs in the endothelial cell may be responsible for shedding of the glycocalyx. This hypothesis is also supported by studies of syndecan-1 shedding from human embryonic kidney cells caused by membrane type matrix metalloproteinase-1 (MT1-MMP) (Endo et al. 2003), shedding of syndecan-1 and syndecan-4 from HeLa tumor cells by MMP-9 (Brule et al. 2006), shedding of syndecan-1 from pancreatic carcinoma cells by MMP-7 (Ding et al. 2005), and shedding of syndecan-1 by MMP-7 during transmigration of neutrophils from the interstitium to alveoli in the lung (Li et al. 2002).

The effects of MMP inhibition on glycan shedding and WBC-EC adhesion in response to topical application of fMLP is illustrated in Fig. 5. Without MMP inhibition, fMLP induces a rapid (<10 min) shedding of glycans and an eightfold increase in the number of WBCs adhered to the walls of post-capillary venules (Mulivor and Lipowsky 2009). Superfusing the tissue with 0.5 μM. doxycycline results in a significant attenuation of glycan shedding and WBC-EC adhesion.

Whereas MMP activity presumably cleaves the protein core of GAG-bearing proteoglycans, cleavage of GAG chains by EC secretion of heparanase may also contribute to shedding (Chappell et al. 2008; Becker et al. 2015). Heparin has long been recognized as an inhibitor of heparanase activity (Bar-Ner et al. 1987), and considerable experimental and clinical evidence supports its anti-inflammatory activity (Page 2013). The anti-inflammatory properties of unfractionated and low-molecular-weight heparins (LMWH) have been studied extensively, although precise mechanisms have not been established (Oduah et al. 2016). Several studies have aimed to delineate the role of heparin in WBC-EC rolling and adhesion, and transmigration trough the microvessel wall. Treatment with LMWH dramatically diminished sepsis-induced neutrophil sequestration in the lung (Ning et al. 2015) and attenuated shedding of the glycocalyx in septic shock (Yini et al. 2015). Heparin has been reported to diminish or protect against reperfusion injury in various animal models (Young 2008). Intradermal administration of heparin attenuated eosinophil accumulation in response to inflammatory stimuli in a dose-dependent manner (Teixeira and Hellewell 1993). Binding of heparins to selectins (Koenig et al. 1998), WBCs (Page 2013; Diamond et al. 1995; Lever et al. 2000), and HSPGs and other constituents of the EC glycocalyx (Nordling et al. 2015; VanTeeffelen et al. 2007) has been shown to inhibit the inflammatory process. Use of low-molecular-weight heparin fractions has shown potential for protecting the endothelial glycocalyx from degradation in nephrosis (Gaddi et al. 2010), diabetes (Eskens et al. 2013), thrombosis (Daniels et al. 2006), retinal neovascularization (Jo et al. 2014), and inflammation (Becker et al. 2015; Kolarova et al. 2014). These studies found that the agent sulodexide, a mixture of low-molecular-weight heparin and dermatan sulfates, afforded significant protection of the glycocalyx from degradation.

The effects of graded concentrations of LMWH (Lovenox®, relative molecular mass, Mr. = 4500) on shedding of glycans and WBC-EC adhesion (Lipowsky and Lescanic 2017) are illustrated in Fig. 5b, d. With increasing doses of LMWH up to 0.22 mg/kg, competitive binding of LMWH to heparanase may attenuate the initial shedding of glycans due to fMLP. With greater doses (>0.6 mg/kg), glycan concentration appears to rise due to a compaction of the glycocalyx as HS chains are cleaved and the layer collapses. Eventually, the inhibition of shedding by LMWH is overwhelmed by activity of either MMPs, heparanase, or other sheddases. The WBC-EC adhesion response to fMLP (Fig. 5d) was significantly attenuated during the initial 10 min at the highest dose of LMWH but eventually rose with prolonged exposure to the chemoattractant. In these studies, WBC adhesion correlated with intensity of the lectin stain for all measurements and revealed a significant 40% reduction in adhesion as intensity increased 50%. This relationship was attributed to LMWH inhibition of heparanase and/or binding to

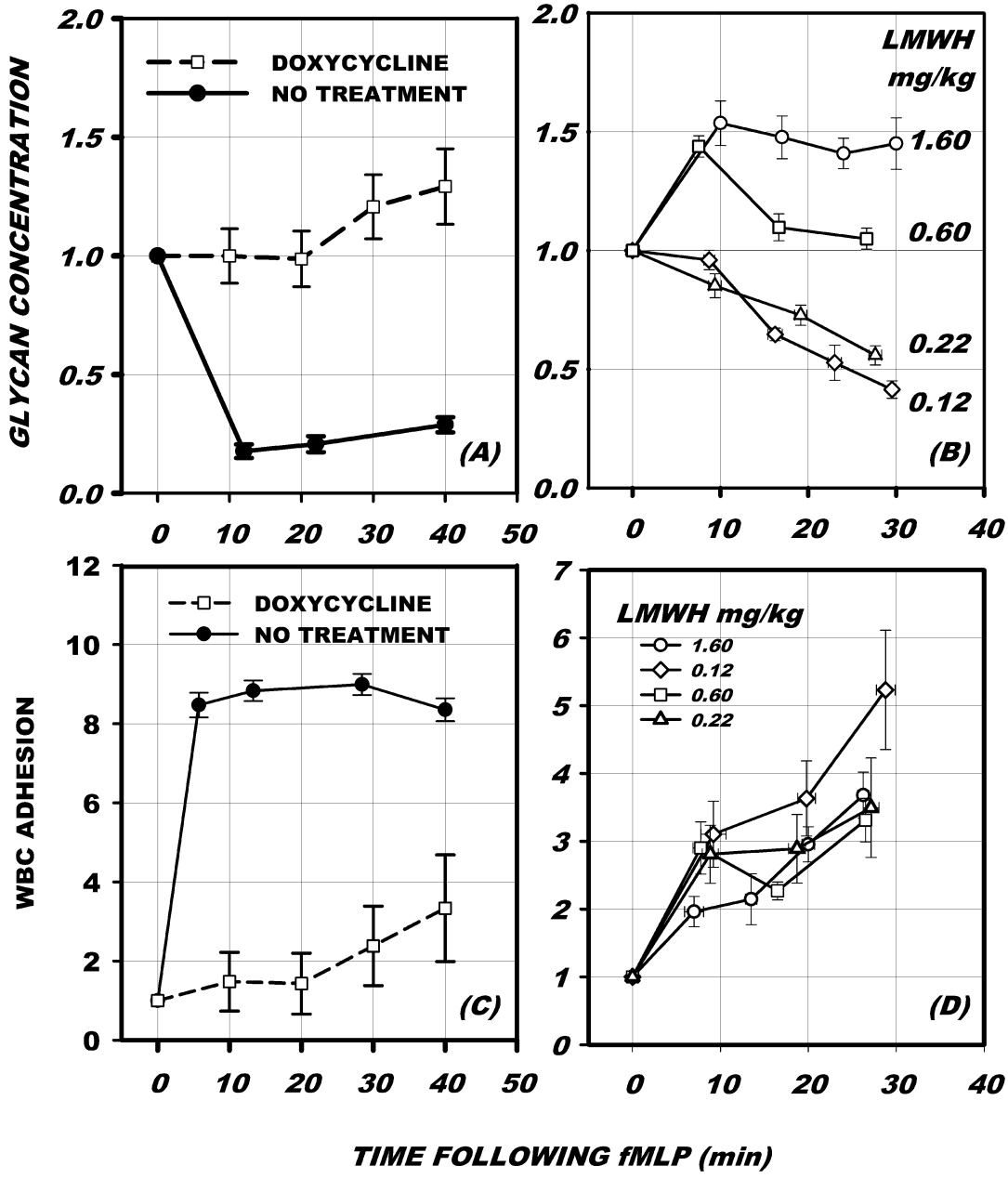

Fig. 5 Enzymatic shedding of the glycocalyx and WBC-EC adhesion in mesenteric venules. Glycan concentration was taken in proportion to the intensity of fluorescently labeled lectin (BS-1), normalized to initial values as a function of time following topical application of fMLP. (**a**) Glycan concentration in the glycocalyx fell dramatically following onset of fMLP stimulation. This fall was completely abolished by superfusion of the tissue with the MMP inhibitor doxycycline at a concentration of 0.5 μM. (**b**) Glycan concentration due to fMLP following IV administration of low-molecular-weight heparin (LMWH) of the indicated doses. Low doses (0.22 mg/kg) inhibited the initial fall during the first 10 min. High doses (>0.60 mg/kg) resulted in a rise in glycan concentration presumably due to ligation of HS chains and subsequent collapse of the glycocalyx. (**c**). The WBC-EC adhesion response to fMLP, with and without superfusion with doxycycline. (**d**) WBC-EC adhesion with infusion of LMWH. The high dose of LMWH initially delayed the rise in WBC-EC adhesion. Data are means ± SE. (**a**) and (**c**) redrawn from Mulivor et al. (Atherton and Born 1972); (**b**) and (**d**) redrawn from Lipowsky et al. (Atherton and Born 1973)

components of the glycocalyx with a resultant mitigation of glycan shedding, compaction of the lectin stain, and stabilization of the glycocalyx.

6 Leukocyte Rolling and Adhesion

Based upon the rolling and adhesion of WBCs on either artificial surfaces coated with receptors for specific ligands (Alon et al. 1995; Lawrence and Springer 1991, 1993) or monolayers of cultured endothelial cells (Arisaka et al. 1995; Hoover et al. 1980; Lawrence et al. 1987), it has long been held that adhesiveness is governed by regulation of the affinity and avidity of the integrin molecules on the WBC and EC (Zarbock and Ley 2009; Kinashi and Katagiri 2004; Laudanna et al. 2002; Luo et al. 2007). In vivo studies of post-capillary venules (Arfors et al. 1987; House and Lipowsky 1987b; Ley et al. 1995) have supported this concept. In addition, the mechanical properties of the glycocalyx may play a role in the adhesion process in light of the ability of microvilli on the surface of rolling WBCs to penetrate the surface layer to reach adhesion receptors (Zhao et al. 2001). WBC microvilli may range in length from 0.3 to 0.7 μm (Weinbaum et al. 2007). The ability to penetrate the glycocalyx may depend on changes in porosity and stiffness attendant to physiological stimuli (Weinbaum et al. 2007; Platts et al. 2003; Platts and Duling 2004). Under normal conditions, the apparent thickness of the glycocalyx significantly exceeds the lengths of endothelial cell (EC) receptors involved in leukocyte (WBC) rolling on the EC (selectins) and firm adhesion to the EC (integrins). The lengths of these receptors range from 20 nm for the β2 integrin ligands to 30–40 nm for E- and P-selectins (Springer 1990). Thus, reduction in thickness of the glycocalyx by either chemoattractants (e.g., fMLP) (Gao and Lipowsky 2010) or cytokines (e.g., TNF-α) (Henry and Duling 2000) accompanied by increased porosity may enhance access to adhesion receptors on the EC surface. It has been shown that perfusion of post-capillary venules with heparinase or superfusion of the tissue with fMLP served to increase binding of circulating antibodies to ICAM-1 on the EC surface (Mulivor and Lipowsky 2002). Although in this study, firm adhesion of WBCs was not stimulated by perfusion of venules with heparinase, most likely because substrates for leukocyte rolling were also removed, subsequent studies using heparitinase (which may cleave less sulfated heparan sulfate chains) produced an increase in firm WBC adhesion (Constantinescu et al. 2003). Alternatively, it has been demonstrated that heparinase reduces stimulated rolling and adhesion of WBCs in post-capillary venules by inhibiting externalization of P-selectin and/or compromising the structural interactions between heparan sulfate proteoglycans and selectins (Hayward et al. 1998).

Changes in the glycocalyx attendant to EC activation also affect WBC rolling adhesive interactions with the EC. Taking the rolling velocity of WBCs (normalized with respect to estimated wall shear rates, S.R.) as a measure of the adhesiveness of the EC surface (the lower the ratio of V_{WBC}/SR, the greater the adhesiveness), it was found that superfusion of the tissue with inhibitors of MMP activity, such as doxycycline or the zinc chelator GM6001, decreased the rolling velocity, thus promoting adhesiveness of the EC surface during WBC rolling. These results suggest that there is a basal level of sheddase activity on the EC surface that may be suppressed by MMP inhibition, which leads to an excessive accumulation of adhesion receptors on the EC surface that retard the rolling motion of WBCs. The presence of a basal level of MMP activity on the EC surface of post-capillary venules has been demonstrated by measuring the fluorescence activity of fluorescence substrates circulating in the plasma, which is reduced with MMP inhibition (Mulivor and Lipowsky 2009). Interestingly, superfusion of the tissue with fMLP alone causes a similar reduction in rolling velocity, presumably due to a combination of conformational changes in adhesion receptors on the EC surface and enhanced externalization of adhesion receptors (e.g., P-selectin) and shedding of the glycocalyx. While inhibition of MMP activation and activation with fMLP both resulted in diminished rolling velocity, the strength of the

adhesive bond during firm adhesion was found to be less with MMP suppression compared to that with fMLP, presumably due to conformational changes of WBC integrin receptors induced by fMLP (Lipowsky et al. 2015).

Similar adhesive interactions have also been observed, in part, by experiments in other tissues and cells. Inhibition of L-selectin shedding from WBCs by the metalloprotease inhibitor KD-IX-73-4 was found to reduce WBC rolling velocity in post-capillary venules of hamster cremaster muscle (Hafezi-Moghadam et al. 2001), which was attributed to inhibition of L-selectin shedding on the leukocyte alone. Although KD-IX-73-4 had no apparent effect on the endothelial glycocalyx, these studies bring to light the potential for metalloprotease inhibition to affect leukocyte rolling and adhesion. Further, comparison of the inhibitory activity of KD-IX-73-4 on the shedding of the endothelial protein C receptor (EPCR) from EA.hy926 endothelial cells, with inhibition of the MMP inhibitor GM6001, revealed that the latter was ineffective in inhibiting the release of EPCR (Xu et al. 2000). Thus, if this endothelial selectivity of the MMP inhibitors GM6001 and doxycycline applies to the reductions of WBC rolling velocity in venules, then the role of MMP inhibition on affecting the adhesive properties of the endothelial glycocalyx is further supported. It has also been shown that reduced rolling velocity of WBCs occurs following exposure of cremaster venules to TNF-α (Jung et al. 1998). Although these results were attributed to conformational changes of adhesion receptors in response to TNF-α, this trend may reflect the shedding of glycans from the EC surface, as noted previously (Henry and Duling 2000), and the enhanced access to adhesion ligands (e.g., ICAM-1).

7 Conclusions

In summary, the endothelial surface layer, which consists of the EC glycocalyx and a layer of adsorbed proteins, has been implicated as a barrier to WBC-EC adhesion. The primary glycoproteins are decorated with the principal glycosaminoglycans (GAGS) heparan sulfate (HS) and chondroitin sulfate (CS) that are encased in a meshwork of hyaluronic acid (HA). Together, these glycans form a layer that can be observed in vivo on the surface of the EC that is on the order of 500 μm thick. Measurement of the precise thickness of the ESL is fraught with many difficulties and is most easily implemented by exclusion of macromolecules from the EC surface. In vitro, the ESL is much smaller, on the order of 1/10th the in vivo thickness. Staining of glycans with carbohydrate-binding proteins (lectins) permits visualization of the ESL and reveals that the composition of the glycocalyx readily changes during the inflammatory process, as evidenced by the shedding of glycans with activation of the endothelium by chemoattractants and cytokines. Reductions in thickness and increases in porosity of the ESL due to an inflammatory stimulus facilitate greater access to WBC adhesion receptors on the EC surface and thus promote WBC-EC adhesion.

The effectors of ESL shedding are most likely members of the family of metalloproteinases, which cleave the core proteoglycans, and endoglycosidases (namely, heparanase), which cleave GAGs attached to the core proteins. Direct intravital microscopic studies of shedding of the glycocalyx have suggested that glycan shedding may be inhibited by MMP inhibitors and competitive binding to EC-derived heparanase. The relative proportions of MMP and heparanase-induced shedding remain to be fully delineated, as well as the extent to which MMPs and heparanase affect their mutual release and activation. Identification of the specific proteases responsible for shedding is further complicated by the ability of specific MMPs to activate other members of the MMP family and for other proteases to activate MMPs. There is also an indirect association between heparanase and MMP expression (Purushothaman et al. 2008, 2011, 2010; Zcharia et al. 2009). For example, blocking activation of MMP-9 inhibited heparanase-induced syndecan-1 shedding in myeloma cells (Purushothaman et al. 2010), and overexpression of heparanase in cultured human mammary carcinoma cells resulted in diminished expression of MMP-2,

MMP-9, and MMP-14 (Zcharia et al. 2009). It is clear, however, that stabilization of the glycocalyx during inflammation may indeed mitigate WBC-EC adhesion. Thus, the development of new strategies to directly target shedding of the glycocalyx may have significant therapeutic value.

Acknowledgments This work was supported in part by NIH R01 HL-39286.

References

Adamson RH, Clough G (1992) Plasma proteins modify the endothelial cell glycocalyx of frog mesenteric microvessels. J Physiol 445:473–486

Alon R, Hammer DA, Springer TA (1995) Lifetime of the p-selectin-carbohydrate bond and its response to tensile force in hydrodynamic flow. Nature 374:539–542

Arfors KE, Lundberg C, Lindbom L, Lundberg K, Beatty PG, Harlan JM (1987) A monoclonal antibody to the membrane glycoprotein complex cd18 inhibits polymorphonuclear leukocyte accumulation and plasma leakage in vivo. Blood 69:338–340

Arisaka T, Mitsumata M, Kawasumi M, Tohjima T, Hirose S, Yoshida Y (1995) Effects of shear stress on glycosaminoglycan synthesis in vascular endothelial cells. Ann N Y Acad Sci 748:543–554

Atherton A, Born GV (1972) Quantitative investigations of the adhesiveness of circulating polymorphonuclear leucocytes to blood vessel walls. J Physiol 222: 447–474

Atherton A, Born GV (1973) Relationship between the velocity of rolling granulocytes and that of the blood flow in venules. J Physiol 233:157–165

Bagge U, Karlsson R (1980) Maintenance of white blood cell margination at the passage through small venular junctions. Microvasc Res 20:92–95

Bar-Ner M, Eldor A, Wasserman L, Matzner Y, Cohen IR, Fuks Z et al (1987) Inhibition of heparanase-mediated degradation of extracellular matrix heparan sulfate by non-anticoagulant heparin species. Blood 70:551–557

Becker BF, Jacob M, Leipert S, Salmon AH, Chappell D (2015) Degradation of the endothelial glycocalyx in clinical settings: searching for the sheddases. Br J Clin Pharmacol 80:389–402

Bennett HS, Luft JH, Hampton JC (1959) Morphological classifications of vertebrate blood capillaries. Am J Phys 196:381–390

Braide M, Amundson B, Chien S, Bagge U (1984) Quantitative studies on the influence of leukocytes on the vascular resistance in a skeletal muscle preparation. Microvasc Res 27:331–352

Bruegger D, Jacob M, Rehm M, Loetsch M, Welsch U, Conzen P et al (2005) Atrial natriuretic peptide induces shedding of endothelial glycocalyx in coronary vascular bed of Guinea pig hearts. Am J Physiol Heart Circ Physiol 289:H1993–H1999

Brule S, Charnaux N, Sutton A, Ledoux D, Chaigneau T, Saffar L et al (2006) The shedding of syndecan-4 and syndecan-1 from hela cells and human primary macrophages is accelerated by sdf-1/cxcl12 and mediated by the matrix metalloproteinase-9. Glycobiology 16:488–501

Cabrales P, Vazquez BY, Tsai AG, Intaglietta M (2007) Microvascular and capillary perfusion following glycocalyx degradation. J Appl Physiol 102:2251–2259

Chappell D, Jacob M, Rehm M, Stoeckelhuber M, Welsch U, Conzen P et al (2008) Heparinase selectively sheds heparan sulphate from the endothelial glycocalyx. Biol Chem 389:79–82

Chappell D, Jacob M, Paul O, Rehm M, Welsch U, Stoeckelhuber M et al (2009a) The glycocalyx of the human umbilical vein endothelial cell: an impressive structure ex vivo but not in culture. Circ Res 104: 1313–1317

Chappell D, Hofmann-Kiefer K, Jacob M, Rehm M, Briegel J, Welsch U et al (2009b) TNF-alpha induced shedding of the endothelial glycocalyx is prevented by hydrocortisone and antithrombin. Basic Res Cardiol 104:78–89

Colburn P, Kobayashi E, Buonassisi V (1994) Depleted level of heparan sulfate proteoglycan in the extracellular matrix of endothelial cell cultures exposed to endotoxin. J Cell Physiol 159:121–130

Constantinescu AA, Vink H, Spaan JA (2001) Elevated capillary tube hematocrit reflects degradation of endothelial cell glycocalyx by oxidized ldl. Am J Physiol Heart Circ Physiol 280:H1051–H1057

Constantinescu AA, Vink H, Spaan JA (2003) Endothelial cell glycocalyx modulates immobilization of leukocytes at the endothelial surface. Arterioscler Thromb Vasc Biol 23:1541–1547

Daniels B, Linhardt RJ, Zhang F, Mao W, Wice SM, Hiebert LM (2006) In vivo antithrombotic synergy of oral heparin and arginine: endothelial thromboresistance without changes in coagulation parameters. Thromb Haemost 95:865–872

DeLano FA, Schmid-Schonbein GW (2008) Proteinase activity and receptor cleavage: mechanism for insulin resistance in the spontaneously hypertensive rat. Hypertension 52:415–423

Desjardins C, Duling BR (1990) Heparinase treatment suggests a role for the endothelial cell glycocalyx in regulation of capillary hematocrit. Am J Phys 258:H647–H654

Diamond MS, Alon R, Parkos CA, Quinn MT, Springer TA (1995) Heparin is an adhesive ligand for the leukocyte integrin mac-1 (cd11b/cd1). J Cell Biol 130: 1473–1482

Ding K, Lopez-Burks M, Sanchez-Duran JA, Korc M, Lander AD (2005) Growth factor-induced shedding of syndecan-1 confers glypican-1 dependence on mitogenic responses of cancer cells. J Cell Biol 171: 729–738

Endo K, Takino T, Miyamori H, Kinsen H, Yoshizaki T, Furukawa M et al (2003) Cleavage of syndecan-1 by membrane type matrix metalloproteinase-1 stimulates cell migration. J Biol Chem 278:40764–40770

Eskens BJM, Zuurbier CJ, van Haare J, Vink H, van Teeffelen J (2013) Effects of two weeks of metformin treatment on whole-body glycocalyx barrier properties in db/db mice. Cardiovasc Diabetol 12:175

Fahraeus R (1929) The suspension stability of blood. Physiol Rev 9:241–274

Feng J, Weinbaum S (2000) Lubrication theory in highly compressible porous media: the mechanics of skiing, from red cells to humans. J Fluid Mech 422:281–317

Fitzgerald ML, Wang Z, Park PW, Murphy G, Bernfield M (2000) Shedding of syndecan-1 and -4 ectodomains is regulated by multiple signaling pathways and mediated by a timp-3-sensitive metalloproteinase. J Cell Biol 148:811–824

Fux L, Ilan N, Sanderson RD, Vlodavsky I (2009) Heparanase: busy at the cell surface. Trends Biochem Sci 34:511–519

Gaddi AV, Cicero AF, Gambaro G (2010) Nephroprotective action of glycosaminoglycans: why the pharmacological properties of sulodexide might be reconsidered. Int J Nephrol Renovasc Dis 3:99–105

Gao L, Lipowsky HH (2010) Composition of the endothelial glycocalyx and its relation to its thickness and diffusion of small solutes. Microvasc Res 80:394–401

Goldsmith HL, Spain S (1984) Margination of leukocytes in blood flow through small tubes. Microvasc Res 27:204–222

Golub LM, Lee HM, Ryan ME, Giannobile WV, Payne J, Sorsa T (1998) Tetracyclines inhibit connective tissue breakdown by multiple non-antimicrobial mechanisms. Adv Dent Res 12:12–26

Gotte M (2003) Syndecans in inflammation. FASEB J 17:575–591

Gouverneur M, Spaan JA, Pannekoek H, Fontijn RD, Vink H (2006) Fluid shear stress stimulates incorporation of hyaluronan into endothelial cell glycocalyx. Am J Physiol Heart Circ Physiol 290:H458–H452

Grant L (1973) The sticking and emigration of white blood cells in inflammation. In: Zweifach BW, Grant L, McClusky R (eds) The inflammatory process, vol 2. Academic Press, Orlando, pp 205–249

Grimm J, Keller R, de Groot PG (1988) Laminar flow induces cell polarity and leads to rearrangement of proteoglycan metabolism in endothelial cells. Thromb Haemost 60:437–441

Gronski TJ, Martin RL, Kobayashi DK, Walsh BC, Holman MC, Huber M et al (1997) Hydrolysis of a broad spectrum of extracellular matrix proteins by human macrophage elastase. J Biol Chem 272:12189–12194

Haas TL, Milkiewicz M, Davis SJ, Zhou AL, Egginton S, Brown MD et al (2000) Matrix metalloproteinase activity is required for activity-induced angiogenesis in rat skeletal muscle. Am J Physiol Heart Circ Physiol 279:1540–1547

Hafezi-Moghadam A, Thomas KL, Prorock AJ, Huo Y, Ley K (2001) L-selectin shedding regulates leukocyte recruitment. J Exp Med 193:863–872

Haldenby KA, Chappell DC, Winlove CP, Parker KH, Firth JA (1994) Focal and regional variations in the composition of the glycocalyx of large vessel endothelium. J Vasc Res 31:2–9

Hayward R, Scalia R, Hopper B, Appel JZ III, Lefer AM (1998) Cellular mechanisms of heparinase iii protection in rat traumatic shock. Am J Phys 275: H23–H30

Henry CB, Duling BR (1999) Permeation of the luminal capillary glycocalyx is determined by hyaluronan. Am J Phys 277:H508–H514

Henry CB, Duling BR (2000) TNF-alpha increases entry of macromolecules into luminal endothelial cell glycocalyx. Am J Physiol Heart Circ Physiol 279:H2815–H2823

Hofmann-Kiefer KF, Kemming GI, Chappell D, Flondor M, Kisch-Wedel H, Hauser A et al (2009) Serum heparan sulfate levels are elevated in endotoxemia. Eur J Med Res 14:526–531

Hoover RL, Folger R, Haering WA, Ware BR, Karnovsky MJ (1980) Adhesion of leukocytes to endothelium: roles of divalent cations, surface charge, chemotactic agents and substrate. J Cell Sci 45:73–86

House SD, Lipowsky HH (1987a) Microvascular hematocrit and red cell flux in rat cremaster muscle. Am J Phys 252:H211–H222

House SD, Lipowsky HH (1987b) Leukocyte-endothelium adhesion: microhemodynamics in mesentery of the cat. Microvasc Res 34:363–379

Huxley VH, Curry FE (1991) Differential actions of albumin and plasma on capillary solute permeability. Am J Phys 260:H1645–H1654

Ihrcke NS, Platt JL (1996) Shedding of heparan sulfate proteoglycan by stimulated endothelial cells: evidence for proteolysis of cell-surface molecules. J Cell Physiol 168:625–637

Ihrcke NS, Wrenshall LE, Lindman BJ, Platt JL (1993) Role of heparan sulfate in immune system-blood vessel interactions. Immunol Today 14:500–505

Iigo Y, Suematsu M, Higashida T, Oheda J, Matsumoto K, Wakabayashi Y et al (1997) Constitutive expression of icam-1 in rat microvascular systems analyzed by laser confocal microscopy. Am J Phys 273:H138–H147

Jo H, Jung SH, Kang J, Yim HB, Kang KD (2014) Sulodexide inhibits retinal neovascularization in a mouse model of oxygen-induced retinopathy. BMB Rep 47:637–642

Jung U, Norman KE, Scharffetter-Kochanek K, Beaudet AL, Ley K (1998) Transit time of leukocytes rolling through venules controls cytokine-induced inflammatory cell recruitment in vivo. J Clin Invest 102:1526–1533

Kinashi T, Katagiri K (2004) Regulation of lymphocyte adhesion and migration by the small GTPase Rap1 and its effector molecule RAPL. Immunol Lett 93:1–5

Klitzman B, Duling BR (1979) Microvascular hematocrit and red cell flow in resting and contracting striated muscle. Am J Phys 237:H481–H490

Koenig A, Norgard-Sumnicht K, Linhardt R, Varki A (1998) Differential interactions of heparin and heparan sulfate glycosaminoglycans with the selectins. Implications for the use of unfractionated and low molecular weight heparins as therapeutic agents. J Clin Invest 101:877–889

Kolarova H, Ambruzova B, Sindlerova LS, Klinke A, Kubala L (2014) Modulation of endothelial glycocalyx structure under inflammatory conditions. Mediat Inflamm 2014:694312

Laudanna C, Kim JY, Constantin G, Butcher EC (2002) Rapid leukocyte integrin activation by chemokines. Immunol Rev 186:37–46

Laurent TC, Fraser JR (1992) Hyaluronan. FASEB J 6:2397–2404

Lawrence MB, Springer TA (1991) Leukocytes roll on a selectin at physiologic flow rates: distinction from and prerequisite for adhesion through integrins. Cell 65:859–873

Lawrence MB, Springer TA (1993) Neutrophils roll on E-selectin. J Immunol 151:6338–6346

Lawrence MB, McIntire LV, Eskin SG (1987) Effect of flow on polymorphonuclear leukocyte endothelial-cell adhesion. Blood 70:1284–1290

Lever R, Hoult JRS, Page CP (2000) The effects of heparin and related molecules upon the adhesion of human polymorphonuclear leucocytes to vascular endothelium in vitro. Br J Pharmacol 129:533–540

Ley K, Bullard DC, Arbones ML, Bosse R, Vestweber D, Tedder TF et al (1995) Sequential contribution of l- and p-selectin to leukocyte rolling in vivo. J Exp Med 181:669–675

Li Z, Li L, Zielke HR, Cheng L, Xiao R, Crow MT et al (1996) Increased expression of 72-kd type iv collagenase (mmp-2) in human aortic atherosclerotic lesions. Am J Pathol 148:121–128

Li Q, Park PW, Wilson CL, Parks WC (2002) Matrilysin shedding of syndecan-1 regulates chemokine mobilization and transepithelial efflux of neutrophils in acute lung injury. Cell 111:635–646

Lipowsky HH, Lescanic A (2013) The effect of doxycycline on shedding of the glycocalyx due to reactive oxygen species. Microvasc Res 90:80–85

Lipowsky HH, Lescanic A (2017) Inhibition of inflammation induced shedding of the endothelial glycocalyx with low molecular weight heparin. Microvasc Res 112:72–78

Lipowsky HH, Sah R, Lescanic A (2011) Relative roles of doxycycline and cation chelation in endothelial glycan shedding and adhesion of leukocytes. Am J Physiol Heart Circ Physiol 300:H415–H422

Lipowsky HH, Lescanic A, Sah R (2015) Role of matrix metalloproteases in the kinetics of leukocyte-endothelial adhesion in post-capillary venules. Biorheology 52:433–445

Luft JH (1966) Fine structures of capillary and endocapillary layer as revealed by ruthenium red. Fed Proc 25:1773–1783

Luo B-H, Carman CV, Springer TA (2007) Structural basis of integrin regulation and signaling. Annu Rev Immunol 25:619–647

Marki A, Esko JD, Pries AR, Ley K (2015) Role of the endothelial surface layer in neutrophil recruitment. J Leukoc Biol 98:503–515

Mulivor AW, Lipowsky HH (2002) Role of glycocalyx in leukocyte-endothelial cell adhesion. Am J Physiol Heart Circ Physiol 283:H1282–H1291

Mulivor AW, Lipowsky HH (2004) Inflammation- and ischemia-induced shedding of venular glycocalyx. Am J Physiol Heart Circ Physiol 286:H1672–H1680

Mulivor AW, Lipowsky HH (2009) Inhibition of glycan shedding and leukocyte-endothelial adhesion in postcapillary venules by suppression of matrixmetalloprotease activity with doxycycline. Microcirculation 16:657–666

Ning F, Wang X, Shang L, Wang T, Lv C, Qi Z et al (2015) Low molecular weight heparin may prevent acute lung injury induced by sepsis in rats. Gene 557:88–91

Nordling S, Hong J, Fromell K, Edin F, Brannstrom J, Larsson R et al (2015) Vascular repair utilising immobilised heparin conjugate for protection against early activation of inflammation and coagulation. Thromb Haemost 113:1312–1322

Oduah EI, Linhardt RJ, Sharfstein ST (2016) Heparin: past, present, and future. Pharmaceuticals (Basel) 9 pii: E38

Padberg JS, Wiesinger A, di Marco GS, Reuter S, Grabner A, Kentrup D et al (2014) Damage of the endothelial glycocalyx in chronic kidney disease. Atherosclerosis 234:335–343

Page C (2013) Heparin and related drugs: beyond anticoagulant activity. ISRN Pharmacol 2013:910743

Park PW, Reizes O, Bernfield M (2000) Cell surface heparan sulfate proteoglycans: selective regulators of ligand-receptor encounters. J Biol Chem 275:29923–29926

Platt JL, Vercellotti GM, Lindman BJ, Oegema TR Jr, Bach FH, Dalmasso AP (1990) Release of heparan sulfate from endothelial cells. Implications for pathogenesis of hyperacute rejection. J Exp Med 171:1363–1368

Platt JL, Dalmasso AP, Lindman BJ, Ihrcke NS, Bach FH (1991) The role of c5a and antibody in the release of heparan sulfate from endothelial cells. Eur J Immunol 21:2887–2890

Platts SH, Duling BR (2004) Adenosine a3 receptor activation modulates the capillary endothelial glycocalyx. Circ Res 94:77–82

Platts SH, Linden J, Duling BR (2003) Rapid modification of the glycocalyx caused by ischemia-reperfusion is inhibited by adenosine a2a receptor activation. Am J Physiol Heart Circ Physiol 284:H2360–H2367

Poiseuille JLM (1835) Recherches sur les causes du mouvement du sang dans les vaisseaux capillaries. C R Acad Sci 6:554–560

Potter DR, Damiano ER (2008) The hydrodynamically relevant endothelial cell glycocalyx observed in vivo is absent in vitro. Circ Res 102:770–776

Pries AR, Secomb TW, Gaehtgens P, Gross JF (1990) Blood flow in microvascular networks. Experiments and simulation. Circ Res 67:826–834

Pries AR, Secomb TW, Jacobs H, Sperandio M, Osterloh K, Gaehtgens P (1997) Microvascular blood flow resistance: role of endothelial surface layer. Am J Phys 273:H2272–H2279

Pries AR, Secomb TW, Gaehtgens P (2000) The endothelial surface layer. Pflugers Arch 440:653–666

Purushothaman A, Chen L, Yang Y, Sanderson RD (2008) Heparanase stimulation of protease expression implicates it as a master regulator of the aggressive tumor phenotype in myeloma. J Biol Chem 283: 32628–32636

Purushothaman A, Uyama T, Kobayashi F, Yamada S, Sugahara K, Rapraeger AC et al (2010) Heparanase-enhanced shedding of syndecan-1 by myeloma cells promotes endothelial invasion and angiogenesis. Blood 115:2449–2457

Purushothaman A, Hurst DR, Pisano C, Mizumoto S, Sugahara K, Sanderson RD (2011) Heparanase-mediated loss of nuclear syndecan-1 enhances histone acetyltransferase (hat) activity to promote expression of genes that drive an aggressive tumor phenotype. J Biol Chem 286:30377–30383

Rapraeger A (1989) Transforming growth factor (type beta) promotes the addition of chondroitin sulfate chains to the cell surface proteoglycan (syndecan) of mouse mammary epithelia. J Cell Biol 109:2509–2518

Rehm M, Bruegger D, Christ F, Conzen P, Thiel M, Jacob M et al (2007) Shedding of the endothelial glycocalyx in patients undergoing major vascular surgery with global and regional ischemia. Circulation 116: 1896–1906

Reitsma S, Slaaf DW, Vink H, van Zandvoort MA, oude Egbrink MG (2007) The endothelial glycocalyx: composition, functions, and visualization. Pflugers Arch 454:345–359

Schmid-Schonbein GW, Usami S, Skalak R, Chien S (1980) The interaction of leukocytes and erythrocytes in capillary and postcapillary vessels. Microvasc Res 19:45–70

Schnitzer JE, Ulmer JB, Palade GE (1990a) A major endothelial plasmalemmal sialoglycoprotein, gp60, is immunologically related to glycophorin. Proc Natl Acad Sci U S A 87:6843–6847

Schnitzer JE, Shen CP, Palade GE (1990b) Lectin analysis of common glycoproteins detected on the surface of continuous microvascular endothelium in situ and in culture: identification of sialoglycoproteins. Eur J Cell Biol 52:241–251

Secomb TW, Hsu R, Pries AR (2001) Motion of red blood cells in a capillary with an endothelial surface layer: effect of flow velocity. Am J Physiol Heart Circ Physiol 281:H629–H636

Simionescu M, Simionescu N, Palade GE (1982) Differentiated microdomains on the luminal surface of capillary endothelium: distribution of lectin receptors. J Cell Biol 94:406–413

Smith ML, Long DS, Damiano ER, Ley K (2003) Near-wall micro-piv reveals a hydrodynamically relevant endothelial surface layer in venules in vivo. Biophys J 85:637–645

Spinale FG (2007) Myocardial matrix remodeling and the matrix metalloproteinases: influence on cardiac form and function. Physiol Rev 87:1285–1342

Springer TA (1990) Adhesion receptors of the immune system. Nature 346:425–434

Springer TA, Lasky LA (1991) Cell adhesion. Sticky sugars for selectins. Nature 349:196–197

Squire JM, Chew M, Nneji G, Neal C, Barry J, Michel C (2001) Quasi-periodic substructure in the microvessel endothelial glycocalyx: a possible explanation for molecular filtering? J Struct Biol 136:239–255

Subramanian SV, Fitzgerald ML, Bernfield M (1997) Regulated shedding of syndecan-1 and -4 ectodomains by thrombin and growth factor receptor activation. J Biol Chem 272:14713–14720

Sutera SP, Seshadri V, Croce PA, Hochmuth RM (1970) Capillary blood flow II. Deformable model cells in tube flow. Microvasc Res 2:420–433

Svennevig K, Hoel T, Thiara A, Kolset S, Castelheim A, Mollnes T et al (2008) Syndecan-1 plasma levels during coronary artery bypass surgery with and without cardiopulmonary bypass. Perfusion 23:165–171

Taraboletti G, D'Ascenzo S, Borsotti P, Giavazzi R, Pavan A, Dolo V (2002) Shedding of the matrix metalloproteinases mmp-2, mmp-9, and mt1-mmp as membrane vesicle-associated components by endothelial cells. Am J Pathol 160:673–680

Teixeira MM, Hellewell PG (1993) Suppression by intradermal administration of heparin of eosinophil accumulation but not oedema formation in inflammatory reactions in Guinea-pig skin. Br J Pharmacol 110:1496–1500

VanTeeffelen JW, Brands J, Jansen C, Spaan JA, Vink H (2007) Heparin impairs glycocalyx barrier properties and attenuates shear dependent vasodilation in mice. Hypertension 50:261–267

Vink H, Duling BR (1996) Identification of distinct luminal domains for macromolecules, erythrocytes, and leukocytes within mammalian capillaries. Circ Res 79:581–589

Vink H, Duling BR (2000) Capillary endothelial surface layer selectively reduces plasma solute distribution volume. Am J Physiol Heart Circ Physiol 278:H285–H289

Vogl-Willis CA, Edwards IJ (2004) High-glucose-induced structural changes in the heparan sulfate proteoglycan, perlecan, of cultured human aortic endothelial cells. Biochim Biophys Acta 1672:36–45

Weinbaum S, Tarbell JM, Damiano ER (2007) The structure and function of the endothelial glycocalyx layer. Annu Rev Biomed Eng 9:121–167

Wiesinger A, Peters W, Chappell D, Kentrup D, Reuter S, Pavenstadt H et al (2013) Nanomechanics of the

endothelial glycocalyx in experimental sepsis. PLoS One 8:e80905
Xu J, Qu D, Esmon NL, Esmon CT (2000) Metalloproteolytic release of endothelial cell protein c receptor. J Biol Chem 275:6038–6044
Yaras N, Sariahmetoglu M, Bilginoglu A, Aydemir-Koksoy A, Onay-Besikci A, Turan B et al (2008) Protective action of doxycycline against diabetic cardiomyopathy in rats. Br J Pharmacol 155:1174–1184
Yini S, Heng Z, Xin A, Xiaochun M (2015) Effect of unfractionated heparin on endothelial glycocalyx in a septic shock model. Acta Anaesthesiol Scand 59: 160–169
Young E (2008) The anti-inflammatory effects of heparin and related compounds. Thromb Res 122:743–752
Yu WH, Woessner JF Jr (2000) Heparan sulfate proteoglycans as extracellular docking molecules for matrilysin (matrix metalloproteinase 7). J Biol Chem 275: 4183–4191
Zarbock A, Ley K (2009) Neutrophil adhesion and activation under flow. Microcirculation 16:31–42
Zcharia E, Jia J, Zhang X, Baraz L, Lindahl U, Peretz T et al (2009) Newly generated heparanase knock-out mice unravel co-regulation of heparanase and matrix metalloproteinases. PLoS One 4:e5181
Zhao Y, Chien S, Weinbaum S (2001) Dynamic contact forces on leukocyte microvilli and their penetration of the endothelial glycocalyx. Biophys J 80:1124–1140
Zuurbier CJ, Demirci C, Koeman A, Vink H, Ince C (2005) Short-term hyperglycemia increases endothelial glycocalyx permeability and acutely decreases lineal density of capillaries with flowing red blood cells. J Appl Physiol 99:1471–1476
Zweifach BW (1955) Structural makeup of capillary wall. Ann N Y Acad Sci 61:670–677

Mechanobiology and Vascular Remodeling: From Membrane to Nucleus

Ying-Xin Qi, Yue Han, and Zong-Lai Jiang

Abstract

Vascular endothelial cells (ECs) and smooth muscle cells (VSMCs) are constantly exposed to hemodynamic forces in vivo, including flow shear stress and cyclic stretch caused by the blood flow. Numerous researches revealed that during various cardiovascular diseases such as atherosclerosis, hypertension, and vein graft, abnormal (pathological) mechanical forces play crucial roles in the dysfunction of ECs and VSMCs, which is the fundamental process during both vascular homeostasis and remodeling. Hemodynamic forces trigger several membrane molecules and structures, such as integrin, ion channel, primary cilia, etc., and induce the cascade reaction processes through complicated cellular signaling networks. Recent researches suggest that nuclear envelope proteins act as the functional homology of molecules on the membrane, are important mechanosensitive molecules which modulate chromatin location and gene transcription, and subsequently regulate cellular functions. However, the studies on the roles of nucleus in the mechanotransduction process are still at the beginning. Here, based on the recent researches, we focused on the nuclear envelope proteins and discussed the roles of pathological hemodynamic forces in vascular remodeling. It may provide new insight into understanding the molecular mechanism of vascular physiological homeostasis and pathophysiological remodeling and may help to develop hemodynamic-based strategies for the prevention and management of vascular diseases.

Y.-X. Qi (✉) · Y. Han · Z.-L. Jiang
Institute of Mechanobiology and Medical Engineering, School of Life Sciences and Biotechnology, Shanghai Jiao Tong University, Shanghai, China
e-mail: qiyx@sjtu.edu.cn

1 Introduction

Biomechanics studies the deformation and movement of living entities based on the organic combination of biological and mechanical principles and tries to recognize the laws of life processes and to solve the scientific issues in the field of life and health. The classical theory of biomechanics is the stress-growth law proposed by Y.C. Fung in his monograph, *Biomechanics: Motion, Flow, Stress, and Growth*, which mentioned that the remodeling of blood vessel involving growth or resorption of cell and extracellular materials is linked to the mechanical stresses (Fung 1990). The stress-growth law is an important

B. M. Fu, N. T. Wright (eds.), *Molecular, Cellular, and Tissue Engineering of the Vascular System*, Advances in Experimental Medicine and Biology 1097,
https://doi.org/10.1007/978-3-319-96445-4_4

and fundamental theory that expounds the intrinsic relationship between mechanical motion and life motion and guides the transformation of biomechanics from mechanics applied to biology to the mechanism in mechanical regulation of life processes. With the accelerated development in molecular biology and cellular biology, mechanobiology becomes a new frontier field of biomechanics, which focuses on how mechanical factors interacting with chemical signals regulate cellular/tissue functions and their molecular mechanisms. Although almost all types of cells in vivo are exposed to mechanical stimuli, much of the researches on mechanobiology have focused on the cardiovascular system, in which mechanical forces play critical roles (Wang et al. 2008). Vascular mechanobiology elucidates the mechanism in which physiologically mechanical factors result in vascular homeostasis or pathophysiologically mechanical factors induce vascular remodeling. Vascular remodeling is characterized as abnormal variations of vascular cell phenotype, morphological structure, and functions such as migration, hypertrophy, proliferation, and apoptosis. Vascular remodeling is the essential pathogenic process of various cardiovascular disorders, including hypertension, atherosclerosis, stroke, and restenosis after vein graft (Chien 2007; Chiu and Chien 2011). The understanding of mechanobiological mechanism in vascular remodeling will play a unique role in solving the key scientific problems of human physiology and disease and will generate important theoretical and clinical significance.

Circulating system, centered on the heart that functions as a mechanical pump, contains amount of mechanical effects, which involves hemodynamic forces caused by the blood flow, deformation of blood cells and blood vessels, and interaction between blood and vessels (Fung 1990). Clinical researches revealed that despite the exposure to the same systemic risk factors such as smoking, hyperlipidemia, hyperglycemia, hypertension, obesity, and diabetes, the earliest lesions of atherosclerosis always occur at some specific area of arteries. These atherosclerosis-prone areas are the bifurcations, branch points and curvatures of arteries and valve sinuses, and poststenotic regions (Fig. 1) (Chiu and Chien 2011). Further observations revealed that hemodynamic forces in these parts are characterized as nonuniform and irregular, including recirculation eddies and changes in direction with space (flow separation and reattachment) and time (reciprocating flow). In contrast, the straight part of the artery, which is generally spared form atherosclerotic lesions, is exposed to sustained laminar blood flow and high shear stress (with a definite direction) (Chien 2007; Chiu and Chien 2011). These relationships between the regional susceptibility of atherosclerosis and the local hemodynamic

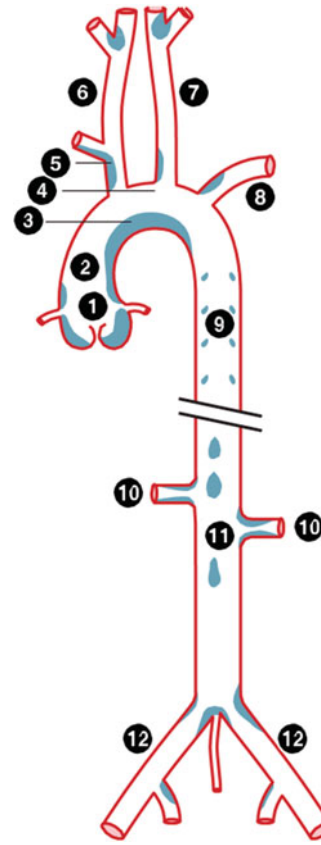

Fig. 1 Schematic drawing shows the atherosclerosis-prone areas (light blue) in the artery system which are the bifurcations and branch points and curvatures of arteries. *1*. Aortic sinus; *2*. ascending aorta; *3*. inner (lesser) curvature of aortic arch; *4*. outer (greater) curvature of aortic arch; *5*. innominate artery; *6*. right common carotid artery; *7*. left common carotid artery; *8*. left subclavian artery; *9*. thoracic aorta; *10*. renal artery; *11*. abdominal aorta; *12*. iliac artery [cited from (Chiu and Chien 2011)]

forces strongly suggested the significant roles of mechanical stimuli in vascular physiology and pathophysiology.

During recent decades, increasing evidences, both in vivo and in vitro, revealed that hemodynamic forces, including fluid shear stress and cyclic stretch, modulate expressions of relevant molecules and subsequently influence the morphology, structure, and function of vascular endothelial cells (ECs) and smooth muscle cells (VSMCs). For example, the experiments using primate thoracic aorta in vivo or the step flow channel in vitro both suggest that disturbed flow induces the polygonal shape of ECs and enhances the endothelial permeability via modulating the distribution of cytoskeleton F-actin filaments and the organization of intercellular junctional protein (Chiu et al. 1998; Davies 1995; Miao et al. 2005). It has been shown that there are various mechanosensors in vascular cell membrane, including integrins (Shyy and Chien 1997; Moiseeva 2001), ion channels (Hoger et al. 2002; Wan et al. 2015), junctional proteins (Tzima et al. 2005; Ye et al. 2014), as well as primary cilia (Egorova et al. 2011; Mohieldin et al. 2016). Recent evidences suggest that the nucleus, as the largest and stiffest organelle in the cell, can also directly sense and respond to mechanical signals and then regulate cell functions. The nucleus interacts with the cytoskeleton via linker of the nucleoskeleton and cytoskeleton (LINC) complexes (Rothballer and Kutay 2013), and this physical linkage allows the direct transmission of mechanical forces exerted on the cell surface to the hallmark of protein complexes in the nucleus of eukaryotic cells. Unlike the widely established mechanotransduction role of molecules in cell membrane and cytoplasm, the roles of nuclear molecules and structures are still in their infant.

Understanding of the effects of hemodynamic forces on signaling transduction, gene expression, and cellular structures and functions will help to identify the molecular and mechanical bases of the roles of complex hemodynamic patterns in the development of vascular pathologies such as atherosclerosis, hypertension, thrombosis, in-stent restenosis, and bypass graft occlusion, as well as their clinical complications. Furthermore, such information may lead to the discovery and identification of new disease-related genes and the development of novel therapeutic strategies.

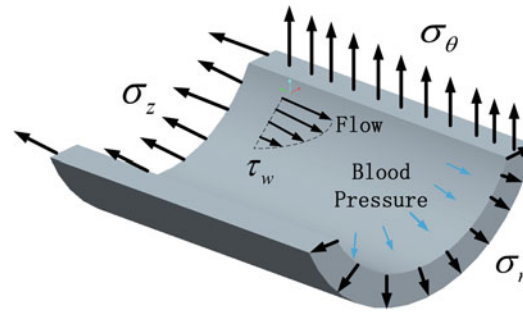

Fig. 2 Schematic drawing shows the relevant hemodynamic forces acting on arteries [modified from (Humphrey et al. 2015)]

2 Hemodynamic Forces, Vascular Homeostasis, and Remodeling

Because of the blood flow, arterial wall is exposed to complicated hemodynamic forces in vivo: wall shear stress (τ_w) caused by frictional interactions between the endothelium and flowing blood; circumferential stress (σ_θ), caused by the blood pressure changing the circumference cyclically; and the radial stress (σ_r), due directly to blood pressure and perivascular constraints (Humphrey et al. 2015) (Fig. 2). Of these main three hemodynamic stresses, circumferential stress is the largest in the aorta, which is about 150 kPa under normal conditions, while wall shear stress in the straight part of the arterial tree is 1–7 kPa (10–70 dyn/cm^2, much smaller than circumferential stress). Regardless of magnitude, all components of hemodynamic forces affect the mechanobiology, with ECs sensitive to changes in shear stress while VSMCs sensitive to cyclic stretch following circumferential stress (Chiu and Chien 2011; Humphrey et al. 2015).

It had been proved that physiological hemodynamic forces are protective factors which play crucial roles in maintaining vascular homeostasis. Whereas, pathological hemodynamic forces induce vascular remodeling. For instance, during hypertension, chronically elevated cyclic stretch stimulates abnormal proliferation and migration of VSMCs, which subsequently cause vascular remodeling (Qi et al. 2016). Whereas, reciprocating shear stress induces the high permeability of vascular endothelium (Miao et al. 2005).

2.1 Shear Stress and EC Mechanobiology

ECs serve as a semipermeable barrier whose homeostasis plays critical roles in the maintenance of vascular physiological functions (Chien 2007, 2008). As the interface between the blood flow and the vessel wall, vascular ECs are constantly exposed to fluid shear stress created by flowing blood. The blood that circulates through the vessels exerts an oscillatory shear stress on the straight part of the arterial wall of around 1–7 Pa (in humans) which varies with the exact location in the arterial tree. The shear stress at arterial branch points and curvature and poststenotic regions is a low net forward flow without a clear direction, and shear stress is less than 0.4 Pa (Giddens et al. 1993; Chiu and Chien 2011). Although typical shear stress acted on ECs is five orders of magnitude lower than circumferential stress, its importance on cell behavior should not be underestimated.

The magnitudes of shear stress are significantly diverse between different species, with a general trend of increased mean shear stress following decreased body size (Suo et al. 2007; Greve et al. 2006). Interestingly, although the volume of shear stress between different species is different, the prone distribution of atherosclerotic lesions is similar. For example, the volume of shear stress in the aorta of mouse is almost twice as that in human, and the similar site specificity of atherogenesis at aortic sinus and lesser curvature of aortic arch were both reported (Suo et al. 2007; Cheng et al. 2006). Furthermore, despite the large differences in wall shear stress between different species, the morphologic changes of ECs (Davies 1995) and spatial distributions of atherogenic molecules such as vascular cell adhesion molecule 1 (VCAM-1) (Suo et al. 2007; Chiu and Chien 2011) are similar at atherosclerotic plaque localization. These results suggest that the relative differences in flow patterns (laminar vs disturbed) and in shear stress gradient of the magnitude, but not the absolute level of the magnitude, may contribute to the flow-mediated vascular homeostasis and remodeling. It is well established that shear stress is attributed to the site selectivity of atherosclerotic lesions and influence phenotype diversity of ECs which is characterized as a series of related changes, including the morphology, orientation, turnover rate (proliferation and apoptosis), migration, and expressions of inflammatory molecules (Chiu and Chien 2011).

Researches on shear-induced morphology and orientation in the past decades have shed much light on the mechanobiology of ECs. During homeostasis in the relative straight portion of an artery, ECs are exposed to laminar flow with a physiological level of shear stress. In both in vivo researches based on the athero-prone and atheroprotective area of arteries and in vitro experiments using flow chamber, physiological shear stress leads to the aligned and elongated direction, with the well organized and parallel actin stress fibers in the central region (Zhou et al. 2014). The turnover rate of these ECs under homeostasis is relatively low, and the expression and distributions of intercellular junctional proteins, such as vascular endothelial cadherin (VE-cadherin), are continuous and in the periphery of cell (Chen et al. 1995; Miao et al. 2005).

In contrast, during vascular remodeling in areas exposed to disturbed flow including the arterial branch points and curvatures, the ECs are more polygonal in appearance without a clear orientation; their actin filaments are short, randomly oriented, and localized mainly at the cell periphery (Kim et al. 1989); the turnover rate of ECs is enhanced. The accelerated cell turnover rate at regions of disturbed flow probably plays a significant role in the disruption of junctional pro-

teins and the consequent increase of permeability to macromolecules such as the low-density lipoproteins which is a crucial pathogenesis process during atherosclerosis (Chen et al. 1995). Miao et al. also revealed that both in vivo (in the aortic arch and the poststenotic dilatation site beyond an experimental constriction) and in vitro (flow chambers), the intercellular junctional proteins—VE-cadherin has discontinuous distribution around the cell borders, which suggests the high permeability of endothelium at the preferential localization of atherosclerosis in regions exposed to complex flow patterns and fluctuating shear stress (Miao et al. 2005).

It has been reported that numerous mechanosensors on vascular cell membrane are involved in shear-induced vascular homeostasis or remodeling. There are five kinds of mechanosensors on membrane of ECs: (1) lipids (Chien 2003); (2) glycocalyx (Florian et al. 2003); (3) proteins, including integrins (Shyy and Chien 1997), ion channels (Hoger et al. 2002), junctional proteins (Haga et al. 2007), growth factor receptors (Tzima et al. 2005), receptor tyrosine kinases (RTKs) (Yang et al. 2016), G protein-coupled receptor (GPCRs) (Scimia et al. 2012), and platelet/endothelial cell adhesion molecule-1 (PECAM-1) (Conway and Schwartz 2015); (4) caveolae (Gilbert et al. 2016); and (5) primary cilia (Egorova et al. 2011). More detailed information about membrane mechanosensors on EC responses to (patho)physiological mechanical situation is referred to the excellent reviews (Chiu et al. 2009; Chiu and Chien 2011; Mohieldin et al. 2016).

Except the mechanosensors that consist in vascular cell membrane that is mentioned above, the cytoskeletal filaments are interconnected and also linked to membrane proteins throughout the cell. Cytoskeletons made of actin filaments, microtubules, and intermediate filaments provide elastic stiffness and maintain the shape and structure of the cell, enabling specific cellular functions (Huber et al. 2015). Interpenetration and interactions among different cytoskeletal networks combined with specific cross-linking are likely to influence cellular overall mechanical responses. Cytoskeletal dynamic assembly has been observed to response to different flow patterns. A lot of studies indicate that shear stress applied to the cell surface is transmitted to cytoplasmic sites via cytoskeletal deformations such as intermediate filament displacement or actin filament deformation (Macek Jilkova et al. 2014; Vartanian et al. 2010). Direct observation of intermediate filament displacement in cells expressing green fluorescent protein suggested that fluid shear stress altered the cytoskeletal mechanics rapidly (Helmke et al. 2001). More than its structural roles, cytoskeleton may also regulate gene transcription through the nucleocytoplasmic shuttling of mechanosensitive transcriptional activators (Speight? et al. 2016).

2.2 Cyclic Stretch and VSMC Mechanobiology

Since the cardiovascular system is pressure-driven, the vascular wall is continuously subjected to cyclic circumferential stress of around 100–150 kPa, which is generated by the pulsatile blood pressure. Following the pulsatile blood pressure, the arterial wall rhythmically distends and relaxes which cause the mechanical stretch on the intramural cells with the magnitude of 5–10% under physiological situation (Anwar et al. 2012). The excessive and pathological mechanical stretch, such as high magnitude stretches of 20% and above that occur during hypertension, has been shown to be harmful as it perturbs the vascular tone and causes inappropriate cellular response of vascular wall that can lead to cardiovascular abnormalities (Anwar et al. 2012; Haga et al. 2007).

VSMCs in vascular media are mainly exposed to mechanical stretch in vivo. In mature vessels, VSMCs are highly differentiated cells whose principal functions are contraction and regulating vessel diameter which is vital to blood vessel tone. Contractile proteins that participate in maintaining the contractility of VSMCs, such as α-actin, SM22α, calponin, and myosin heavy chain, have been shown to be the specific

differentiation markers of VSMCs (Owens et al. 2004). There is a strong evidence that the dedifferentiation (phenotypic transformation) of VSMCs, defined by the decreased expressions of contractile proteins, accompanied with increased proliferation, migration, and synthetic capacity, contributes to pathogenesis of vascular remodeling (Parizek et al. 2011).

Another important mechanobiological process that involved cyclic stretch is venous bypass graft, which is the most commonly employed clinical solution for a heart attack caused by atherosclerosis. The exposure of the grafting autologous veins to the new hemodynamic environment of the arterial circulation is thought to be an important stimulus for the venous remodeling, which induces neointima hyperplasia and causes late graft failure in the patient (Cheng and Du 2007; Cohen et al. 2014). The insertion of a grafting vein into the arterial system exposes the thin- walled and compliant vein to the arterial mechanical system that is much higher than what the venous wall is previously accommodated. Arterial cyclic stretch changes the functions of VSMCs in grafted veins, including excessive proliferation and migration, which mediates neointima formation during grafted vein remodeling (Cheng and Du 2007; Huang et al. 2017).

The mechanisms of mechanosensing of VSMCs in response to stretch is less well understood than that in ECs subjected to flowing shear stress. However, just as the cases in shear stress sensing, several membrane structures and proteins, such as primary cilium, connection proteins, and ion channel, have been shown to be mechanosensitive to cyclic stretch.

Primary cilium, which is an integral component of apical organelles on membrane, is widely accepted as a mechanosensor in ECs that is regulated by different flow patterns (Egorova et al. 2011; Nauli et al. 2008). Recent studies have successfully demonstrated the presence of primary cilia throughout the cardiovascular system, including arterial VSMCs. Primary cilia localize to VSMCs with their long axis aligned at 58.3 degrees angle in relation to the cross-sectional plane of the artery, projecting into the extracellular matrix (ECM). This preferentially oriented pattern may help primary cilia to detect a sudden increase in blood pressure, which in turn leads to a subsequent influx of calcium ions and increase in intracellular calcium concentration (Lu et al. 2008; Mohieldin et al. 2016). As a result, primary cilia enable cells to translate the extracellular mechanics into a variation of intracellular second messenger which triggers complex signaling cascades. Although in ECs, the primary cilia-triggered calcium induces the activation of endothelial nitric oxide synthase (eNOS), which modulates the synthesis of nitric oxide gas and vascular tone (AbouAlaiwi et al. 2009; Mohieldin et al. 2016), their roles in VSMCs has not been clearly defined.

Integrin proteins are transmembrane heterodimeric receptors comprising α- and β-subunits, which directly couple the ECM to actin filaments within the cell and allow the transmission of mechanical forces from outside microenvironment to inside biochemical reactions of the cells. To date, 24 kinds of integrin members have been described, and among them, 13 are found in VSMCs (Moiseeva 2001; Ye et al. 2014). The stretch induces integrin-dependent mechanotransduction through both large conductance calcium and voltage-activated potassium (BK) ion channel (Wu et al. 2008) and Src-dependent pathways (Min et al. 2012).

Besides cell-ECM connections, VSMCs on the cell membrane contain a variety of cadherin junctions which directly connect adjacent cells together and transfer mechanical signals from one cell to the next (Ye et al. 2014). The cadherins bind adjacent VSMCs and link them intracellularly to actin filaments via catenins, which is associated with various cellular functions, i.e., migration, proliferation, and survival. Among multiple subtypes of cadherins expressed on VSMC membrane, N-cadherin is highly expressed in both venous and arterial VSMCs and may play a significant role in mechanosensing and regulation of arteriolar contraction (Ye et al. 2014).

In addition, BK channels are predominantly expressed in VSMC membrane and play important roles in modulating cellular contraction to change blood vessel diameter, which then regulate vascular tone and mechanical flow (Pang and Rusch 2009; Sausbier et al. 2005). BK channel is composed of the α-subunit that forms the pore structure and the accessory β-subunit. Recent study revealed that hypertensive mechanical stretch decreased the expression of the BK channel α-subunit but increased its activity via endoplasmic reticulum (ER) stress-induced alternative splicing, which subsequently modulated BK activation and VSMC dedifferentiation. The alternative splicing of the stress axis-regulated exons of BK channel induced by elevated mechanical stretch may be an important determinant of BK channel activity under different hemodynamic conditions (Wan et al. 2015).

Vascular homeostasis or remodeling requires ECs and VSMCs to sense their local mechanical environments and switch the extracellular mechanical stimuli to the intracellular biochemical reactions. It had been established that via the activation or deformation of the membrane molecules and structures mentioned above, various intracellular signaling pathways are triggered, which is excellent reviewed by Haga et al. (2007) and Jufri et al. (2015). Recent researches demonstrated that noncoding RNA, including microRNA, long noncoding RNA (lncRNA), and circular RNA (cirRNA), may also participate in the mechanobiological regulation of vascular homeostasis and remodeling via posttranscriptional epigenetic regulations. Noncoding RNA-based therapies represent one of new frontier in the clinical development of targets and biomarkers of human cardiovascular diseases (Zhou et al. 2014). However, there are still many unknown areas in the research of noncoding RNAs under mechanotransduction. Multiple transcriptional factors, coactivators, or co-suppressors are involved in the regulation of noncoding RNA expression under mechanical regulation which needs to be elucidated. The unknown area is not only a challenge but also an opportunity scientists and clinicians need to work together to overcome the difficulties.

3 Role of Nuclear Envelope in Vascular Mechanotransduction

Nucleus is the largest and stiffest organelle in most cells, which plays an important role in housing and protecting the genetic information and serving as the site of DNA and RNA synthesis, transcription, and processing, as well as coordinating the intricate cellular architecture (Caille et al. 2002). As mentioned above, there are various mechanosensors in the membrane of vascular cells which transduce the mechanical stresses from the environment, including ECM and blood flow, to intracellular biochemical signals and subsequently transmit the related information into the nucleus. Cells under mechanical stimuli show altered cell signaling and cytoskeletal reorganization leading to changes in cellular phenotype ultimately. During recent years, the direct roles of nucleus especially the role of nuclear envelope (NE) in mechanosensing and mechanotransduction have gained more and more attention. Nucleus is also the force-responsive element, and the mechanical environment not only affects the position of nucleus in the cell but also affects the subnuclear structures and changes in subnuclear movement (Booth-Gauthier et al. 2013).

NE is the physical barrier between the cytoplasm and the genome and is composed of two lipid bilayers, i.e., inner nuclear membrane (INM) and outer nuclear membrane (ONM), nuclear membrane proteins, nuclear pore complexes (NPCs), as well as the nuclear lamina (Shah et al. 2017) (Fig. 3a). The INM and ONM, extensions of the rough ER, fuse at the NPCs and delineate a periplasmic space, which is continuous with the ER lumen. NPCs mediate the selective transport of macromolecules and the diffusion of small substances between the nucleoplasm and cytoplasm, like gatekeepers of the nucleus (Shah et al. 2017; Ungricht and Kutay 2017). In contrast to the understanding of the exchange of different sizes of molecules via NE, the role of NE in mechanotransduction and gene regulation is far from clear. LINC complexes, the nuclear membrane proteins which across the nuclear mem-

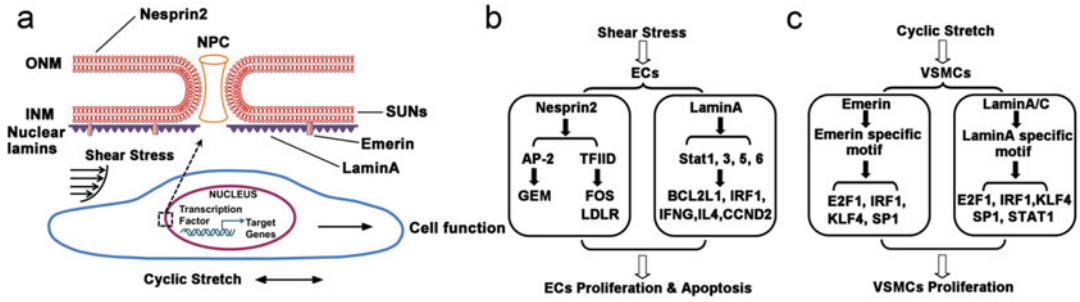

Fig. 3 Schematic diagram of the roles of NE in vascular mechanotransduction. (**a**) The schematic diagram of the components of NE that may be involved in the mechanotransduction in response to mechanical forces. (**b**). Low shear stress (0.5 Pa) represses the expressions of Nesprin2 and Lamin A, which impact the activations of transcription factors AP-2, TFIID, and Stat1, 3, 5, and 6, respectively; then regulate the mRNA levels of their downstream target genes; and induce the proliferation and apoptosis of ECs eventually. (**c**) Pathological cyclic stretch depresses the expression of Emerin and Lamin A/C, which bind to specific motifs in the DNA segments, respectively; decrease the binding of Emerin to promoter regions of E2F1, IRF1, KLF4, and SP1 and the binding of Lamin A/C to the promoter regions of E2F1, IRF1, KLF4, KLF5, SP1, and STAT1; and eventually induce VSMC proliferation [modified from (Han et al. 2017)]

brane and physically connected with both cytoskeleton and the nuclear lamina which form the scaffold beneath the INM. Recent researches suggested that LINC and nuclear lamina are two crucial parts of NE that may participate in the direct force transmission from the environment to the nucleus.

3.1 LINC Complexes in Mechanotransduction

Cytoskeleton is the major determinant of the physical and mechanical properties of a cell and mediates its responses to respective cues from the surrounding. All cytoskeletal polymers, including actin filaments, microtubules, and intermediate filaments, can connect to the NE via LINC complexes (Spichal and Fabre 2017). These physical connections of LINC complexes allow the direct transfer of mechanical signals along the cytoskeletal into the nucleus, and the components of LINC complexes may participate in maintaining nuclear and cellular organization as well as signal transduction (Tapley and Starr 2013).

LINC complexes, conserved from yeast to human being, are composed of the ONM- and INM-associated proteins including NE spectrin-repeat proteins (Nesprins) and Sad1/UNC-84 (SUN) proteins (Rothballer and Kutay 2013; Tapley and Starr 2013). Nesprins reside at the ONM and associate with all three kinds of cytoskeleton, i.e., actin filaments, microtubules, and intermediate filaments. The transmembrane structure of Nesprins provides a physical link which connects with cytoskeletal filaments on the cytoplasm side and with SUN proteins on the nucleoplasm side via Klarsicht, Anc-1, and Syne homology (KASH) domain, which is a 30-amino acid typically ending with the conserved motif, PPPX or PPPT (Hieda 2017).

The acronym KASH is derived from the conservation of the same domain in Klarsicht from *D. melanogaster*, ANC-1 from *C. elegans*, and Syne homology from mammals. Human genome contains six genes encoding proteins consisting KASH domain, and four of them are Nesprins (Nesprin1–4) (Rajgor and Shanahan 2013). Compared with Nesprin 4, Nesprin 1–3 are widely expressed in most cells. Nesprins have been shown to regulate cellular responses to mechanical forces. For example, Nesprin1 knockdown increases the number of focal adhesions and substrate traction while decreases the speed of EC migration induced by cyclic strain, accompanied by abnormal adhesion, migration, and cyclic strain-induced reorientation

(Chancellor et al. 2010). Recent study reported that Nesprin2 is sensitive to the fluid shear stress and closely related to EC functions. Low shear stress application represses expression of Nesprin2 which subsequently modulates the activation of some key transcription factors, then regulates the expressions of their target genes, and eventually increases both the proliferation and apoptosis of ECs (Fig. 3b) (Han et al. 2015). The physical link among the cytoskeleton-Nesprins-SUN is crucial for correct mechanotransduction, and the disruption of Nesprin-SUN complexes significantly reduces the force transmission from the cytoskeleton to nucleus, which perturbs the mechanical control of cell differentiation and abrogates the stretch-induced proliferation (Lombardi et al. 2011).

SUN proteins are firstly defined as a domain of shared homology between Sad1 in *Schizosaccharomyces pombe* and UNC-84 in *Caenorhabditis elegans* and are conserved across eukaryotes. Most SUN proteins contain a short coiled-coil domain that aids in dimerization or multimerization; meanwhile, the nucleoplasmic domain of SUN proteins interacts with nuclear lamina and chromatin-binding proteins (Bone et al. 2014). SUN proteins are at least one transmembrane protein specifically localized to the INM. Both human and mouse genomes encode at least six SUN proteins, in which SUN1 and SUN2 are widely expressed, whereas the other SUN proteins, SUN3 and SPAG4, appear to be expressed in a limited amount of tissues (Tapley and Starr 2013). The direct interactions between SUN proteins and KASH domain across the NE provide the core of linkers of the nucleoskeleton to the cytoskeleton and physically connect the nucleus interior to cytoskeletal networks. Removing of SUN1 weakens the nucleoskeleton, which reduces the mechanical forces transferred to nuclear (Starr 2012). Brosig et al. had proved that dominant negative Nesprin and SUN protein constructs enhanced transcriptional activity of NFκB, suggesting the degradation of nuclear LINC complexes contributes to conformational changes in chromatin structure and organization and then modulates transcription factor binding or transcriptional processes (Brosig et al. 2010).

Except the direct mechanical transmit effect of LINC complexes, the components of the complexes also play crucial roles in maintaining the structural integrity of nucleus. The transmission electron microscope (TEM) analysis revealed that either Nesprin2 or A-type lamin knockdown results in the degradation of NE phospholipid bilayer, suggesting that Nesprin2 and A-type lamins have essential roles in maintaining NE stability and normal structure (Han et al. 2015).

3.2 Lamina in Mechanotransduction

The nuclear lamina forms a mesh-like network of intermediate filaments localized mainly beneath the INM and plays a major role in maintaining the mechanical stability and shape of the nucleus (Goldman et al. 2002; Swift et al. 2013). There are four isoforms of lamins in mammalian cells: A-type lamins including LaminA and LaminC which are splice variants encoded by the LMNA gene and B-type lamins including LaminB1 and LaminB2 encoded by LMNB1 and LMNB2 genes, respectively (Goldman et al. 2002; Holaska 2008). Lamins are absent from unicellular organisms and plants, but all metazoan cells express at least one kind of B-type lamins. B-type lamins are essential proteins that are expressed in all cells throughout development, whereas A-type lamins are expressed only in differentiated cells (Dechat et al. 2008). The differential expression patterns of lamins suggest that A-type lamins may be important for inducing or maintaining the differentiated state. Recently, the differential expression of A-type lamins has been detected in cells subjected to different kinds of mechanical stimuli and shown to be involved in differential cellular functions, including DNA replication and repair, higher-order chromatin organization, signal transduction, and gene transcription (Dechat et al. 2008; Tzima et al. 2005). In human mesenchymal stem cells and two cancer cell lines, the differentially expressed A-type lamins can modulate cell migration and survival (Harada et al. 2014). Swift et al. found

that LaminA, but not LaminB, is changed by matrices with different stiffness and participates in the differentiation of mesenchymal stem cells induced by the stiffness of culture matrix (Swift et al. 2013).

Evidence is accumulating that A-type lamins and associated NE proteins are key regulators of mechanotransduction. It is supported by the finding that deficiency of A-type lamins ($LMNA^{-/-}$) increases nuclear deformation and attenuates NFκB-regulated transcription under mechanical strain, which suggests that deficiency of A-type lamins is thus associated with both defective nuclear mechanics and impaired mechanotransductions (Lammerding et al. 2004). Furthermore, downregulation of A-type lamins in ECs facilitates T cell migration through EC layers, suggesting that regulation of EC nuclear stiffness by both Lamin A and LaminC may modulate subendothelial migration of blood-borne immune cells, which is a key process in the developing of atherosclerosis (Song et al. 2016). Under pathological cyclic stretch, the expression of A-type lamins is depressed, which regulates a sequence-specific binding of A-type lamins to motifs of specific transcription factors and ultimately increases proliferation of VSMCs (Qi et al. 2016). In addition, LaminA is also involved in force sensing generated from cells within a tissue in differentiation. Matrix stiffness directly influenced LaminA protein levels, and LaminA transcription was regulated by the vitamin A/retinoic acid pathway with broad roles in development (Swift et al. 2013).

Emerin is another ubiquitous integral membrane protein that localizes to the INM and associates with Nesprin1, Nesprin2, SUN1/2, and A-type lamins. Emerin has a LEM domain and therefore binds barrier-to-autointegration factor (BAF), a conserved chromatin protein essential for cell division. BAF recruits Emerin to chromatin and regulates higher-order chromatin structure during nuclear assembly (Holaska 2008). The mutations in EMD (encoded Emerin) and LMNA are related to similar diseases, which are characterized by progressive skeletal muscle weakening, abnormal fat deposition, premature aging, and complex cardiac syndrome, including dilated cardiomyopathy and life-threatening irregular heart rhythms (Muchir and Worman 2007). Embryo fibroblasts cultured from LaminA-deficient mice ($LMNA^{-/-}$) (Lammerding et al. 2004) and Emerin-deficient mice ($EMD^{-/y}$ for males or $EMD^{-/-}$ for females, EMD located on the chromosome X in human and mouse) (Lammerding et al. 2005) are both associated with defective nuclear mechanics and impaired transcription of mechanically activated genes. In aorta media, the single nucleotide mutation of LMNA at G608G decreases the expressions of mechanotransduction proteins such as vinculin, transgelin, and vimentin in VSMCs under high, but not normal, shear stress (Song et al. 2014). The results of the current study on the hypertensive animal model and cultured VSMCs suggest that Emerin and A-type lamins have protective effects, and the repressed expressions of Emerin and A-type lamins by pathologically elevated cyclic stretch (15% cyclic stretch), which modulates their binding to the respective sequencing-specific motifs of transcription factors, induce the VSMC dysfunctions (Fig. 3c) (Qi et al. 2016). Using magnetic tweezers, Guilluy et al. introduces mechanical stretch to the isolated nuclei directly and revealed that mechanotransduction can occur within the nucleus that requires intact nuclear A-type lamins and Emerin (Guilluy et al. 2014). All these results suggest that both A-type lamins and Emerin are important mechano-responsive molecules and modulate the proliferation of vascular ECs and VSMCs in arterial walls in response to cyclic strain and shear stress. Other studies have found that the reduction in A-type lamins and Emerin reduces the viability of the nucleus and cytoskeletal microfilaments and results in a decrease in the activity and translocation of the transcription factor MRTF-A which is a kind of cardiomyocyte-related mechanically sensitive transcription factor that plays an important role in the development of the heart (Ho et al. 2013).

All these researches showed that A-type lamins and Emerin modulate nuclear structure, which directly affects gene regulation. On the other hand, NE elements can also interact directly

with chromosomes or multiple transcriptional regulators. For example, A-type lamins bind to pRb, c-Fos, and ERK1/2 (Ho and Lammerding 2012); Emerin interacts with β-catenin, BAF, and GCL (Wilson and Berk 2010). The results suggest that the structure of the nucleus, plasticity, and mechanical transmission between the nucleus and the cytoskeleton compose a complex intracellular signaling mechanotransduction network.

4 Summary and Perspectives

Vascular cells sense the extracellular mechanical stimuli, trigger complex intracellular signaling networks by mechanotransduction, and then modulate cell functions. The key point of mechanotransduction is the mechanosensing which transfers the outside mechanical stimuli to the inside biochemical signals. Growing evidences suggest that except the structures and molecules on cytomembrane, such as primary cilium, cell adhesion complex, connection proteins, as well as ion channels, structures and molecules associated with nuclear membrane, especially the LINC complexes and lamina of NE, also play important roles in sensing the mechanical environment and regulating multiple cell functions, including chromatin organization, DNA replication, and gene transcription.

In recent years, several new processes that are associated with NE remodeling have been discovered, including NE rupture and repair (Shah et al. 2017), NE assembly during interphase (Ungricht and Kutay 2017), NE autophagy (Dou et al. 2015), and NE mechanotransduction (Aureille et al. 2017; Osmanagic-Myers et al. 2015). Although in the last decade there are amount of progresses made in NE mechanotransduction that different components sense the mechanical force directly from extracellular environment or via cytoskeleton, many outstanding questions remain to be answered. For instance, a recent model hypothesizes a mirror structure between LINC complexes in the nucleus and integrin-based adhesions in the cell membrane (Aureille et al. 2017; Osmanagic-Myers et al. 2015); whether LINC complexes also have an "inside-out" regulation on the organization and structure of cytoskeleton or ECM still needs further demonstration. On the nuclear side of NE, researches revealed that mechanical forces modulate the binding ability of NE proteins to DNA (Qi et al. 2016); however, the components and structures involved in the DNA-binding process are still unclear. Furthermore, the present researches on mechanotransduction of NE are mainly based on the 2D culture system and whether the mechanisms in 3D system and in vivo situation are similar or not. So far, many NE proteins still remain poorly characterized, especially those that are only expressed in specific tissues.

Deeper researches on mechanotransduction will shed lights to understand the molecular mechanisms in both vascular homeostasis and remodeling; help to reveal the mechanical basis of cardiovascular diseases on tissue, cellular, and molecular levels; and might also provide potentiate novel targets to therapy for cardiovascular diseases.

Acknowledgments Work in our laboratory is supported by grants from the National Natural Science Foundation of China (Nos. 11625209, 11572199, and 11232010).

References

AbouAlaiwi WA, Takahashi M, Mell BR, Jones TJ, Ratnam S, Kolb RJ, Nauli SM (2009) Ciliary polycystin-2 is a mechanosensitive calcium channel involved in nitric oxide signaling cascades. Circ Res 104(7):860–869

Anwar MA, Shalhoub J, Lim CS, Gohel MS, Davies AH (2012) The effect of pressure-induced mechanical stretch on vascular wall differential gene expression. J Vasc Res 49(6):463–478

Aureille J, Belaadi N, Guilluy C (2017) Mechanotransduction via the nuclear envelope: a distant reflection of the cell surface. Curr Opin Cell Biol 44:59–67

Bone CR, Tapley EC, Gorjánácz M, Starr DA (2014) The Caenorhabditis elegans SUN protein UNC-84 interacts with Lamin to transfer forces from the cytoplasm to the nucleoskeleton during nuclear migration. Mol Biol Cell 25(18):2853–2865

Booth-Gauthier EA, Du V, Ghibaudo M, Rape AD, Dahl KN, Ladoux B (2013) Hutchinson-Gilford progeria syndrome alters nuclear shape and reduces cell motility in three dimensional model substrates. Integr Biol 5(3):569–577

Brosig M, Ferralli J, Gelman L, Chiquet M, Chiquet-Ehrismann R (2010) Interfering with the connection between the nucleus and the cytoskeleton affects nuclear rotation, mechanotransduction and myogenesis. Int J Biochem Cell Biol 42(10):1717–1728

Caille N, Thoumine O, Tardy Y, Meister JJ (2002) Contribution of the nucleus to the mechanical properties of endothelial cells. J Biomech 35(2):177–187

Chancellor TJ, Lee J, Thodeti CK, Lele T (2010) Actomyosin tension exerted on the nucleus through nesprin-1 connections influences endothelial cell adhesion, migration, and cyclic strain-induced reorientation. Biophys J 99(1):115–123

Chen YL, Jan KM, Lin HS, Chien S (1995) Ultrastructural studies on macromolecular permeability in relation to endothelial cell turnover. Atherosclerosis 118(1): 89–104

Cheng J, Du J (2007) Mechanical stretch simulates proliferation of venous smooth muscle cells through activation of the insulin-like growth factor-1 receptor. Arterioscler Thromb Vasc Biol 27:1744–1751

Cheng C, Tempel D, van Haperen R, van der Baan A, Grosveld F, Daemen MJ, Krams R, de Crom R (2006) Atherosclerotic lesion size and vulnerability are determined by patterns of fluid shear stress. Circulation 113(23):2744–2753

Chien S (2003) Molecular and mechanical bases of focal lipid accumulation in arterial wall. Prog Biophys Mol Biol 83(2):131–151

Chien S (2007) Mechanotransduction and endothelial cell homeostasis: the wisdom of the cell. Am J Physiol Heart Circ Physiol 292(3):H1209–H1224

Chien S (2008) Effects of disturbed flow on endothelial cells. Ann Biomed Eng 36(4):554–562

Chiu JJ, Chien S (2011) Effects of disturbed flow on vascular endothelium: pathophysiological basis and clinical perspectives. Physiol Rev 91(1):327–387

Chiu JJ, Wang DL, Chien S, Skalak R, Usami S (1998) Effects of disturbed flow on endothelial cells. J Biomech Eng 120(1):2–8

Chiu JJ, Usami S, Chien S (2009) Vascular endothelial responses to altered shear stress: pathologic implications for atherosclerosis. Ann Med 41(1):19–28

Cohen DJ, Osnabrugge RL, Magnuson EA, Wang K, Li H, Chinnakondepalli K, Pinto D, Abdallah MS, Vilain KA, Morice MC, Dawkins KD, Kappetein AP, Mohr FW, Serruys PW (2014) Cost-effectiveness of percutaneous coronary intervention with drug-eluting stents versus bypass surgery for patients with 3-vessel or left main coronary artery disease: final results from the synergy between percutaneous coronary intervention with TAXUS and cardiac surgery (SYNTAX) trial. Circulation 130:1146–1157

Conway DE, Schwartz MA (2015) Mechanotransduction of shear stress occurs through changes in VE-cadherin and PECAM-1 tension: implications for cell migration. Cell Adhes Migr 9(5):335–339

Davies PF (1995) Flow-mediated endothelial mechanotransduction. Physiol Rev 75(3):519–560

Dechat T, Pfleghaar K, Sengupta K, Shimi T, Shumaker DK, Solimando L, Goldman RD (2008) Nuclear lamins: major factors in the structural organization and function of the nucleus and chromatin. Genes Dev 22(7):832–853

Dou Z, Xu C, Donahue G, Shimi T, Pan JA, Zhu J, Ivanov A, Capell BC, Drake AM, Shah PP, Catanzaro JM, Ricketts MD, Lamark T, Adam SA, Marmorstein R, Zong WX, Johansen T, Goldman RD, Adams PD, Berger SL (2015) Autophagy mediates degradation of nuclear lamina. Nature 527(7576):105–109

Egorova AD, Khedoe PP, Goumans MJ, Yoder BK, Nauli SM, ten Dijke P, Poelmann RE, Hierck BP (2011) Lack of primary cilia primes shear-induced endothelial-to-mesenchymal transition. Circ Res 108(9):1093–1101

Florian JA, Kosky JR, Ainslie K, Pang Z, Dull RO, Tarbell JM (2003) Heparan sulfate proteoglycan is a mechanosensor on endothelial cells. Circ Res 93(10):e136–e142

Fung YC (1990) Biomechanics: motion, flow, stress, and growth. Springer-Verlag, New York

Giddens DP, Zarins CK, Glagov S (1993) The role of fluid mechanics in the localization and detection of atherosclerosis. J Biomech Eng 115(4B):588–594

Gilbert G, Ducret T, Savineau JP, Marthan R, Quignard JF (2016) Caveolae are involved in mechanotransduction during pulmonary hypertension. Am J Physiol Lung Cell Mol Physiol 310(11):L1078–L1087

Goldman RD, Gruenbaum Y, Moir RD, Shumaker DK, Spann TP (2002) Nuclear lamins: building blocks of nuclear architecture. Genes Dev 16(5):533–547

Greve JM, Les AS, Tang BT, Draney Blomme MT, Wilson NM, Dalman RL, Pelc NJ, Taylor CA (2006) Allometric scaling of wall shear stress from mice to humans: quantification using cine phase-contrast MRI and computational fluid dynamics. Am J Physiol Heart Circ Physiol 291(4):H1700–H1708

Guilluy C, Osborne LD, Van Landeghem L, Sharek L, Superfine R, Garcia-Mata R, Burridge K (2014) Isolated nuclei adapt to force and reveal a mechanotransduction pathway in the nucleus. Nat Cell Biol 16(4):376–381

Haga JH, Li YS, Chien S (2007) Molecular basis of the effects of mechanical stretch on vascular smooth muscle cells. J Biomech 40(5):947–960

Han Y, Wang L, Yao QP, Zhang P, Liu B, Wang GL, Shen BR, Cheng BB, Wang YX, Jiang ZL, Qi YX (2015) Nuclear envelope proteins Nesprin2 and LaminA regulate proliferation and apoptosis of vascular endothelial cells in response to shear stress. Biochim Biophys Acta 1853(5):1165–1173

Han Y, Huang K, Yao QP, Jiang ZL (2017) Mechanobiology in Vascular Remodeling. Natl Sci Rev nwx153

Harada T, Swift J, Irianto J, Shin JW, Spinler KR, Athirasala A, Diegmiller R, Dingal PC, Ivanovska IL, Discher DE (2014) Nuclear lamin stiffness is a barrier to 3D migration, but softness can limit survival. J Cell Biol 204(5):669–682

Helmke BP, Thakker DB, Goldman RD, Davies PF (2001) Spatiotemporal analysis of flow-induced intermediate

filament displacement in living endothelial cells. Biophys J 80(1):184–194
Hieda M (2017) Implications for diverse functions of the LINC complexes based on the structure. Cell 6(1):pii: E3
Ho CY, Lammerding J (2012) Lamins at a glance. J Cell Sci 125(Pt 9):2087–2093
Ho CY, Jaalouk DE, Vartiainen MK, Lammerding J (2013) Lamin a/C and emerin regulate MKL1-SRF activity by modulating actin dynamics. Nature 497(7450): 507–511
Hoger JH, Ilyin VI, Forsyth S, Hoger A (2002) Shear stress regulates the endothelial Kir2.1 ion channel. Proc Natl Acad Sci U S A 99(11):7780–7785
Holaska JM (2008) Emerin and the nuclear lamina in muscle and cardiac disease. Circ Res 103(1):16–23
Huang K, Bao H, Yan ZQ, Wang L, Zhang P, Yao QP, Shi Q, Chen XH, Wang KX, Shen BR, Qi YX, Jiang ZL (2017) MicroRNA-33 protects against neointimal hyperplasia induced by arterial mechanical stretch in the grafted vein. Cardiovasc Res 113(5):488–497
Huber F, Boire A, López MP, Koenderink GH (2015) Cytoskeletal crosstalk: when three different personalities team up. Curr Opin Cell Biol 32:39–47
Humphrey JD, Schwartz MA, Tellides G, Milewicz DM (2015) Role of mechanotransduction in vascular biology: focus on thoracic aortic aneurysms and dissections. Circ Res 116(8):1448–1461
Jufri NF, Mohamedali A, Avolio A, Baker MS (2015) Mechanical stretch: physiological and pathological implications for human vascular endothelial cells. Vasc Cell 7:8
Kim DW, Langille BL, Wong MK, Gotlieb AI (1989) Patterns of endothelial microfilament distribution in the rabbit aorta in situ. Circ Res 64(1):21–31
Lammerding J, Schulze PC, Takahashi T, Kozlov S, Sullivan T, Kamm RD, Stewart CL, Lee RT (2004) LaminA/C deficiency causes defective nuclear mechanics and mechanotransduction. J Clin Invest 113(3): 370–378
Lammerding J, Hsiao J, Schulze PC, Kozlov S, Stemart CL, Lee RT (2005) Abnormal nuclear shape and impaired mechanotransduction in emerin-deficient cells. J Cell Biol 170(5):781–791
Lombardi ML, Jaalouk DE, Shanahan CM, Burke B, Roux KJ, Lammerding J (2011) The interaction between nesprins and sun proteins at the nuclear envelope is critical for force transmission between the nucleus and cytoskeleton. J Biol Chem 286(30):26743–26753
Lu CJ, Du H, Wu J, Jansen DA, Jordan KL, Xu N, Sieck GC, Qian Q (2008) Non-random distribution and sensory functions of primary cilia in vascular smooth muscle cells. Kidney Blood Press Res 31(3):171–184
Macek Jilkova Z, Lisowska J, Manet S, Verdier C, Deplano V, Geindreau C, Faurobert E, Albigès-Rizo C, Duperray A (2014) CCM proteins control endothelial β1 integrin dependent response to shear stress. Biol Open 3(12):1228–1235
Miao H, Hu YL, Shiu YT, Yuan S, Zhao Y, Kaunas R, Wang Y, Jin G, Usami S, Chien S (2005) Effects of flow patterns on the localization and expression of VE-cadherin at vascular endothelial cell junctions: in vivo and in vitro investigations. J Vasc Res 42(1):77–89
Min J, Reznichenko M, Poythress RH, Gallant CM, Vetterkind S, Li Y, Morgan KG (2012) Src modulates contractile vascular smooth muscle function via regulation of focal adhesions. J Cell Physiol 227(11):3585–3592
Mohieldin AM, Zubayer HS, Al Omran AJ, Saternos HC, Zarban AA, Nauli SM, AbouAlaiwi WA (2016) Vascular endothelial primary Cilia: mechanosensation and hypertension. Curr Hypertens Rev 12(1):57–67
Moiseeva EP (2001) Adhesion receptors of vascular smooth muscle cells and their functions. Cardiovasc Res 52(3):372–386
Muchir A, Worman HJ (2007) Emery-Dreifuss muscular dystrophy. Curr Neurol Neurosic Rep 7(1):78–83
Nauli SM, Kawanabe Y, Kaminski JJ, Pearce WJ, Ingber DE, Zhou J (2008) Endothelial cilia are fluid shear sensors that regulate calcium signaling and nitric oxide production through polycystin-1. Circulation 117(9):1161–1171
Osmanagic-Myers S, Dechat T, Foisner R (2015) Lamins at the crossroads of mechanosignaling. Genes Dev 29(3):225–237
Owens GK, Kumar MS, Wamhoff BR (2004) Molecular regulation of vascular smooth muscle cell differentiation in development and disease. Physiol Rev 84: 767–801
Pang L, Rusch NJ (2009) High-conductance, Ca(2+) -activated K+ channels: altered expression profiles in aging and cardiovascular disease. Mol Interv 9: 230–233
Parizek M, Novotna K, Bacakova L (2011) The role of smooth muscle cells in vessel wall pathophysiology and reconstruction using bioactive synthetic polymers. Physiol Res 60:419–437
Qi YX, Yao QP, Huang K, Shi Q, Zhang P, Wang GL, Han Y, Bao H, Wang L, Li HP, Shen BR, Wang Y, Chien S, Jiang ZL (2016) Nuclear envelope proteins modulate proliferation of vascular smooth muscle cells during cyclic stretch application. Proc Natl Acad Sci U S A 113(19):5293–5298
Rajgor D, Shanahan CM (2013) Nesprins: from the nuclear envelope and beyond. Expert Rev Mol Med 15:e5
Rothballer A, Kutay U (2013) The diverse functional LINCs of the nuclear envelope to the cytoskeleton and chromatin. Chromosoma 122(5):415–429
Sausbier M, Arntz C, Bucurenciu I, Zhao H, Zhou XB, Sausbier U, Feil S, Kamm S, Essin K, Sailer CA, Abdullah U, Krippeit-Drews P, Feil R, Hofmann F, Knaus HG, Kenyon C, Shipston MJ, Storm JF, Neuhuber W, Korth M, Schubert R, Gollasch M, Ruth P (2005) Elevated blood pressure linked to primary hyperaldosteronism and impaired vasodilation in BK channel-deficient mice. Circulation 112:60–68
Scimia MC, Hurtado C, Ray S, Metzler S, Wei K, Wang J, Woods CE, Purcell NH, Catalucci D, Akasaka T, Bueno OF, Vlasuk GP, Kaliman P, Bodmer R, Smith LH, Ashley E, Mercola M, Brown JH, Ruiz-Lozano P

(2012) APJ acts as a dual receptor in cardiac hypertrophy. Nature 488(7411):394–398
Shah P, Wolf K, Lammerding J (2017) Bursting the bubble—nuclear envelope rupture as a path to genomic instability? Trends Cell Biol 27(8):546–555
Shyy JY, Chien S (1997) Role of integrins in cellular responses to mechanical stress and adhesion. Cur Opin Cell Biol. 9(5):707–713
Song M, San H, Anderson SA, Cannon RO 3rd, Orlic D (2014) Shear stress-induced mechanotransduction protein deregulation and vasculopathy in a mouse model of progeria. Stem Cell Res Ther 5(2):41
Song KH, Lee J, Park H, Kim HM, Park J, Kwon KW, Doh J (2016) Roles of endothelial A-type lamins in migration of T cells on and under endothelial layers. Sci Rep 6:23412
Speight P, Kofler M, Szászi K, Kapus A (2016) Context-dependent switch in chemo/mechanotransduction via multilevel crosstalk among cytoskeleton-regulated MRTF and TAZ and TGFβ-regulated Smad3. Nat Commun 7:11642
Spichal M, Fabre E (2017) The emerging role of the cytoskeleton in chromosome dynamics. Front Genet 8:60
Starr DA (2012) Laminopathies: too much SUN is a bad thing. Curr Biol 22(17):R678–R680
Suo J, Ferrara DE, Sorescu D, Guldberg RE, Taylor WR, Giddens DP (2007) Hemodynamic shear stresses in mouse aortas: implications for atherogenesis. Arterioscler Thromb Vasc Biol 27(2):346–351
Swift J, Ivanovska IL, Buxboim A, Harada T, Dingal PC, Pinter J, Pajerowski JD, Spinler KR, Shin JW, Tewari M, Rehfeldt F, Speicher DW, Discher DE (2013) Nuclear Lamin-a scales with tissue stiffness and enhances matrix-directed differentiation. Science 341(6149):1240104
Tapley EC, Starr DA (2013) Connecting the nucleus to the cytoskeleton by SUN-KASH bridges across the nuclear envelope. Curr Opin Cell Biol 25(1):57–62
Tzima E, Irani-Tehrani M, Kiosses WB, Dejana E, Schultz DA, Engelhardt B, Cao G, DeLisser H, Schwartz MA (2005) A mechanosensory complex that mediates the endothelial cell response to fluid shear stress. Nature 437(7057):426–431
Ungricht R, Kutay U (2017) Mechanisms and functions of nuclear envelope remodelling. Nat Rev Mol Cell Biol 18(4):229–245
Vartanian KB, Berny MA, McCarty OJ, Hanson SR, Hinds MT (2010) Cytoskeletal structure regulates endothelial cell immunogenicity independent of fluid shear stress. Am J Physiol Cell Physiol 298(2):C333–C341
Wan XJ, Zhao HC, Zhang P, Huo B, Shen BR, Yan ZQ, Qi YX, Jiang ZL (2015) Involvement of BK channel in differentiation of vascular smooth muscle cells induced by mechanical stretch. Int J Biochem Cell Biol 59:21–29
Wang Y, Shyy JY, Chien S (2008) Fluorescence proteins, live-cell imaging, and mechanobiology: seeing is believing. Annu Rev Biomed Eng 10:1–38
Wilson KL, Berk JM (2010) The nuclear envelope at a glance. J Cell Sci 123(Pt 12):1973–1978
Wu X, Yang Y, Gui P, Sohma Y, Meininger GA, Davis GE, Braun AP, Davis MJ (2008) Potentiation of large conductance, Ca2+−activated K+ (BK) channels by α5β1 integrin activation in arteriolar smooth muscle. J Physiol 586(6):1699–1713
Yang B, Lieu ZZ, Wolfenson H, Hameed FM, Bershadsky AD, Sheetz MP (2016) Mechanosensing controlled directly by tyrosine kinases. Nano Lett 16(9):5951–5961
Ye GJ, Nesmith AP, Parker KK (2014) The role of mechanotransduction on vascular smooth muscle myocytes cytoskeleton and contractile function. Anat Rec 297(9):1758–1769
Zhou J, Li YS, Chien S (2014) Shear stress-initiated signaling and its regulation of endothelial function. Arterioscler Thromb Vasc Biol 34(10):2191–2198

Endothelial Nuclear Lamina in Mechanotransduction Under Shear Stress

Julie Y. Ji

Abstract

Endothelial cells that line the lumen of blood vessels are at the interface between hemodynamic forces and vascular wall biology. Endothelial cells transduce mechanical and biological signals from blood flow into intracellular signaling cascades through a process called mechanotransduction. Mechanotransduction is an important part of normal cell functions, as well as endothelial dysfunction which leads to inflammation and pathological conditions. For example, atherosclerosis preferentially develops in regions of disturbed fluid flow and low shear stress. The nuclear lamina, which sits underneath the nuclear envelope, serves to maintain the nuclear structure while acting as a scaffold for heterochromatin and many transcriptional proteins. Defects in lamina and its associated proteins cause a variety of human diseases including accelerated aging diseases such as Hutchinson-Gilford Progeria syndrome. The role of nuclear lamina in endothelial mechanotransduction, specifically how nuclear mechanics impact gene regulation under shear stress, is not fully understood. In one study, lamin A/C was silenced in bovine aortic endothelial cells to determine its role in both glucocorticoid receptor (GR) nuclear translocation and glucocorticoid response element (GRE) transcriptional activation in response to its natural ligand dexamethasone as well as fluid shear stress. Results suggest that absence of lamin A/C does not hinder passage of GR into the nucleus but nuclear lamina is important to properly regulate GRE transcription. Ongoing research continues to investigate how nuclear lamins contribute to endothelial mechanotransduction and to better understand the role of Lamin A in vascular aging and in the progression of cardiovascular diseases.

J. Y. Ji (✉)
Department of Biomedical Engineering, Indiana University Purdue University Indianapolis, Indianapolis, IN, USA
e-mail: jji@iupui.edu

1 Background

1.1 Introduction to Arterial Morphology

Cardiovascular biomechanics is focused on understanding the interaction between mechanical forces of the vasculature and thephysiology of the

B. M. Fu, N. T. Wright (eds.), *Molecular, Cellular, and Tissue Engineering of the Vascular System*, Advances in Experimental Medicine and Biology 1097,
https://doi.org/10.1007/978-3-319-96445-4_5

circulatory system. Human circulation including the heart and the systemic and pulmonary circulation plays a vital role in ensuring constant delivery of oxygen and nutrients to all body parts depending on needs while also removing toxic waste products from metabolism. The vascular network is in constant contact with circulating molecular signals in blood and vital to communication and transport between different organs and parts of a body. It is also the first layer or protection against any blood-borne pathogens. The organized structure and properties of the vascular network are optimized to carry out this vital function. The pumping of the heart drives blood flow through the network of blood vessels, and the hemodynamic forces of blood flow are continuously impacting the vessel walls. On the other hand, the physiology of the vessel structure is designed to adapt and react to mechanical stimuli from its environment. Therefore, the blood vessel network must integrate biochemical and mechanical signals as part of its normal functions. To understand how blood flow impacts the biomechanics of the vasculature, we need to understand the basic structures of the arterial wall.

The arterial wall can be considered as a three-layer structure. The innermost layer that is in direct contact with blood flow is the intima, which contains a single layer of endothelial cells that sit on top of a thin layer of basement membrane consisting of elastin, collagen, and laminin fibers. This layer of endothelium is extremely important because it serves as the interface for exchange of nutrients, sugar, hormones, electrolytes, and other important molecules between blood and the tissues beyond. It is also a target for penetration by blood-borne pathogens and for drug delivery, all while under the hemodynamic forces of blood flow. Endothelial cells therefore play many roles. They act as a medium of transport, with select permeability, from blood to tissues; they are susceptible to hormones and other signaling molecules distributed by blood; and they are constantly exposed to mechanical forces due to pulsatile blood flow. The middle layer is the media, which consists mostly of vascular smooth muscle cells (VSMC) with different elastin and collagen contents. The smooth muscle cells actively regulate blood vessel width by contracting and relaxing in response to signaling molecules such as nitric oxide, thereby modulating the amount of blood flow entering the subsequent regions. The outermost layer is the adventitia, containing mostly fibroblasts and other connective tissues that help attach a vessel to its immediate environment. Embedded throughout these layers are various amounts of elastin, collagen, and extracellular matrix that help yield different mechanical properties for each layer.

In order to provide blood supply throughout a body, the arterial vessel network ranges in size from aorta, which is a few centimeters in diameter, down to capillaries that are wrap around a single red blood cells. Wall thickness and composition of muscle and elastic fibers vary greatly depending on location. The primary connective tissue fibers in the arterial wall are elastin and collagen. The elastic modulus of collagen fiber is typically an order of magnitude higher under physiological conditions than that of an elastin fiber (Shadwick 1999). Elastin is easily stretched, while collagen fibers are stiffer and form networks throughout the media and adventitia layers. Together elastin and collagen fibers in the vascular wall produce a nonlinear deformation response to transmural pressures. A combination of tensile and compressive forces within the vessel wall results in residual stress native to a living vessel tissue, which is part of the vessel remodeling process in response to blood pressure. VSMC themselves are active participants of vessel wall mechanics. They relax or contract under physiological signals as a way to help modulate vessel diameter. Changes in vessel diameter are directly related to volumetric flow rate and tissue resistance to flow. Thus, the media and adventitia layers are primarily responsible for structural and mechanical support of the vessel wall against continuous hemodynamics forces of blood flow. The single lumenal endothelial layer does not contribute to the mechanical properties of the vessel wall but is instead an active interface for signaling and transport. Endothelial to VSMC signals, for example, include as nitric oxide (NO) a potent vessel dilator. Activated endothelial cells in response to inflammation help

recruit neutrophils and other immune cells that infiltrate into tissues toward sites of inflammation. Endothelial cells are also first barrier to transport of drugs delivered to circulation. Thus the layers of vessel wall have distinct functions that work together to maintain optimal vascular condition under homeostasis.

1.2 Atherosclerosis and the Endothelium

Cardiovascular disease is the leading cause of death in developed countries. Atherosclerosis is a chronic inflammatory disease that develops over time in adults, with common risk factor such as poor diet, sedentary lifestyle, smoking, and age. It is initiated with the progressive buildup of oxidized low-density lipoproteins (LDL) in the arterial walls (Ross 1999). In the vascular networks, localized differences in hemodynamic forces that impact endothelial cells contribute to plaque formation. Reversing, disturbed flow patterns with low or alternating shear stress levels over time tend to promote an inflammatory endothelial expression profile, leading to endothelial cell dysfunction. These cells with activated inflammatory response cascades enhance further accumulation of LDL, as well as cholesterol and fats, underneath the endothelium. These pockets of reversing or low levels of flow and shear stress are also where disease-causing agents can accumulate, leading to increased mass transfer across the endothelium by diffusion. Any endothelial damage or disruption can also cause inflammatory response and infiltration of LDL and cholesterol. LDLs in subendothelial space become oxidized (ox-LDLs) and trigger the recruitment and infiltration of monocytes, which turn into macrophages. As these cells continue to accumulate LDL, they become foam cells. Eventually, smooth muscle cells (SMC) infiltrate and form a cover of fibrous tissue over the inflammation site as the lesion in the arterial wall is developed into an atherosclerotic plaque. The thickness of the SMC layer and its extracellular matrix changes over time, and rupture of this fibrous cap would result in an acute thrombotic event, resulting in heart attack or stroke.

Healthy functioning endothelium ensures proper circulation to tissues, delivery of oxygen, nutrients, and drugs, provides first line of defense against pathogens, and helps fight infections and inflammations. On the other hand, endothelial cells of the vessel wall also play an important role in the initiation and progression of atherosclerotic lesions (Teichert et al. 2008). Progression of vascular disease often begins with endothelial dysfunction. The endothelium has been an important topic of research on vascular physiology in part because of its important role in modulating the effects of both biological signals and mechanical stress from hemodynamics. Endothelial cells respond differently to their local hemodynamic environment and the corresponding mechanical stresses due to blood flow. As a result, they play an important role in help preventing or promoting the development of atherosclerotic plaques.

1.3 Hemodynamics of Blood Flow and Shear Stress

The heart works to pump blood throughout the circulation system. The pressure pulse of each heartbeat is largest at the aorta or larger arteries and dissipates down to descending arteries before reaching around zero in the capillaries. The structure of the arterial wall is designed to withstand each pressure pulse. Pumping of the heart is pulsatile in nature. With each heartbeat, the vessel wall is extended in the radial direction as forces of blood flow passes in the tangential direction. The mechanical stress generated by blood flow, in unit of force per area, is in two directions: either perpendicular (circumferential direction) or tangential (axial direction) to the vessel wall (Fig. 1A). The circumferential stress is due to blood pressure acting on the perimeter of the vessel wall, resulting in circumferential stretch. The axial stress, or shear stress, is the frictional force from blood flow parallel to the endothelium. Shear stress acts parallel to the vessel wall and is a result of blood viscosity and the

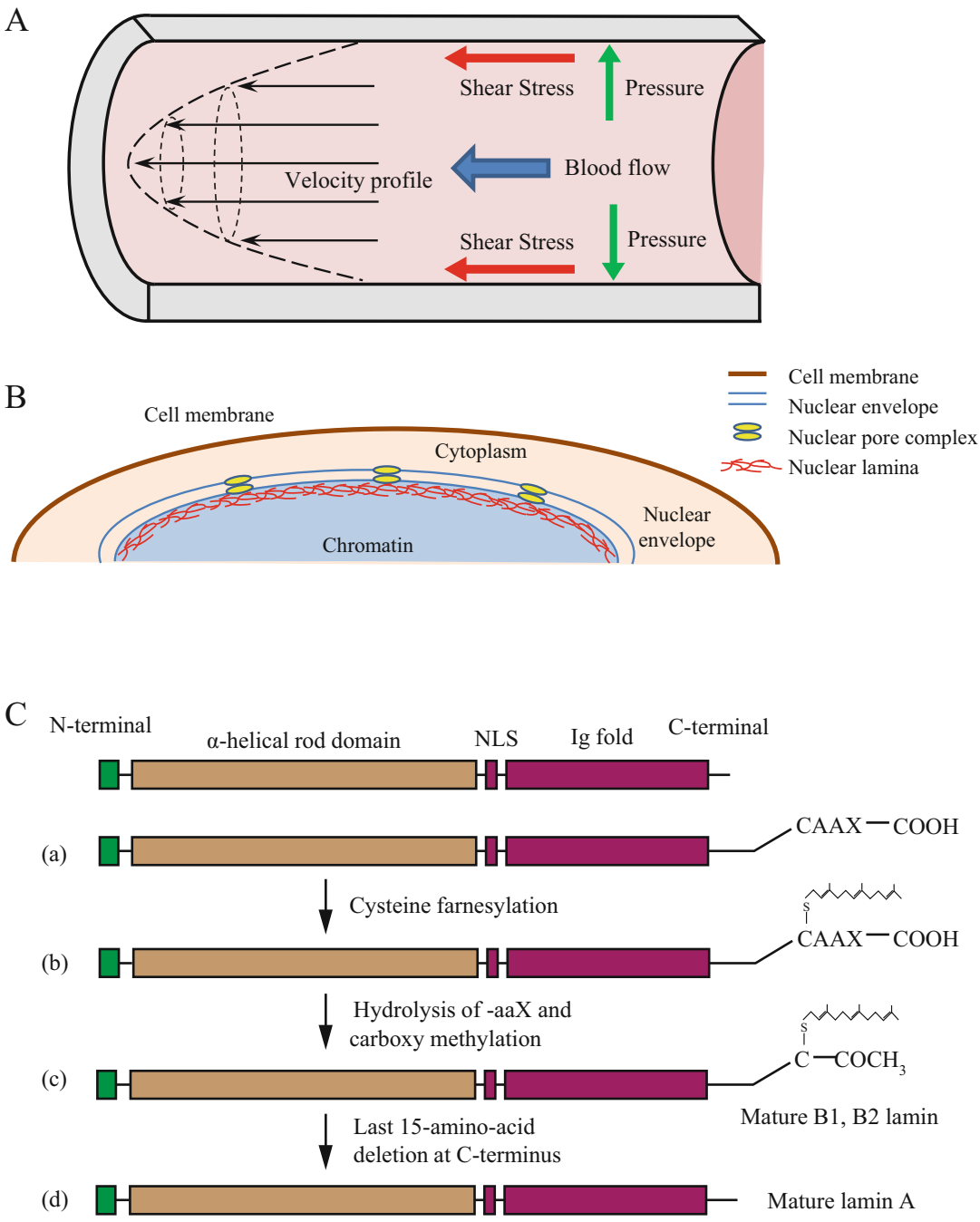

Fig. 1 (**A**) Diagram of hemodynamic forces from blood flow on the vessel wall. Shear stress is tangential to vessel wall, while pressure is perpendicular. (**B**) Cell structure at the nucleus. Then nuclear lamina sits underneath the nuclear envelope. (**C**) Top: schematic drawing of typical lamin structures, including a highly conserved α-helix rod domain and a more divergent N-terminal head and a C-terminal tail that contains NLS (nuclear localization signal that contains chromatin binding site) and Ig-fold domain. Posttranslational modifications in lamin proteins. Lamins after protein synthesis contain a complete—CAAX motif at C-terminus (a), and the cysteine in—CAAX motif is farnesylated by farnesyltransferase (b). The aaX residues are removed and the cysteine at the C-terminus is methylated (c), which produces mature B-type lamins. Mature lamin A will be generated after the last 15 amino acids being removed by ZMPSTE24

velocity gradient at the wall. These stresses are constantly being experienced by the endothelium on the lumen side and play an important role in the morphology, expression, and signaling of these cells. Exposure to shear stress is an integral part of basic functions of the endothelium. Imagine blood vessels to be a system of soft flexible cylindrical tubes. Then the complex geometry of the vasculature, with all its curvatures and bifurcations and other irregularities, will create distinct localized flow dynamics that will results in shear stress of varying magnitude and direction (Malek et al. 1999).

In particular, shear stress in straight section of the vasculature tend to be one-directional, constant, and higher in magnitude, between 10 and 70 dynes/cm^2 (Malek et al. 1999). High uniform shear stress is associated with a protective effect on endothelial cells, and these areas are more likely to stay free of pathological blockages. On the other hand, when blood flows into curved or branching sections, the hemodynamics changes significantly. As flow bends and curves, shear stress experienced by endothelial cells is more varied in direction and magnitude, as uniform flow becomes disturbed flow. Low shear stress (<5 dynes/cm^2) that is oscillating or reversing in direction is observed at curved or bifurcation sections, and the endothelium at these area has significantly different responses. The sections of the vasculature, around branching or bending points, are preferred sites for disease pathologies such as plaque formation and atherosclerosis. The endothelium at these sites under low or reversing flow tends to have completely different morphologies from those at straight sections. Moreover, these endothelial cells tend to pro-inflammatory and pro-atherosclerotic expression profiles, resulting in cellular damage under shear stress and possibly contributing to vascular diseases.

1.4 Shear Stress and Endothelial Cell Response

In general, endothelial responses to unidirectional steady laminar shear stress are very different from low, oscillatory shear stress. There is a significant body of work with extensive research on the different ways endothelial cells respond to mechanical stresses. Because endothelial cells sit at the interface between blood flow on the lumen side and the vessel wall tissues underneath, they are responsible for a variety of effects described as mechanotransduction. As the name implies, mechanotransduction is the translation of mechanical signals (such as shear stress, pressure, or environmental mechanical properties) into biochemical or biological responses in endothelial or other vascular cells.

The effect of shear stress on endothelium is an integral part of maintaining and modulating homeostasis in the vasculature. Fluid shear stress, at varying magnitude and direction, affects both normal and pathological endothelial functions, for example, in atherosclerosis pathology. In in vitro studies, shear stress between 10 and 25 dynes/cm^2 is commonly used for high shear stress. On the other hand, low shear stress of <5 dynes/cm^2) is used in oscillating or disturbed flow conditions (Chien 2007).

Endothelial gene expression profiles in vivo at regions of undeveloped or disturbed flow or developed or laminar flow were examined using gene microarray analysis. Cells were extracted from adult male pigs, at regions such as inner curvature of the aortic arch, where disturbed flow is present, and the descending thoracic aorta, where more laminar flow exists. Using reverse transcription polymerase chain reaction (RT-PCR) to amplify endothelial RNA samples, and a nearly 2000 gene microarray analysis, Passerini et al. identified specific gene expression profiles at these different regions. Low shear or oscillatory flow promotes an atherogenic endothelial phenotype with increased endothelial cell turnover and proliferation (Davies et al. 2002; Volger et al. 2007). Upregulated inflammatory cytokines were confirmed in the disturbed flow region. Similarly, there was an enhanced apoptosis and antioxidative transcription profile present in the disturbed flow regions (Passerini et al. 2004). Thus, endothelial mechanotransduction generally follows the paradigm that oscillating, reversing, and low shear stress tend to be associated with regions preferential to developing atherosclerosis, while laminar, uniform, high

levels of shear stress tend to be protective against atherosclerotic plaque formation.

1.5 Shear Stress and Endothelial Cell Signaling

Fluid shear stress influences endothelial cell phenotypes and functions, and mechanotransduction is carried out via a myriad of signaling pathways in endothelial cells. Some key findings are summarized in Table 1. Endothelial responses to shear stress can be categorized as immediate (rapid release of nitric oxide, NO (Kuchan and Frangos 1994)), short-term (upregulation of tissue plasminogen activator (tPA) gene (Diamond et al. 1990)), or long term. Sustained exposure to shear stress leads to endothelial cell realignment in the direction of flow and changes in structural organization, mechanical properties, and nuclear activities (Dewey et al. 1981). Endothelial mechanotransduction involves a variety of signaling molecules such as heat shock proteins, transcription factors, mitogen-activated protein kinases (MAPKs), and phosphoinositide 3 (PI3) kinase (Tseng et al. 1995). Ongoing research is mapping out the shear-induced endothelial

Table 1 Cellular response to laminar flow profile vs. disturbed flow profile

Endothelial cell response	Key signaling constituents	Laminar flow—physiological shear stress ($\geq \sim$10 dyne/cm^2)	Disturbed flow—low, oscillatory shear stress (0–4 dyne/cm^2)
		Cell response compared to static state conditions (no fluid flow)	
Apoptosis	Various activation pathways (Kaiser et al. 1997; Masuda et al. 1989)	Decreased	Increased
Proliferation	Cell division and vascular wall remodeling (Malek and Izumo 1994)	Decreased	Increased
Adhesion	Vascular cell adhesion molecule 1 (VCAM-1) (Ando et al. 1994; Hishikawa et al. 1995; Shyy et al. 1995)	Decreased	Increased
Vascular constriction	Endothelin 1 (ET-1) (Hishikawa et al. 1995; Malek and Izumo 1992)	Decreased	Increased
Vascular dilation	Endothelial nitric oxide synthase (eNOS) (Fleming et al. 1997; Palmer et al. 1988; Ranjan et al. 1995)	Increased	Decreased
Anti-oxidative response	Cyclooxygenase 1 (COX-1) and Mn superoxide dismutase (Mn SOD) (Topper et al. 1996)	Increased	Decreased
Inflammatory response	Monocyte chemotactic peptide 1 (MCP-1) (Korenaga et al. 1997)	Decreased	Increased
Thrombosis mediators	Tissue plasminogen activator (TPA) (Diamond et al. 1989; Malek and Izumo 1994)	Increased	Decreased
Growth mediators	Platelet derived growth factor (PDGF) A or B (Malek and Izumo 1994, Resnick et al. 1993; Shyy et al. 1995)	Decreased	Increased
Growth mediators	Growth inhibitor—transforming growth factor β1 (TGF-β1) (Ohno et al. 1995)	Increased	Decreased
Alignment/shape	Cell motility and focal adhesion kinase (FAK) (Dewey et al. 1981, Gimbrone et al. 1997, Zebda et al. 2012)	Aligned w/flow direction—elongated	No alignment—Random, polygon

pathways and their interplay with other cellular processes such as apoptosis.

In arterial regions susceptible to atherosclerotic lesions, inflammatory, thrombotic, and proliferative genes are upregulated (Malek et al. 1999). Low shear stress in these regions changes endothelial expression and increases cell turnover. Increased apoptosis disrupts the local endothelial layer and exposes the underlying layers to lipid accumulation and inflammation (Volger et al. 2007; Davies et al. 2002). Studies have identified various key signaling molecules that respond to endothelial shear, although their specific role in apoptosis and atherosclerosis remains ambiguous (Diamond et al. 1990; Kaiser et al. 1997; Passerini et al. 2004). One key mechanotransduction element, MAPK, is also transiently activated in immune response cascades by inflammatory cytokines such as those found in regions of low shear stress (Shyy et al. 1995). Tissue necrosis factor α (TNFα) and interleukin (IL) 1β are inflammatory cytokines that regulate endothelial responses. Cytokine induction of endothelial cells stimulates MAPKs such as c-Jun N-terminal kinase (JNK), extracellular signal-regulated kinase (ERK), and p38 proteins that play a significant role in mediating inflammatory responses including apoptosis.

Alternatively, high laminar shear stress was shown to inhibit cytokine activation of key MAPK signaling constituents. For example, shear stress phosphorylates MAPK which results in the activation of (ERK). Surapisitchat et al. confirmed that laminar shear stress inhibits downstream inflammatory signaling in endothelial cells (Surapisitchat et al. 2001). For each experiment, laminar shear stress (12 dynes/cm^2) was applied for 10 min followed by a 15 min cytokine, TNFα (10 ng/mL), incubation of sheared human umbilical vein endothelial cells (HUVECs). Shear stress alone was shown to stimulate ERK and p38 activity, while JNK expression was decreased compared to non-sheared controls. Furthermore, theexposure of shear stress decreased JNK expression by nearly 46%, while ERK and p38 activation under cytokine induction was not significantly affected by shear (Surapisitchat et al. 2001). This study highlights a key role of laminar shear stress in mitigating downstream inflammatory response stimulated by cytokine exposure. Mitogen-activated protein kinase phosphatase 1 (MKP-1) is a negative mediator of inflammatory signals and dephosphorylates both p38 and JNK. Laminar shear increased MKP-1 expression and downregulated vascular cell adhesion molecule 1 (VCAM-1) expression in HUVECs. These findings suggest that laminar shear stress induced MKP-1 expression to suppress JNK and p38 MAPK expression, both of which were stimulated by inflammatory cytokines. These studies emphasize the importance of laminar shear stress in suppressing inflammatory responses, which also overlaps with endothelial apoptosis signaling cascades.

At the same time, the endothelium is susceptible to signaling molecules and hormones circulating in blood. Endothelial cells possess a family of nuclear hormone receptors including the glucocorticoid receptor (GR) (Eickelberg et al. 1999). The anti-inflammatory effects of glucocorticoids such as dexamethasone on the endothelium suggest a protective role against development of atherosclerosis (Brostjan et al. 1997). Following ligand binding, the GR receptors undergo conformational changes, dimerization, and translocation from the cytoplasm to the nucleus, where they bind to specific DNA sequences (e.g., glucocorticoid response elements, GRE) to regulate genes via transactivation or transrepression (Zanchi et al. 2010). In fact, shear stress alone activates nuclear transport of GR and the GRE transcription pathway, through processes that were sensitive to mitogen-activated protein kinase (MAPK) and phosphatidylinositol 3-kinase (PI 3-kinase) inhibition (Ji et al. 2003). Arterial hemodynamic force may prove as potent as Dex in steroid-independent GR activation, further emphasizing the connections between shear stress, inflammation, and athero-pathology.

1.6 Nuclear Lamina

The nucleus is the biggest and most important organelle inside a cell, and its role in endothelial mechanotransduction can be potentially two parts: structural and mechanical as well as in regulating transcription or other signaling pathways. The nucleus is separated from the cytoplasm by the nuclear envelope (NE), which is composed of outer nuclear membrane (ONM) and inner nuclear membrane (INM) connected by nuclear pore complexes (NPCs) (Burke and Stewart 2013). Just beneath the nuclear envelope is the nuclear lamina, a dynamic network of lamin polymers and lamin-associated proteins (Gruenbaum et al. 2005). Lamins are type V intermediate filament (IF) proteins that form a filamentous network. Besides giving the nucleus structural support, the nuclear lamina is also home to a family of nuclear proteins that participate in chromatin organization, DNA replication, and repair, as well as gene regulation through interactions with peripheral heterochromatins or transcription factors (TFs) (Ho and Lammerding 2012; Gruenbaum et al. 2005). As a result, lamins also have a significant role in regulating epigenetic events. Furthermore, the nuclear lamina also links the cytoskeleton through nesprin and SUN proteins in the linker of nucleoskeleton and cytoskeleton (LINC) complex (Wilson and Berk 2010; Hutchison 2002; Crisp et al. 2006).

There are two types of lamins, A-type lamins and B-type lamins, according to their isoelectric values, (Krohne and Benavente 1986) that have similar protein structures. There is a highly conserved central rod domain which forms parallel coiled-coiled homodimers. The N-terminal head is short and globular, while long C-terminal tails of dimers join longitudinally to form polymers in vivo (Ho and Lammerding 2012; Kolb et al. 2011). Final lamin filaments are typically 10 nm in diameter (Dittmer and Misteli 2011) (Fig. 1B). There are three Lamin genes in mammals: LMNA, LMNB1, and LMNB2. LMNA encodes A-type lamins that have at least two major isoforms (Lamin A and Lamin C) and two minor forms (AΔ10 and Lamin C2) by alternative splicing (Wydner et al. 1996). B-type lamins, B1 and B2, are encoded by LMNB1 and LMNB2, respectively (Alsheimer et al. 2000; Biamonti et al. 1992; Burke and Stewart 2013). It is thought that A-type lamin, or lamin A/C, is a greater contributor to maintaining nuclear shape and stiffness, since deletion or mutation of lamin A/C resulted significantly distorted nuclei morphology as well as phenotypes (Lammerding et al. 2006). Lamin A is first transcribed as prelamin, the lamin A precursor, which has a CAAX motif at carboxyl-terminus, where the cysteine is farnesylated by farnesyltransferase (FT) after protein synthesis to facilitate its localization at nuclear envelope. Next, the -aaX residues are hydrolyzed by a zinc metallo-endoprotease (Zmpste24 or FACE-1) on prelamin A. The farnesylated cysteine is methylated afterward. B-type lamins have permanently farnesylated tails. In prelamin A, the last 15 amino acids (including the farnesylated cysteine) is removed by Zmpste24, resulting in mature Lamin A (Burke and Stewart 2013).

1.7 Laminopathies

Mutations of the Lamin protein cause a wide range of human diseases called laminopathies (Bonne et al. 1999; Bione et al. 1994; Fatkin et al. 1999; Cao and Hegele 2000; De Sandre-Giovannoli et al. 2002; Eriksson et al. 2003). Laminopathies cover a multitude of overlapping phenotypes, including loss of skeletal and cardiac muscle tissues and subcutaneous adipose tissue, such as Emery-Dreifuss muscular dystrophy (EDMD) and Dunnigan-type familial partial lipodystrophy (FPLD), as well as peripheral nerve dysfunctions, such as Charcot-Marie-tooth disease (CMT). Cells from patients with Lamin A/C mutations that cause muscular disorders had abnormal and disrupted lamina network resulting dramatically distorted nuclei. Instead of being circular in shape, these nuclei look distorted, flattened, with blebbings. The distorted nuclei could contribute to their increased mechano-sensitivity to stresses, and that might partially explain significant damages in skeletal and cardiac muscles that are often exposed to more stress in vivo (Muchir et al. 2007).

One type of laminopathy, Hutchinson-Gilford progeria syndrome (HGPS), is a disease caused by a point mutation in lamin A gene, which leads to premature aging in children (Butin-Israeli et al. 2012; Gruenbaum et al. 2005; Hutchison and Worman 2004). In HGPS, a rare point mutation on the lamin A gene *LMNA* G608G unveils a cryptic splice site that eventually yield a truncated and farnesylated prelamin mutant form called progerin (Δ50 lamin A). HGPS cells were reported to have missense mutations on exon 11 on LMNA that create a cryptic splice site responsible for the deletion of 50 amino acids near C-terminus, resulting in an absence of the recognition site of Zmpste24 for the final 15 amino acid removal on prelamin A. This lack of posttranslational modification will lead to the generation of a truncated prelamin A called progerin that has permanently farnesylated tail.

Except for the resemblance in appearance between patients with progeroid syndromes (mainly HGPS) and elderly people, they also share similarities at cellular level that include increased DNA damage, defects in DNA repair, and shortened telomere length, which significantly impair cell proliferation capacity (Dreesen and Stewart 2011). More importantly, they are both prone to developing advanced atherosclerotic lesions, although the extensive loss of smooth muscle cells (SMCs) in arteries and thickened adventitial fibrosis in veins were only observed in HGPS patients than in elderly people (Olive et al. 2010). Children with HGPS exhibit premature signs of aging and typically die in their teens from myocardial infarction or stroke from advanced atherosclerosis typical of much older people (Scaffidi et al. 2005). HGPS patients develop signs of old age early in life, such as hair loss, hard skin, and lipoatrophy (Scaffidi et al. 2005). On the other hand, they are without other typical symptoms of aging such as cataracts, cancer, osteoporosis, or mental deterioration (Hennekam 2006). High blood pressure and difficulty to control blood pressure starts early in life, and their cholesterol levels are at the high adult levels (Stehbens et al. 1999). Cells with progerin demonstrate abnormal nuclear shape and morphology. Interestingly, progerin is also found in healthy older individuals whose cells also exhibit abnormal nuclear shape like HGPS cells (Scaffidi and Misteli 2006).

The characteristics of vascular dysfunction in HGPS are strikingly similar to those developed with normal aging. Despite their age, lack of family history, and other risk factors such as smoking or diet, they develop an aggressive form of atherosclerosis. In the cardiovascular system, HGPS is marked by gradual disappearance of VSMC, increased collagen deposits, and hardening of the arteries (Merideth et al. 2008). Other similarities between HGPS and aging vessels include expression of inflammatory markers, arterial calcification, extracellular matrix (ECM) deposition, media and adventitia thickening, increased senescence, and loss of VSMC (Brassard et al. 2016). However, in HGPS, intimal lesions are often fibrotic and acellular, and HGPS patients had significantly greater VSMC depletion in media layer where disorganized type I collagen and fibrous tissue are found instead (Olive et al. 2010), which likely contribute to an increased vessel stiffness. Interestingly, the endothelium in HGPS patients or mice is less affected by HGPS and remains mostly intact (Varga et al. 2006).

Disease mechanisms of laminopathies responsible for tissue-specific phenotypes are not fully characterized. Two interrelated hypothesis have been proposed. Lamin mutations either lead to a more fragile nucleus, resulting in increased susceptibility to mechanical forces (structural hypothesis) or disrupt gene transcriptional regulation (gene regulation hypothesis). Research on the disease mechanisms of laminopathies suggests a crucial role for lamins as a load-bearing structure necessary for withstanding mechanical stresses to the nucleus and structural integrity and normal nuclear mechanics (Lammerding et al. 2004; Dahl et al. 2008). (Lammerding et al. 2004, 2006). Endothelial cells of patients with laminopathies show hindered regeneration after injury, resulting in suboptimal intimal integrity (Al-Shali and Hegele 2004). While long-term sustained exposure to shear stress leads to both endothelial cell realignment with flow and changes in structural organization, mechanical properties, and nuclear activities (Dewey et al. 1981), the role of lamins in endothelial mechanotransduction is not yet fully understood. Ongo-

ing research continues to reveal the correlations between truncated prelamin A and normal aging process, which might shed light on discovering aging mechanisms and treatments for those patients suffered from accelerated aging diseases. (Cao et al. 2011; Yang et al. 2006).

2 Using Image Analysis Tools to Study Endothelial Nuclear Lamina in Mechanotransduction

2.1 Introduction

The rest of this chapter will highlight a study on mechanotransduction in endothelial cells at the nucleus (Nayebosadri et al. 2012; Nayebosadri and Ji 2013). This study demonstrates the ability of mechanical stress to induce ligand-independent receptor activation, nuclear import, and subsequent gene activation. Endothelial cells, as do most cell types, possess nuclear receptors such as the glucocorticoid receptor (GR) (Eickelberg et al. 1999) that respond to steroid hormones under physiological conditions. GR is part of the superfamily of nuclear receptors that function as DNA-binding, transcription regulators. Following passive transport through the cell membrane, glucocorticoids such as Dex bind to GR and initiate conformational change, dimerization, and release of heat shock proteins. GR has also been shown to become activated in a ligand-independent manner via phosphorylation of specific serine residues at the N-terminus by ERK, MAPK, glycogen synthase kinase-3, and protein kinases A and C (Adcock 2001; Adcock and Caramori 2001; Itoh et al. 2002). Subsequently, GR's nuclear localization signal is exposed which allows the complex to translocate into the nucleus through the nuclear pore complex and bind to GRE to regulate target genes (Barnes 1998). Specifically, it can induce transcription of anti-inflammatory genes via a process known as transactivation or suppress inflammatory gene expression by inhibitory protein-protein interactions, referred to as transrepression (Beck et al. 2009).

As discussed above, the lamina serves as a scaffold for nuclear proteins, influences gene expression, supports chromatin organization and DNA replication, and links the cytoskeleton through nesprin and SUN proteins in the LINC complex (Wilson and Berk 2010; Hutchison 2002; Crisp et al. 2006). Cells with defective lamina demonstrate deformed nuclei, disorganized heterochromatin, and a defective DNA damage response pathway (Dahl et al. 2008; Sieprath et al. 2012). It is hypothesized that signaling cascades are hindered when the lamina is disrupted and the nucleus becomes fragile and deformed. Specifically, a defective lamina, cytoskeleton, and integrin relay may affect the proper transduction of extracellular stress, thus leading to altered transcriptional regulation or deregulation.

GR has already described as an anti-inflammatory nuclear receptor that can be regulated by shear stress (Ji et al. 2003). Using a unique expectation-maximization algorithm based on Bayesian statistics, GR subcellular movement can be quantified based on changes of fluorescently labeled GR (GFP-GR). An image analysis process was developed based on segmentation tools to quantitatively show the time progression of intracellular GFP-GR fluorescence. By quantifying minute local variations in brightness over time as activated GR moves into the cell nucleus, cytoplasm and nuclear presence of GFP-GR under chemical or mechanical stimulation was successfully tracked over time. Image-based results also correlated with protein analysis of GR in the cytoplasm and nuclear fractions. This method of quantifying intracellular movement of fluorescently labeled receptors is important in studies to better understand nuclear receptors pathways in endothelial mechanotransduction.

2.2 Methods

2.2.1 Cell Culture and Shear Stress

In this study, bovine aortic endothelial cells (BAEC) were used. Cells at passages 10 or less were cultured under standard cell culture conditions and seeded on 38 × 75 mm glass

slides coated with fibronectin (1 mg/mL), at density of 5 to 6 $\times$ 10^5 cells per slide. To prepare cells for experiments, cells were maintained in in regular growth media with 10% charcoal/dextran-treated fetal bovine serum (FBS), instead of regular FBS. Charcoal/dextran treatment ensures removal of hormones and potential glucocorticoid analogs that would interfere with background readings. In order to highlight GR receptors as well as the nuclear lamina inside cells, cells were transfected with fluorescently labeled GR and lamin A. In the GFP-GR plasmid vector, the mouse GR cDNA N-terminus was fused in frame to the C-terminus of green fluorescence protein (GFP) (Ji et al. 2003). The pRFP-laminA plasmid contains full-length human lamin A, placed at the carboxyl-terminus of the fluorescence tags (Ji et al. 2007). BAECs on slides were transfected for 4 h with both pGFP-GR and pRFP-LaminA and allowed to recover overnight. Alternatively, BAECs were incubated with blue nuclear chromatin Hoechst stain (1:1000 dilution) for 15 min for nuclear fluorescence imaging.

For shear experiments, cells on slides were placed in parallel plate flow chambers attached to a sterile, laminar flow system as previously described (Frangos et al. 1988; Pavalko et al. 2003). Everything is placed in an environmental chamber kept at 37 °C with 5% CO_2. The magnitude of shear stress (τ) on the cell monolayer is calculated based on the Navier-Stokes equation for a Newtonian fluid in a parallel plate geometry. The equation for wall shear stress simplifies to $\tau = \frac{6\mu Q}{bh^2}$, where μ is the viscosity of the media (0.01 dynes/cm^2), Q is the volumetric flow rate ($\sim$0.5 mL/s), b is the width of the flow chamber (2.5 cm), and h is the separation distance between the chamber and the glass slide (0.025 cm). Using this system, cells were exposed to 10 or 25 dynes/cm^2 laminar wall shear stress. Flow experiments were carried out in regular growth media (10% charcoal/dextran-treated FBS). For live cell imaging, the flow chamber is placed flat on a fluorescence microscope stage enclosed inside a 37°C chamber. Phase contrast and fluorescence images were captured through a CCD camera at 10$\times$ or 40$\times$ magnification.

2.2.2 Development of Segmentation Image Analysis Tools

Time-lapse images of live cells under flow or Dex induction were subjected to quantitative image analysis. The Bayesian-based image analysis algorithm is a much more efficient, robust, and consistent way of analyzing fluorescence images of cells over time compared to current methods in literature. Statistical Bayesian techniques have been successfully applied to the segmentation of medical images with low signal-to-noise ratios (Marroquin et al. 1987; Chen et al. 2003). Due to the low signal levels and noise in the fluorescence imaging, a statistical approach was used to obtain segmented measurements from the digital image data. Optimal estimate of both the image segmentation and of the mean and variance of the segmented areas was automatically provided by the expectation-maximization/maximization of posterior marginal (EM/MPM) algorithm (Chen et al. 2003).

Briefly, for this application the input images for the segmentation, denoted here as Y, are modeled as a signal X, with additive noise: $Y = X + \eta$. This statistical approach treats the GFP image data as Markov random fields (MRF) and uses Bayes rule to take advantage of a prior model. The mathematical formulation begins with Gaussian iid (independent, identically distributed) statistics (mean and variances) for N segmentation classes denoted in a vector: $\theta = (\mu_1, \sigma_1, \mu_2, \sigma_2, \ldots, \mu_N, \sigma_N)$. The probability mass function for X given the noisy image Y, $p_{X\,|\,Y}(x|\,y, \theta)$, is iteratively maximized. The best estimate at each pixel, $\widehat{x}$, of the total image, X, is developed from Bayes rule.

$$p_{X|Y}\,(x|y,\theta) = \frac{f_{Y|X}\,(y|x,\theta)\;p_X(x)}{f_Y\,(y|\theta)}$$

The joint probability density function, $f_{Y\,|\,X}(y|\,x, \theta)$, also called the likelihood function, is the multiplication of the Gaussians over the whole set of pixels in the image $s \in S$, where x_s is the segmentation at a particular pixel being analyzed.

The model for the prior, $p_X(x)$, is developed with two parts. First, a neighborhood is devel-

oped, denoted as C, containing the four nearest neighbors to a pixel. Using a counting function, $t\,(x_s, x_r) = \left\{ \begin{matrix} 0 \forall x_r = x_s \\ 1 \forall x_r \neq x_s \end{matrix} \right\}$, the current pixel, x_s, is compared to its neighbors, x_r. This $t(x_s, x_r)$ function will increase the likelihood that near neighbors in an image will be the same segmented value. Second, the RFP-LaminA images are used to assign a probability value: γ_{x_s} for the pixels in the nucleus, taking advantage of the prior knowledge identifying the cell nucleus.

$$\widehat{x} = \arg\max_{x} \left\{ \sum_{s \in S} -\log \sigma_{x_s} - \frac{\left(y_s - \mu_{x_s}\right)^2}{\sigma_{x_s}^2} - \sum_{[r,s] \in C} \beta t\,(x_s, x_r) - \sum_{s \in S} \gamma_{x_s} \right\}$$

The above equation is used to find the best estimate of x, by iterating through the image, using this formula at each pixel with maximization of posterior marginals (MPM) (Marroquin et al. 1987). The optimal Gaussian means and variances for the segmented image, the vector $\theta = (\mu_1, \sigma_1, \mu_2, \sigma_2, \ldots, \mu_N, \sigma_N)$, are found using the expectation-maximization (EM) optimization in conjunction with MPM. The user begins the sequence by providing the input of the number of segmentation classes in the image (in this case, corresponding to three biological structures: background, cell nucleus, and cytoplasm). Next, a starting point for θ is established automatically. Once the first few iterations of the MPM are completed, providing the current $\widehat{x}$; a new estimate of theta is developed from statistics of the MPM. This new estimate of theta is then used in the next iterations of MPM. These processes alternate until a test for convergence is met.

2.2.3 Quantitative Image Analysis

Quantitative assessment of GFP-GR translocation was done using the following process:

1. First, GFP-GR images were converted to 8-bit black and white (Fig. 1Aa, b).
2. RFP-LaminA or Hoechst stain images were also converted to 8-bit black/white images and then thresholded to obtain the nucleus, which is then used as a prior atlas (Fig. 1Ac, d).
3. For each time point, the new RFP-LaminA and GFP-GR images were processed to form the segmentations: Background, cell nucleus, and cytoplasm (Fig. 1Ae). This produced a time sequence of segmentations of the GFP-GR images with each sample treated independently.

The pixel data's brightness, measured by mean and variance of each segmented class, was provided as an output and then a plot of time series data provides the variation of nucleus and cytoplasm brightness. For each time point, the nucleus value was divided by the cytoplasm value to obtain a normalized nucleus brightness and to account for changes in brightness that may have occurred due to focus drift. Then value at each time point was normalized to the brightness at $t = 0$. Average and standard error were obtained for n number of cells analyzed.

2.3 Results

2.3.1 Dexamethasone Induced up to 60% GR Nuclear Translocation Within 20 Min

BAECs transfected with GFP-GR showed localization of the protein throughout the cytoplasm and nucleus. Upon addition of a synthetic glucocorticoid dexamethasone (Dex), GFP-GR began to show immediate signs of nuclear translocation as the brightness of the nucleus increased and that of the cytoplasm decreased. Within 20 min, GFP-GR had significantly translocated to the nucleus as outlined by the RFP-LaminA. Figure 2B shows images of a cell with green fluorescence labeled GR, red fluorescence labeled lamina, and their merged images, at 0 and 20 min with Dex. The nuclear lamina, on the other hand, remained unchanged. Nuclear translocation of GFP-GR was quantitatively track over time based on segmentation analysis of time-lapse images for the first 20 min after adding Dex (25 μM) (Fig. 2C).

A steady increase in green fluorescence at the nucleus as outlined by RFP labeled lamina was observed, up to 58.5 ± 0.7% ($n = 11$) increase in 20 min. A rapid nuclear localization of GFP-GR with Dex induction was anticipated, as reported previously (Ji et al. 2003); however the dynamics of GR nuclear movement has not been quantified till now. This image analysis result suggests that within the first 15 min of Dex induction, almost 60% of cytoplasm GFP-GR has translocated into the nucleus. Western blots of endogenous GR showed similar trend.

2.3.2 Laminar Shear Stress Induced GR Nuclear Translocation in a Dose-Dependent Manner

Physiologically relevant shear stresses of 10 and 25 dynes/cm^2 were applied on BAECs in a parallel plate flow chamber to further assess ligand-independent GR activation and intracellular movement. It was previously reported that GR localizes to the nucleus within 2 h (Ji et al. 2003). In those cases, cells were sheared for 2 h and then removed from flow chambered and imaged. This current setup allows for real-time time-lapse imaging of cells as they are being sheared. Compared to Dex induction, GR movement is slower, and nuclear localization is less pronounced, occurring within 2 h, compared to about 20 min with Dex. Figure 2D shows an example of a cell sheared with 25 dynes/cm^2. While the red nuclear lamina does not change in shape or brightness within 2 h of shear, GFP-GR becomes increasingly nuclear concentrated. Quantitative image analysis algorithm allowed for more precise, quantitative assessment of GR nuclear movement (Fig. 2E). When BAECs were exposed to 25 dynes/cm^2, there is a steady and gradual increase of fluorescence in the nucleus throughout the 2 h time frame, with the greatest increase in nuclear brightness occurring between 30 and 60 min, at an average 0.286% increase per minute. Expectation-maximization (EM) algorithm results demonstrate that there is a 16.1% change in the nucleus within the first hour and a 22.1 ± 0.02% change after 2 h. With shear stress of 10 dynes/cm^2, the greatest change in nuclear brightness occurred between 60 and 90 min, at an average 0.264% increase per minute. The total brightness change over 2 h was 20.2 ± 0.02% for the nucleus. Image analysis algorithm provided quantitative assessment of GR intracellular movement that would not be otherwise revealed in time-lapse videos alone. The finding that GFP-GR nuclear localization occurred faster with higher shear stress of 25 dynes/cm^2 suggests a dose-dependent effect of shear stress on the rate of GR nuclear localization, particularly within the first 90 min of shearing. In fact, at 60 and 70 min of shearing, the nuclear brightness is significantly higher in cells exposed to 25 dynes/cm^2 compared to 10 dynes/cm^2 ($P < 0.05$).

The finding that arterial shear stress may act similarly to glucocorticoids to induce GR nuclear localization through a steroid-independent mechanism is significant because it suggests that mechanical forces alone can trigger intracellular movement of GR into the nucleus. The nuclear matrix has been shown to serve as a scaffold and stabilizer for GR and other transcription factors upon the formation of protein complexes (Lloyd et al. 2002). It is not known, however, how GR nuclear functions would be affected by the absence of lamina. Understanding the role of endothelial lamina in shear-induced GR nuclear localization and transcription regulation would help elucidate how force transduction and nuclear mechanics impact gene regulation.

2.3.3 Lamin Silencing Did Not Hinder GR Nuclear Translocation under Shear Stress or Dexamethasone

Lamin A/C in BAECs was successfully silenced using stable transfection with shRNA lentiviral particles. Western blot of whole cell lysate revealed an absence of lamin A/C proteins in cells treated with lentiviral particles containing the lamin shRNA plasmid (Fig. 3A). Cells treated with non-targeting plasmid still demonstrated consistent lamin A/C expression. Fluorescence labeling of cell nuclei with lamin shRNA using nuclear Hoechst stain also revealed distorted nuclear shapes compared to cells with control shRNA (Fig. 3B) that showed the characteristic

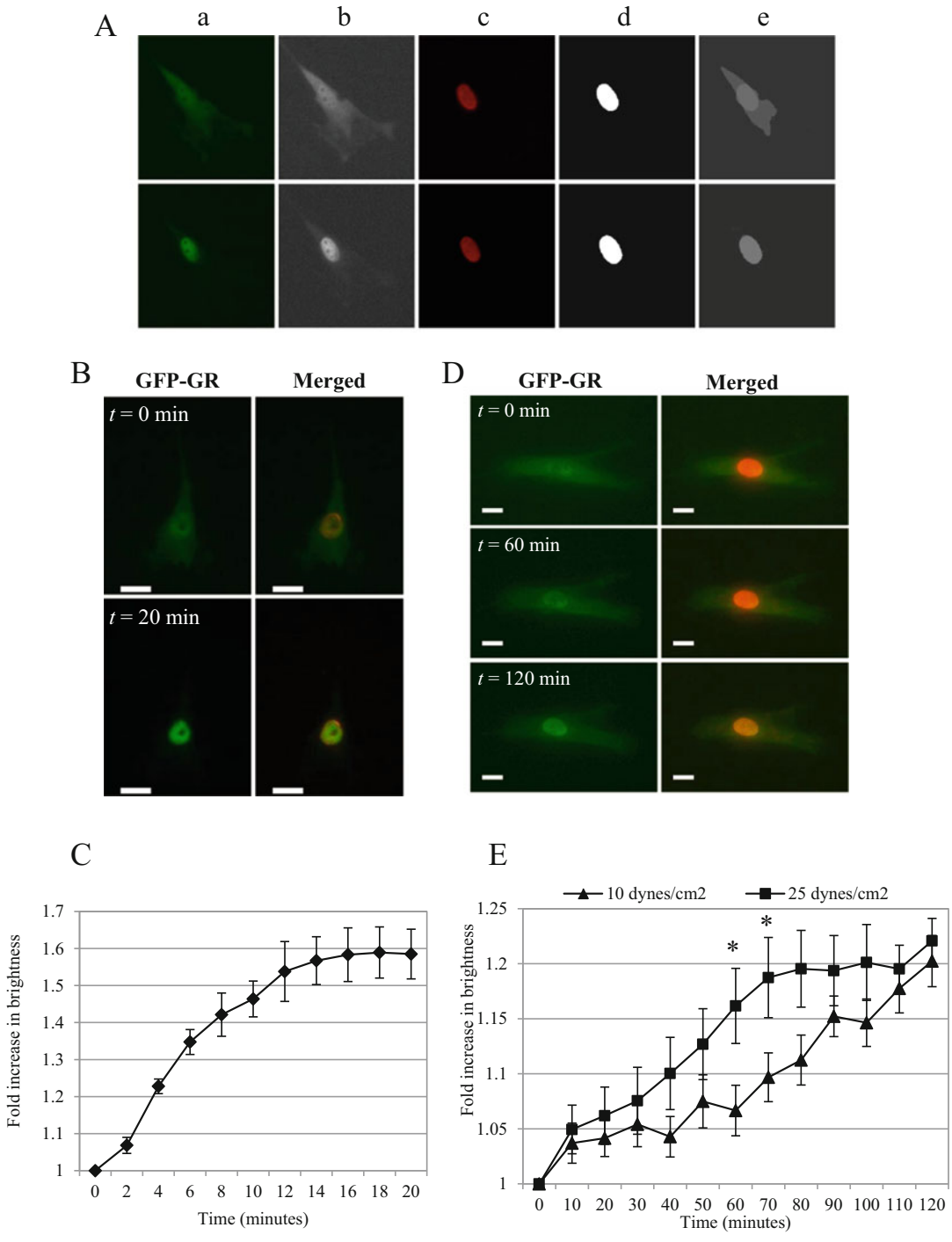

Fig. 2 (**A**) Analysis method of GFP-GR translocation in Dex-treated cells. At each time point, GFP-GR images (a) were first converted to an 8-bit black and white image (b). RFP-LaminA images (c) were converted to an 8-bit black and white image and then thresholded to obtain an outline, or atlas, of the nucleus (d) to improve segmentation. Images (b) and (d) were then imported into the algorithm for each time point, and a merged image (e) was exported along with brightness data for the cytoplasm, nucleus, and background. (**B**) Cells transfected with GFP-GR show

circular nuclear shape. Deformed nuclear shape is a marker of defective nuclear lamina (Dahl et al. 2008). Thus, images of Hoechst-stained nuclei further demonstrated the absence of nuclear lamina in lamin shRNA cells.

Cells with either control or lamin A/C shRNA were then transfected with GFP-GR plasmid and treated with 25 μM Dex. Both green (GFP-GR) and blue (Hoechst) fluorescence time-lapse images were used in the Bayesian image analysis algorithm to quantify the dynamic nuclear localization of GFP-GR based on fluorescence brightness. In both cases, prior to Dex treatment, GFP-GR was distributed evenly in the cytoplasm and nucleus. Within 20 min of adding Dex, GFP-GR was mostly localized inside of the nucleus. The absence of nuclear lamina did not hinder GFP-GR nuclear localization under Dex activation. Both cell types demonstrated similar rates of nuclear movement of GFP-GR, around 50% after 20 min (Nayebosadri et al. 2012).

The effect of nuclear lamina on ligand-independent GR translocation under high shear stress was also examined at 25 dynes/cm^2 for up to 2 h. Both types of cells demonstrated more consistent GFP-GR nuclear movement at 25 dynes/cm^2. By 90 min, however, GFP-GR brightness in lamin shRNA cells approached its maximum value before leveling out at 22.2 ± 1.8%. Control shRNA cells reached a maximum of 24.1 ± 3.0% increase in nuclear brightness at 120 min (Fig. 3C). Thus, even in the absence of lamin A/C, GFP-GR was still able to translocate into the nucleus under shear stress within 2 h, independent of agonist binding. Western blots of endogenous GR protein agreed with time-lapse image analysis results. These results indicate that shear-induced GFP-GR nuclear localization occurred independent of lamin A/C proteins. The overall trends and the final GFP-GR nuclear brightness at 120 min correspond well with what was reported previously for control cells.

2.3.4 Lower Shear Stress Reduced GR Nuclear Translocation in Control, but Not in Lamin shRNA Cells

To determine if GR translocation also occurs under lower shear stress, BAECs were sheared at 5 dynes/cm^2. Fluorescence images again demonstrated deformed nuclei in lamin shRNA cells, as well as GFP-GR nuclear localization for either cell types with shear. Quantitative image analysis revealed that greater nuclear localization was observed in lamin shRNA cells than control cells. Lamin shRNA cells reached a maximum of 20% increase in nuclear brightness versus 13% for control cells after 100 min (Fig. 3D). The difference was significant at $t = 40$, 100, and 120 min ($^*P < 0.05$). Compared to higher shear magnitudes, control shRNA cells with an intact lamina demonstrated a lower nuclear brightness change within the same 2-h time frame, while nuclear brightness change observed in lamin shRNA cells was similar to those treated with 25 dynes/cm^2 shear stress.

2.3.5 Luciferase Expression Based on GRE Promoter Is Upregulated in the Absence of Lamin A/C

Even as GR nuclear localization was observed with either Dex or shear stress, does it necessarily lead to transcriptional changes? To further

Fig. 2 (continued) initial localization of the protein in both the cytoplasm and nucleus. Following addition of Dex, GFP-GR translocated to the nucleus (as outlined by RFP-LaminA) within 20 min. Image was taken at 40× magnification. Scale bar = 15 μm. (**C**) Quantitative analysis of images shows that after 20 min of Dex treatment, GFP-GR nuclear brightness increases 58.5 ± 0.7% ($n = 11$). (**D**) GFP-GR nuclear translocation under shear stress. GFP-GR is initially distributed evenly throughout the cytoplasm and nucleus. After 1 h of 25 dynes/cm^2 shear, the nucleus becomes distinguished with increased brightness relative to the cytoplasm. At 2 h, GFP-GR has translocated into the nuclear boundary outlined by RFP-LaminA. Cell was imaged at 40× magnification. Scale bar = 15 μm. (**E**) Fold increase in relative brightness of nuclear GFP-GR under 10 ($n = 11$) and 25 ($n = 13$) dynes/cm^2 shear stress. After 2 h, GFP-GR nuclear brightness increased by approximately 20.2 ± 0.02% and 22 ± 0.02% for 10 and 25 dynes/cm^2, respectively. ($^*P < 0.05$ for 10 vs. 25 dynes/cm^2)

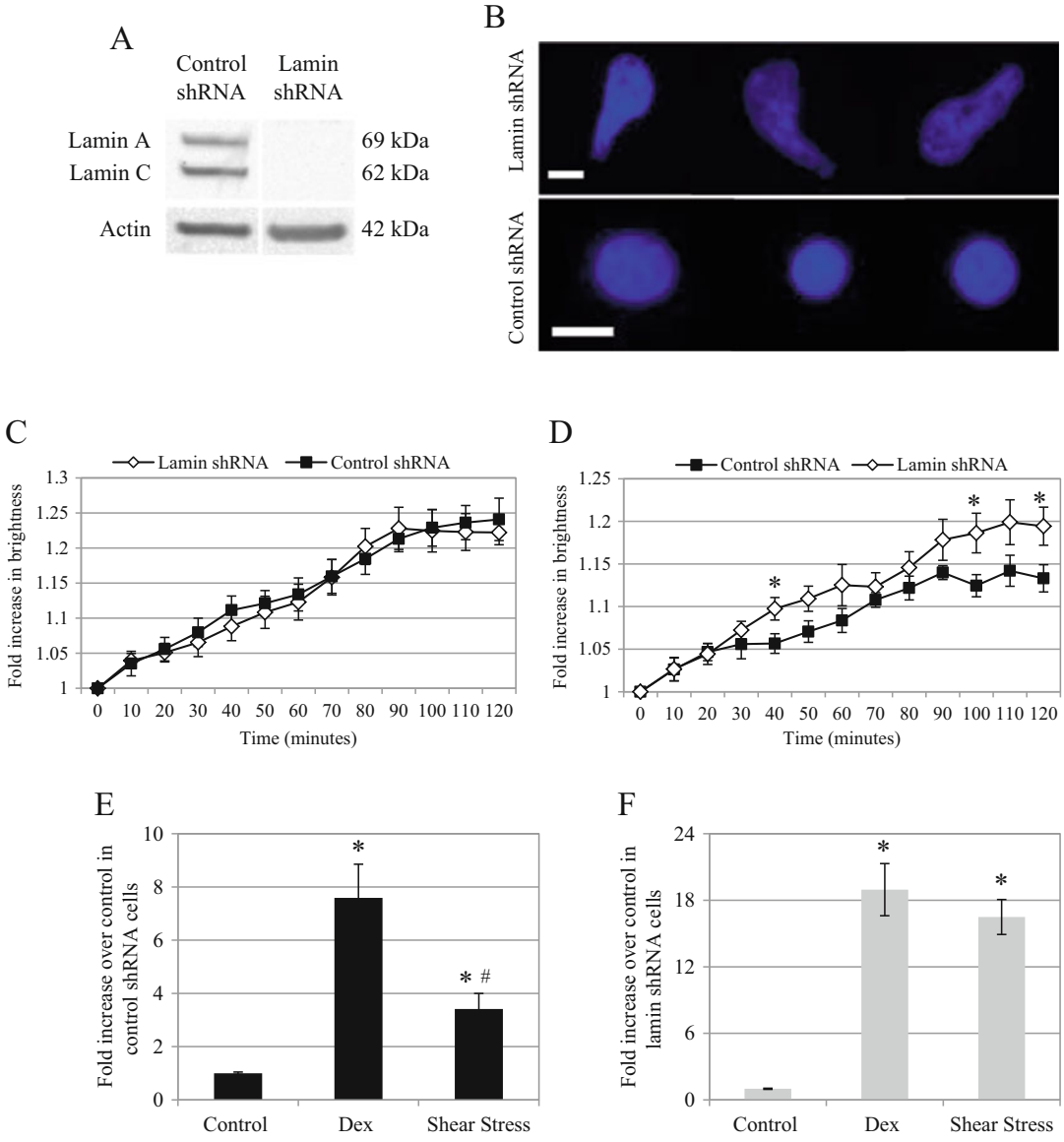

Fig. 3 (**A**) Confirmation of lamin A/C silencing: Western blot of whole cell protein extractions from control and lamin shRNA BAECs confirm the presence and absence of lamin A/C, respectively. Actin was used as the loading control. (**B**) Hoechst staining of live cell nuclei showed that cells with lamin shRNA have irregularly shaped nuclei, and cells with non-targeting control shRNA had the characteristic circular nuclei. Images were taken at 40× magnification. Scale bar = 15 μm. (**C**) GFP-GR nuclear movement is independent of lamin A/C under shear stress of 25 dynes/cm^2. Quantitative image analysis of GFP-GR subcellular movement shows a 22.2 ± 1.8% and 24.1 ± 3.0% increase in nuclear brightness for lamin ($n = 7$) and control($n = 9$) shRNA treated BAECs, respectively, after 120 min. (**D**) GR nuclear translocation is reduced in control compared to lamin shRNA cells under shear stress of 5 dynes/cm^2. Quantitative image analysis of GFP-GR subcellular movement shows a 19.4 ± 2.2% and 13.3 ± 1.6% increase in nuclear brightness for lamin and control shRNA treated BAECs, respectively ($n = 11$), after 120 min. *$P < 0.05$ at $t = 40$, 100, and 120 min for control vs. lamin shRNA treated BAEC. (**E**) Dex and shear-induced GRE promoter activation is affected by nuclear lamina and HDAC. In BAEC with control shRNA, Dex (25 μM) and shear stress (25 dynes/cm^2) upregulated luciferase expression based on GRE reporter plasmid by 7.6- ± 1.3- and 3.4- ± 0.6-fold compared to untreated cells,

examined if subsequent transcription from GRE promoters was also increased, a dual-luciferase reporter plasmid was used. Activated GR in the nucleus is hypothesized to bind to GRE promoters and initiates transcription of the reporter gene. For cells with control, non-targeting shRNA and intact nuclear lamina, treatment with Dex (25 μM) resulted in a 7.6- ± 1.3-fold increase in luciferase expression over untreated cells, while cells sheared at 25 dynes/cm^2 showed a 3.4- ± 0.6-fold increase (Fig. 3E). There was significantly higher luciferase expression under Dex induction compared to shear stress, which is consistent with the levels of nuclear localization observed in image and Western analyses. Since Dex induced greater GR nuclear localization, this data suggested that Dex also yielded stronger activation of the GRE promoter compared to shear stress. On the other hand, in lamin A/C-silenced BAEC, significantly higher increase in luciferase was observed for cells treated with either Dex or shear stress, compared to control shRNA ($P < 0.05$): 18.9- ± 2.4- and 16.5- ± 1.6-fold increase, respectively (Fig. 3F). There was no significant difference in luciferase expression between Dex and shear stress induction. This data suggests the expression of the GRE promoter is enhanced in the absence of nuclear lamina, regardless of induction.

2.4 Discussion

Using the image analysis algorithm that was developed based on Bayesian statistics, it is possible to quantify time-dependent intracellular movement of fluorescently labeled GR. This imaging-based study demonstrated that nuclear lamina is not required for nuclear import of GR after induction with either Dex or shear tress. After treatment with Dex or shear stress, cells with control or lamin A/C gene silencing shRNA demonstrated a similar extent of GFP-GR nuclear localization to what was reported for non-shRNA treated cells (Nayebosadri et al. 2012).

Lamins participate in linking the nucleus to the cytoskeleton networks through the LINC complex (Crisp et al. 2006) by attaching to SUN proteins within the nuclear envelope, which are further connected to nesprin proteins on the outer nuclear envelope. Nesprins in turn attach to actin and microtubules via dynein and intermediate filaments via plectin (Zwerger et al. 2013). Disrupting the endothelial actin and microtubule networks does not prevent nuclear localization of GFP-GR with Dex or shear stress, suggesting that GR may utilize alternative methods, such as diffusion, to translocate (Nayebosadri et al. 2012). It is not surprising then that silencing lamin proteins also would not interfere with nuclear localization of GR proteins. Nuclear import of GR appears to be independent of the lamin-dependent, nucleus-cytoskeleton link.

Nuclear lamina plays an important role in maintaining nuclear structure and mechanics (De Vos et al. 2011; Lammerding et al. 2004). In cells with intact nuclei, a greater degree of GFP-GR nuclear localization under higher shear stress was observed, but this distinction was less obvious in lamin-deficient cells. This could be in part due to increased nuclear stiffness in cells with intact lamina and proper signal transduction cascades. In cells lacking lamin A/C, nuclei are more deformed and fragile with decreased nuclear mechanical stiffness as well as impaired activation of mechanosensitive genes (Ho and Lammerding 2012; Dahl et al. 2008). As a result, they are potentially more susceptible to all levels of shear stress. This would also suggest disruption of lamina-dependent signal transduction cascade, for example, the MAPK signaling pathway which phosphorylates GR independent

Fig. 3 (continued) respectively. For all cases, $n = 3$. *$P < 0.05$ compared to control. In addition, Dex-induced luciferase expression was significantly higher than that of shear stress. #$P < 0.05$ compared to Dex. (**F**) In BAEC with lamin shRNA, treatment with Dex ($n = 5$) and shear stress ($n = 6$) significantly increased luciferase expression: 18.9- ± 2.4- and 16.5- ± 1.6-fold increases, respectively, compared to untreated cells ($n = 5$). *$P < 0.05$ compared to control

of a ligand (Muchir et al. 2007; Galliher-Beckley et al. 2011).

The data suggest that lower shear stress (5 dynes/cm^2) may have a different effect on GR nuclear translocation in cells with intact lamina. Less GFP-GR brightness in the nucleus and a greater cytoplasmic GR presence was observed, which suggests that GR translocation under atherogenic levels of shear stress is more hindered compared to atheroprotective levels (10 or 25 dynes/cm^2). This would be consistent with atheroprotective property of higher shear stress, including upregulation of anti-inflammatory glucocorticoid-responsive genes. In the absence of lamina, the level of GR nuclear localization was similar to those sheared at higher magnitudes. Again, this may be due to the nuclei becoming more susceptible to mechanical stresses as well as disrupted signaling cascade.

In lamin-deficient cells, Dex and shear stress both induced significant increases in luciferase expression compared to untreated or control shRNA treated cells. This data suggested that in the absence of lamin A/C, there was increased transcriptional activity and gene expression from GRE promoter plasmid. Recently, lamin proteins have been shown to be mediators of oxidative stress (Sieprath et al. 2012; Malhas et al. 2009). In the absence of lamin proteins, there is an increase in reactive oxygen species, which causes the 14-3-3 zeta isoform proteins to bind to GR, and Cidlowski et al. showed that in oxidative stress induced by H_2O_2, more 14-3-3 zeta is recruited to the gene promoter region (Galliher-Beckley et al. 2011). Thus, there are other mechanisms, such as in during oxidative stress, through which lamin deficiency could affect signal mechanisms, ultimately leading to altered transcription of target genes. Furthermore, some studies have represented the nuclear lamina as a genetically repressive environment (Demmerle et al. 2012; Shevelyov and Nurminsky 2012). The absence of the nuclear lamina would therefore lead to a loss of heterochromatin at the inner nuclear membrane and certain transcription factors no longer being sequestered there as inactive complexes, resulting in unregulated gene transcription (Ho and Lammerding 2012).

3 Summary

The study described above has led to further understanding of endothelial mechanotransduction at the nuclear level. While GR activation under shear stress may be unique to endothelial cells, this study also contributes to our understanding of the disease mechanisms of laminopathies by linking effects of mechanical stress and chromatin regulation at the nuclear lamina. On the other hand, atherosclerotic lesions develop preferentially at regions of low shear and disturbed flow, while sustained unidirectional high shear is associated with protected endothelium. Endothelial cells lose their protective effects of shear stress with increasing passage, e.g., decreased upregulation of nitric oxide and suppression of apoptosis. The accumulation of progerin in endothelial cells due to HGPS or normal aging may interfere with these processes especially under hemodynamic conditions.

Considering the mechanosensitive roles that lamin A plays in vascular cells, it is important to investigate whether lamin A mediates these stress-induced responses, which may underlie one of the mechanisms of how aging contributes to the initiation of cardiovascular diseases, such as atherosclerosis. Given the pivotal roles of lamins in nuclear mechanics and numerous cellular events, it is of great importance to understand the mechanisms underlying those regulations. Recent findings indicate the correlations between mutated lamins, atherosclerosis, and aging process, suggesting a potential therapy for CAD and advances in understanding normal aging process (Broers et al. 2006; Ragnauth et al. 2010). Research continues to investigate the impact of fluid shear stress on transcriptional regulation at the nucleus and to further elucidate the interactions between nuclear proteins and mechanotransduction pathways involved in gene transcription.

References

Adcock IM (2001) Glucocorticoid-regulated transcription factors. Pulm Pharmacol Ther 14:211–219

Adcock IM, Caramori G (2001) Cross-talk between pro-inflammatory transcription factors and glucocorticoids. Immunol Cell Biol 79:376–384

Al-Shali KZ, Hegele RA (2004) Laminopathies and atherosclerosis. Arterioscler Thromb Vasc Biol 24:1591–1595

Alsheimer M, Von Glasenapp E, Schnolzer M, Heid H, Benavente R (2000) Meiotic lamin C2: the unique amino-terminal hexapeptide GNAEGR is essential for nuclear envelope association. Proc Natl Acad Sci U S A 97:13120–13125

Ando J, Tsuboi H, Korenaga R, Takada Y, Toyama-Sorimachi N, Miyasaka M et al (1994) Shear stress inhibits adhesion of cultured mouse endothelial cells to lymphocytes by downregulating VCAM-1 expression. Am J Physiol 267:C679–C687

Barnes PJ (1998) Anti-inflammatory actions of glucocorticoids: molecular mechanisms. Clin Sci (Lond) 94:557–572

Beck IM, Vanden Berghe W, Vermeulen L, Yamamoto KR, Haegeman G, De Bosscher K (2009) Crosstalk in inflammation: the interplay of glucocorticoid receptor-based mechanisms and kinases and phosphatases. Endocr Rev 30:830–882

Biamonti G, Giacca M, Perini G, Contreas G, Zentilin L, Weighardt F, Guerra M, Della Valle G, Saccone S, Riva S et al (1992) The gene for a novel human Lamin maps at a highly transcribed locus of chromosome 19 which replicates at the onset of S-phase. Mol Cell Biol 12:3499–3506

Bione S, Maestrini E, Rivella S, Mancini M, Regis S, Romeo G, Toniolo D (1994) Identification of a novel X-linked gene responsible for Emery-Dreifuss muscular dystrophy. Nat Genet 8:323–327

Bonne G, Di Barletta MR, Varnous S, Becane HM, Hammouda EH, Merlini L, Muntoni F, Greenberg CR, Gary F, Urtizberea JA, Duboc D, Fardeau M, Toniolo D, Schwartz K (1999) Mutations in the gene encoding lamin A/C cause autosomal dominant Emery-Dreifuss muscular dystrophy. Nat Genet 21:285–288

Brassard JA, Fekete N, Garnier A, Hoesli CA (2016) Hutchinson-Gilford progeria syndrome as a model for vascular aging. Biogerontology 17:129–145

Broers JLV, Ramaekers FCS, Bonne G, Ben Yaou R, Hutchison CJ (2006) Nuclear lamins: Laminopathies and their role in premature ageing. Physiol Rev 86:967–1008

Brostjan C, Anrather J, Csizmadia V, Natarajan G, Winkler H (1997) Glucocorticoids inhibit E-selectin expression by targeting NF-kappaB and not ATF/c-Jun. J Immunol 158:3836–3844

Burke B, Stewart CL (2013) The nuclear lamins: flexibility in function. Nat Rev Mol Cell Biol 14:13–24

Butin-Israeli V, Adam SA, Goldman AE, Goldman RD (2012) Nuclear lamin functions and disease. Trends Genet 28:464–471

Cao H, Hegele RA (2000) Nuclear lamin A/C R482Q mutation in Canadian kindreds with Dunnigan-type familial partial lipodystrophy. Hum Mol Genet 9:109–112

Cao K, Graziotto JJ, Blair CD, Mazzulli JR, Erdos MR, Krainc D, Collins FS (2011) Rapamycin reverses cellular phenotypes and enhances mutant protein clearance in Hutchinson-Gilford progeria syndrome cells. Sci Transl Med 3:89ra58

Chen XL, Varner SE, Rao AS, Grey JY, Thomas S, Cook CK, Wasserman MA, Medford RM, Jaiswal AK, Kunsch C (2003) Laminar flow induction of antioxidant response element-mediated genes in endothelial cells. A novel anti-inflammatory mechanism. J Biol Chem 278:703–711

Chien S (2007) Mechanotransduction and endothelial cell homeostasis: the wisdom of the cell. Am J Physiol Heart Circ Physiol 292:H1209–H1224

Crisp M, Liu Q, Roux K, Rattner JB, Shanahan C, Burke B, Stahl PD, Hodzic D (2006) Coupling of the nucleus and cytoplasm: role of the LINC complex. J Cell Biol 172:41–53

Dahl KN, Ribeiro AJ, Lammerding J (2008) Nuclear shape, mechanics, and mechanotransduction. Circ Res 102:1307–1318

Davies PF, Polacek DC, Shi C, Helmke BP (2002) The convergence of haemodynamics, genomics, and endothelial structure in studies of the focal origin of atherosclerosis. Biorheology 39:299–306

De Sandre-Giovannoli A, Chaouch M, Kozlov S, Vallat JM, Tazir M, Kassouri N, Szepetowski P, Hammadouche T, Vandenberghe A, Stewart CL, Grid D, Levy N (2002) Homozygous defects in LMNA, encoding lamin A/C nuclear-envelope proteins, cause autosomal recessive axonal neuropathy in human (Charcot-Marie-Tooth disorder type 2) and mouse. Am J Hum Genet 70:726–736

De Vos WH, Houben F, Kamps M, Malhas A, Verheyen F, Cox J, Manders EM, Verstraeten VL, Van Steensel MA, Marcelis CL, Van den Wijngaard A, Vaux DJ, Ramaekers FC, Broers JL (2011) Repetitive disruptions of the nuclear envelope invoke temporary loss of cellular compartmentalization in laminopathies. Hum Mol Genet 20:4175–4186

Demmerle J, Koch AJ, Holaska JM (2012) The nuclear envelope protein Emerin binds directly to histone Deacetylase 3 (HDAC3) and activates HDAC3 activity. J Biol Chem 287:22080–22088

Dewey CF Jr, Bussolari SR, Gimbrone MA Jr, Davies PF (1981) The dynamic response of vascular endothelial cells to fluid shear stress. J Biomech Eng 103:177–185

Diamond SL, Eskin SG, McIntire LV (1989) Fluid flow stimulates tissue plasminogen activator secretion by cultured human endothelial cells. Science 243:1483–1485

Diamond S, Sharefkin J, Dieffenbach C, Frasier-Scott K, Mcintire L, Eskin S (1990) Tissue plasminogen activator messenger RNA levels increase in cultured human endothelial cells exposed to laminar shear stress. J Cell Physiol 143:364–371

Dittmer TA, Misteli T (2011) The Lamin protein family. Genome Biol 12:222

Dreesen O, Stewart CL (2011) Accelerated aging syndromes, are they relevant to normal human aging? Aging (Albany NY) 3:889–895

Eickelberg O, Roth M, Lorx R, Bruce V, Rudiger J, Johnson M, Block LH (1999) Ligand-independent activation of the glucocorticoid receptor by beta2-adrenergic receptor agonists in primary human lung fibroblasts and vascular smooth muscle cells. J Biol Chem 274:1005–1010

Eriksson M, Brown WT, Gordon LB, Glynn MW, Singer J, Scott L, Erdos MR, Robbins CM, Moses TY, Berglund P, Dutra A, Pak E, Durkin S, Csoka AB, Boehnke M, Glover TW, Collins FS (2003) Recurrent de novo point mutations in Lamin A cause Hutchinson-Gilford progeria syndrome. Nature 423:293–298

Fatkin D, Macrae C, Sasaki T, Wolff MR, Porcu M, Frenneaux M, Atherton J, Vidaillet HJ Jr, Spudich S, De Girolami U, Seidman JG, Seidman C, Muntoni F, Muehle G, Johnson W, Mcdonough B (1999) Missense mutations in the rod domain of the lamin A/C gene as causes of dilated cardiomyopathy and conduction-system disease. N Engl J Med 341:1715–1724

Fleming I, Bauersachs J, Busse R (1997) Calcium-dependent and calcium-independent activation of the endothelial NO synthase. J Vasc Res 34:165–174

Frangos JA, Mcintire LV, Eskin SG (1988) Shear stress induced stimulation of mammalian cell metabolism. Biotechnol Bioeng 32:1053–1060

Galliher-Beckley AJ, Williams JG, Cidlowski JA (2011) Ligand-independent phosphorylation of the glucocorticoid receptor integrates cellular stress pathways with nuclear receptor signaling. Mol Cell Biol 31:4663–4675

Gimbrone MA Jr, Resnick N, Nagel T, Khachigian LM, Collins T, Topper JN (1997) Hemodynamics, endothelial gene expression, and atherogenesis. Ann N Y Acad Sci 811:1–10; discussion 1

Gruenbaum Y, Margalit A, Goldman RD, Shumaker DK, Wilson KL (2005) The nuclear lamina comes of age. Nat Rev Mol Cell Biol 6:21–31

Helmlinger G, Berk BC, Nerem RM (1995) Calcium responses of endothelial cell monolayers subjected to pulsatile and steady laminar flow differ. Am J Physiol 269:C367–C375

Hennekam RC (2006) Hutchinson-Gilford progeria syndrome: review of the phenotype. Am J Med Genet A 140:2603–2624

Hishikawa K, Nakaki T, Marumo T, Suzuki H, Kato R, Saruta T (1995) Pressure enhances endothelin-1 release from cultured human endothelial cells. Hypertension 25:449–452

Ho CY, Lammerding J (2012) Lamins at a glance. J Cell Sci 125:2087–2093

Hutchison CJ (2002) Lamins: building blocks or regulators of gene expression? Nat Rev Mol Cell Biol 3:848–858

Hutchison CJ, Worman HJ (2004) A-type lamins: guardians of the soma? Nat Cell Biol 6:1062–1067

Itoh M, Adachi M, Yasui H, Takekawa M, Tanaka H, Imai K (2002) Nuclear export of glucocorticoid receptor is enhanced by c-Jun N-terminal kinase-mediated phosphorylation. Mol Endocrinol 16:2382–2392

Ji JY, Jing H, Diamond SL (2003) Shear stress causes nuclear localization of endothelial glucocorticoid receptor and expression from the GRE promoter. Circ Res 92:279–285

Ji JY, Lee RT, Vergnes L, Fong LG, Stewart CL, Reue K, Young SG, Zhang Q, Shanahan CM, Lammerding J (2007) Cell nuclei spin in the absence of Lamin B1. J Biol Chem 282:20015–20026

Kaiser D, Freyberg MA, Friedl P (1997) Lack of hemodynamic forces triggers apoptosis in vascular endothelial cells. Biochem Biophys Res Commun 231:586–590

Kolb T, Maass K, Hergt M, AEBI U, Herrmann H (2011) Lamin A and lamin C form homodimers and coexist in higher complex forms both in the nucleoplasmic fraction and in the lamina of cultured human cells. Nucleus 2:425–433

Korenaga R, Ando J, Kosaki K, Isshiki M, Takada Y, Kamiya A (1997) Negative transcriptional regulation of the VCAM-1 gene by fluid shear stress in murine endothelial cells. Am J Physiol 273:C1506–C1515

Krohne G, Benavente R (1986) The nuclear lamins. A multigene family of proteins in evolution and differentiation. Exp Cell Res 162:1–10

Kuchan M, Frangos J (1994) Role of calcium and calmodulin in flow-induced nitric oxide production in endothelial cells. Am J Phys 266:C628–C636

Lammerding J, Schulze PC, Takahashi T, Kozlov S, Sullivan T, Kamm RD, Stewart CL, Lee RT (2004) Lamin A/C deficiency causes defective nuclear mechanics and mechanotransduction. J Clin Invest 113:370–378

Lammerding J, Fong LG, JI JY, reue K, Stewart CL, Young SG, Lee RT (2006) Lamins a and C but not Lamin B1 regulate nuclear mechanics. J Biol Chem 281:25768–25780

Lloyd DJ, Trembath RC, Shackleton S (2002) A novel interaction between Lamin A and SREBP1: implications for partial lipodystrophy and other laminopathies. Hum Mol Genet 11:769–777

Malek A, Izumo S (1992) Physiological fluid shear stress causes downregulation of endothelin-1 mRNA in bovine aortic endothelium. Am J Physiol 263:C389–C396

Malek AM, Izumo S (1994) Molecular aspects of signal transduction of shear stress in the endothelial cell. J Hypertens 12:989–999

Malek AM, Alper SL, Izumo S (1999) Hemodynamic shear stress and its role in atherosclerosis. JAMA 282:2035–2042

Malhas AN, Lee CF, Vaux DJ (2009) Lamin B1 controls oxidative stress responses via Oct-1. J Cell Biol 184:45–55

Marroquin J, Mitter S, Poggio T (1987) Probabalistic solution of ill-posed problems in computational vision. J Am Stat Assoc 82:76–89

Masuda H, Kawamura K, Tohda K, Shozawa T, Sageshima M, Kamiya A (1989) Increase in endothelial cell density before artery enlargement in flow-loaded canine carotid artery. Arteriosclerosis 9:812–823

Merideth MA, Gordon LB, Clauss S, Sachdev V, Smith AC, Perry MB, Brewer CC, Zalewski C, Kim HJ, Solomon B, Brooks BP, Gerber LH, Turner ML, Domingo DL, Hart TC, Graf J, Reynolds JC, Gropman A, Yanovski JA, Gerhard-Herman M, Collins FS, Nabel EG, Cannon RO 3rd, Gahl WA, Introne WJ (2008) Phenotype and course of Hutchinson-Gilford progeria syndrome. N Engl J Med 358:592–604

Muchir A, Pavlidis P, Decostre V, Herron AJ, Arimura T, Bonne G, Worman HJ (2007) Activation of MAPK pathways links LMNA mutations to cardiomyopathy in Emery-Dreifuss muscular dystrophy. J Clin Invest 117:1282–1293

Nayebosadri A, Ji JY (2013) Endothelial nuclear lamina is not required for glucocorticoid receptor nuclear import but does affect receptor-mediated transcription activation. Am J Physiol Cell Physiol 305:C309–C322

Nayebosadri A, Christopher L, Ji JY (2012) Bayesian image analysis of dexamethasone and shear stress-induced glucocorticoid receptor intracellular movement. Ann Biomed Eng 40:1508–1519

Ohno M, Cooke JP, Dzau VJ, Gibbons GH (1995) Fluid shear stress induces endothelial transforming growth factor beta-1 transcription and production. Modulation by potassium channel blockade. J Clin Invest 95:1363–1369

Olive M, Harten I, Mitchell R, Beers JK, Djabali K, Cao K, Erdos MR, Blair C, Funke B, Smoot L, Gerhard-Herman M, Machan JT, Kutys R, Virmani R, Collins FS, Wight TN, Nabel EG, Gordon LB (2010) Cardiovascular pathology in Hutchinson-Gilford progeria: correlation with the vascular pathology of aging. Arterioscler Thromb Vasc Biol 30:2301–2309

Palmer RM, Ashton DS, Moncada S (1988) Vascular endothelial cells synthesize nitric oxide from L-arginine. Nature 333:664–666

Passerini AG, Polacek DC, Shi C, Francesco NM, Manduchi E, Grant GR, Pritchard WF, Powell S, CHANG GY, Stoeckert CJ Jr, Davies PF (2004) Coexisting proinflammatory and antioxidative endothelial transcription profiles in a disturbed flow region of the adult porcine aorta. Proc Natl Acad Sci U S A 101:2482–2487

Pavalko FM, Gerard RL, Ponik SM, Gallagher PJ, Jin Y, Norvell SM (2003) Fluid shear stress inhibits TNF-alpha-induced apoptosis in osteoblasts: a role for fluid shear stress-induced activation of PI3-kinase and inhibition of caspase-3. J Cell Physiol 194:194–205

Ragnauth CD, Warren DT, Liu Y, McNair R, Tajsic T, Figg N, Shroff R, Skepper J, Shanahan CM (2010) Prelamin A acts to accelerate smooth muscle cell senescence and is a novel biomarker of human vascular aging. Circulation 121:2200–2210

Ranjan V, Xiao Z, Diamond SL (1995) Constitutive NOS expression in cultured endothelial cells is elevated by fluid shear stress. Am J Physiol 269:H550–H555

Resnick N, Collins T, Atkinson W, Bonthron DT, Dewey CF Jr, Gimbrone MA Jr (1993) Platelet-derived growth factor B chain promoter contains a cis-acting fluid shear-stress-responsive element. Proc Natl Acad Sci U S A 90:4591–4595

ROSS R (1999) Atherosclerosis–an inflammatory disease. N Engl J Med 340:115–126

Scaffidi P, Misteli T (2006) Lamin A-dependent nuclear defects in human aging. Science 312:1059–1063

Scaffidi P, Gordon L, Misteli T (2005) The cell nucleus and aging: tantalizing clues and hopeful promises. PLoS Biol 3:e395

Shadwick RE (1999) Mechanical design in arteries. J Exp Biol 202:3305–3313

Shevelyov YY, Nurminsky DI (2012) The nuclear lamina as a gene-silencing hub. Curr Issues Mol Biol 14:27–38

Shyy JY, Li YS, Lin MC, Chen W, Yuan S, Usami S, Chien S (1995) Multiple cis-elements mediate shear stress-induced gene expression. J Biomech 28:1451–1457

Sieprath T, Darwiche R, De Vos WH (2012) Lamins as mediators of oxidative stress. Biochem Biophys Res Commun 421:635–639

Stehbens WE, Wakefield SJ, Gilbert-Barness E, Olson RE, Ackerman J (1999) Histological and ultrastructural features of atherosclerosis in progeria. Cardiovasc Pathol 8:29–39

Surapisitchat J, Hoefen RJ, Pi X, Yoshizumi M, Yan C, Berk BC (2001) Fluid shear stress inhibits TNF-alpha activation of JNK but not ERK1/2 or p38 in human umbilical vein endothelial cells: inhibitory crosstalk among MAPK family members. Proc Natl Acad Sci U S A 98:6476–6481

Teichert AM, Scott JA, Robb GB, Zhou YQ, Zhu SN, Lem M, Keightley A, Steer BM, Schuh AC, Adamson SL, Cybulsky MI, Marsden PA (2008) Endothelial nitric oxide synthase gene expression during murine embryogenesis: commencement of expression in the embryo occurs with the establishment of a unidirectional circulatory system. Circ Res 103:24–33

Topper JN, Cai J, Falb D, Gimbrone MA Jr (1996) Identification of vascular endothelial genes differentially responsive to fluid mechanical stimuli: cyclooxygenase-2, manganese superoxide dismutase, and endothelial cell nitric oxide synthase are selectively up-regulated by steady laminar shear stress. Proc Natl Acad Sci U S A 93:10417–10422

Tseng H, Peterson T, Berk B (1995) Fluid shear stress stimulates mitogen-activated protein kinase in endothelial cells. Circ Res 77:869–878

Varga R, Eriksson M, Erdos MR, Olive M, Harten I, Kolodgie F, Capell BC, Cheng J, Faddah D, Perkins S, Avallone H, San H, Qu X, Ganesh S, Gordon LB, Virmani R, Wight TN, Nabel EG, Collins FS (2006) Progressive vascular smooth muscle cell defects in a mouse model of Hutchinson-Gilford progeria syndrome. Proc Natl Acad Sci U S A 103:3250–3255

Volger OL, Fledderus JO, Kisters N, Fontijn RD, Moerland PD, Kuiper J, Van Berkel TJ, Bijnens AP, Daemen MJ, Pannekoek H, Horrevoets AJG (2007) Distinctive expression of chemokines and transforming growth factor-beta signaling in human arterial endothelium during atherosclerosis. Am J Pathol 171:326–337

Wilson KL, Berk JM (2010) The nuclear envelope at a glance. J Cell Sci 123:1973–1978

Wydner KL, Mcneil JA, Lin F, Worman HJ, Lawrence JB (1996) Chromosomal assignment of human nuclear envelope protein genes LMNA, LMNB1, and LBR by fluorescence in situ hybridization. Genomics 32:474–478

Yang SH, Meta M, Qiao X, Frost D, Bauch J, Coffinier C, Majumdar S, Bergo MO, Young SG, Fong LG (2006) A farnesyltransferase inhibitor improves disease phenotypes in mice with a Hutchinson-Gilford progeria syndrome mutation. J Clin Invest 116:2115–2121

Zanchi NE, Filho MA, Felitti V, Nicastro H, Lorenzeti FM, Lancha AH Jr (2010) Glucocorticoids: extensive physiological actions modulated through multiple mechanisms of gene regulation. J Cell Physiol 224:311–315

Zebda N, Dubrovskyi O, Birukov KG (2012) Focal adhesion kinase regulation of mechanotransduction and its impact on endothelial cell functions. Microvasc Res 83:71–81

Zwerger M, Jaalouk DE, Lombardi ML, Isermann P, Mauermann M, Dialynas G, Herrmann H, Wallrath LL, Lammerding J (2013) Myopathic Lamin mutations impair nuclear stability in cells and tissue and disrupt nucleo-cytoskeletal coupling. Hum Mol Genet 22(12):2335–2349

Regional Heterogeneity in the Regulation of Vasoconstriction in Arteries and Its Role in Vascular Mechanics

Sae-Il Murtada and Jay D. Humphrey

Abstract

Vasoconstriction and vasodilation play important roles in the circulatory system and can be regulated through different pathways that depend on myriad biomolecules. These different pathways reflect the various functions of smooth muscle cell (SMC) contractility within the different regions of the arterial tree and how they contribute to both the mechanics and the mechanobiology. Here, we review the primary regulatory pathways involved in SMC contractility and highlight their regional differences in elastic, muscular, and resistance arteries. In this way, one can begin to assess how these properties affect important biomechanical and mechanobiological functions in the circulatory system in health and disease.

1 Introduction

The vascular system consists of a network of blood vessels for transporting blood and thus carries vital nutrients and oxygen to or waste products and carbon dioxide from cells, tissues, and organs throughout the body. Blood flow is regulated by multiple factors such as heart rate, cardiac contractility, vascular geometry and stiffness, and smooth muscle cell (SMC) tone. Blood vessels branch out and divide into increasingly smaller vessels, which can be categorized depending on their position along the vascular tree. Vessels in different regions are characterized by different values of luminal radius, different wall composition, and SMC phenotype. Nevertheless, all arteries have three primary structural constituents that contribute to the overall mechanical integrity: elastic fibers, collagen fibers, and proteoglycans. The fraction of each of these vascular constituents varies, however, depending on the type of vessel and region (Fig. 1). Importantly, these constituents are established, maintained, and repaired primarily by the SMCs of the middle (medial) layer and the fibroblasts of the outer (adventitial) layer. SMCs can also contract and relax, thereby serving as a fourth key structural component. The fractions of these four structural constituents reflect their roles and function in the circulatory system. Larger systemic arteries located closer to the heart, also referred to as elastic or conduit vessels, have a higher elastin-collagen ratio and store significant elastic energy during cyclic pressurization that helps to dampen blood pressure oscillations and augment

S.-I. Murtada · J. D. Humphrey (✉)
Department of Biomedical Engineering, Yale University, New Haven, CT, USA
e-mail: jay.humphrey@yale.edu

B. M. Fu, N. T. Wright (eds.), *Molecular, Cellular, and Tissue Engineering of the Vascular System*, Advances in Experimental Medicine and Biology 1097,
https://doi.org/10.1007/978-3-319-96445-4_6

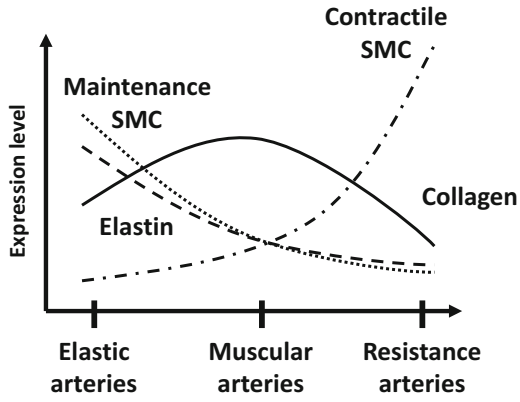

Fig. 1 Regional expression of collagen (solid), elastin (dashed), maintenance SMC (dotted), and contractile SMC (dash-dotted) in different elastic, muscular, and resistance arteries

flow during diastole. This so-called Windkessel effect helps to provide continuous blood flow to distally located vessels. Healthy elastic arteries have a high SMC content, although not of a truly strong contractile phenotype. In contrast, mid-sized muscular arteries are primarily responsible for regulating the distribution of blood flow via contraction and relaxation of SMCs, which are of a strong contractile phenotype. The muscular arteries connect to the microcirculation, which consists of arterioles, capillaries, and venules. Arterioles are small resistance vessels with a lower elastin-collagen ratio and a high fraction of highly contractile SMCs. Vasoconstriction and vasodilation of resistance arteries contribute significantly to overall (peripheral) vascular resistance, which in turn largely dictates mean systemic arterial pressure. The capillaries are the delivery sites of important nutrients, oxygen, and hormones to target cells, tissues, and organs. The venous tree starts with venules and transitions to increasingly larger veins, which do not provide much resistance to flow; instead, veins serve as capacitance vessels (i.e., a large volume of blood can be stored in veins, which can cause large changes in blood flow through small changes in the inner diameter (Milnor 1990)). Importantly, structure thus reflects function throughout the circulatory system.

In addition to regional differences in the content of vascular constituents, SMCs manifest a wide spectrum of phenotypes regionally, with the two ends of the spectrum generally represented as contractile and synthetic (Rensen et al. 2007). There are several ways to classify vascular SMC phenotype, as, for example, via the expression of contractile protein markers (e.g., smooth muscle alpha-actin, smooth muscle myosin heavy chain, SM22 alpha, calponin, caldesmon, smoothelin, and telokin) (Fisher 2010), by the time course of the contractile response (e.g., phasic vs. tonic) (Somlyo and Somlyo 1968), or by the regulation of contractile activation (e.g., electromechanical vs. pharmacomechanical) (Somlyo and Somlyo 1994). SMCs are also categorized simply depending on regional position and vessel type. SMCs in peripheral small resistance arteries produce a rapid and strong active tone and are considered to exhibit a strong contractile phenotype (Brozovich et al. 2016), whereas those in large elastic arteries exhibit less tone and instead primarily regulate the extracellular matrix and are hence considered to exhibit a mild synthetic (maintenance) phenotype. SMCs do not exhibit a terminal differentiation status and are thus able to de-differentiate into migratory, proliferative, and highly synthetic phenotypes during injury and disease. More recent findings suggest that SMCs can also transdifferentiate to have a more pro-inflammatory phenotype (Orr et al. 2010). Hence, depending on the local presentation of biochemical and biomechanical factors, a vessel can accommodate SMCs having different or diverse (coexisting) phenotypes. Indeed, a heterogeneous expression of contractile and synthetic SMC phenotypes equips an artery with the ability to constrict and vasoregulate blood flow or to sense and regulate extracellular matrix components without the extensive phenotypic modulation that occurs during injury responses or disease progression. Moreover, we emphasize that SMC contractility is vital on a local level in sensing and regulating the extracellular matrix, thus promoting wall homeostasis under normal conditions or growth and remodeling responses under pathophysiological conditions (Wang et al. 2010; Doyle et al. 2015).

SMC contractility is driven by the power-stroke motion generated by myosin motors, which is activated when myosin regulatory light chains (MRLCs) are phosphorylated. MRLC phosphorylation is regulated through different catalyzing components, acting with different time courses and through different pathways. Many of the different signaling pathways regulating SMC contractility have been analyzed and reviewed, but few address or emphasize regional differences in cell properties. That is, SMCs are often considered as equivalent, and regional differences in the regulation of contractility for global (vessel level) or local (matrix level) function are not separated. Among the few studies of regional differences in active properties and regulatory pathways as well as some passive responses, consider the following. Cox compared active and passive biomechanical responses by the internal thoracic artery, carotid artery, renal artery, mesenteric artery, iliac artery, and coronary artery to chemical stimuli and mechanical loading, with stronger active stress responses found in the muscular, renal, mesenteric, and iliac arteries and weaker responses in coronary and internal thoracic arteries (Cox 1978). Wede and colleagues reported a significantly higher active stress response in the mesenteric artery than in the carotid artery or thoracic aorta but a reverse trend in the passive stress response (Wede et al. 2002). Deeper investigations of the mechanisms responsible for regional differences in active stress response are often not addressed. A notable example, however, is Kitazawa and colleague who reported different regulatory pathways in the thoracic aorta and caudal and mesenteric arteries (Kitazawa and Kitazawa 2012).

The regionally heterogeneous pathways regulating vasoconstriction and vasodilation are related to critical functions of SMCs in arteries and play important roles in the acute mechanics (e.g., regulating luminal radius and vascular resistance) as well as the chronic mechanobiology (e.g., extracellular matrix maintenance or vascular remodeling). A broader consistent comparison of the degree of contractile capacity and associated signaling pathways as a function of vascular region would promote a better understanding of the function of SMC phenotype in the circulatory system. Here, we review the main regulatory pathways in SMC contractility and their regional differences in elastic, muscular, and resistance arteries. We also address how these properties affect important mechanical and mechanobiological functions in the circulatory system.

2 Mechanical and Mechanobiological Functions

Arterial mechanics is complicated by the nonlinear, anisotropic material properties intrinsic to the wall and the large cyclic deformations it experiences with each beat of the heart. Notwithstanding the need for sophisticated methods of biomechanical analysis (Humphrey 2002), simple mechanical analyses provide some insight. In particular, good estimates of mean pressure-induced radial wall stress, mean pressure-induced circumferential wall stress, mean axial force-induced axial stress, and mean flow-induced wall shear stress are

$$\sigma_r \approx \frac{-P}{2}, \quad \sigma_\theta = \frac{Pa}{h}, \quad \sigma_z = \frac{f}{\pi h\,(2a+h)}, \quad \tau_w = \frac{4\mu Q}{\pi a^3} \tag{1}$$

where P is the distending pressure, a the luminal radius, h the wall thickness, f the axial force, Q the volumetric flow rate, and μ the viscosity of the blood. Importantly, order of magnitude values for these four components of Cauchy stress are $\sigma_r \sim -6$ kPa, $\sigma_\theta \sim \sigma_z \sim 100$ kPa, and $\tau_w \sim 1$ Pa. For this reason, one often neglects mechanical contributions of the radial component relative to the in-plane (circumferential and axial) components when studying wall mechanics. Similarly, given the five orders of magnitude differences between the pressure-induced intramural stresses and the flow-induced wall shear stress, the latter is typically neglected in analyses of wall mechanics.

Nevertheless, wall shear stress is as important to mechanobiological responses of ECs as are circumferential and axial wall stresses to mechanobiological responses of medial SMCs and adventitial fibroblasts (Davies 2009; Haga et al. 2007; Chiquet et al. 2003). This chapter is motivated by the mechanics and mechanobiology of SMCs, so let us consider the circumferential stress in more detail. Clearly, increasing pressure increases the circumferential stress via associated distension (increase in radius) and isochoric thinning (decrease in wall thickness) of the pseudoelastic wall. Conversely, increasing smooth muscle contraction decreases circumferential stress by reducing the luminal radius and isochorically increasing the wall thickness. The Laplace equation should thus be written as

$$\sigma_\theta = \frac{Pa\,(P,C)}{h\,(P,C)}$$

where C denotes vessel-level contractility. Hence, although it is often neglected in studies of arterial mechanics, SMC contractility is fundamental to the mechanics, not only to the regulation of blood flow.

In addition to contributing to the biomechanical functionality at the vessel level, SMCs are also largely responsible for establishing, maintaining, and refashioning the extracellular matrix of the media. To accomplish this important function, SMCs must actively mechano-sense and mechano-regulate the matrix (Humphrey et al. 2014). Both of these mechanobiological functions are enabled via actin-myosin activity and interactions between the cells and matrix that are facilitated by multiple types of integrins (i.e., transmembrane proteins that connect the extracellular matrix and intracellular cytoskeleton). In this way, both the macromechanics (vessel-level contractility) and micromechanics (extracellular matrix function and integrity) are dictated in large part by the ability of SMCs to contract and relax, which interestingly also involve similar intracellular signaling pathways. Fundamental to understanding and controlling SMC contributions to arterial health and disease, therefore, is a detailed understanding of actin-myosin regulation.

3 Regulation of SMC Contractility

SMCs produce active force when intracellular myosin motors interact with neighboring actin filaments. The myosin motors can be described using a lever-arm model with a head region and tail region. The head region consists of an actin-binding domain, a converter domain, and a regulatory domain carrying the MRLCs that activate the myosin motor when phosphorylated. The tail region acts as an elastic spring and is able to bind to other myosin motors, thus forming long thick myosin filaments. These thick filaments are surrounded by thin actin filaments and can form load-bearing crossbridges between the myosin and actin when myosin motors attach to the actin filaments. The crossbridges cause relative filament sliding through a power-stroke motion, which causes the SMC to contract. The magnitude of cell contraction depends on many factors, including activated myosin motors, myosin thick filament length, actin network organization, and filament lattice spacing; of course the magnitude of vessel contraction depends on the number of SMCs (Murtada et al. 2017).

Phosphorylation of the MRLC is governed by the phosphorylation of myosin light-chain kinase (MLCK) and the dephosphorylation of myosin light-chain phosphatase (MLCP), which are coordinated through a network of signaling pathways. Excitation-contraction coupling in SMCs can be categorized into electromechanical versus pharmacomechanical coupling (Somlyo and Somlyo 1994). The former moderates contraction mainly through changes in membrane depolarization affecting intracellular calcium and regulating MLCK activity; the latter moderates contraction through G-protein-coupled receptors activating calcium-sensitizing pathways without significant changes in membrane potential and MLCK activity. Endothelial-driven vasodilation acts through pathways shared with the calcium-sensitizing

pathways but promotes MLCP activity through a calcium-desensitizing manner. These calcium-sensitizing and calcium-desensitizing pathways are linked to receptors and targets for physiological vasoconstrictors (e.g., norepinephrine, angiotensin II, and endothelin-1) and vasodilators (e.g., acetylcholine, nitric oxide, and adenosine) and can activate both electromechanical and pharmacomechanical coupling pathways that independently or through cross talk influence vascular tone in arteries. In the following section, we address the calcium-dependent MLCK pathway as well as the calcium-sensitizing and calcium-desensitizing MLCP pathways and their regional differences in arteries.

3.1 Intracellular Calcium: Electromechanical Coupling

Intracellular calcium is one of the most important central secondary messengers in most cells and is crucial for regulating contractility in SMCs. There are two sources of intracellular calcium in SMCs: the extracellular matrix and associated interstitial fluid, with a concentration of calcium that is higher than that in the intracellular cytoplasm, and the sarcoplasmic reticulum (SR), which acts as an intracellular storage for calcium ions. The exchange of calcium between intracellular and extracellular spaces occurs mainly through a spectrum of ion channels, whereas the sarcoplasmic reticulum is triggered mainly by receptor activation.

3.1.1 SMC Membrane Ion Channels

The resting membrane potential, that is, the difference between intracellular and extracellular potential, is negative in SMCs (from −50 to −40 mV). When the membrane is depolarized (i.e., an increased membrane potential and a higher positive charge inside the cell), an exchange of potassium (K^+), sodium (Na^+), chloride (Cl^-), and most importantly calcium (Ca^{2+}) ions takes place between the extracellular and intracellular spaces through different membrane ion channels, pumps, and exchangers; this results in an action potential. The calcium concentration is ∼10,000-fold higher in the extracellular space than in the intracellular space of a SMC, and depolarization of the cell membrane by ∼15 mV will elevate intracellular calcium to ∼300–400 nM. Membrane hyperpolarization (i.e., a decreased membrane potential and higher negative charge inside the cell) of ∼15 mV will lower the intracellular calcium to ∼100 nM (Hill-Eubanks et al. 2011). There are several different types of ion channels and exchangers that regulate SMC contractility in arteries, such as voltage-dependent channels, ligand-operated channels, and mechanosensitive cation channels.

One of the most important groups of ion channels regulating intracellular calcium in SMCs is the voltage-dependent calcium channels (VDCCs). Depolarization causes VDCCs to open, thus increasing the influx of calcium ions and promoting vasoconstriction; hyperpolarization, in contrast, causes VDCC to close, thus decreasing the influx of calcium and vasodilation. There are three different types of VDCCs in SMCs: L-type ($Ca_V1.2$), P/Q-type ($Ca_V2.1$), and T-type ($Ca_V3.1$, $Ca_V3.2$) (Martinsen et al. 2014). The L-type calcium channel (LTCC) is the most abundant VDCC in SMCs and found in both elastic and resistance arteries. The LTCC is characterized by its high-voltage and long-lasting activation. The P/Q-type calcium channels have been reported to be slower than LTCCs and have a calcium-independent rate of inactivation, thus providing a longer time for calcium influx. The P/Q-type channels also feature hormonal regulation properties (Andreasen et al. 2006). The T-type calcium channel (TTCC) is characterized by its low-voltage and transient activation and is more sensitive to depolarization; it activates and inactivates more rapidly than the LTCC. This unique characteristic makes the TTCC able to respond to small and fast changes in stimuli, which is necessary in resistance arteries. When comparing effects of LTCC blockers and TTCC blockers in the rat aorta versus mesenteric arteries, in response to high K^+-induced depolarization, TTCC blockers have a significantly greater effect in resistance arteries (Ball et al. 2009). VDCCs can also be classified into calcium channels sensitive or insensitive to dihydropyridine, a group of calcium channel

blockers used to treat hypertension (Hill-Eubanks et al. 2011). Some of the dihydropyridine-insensitive calcium channel blockers are more effective in resistance arteries than in elastic arteries (Martinsen et al. 2014).

Potassium channels are abundantly expressed in all SMCs and are considered to play important roles in regulating the membrane potential. When these channels open, positively charged potassium ions diffuse from the intracellular to the extracellular space, resulting in membrane hyperpolarization, thereby causing the VDCCs to close and the vessel to dilate. When the potassium channels close, the reduced efflux of potassium ions leads to membrane depolarization, causing VDCCs to open and the vessel to constrict. Several subgroups of potassium channels regulate the transportation of potassium ions in SMCs. Four important channels are the calcium-activated potassium channel ($K_{Ca}C$), voltage-activated potassium channel (K_vC), ATP-sensitive potassium channel ($K_{ATP}C$), and inwardly rectifying potassium channel ($K_{IR}C$). The $K_{ATP}C$ is an ATP-sensitive potassium channel that closes with increased ATP concentration (Jackson 2000). The $K_{IR}C$ is unique because of its ability to increase intracellular potassium ion concentrations (inward flow) for physiological values of membrane potential (Ko et al. 2008). Here, we will focus on $K_{Ca}C$ and K_vC, which have differential activity. The $K_{Ca}C$ is a key player in responding to an increase in intracellular calcium and is the predominant potassium channel regulating vascular tone. These channels have a negative feedback role causing hyperpolarization and inhibiting vasoconstriction in response to increased intracellular calcium. The $K_{Ca}C$ can be divided into three subfamilies: small-, intermediate-, and large-conductance subfamilies. The small- and intermediate-conductance $K_{Ca}C$ are found in endothelial cells (ECs), and the large-conductance ("big") $K_{Ca}C$ ($BK_{Ca}C$) is found in SMCs. The $BK_{Ca}C$ is expressed in elastic and resistance arteries and regulated by both voltage and intracellular calcium (Jackson 2000). Thus, both membrane depolarization and increases in intracellular calcium above a threshold level are necessary to activate the $BK_{Ca}C$. The $BK_{Ca}C$ is an important modulator of resting membrane potential and the myogenic tone particular to resistance arteries. $BK_{Ca}C$ activity increases in all types of arteries in response to chronic hypertension as a protective mechanism to restrict vascular contraction and blood pressure (Sobey 2001). Voltage-dependent potassium channels (K_vC) serve as delayed rectifiers and are regulated by the membrane potential; they function as a buffer against depolarization and vasoconstriction. There are many alpha-subunits (Kv1.1–1.6) and beta-subunits (KvB1.1, KvB1.2) for K_vC, with each subunit relating to a distinct gene. These subunit genes are expressed differently in elastic versus muscular arteries, with most K_vC genes expressed more in the latter (Cox et al. 2001). In the same study, expression levels of Kv1.2 and Kv1.3 were reported to be significantly elevated in the aorta (elastic) and mesenteric (muscular) arteries in hypertensive rats. Yet, in a separate study in hypertensive rats, a lower activity in both K_vC and $BK_{Ca}C$ was reported in interlobar (resistance) arteries (Martens and Gelband 1996). These regional differences in potassium channel activity relate to a higher SMC contractile activity in resistance arteries and a lower activity in large arteries during hypertension. An impaired function of the K_vC would increase membrane depolarization and levels of intracellular calcium, causing a positive feedback mechanism for hypertension. Notwithstanding the significant difference between the systemic and pulmonary circulation, there are reports of equal expression levels of $BK_{Ca}C$ and K_vC in SMCs in larger pulmonary arteries, whereas K_vC is more highly expressed in smaller pulmonary arteries (Archer et al. 1996).

The chloride ion channel is an outward permeable ion channel expressed in different tissues and types of SMCs. The calcium-activated chloride channel ($Cl_{Ca}C$) is present in SMCs in different arteries (Bulley and Jaggar 2014). Increased intracellular calcium opens the $Cl_{Ca}Cs$ causing a discharge of negatively charged chloride ions from the intracellular to the extracellular space, thus leading to membrane depolarization. The $Cl_{Ca}Cs$ play important roles in ligand-gated pathways where they can depolarize the membrane

in response to calcium release from intracellular storages, which increases the activity of VDCCs and the concentration of intracellular calcium. Inactivation of chloride channels in both the aorta and mesenteric arteries reduces the response to norepinephrine (NE) but not to high KCl-induced contraction (Criddle et al. 1996, 1997). Activation of $Cl_{Ca}Cs$ has opposite depolarizing effects on membrane potential compared with the hyperpolarizing effect of $BK_{Ca}Cs$, and the ratio of these two channels has an important effect on the membrane potential in response to increased intracellular calcium.

The sodium-calcium exchanger (NaCaX) is a voltage-dependent ion exchanger that discharges intracellular calcium ions with an influx of extracellular sodium ions. Overexpression of NaCaX activity leads to decreased intracellular calcium and a decreased rate of contraction, thus promoting relaxation. NaCaX activity declines in response to membrane depolarization, inhibiting a decrease in intracellular calcium and thus SMC contraction. Despite a reverse-mode activity, NaCaX is less sensitive to membrane depolarization than VDCC (Nelson et al. 1990).

Pressure-induced membrane depolarization is an important controller of myogenic tone in resistance arteries. In cases of a sudden increase in pressure, elastic arteries expand and store elastic energy, while resistance arteries exhibit a unique ability to do the opposite and constrict. The latter is known as the Bayliss effect where a sudden increase in pressure causes arteriolar vasoconstriction to maintain flow despite fluctuations in loading. The mechanistic basis behind this effect includes a group of mechanosensitive (pressure-sensitive) nonselective cation channels located on the SMC membrane, also known as stretch-activated ion channels (SACs) that cause membrane depolarization when stretched. SACs are interesting due to their mechanosensitive properties and have been studied in peripheral and coronary artery SMCs as well as in ECs. Recent studies identified a new group of mechanosensitive ion channels called Piezo1 channel (PIEZO1), with high expression in the caudal artery and low expression in the aorta, again with important roles in hypertension-driven remodeling (Retailleau et al. 2015). In both angiotensin II- and DOCA salt-induced hypertension models, Piezo1 plays a crucial role in remodeling of the caudal arterial wall.

Ion channels can be targeted to treat hypertension, but because of their regional differences in expression and interdependence with other ion channels, (e.g., through the membrane potential and intracellular calcium), global inhibition of a certain ion channel may also cause undesired effects. If understood better, however, this regional difference in ion channel expression could be used as an advantage when targeting certain regions. Figure 2 shows relationships among some of the many different ion channels.

3.1.2 Sarcoplasmic Reticulum

The sarcoplasmic reticulum (SR) is an important alternative source of intracellular calcium that can activate calcium-sensitive ion channels and calcium-dependent pathways independent of changes in membrane potential. These internal stores of calcium exist in most vessel types (Devine et al. 1972) but tend to be localized more centrally in SMCs of elastic arteries and more peripherally in SMCs of muscular arteries (Nixon et al. 1994). Two main receptors release intracellular calcium from the SR: inositol-1,4,5-triphosphate (IP3) receptors and ryanodine receptors (RyR). IP3 and diacylglycerol (DAG) are by-products of the hydrolysis of phosphatidylinositol 4,5-biphosphate (PIP2) by phospholipase C (PLC), which is an important pathway between intracellular calcium and pharmacomechanical coupling activation. RyR are named after the plant alkaloid ryanodine. Myriad molecules can bind and activate RyR, such as ions, calmodulin, kinases, and phosphatases (Zalk et al. 2007). Exposure to ryanodine will cause calcium depletion in the SMC SR, which is thereby an effective method to suspend the effect of sudden SR calcium release. Similar to the SMC itself, the SR has a pump to recover its basal level of intracellular calcium. Calcium is restored in the SR through an ATP-dependent calcium pump (SERCA). Activation of this pump causes a decrease in cytoplasmic calcium and associated increase in calcium in the SR. The SERCA pump can be regulated by phospholamban, a

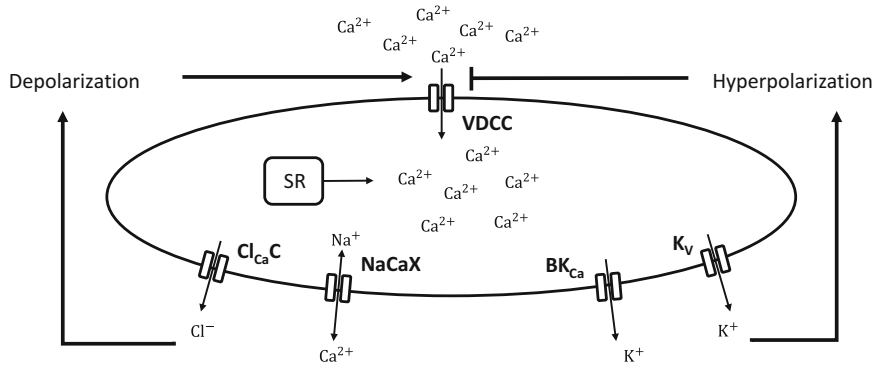

Fig. 2 Regulation of intracellular calcium through electromechanical coupling

protein targeted by protein kinase A (PKA) or protein kinase G (PKG), which inactivates calcium release from the SR causing a reduced cytoplasmic calcium concentration (Pozzan et al. 1994).

3.1.3 Myosin Light-Chain Kinase (MLCK)

Intracellular calcium is an important secondary messenger, which in SMCs has several targets. A key target in regulating vasoconstriction is calmodulin (CaM), a calcium-modulated protein that can activate several important kinases and phosphatases that regulate vascular contraction. CaM has four calcium-binding sites. Binding of calcium ions to CaM forms a calcium-calmodulin complex (CaCaM) which, among other functions, activates the myosin-phosphorylating MLCK. Noted above, MLCK is a serine/threonine protein kinase enzyme that phosphorylates the myosin regulatory light chains (MRLCs) and activates myosin motors, thus enabling interactions with attachments to neighboring acting filaments. There are several isoforms of MLCK, one of which is SMC specific and encoded in humans by the *MYLK1* gene (Herring et al. 2006). MLCK is a long and flexible molecule that has both an actin- and a myosin-binding site, both of which are weakened when activated by CaCaM. These binding sites are located on each end of the MLCK and suggest that MLCK is readily available to the actomyosin complex and could affect actin and myosin interactions at low concentration of CaCaM (Hong et al. 2011). MLCK expression is higher in the mesenteric artery than in the aorta (Martinsen et al. 2014), consistent with the faster phasic contractile response in the mesenteric. Despite the lower expression in the aorta, MLCK regulates calcium channel activity more in the aorta than in mesenteric arteries. It also appears that MLCK is important in regulating the homeostatic level of cytoplasmic calcium and thus the basal tone in the aorta.

3.2 Calcium Sensitization: Pharmacomechanical Coupling

Myosin phosphorylation can be increased at the same level of intracellular calcium and MLCK activity by inhibiting the dephosphorylating myosin light-chain phosphatase (MLCP) enzyme activity. Inhibition of MLCP is also known as calcium sensitization, which can be initiated through different pathways. Several components are involved in the calcium sensitization signaling network, ranging from activation of G-protein-coupled receptors (GPCR) by adrenergic agonists to inhibition of MLCP subunits by the inhibitory protein CPI-17 and the Rho-associated protein kinase (ROCK).

3.2.1 Adrenergic Receptors

SMCs, and similarly cardiomyocytes, are controlled in part by the autonomic nervous system, which regulate unconscious functions such

as heart rate and the fight-or-flight response. The autonomic nervous system can be divided into sympathetic and parasympathetic. In arteries, the sympathetic nervous system is characterized by postganglionic release of adrenergic norepinephrine (NE), causing vasoconstriction through adrenergic receptors located on the SMC membrane. The parasympathetic nervous system is characterized by release of cholinergic acetylcholine, causing vasodilation through muscarinic cholinergic receptors located on the EC membrane. It should be noted that muscarinic receptors are located on SMC in certain veins and coronary arteries where acetylcholine acts as a vasoconstrictor (Milnor 1990).

Adrenergic receptors are widely expressed in different tissues (e.g., liver, heart, bladder, and blood vessels) and are common targets for clinical treatment. In 1948, the pharmacologist Raymond Ahlquist categorized adrenergic receptors into α and β types, which have since been divided into additional subtypes. In arteries, SMC tone is controlled primarily by α_1-, α_2-, and β_2-adrenergic receptors, where primarily α_1 regulates vasoconstriction, α_2 regulates presynaptic release of NE, and β_2 regulates vasodilation (Michelotti et al. 2000). The α_1-adrenergic receptor can be classified into three subtypes: α_{1A}, α_{1B}, and α_{1D}. Each subtype contributes to vascular tone, but they differ in regional distribution and pharmacologic response to agonists and antagonists. In the cardiovascular system, α_{1A}-adrenergic receptors are predominantly expressed in the heart and resistance arteries, α_{1D} in elastic and muscular arteries, and α_{1B} in the heart and all vessels (Michelotti et al. 2000).

In murine arteries, the α_{1A} receptor was reported to be absent in the ascending and descending thoracic aorta, carotid artery, and pulmonary artery, with low expression in the suprarenal abdominal artery but high expression in the infrarenal abdominal aorta and in the celiac, renal, mesenteric, iliac, and femoral arteries (Rokosh and Simpson 2002). The α_{1A}-adrenergic selective agonist A61603 has been reported to be much more potent than norepinephrine (NE) in rat vas deferens (Knepper et al. 1995) and equivalent to the nonselective α_{1A}-adrenergic agonist phenylephrine (PE) in rat mesenteric arteries (Kitazawa and Kitazawa 2012). This trend was also observed in the rat caudal artery where both the active response and sensitivity to A61603 were much stronger than in the aorta (Mueed et al. 2004). This distribution suggests a gradual trend toward a stronger response to the α_{1A}-adrenergic selective agonist A61603 in resistance arteries compared to that in elastic arteries. The α_{1A} selective antagonist RS100329 has a 100-fold higher potency to α_{1A}- than to α_{1B}- or α_{1D}-adrenergic receptors (Williams et al. 1999). In vitro contractions of rat arterial rings stimulated with PE reveal further that RS100329 has high potency in the mesenteric artery, less in the caudal artery, and least in the thoracic aorta, among these three vessels (Kitazawa and Kitazawa 2012), thus corroborating that α_{1A} is more pronounced in resistance arteries than in elastic arteries.

In rat arteries, α_{1D}-adrenergic receptor expression (protein level) has been found in the aorta, iliac artery, and femoral artery but less in the mesenteric artery (Michelotti et al. 2000). No selective α_{1D}-adrenergic agonists are available, but the α_{1D} selective antagonist BMY7378 has approximately 100 times higher potency toward α_{1D} compared to α_{1A} and α_{1B} receptors. Active responses to NE are higher in the suprarenal abdominal aorta and mesenteric artery than in the infrarenal abdominal aorta, and the α_{1D}-adrenergic selective antagonist BMY7378 is most efficient in the suprarenal abdominal aorta and least effective in the infrarenal abdominal aorta (Yamamoto and Koike 2001). These observations are interesting for two reasons. First, NE elicits stronger responses in proximal regions of the abdominal aorta and in the mesenteric artery than in the distal regions of the abdominal aorta. Second, higher concentrations of BMY7378 are necessary to inhibit vasoconstriction stimulated by NE in the distal region of the abdominal aorta than in the mesenteric artery or in the proximal region of the abdominal aorta. Hence, there exists a regional heterogeneity of α_1-adrenergic receptor subtypes not only between muscular and elastic arteries but also within elastic

arteries, with the suprarenal abdominal aorta primarily regulated by α_{1D} receptors, whereas the infrarenal abdominal aorta is regulated mainly through α_{1A} receptors. Other reports have confirmed the dominant influence of α_{1D} receptors in proximal regions of the aorta. In vitro contractions of rat arterial rings stimulated with PE demonstrated that the α_{1D} selective antagonist had its largest effect in the thoracic aorta, with an attenuated effect in the caudal artery and the least effect in the mesenteric artery (Kitazawa and Kitazawa 2012). Similar trends in regional distributions of α_{1A}- and α_{1D}-adrenergic receptor expression have been reported in rats and humans, with more α_{1D} receptors in the elastic aorta and more α_{1A} receptors in the muscular mesenteric arteries (Michelotti et al. 2000; Rudner et al. 1999).

The role of α_{1B} receptors has been more difficult to isolate due to the lack of α_{1B} selective adrenergic receptor agonists. The antagonist 5-methyl urapidil (5-MU) has higher selectivity to α_{1A}- and α_{1D}-adrenergic receptors ($\alpha_{1A} > \alpha_{1D} > \alpha_{1B}$) and has been used to favor α_{1B} stimulation. The antagonist chloroethylclonidine (CEC) has higher selectivity to α_{1B} receptors ($\alpha_{1B} > \alpha_{1D} > \alpha_{1A}$) and can be used to inhibit α_{1B} stimulation. These two compounds have been used to demonstrate a potential role of α_{1B}-adrenergic receptors during SMC development (Chen et al. 1995). Knockout studies provide some clues on the function of the α_{1B} receptors but not without controversy. It has been observed that contractility of the thoracic aorta is both affected and not affected by NE and PE in ${\alpha_{1B}}^{-/-}$ mice (Cavalli et al. 1997; Hosoda et al. 2005).

Single knockout models of α_{1A} (Rokosh and Simpson 2002), α_{1B} (Cavalli et al. 1997), and α_{1D} (Tanoue et al. 2002) all cause hypotension in mice despite their heterogeneous distribution along the arterial tree. This finding suggests that all subtypes may participate cooperatively in blood pressure regulation, with the controversial α_{1B} -adrenergic receptors possibly contributing through vasoconstriction of elastic, muscular, and resistance arteries. Figure 3 summarizes the regional activity of α_1 adrenergic receptors in elastic, muscular, and resistance arteries.

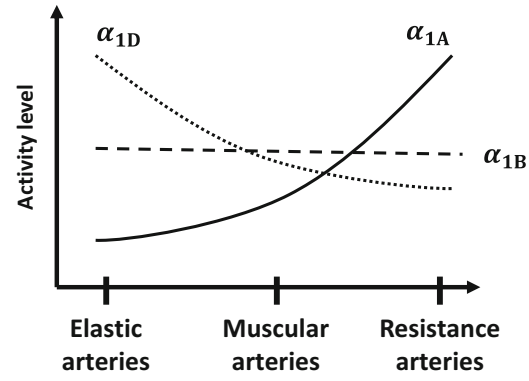

Fig. 3 Regional activity of α_1-adrenergic receptor subtypes A (solid), B (dashed), and D (dotted) in elastic, muscular, and resistance arteries

3.2.2 G-Protein-Coupled Receptors

G-proteins are membrane proteins that act as common mediators of cellular responses to hormones and neurotransmitters in SMCs. When connected to adrenergic receptors, G-proteins form G-protein-coupled receptors (GPCR) that activate numerous cellular responses, including those regulating active tone in arteries. G-proteins can be divided into four classes: G_q, $G_{12/13}$, G_s, and G_i (Simon et al. 1991). The G-protein family G_q activates phospholipase C (PLC) and the IP3/DAG pathway, whereas $G_{12/13}$ activates RhoA and the Rho-Rho-Kinase pathway. The β-adrenergic receptors are coupled to the G-protein family G_s (stimulator), which activates adenylyl cyclase and produces cAMP (cyclic adenosine-3′3, 5′ monophosphate) from ATP (adenosine triphosphate). This process has different effects in different cells. β-adrenergic receptors enhance contraction in cardiomyocytes but cause relaxation in SMCs by reducing intracellular calcium through activation of a cAMP-dependent protein kinase (PKA). The G-protein class G_i (inhibitor) mainly inhibits adenylyl cyclase and production of cAMP. Here, we focus on the G_q and $G_{12/13}$ G-proteins and their signaling cascades regulating SMC contractility (see Fig. 4).

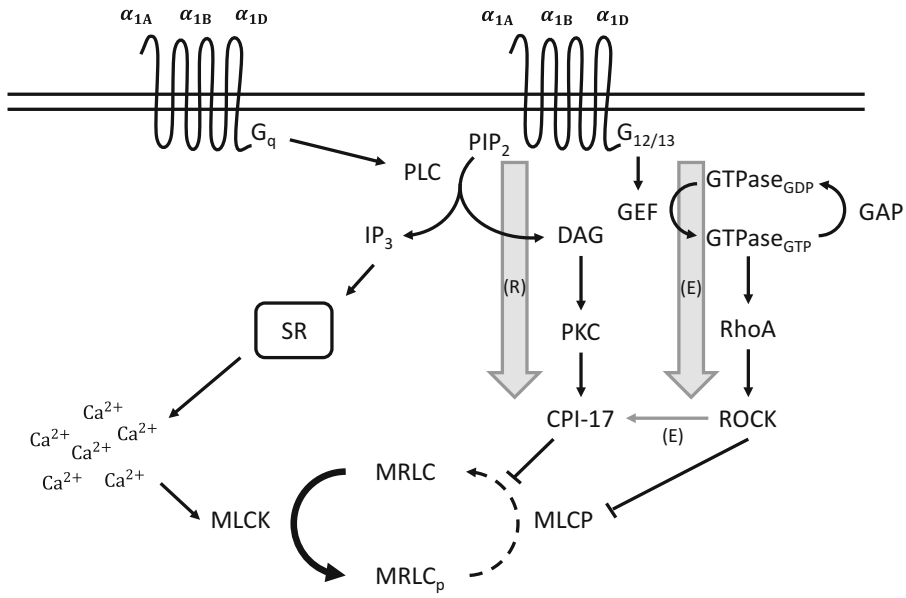

Fig. 4 Calcium-sensitizing pathways regulating vasoconstriction. Pathways more active in resistance arteries are denoted by (R) and in elastic arteries by (E)

3.2.3 G_q–PLC–PKC/IP3

The G-protein family G_q activates PLC, a membrane-associated enzyme that catalyzes the hydrolysis of phosphatidylinositol 4,5-biphosphate (PIP2) into 1,2-diacylglycerol (DAG) and 1,4,5-triphosphate (IP3) (Berridge and Irvine 1984). IP3 binds to IP3 receptors located in the SR activating release of calcium, which in turn triggers cytosolic calcium-dependent activities that include activation of calcium-dependent ion channels (e.g., $Cl_{Ca}C$) that induce membrane depolarization and open VDCCs to further elevate intracellular calcium concentration. DAG binds and activates the phosphorylating enzyme protein kinase C (PKC), which exists in several isoforms. αPKC is expressed in the cytosol of most SMCs whereas δPKC associates with the SMC cytoskeleton and membrane (Salamanca and Khalil 2005). The PKCs consist of a regulatory and a catalytic domain. The regulatory domain has binding sites for DAG and calcium; the catalytic domain can activate substrates involved in important cellular functions such as exocytosis, gene expression, proliferation, growth, and regulation of vascular contraction. Several substitutes can bind to the regulatory domain instead of DAG and activate PKC. Examples include PDBu as well as several PKC inhibitors such as GF109203x that inhibit the catalytic domain. An important PKC-dependent pathway that regulates vascular contractility is phosphorylation and activation of a 17 kDa PKC-potentiated MLCP inhibitor (CPI-17), which is predominantly expressed in vascular SMCs.

PKC expression has been reported to be comparable in rat thoracic aorta, caudal artery, and small mesenteric artery, whereas CPI-17 expression is higher in the second- and third-generation mesenteric artery compared with the aorta and caudal artery (Kitazawa and Kitazawa 2012). High expression of CPI-17 in resistance arteries is supported by in vitro contraction studies of rat arterial rings with PE and relaxation with the PKC inhibitor GF109203x, with active force development significantly reduced in the second- and third-generation mesenteric arteries, less reduced in the caudal and superior mesenteric arteries, and least reduced in the thoracic aorta. Increased vascular contractility in mesenteric arteries and increased blood pressure in transgenic mouse models with increased expression of CPI-

17 have also been reported (Su et al. 2013). Other studies report higher expression of PKC and CPI-17 and sensitivity to the PKC inhibitor PDBu in the rat aorta compared with the caudal artery (Mueed et al. 2004) and a higher expression of CPI-17 in the rabbit aorta than in the femoral artery (Woodsome et al. 2001). Further studies could clarify differences in PKC-mediated contraction in different vessel types, in particular between muscular and elastic arteries. Nonetheless, it is evident that there is a regional distribution and activity of PKC/CPI-17, with the highest expression found in resistance arteries and lower expression in muscular and elastic arteries.

When inhibiting PKC with GF109203x in PE-stimulated contractions, the sustained level of intracellular calcium decreases in the small mesenteric artery but not in the thoracic aorta (Kitazawa and Kitazawa 2012) or the femoral artery (Dimopoulos et al. 2007), suggesting that PKC could have a role in calcium handling in resistance arteries but not in elastic or muscular arteries. Other reports suggest that PKC can activate the store-operated ion channel (SOC) (Leung et al. 2008) and inhibit activation of BK_{Ca} (Barman et al. 2004) in pulmonary arteries, which would increase the intracellular calcium.

3.2.4 $G_{12/13}$–RhoA–ROCK

The G-protein family $G_{12/13}$ activates a cascade of signaling proteins that includes members of the small Rho family GTPases, which play important roles in cytoskeletal changes, vesicle trafficking, cell progression, and myosin phosphorylation. GTPase activity is regulated by two proteins, guanine nucleotide exchange factor (GEF) and GTPase-activating protein (GAP); GTPase is activated when attached to guanosine triphosphate (GTP) and deactivated when attached to guanosine diphosphate (GDP). GEF promotes activation by exchanging GDP with GTP, while GAP promotes hydrolysis of GTP to GDP. The main members in the Rho family are RhoA, Rac1, and Cdc42, with more than 70 potential downstream effectors involved in important cellular functions, including Dia1,2 (downstream of RhoA, Rac1), Wasp (downstream of Rac1), N-Wasp (downstream of Cdc42), MEKK4/Jnk (downstream of Cdc42), and ROCK (downstream of RhoA) (Bustelo et al. 2007). RhoA is an important activator of Rho-Kinase (ROCK), a kinase involved in cytoskeletal reorganization and calcium sensitization. ROCK is a member of the serine/threonine kinase family and has two isoforms, ROCK1 and ROCK2. Both isoforms are expressed in vascular SMCs and are involved in regulating MLCP activity with cooperative roles, with ROCK2 reported to be the predominant isoform to regulate vascular contractility (Wang et al. 2009).

RhoA has been reported to be expressed more in elastic (aorta) and muscular (caudal) arteries than resistance (small mesenteric) arteries. Expressions of ROCK1 and ROCK2 were nevertheless equivalent in the different vessel types. Regional differences in the RhoA-ROCK pathway were found through in vitro contraction tests induced with PE together with the ROCK inhibitor Y27632, where the largest effect (inhibition) was observed in the aorta, a decreased effect in the caudal artery, and the least effect in the small mesenteric artery (Kitazawa and Kitazawa 2012).

Inhibiting ROCK with Y27642 reduces the sustained level of intracellular calcium in the aorta but not in the small mesenteric artery, suggesting that ROCK has a role in calcium handling in elastic arteries. ROCK is required for non-voltage and non-capacitive-dependent calcium entry in arteries, and inhibition of these channels has a larger effect on the aorta than the mesenteric artery (Martinsen et al. 2014). This could explain the reduction of intracellular calcium when inhibiting ROCK in the aorta and not in the mesenteric artery. The sensitivity and maximal effect of ROCK on intracellular calcium are higher when stimulated by NE in the aorta than in the mesenteric artery (Ghisdal et al. 2003). It was also found that Y27632-dependent inhibition of intracellular calcium is not related to any potassium ion channel, PLC activity, or IP3 receptor. It should be noted that there have been reports where inhibiting ROCK with Y27632 had very little effect in rat aorta (Mueed et al. 2004). Regional differences in RhoA expression, with higher expression in elastic arteries than in resistance arteries, will affect both intracellular

calcium levels and calcium sensitization through a ROCK-dependent pathway.

Interestingly, some reports suggest that ROCK could be involved in phosphorylating and activating CPI-17 (Kitazawa and Kitazawa 2012; Koyama et al. 2000). CPI-17 phosphorylation was reduced in the aorta but not in the small mesenteric artery when inhibiting ROCK with Y27632, suggesting that $G_{12/13}$ G-protein activation could inhibit MLCP through both a RhoA-ROCK pathway and a PKC-CPI-17 pathway in elastic arteries, thus rendering it efficient in regulating contraction in elastic arteries. It should be noted that electromechanical activation (exposure to high KCl) was able to phosphorylate MYPT1 through RhoA activation (Sakurada et al. 2003) but with no activation of CPI-17 (Dimopoulos et al. 2007), suggesting that ROCK phosphorylation of CPI-17 could be dose-dependent or that other factors are necessary to phosphorylate CPI-17 through ROCK.

3.2.5 Myosin Light-Chain Phosphatase

MLCP consists of three subunits: a large 110–130 kDa regulatory subunit MYPT1, a 38 kDa catalytic subunit PP1c, and a small 20 kDa subunit with a function yet unknown. The MYPT1 subunit is responsible for activating the PP1c subunit through a conformational change that allows PP1c to activate MLCP. The MLCP can be inhibited through two main pathways, phosphorylation of MYPT1 (at Thr696 and Thr853 sites) and direct inhibition of MLCP (Dimopoulos et al. 2007). MYPT1 (Thr853 site) can be phosphorylated by ROCK through the $G_{12/13}$/RhoA/ROCK pathway but also phosphorylated (Thr696 site) by different kinases, including integrin-linked kinase (ILK), zipper-interacting protein kinase (ZIPK), p21-activated kinase (PAK), and dystrophia myotonica protein kinase (DMPK) (Somlyo and Somlyo 2003). The second pathway of directly inhibiting MLCP is phosphorylation and activation of the SMC-specific MLCP inhibitor CPI-17 through the G_q/PLC/DAG/PKC/CPI-17 (primary) or the $G_{12/13}$/RhoA/ROCK/CPI-17 (secondary) pathway. Phosphorylation of Thr38 on CPI-17 increases the effect of its inhibition of MLCP by 1000-fold. The ratio of CPI-17 to MYPT1 expression varies and depends on SMC type and regional differences (Dimopoulos et al. 2007).

Vascular contraction is characterized by a rapid transient increase in intracellular calcium, which decreases to a steady-state value after reaching its peak. MLC phosphorylation behaves similarly with an initial peak but higher maintained levels. Intracellular calcium can be directly linked to MLCK activity. The maintained level of MLC phosphorylation despite loss of MLCK activity is thought to be related to a reduced MLCP activity regulated by the two (CPI-17/ROCK) calcium-sensitizing pathways. These pathways differ in the time course of MLCP inhibition, with phosphorylation of CPI-17 occurring faster than phosphorylation of MYPT1 (Dimopoulos et al. 2007). The fast transient increase in MLC phosphorylation can be eliminated by inhibiting an increase in intracellular calcium by blocking VDCC and depleting intracellular calcium from the SR or by inhibiting PKC. The steady-state value of MLC phosphorylation reduces when inhibiting ROCK, which also affects the steady-state value of CPI-17 phosphorylation, thus confirming that ROCK can phosphorylate CPI-17 independently of PKC (Kitazawa and Kitazawa 2012). The ROCK pathway regulates the late sustained phase of contraction, while the early phase associates with MLCK activity and phosphorylation of CPI-17 (Dimopoulos et al. 2007), which most likely dictates the regionally different contractile responses in arteries. The G_q/PLC/DAG/PKC/CPI-17 pathway, with highest activity in resistance arteries and lower activity in muscular and elastic arteries, acts faster than the $G_{12/13}$/RhoA/ROCK pathway, which is most active in elastic arteries (see Fig. 5). These observations suggest that the time course of regulating active tone is important in arteries and that different vessel types utilize a variety of pathways to generate different acute responses and chronic regulations of the active tone.

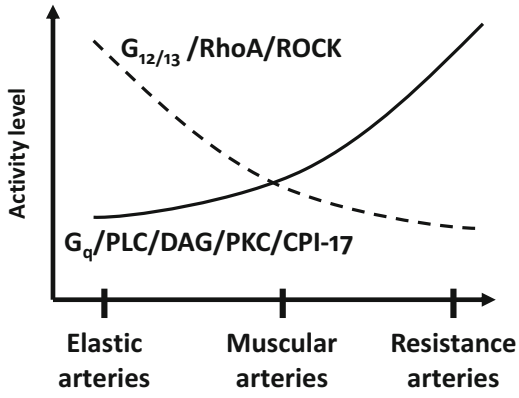

Fig. 5 Regional activity of CPI-17 (solid) and ROCK (dashed) in elastic, muscular, and resistance arteries

Interestingly, inhibiting an increase in intracellular calcium during PE-induced contraction significantly reduces active tone in the femoral artery, although without changes in the steady-state value of MLC phosphorylation when compared to contraction with normal levels of calcium (Dimopoulos et al. 2007). Moreover CPI-17 phosphorylation is significantly reduced, while phosphorylation of MYPT1 is not affected. This weak, however existing, calcium transient-independent contraction was confirmed in the thoracic aorta but was not observed in the small mesenteric artery (Kitazawa and Kitazawa 2012). This suggests that basal levels of intracellular calcium are enough to trigger calcium-sensitizing active tone in elastic arteries, while calcium transients above basal level are necessary to trigger contraction in resistance arteries.

3.3 Calcium Desensitization: EC-Driven Relaxation

Vascular ECs line the innermost layer of the arterial wall, the intima, and have many important functions including clearance of specific vasoactive substances from the circulation, synthesis of prostaglandins, antithrombogenic activity, regulation of mitosis and development of SMC, and release of endothelium-derived factors such as nitric oxide (NO) or endothelin-1 (ET-1) (Milnor 1990). NO is an important signaling molecule with anti-inflammatory, antithrombotic, vasodilatory, and matrix-modulating roles. NO synthesis in ECs is mediated by endothelial NO synthase (eNOS), which facilitates conversion of the amino acid L-arginine to L-citrulline, with NO as a by-product. As in SMCs, intracellular calcium in ECs is regulated in part by membrane ion channels and receptors. ECs also possess a range of different membrane ion channels, including receptor-activated cation channels, nonselective cation channels, potassium channels, chloride channels, and mechanosensitive ion channels. Membrane potential is an important driving force regulating the intracellular calcium in ECs and is, as in SMCs, regulated through an exchange of different ions within the extracellular space. Central ion channels in ECs are the potassium ion channels, in particular inwardly rectifying K_{ir} channels, which are important for the resting potential, chloride channels, and voltage-dependent sodium and calcium channels. ECs are also equipped with stretch- and shear-sensitive nonselective cation channels that regulate intracellular calcium in response to changes in blood pressure and flow (Nilius and Droogmans 2001). Calcium entry into ECs can also be activated though a G-protein-coupled receptor pathway activating nonselective cation, store-operated channels, and membrane receptors. Membrane receptors in ECs are cholinergic receptors of the muscarinic type, which also exist in SMCs. Cholinergic nerves release acetylcholine, which binds to muscarinic receptors coupled to the G_q-protein, thus activating the PLC/IP3 pathway and increasing intracellular calcium. Depending on the ratio of expression and affinity to muscarinic receptors in endothelial and SMCs, the total response may be vasodilation or vasoconstriction. In most arteries, however, activation of muscarinic receptors causes vasodilation though it causes vasoconstriction in coronary arteries and veins (Milnor 1990). Intracellular calcium in ECs can also activate MLCK-dependent contraction in a fashion similar to that in SMCs. However, the active tone produced in vascular ECs is ~20 times smaller than in SMCs and does not contribute to the mechanical function of the arterial wall. Rather,

active tone in ECs is believed to relate to vessel permeability for controlling transportation of important molecules through intracellular junctions (Sukriti et al. 2014).

When NO produced by ECs diffuses into the wall and reaches the SMCs, it activates NO-guanylyl cyclase (NO-GC) which triggers the synthesis of GTP to cyclic guanosine monophosphate (cGMP). The concentration of cGMP is determined by NO-GC and the enzyme phosphodiesterase (PDE), which breaks down cGMP. cGMP is an important messenger in NO-mediated vasodilation and acts mainly through cGMP-dependent protein kinase (PKG) regulating intracellular calcium and calcium desensitization in the SMCs. There are two families of PKG: PKGI and PKGII, which are encoded by two separate genes, with PKGI more involved in cGMP-regulated signaling (Francis et al. 2010). PKG can regulate both electromechanical- and pharmacomechanical-driven SMC contractility by changing intracellular calcium regulation and calcium-desensitizing pathways (Lincoln et al. 2001). PKG decreases MLCK activity by reducing intracellular calcium mainly by enhancing the activity of $BK_{Ca}C$ and $K_{ATP}C$, leading to membrane repolarization and hyperpolarization (Ko et al. 2008). PKG is also able to phosphorylate IP3 receptors reducing PLC-activated calcium release from the SR (Lincoln et al. 2001). PKG increases MLCP activity by inhibiting CPI-17- and ROCK-dependent pathways, leading to calcium desensitization. PKG phosphorylates Ser695 located on the MYPT1, which prevents phosphorylation of Thr696 and deactivation of MLCP. PKG also dephosphorylates CPI-17, which prevents CPI-17 from inhibiting MLCP (Lincoln 2007). This makes PKG a powerful and important component regulating vasodilation. See Fig. 6 for a summary of the EC-driven calcium-desensitizing pathways in VSMCs.

Acetylcholine causes EC-dependent vasodilation in the aorta and femoral, hepatic, mesenteric, and renal arteries to both KCl- and PE-induced contraction with comparable sensitivity (Zygmunt et al. 1995). However, when inhibiting acetylcholine-triggered NO formation through the L-arginine analog L-NOARG, a regional inhibitory effect to L-NOARG was observed for PE-induced contraction with no relaxation in the femoral and renal arteries. The L-NOARG-resistant relaxation in the aorta and hepatic and mesenteric arteries was suggested to be due to a regional endothelium-derived hyperpolarizing mechanism (Zygmunt et al. 1995).

The NO content has been reported to be more than two times higher in the aorta than in the mesenteric artery (Burgoyne et al. 2012) suggesting that NO-regulated vasodilation could require a higher level of NO in elastic arteries than in resistance arteries (sensitivity) or produce higher levels NO-regulated vasodilation in elastic arteries than in mesenteric arteries (magnitude). The higher NO content in the aorta is also believed to have a desensitizing effect to PKG oxidation. Besides activation through NO-cGMP, PKG can also be activated through a competing oxidation mechanism where activation through cGMP attenuates PKG oxidation (Burgoyne et al. 2007). Hence, a higher level of NO-cGMP, as reported in the aorta compared to the mesenteric artery, would better resist PKG to oxidation. This property was also reflected by the aorta, which was much less sensitive than the mesenteric artery to H_2O_2-induced relaxation.

3.4 Basal Active Tone in Arteries

Similar to how the kinetics of the phosphorylating MLCK and dephosphorylating MLCP regulate total myosin phosphorylation, the kinetics of the basal SMC activity and basal EC activity likely regulate basal vascular tone (Fig. 7). Basal SMC activity is set by the regulatory components involved in defining SMC contractility, including basal levels of adrenergic agonist concentration, SMC intracellular calcium, blood pressure, and mechanical wall tensile stress. Likewise, basal EC activity depends on basal levels of EC intracellular calcium, blood flow, and mechanical wall shear stress.

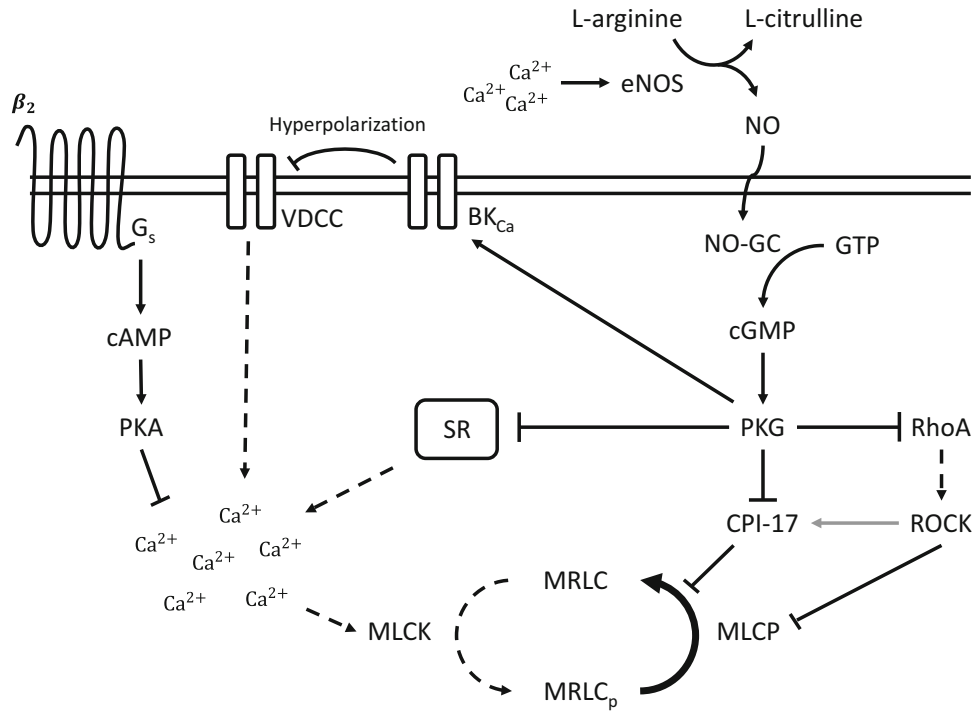

Fig. 6 Endothelial cell-driven calcium-desensitizing pathways regulating myosin regulatory light-chain (MRLC) dephosphorylation and vasodilation

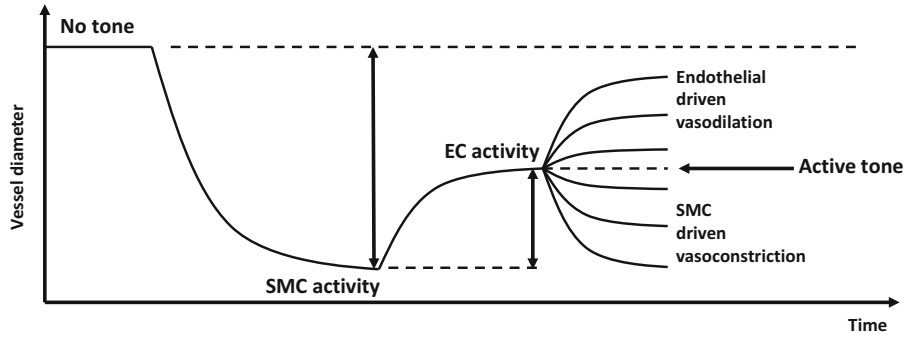

Fig. 7 Active tone in arteries regulates vessel diameter and is defined by the combined activity of smooth muscle cells (SMCs) and endothelial cells (ECs)

Basal SMC activity likely sets the maximal resting tone and is not trivial to measure ex vivo. Theoretically, this could be accomplished in vitro by comparing active tone at basal and zero intracellular calcium with inhibited EC activity. The endothelium is considered as an important player in regulating basal vascular tone. Basal NO production by ECs at zero flow has been reported to be higher in the thoracic aorta and carotid artery compared to mesenteric and femoral arteries. By inhibiting constitutive NO synthase with N^{Ω}-nitro-L-arginine methyl ester (L-NAME) during PE-stimulated contraction, ring segments from the thoracic aorta and carotid artery produce

higher active tension, while tension remains unchanged in the mesenteric artery and even reduced in the femoral artery (Leloup and Fransen 2015). This observation is supported by direct measurements of NO where a 2.7-fold higher level was reported in the thoracic aorta than in the mesenteric artery during basal conditions (Burgoyne et al. 2012). Lower basal NO production (i.e., lower production at zero flow) would give ECs a higher capability to regulate vascular tone. One remarkable observation was a decrease in active tone in the femoral artery in response to L-NAME. Vascular relaxation was observed when a denuded femoral artery was subjected to the NO-donor sodium nitroprusside (SNP) (Kitazawa et al. 2009), suggesting that the difference could be in femoral endothelial function and eNOS activity rather than a reduced signaling to NO in femoral SMCs. When inhibiting eNOS activity during electromechanical stimulation (high KCl), the increased active response was diminished in the thoracic aorta and reduced in the carotid artery. This would suggest that basal NO does significantly affect the thoracic aorta or the carotid artery when stimulating SMCs through membrane depolarization. Yet, the basal effect of EC always depends on the basal level of SMC contractile capacity unless SMCs could be regulated through endothelium-dependent contractility.

Besides EC-dependent relaxation regulated through eNOS, ECs are also able to produce endothelium-dependent contraction, regulated by thromboxane A_2 (TxA_2) through cyclooxygenase (COX) in mouse abdominal aorta, femoral, and carotid arteries (Zhou et al. 2005). When stimulating these arteries with acetylcholine while inhibiting eNOS with L-NAME, the largest endothelium-dependent contraction to acetylcholine was observed in the carotid artery, followed by the abdominal aorta, and then the femoral artery. This contraction was not seen in endothelium-denuded vessels, confirming its endothelial dependency and not due to SMC muscarinic receptors. These results suggest a regional difference in functional competition between endothelium-dependent and endothelium-independent tone in arteries.

3.5 Local Versus Remote Control Vascular Response

Vascular tone is regulated in vivo by several different systems, which can be separated by factors regulated by local versus remote control systems (Mellander 1970). Local control results from locally produced factors (e.g., endothelial-dependent NO secretion or stretch-dependent activation), while remote control mechanisms stem from the parasympathetic and sympathetic nervous system as well as the renal and adrenal gland-dependent renin-angiotensin system. Remote control can affect a larger domain of the circulatory system and often acts in synergy with the local control system. Blood pressure and flow are thus affected by both local and remote control systems. Again, however, different types of arteries can respond differently to both control systems, as, for example, release of norepinephrine (NE) can cause a weaker response in the infrarenal abdominal artery than in the suprarenal abdominal aorta (Yamamoto and Koike 2001). Another interesting example is angiotensin II.

Angiotensin II is a key effector molecule of the renin-angiotensin system. It binds mainly to two receptors: the AT1 receptor, which affects growth, remodeling, and vasoconstriction, and the AT2 receptor, which affects vasodilation and opposes effects of the AT1 receptor. The AT1 receptor activates G_q, G_i, and $G_{12/13}$ G-proteins (Wynne et al. 2009) and, in mice, can be divided into two subgroups, the AT1a and AT1b receptors. AT1a is thought to play a major role in regulating transient cardiovascular function as well as long-term growth and remodeling via extracellular matrix protein turnover in the arterial wall, while AT1b is linked more to the contractile response to agonist stimulation (Zhou et al. 2003). Regional variations in response to angiotensin II have been reported in murine arteries due to differences in AT1b receptor expression, with the highest response in the infrarenal abdominal aorta and femoral artery, lower responses in the carotid artery, and lower yet in the thoracic aorta (Zhou et al. 2007). These differential responses reflect a regional gradient in AT1a and AT1b gene expression in the mouse aorta, with highest

expression in the infrarenal abdominal aorta and lowest in the suprarenal abdominal aorta (Poduri et al. 2012). Therefore, an increase in angiotensin II in the circulation will cause regional differences in vasoconstriction with greater active responses in distal regions of the abdominal aorta and the femoral artery.

Endothelin-1 is endothelium-derived vasoconstrictor with similar regional responses as angiotensin II due to endothelin receptor distributions, with greater responses in the abdominal aorta and less response in the thoracic aorta and carotid artery (Zhou et al. 2004). Endothelin-1 binds to two major receptors in SMCs, ET_A and ET_B. These receptors are also coupled to G-protein family members G_q, G_s, and G_i (Wynne et al. 2009) and trigger the PLC/DAG/PKC/CPI-17 pathway.

4 SMC Cytoskeleton Regulation

SMC cytoskeletal filaments, mainly the actin (thin) but also intermediate filaments (namely, desmin and vimentin), play fundamental roles in vascular contractility. The RhoA-ROCK pathway regulates actin cytoskeletal remodeling through two separate pathways, by promoting polymerization or inhibiting depolymerization to promote active tension development. RhoA activates mammalian diaphanous-related formins (mDia) which play an important role in the polymerization of actin filaments and formation of actin stress fibers. ROCK triggers LIM kinase, which inactivates cofilin-driven f-actin depolymerization, thus stabilizing actin filament networks (Tang and Anfinogenova 2008). There are reports of higher actin filament concentration in resistance arteries (second generation of mesenteric arteries) than in muscular (mesenteric artery) or in elastic (aorta) arteries (Wede et al. 2002). Yet, the dominant ROCK regulation of active tension in elastic versus resistance arteries suggests that actin polymerization could be an important regulatory mechanism in all arteries. Actin polymerization, which strengthens the intracellular cytoskeletal network, not only promotes active tension development, it also increases the ability of a SMC to sense, through integrins, mechanical forces acting on the surrounding extracellular matrix (Humphrey et al. 2014).

CaCaM activates several important components in SMCs, such as caldesmon (CaD), calponin (CaP), and MLCK. CaD and CaP are actin filament-associated proteins that are believed to regulate actin availability for myosin through extracellular regulated kinase 1/2 (ERK1/2) and PKC, similar to the function of troponin in the skeletal muscle (Kim et al. 2008).

The intermediate filament vimentin is well expressed in most vessels, while desmin is more expressed in more distal arteries. This regional variation is also reflected by active tone generation, where active stress is significantly less in resistance arteries but not significantly affected in muscular and elastic arteries in desmin-deficient mice (Wede et al. 2002).

5 Multiscale Vascular Contractility

The active tone developed by SMC contraction deforms the vascular wall and thus alters overall wall mechanics, including stress and stiffness. SMC force generation at a tissue level is determined mainly by SMC-SMC connections and the number of intracellular attached myosin crossbridges activated by MRLC phosphorylation. Active myosin crossbridges perform power-stroke movements, attaching and pulling neighboring actin filaments resulting in filament sliding and SMC deformation. This deformation, primarily in the circumferential direction, causes the vascular wall to reduce its inner radius and increase its wall thickness, both of which tend to decrease wall stress (including that borne by the passive extracellular matrix) according to the aforementioned Laplace equation. This reduction in inner radius also increases vascular resistance, which can affect local flow. This is a particularly important function of the resistance arteries but muscular arteries as well.

A Hill-type muscle model, which is frequently used to study muscle contraction, describes mus-

cular tissue via a Maxwell-like or Kelvin-Voigt arrangement of the contractile components. In the Maxwell-like Hill model, the vascular wall can be modeled using a parallel elastic component, a serial elastic component, and a contractile component (Cox 1978). While the serial elastic component represents the elasticity of the attached crossbridges and the contractile component represents average filament sliding causing the cell to contract, the parallel elastic component represents the elasticity of the extracellular matrix components. More attached crossbridges and more active SMCs are modeled by a stiffer elastic modulus for the serial component. Deformation of the contractile component will depend on boundary and loading conditions. The fraction of active SMCs and passive extracellular matrix components (e.g., elastin and collagen) defines which vascular wall component will be responsible for the main mechanical load-bearing component in the vascular wall. It is well known that elastin area fraction differs by region, higher in the thoracic aorta, lower in the abdominal aorta, and less in the mesenteric and femoral artery (Kleinbongard et al. 2013; Akata et al. 2003). In both elastic and muscular mouse arteries, the SMC and elastin area fractions are often proportional, with the largest fraction of SMCs (mainly maintenance phenotype) and elastin in the thoracic region, a lower fraction in the abdominal region of the aorta, and lower yet in the carotid artery (Ferruzzi et al. 2015). The active force produced via electromechanical stimulation is highest in the thoracic aorta, less in the abdominal aorta, and least in the carotid artery (Kleinbongard et al. 2013). This trend is maintained when normalizing the active force with morphological data of the respective arterial region (Ferruzzi et al. 2015), but when normalized with the SMC area, only the active stresses generated by the SMCs are found to be highest in the carotid artery (SMC only, 85.6 kPa; entire wall, 13.7 kPa), lower in the abdominal aorta (SMC only, 71.7 kPa; entire wall, 14.6 kPa), and lower yet in the thoracic aorta (SMC only, 62.7 kPa; entire wall, 22.1 kPa). Despite the higher SMC area fraction in elastic arteries, the active stress produced by the SMCs is higher in muscular arteries, which likely derives from different SMC phenotypes in muscular and elastic arteries. Resistance arteries have the highest SMC fraction and active stress production (Wede et al. 2002; Intengan et al. 1999) but a low fraction of elastin; thus, they do not share the same proportionality of elastin and SMC content as observed in elastic and muscular arteries. Interestingly, the fraction of collagen has an opposite trend to SMC fractions in all regions of arteries and to elastin in elastic and muscular arteries but not in resistance arteries (Ferruzzi et al. 2015; Intengan et al. 1999).

Degradation of elastin, as in aging or disease progression, is often compensated by increased collagen deposition in the arterial wall. Hence, it could be informative to compare collagen to SMC content in arteries throughout vascular remodeling, noting that loss of elastin in elastic arteries may promote SMC apoptosis. For example, to maintain the same level of stress in the vascular wall for a particular loading condition, a reduction of SMC active tone (serial component) would have to be compensated by an increase in collagen (parallel component). This has been reported in hypertensive rats where a significant increase of collagen and loss of SMCs in resistance arteries have been observed (Intengan et al. 1999). Adaptation of vascular wall components has been observed in both resistance (Tuna et al. 2013) and elastic (Arner et al. 1984) arteries where a loss of active stress is compensated by an increase in passive wall stress. It has been suggested that an underlying remodeling process also occurs within SMCs, reflected by changes in contractile capacity, before any detectable changes are observed in the extracellular matrix components (Martinez-Lemus et al. 2009). Acute vascular remodeling of active tone without any changes in passive behavior of the vascular wall has been reported in the descending thoracic aorta where activation of GPCR was necessary (Murtada et al. 2016a).

SMC tone has been suggested to direct the development and direction of arterial remodeling (Bakker et al. 2008). This is apparent during hypertension where regulation of vascular contractility mirrors regional differences in arterial

remodeling, with reduced activity in K_vC and $BK_{Ca}C$ (increased contractility) commonly arising with inward remodeling in resistance arteries and elevated expression of K_vC (reduced contractility) commonly associating with outward remodeling in elastic arteries.

There are several reports where dysfunctional SMC contractility, through mutations in genes encoding SMC contractile proteins, causes pathological conditions in the vascular wall (Humphrey et al. 2015), as well as where dysfunctional extracellular matrix causes reductions in SMC tone (Murtada et al. 2016b), suggesting a significant coupling between passive and active properties in arteries. SMC contractility has a demonstrated important role in maintaining geometrical and mechanical properties near homeostatic levels by reducing wall stresses and modulating vascular remodeling during elevated blood pressure (Bersi et al. 2017). Furthermore, SMC tone has been suggested to have a stress-shielding role in a vulnerable extracellular matrix (Ferruzzi et al. 2016). Postnatal disruption of the transforming growth factor beta receptor II (Tgfbr2) in SMC compromises both contractile and structural biomechanical vessel properties. Treating with rapamycin, an mTOR inhibitor, did not recover the passive structural biomechanical properties but restored biaxial SMC contractile properties and prevented pressure-induced delaminations.

Calcium channel blockers are used to reduce blood pressure by reducing SMC contractility. Inhibition of the LTCC using dihydropyridine (affecting both vascular and cardiac LTCC) or non-dihydropyridine (affecting mainly cardiac LTCC) calcium channel blockers has, however, accelerated aneurysm growth and rupture in Marfan syndrome mice despite reducing blood pressure (Doyle et al. 2015). Although both types of calcium channel blockers enhance enlargement of the ascending thoracic aorta, inhibiting LTCC had a more severe pathological effect. In contrast, inhibiting PKC (using enzastaurin), which is less active in elastic arteries and also an upstream regulator of the mitogen-activated kinase (MAPK) signaling component ERK1/2, led to a reduction in aneurysmal growth. Similar reduction in lesion growth was observed when relaxing only the resistance arteries using the antihypertensive agent hydralazine, thus revealing the importance of mechanical loads. These studies collectively demonstrate that SMC components at different length scales can lead to different consequences on the extracellular matrix and overall vascular phenotype in different regions in the arterial tree.

6 Summary

SMC contractility plays many important roles in the circulatory system and can be regulated through many different pathways with differential effects on distinct functions and behavior. A summary of the VSMC regulatory components in different types of arteries is given in Table 1. These pathways, in turn, are regulated by different proteins and have different response times. These many differences reflect the various functions of SMC contractility in the different regions within the arterial tree. Intracellular calcium plays an important role in the rapid activation of MLCK through activation of multiple ion channels but also in the rapid phosphorylation of CPI-17 and inhibition of MLCP. Calcium-sensitizing pathways play important complementary roles in regulating active tone but also in linking endothelial-dependent regulation of calcium-desensitizing vasodilation with the regulation of extracellular matrix components. Despite the many regional differences in regulating vascular contractility, the regions work together in health through synergistic interactions where local changes in vascular tone can affect the global hemodynamics (Humphrey et al. 2016). To better understand the function and impact of SMC contraction, further attention needs to be given to regional differences in arteries.

In conclusion, we hope that this brief overview of regulatory pathways in SMC contractility and their regional heterogeneity gives better insight into and understanding of roles of vascular contractility in the different regions of the systemic circulation. Understanding SMC contractility is critical for understanding vascular health and disease, including the ability of the vasculature

Table 1 Regional activity (+++, high; ++, medium; +, low) of vascular smooth muscle cell regulatory components in elastic, muscular, and resistance arteries. The (?) indicates the need for further information

	Elastic	Muscular	Resistance
MLCK	++	++(?)	+++
MLC	+	+++	+++
α_{1A} AR	+	++	+++
α_{1B} AR	++(?)	++(?)	++(?)
α_{1D} AR	+++	++	++(?)
PKC	++	++	++
CPI-17	++(?)	++(?)	+++
RhoA	+++	+++	+
ROCK	++	++	++
MYPT1	++	+++	+++

to adapt to sustained changes in mechanical loading (cf. Dajnowiec and Langille (2007), Valentin et al. (2009)). Multiscale, multiphysics models of the vascular wall promise to increase greatly our understanding of how genetic mutations, drug treatments, and mechanical interventions affect vascular biology and physiology and thus diagnosis and treatment.

Acknowledgments This work was supported, in part, by grants from the NIH: R01 HL105297, U01 HL116323, and R01 HL134712.

References

Akata T, Kanna T, Yoshino J, Takahashi S (2003) Mechanisms of direct inhibitory action of isoflurane on vascular smooth muscle of mesenteric resistance arteries. Anesthesiology 99(3):666–677

Andreasen D, Friis UG, Uhrenholt TR, Jensen BL, Skøtt O, Hansen PB (2006) Coexpression of voltage-dependent calcium channels Cav1.2, 2.1a, and 2.1b in vascular myocytes. Hypertension 47(4):735–741

Archer SL, Huang JM, Reeve HL, Hampl V, Tolarová S, Michelakis E, Weir EK (1996) Differential distribution of electrophysiologically distinct myocytes in conduit and resistance arteries determines their response to nitric oxide and hypoxia. Circ Res 78(3):431–442

Arner A, Malmqvist U, Uvelius B (1984) Structural and mechanical adaptations in rat aorta in response to sustained changes in arterial pressure. Acta Physiol Scand 122:119–126

Bakker ENTP, Matlung HL, Bonta P, De Vries CJ, Van Rooijen N, Vanbavel E (2008) Blood flow-dependent arterial remodelling is facilitated by inflammation but directed by vascular tone. Cardiovasc Res 78(2): 341–348

Ball CJ, Wilson DP, Turner SP, Saint DA, Beltrame JF (2009) Heterogeneity of L- and T-channels in the vasculature: rationale for the efficacy of combined L- and T-blockade. Hypertension 53(4): 654–660

Barman SA, Zhu S, White RE (2004) Protein kinase C inhibits BKCa channel activity in pulmonary arterial smooth muscle. Am J Physiol Lung Cell Mol Physiol 286(1):L149–L155

Berridge MJ, Irvine RF (1984) Inositol trisphosphate, a novel second messenger in cellular signal transduction. Nature 312(5992):315–321

Bersi MR, Khosravi R, Wujciak AJ, Harrison DG, Humphrey JD (2017) Differential cell-matrix mechanoadaptations and inflammation drive regional propensities to aortic fibrosis, aneurysm or dissection in hypertension. J R Soc Interface 14(136):327

Brozovich FV, Nicholson CJ, Degen CV, Gao YZ, Aggarwal M, Morgan KG (2016) Mechanisms of vascular smooth muscle contraction and the basis for pharmacologic treatment of smooth muscle disorders. Pharmacol Rev 68(2):476–532

Bulley S, Jaggar JH (2014) Cl^- channels in smooth muscle cells. Pflugers Arch 466(5):861–872

Burgoyne JR, Madhani M, Cuello F, Charles RL, Brennan JP, Schroder E, Browning DD, Eaton P (2007) Cysteine redox sensor in PKGIa enables oxidant-induced activation. Science 317(5843):1393–1397

Burgoyne JR, Prysyazhna O, Rudyk O, Eaton P (2012) cGMP-dependent activation of protein kinase G precludes disulfide activation: implications for blood pressure control. Hypertension 60(5):1301–1308

Bustelo XR, Sauzeau V, Berenjeno IM (2007) GTP-binding proteins of the rho/Rac family: regulation, effectors and functions in vivo. BioEssays 29(4): 356–370

Cavalli A, Lattion AL, Hummler E, Nenniger M, Pedrazzini T, Aubert JF, Michel MC, Yang M, Lembo G, Vecchione C, Mostardini M, Schmidt A, Beermann F, Cotecchia S (1997) Decreased blood pressure response in mice deficient of the alpha1b-adrenergic receptor. Proc Natl Acad Sci U S A 94(21): 11589–11594

Chen L, Xin X, Eckhart AD, Yang N, Faber JE (1995) Regulation of vascular smooth muscle growth by alpha 1-adrenoreceptor subtypes in vitro and in situ. J Biol Chem 270(52):30980–30988

Chiquet M, Renedo AS, Huber F, Flück M (2003) How do fibroblasts translate mechanical signals into changes in extracellular matrix production? Matrix Biol 22(1): 73–80

Cox RH (1978) Regional variation of series elasticity in canine arterial smooth muscles. Am J Phys 234(18):H542–H551

Cox RH, Folander K, Swanson R (2001) Differential expression of voltage-gated K(+) channel genes in arteries from spontaneously hypertensive and Wistar-Kyoto rats. Hypertension 37(5):1315–1322

Criddle DN, de Moura RS, Greenwood IA, Large WA (1996) Effect of niflumic acid on noradrenaline-induced contractions of the rat aorta. Br J Pharmacol 118(4):1065–1071

Criddle DN, de Moura RS, Greenwood IA, Large WA (1997) Inhibitory action of niflumic acid on noradrenaline- and 5-hydroxytryptamine-induced pressor responses in the isolated mesenteric vascular bed of the rat. Br J Pharmacol 120(5):813–818

Dajnowiec D, Langille BL (2007) Arterial adaptations to chronic changes in haemodynamic function: coupling vasomotor tone to structural remodelling. Clin Sci 113(1):15–23

Davies PF (2009) Hemodynamic shear stress and the endothelium in cardiovascular pathophysiology. Nat Clin Pract Cardiovasc Med 6(1):16–26

Devine CE, Somlyo AV, Somlyo AP (1972) Sarcoplasmic reticulum and excitation-contraction coupling in mammalian smooth muscles. J Cell Biol 52(3): 690–718

Dimopoulos GJ, Semba S, Kitazawa K, Eto M, Kitazawa T (2007) Ca2-dependent rapid Ca2 sensitization of contraction in arterial smooth muscle. Circ Res 100(1):121–129

Doyle JJ, Doyle AJ, Wilson NK, Habashi JP, Bedja D, Whitworth RE, Lindsay ME, Schoenhoff F, Myers L, Huso N, Bachir S, Squires O, Rusholme B, Ehsan H, Huso D, Thomas CJ, Caulfield MJ, Van Eyk JE, Judge DP, Dietz HC, Farrar C, Ravekes W, Dietz HC, Lurman K, Holmes KW, Habashi J, Milewicz DM, Prakash SK, Terry M, Lemaire SA, Morris SA, Volguina I, Maslen CL, Song HK, Silberbach GM, Pyeritz RE, Bavaria JE, Milewski K, Parker A, Devereux RB, Weinsaft JW, Roman MJ, Latortue T, Shohet R, Kennedy F, McDonnell N, Griswold B, Asch FM, Weissman NJ, Eagle KA, Tolunay HE, Desvigne-Nickens P, Stylianou MP, Mitchell M, Tseng H, Kroner BL, Hendershot T, Whitworth R, Ringer D, Dietz HC, McCallion A, Loeys B, Van Laer L, Eriksson P, Franco-Cereceda A, Mertens L, Mittal S, Mohamed SA, Andelfinger G, Dietz HC (2015) A deleterious gene-by-environment interaction imposed by calcium channel blockers in Marfan syndrome. elife 4:1–18

Ferruzzi J, Bersi MR, Uman S, Yanagisawa H, Humphrey JD (2015) Decreased elastic energy storage, not increased material stiffness, characterizes central artery dysfunction in fibulin-5 deficiency independent of sex. J Biomech Eng 137(3):31007

Ferruzzi J, Murtada S-I, Li G, Jiao Y, Uman S, Ting MYL, Tellides G, Humphrey JD (2016) Pharmacologically improved contractility protects against aortic dissection in mice with disrupted transforming growth factor-?? Signaling despite compromised extracellular matrix properties. Arterioscler Thromb Vasc Biol 36(5): 919–927

Fisher SA (2010) Vascular smooth muscle phenotypic diversity and function. Physiol Genomics 42(3): 169–187

Francis SH, Busch JL, Corbin JD, Sibley D (2010) cGMP-dependent protein kinases and cGMP phosphodiesterases in nitric oxide and cGMP action. Pharmacol Rev 62(3):525–563

Ghisdal P, Vandenberg G, Morel N (2003) Rho-dependent kinase is involved in agonist-activated calcium entry in rat arteries. J Physiol 551(Pt 3):855–867

Haga JH, Li Y-SJ, Chien S (2007) Molecular basis of the effects of mechanical stretch on vascular smooth muscle cells. J Biomech 40(5):947–960

Herring BP, El-Mounayri O, Gallagher PJ, Yin F, Zhou J (2006) Regulation of myosin light chain kinase and telokin expression in smooth muscle tissues. Am J Physiol Cell Physiol 291(5):C817–C827

Hill-Eubanks DC, Werner ME, Heppner TJ, Nelson MT (2011) Calcium signaling in smooth muscle. Cold Spring Harb Perspect Biol 3(9):a004549

Hong F, Haldeman BD, Jackson D, Carter M, Baker JE, Cremo CR (2011) Biochemistry of smooth muscle myosin light chain kinase. Arch Biochem Biophys 510(2):135–146

Hosoda C, Koshimizu T-A, Tanoue A, Nasa Y, Oikawa R, Tomabechi T, Fukuda S, Shinoura H, Oshikawa S, Takeo S, Kitamura T, Cotecchia S, Tsujimoto G (2005) Two alpha1-adrenergic receptor subtypes regulating the vasopressor response have differential roles in blood pressure regulation. Mol Pharmacol 67(3):912–922

Humphrey JD (2002) Cardiovascular solid mechanics. Springer, New York, NY

Humphrey JD, Dufresne ER, Schwartz MA (2014) Mechanotransduction and extracellular matrix homeostasis. Nat Rev Mol Cell Biol 15(12):802–812

Humphrey JD, Schwartz MA, Tellides G, Milewicz DM (2015) Role of mechanotransduction in vascular biology: focus on thoracic aortic aneurysms and dissections. Circ Res 116(8):1448–1461

Humphrey JD, Harrison DG, Figueroa CA, Lacolley P, Laurent S (2016) Central artery stiffness in hypertension and aging: a problem with cause and consequence. Circ Res 118(3):379–381

Intengan HD, Thibault G, Li JS, Schiffrin EL (1999) Resistance artery mechanics, structure, and extracellular components in spontaneously hypertensive rats: effects of angiotensin receptor antagonism and converting enzyme inhibition. Circulation 100(22):2267–2275

Jackson WF (2000) Ion channels and vascular tone. Hypertension 35(1 Pt 2):173–178

Kim HR, Appel S, Vetterkind S, Gangopadhyay SS, Morgan KG (2008) Smooth muscle signalling pathways in health and disease. J Cell Mol Med 12(6A):2165–2180

Kitazawa T, Kitazawa K (2012) Size-dependent heterogeneity of contractile Ca2+ sensitization in rat arterial smooth muscle. J Physiol 590(Pt 21):5401–5423

Kitazawa T, Semba S, Huh YH, Kitazawa K, Eto M (2009) Nitric oxide-induced biphasic mechanism of

vascular relaxation via dephosphorylation of CPI-17 and MYPT1. J Physiol 587(Pt 14):3587–3603
Kleinbongard P, Schleiger A, Heusch G (2013) Characterization of vasomotor responses in different vascular territories of C57BL/6J mice. Exp Biol Med (Maywood) 238(10):1180–1191
Knepper SM, Buckner SA, Brune ME, DeBernardis JF, Meyer MD, Hancock AA (1995) A-61603, a potent alpha 1-adrenergic receptor agonist, selective for the alpha 1A receptor subtype. J Pharmacol Exp Ther 274(1):97–103
Ko EA, Han J, Jung ID, Park WS (2008) Physiological roles of K+ channels in vascular smooth muscle cells. J Smooth Muscle Res 44(2):65–81
Koyama M, Ito M, Feng J, Seko T, Shiraki K, Takase K, Hartshorne DJ, Nakano T (2000) Phosphorylation of CPI-17, an inhibitory phosphoprotein of smooth muscle myosin phosphatase, by rho-kinase. FEBS Lett 475(3):197–200
Leloup AJA, Fransen P (2015) Elastic and muscular arteries differ in structure, basal NO production and voltage-gated Ca (2+)-channels. Front Physiol 6:1–9
Leung FP, Yung LM, Yao X, Laher I, Huang Y (2008) Store-operated calcium entry in vascular smooth muscle. Br J Pharmacol 153(5):846–857
Lincoln TM (2007) Myosin phosphatase regulatory pathways: different functions or redundant functions? Circ Res 100(1):10–12
Lincoln TM, Dey N, Sellak H (2001) Invited review: cGMP-dependent protein kinase signaling mechanisms in smooth muscle: from the regulation of tone to gene expression. J Appl Physiol 91(3):1421–1430
Martens JR, Gelband CH (1996) Alterations in rat interlobar artery membrane potential and K+ channels in genetic and nongenetic hypertension. Circ Res 79(2):295–301
Martinez-Lemus LA, Hill MA, Meininger GA (2009) The plastic nature of the vascular wall: a continuum of remodeling events contributing to control of arteriolar diameter and structure. Physiology 24(1):45–57
Martinsen A, Dessy C, Morel N (2014) Regulation of calcium channels in smooth muscle: new insights into the role of myosin light chain kinase. Channels (Austin) 8(5):402–413
Mellander S (1970) Systemic circulation: local control. Annu Rev Physiol 32:313–344
Michelotti GA, Price DT, Schwinn DA (2000) Alpha 1-adrenergic receptor regulation: basic science and clinical implications. Pharmacol Ther 88(3):281–309
Milnor WR (1990) Cardiovascular physiology. Oxford University Press, Oxford, UK
Mueed I, Bains P, Zhang L, Macleod KM (2004) Differential participation of protein kinase C and rho kinase in ⌴ 1 -adrenoceptor mediated contraction in rat arteries 1. Can J Physiol Pharmacol 902:895–902
Murtada S-I, Lewin S, Arner A, Humphrey JD (2016a) Adaptation of active tone in the mouse descending thoracic aorta under acute changes in loading. Biomech Model Mechanobiol 15(3):579–592
Murtada S-I, Ferruzzi J, Yanagisawa H, Humphrey JD (2016b) Reduced biaxial contractility in the descending thoracic aorta of fibulin-5 deficient mice. J Biomech Eng 138(5):51008
Murtada S-I, Humphrey JD, Holzapfel GA (2017) Multiscale and multiaxial mechanics of vascular smooth muscle. Biophys J 113(3):714–727
Nelson MT, Patlak JB, Worley JF, Standen NB (1990) Calcium channels, potassium channels, and voltage dependence of arterial smooth muscle tone. Am J Phys 259(1 Pt 1):C3–C18
Nilius B, Droogmans G (2001) Ion channels and their functional role in vascular endothelium. Physiol Rev 81(4):1415–1459
Nixon GF, Mignery GA, Somlyo AV (1994) Immunogold localization of inositol 1,4,5-trisphosphate receptors and characterization of ultrastructural features of the sarcoplasmic reticulum in phasic and tonic smooth muscle. J Muscle Res Cell Motil 15(6): 682–700
Orr AW, Hastings NE, Blackman BR, Wamhoff BR (2010) Complex regulation and function of the inflammatory smooth muscle cell phenotype in atherosclerosis. J Vasc Res 47(2):168–180
Poduri A, Owens AP, Howatt DA, Moorleghen JJ, Balakrishnan A, Cassis LA, Daugherty A (2012) Regional variation in aortic AT1b receptor mRNA abundance is associated with contractility but unrelated to atherosclerosis and aortic aneurysms. PLoS One 7(10):1–8
Pozzan T, Rizzuto R, Volpe P, Meldolesi J (1994) Molecular and cellular physiology of intracellular calcium stores. Physiol Rev 74(3):595–636
Rensen SSM, Doevendans PAFM, van Eys GJJM (2007) Regulation and characteristics of vascular smooth muscle cell phenotypic diversity. Neth Heart J 15(3):100–108
Retailleau K, Duprat F, Arhatte M, Ranade SS, Peyronnet R, Martins JR, Jodar M, Moro C, Offermanns S, Feng Y, Demolombe S, Patel A, Honoré E (2015) Piezo1 in smooth muscle cells is involved in hypertension-dependent arterial remodeling. Cell Rep 13(6): 1161–1171
Rokosh DG, Simpson PC (2002) Knockout of the alpha 1A/C-adrenergic receptor subtype: the alpha 1A/C is expressed in resistance arteries and is required to maintain arterial blood pressure. Proc Natl Acad Sci U S A 99(14):9474–9479
Rudner XL, Berkowitz DE, Booth JV, Funk BL, Cozart KL, D'Amico EB, El-Moalem H, Page SO, Richardson CD, Winters B, Marucci L, Schwinn DA (1999) Subtype specific regulation of human vascular alpha(1)-adrenergic receptors by vessel bed and age. Circulation 100(23):2336–2343
Sakurada S, Takuwa N, Sugimoto N, Wang Y, Seto M, Sasaki Y, Takuwa Y (2003) Ca2+−dependent activation of rho and rho kinase in membrane depolarization-induced and receptor stimulation-induced vascular smooth muscle contraction. Circ Res 93(6): 548–556

Salamanca DA, Khalil RA (2005) Protein kinase C isoforms as specific targets for modulation of vascular smooth muscle function in hypertension. Biochem Pharmacol 70(11):1537–1547

Simon MI, Strathmann MP, Gautam N (1991) Diversity of G proteins in signal transduction. Science 252(5007):802–808

Sobey CG (2001) Potassium channel function in vascular disease. Arterioscler Thromb Vasc Biol 21(1):28–38

Somlyo AP, Somlyo AV (1968) Vascular smooth muscle. I. Normal structure, pathology, biochemistry, and biophysics. Pharmacol Rev 20(4):197–272

Somlyo AP, Somlyo AV (1994) Smooth muscle—excitation-contraction coupling, contractile regulation, and the cross-bridge cycle. Alcohol Clin Exp Res 18(1):138–143

Somlyo AP, Somlyo AV (2003) Ca2+ sensitivity of smooth muscle and nonmuscle myosin II: modulated by G proteins, kinases, and myosin phosphatase. Physiol Rev 83(4):1325–1358

Su W, Xie Z, Liu S, Calderon LE, Guo Z, Gong MC (2013) Smooth muscle-selective CPI-17 expression increases vascular smooth muscle contraction and blood pressure. Am J Physiol Heart Circ Physiol 305(1):H104–H113

Sukriti S, Tauseef M, Yazbeck P, Mehta D (2014) Mechanisms regulating endothelial permeability. Pulm Circ 4(4):535–551

Tang DD, Anfinogenova Y (2008) Physiologic properties and regulation of the actin cytoskeleton in vascular smooth muscle. J Cardiovasc Pharmacol Ther 13(2):130–140

Tanoue A, Nasa Y, Koshimizu T, Shinoura H, Oshikawa S, Kawai T, Sunada S, Takeo S, Tsujimoto G (2002) The alpha(1D)-adrenergic receptor directly regulates arterial blood pressure via vasoconstriction. J Clin Invest 109(6):765–775

Tuna BG, Bakker ENTP, VanBavel E (2013) Relation between active and passive biomechanics of small mesenteric arteries during remodeling. J Biomech 46(8):1420–1426

Valentin A, Cardamone L, Baek S, Humphrey J (2009) Complementary vasoactivity and matrix remodelling in arterial adaptations to altered flow and pressure. J R Soc Interface 6(32):293–306

Wang Y, Zheng XR, Riddick N, Bryden M, Baur W, Zhang X, Surks HK (2009) ROCK isoform regulation of myosin phosphatase and contractility in vascular smooth muscle cells. Circ Res 104(4):531–540

Wang L, Guo DC, Cao J, Gong L, Kamm KE, Regalado E, Li L, Shete S, He WQ, Zhu MS, Offermanns S, Gilchrist D, Elefteriades J, Stull JT, Milewicz DM (2010) Mutations in myosin light chain kinase cause familial aortic dissections. Am J Hum Genet 87(5):701–707

Wede OK, Löfgren M, Li Z, Paulin D, Arner A (2002) Mechanical function of intermediate filaments in arteries of different size examined using desmin deficient mice. J Physiol 540(Pt 3):941–949

Williams TJ, Blue DR, Daniels DV, Davis B, Elworthy T, Gever JR, Kava MS, Morgans D, Padilla F, Tassa S, Vimont RL, Chapple CR, Chess-Williams R, Eglen RM, Clarke DE, Ford AP (1999) In vitro alpha1-adrenoceptor pharmacology of Ro 70-0004 and RS-100329, novel alpha1A-adrenoceptor selective antagonists. Br J Pharmacol 127(1):252–258

Woodsome TP, Eto M, Everett A, Brautigan DL, Kitazawa T (2001) Expression of CPI-17 and myosin phosphatase correlates with Ca2+ sensitivity of protein kinase C-induced contraction in rabbit smooth muscle. J Physiol 535(2):553–564

Wynne BM, Chiao C-W, Webb RC (2009) Vascular smooth muscle cell signaling mechanisms for contraction to angiotensin II and endothelin-1. J Am Soc Hypertens 3(2):84–95

Yamamoto Y, Koike K (2001) Alpha(1)-adrenoceptor subtypes in the mouse mesenteric artery and abdominal aorta. Br J Pharmacol 134(5):1045–1054

Zalk R, Lehnart SE, Marks AR (2007) Modulation of the ryanodine receptor and intracellular calcium. Annu Rev Biochem 76:367–385

Zhou Y, Chen Y, Dirksen WP, Morris M, Periasamy M (2003) AT1b receptor predominantly mediates contractions in major mouse blood vessels. Circ Res 93(11):1089–1094

Zhou Y, Dirksen WP, Zweier JL, Periasamy M (2004) Endothelin-1-induced responses in isolated mouse vessels: the expression and function of receptor types. Am J Physiol Heart Circ Physiol 287(2):H573–H578

Zhou Y, Varadharaj S, Zhao X, Parinandi N, Flavahan NA, Zweier JL (2005) Acetylcholine causes endothelium-dependent contraction of mouse arteries. Am J Physiol Heart Circ Physiol 289(3):H1027–H1032

Zhou Y, Dirksen WP, Babu GJ, Periasamy M (2007) Differential vasoconstrictions induced by angiotensin II: role of AT1 and AT2 receptors in isolated C57BL/6J mouse blood vessels. Am J Physiol Heart Circ Physiol 43210:2797–2803

Zygmunt PM, Ryman T, Högestätt ED (1995) Regional differences in endothelium-dependent relaxation in the rat: contribution of nitric oxide and nitric oxide-independent mechanisms. Acta Physiol Scand 155(3):257–266

Microcalcifications, Their Genesis, Growth, and Biomechanical Stability in Fibrous Cap Rupture

Luis Cardoso and Sheldon Weinbaum

Abstract

For many decades, cardiovascular calcification has been considered as a passive process, accompanying atheroma progression, correlated with plaque burden, and apparently without a major role on plaque vulnerability. Clinical and pathological analyses have previously focused on the total amount of calcification (calcified area in a whole atheroma cross section) and whether more calcification means higher risk of plaque rupture or not. However, this paradigm has been changing in the last decade or so. Recent research has focused on the presence of microcalcifications (μCalcs) in the atheroma and more importantly on whether clusters of μCalcs are located in the cap of the atheroma. While the vast majority of μCalcs are found in the lipid pool or necrotic core, they are inconsequential to vulnerable plaque. Nevertheless, it has been shown that μCalcs located within the fibrous cap could be numerous and that they behave as an intensifier of the background circumferential stress in the cap. It is now known that such intensifying effect depends on the size and shape of the μCalc as well as the proximity between two or more μCalcs. If μCalcs are located in caps with very low background stress, the increase in stress concentration may not be sufficient to reach the rupture threshold. However, the presence of μCalc(s) in the cap with a background stress of about one fifth to one half the rupture threshold (a stable plaque) will produce a significant increase in local stress, which may exceed the cap rupture threshold and thus transform a non-vulnerable plaque into a vulnerable one. Also, the classic view that treats cardiovascular calcification as a passive process has been challenged, and emerging data suggest that cardiovascular calcification may encompass both passive and active processes. The passive calcification process comprises biochemical factors, specifically circulating nucleating complexes, which would lead to calcification of the atheroma. The active mechanism of atherosclerotic calcification is a cell-mediated process via cell death of macrophages and smooth muscle cells (SMCs) and/or the release of matrix vesicles by SMCs.

L. Cardoso (✉) · S. Weinbaum
Department of Biomedical Engineering, The City College of New York, New York, NY, USA
e-mail: Cardoso@ccny.cuny.edu

B. M. Fu, N. T. Wright (eds.), *Molecular, Cellular, and Tissue Engineering of the Vascular System*, Advances in Experimental Medicine and Biology 1097,
https://doi.org/10.1007/978-3-319-96445-4_7

1 Atherosclerotic Plaque Development

Atherosclerosis is a slow progressive disease of the intimal layer of blood vessels that generally takes several years to develop in humans. Atherosclerosis is highly prevalent worldwide, particularly in the sixth and seventh decades of life, resulting in different cardiovascular disease complications, including myocardial infarction, unstable and stable angina, sudden coronary death, stroke, transient ischemic attack, critical limb ischemia, and claudication. In particular, coronary thrombosis preceding myocardial infarction is generally caused by acute plaque rupture and in some cases due to plaque erosion or the presence of calcified nodules. The progression of atherosclerosis is characterized by several distinct stages, comprising adaptive intimal thickening (AIT), pathological intimal thickening (PIT), fibroatheroma (FA), and thin-cap fibroatheroma (TCFA) formation (Virmani et al. 2000, 2003). The first stage, AIT, exhibits an increase in smooth muscle cells (SMCs) and an enriched proteoglycan-collagen matrix, without the presence of inflammatory cells. Following AIT, atherosclerotic plaques become apparent with the presence of fatty streaks, macrophages, and SMCs (Stary et al. 1994). PIT is then developed when acellular lipid pools are formed within the intima layer of the vessel, close to the internal elastic lamina, at the boundary with the media layer. At this stage, lipid pools are rich in proteoglycans, and SMCs in this region are scarce (Virmani et al. 2000, 2003; Stary et al. 1994). In the next stage of atheroma development, both macrophages and T lymphocytes are attracted by the lipid content in the atheroma and migrate from the luminal blood stream into the lipid pool. Many of those macrophages will be transformed into foam cells, produce matrix metalloproteinases (MMPs), die in situ, and thus transform the lipid pool into a necrotic core that is a characteristic of a FA (Virmani et al. 2003; Stary et al. 1995). SMCs that would have migrated to the atheroma cap, the region separating the core from the lumen, will transform the extracellular matrix of this region into fibrotic tissue. A necrotic core in an advanced FA will contain extensive acellular debris, free cholesterol, and lack of extracellular matrix (Virmani et al. 2000, 2003). Further progression of the disease and the accumulation of macrophages (Libby et al. 2002; Libby 2002) secreting MMPs at the boundary between the core and the cap will produce the thinning of fibrotic cap tissue. A TCFA is then formed, comprising a large necrotic core over a thin cap (<65 μm) heavily infiltrated by macrophages, but with a small presence of T lymphocytes and few if any SMCs. The rupture of the thin fibrous cap overlying the necrotic core of a vulnerable plaque is widely viewed as the primary cause of acute coronary syndrome (Virmani et al. 2003, 2007; Burke et al. 1999).

2 Determinants of Plaque Rupture

Based on histological analyses of plaque morphology and tissue composition, vulnerable plaque has been defined as a positively remodeled lesion containing a lipid-rich pool with a fibrous cap that is infiltrated by macrophages (Virmani et al. 2003, 2007; Burke et al. 1997, 1999), characterized by the presence of inflammation (Libby et al. 2002; Libby 2002; Berliner et al. 1995; Demer 2002), matrix metalloproteinases (Virmani et al. 2007), smooth muscle cell apoptosis (Bennett et al. 1995; Isner et al. 1995), neovascularization, and intraplaque hemorrhage (Kolodgie et al. 2003). In addition to these biological factors, biomechanical determinants of fibrous cap tissue rupture have been identified. These include the mechanical properties of the cap tissue and the atheroma (Akyildiz et al. 2011; Finet et al. 2004; Wenk 2011), 3D morphology of plaque and vessel (Finet et al. 2004; Cheng et al. 1993; Rambhia et al. 2012; Tang et al. 2005; Vengrenyuk et al. 2008), circumferential stresses developed in the cap under the action of blood pressure (Finet et al. 2004; Cheng et al. 1993; Vengrenyuk et al. 2008; Hoshino et al. 2009; Ohayon et al. 2008), fluid-induced shear

stresses (Rambhia et al. 2012; Bluestein et al. 2008), residual stresses (Ohayon et al. 2007), and the presence of microcalcifications (μCalcs) in the cap proper (Vengrenyuk et al. 2006, 2008; Bluestein et al. 2008; Maldonado et al. 2012, 2013; Kelly-Arnold et al. 2013). Indeed, many of the biomechanical factors are intrinsically related to the morphology, tissue composition, and biochemical and biological environment in the atheroma.

Plaque rupture occurs when the soft tissue in the atheroma cap is compromised under the action of high blood pressure (Burke et al. 1999; Davies and Thomas 1981, 1985). Cap rupture co-localizes with thrombus formation in the cap tissue (Davies and Thomas 1981, 1985) where increased mechanical stresses are observed (Richardson et al. 1989; Born and Richardson 1989). Plaque rupture is initiated when the ultimate stress (i.e., maximum stress at failure) of the fibrous cap tissue is exceeded (Richardson et al. 1989; Born and Richardson 1989). Importantly, the presence of a lipid pool leads to a concentration of tissue stress in the overlying fibrous cap (Richardson et al. 1989), the size of the lipid pool correlating with the risk of cap rupture (Davies et al. 1993). Caps are also mechanically weakened in regions where there is a locally increased macrophage density (Lendon et al. 1991). Furthermore, the strength of the cap depends on its collagen content (Burleigh et al. 1992). However, 37% of cap ruptures occurred in the cap center (Richardson et al. 1989), as opposed to the cap shoulders, where 2D finite element analysis (FEA) predicted peak circumferential stress (PCS) and macrophages were present in greater concentration. This critical observation was subsequently confirmed in a more recent extensive study of 300 rupture sites where again 37% of cap tears were at the center (Maehara et al. 2002).

The presence of calcification increases the stiffness (elastic modulus E) of the cap in the abdominal aorta (Lee et al. 1991). Two-dimensional FEA demonstrated that larger stenosis decreased PCS, while decreasing cap thickness greatly increased PCS in coronary arteries (Loree et al. 1992). This analysis was then applied to 24 coronary artery lesions, 12 ruptured and 12 intact (Cheng et al. 1993). This widely cited study predicted that the threshold PCS for rupture was 300 kPa and that the average rupture stress was 545 kPa, but surprisingly in only 7 of the 12 ruptured lesions did the site of rupture occur at the predicted location of PCS. This was attributed at the time to variation in cap tissue properties. Subsequently, these investigators demonstrated using 2D FEA that PCS did not correlate with the presence of large size calcifications located in the back of the core and that PCS would decrease substantially if the lipid pool was replaced by fibrous tissue (Huang et al. 2001).

2.1 Fibrous Cap Thickness

The prediction that decreasing cap thickness could significantly increase the risk of cap rupture (Loree et al. 1992) led to a series of experimental investigations eventually leading to the widely cited criterion that caps ≤65 μm were prone to rupture (Virmani et al. 2003). This criterion was based on the frequently quoted results in Burke et al. (1997) where the mean ± SD cap thickness for rupture is given as 23 ± 19 μm and that 95% of ruptured caps were < 65 μm. These measurements were based on the measured thickness at the tear. However, if one examines the tears in Fig. 1 of Burke et al. (1997), they are at an acute angle where the tissue is severely tapered toward the thin edge of the tear as opposed to where the tear had started. More recent results indicate that caps as thick as 100 μm can rupture (Maehara et al. 2002), and in the case of exertion, ruptured caps as thick as 160 μm were observed (Tanaka et al. 2008). The <65 μm criterion has been challenged by the detailed 3D FEA in Maldonado et al. (2012). In the latter study, the PCS has been quantitatively analyzed in 62 non-ruptured fibrous caps in all 3 coronary arteries. The thinnest non-ruptured cap was 66 μm, very close to the <65 μm criterion, but the PCS in this cap was only 107 kPa, far less than the 300 kPa threshold proposed in Cheng et al. (1993), and the predicted cap thickness for this threshold

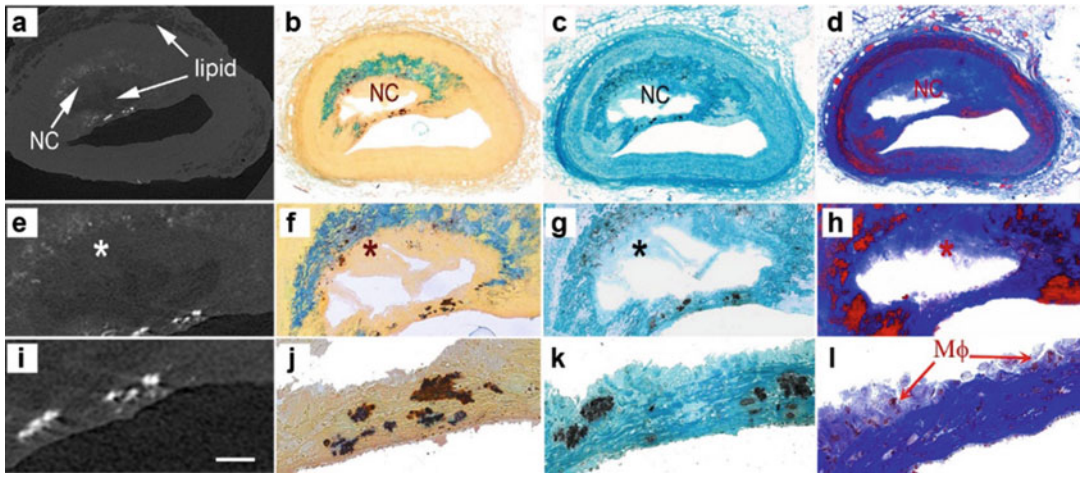

Fig. 1 Images of human atheroma obtained using HR-μCT and undecalcified plastic-embedded histology. (**a**) HR-μCT at 2.1 μm resolution, (**b**) alizarin red S, (**c**) von Kossa, and (**d**) trichrome staining. Magnified views of the atheroma core and cap are shown in (**e**–**h**) and (**i**–**l**), respectively. Calcified tissue stained red for calcium with alizarin red S and black for phosphate with von Kossa. Comparison of HR-μCT images with histology confirmed that the darker gray color in HR-μCT images corresponds to lipid, as shown at the center of the core and the outermost tunica adventitia layer of the vessel. Also, regions in dark gray color in HR-μCT images appear as void regions in histology, since lipid is removed by the histological processing employed. Smooth muscle cells shown in red color in trichrome staining can be distinguished in the media layer and invade the cap shoulders. The necrotic core (NC) is shown in light blue in color that corresponds to degraded ECM (*). A magnified view of the cap displays μCalcs within the cap and multinucleated cells, possibly macrophages (μφ), at the boundary of the cap from the core side of the lesion in **l**. Reproduced with permission from Maldonado et al. (2015)

to be achieved was only 30 μm. This 3D FEA confirmed the earlier 2D predictions in Finet et al. (2004) that fibrous caps >65 μm thickness had PCS less than the 300 kPa threshold, and this result appeared to be insensitive to lipid pool geometry. These predictions and the observation that caps >100 μm do rupture strongly suggest that cap thickness, though important, is not the only criterion for rupture, as discussed next.

2.2 Other Criteria for Rupture

The inability to explain rupture in thick caps and the fact that in only 58% of caps did rupture occur at the location of PCS (Cheng et al. 1993) prompted a number of studies where other biomechanical aspects of cap rupture were examined. This included lipid core composition (Finet et al. 2004), necrotic core size (Ohayon et al. 2008), location and shape of lipid pool (Akyildiz et al. 2011; Tang et al. 2004), residual stresses (Ohayon et al. 2007), and the proximity of calcifications to the lipid pool (Hoshino et al. 2009). Collectively, these studies indicated that large, thick lipid pools increased risk of rupture (Ohayon et al. 2008), residual stresses reduced the PCS in the fibrous cap proper (Ohayon et al. 2007), that the PCS was increased near the edges of calcifications (Hoshino et al. 2009), and that the PCS could occur in healthy thin regions of a vessel wall opposite a lesion or regions of high lumen curvature (Tang et al. 2005). The fluid-structure interaction (FSI) analyses in Tang et al. (2004, 2005) were the first 3D numerical studies to calculate tissue stresses in actual in vivo MRI images of human coronary arteries. Shortly thereafter, Ohayon et al. (2005) provided the first 3D FEA of human coronary arteries as seen using IVUS imaging. The latter study pointed out the major limitations of 2D FEA and showed that the predictions of the PCS in 2D cross sections could be off by as much as a factor of 2. Despite these advances, the basic paradoxes

as to (1) why so many cap tears occurred in the center of the cap, (2) why ruptures frequently did not coincide with location of PCS, and (3) why caps >65 μm thickness could rupture at tissue stresses far below the 300 kPa critical threshold still remained unresolved. The answer to those paradoxes may reside on an aspect of atheroma progression that has received less attention, the calcification of atherosclerotic tissues (Cardoso and Weinbaum 2014).

3 Calcification of Atherosclerotic Tissues

Calcification of atherosclerotic tissues is associated with the progression of atherosclerosis itself. Atherosclerotic calcification is generally an amorphous type of mineralization, observed in thick-walled elastic arteries in the systemic circulation, including peripheral arteries, coronary and carotid vessels, mainly at the base of the intimal lesion, bound by the internal elastic lamina, in proximity to the media layer of the vessel. In Monckeberg's disease, however, where media sclerosis is associated with diabetes, chronic kidney disease, and aging, calcification is present along the elastic lamellae in the media and may extend up to the internal elastic lamina. While amorphous calcification is most frequent in atheroma, well-organized, structured, bone-like tissue calcification is less frequent. Arterial calcification involves chondrocyte and osteoblast differentiation, as well as bone-related proteins such as bone morphometric proteins 2 and 4 (BMP-2, BMP-4), osteocalcin, and osteoprotegerin.

The morphology and composition of atheromatous plaque and calcification have been investigated both ex vivo using histology and in vivo by diverse clinical imaging technologies. There are three main types of noninvasive imaging technologies used in vivo, including cardiac computed tomography (CT) (Kopp et al. 2001; Choi et al. 2008; Knollmann et al. 2008; Motoyama et al. 2007). Cardiac magnetic resonance imaging (MRI) (Yang et al. 2003; Choudhury et al. 2002), and single-positron emission computed tomography (SPECT) (Tsimikas and Shaw 2002; Sinusas 2010; Strauss et al. 2004; Russell and Zaret 2006). Clinical CT has shown potential to identify soft, intermediate, and calcified plaques, as well as spotty macrocalcifications. MRI has the ability to identify different tissue densities present in the necrotic core, fibrous cap, and tissue inflammation. These imaging approaches allow a rapid, noninvasive identification of advanced lesions. However, their main limitation is the resolution, ~250 μm for CT, ~400 μm for MRI, and 1000 μm for SPECT, which does not allow identifying either early plaques or thin caps prone to rupture. Therefore, invasive vascular imaging approaches have been developed to achieve in vivo and ex vivo images with greater contrast and resolution. Among current invasive in vivo approaches, we can include intravascular ultrasound (IVUS) (Maehara et al. 2002; Potkin et al. 1990), IVUS elastography (de Korte et al. 1998; Schaar et al. 2003), virtual histology and tissue characterization (Nasu et al. 2006; Rodriguez-Granillo et al. 2005), optical coherence tomography (Patwari et al. 2000; Yabushita et al. 2002), near-infrared (NIR) spectroscopy (Moreno et al. 2002), intracoronal magnetic resonance imaging (MRI) (Larose et al. 2005, 2008), and molecular imaging (MI) (New and Aikawa 2011). Ultrasound-based approaches can provide morphology, tissue characterization (i.e., fibrotic, lipid, calcification, etc.), and mechanical properties; however, current clinical systems at 40–45 MHz have an axial resolution of about 80–100 μm and lateral resolution of 200–250 μm, which are greatly limited in distinguishing thin caps. The intravascular ultrasound PROSPECT study confirmed predictive in vivo determinants of coronary complications, such as thin-cap fibroatheroma, luminal area, plaque burden, and dense calcium volume. OCT has a much greater resolution than IVUS, reaching ~10–15 μm axial resolution, and provides information on tissue composition (Lowe et al. 2011; Bezerra et al. 2009). Recent developments have reached 1 μm axial resolution using micro-OCT (Liu et al. 2011) in a laboratory setup, with the potential to translate it to the clinic. The drawback of OCT is its limited depth of penetration and the

light scattering due to red blood cells. The latter requires "flushing" the artery with a transparent saline solution to image the vessel wall.

Prior to the studies by Vengrenyuk et al. (2006, 2008, 2010) (Maldonado et al. 2012, 2013; Kelly-Arnold et al. 2013), where the focus of calcification shifted from large calcification into very small calcifications within the fibrous cap, there was no apparent need for 3D imaging of an entire vessel preserving cellular level microcalcifications (μCalcs) (Cardoso and Weinbaum 2014). Nearly all studies of coronary artery calcification were based on macrocalcifications that could be seen using available in vivo imaging techniques IVUS, MRI, and OCT. Except for OCT, the two main in vivo imaging modalities, IVUS and MRI, detected primarily mm size calcifications and the rough boundaries of lipid pools. The gold standard for visualization was histology, which required fixation, dehydration, and/or some degree of decalcification before paraffin embedding to allow for sectioning. The most important limitation was that one was restricted to a small number of 2D sections and was, therefore, unable to obtain 3D reconstructions of entire intact lesions. At the electron microscopic level, one could see 100–300 nm matrix vesicles, a small fraction of which were calcified (Bobryshev et al. 2008; Aikawa et al. 2007).

Calcification becomes apparent in histological sections first as microcalcifications (μCalcs), small calcified particles 1–100 μm in size, which are detected using von Kossa staining for phosphate or alizarin red for calcium composition. Electron microscopy has shown that μCalcs can start as small as 100 nm. Microcalcifications may either coalesce or grow to larger size to form calcifications >1 mm that can then be detected using conventional clinical imaging systems (CT, MRI, SPECT). Large calcifications are generally measured using the quantitative Agatston's calcium scoring method using CT (Agatston et al. 1990), which quantify the amount of calcification in the whole atheroma. Recently, metabolic imaging using PET scanning using ^{18}F-fluorodeoxyglucose has been shown to be capable of identifying inflammation and microcalcifications in vivo (Joshi et al. 2014; Tawakol et al. 2006). This approach has demonstrated the ability to identify the culprit plaque responsible for a recent acute coronary event, as well as high-risk plaques in stable coronary artery disease, which are also identified by IVUS (Joshi et al. 2014). The limitation of PET is its resolution. On the other hand, high-resolution micro-computed tomography (HR-μCT) can be used to obtain the 3D morphology of fibroatheromas and calcifications ex vivo, allowing us to quantitatively analyze the number and size of calcifications in atheroma, spatial changes and patterns of calcification, and their relation to lipid and necrotic cores.

High-resolution μCT is highly sensitive to calcified tissue and has been shown to also distinguish lipid from necrotic core and soft tissue in human coronary arteries (Vengrenyuk et al. 2006, 2008, 2010; Maldonado et al. 2012, 2013; Kelly-Arnold et al. 2013). Vengrenyuk et al. (2006) provided the first use of μCT to visualize cellular level μCalcs in human coronary vessels. The imaging and characterization of hundreds and even thousands of μCalcs using μCT have been refined in recent studies (Maldonado et al. 2012, 2013; Kelly-Arnold et al. 2013) with up to ~2 μm resolution. This greatly enhanced resolution has enabled one to quantify the number, location, shape, clustering, and degree of mineralization of microcalcifications in unprocessed (non-dehydrated, infiltrated, nor embedded) whole coronary vessels. HR-μCT images taken at 2.1 μm resolution (Maldonado et al. 2015) in Fig. 1a reveal several important atheroma features: (1) a narrowing of the lumen cross-sectional area and asymmetric thickening of the vessel wall and outer boundary of the vessel wall; (2) atheroma soft tissue displayed as a light gray color; (3) a semi-annular core region with a gray color shade darker than the color in soft tissue; (4) an outer region corresponding to lipid in the adventitia, with a gray color shade darker than the color in soft tissue, similar to the gray color level in the core; and (5) calcified tissue represented by a much brighter shade of white. Calcified tissue stained red for calcium with alizarin red S and black for phosphate with von Kossa in histology section is shown

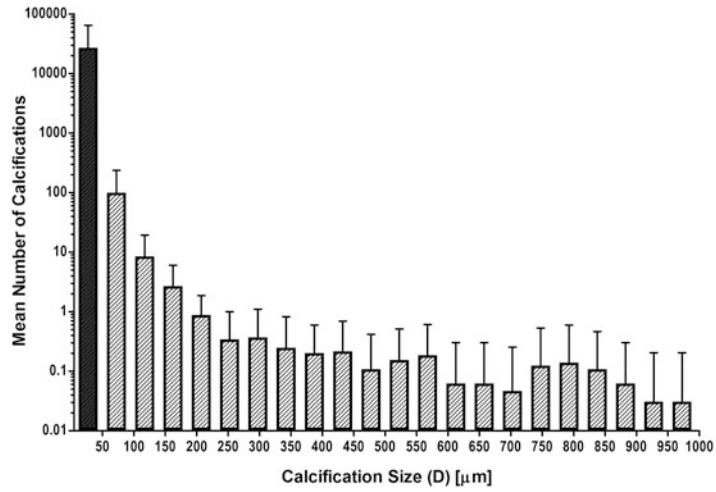

Fig. 2 Mean number of calcifications classified by equivalent spherical diameter (D) that were identified using HR-μCT at 2.1 μm resolution in whole atheroma ($n = 72$). Reproduced with permission from Maldonado et al. (2015)

in Fig. 1b, c, respectively. Collagen is shown in blue and smooth muscle cells in red in trichrome-stained sections (Fig. 1d). Magnified views of the core are shown in Fig. 1e–h and magnified views of the cap in Fig. 1i–l. The core in HR-μCT images (Fig. 1a, e) is generally darker than the surrounding soft tissue; however, its color is not always homogeneous, and the boundary of the core may not be a well-defined line. Comparison of HR-μCT images with histology confirmed that the darker gray color in HR-μCT images corresponds to lipid, as shown at the center of core and the outermost tunica adventitia layer of the coronary in Fig. 1a. Also, regions in dark gray color in HR-μCT images appear as void regions in histology, since lipid is removed by the histological processing employed (Fig. 1e–h). Cores that show both light and dark gray colors correspond thus to lipid and necrotic cores, respectively. In addition to the difference in gray color level, the presence of microcalcifications often helps to distinguish the boundary of the core, which is important to identify the cap and to determine the minimum cap thickness in 3D image reconstructions. The region that corresponds to lighter hue of gray within the lipid core in HR-μCT (Fig. 1a, e) is a region containing degraded extracellular matrix (ECM) where no cells were highlighted, thus identified as a necrotic core (NC) in Fig. 1d, h. Microcalcifications can be observed within and around the core (Fig. 1e–h) and within the cap (Fig. 1i, l). Smooth muscle cells shown in red can be distinguished in the media layer and invade the cap shoulders (Fig. 1h). A magnified view of the cap displays multinucleated cells, possibly macrophages (MΦ), at the boundary of the cap from the core side of the lesion (Fig. 1l) (Maldonado et al. 2015).

Figure 2 describes the mean number of calcifications classified by equivalent spherical diameter (D) that were identified using HR-μCT at 2.1 μm resolution in 72 human atheromas. It can be clearly observed that the most abundant type of calcification are microcalcifications <50 μm in diameter (Maldonado et al. 2015).

3.1 Progression of Calcification in Atheroma Core

While microcalcifications are by far the most abundant type of calcification in atheroma (Fig. 2), it is important to identify the morphology and spatial distribution of calcifications within the atheroma. Based on those observations, four different calcification patterns were proposed (Maldonado et al. 2015):

3.1.1 Microcalcifications at the Core Boundary

In what seems to be the initial stage of calcification development, submicron- and micron-sized calcified particles (Wenk 2011; Cheng et al. 1993; Rambhia et al. 2012; Tang et al. 2005) are aligned at the interface between the soft tissue and the necrotic core, possibly constrained

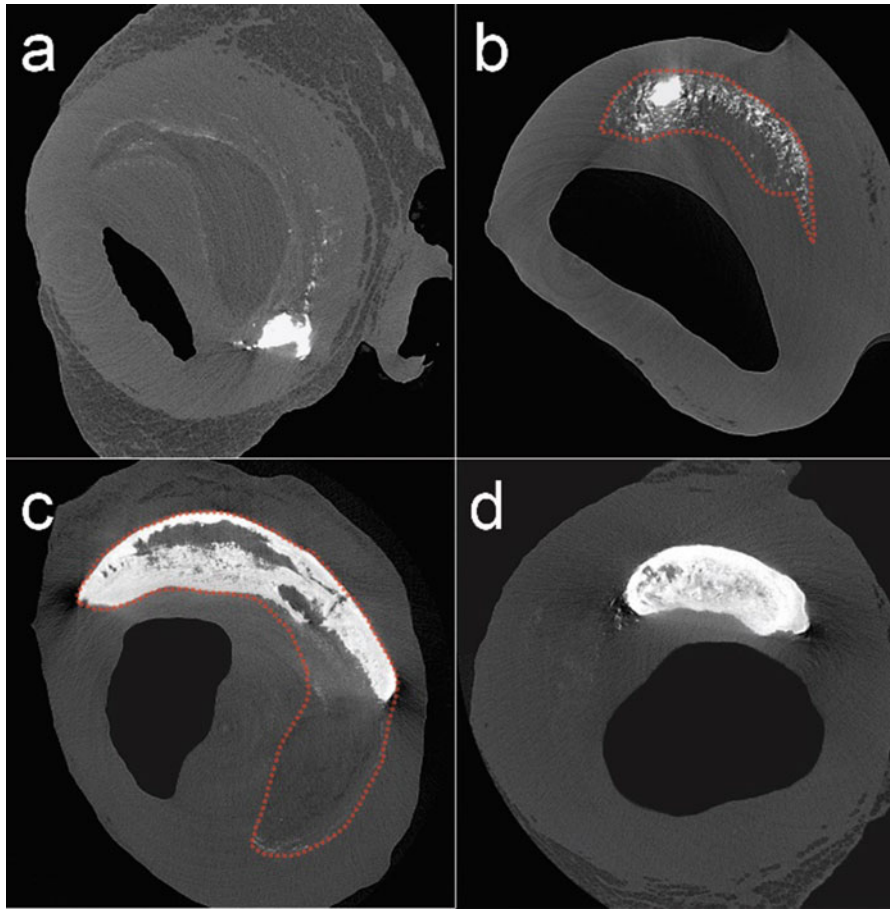

Fig. 3 Calcification patterns A to D distinguished in different human coronary fibroatheromas under HR-μCT imaging at 2.1 μm resolution. Calcification patterns are described based on their location, size, and stage of calcification. Dotted red lines added to delimit the lipid/necrotic core. (**a**) Microcalcifications along the core boundary, (**b**) microcalcifications within the core, (**c**) large calcifications forming the boundary and within the core, (**d**) advanced macrocalcifications. Reproduced with permission from Maldonado et al. (2015)

by the internal elastic lamina. In Fig. 3a, the atheroma looks like a soft plaque, characterized by a mixed lipid/necrotic core, containing a few isolated μCalcs within the core, and also 0.5–5 μm size μCalcs were appearing as a fuzzy/dotted border at the core boundary because they are too small to be clearly resolved in HR-μCT at the current 2.1 μm resolution.

3.1.2 Microcalcifications Within the Core

This calcification pattern comprises small calcified particles <100 μm diameter that are dispersed within the necrotic core. As shown in Fig. 3b, μCalcs >5 μm visible at 2.1 μm resolution cluster to form more abundant and larger μCalcs within the core.

3.1.3 Large Calcifications Within the Core

These are calcifications >100 μm diameter that either fuse together or grow through a crystallization process forming a calcification front and large calcifications in the core (Fig. 3c). Large calcifications within the core may form large shells, which may fracture radially.

3.1.4 Advanced Calcifications

Calcifications can grow until they completely fill the entire core area forming an advanced calcified plaque (Fig. 3d), in some cases growing beyond the core and extending into the tunica media. Advance calcifications may also undergo fracture and form calcified nodules with fibrin deposition. These calcified nodules are sometimes seen protruding into the lumen, where they have been associated with a thrombogenic response and cardiovascular events.

The majority of the atheroma (75.4%) exhibits a combination of two or more of patterns A to D. As shown in Fig. 4, all four calcification patterns are found at contiguous locations in this single atheroma along its axial length (Maldonado et al. 2015). These cross-sectional images are displayed in sequence, each of them taken ~250 μm apart, advancing in the axial direction of the atheroma (Fig. 4a–d). In 69 out of 72 atheroma analyzed, 1 or more of the 4 calcification morphologies are present. In the remaining three, no calcification was detected with HR-μCT at 2.1 μm resolution. This analysis indicates that pattern A is the most common in the atheroma, as 75.4% have at least one region of μCalcs accumulating at a boundary of the core, followed by pattern C, present in 68.1% of atheroma, with large calcifications forming at the boundaries of the core. Patterns B and D appear in 52.1% and 43.5% of the samples, respectively.

4 Role of Calcification on Plaque Vulnerability

There is a lack of agreement on whether coronary calcification predicts plaque vulnerability or it is a marker of plaque burden only (Otsuka et al. 2014). Calcifications are frequently seen in healed plaque ruptures but less frequently in fibroatheromas, TCFA, and plaque rupture, and even less calcification is observed in plaque erosion at pathological intimal thickening (Burke et al. 2001). Such observations indicate that calcification is first formed in PIT and becomes more prominent with the progression of the atheroma. The degree and type of calcification at the different stages of atheroma progression in sudden cardiovascular death (SCD) victims are shown in Fig. 5.

Importantly, acute ruptures in Fig. 5 show that 100% of such plaques include diffuse, speckled, or fragmented calcifications. Almost all healed ruptures, approximately 85% of vulnerable plaques and about 65% of erosions, are also associated with some type of calcification. While mean calcification area is a sensitive biomarker of plaque burden, the analysis in Fig. 5c demonstrates that the mean calcification area measured in histological sections is not a specific marker of vulnerability. However, this study does not report whether the speckled and diffuse calcification was observed within the core or the fibroatheroma cap. Calcification was also found be a distinctive biomarker in patients with acute myocardial infarction relative to controls dying from non-cardiac events with at least one coronary artery showing >50% stenosis (Mauriello et al. 2013). Unfortunately, once again, coronary calcification as measured did not correlate with the presence of unstable plaque characteristics.

Larger amounts of calcification are generally observed at proximal locations of the three main coronary arteries, when compared to distal segments (Maldonado et al. 2012; Sangiorgi et al. 1998; Burke et al. 2002). The amount of arterial calcification has been shown to be correlated with plaque burden, so that the larger the atheroma, the more extensive the calcification is (Sangiorgi et al. 1998). However, in the same study, the correlation between calcification area and lumen narrowing was found to be weak. On the contrary, a strong correlation was found between percent stenosis and the percentage of calcification and mean calcification area in other studies (Burke et al. 2001, 2002). A plausible explanation is that advanced lesions, specially healed plaque ruptures, display larger stenosis and greater amount of calcification.

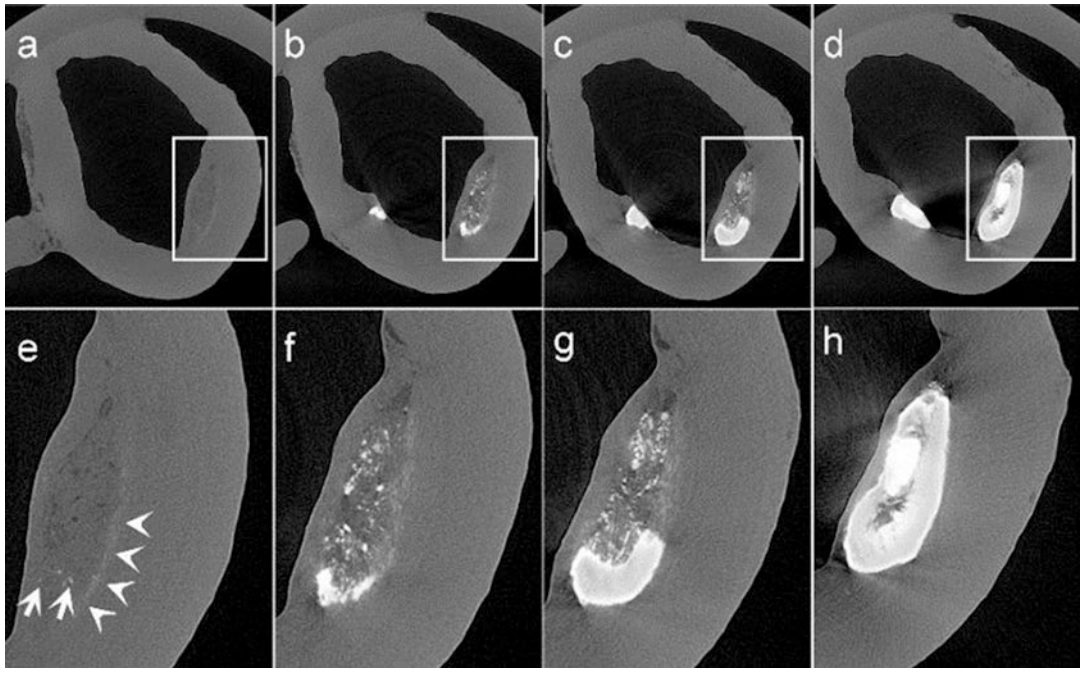

Fig. 4 Sequence of images from a human atheroma taken approximately 250 μm apart from each other displaying the spatial progression of calcification process in atheroma. (**a**, **e**) A soft plaque, characterized by a mixed lipid/necrotic core, containing few isolated μCalcs within the core, and 0.5–5 μm size μCalcs that cannot be fully resolved in HR-μCT at 2.1 μm resolution, appearing as a fuzzy white line at the bottom of the atheroma, (**b**, **f**) submicron μCalcs cluster to form more abundant and larger μCalcs within the core of the lesion, (**c**, **g**) microcalcifications further agglomerate to create a larger macrocalcification within the core, (**d**, **h**) the calcification fills the entire core area. Reproduced with permission from Maldonado et al. (2015)

Several decades of research have provided evidence that large calcification located near the intimal-medial boundary does not increase plaque vulnerability. To the contrary, biomechanical studies demonstrated that plaques may even become less vulnerable. However, emerging evidence in the last 10 years indicates the opposite behavior when very small calcifications located within the cap tissue proper are taken into consideration. Such microcalcifications and their location are not singled out in calcium score and calcified area measurements, the clinical standard by which the role of calcification on plaque vulnerability is analyzed. The presence of microcalcifications in the fibrous cap and their role on plaque vulnerability are discussed next.

4.1 Presence of Microcalcifications in the Fibrous Cap

As shown in Fig. 1i–l μCalcs can be found embedded in the fibrous cap of the atheroma (Maldonado et al. 2015), where they lead to a significant increase in plaque vulnerability (Virmani et al. 2007; Berliner et al. 1995). In 27 out of 72 atheromas herein analyzed, we were able to detect the presence of μCalcs in the fibrous cap with diameters between 5 and 50 μm (Maldonado et al. 2015). The total number of μCalcs located within the cap region of these atheromas represents a small fraction, ~2% (Fig. 6a), of all μCalcs in atheromas (Fig. 2). On average, each cap had 2088 μCalcs, within this size range.

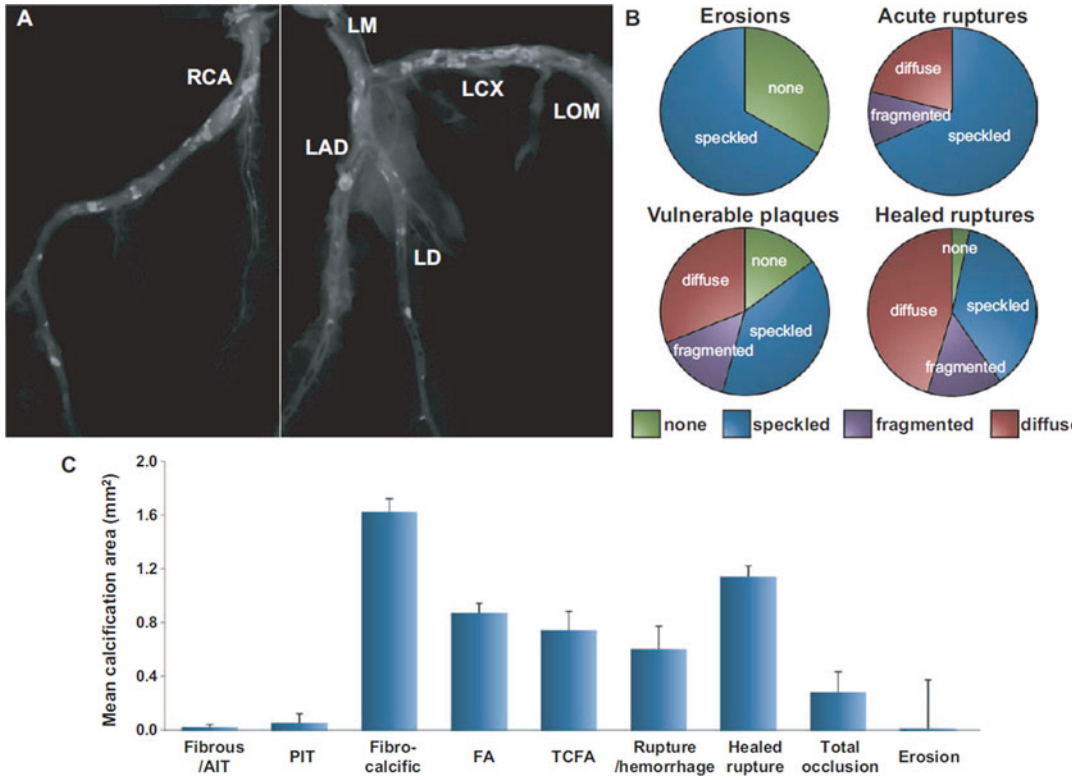

Fig. 5 Coronary calcification and plaque morphology in humans. (**a**) Radiograph of the coronary arteries following removal from the heart. (**b**) Type of radiographic calcification in different plaques. Radiographic calcification was typed according to the classification of Friedrich et al. (1994) and in brief absence of calcification, speckled, and fragmented (linear or wide, single focus of calcium >2 mm in diameter), or diffuse (≥5 mm segment of continuous calcium). (**c**) Bar graph shows the mean area of calcification in different plaquemorphologies in sudden coronary death victims. T bars indicate SEM. AIT indicates adaptive intimal thickening; FA, fibroatheroma; LAD, left anterior descending artery; LCX, left circumflex artery; LD, left diagonal artery; LM, left main coronary artery; LOM, left obtuse marginal branch; PIT, pathological intimal thickening; RCA, right coronary artery; and TCFA, thin-cap fibroatheroma. Reproduced with permission from Burke et al. (2001) and Otsuka et al. (2014)

The number of μCalcs was analyzed based on their location in the shoulders or center of the cap and their position between the necrotic core and the lumen. Our results indicate that 61.3% of caps had μCalcs at both the center and the shoulders, 16.1% just at the center, and 22.6% at just the shoulder. In addition, we found that most μCalcs are located closer to the necrotic core than to the lumen (Fig. 6b), which indicates that the source of these particles would, most likely, be on the necrotic core side of the cap. Roijers et al. showed that microcalcifications were observed in adaptive intimal thickening, fatty streak, pathological intimal thickening, and fibroatheroma (Roijers et al. 2011).

4.2 Microcalcifications in Fibrous Caps Increase Plaque Vulnerability

A new paradigm capable of explaining (1) why many cap tears occurred in the center of the cap, not at the shoulders where macrophages are more abundant, (2) why ruptures frequently did not coincide with location of PCS, and (3) why caps >65 μm thickness could rupture at tissue stresses far below the 300 kPa critical threshold was proposed in Vengrenyuk et al. (2008). It was hypothesized that small calcifications (μCalcs diameter < cap thickness) located within the fibrous cap proper should increase significantly the

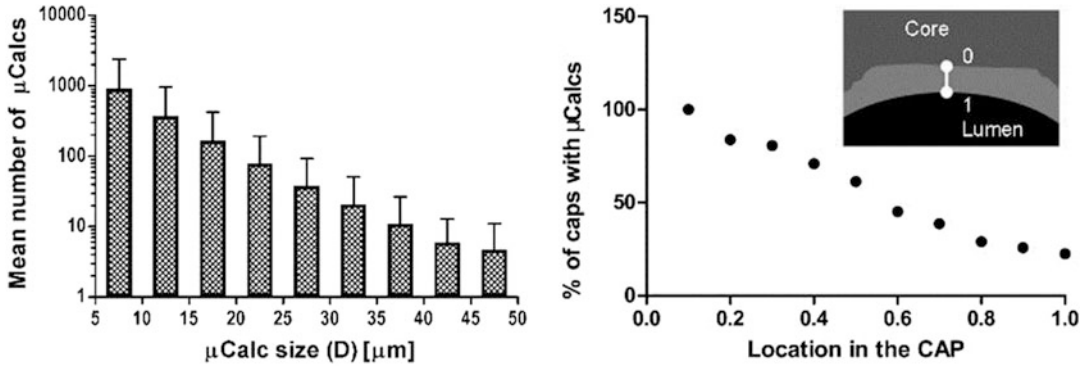

Fig. 6 Mean number of calcifications classified by equivalent spherical diameter, D, that were identified using HR-μCT at 2.1-μm resolution in the cap of atheromas ($n = 27$). Microcalcifications, with 5 μm < D < 50 μm are shown in the shaded bar in the left panel. Percentage of fibrous caps with microcalcifications located at different positions in trough the cap thickness, where 0 is closer to the lipid/necrotic core and 1 is closest to the lumen (right panel), showing how the majority of microcalcifications are located close to the core boundary. Reproduced with permission from Maldonado et al. (2015)

tensile stresses at the interface between the calcification and the fibrous cap tissue (Vengrenyuk et al. 2008). The study also provided the first experimental evidence on the presence of such μCalcs in human atheroma. The authors used HR-μCT imaging at 6.7 μm resolution, to create 3D numerical models of coronary vessels, and determined that μCalcs increased the cap tissue PCS by 200% for spherical calcifications and by more than 400% for elongated, elliptical-shaped μCalcs when aligned with the tensile axis of the cap (Cardoso et al. 2014). Therefore, μCalcs can produce tears in the cap center, even if the most abundant region with macrophages is the shoulders. Also, μCalcs can shift the location of PCS in the cap from shoulders to wherever they are located within the cap and thus can explain why ruptures may not coincide with the location of PCS that was calculated without realizing the presence of μCalcs. Third, μCalcs were shown to act as rigid stress concentrators in a largely deformable soft tissue, raising the PCS by at least 200–400%, with the potential to transform a stable lesion (i.e., with PCS below 300 kPa) into a vulnerable plaque prone to rupture (i.e., with PCS above 300 kPa) (Finet et al. 2004; Cheng et al. 1993; Maldonado et al. 2012; Kelly-Arnold et al. 2013; Ohayon et al. 2005; Goodier 1933).

The prediction in Vengrenyuk et al. (2006) is shown in Fig. 7 where the increase in PCS is shown as a function of cap thickness for three different cases, a cap without a microinclusion using the 2D FEA in Finet et al. (2004) curve 1 and how this PCS would increase for a solid spherical inclusion of 10–20 μm diameter, curves 2–3, respectively. The key observations are that caps significantly thicker than 65 μm could exceed the 300 kPa threshold for rupture if they contained μCalcs, curves 2–3, and that the cap thickness required to achieve an average rupture stress of 545 kPa was ~75 μm if μCalcs were present and not 25 μm as predicted for a cap without μCalcs. These results assume that the inclusions are located in a region where the background tissue stress without the spherical μCalcs was close to the PCS of curve 1.

Importantly, prior to 2005, PCS estimates were based on 2D FEA as shown by curve 1 in Fig. 7. While curve 1 intersects the 300 kPa threshold at 65 μm thickness, where it was predicted that 95% of caps would rupture (Burke et al. 1997), this estimate has been greatly changed as a result of more recent 3D FEA. Ohayon et al. (2005, 2007, 2008) were the first to show that 2D FEA overestimated PCS on average by 73%, 113.8 kPa compared to 65.6 kPa for 3D FEA, and that the 2D analysis was an unreliable predictor of the actual rupture site. In other words, curve 1 in Fig. 3 should lie significantly below where it is now shown, and if the PCS

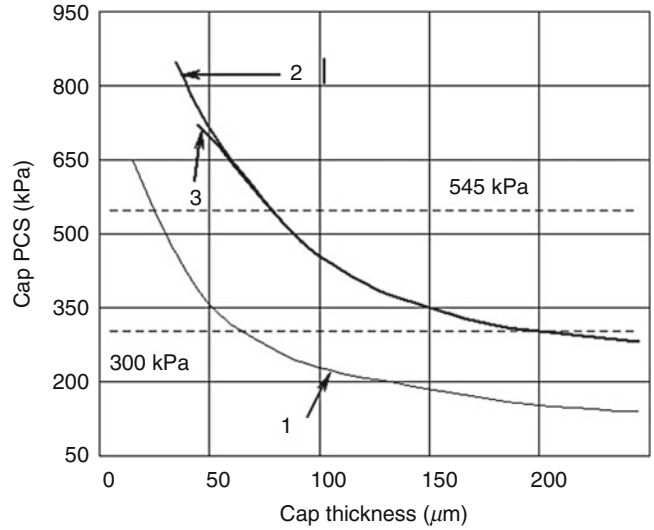

Fig. 7 Changes in cap peak circumferential stress (PSC) with cap thickness for the case when cap tissue is homogeneous (line 1) and when it contains a rigid inclusion of 10–20 μm in diameter (lines 2 and 3, respectively). Reproduced with permission from Vengrenyuk et al. (2006). Copyright (2006) National Academy of Sciences, USA

were corrected by this 73% factor, the revised curve 1 would intersect the 300 kPa threshold at ~30 μm.

In a subsequent study (Bluestein et al. 2008), a 3D FSI simulation was developed for larger μCalcs and then refined and applied to the patient-specific 3D reconstruction of the coronary artery in Fig. 2 of Rambhia et al. (2012). The results of the 3D FEA and the FSI model agreed closely. The FSI simulation had the additional feature that it could predict fluid shear stresses (FSS) and relate these stresses to the time-varying pressure in the lumen. While FSS on endothelial cells are typically five orders of magnitude less than the tissue stresses required for cap rupture, they play an important role in LDL permeability and atherogenesis (Tarbell 2010). In Maldonado et al. (2012), 62 non-ruptured fibrous cap atheroma were examined in 92 of the 3 major coronary arteries using HR-μCT at 6.7 μm resolution. These 92 arteries had on average 4160 μCalcs, 85% μCalcs <50 μm, the vast majority residing in lipid pools. Only 0.2% of these μCalcs (81 total) were in the fibrous cap proper where they could act as tissue stress concentrators. Strikingly, all 81 of the imbedded μCalcs were confined to just 9 (15%) of the 62 fibroatheroma, and their average size was 28 ± 13 μm. The remaining 53 non-ruptured atheroma had no visible μCalcs at 6.7 μm resolution μCT, the thinnest non-ruptured cap being 66 μm in thickness. The spatial distribution of the 81 μCalcs within their respective caps was determined, and 42% were observed to occur in the cap mid-region correlating well with the 37% of tears found in the cap center (Richardson et al. 1989; Maehara et al. 2002). The highest predicted tissue stress for all atheroma cap with μCalcs was 275 kPa, confirming the 300 kPa threshold for rupture proposed in Cheng et al. (1993). FEA also predicted that their caps would need to thin to 30 μm in order to reach the 300 kPa threshold, yet there was not a single non-ruptured cap between 30 and 66 μm. Maldonado et al. (2012) conjectured that this observation could be explained if all caps between 30 and 66 μm had ruptured, not due to their thickness but due to the presence of μCalcs that were just not visible using 6.7 μm resolution μCT. This hypothesis is discussed next.

A much more detailed HR-μCT study at 2.1 μm resolution (Kelly-Arnold et al. 2013) using the same 92 coronary vessels as Maldonado et al. (2012) has led to the identification of nearly 35,000 μCalcs in the caps of 22 out of 66 atheroma. At this resolution, it was possible to observe all μCalcs >5 μm with particular emphasis on just those in the fibrous caps. In the study by Kelly-Arnold et al. (2013), 80% of the visible μCalcs were between 5 and 15 μm.

Second, what was thought to be a single inclusion at 6.7 μm resolution was in many cases a cluster of smaller μCalcs. In Maldonado et al. (2012) and Kelly-Arnold et al. (2013) it was realized that the stress in the region between two μCalcs could be substantially increased (200–500%) if the particles were in close proximity and aligned along their tensile axis, the alignment for the maximum increase in stress. The probability of finding two or more μCalcs in close proximity to each other in a cluster of μCalcs is high, thus potentially increasing the stress concentration beyond the effect of a single μCalc. This study estimated the maximum increase in stress concentration factor (SCF) produced by μCalcs by first determining the proximity (separation distance to μCalc diameter ratio, h/D) for all particle pairs, computing the background stress for the lesion geometry without the μCalcs and then applying the SCF. This simplified approach for estimating the PCS has made it possible to analyze all 35,000 μCalcs in the 22 fibrous caps (Kelly-Arnold et al. 2013) in less than 1 h of computer time. There were only 193 μCalc pairs with $h/D < 2.0$, and of these pairs, only 3 had an $h/D < 0.4$ where the SCF would be >5 if the particles were located along the local tensile axis. Two of these three pairs were in a thick region of the cap where the background stress was low, and in the third pair, the μCalcs were oriented more transverse than parallel to the tensile axis, the net result being that there was not a single μCalc pair among the 35,000 μCalcs observed where the threshold stress of 300 kPa was exceeded. Moreover, in Table 3 of Kelly-Arnold et al. (2013), where a cap thinned to 35 μm at its shoulder without rupturing, the predicted PCS was 313 kPa, very close to the 300 kPa threshold. This cap had over 600 μCalcs >5 μm, but the shoulder itself was devoid of μCalcs. This cap was the thinnest of the 66 non-ruptured caps reported in reference (Kelly-Arnold et al. 2013). Thus, caps can rupture at their shoulders when they thin to 30–35 μm in the absence of μCalcs, but it is clear that this risk would be far greater if even a single μCalc with effective diameter > 5 μm was present.

4.3 Rupture Mechanism due to Microcalcifications

While the microcalcification hypothesis can explain why caps can rupture when the background tissue stress is below the 300 kPa threshold, it does not describe the actual rupture mechanism of the cap. Why from basic mechanics does one have a 300 kPa threshold? In Vengrenyuk et al. (2006) it was proposed that rupture was triggered by an interfacial debonding at the tensile poles of the microinclusion due to a large mismatch in the elastic moduli E of the tissue and the μCalc. In interfacial debonding a small detachment or void at the tensile poles of the particle will explosively grow if the energy stored in the deformed tissue near its poles exceeds the bonding energy of the tissue adhesions at the inclusion interface, frequently referred to as the Griffith criterion (Gent 1980; Gent and Park 1984). This critical debonding stress is denoted as σ_d. The other possible mechanism is cavitation in a hyperelastic medium, not to be confused with cavitation in a liquid where a bubble will grow when it is subjected to pressures at or below its vapor pressure. When cavitation in a hyperelastic medium occurs, a tiny void, such as a gas bubble within the connective tissue itself, will grow when the tensile forces exceed the elastic strength of the tissue to hold itself together. The theory for predicting which failure mechanism will occur, interfacial debonding or cavitation, is described in detail in Maldonado et al. (2013).

The preferential mode of failure is determined by the size of the μCalc, the strength of the bond between the μCalc and the cap tissue, the size of the initial void, and Young's modulus of elasticity E. For a particle of a given size, cavitation will occur if $\sigma_c < \sigma_d$, and debonding will happen if $\sigma_d < \sigma_c$. In the analysis performed by Maldonado et al. (2013), three important results were drawn. First, $\sigma_c < \sigma_d$ for all particles <65 μm, suggesting that cavitation is clearly the preferential mode of failure for μCalcs reported in Maldonado et al. (2012). Second, using a representative elastic modulus for the fibrous cap, the analysis again strongly indicates that cavitation is the primary mode of failure. Third, as the particle size falls

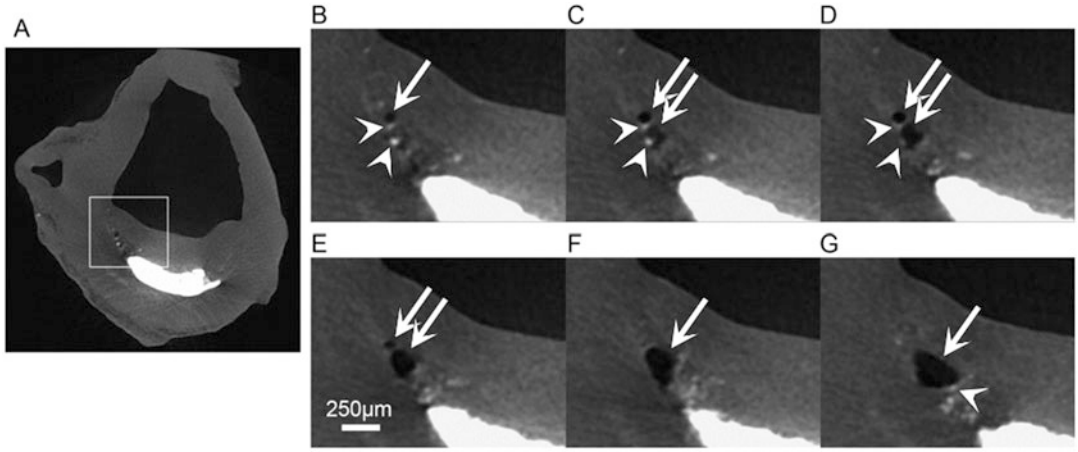

Fig. 8 μCT images at 6.7 μm resolution showing a bubble growing in a fibrous cap in the vicinity of μCalcs. (**a**) Dark area corresponds to air and gray to soft tissue, and bright areas are calcifications. (**b**) Images corresponding to highlighted area in panel A, (**c**, **d**) sequence of images 67 μm apart from panel B (scale bar is 250 μm). Reproduced with permission from Cardoso and Weinbaum (2014)

below ~5 μm, σ_c rises rapidly exceeding the average rupture stress due to the large surface tension energy required for a very small void to grow. This last result implies that before the ultimate stresses needed for cavitation can be reached, the threshold for cap tissue failure will be attained, thus indicating that fibrous caps containing μCalcs <5 μm in diameter may undergo tissue failure only if the cap is thin enough to develop more than 300 kPa, but μCalcs <5 μm would play no role in the tissue rupture. When these results for μCalcs >5 μm are combined with the requirements for cavitation, which show that μCalcs <5 μm are not dangerous because of the large surface energy of their voids, one has a very plausible explanation as to why none of the 66 fibroatheroma examined in Kelly-Arnold et al. (2013) ruptured. Detailed results for all 22 caps with μCalcs >5 μm visible at 2.1 μCT resolution are presented in Kelly-Arnold et al. (2013). Finally, while it is not currently possible to observe tiny initial voids, one does occasionally see larger voids in thick caps where the void started to grow in a region of high local stress and then spread to a region of less stress where it stabilized without breaking through the cap to the lumen of the vessel. Figure 8 is the first direct experimental evidence of this behavior where two voids were created in the space between neighboring μCalcs which then merged and stabilized without causing final cap rupture (Maldonado et al. 2013).

4.4 Growth and Agglomeration of μCalcs

In Kelly-Arnold et al. (2013), using non-decalcified histology, μCalcs >0.5 μm were shown to provide the critical connecting link between the agglomeration of calcified matrix vesicles (Bobryshev et al. 2008; Aikawa et al. 2007; Hsu and Camacho 1999) and the smallest μCalcs visible at 2.1 μm resolution μCT. The non-decalcified histology in Kelly-Arnold et al. (2013) revealed that nearly all of the 44 remaining fibrous caps had μCalcs that were < 5 μm and, thus, too small to detect at 2.1 μm resolution μCT. These very small μCalcs are not dangerous, but they do provide

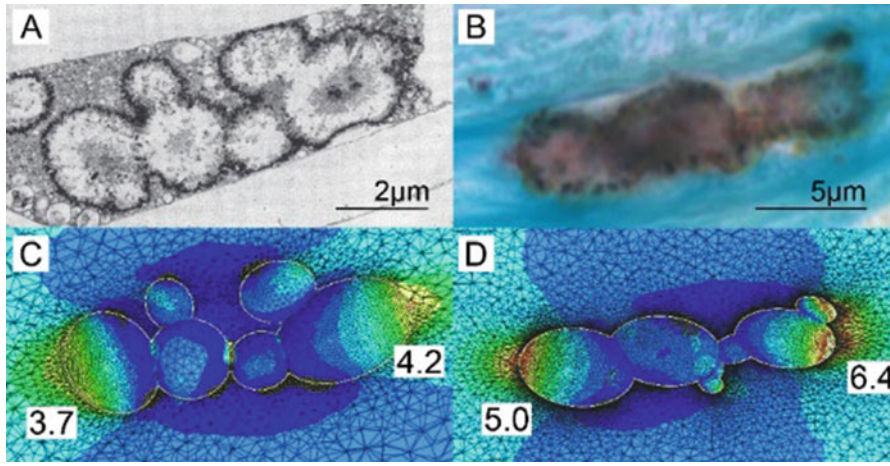

Fig. 9 TEM- and histology-based FEA. (**a**) TEM image of aggregated calcifying matrix vesicles forming μCalcs in a mouse atheroma. (**b**) Image of a μCalc embedded in a human fibrous cap, obtained from non-decalcified histology, stained von Kossa. (**c**, **d**) Stress distribution at the interface of the μCalcs in A and B, respectively, assuming they are embedded in fibrous caps under tension. Numbers show calculated stress concentration factor at the poles. (Reproduced with permission from Kelly-Arnold et al. (2013))

crucial insights into how μCalcs grow and agglomerate starting as matrix vesicles and also their typical shape after they have grown to a size large enough, ~5 μm, to be seen at 2.1 μm resolution μCT. Figure 9a, which is a TEM from E. Aikawa's laboratory, and 9B, which is from our own laboratory using von Kossa stain, show μCalcs embedded in a mouse atheroma and human fibrous cap, respectively. Both μCalcs have a shape consistent with the agglomeration of several enlarged cell-derived matrix vesicles where the region beneath membrane has started calcifying after coalescence. As observed in Fig. 9a, b an elongated μCalc is an agglomeration of smaller calcified particles which individually have the shape of ellipsoids of revolution. These figures strongly suggest that the matrix vesicles described in Bobryshev et al. (2008) first fuse to form larger vesicular bodies typically 1–2 μm diameter that then calcify and agglomerate. Calcification appears to start at the membrane and then may proceed inward. Even at 2.1 μm resolution μCT, it is difficult to image the shape of small μCalcs.

5 Mechanisms and Pathways of Calcification in Atheroma

5.1 Passive Calcification (Biochemical) due to Circulating Nucleating Complexes

Cardiovascular calcification has traditionally been considered a passive mineralization process, associated with vascular degeneration, aging, and metabolic disorders (i.e., chronic renal insufficiency, hyperphosphatemia, diabetes mellitus) (Otsuka et al. 2014; Yahagi et al. 2017). Passive calcification is independent of local cellular activity, lipid accumulation, and inflammation in the atheroma and characterized by calcium and phosphate deposition that leads to amorphous calcification. It is indeed considered that passive calcification accounts for the majority of vascular calcification (Demer and Tintut 2014), appearing late in the progression timeline of the atheroma, and thus is not associated with the risk of plaque rupture (Otsuka et al. 2014; Yahagi et al. 2017).

Passive mineralization is however strongly regulated systemically by hormones and by local signals. Calcium is present in the circulation as both ionized-free form and as a protein-bound form. Calcium ions have spontaneous affinity for elastin- and collagen-binding sites, transforming their neutrally charged structures into positively charged ones, with the capacity of attracting negatively charged phosphate and carbonate ions to ignite the mineralization process (Urry 1971). When calcium is found elevated in plasma, it has been associated with coronary artery calcification (Grønhøj et al. 2016). Elevated serum phosphorus has also been linked to cardiovascular calcification (Cancela et al. 2012) and vascular events (Dhingra et al. 2007; Tonelli et al. 2005). Inorganic phosphate can directly induce osteogenic differentiation of local cells. Nucleotide pyrophosphatase/phosphodiesterase 1 (NPP1) produces extracellular inorganic pyrophosphate (ePPi), which is a potent calcification inhibitor, from ATP released by cells during mineralization (Rutsch et al. 2008). In turn, tissue-nonspecific alkaline phosphatase (TNAP) hydrolyzes and eliminates ePPI. Indeed, overexpression of TNAP could lead to vascular calcification due to enhanced phosphate levels (Sheen et al. 2015). Calcium can increase PiT1 expression on the membrane of VSMCs and MVs, leading to osteoblastic-like cells and phosphate accumulation (Yang et al. 2004), while increased calcium and phosphorus can increase the release of MVs (Reynolds et al. 2004). Calcium is believed to activate MMP2 in MVs, increasing elastin degradation and calcification. Serum calcium and phosphorus are regulated by the parathyroid hormone (PTH) and 1,25-dihydroxyvitamin D. While PTH has not been linked to coronary calcification by calcium scoring (Grønhøj et al. 2016; Arad et al. 1998), 1,25-dihydroxyvitamin D deficiency seems to be associated with cardiovascular events and calcification (de Boer et al. 2009; Watson et al. 1997). Hyperphosphatemia is associated with impaired renal secretion of phosphate and stimulation of vascular calcification (Lanzer et al. 2014; Schlieper et al. 2016). The fibroblast growth factor 23 (FGF-23)/Klotho system is another regulator of mineral metabolism that promotes phosphate excretion through the kidneys, thereby limiting the pro-calcific actions of phosphate. FGF23 has been associated with coronary artery disease and cardiovascular events (Brandenburg et al. 2014; Kestenbaum et al. 2014; Lutsey et al. 2014; Mathew et al. 2014; Parker et al. 2010; Evrard et al. 2015; Lim et al. 2012); however, the role of FGF23 on vascular calcification remains controversial due to mixed results in clinical studies (Kestenbaum et al. 2014; Masai et al. 2013; Scialla et al. 2013) and because FGF23 increases the expression of osteoprotegerin, a vascular calcification inhibitor (Nakahara et al. 2016). Another major calcification inhibitor is inorganic pyrophosphate (Lomashvili et al. 2004), which prevents calcium phosphate aggregation (Fleisch et al. 1970), growing of hydroxyapatite crystals (Francis 1969), and aggregation of hydroxyapatite crystals (Hansen et al. 1976; Villa-Bellosta and Sorribas 2011; Villa-Bellosta et al. 2011). Indeed, pathological increase in inorganic pyrophosphate hydrolysis by tissue-nonspecific alkaline phosphatase (TNAP) induces severe cardiovascular calcification (St Hilaire et al. 2011; Villa-Bellosta et al. 2013). Fetuin, a circulating glycoprotein, is a major inhibitor of apatite found in the circulation, and hence a decrease in fetuin levels results in augmented vascular calcification and higher cardiovascular mortality in hemodialysis patients. Calcifications developed due to chronic kidney disease and renal failure have also been correlated with dysregulation of parathyroid hormone and vitamin D signaling (Lanzer et al. 2014; Schlieper et al. 2016).

5.2 Cell-Mediated (Active) Calcification

Many studies in the last 10 years have contributed to changing the vascular calcification paradigm from a passive process into a passive + active process in which different vascular cells are involved in regulating (i.e., activating/inhibiting) the mineralization of vascular

tissues and atherosclerosis (Otsuka et al. 2014; Leopold 2015; Panh et al. 2017; Nakahara et al. 2017; Boström 2016). The current paradigm of cardiovascular calcification is shown in Fig. 10 (Panh et al. 2017). In the cell-mediated calcification approach, local vascular cells will differentiate into an osteoblast-like phenotype. Those cells include intimal vascular smooth muscle cells (VSMCs) (Leopold 2015; Speer et al. 2009) derived from the media layer and calcifying vascular cells, a subpopulation of VSMCs with an spontaneous capacity for mineralization (Demer and Tintut 2014; Abedin et al. 2004) via the release of matrix vesicles MVs (Reynolds et al. 2004; Anderson 1984), as well as pericytes and pericyte-like cells in the intima and media layer of vasa vasorum of small- and middle-sized arteries (Collett and Canfield 2005).

The active, cell-mediated, mechanisms of vascular calcification are strongly regulated, in particular the differentiation of multipotent cells and VSMCs into osteoblast-like cells. This cell differentiation process is regulated by the BMP-MGP imbalance (described below). Osteochondrogenic transformation of SMCs in the vasculature initiates the formation and release of specialized phospholipidic membrane-bound bilayer structures with submicron diameter size named matrix vesicles (MVs) (Hutcheson et al. 2014, 2016; Ruiz et al. 2016). It is believed that the origin of MVs is exosomes from intracellular multivesicular bodies, secreted in response to upregulation of sphingomyelin phosphodiesterase 3 (SMPD3). The release of MVs from SMCs is an active cell process, regulated by pro-calcification environment/stimulus (Kapustin et al. 2015). MVs can diffuse into collagen fibers and may fuse and form larger vesicles if they have not yet been mineralized. The MVs membrane has phosphate and calcium transporters and pumps, as well as mechanisms for influx regulation. Several transporters have been identified in MVs, including PiT1 and PiT2 for transport of inorganic phosphate, and A2, A5, and A6 from the annexin calcium-binding protein family. Extracellular matrix vesicles (MVs) calcify when calcium phosphate accumulates inside these matrix vesicles, forming hydroxyapatite crystals, similar to bone formation (Amizuka et al. 2012; Kapustin et al. 2011; Naik et al. 2012). Once the mineral inside the MV grows and penetrates the membrane of the MV, it can mineralize in the interstitial space (Golub 2011) and grow, possibly following a passive crystal growth mechanism.

Apoptotic cell death of SMCs and macrophages in the atheroma is another cell-mediated mechanism of vascular calcification. Apoptotic cell death debris generated from SMCs and macrophages calcify in the extracellular environment, inducing nucleation of hydroxyapatite mineral crystals (Clarke et al. 2008). Some research groups believe that chronic low levels of SMCs and macrophage apoptosis are the main driving force behind atherosclerotic calcification in humans (Clarke et al. 2008; Kockx et al. 1998; Proudfoot et al. 2000). Clarke et al. (2010) showed that vascular SMC apoptosis accelerates calcification. While SMC apoptosis is natural, the clearing of apoptotic debris in the atheroma by phagocytes may be incomplete and result in release of proinflammatory cytokines and accumulation of nucleation foci. Lutgens et al. (1999) showed that apoptosis was more predominant in the core of type IV lesions, equally divided in lipid core and fibrous cap in type V lesions, and in ruptured plaques, apoptosis was equally prevalent in the core, the fibrous cap, and the ruptured cap (Lutgens et al. 1999). Kockx et al. (1998) showed that SMC apoptosis is rare in fatty streak lesions. There are a dense infiltration of macrophages accompanied by apoptosis toward the luminal surface of the necrotic core (Kolodgie et al. 2000) and a much denser concentration of apoptotic bodies within the necrotic core when compared to other regions of the atheroma (Schrijvers et al. 2005). Proudfoot et al. (2000) showed in a culture model that SMC nodules calcify at sites of apoptosis and that this can be prevented by inhibiting apoptosis.

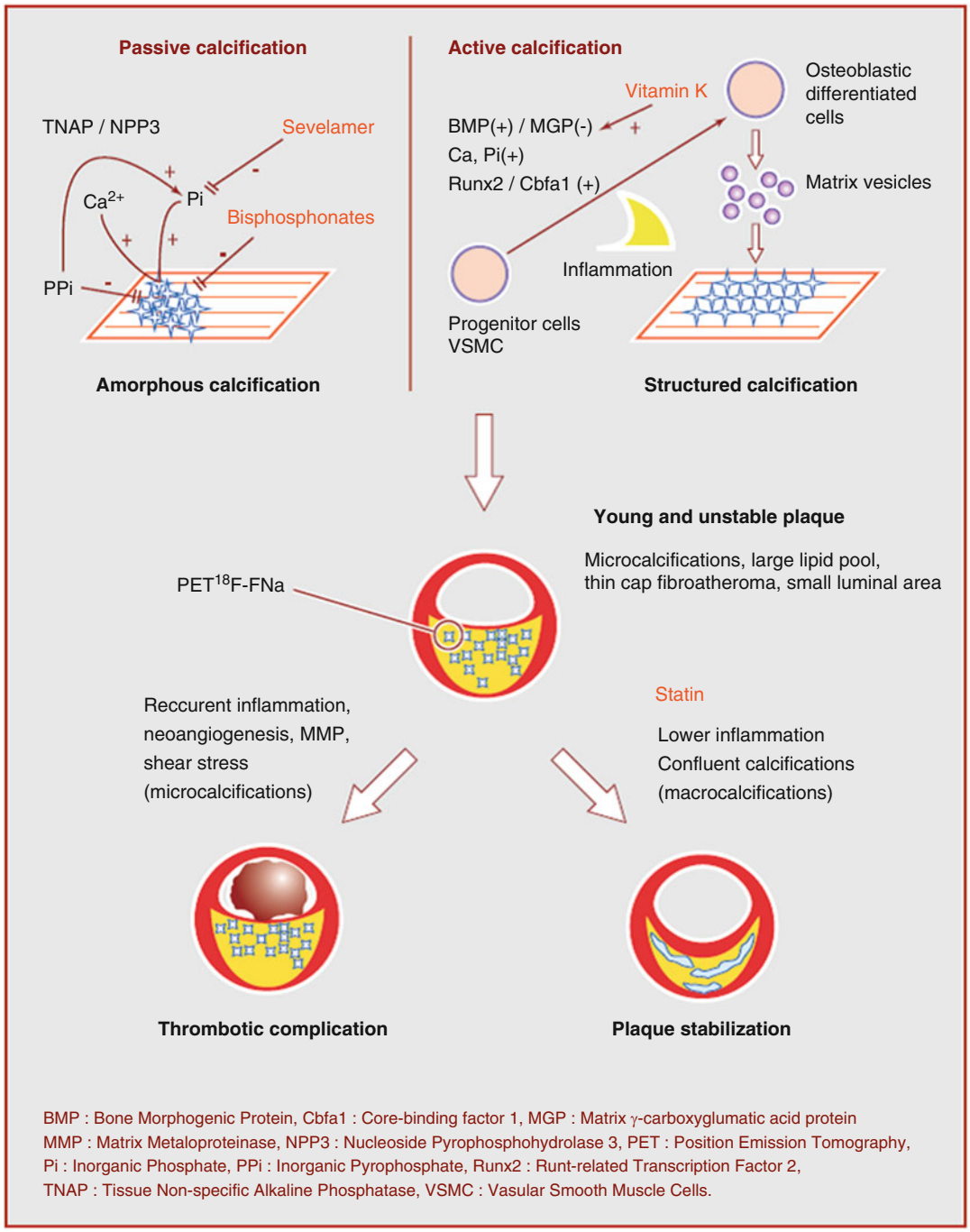

Fig. 10 Coronary calcification pathways. BMP, bone morphogenic protein; Ca, calcium; Cbfa1, core-binding factor 1; FNa, sodium fluoride; MGP, matrix-carboxyglutamic acid protein; MMP, matrix metalloproteinase; NPP3, nucleoside pyrophosphohydrolase 3; PET, positron emission tomography; Pi, inorganic phosphate; PPi, inorganic pyrophosphate; Runx-2, runt-related transcription factor 2; TNAP, tissue-nonspecific alkaline phosphatase; VSMC, vascular smooth muscle cells. Reproduced with permission from Panh et al. (2017)

5.3 Activators of Vascular Calcification

Bone morphometric proteins (BMPs) are part of the tumor growth factor-beta family (TGFβ). BMPs are potent activators of osteogenic differentiation, and a number of them have been associated with the calcification of arteries (Boström et al. 1993) and other disorders such as diabetic vasculopathy, chronic kidney disease, and high levels of circulating phosphate (Yao et al. 2010; Boström et al. 2011; Li et al. 2008). BMP4 seems responsible for increasing vascular calcification in the endothelium via deficiency of matrix Gla protein (MGP), diabetes (Yao et al. 2013), inflammation, and EndMTs (Yao et al. 2015; Jo et al. 2006). Other BMPs seem to function in the media layer through Runx2 and microRNA-30b and 30c (Li et al. 2008; Balderman et al. 2012). In the adventitia, BMP2 has been shown to affect myofibroblasts via Msx2 and LRP6 in diabetic and hyperlipidemic mice (Shao et al. 2007; Cheng et al. 2015) and may mediate hyperphosphatemia and formation of nanocrystals (Li et al. 2008; Sage et al. 2011). Interestingly, Roijers et al. (2011) showed that microcalcifications preceded the presence of calcification proteins such as osteocalcin and BMP-2.

There are at least three Wnt signaling pathways that describe proteins that pass signals into cells via cell surface receptors. The first pathway is the canonical Wnt pathway, the second is the noncanonical planar cell polarity pathway, and the third is the noncanonical Wnt/calcium pathway. There is evidence suggesting that both activators and inhibitors of Wnt signaling affects the development of vascular calcification. It has been reported that a Wnt receptor, LRP6, reduces osteochondrogenic differentiation in vascular SMCs (Cheng et al. 2015). However, Dkk1, a Wnt antagonist, enhances EndMTs and calcification in aortic endothelial cells (ECs), while Wnt7b helps in maintaining a stable ECs phenotype, reducing osteochondrogenesis of ECs (Cheng et al. 2013).

Atherosclerosis is intrinsically a chronic inflammatory process in which the presence of calcification increases with the progression of the disease; however, the relationship between calcification and inflammation is not fully understood. Several inflammatory cytokines are activators (Sage et al. 2011) of calcification in the intima layer of blood vessels (Demer and Tintut 2014; Bessueille and Magne 2015). In addition, pro-inflammatory cytokines, such as saturated fatty acids (e.g., palmitic acid), induce the osteogenic differentiations of VSMCs, while unsaturated fatty acids (e.g., eicosapentaenoic acid) reduce the expression of BMP-2 and other osteoblastic factors and in general osteogenic differentiation (Kageyama et al. 2013). Macrophages, which are specialized inflammatory cells, have also been reported to release MVs (New et al. 2013). Progression of calcification can enhance the inflammatory process in vessels when calcification is present as hyperphosphatemia-induced nanocrystals or calcium phosphate crystals (Sage et al. 2011; Nadra et al. 2005). Interestingly, some infectious diseases, such as tuberculosis, result in ectopic calcifications.

5.4 Inhibitors of Vascular Calcification

Loss of calcification inhibitors is also a cell-mediated mechanism that may lead to atherosclerotic calcification. In normal tissue, calcification inhibitors such as MGP, osteopontin, fetuin, pyrophosphates, etc. are secreted in the vessel wall, preventing the initiation of calcification.

MGP is a calcification inhibitor that regulates BMPs activity via protein-protein interactions and prevents mineral nucleation on elastic sites by binding to mineral crystals (Yao et al. 2008; Khavandgar et al. 2014). MGP can prevent EndMT in the endothelium of aortas (Yao et al. 2013) and differentiation of medial SMCs into osteochondrogenic cells (Speer et al. 2009). Deficiency of MGP in humans (i.e., Keutel syndrome) leads to abnormal calcification, while increased expression of MGP has been reported to reduce atherosclerotic calcification (Yao et al. 2010; Boström et al. 2011).

Other BMP inhibitors have also been shown to reduce vascular calcification. For instance, blocking the activing receptor-like kinase (ALK)3, which is a BMP receptor, reduces vascular calcification, while the BMP inhibitor LDN-193,189 can prevent calcification. Suppression of another inhibitory transcription factor within the BMP cascade, Smad6, could result in osteochondrogenesis (Galvin et al. 2000).

Reduction or complete suppression of osteoprotegerin (OPG) may cause a significant increase in vascular calcification and osteoporosis (Bucay et al. 1998). OPG combined with RANK and RANKL represents a control system for the formation of osteoclasts, which are important for bone turnover, remodeling, circulating calcium, and vascular calcification (Evrard et al. 2015). OPG expressed in vascular tissues seems to block vascular calcification, even though the presence of vascular calcification has been observed despite high serum levels of OPG (Morena et al. 2009). Another potential action of OPG is through suppression of TNF-related apoptosis-inducing ligand (TRAIL), which is a strong activator of apoptosis (Collin-Osdoby et al. 2002), thus reducing the possibility of initiating calcification via the genesis of apoptotic bodies.

6 Summary

The longstanding paradigm is that the culprit plaque of an acute coronary event is not calcified, or has a low amount of calcification, when compared with non-ruptured advanced lesions, which show much larger calcium scores. This supports the notion that large calcifications lead to mechanical stabilization of the atheroma. Clinical and pathological analyses have previously focused on the total amount of calcification (calcified area in a whole atheroma cross section) and whether more calcification means higher risk of plaque rupture or not. However, this paradigm has been changing in the last decade or so. Recent research has focused on the presence of microcalcifications in the atheroma, and more importantly on whether clusters of μCalcs are located in the cap of the atheroma. The fact that one could see μCalcs using HR-μCT was an important breakthrough since μCalcs in the cap proper were thought to be rare and, therefore, hard to find by either histology or confocal sectioning. Indeed, it has been shown that μCalcs in fibrous caps are not rare but numerous and that the overall effect of microcalcifications in plaque vulnerability can be summarized as an intensifier of the background circumferential stress in the cap. The stress concentration factor (SCF) produced by μCalcs does not depend on the specific μCalc location within the cap (center or shoulders); it is now known that it depends on the size and shape of the μCalc as well as the proximity between two or more μCalcs where the SCF, which is typically in the range of 2–5, can exceed five or more if the μCalcs are very closely spaced and aligned along the tensile axis of the cap. It has also been shown based on analysis of failure mechanisms that there is a minimum critical size ~5 μm for μCalcs to be potentially dangerous. In turn, the magnitude of the background stress in the cap depends on the atheroma morphology (i.e., cap thickness, necrotic core size, location and shape of lipid core) and tissue composition (i.e., lipid core composition, residual stresses). Therefore, if the cap has no μCalcs, the cap needs to thin to ~30 μm to reach the rupture threshold and become prone to rupture. Also, if μCalc(s) are located in caps with very low background stress, the increase in stress concentration produced by μCalcs may not be sufficient to reach the rupture threshold. However, the presence of μCalc(s) in the cap with a background stress of about one fifth to one half the rupture threshold (a stable plaque) will produce a significant increase in local stress, which may exceed the cap rupture threshold and thus transform a non-vulnerable plaque into a vulnerable one. However, not only size but location matters significantly, since the thousands of μCalcs observed in the lipid pool can be thought of as floating debris and, thus, inconsequential to vulnerable plaque.

For many decades, cardiovascular calcification has been considered as a passive process, accompanying atheroma progression, correlated with plaque burden, and apparently without a major role on plaque vulnerability. Even though

there is no consensus on the mechanisms leading to calcification of the atherosclerotic intima layer in humans, the classic view of cardiovascular calcification has significantly changed in the last 10 years. In recent studies, the classic view that treats cardiovascular calcification as a passive process has been challenged, and emerging data suggest that cardiovascular calcification may encompass both passive and active processes. The passive calcification process comprises biochemical factors, specifically circulating nucleating complexes, which would lead to calcification of the atheroma. The active mechanism of atherosclerotic calcification is a cell-mediated process via cell death of macrophages and SMCs and/or the release of matrix vesicles by SMCs. A number of activators and inhibitors of vascular calcification have been identified. Among the activators, BMPs, Wnt, inflammatory cytokines, and macrophages play an important role in promoting vascular mineralization, while MGP, osteopontin, fetuin, and pyrophosphates prevent calcification. The regulation of such process seems to be the result of imbalance between activators and inhibitors. Once mineralization is initiated via the active mechanism, calcification may further proceed through a passive mineralization process.

Acknowledgments This research has been supported by NIH grants 1R01HL136431 and 1SC1DK103362; NSF grants CMMI-1662970, CMMI-1333560, MRI-0723027, and MRI-1229449; and NYS DOH grant C31291GG.

Conflict of Interest The authors have no conflict of interest.

References

Abedin M, Tintut Y, Demer LL (2004) Vascular calcification: mechanisms and clinical ramifications. Arterioscler Thromb Vasc Biol 24(7):1161–1170

Agatston AS et al (1990) Quantification of coronary artery calcium using ultrafast computed tomography. J Am Coll Cardiol 15(4):827–832

Aikawa E et al (2007) Osteogenesis associates with inflammation in early-stage atherosclerosis evaluated by molecular imaging in vivo. Circulation 116(24):2841–2850

Akyildiz AC et al (2011) Effects of intima stiffness and plaque morphology on peak cap stress. Biomed Eng Online 10:25

Amizuka N et al (2012) Histology of epiphyseal cartilage calcification and endochondral ossification. Front Biosci (Elite Ed) 4:2085–2100

Anderson, H.C., Mineralization by matrix vesicles. Scan Electron Microsc. 1984;(Pt 2):953–964

Arad Y et al (1998) Serum concentration of calcium, 1,25 vitamin D and parathyroid hormone are not correlated with coronary calcifications. An electron beam computed tomography study. Coron Artery Dis 9(8): 513–518

Balderman JA et al (2012) Bone morphogenetic protein-2 decreases microRNA-30b and microRNA-30c to promote vascular smooth muscle cell calcification. J Am Heart Assoc 1(6):e003905

Bennett MR, Evan GI, Schwartz SM (1995) Apoptosis of human vascular smooth muscle cells derived from normal vessels and coronary atherosclerotic plaques. J Clin Invest 95(5):2266–2274

Berliner JA et al (1995) Atherosclerosis: basic mechanisms. Oxidation, inflammation, and genetics. Circulation 91(9):2488–2496

Bessueille L, Magne D (2015) Inflammation: a culprit for vascular calcification in atherosclerosis and diabetes. Cell Mol Life Sci 72(13):2475–2489

Bezerra HG et al (2009) Intracoronary optical coherence tomography: a comprehensive review clinical and research applications. JACC Cardiovasc Interv 2(11):1035–1046

Bluestein D et al (2008) Influence of microcalcifications on vulnerable plaque mechanics using FSI modeling. J Biomech 41(5):1111–1118

Bobryshev YV et al (2008) Matrix vesicles in the fibrous cap of atherosclerotic plaque: possible contribution to plaque rupture. J Cell Mol Med 12(5B): 2073–2082

de Boer IH et al (2009) 25-hydroxyvitamin D levels inversely associate with risk for developing coronary artery calcification. J Am Soc Nephrol 20(8): 1805–1812

Born GVR, Richardson PD (1989) Mechanical properties of human atherosclerotic lesions. In: Glagov S, Newman WP, Shaffer S (eds) Pathology of the human atherosclerotic plaque. Springer, Berlin

Boström KI (2016) Where do we stand on vascular calcification? Vasc Pharmacol 84:8–14

Boström K et al (1993) Bone morphogenetic protein expression in human atherosclerotic lesions. J Clin Invest 91(4):1800–1809

Boström KI et al (2011) Activation of vascular bone morphogenetic protein signaling in diabetes mellitus. Circ Res 108(4):446–457

Brandenburg VM et al (2014) Fibroblast growth factor 23 (FGF23) and mortality: the Ludwigshafen risk and cardiovascular health study. Atherosclerosis 237(1): 53–59

Bucay N et al (1998) Osteoprotegerin-deficient mice develop early onset osteoporosis and arterial calcification. Genes Dev 12(9):1260–1268

Burke AP et al (1997) Coronary risk factors and plaque morphology in men with coronary disease who died suddenly. N Engl J Med 336(18):1276–1282

Burke AP et al (1999) Plaque rupture and sudden death related to exertion in men with coronary artery disease. JAMA 281(10):921–926

Burke AP et al (2001) Pathophysiology of calcium deposition in coronary arteries. Herz 26(4): 239–244

Burke AP et al (2002) Morphological predictors of arterial remodeling in coronary atherosclerosis. Circulation 105(3):297–303

Burleigh MC et al (1992) Collagen types I and III, collagen content, GAGs and mechanical strength of human atherosclerotic plaque caps: span-wise variations. Atherosclerosis 96(1):71–81

Cancela AL et al (2012) Phosphorus is associated with coronary artery disease in patients with preserved renal function. PLoS One 7(5):e36883

Cardoso L, Weinbaum S (2014) Changing views of the biomechanics of vulnerable plaque rupture: a review. Ann Biomed Eng 42(2):415–431

Cardoso L et al (2014) Effect of tissue properties, shape and orientation of microcalcifications on vulnerable cap stability using different hyperelastic constitutive models. J Biomech 47(4):870–877

Cheng GC et al (1993) Distribution of circumferential stress in ruptured and stable atherosclerotic lesions. A structural analysis with histopathological correlation. Circulation 87(4):1179–1187

Cheng SL et al (2013) Dkk1 and MSX2-Wnt7b signaling reciprocally regulate the endothelial-mesenchymal transition in aortic endothelial cells. Arterioscler Thromb Vasc Biol 33(7):1679–1689

Cheng SL et al (2015) Vascular smooth muscle LRP6 limits arteriosclerotic calcification in diabetic LDLR−/− mice by restraining noncanonical Wnt signals. Circ Res 117(2):142–156

Choi BJ et al (2008) Comparison of 64-slice multidetector computed tomography with spectral analysis of intravascular ultrasound backscatter signals for characterizations of noncalcified coronary arterial plaques. Am J Cardiol 102(8):988–993

Choudhury RP et al (2002) MRI and characterization of atherosclerotic plaque: emerging applications and molecular imaging. Arterioscler Thromb Vasc Biol 22(7):1065–1074

Clarke MC et al (2008) Chronic apoptosis of vascular smooth muscle cells accelerates atherosclerosis and promotes calcification and medial degeneration. Circ Res 102(12):1529–1538

Clarke MC et al (2010) Vascular smooth muscle cell apoptosis induces interleukin-1-directed inflammation: effects of hyperlipidemia-mediated inhibition of phagocytosis. Circ Res 106(2):363–372

Collett GD, Canfield AE (2005) Angiogenesis and pericytes in the initiation of ectopic calcification. Circ Res 96(9):930–938

Collin-Osdoby P et al (2002) Basic fibroblast growth factor stimulates osteoclast recruitment, development, and bone pit resorption in association with angiogenesis in vivo on the chick chorioallantoic membrane and activates isolated avian osteoclast resorption in vitro. J Bone Miner Res 17(10):1859–1871

Davies MJ, Thomas T (1981) The pathological basis and microanatomy of occlusive thrombus formation in human coronary arteries. Philos Trans R Soc Lond Ser B Biol Sci 294(1072):225–229

Davies MJ, Thomas AC (1985) Plaque fissuring—the cause of acute myocardial infarction, sudden ischaemic death, and crescendo angina. Br Heart J 53(4):363–373

Davies MJ et al (1993) Risk of thrombosis in human atherosclerotic plaques: role of extracellular lipid, macrophage, and smooth muscle cell content. Br Heart J 69(5):377–381

Demer LL (2002) Vascular calcification and osteoporosis: inflammatory responses to oxidized lipids. Int J Epidemiol 31(4):737–741

Demer LL, Tintut Y (2014) Inflammatory, metabolic, and genetic mechanisms of vascular calcification. Arterioscler Thromb Vasc Biol 34(4):715–723

Dhingra R et al (2007) Relations of serum phosphorus and calcium levels to the incidence of cardiovascular disease in the community. Arch Intern Med 167(9):879–885

Evrard S et al (2015) Vascular calcification: from pathophysiology to biomarkers. Clin Chim Acta 438: 401–414

Finet G, Ohayon J, Rioufol G (2004) Biomechanical interaction between cap thickness, lipid core composition and blood pressure in vulnerable coronary plaque: impact on stability or instability. Coron Artery Dis 15(1):13–20

Fleisch HA et al (1970) The inhibitory effect of phosphonates on the formation of calcium phosphate crystals in vitro and on aortic and kidney calcification in vivo. Eur J Clin Investig 1(1):12–18

Francis MD (1969) The inhibition of calcium hydroxypatite crystal growth by polyphosphonates and polyphosphates. Calcif Tissue Res 3(2):151–162

Friedrich GJ et al (1994) Detection of intralesional calcium by intracoronary ultrasound depends on the histologic pattern. Am Heart J 128:435–41

Galvin KM et al (2000) A role for smad6 in development and homeostasis of the cardiovascular system. Nat Genet 24(2):171–174

Gent AN (1980) Detachment of an elastic matrix from a rigid spherical inclusion. J Mater Sci 15(11): 2884–2888

Gent AN, Park B (1984) Failure processes in elastomers at or near a rigid spherical inclusion. J Mater Sci 19(6):1947–1956

Golub EE (2011) Biomineralization and matrix vesicles in biology and pathology. Semin Immunopathol 33(5):409–417

Goodier JN (1933) Concentration of stress around spherical and cylindrical inclusion and flaws. Trans ASME 55:39–44

Grønhøj MH et al (2016) Associations between calcium-phosphate metabolism and coronary artery calcification; a cross sectional study of a middle-aged general population. Atherosclerosis 251:101–108
Hansen NM et al (1976) Aggregation of hydroxyapatite crystals. Biochim Biophys Acta 451(2):549–559
Hoshino T et al (2009) Mechanical stress analysis of a rigid inclusion in distensible material: a model of atherosclerotic calcification and plaque vulnerability. Am J Physiol Heart Circ Physiol 297(2):H802–H810
Hsu HH, Camacho NP (1999) Isolation of calcifiable vesicles from human atherosclerotic aortas. Atherosclerosis 143(2):353–362
Huang H et al (2001) The impact of calcification on the biomechanical stability of atherosclerotic plaques. Circulation 103(8):1051–1056
Hutcheson JD, Maldonado N, Aikawa E (2014) Small entities with large impact: microcalcifications and atherosclerotic plaque vulnerability. Curr Opin Lipidol 25(5):327–332
Hutcheson JD et al (2016) Genesis and growth of extracellular-vesicle-derived microcalcification in atherosclerotic plaques. Nat Mater 15(3):335–343
Isner JM et al (1995) Apoptosis in human atherosclerosis and restenosis. Circulation 91(11):2703–2711
Jo H, Song H, Mowbray A (2006) Role of NADPH oxidases in disturbed flow- and BMP4- induced inflammation and atherosclerosis. Antioxid Redox Signal 8(9–10):1609–1619
Joshi NV et al (2014) 18F-fluoride positron emission tomography for identification of ruptured and high-risk coronary atherosclerotic plaques: a prospective clinical trial. Lancet 383(9918):705–713
Kageyama A et al (2013) Palmitic acid induces osteoblastic differentiation in vascular smooth muscle cells through ACSL3 and NF-κB, novel targets of eicosapentaenoic acid. PLoS One 8(6):e68197
Kapustin AN et al (2011) Calcium regulates key components of vascular smooth muscle cell-derived matrix vesicles to enhance mineralization. Circ Res 109(1):e1–e12
Kapustin AN et al (2015) Vascular smooth muscle cell calcification is mediated by regulated exosome secretion. Circ Res 116(8):1312–1323
Kelly-Arnold A et al (2013) Revised microcalcification hypothesis for fibrous cap rupture in human coronary arteries. Proc Natl Acad Sci U S A 110(26):10741–10746. https://doi.org/10.1073/pnas.1308814110
Kestenbaum B et al (2014) Fibroblast growth factor-23 and cardiovascular disease in the general population: the multi-ethnic study of atherosclerosis. Circ Heart Fail 7(3):409–417
Khavandgar Z et al (2014) Elastin haploinsufficiency impedes the progression of arterial calcification in MGP-deficient mice. J Bone Miner Res 29(2):327–337
Knollmann F et al (2008) Quantification of atherosclerotic coronary plaque components by submillimeter computed tomography. Int J Cardiovasc Imaging 24(3):301–310
Kockx MM et al (1998) Apoptosis and related proteins in different stages of human atherosclerotic plaques. Circulation 97(23):2307–2315
Kolodgie FD et al (2000) Localization of apoptotic macrophages at the site of plaque rupture in sudden coronary death. Am J Pathol 157(4):1259–1268
Kolodgie FD et al (2003) Intraplaque hemorrhage and progression of coronary atheroma. N Engl J Med 349(24):2316–2325
Kopp AF et al (2001) Non-invasive characterisation of coronary lesion morphology and composition by multislice CT: first results in comparison with intracoronary ultrasound. Eur Radiol 11(9):1607–1611
de Korte CL et al (1998) Intravascular ultrasound elastography: assessment and imaging of elastic properties of diseased arteries and vulnerable plaque. Eur J Ultrasound 7(3):219–224
Lanzer P et al (2014) Medial vascular calcification revisited: review and perspectives. Eur Heart J 35(23):1515–1525
Larose E et al (2005) Characterization of human atherosclerotic plaques by intravascular magnetic resonance imaging. Circulation 112(15):2324–2331
Larose E et al (2008) Improved characterization of atherosclerotic plaques by gadolinium contrast during intravascular magnetic resonance imaging of human arteries. Atherosclerosis 196(2):919–925
Lee RT et al (1991) Structure-dependent dynamic mechanical behavior of fibrous caps from human atherosclerotic plaques. Circulation 83(5):1764–1770
Lendon CL et al (1991) Atherosclerotic plaque caps are locally weakened when macrophages density is increased. Atherosclerosis 87(1):87–90
Leopold JA (2015) Vascular calcification: mechanisms of vascular smooth muscle cell calcification. Trends Cardiovasc Med 25(4):267–274
Li X, Yang HY, Giachelli CM (2008) BMP-2 promotes phosphate uptake, phenotypic modulation, and calcification of human vascular smooth muscle cells. Atherosclerosis 199(2):271–277
Libby P (2002) Inflammation in atherosclerosis. Nature 420(6917):868–874
Libby P, Ridker PM, Maseri A (2002) Inflammation and atherosclerosis. Circulation 105(9):1135–1143
Lim K et al (2012) Vascular Klotho deficiency potentiates the development of human artery calcification and mediates resistance to fibroblast growth factor 23. Circulation 125(18):2243–2255
Liu L et al (2011) Imaging the subcellular structure of human coronary atherosclerosis using micro-optical coherence tomography. Nat Med 17(8):1010–1014
Lomashvili KA et al (2004) Phosphate-induced vascular calcification: role of pyrophosphate and osteopontin. J Am Soc Nephrol 15(6):1392–1401
Loree HM et al (1992) Effects of fibrous cap thickness on peak circumferential stress in model atherosclerotic vessels. Circ Res 71(4):850–858

Lowe HC et al (2011) Intracoronary optical diagnostics current status, limitations, and potential. JACC Cardiovasc Interv 4(12):1257–1270

Lutgens E et al (1999) Biphasic pattern of cell turnover characterizes the progression from fatty streaks to ruptured human atherosclerotic plaques. Cardiovasc Res 41(2):473–479

Lutsey PL et al (2014) Fibroblast growth factor-23 and incident coronary heart disease, heart failure, and cardiovascular mortality: the atherosclerosis risk in communities study. J Am Heart Assoc 3(3):e000936

Maehara A et al (2002) Morphologic and angiographic features of coronary plaque rupture detected by intravascular ultrasound. J Am Coll Cardiol 40(5):904–910

Maldonado N et al (2012) A mechanistic analysis of the role of microcalcifications in atherosclerotic plaque stability: potential implications for plaque rupture. Am J Physiol Heart Circ Physiol 303(5):H619–H628

Maldonado N et al (2013) The explosive growth of small voids in vulnerable cap rupture; cavitation and interfacial debonding. J Biomech 46(2):396–401

Maldonado N et al (2015) Imaging and analysis of microcalcifications and lipid/necrotic core calcification in fibrous cap atheroma. Int J Cardiovasc Imaging 31(5):1079–1087

Masai H et al (2013) A preliminary study of the potential role of FGF-23 in coronary calcification in patients with suspected coronary artery disease. Atherosclerosis 226(1):228–233

Mathew JS et al (2014) Fibroblast growth factor-23 and incident atrial fibrillation: the multi-ethnic study of atherosclerosis (MESA) and the cardiovascular health study (CHS). Circulation 130(4):298–307

Mauriello A et al (2013) Coronary calcification identifies the vulnerable patient rather than the vulnerable plaque. Atherosclerosis 229(1):124–129

Morena M et al (2009) A cut-off value of plasma osteoprotegerin level may predict the presence of coronary artery calcifications in chronic kidney disease patients. Nephrol Dial Transplant 24(11):3389–3397

Moreno PR et al (2002) Detection of lipid pool, thin fibrous cap, and inflammatory cells in human aortic atherosclerotic plaques by near-infrared spectroscopy. Circulation 105(8):923–927

Motoyama S et al (2007) Multislice computed tomographic characteristics of coronary lesions in acute coronary syndromes. J Am Coll Cardiol 50(4):319–326

Nadra I et al (2005) Proinflammatory activation of macrophages by basic calcium phosphate crystals via protein kinase C and MAP kinase pathways: a vicious cycle of inflammation and arterial calcification? Circ Res 96(12):1248–1256

Naik V et al (2012) Sources of cells that contribute to atherosclerotic intimal calcification: an in vivo genetic fate mapping study. Cardiovasc Res 94(3):545–554

Nakahara T et al (2016) Fibroblast growth factor 23 inhibits osteoblastic gene expression and induces osteoprotegerin in vascular smooth muscle cells. Atherosclerosis 253:102–110

Nakahara T et al (2017) Coronary artery calcification: from mechanism to molecular imaging. JACC Cardiovasc Imaging 10(5):582–593

Nasu K et al (2006) Accuracy of in vivo coronary plaque morphology assessment: a validation study of in vivo virtual histology compared with in vitro histopathology. J Am Coll Cardiol 47(12):2405–2412

New SEP, Aikawa E (2011) Molecular imaging insights into early inflammatory stages of arterial and aortic valve calcification. Circ Res 108(11):1381–1391

New SE et al (2013) Macrophage-derived matrix vesicles: an alternative novel mechanism for microcalcification in atherosclerotic plaques. Circ Res 113(1):72–77

Ohayon J et al (2005) A three-dimensional finite element analysis of stress distribution in a coronary atherosclerotic plaque: in-vivo prediction of plaque rupture location. Biomech Appl Comput Assist Surg 661: 225–241

Ohayon J et al (2007) Influence of residual stress/strain on the biomechanical stability of vulnerable coronary plaques: potential impact for evaluating the risk of plaque rupture. Am J Physiol Heart Circ Physiol 293(3):H1987–H1996

Ohayon J et al (2008) Necrotic core thickness and positive arterial remodeling index: emergent biomechanical factors for evaluating the risk of plaque rupture. Am J Physiol Heart Circ Physiol 295(2):H717–H727

Otsuka F et al (2014) Has our understanding of calcification in human coronary atherosclerosis progressed? Arterioscler Thromb Vasc Biol 34(4):724–736

Panh L et al (2017) Coronary artery calcification: from crystal to plaque rupture. Arch Cardiovasc Dis 110(10):550–561

Parker BD et al (2010) The associations of fibroblast growth factor 23 and uncarboxylated matrix Gla protein with mortality in coronary artery disease: the heart and soul study. Ann Intern Med 152(10):640–648

Patwari P et al (2000) Assessment of coronary plaque with optical coherence tomography and high-frequency ultrasound. Am J Cardiol 85(5):641–644

Potkin BN et al (1990) Coronary artery imaging with intravascular high-frequency ultrasound. Circulation 81(5):1575–1585

Proudfoot D et al (2000) Apoptosis regulates human vascular calcification in vitro: evidence for initiation of vascular calcification by apoptotic bodies. Circ Res 87(11):1055–1062

Rambhia SH et al (2012) Microcalcifications increase coronary vulnerable plaque rupture potential: a patient-based micro-CT fluid-structure interaction study. Ann Biomed Eng 40(7):1443–1454

Reynolds JL et al (2004) Human vascular smooth muscle cells undergo vesicle-mediated calcification in response to changes in extracellular calcium and phosphate concentrations: a potential mechanism for accelerated vascular calcification in ESRD. J Am Soc Nephrol 15(11):2857–2867

Richardson PD, Davies MJ, Born GV (1989) Influence of plaque configuration and stress distribution on fissuring of coronary atherosclerotic plaques. Lancet 2(8669):941–944

Rodriguez-Granillo GA et al (2005) In vivo intravascular ultrasound-derived thin-cap fibroatheroma detection using ultrasound radiofrequency data analysis. J Am Coll Cardiol 46(11):2038–2042

Roijers RB et al (2011) Microcalcifications in early intimal lesions of atherosclerotic human coronary arteries. Am J Pathol 178(6):2879–2887

Ruiz JL et al (2016) Zooming in on the genesis of atherosclerotic plaque microcalcifications. J Physiol 594(11):2915–2927

Russell RR 3rd, Zaret BL (2006) Nuclear cardiology: present and future. Curr Probl Cardiol 31(9): 557–629

Rutsch F et al (2008) Hypophosphatemia, hyperphosphaturia, and bisphosphonate treatment are associated with survival beyond infancy in generalized arterial calcification of infancy. Circ Cardiovasc Genet 1(2):133–140

Sage AP et al (2011) Hyperphosphatemia-induced nanocrystals upregulate the expression of bone morphogenetic protein-2 and osteopontin genes in mouse smooth muscle cells in vitro. Kidney Int 79(4): 414–422

Sangiorgi G et al (1998) Arterial calcification and not lumen stenosis is highly correlated with atherosclerotic plaque burden in humans: a histologic study of 723 coronary artery segments using nondecalcifying methodology. J Am Coll Cardiol 31(1):126–133

Schaar JA et al (2003) Characterizing vulnerable plaque features with intravascular elastography. Circulation 108(21):2636–2641

Schlieper G et al (2016) Vascular calcification in chronic kidney disease: an update. Nephrol Dial Transplant 31(1):31–39

Schrijvers DM et al (2005) Phagocytosis of apoptotic cells by macrophages is impaired in atherosclerosis. Arterioscler Thromb Vasc Biol 25(6):1256–1261

Scialla JJ et al (2013) Fibroblast growth factor 23 is not associated with and does not induce arterial calcification. Kidney Int 83(6):1159–1168

Shao JS et al (2007) Vascular bmp Msx2 Wnt signaling and oxidative stress in arterial calcification. Ann N Y Acad Sci 1117:40–50

Sheen CR et al (2015) Pathophysiological role of vascular smooth muscle alkaline phosphatase in medial artery calcification. J Bone Miner Res 30(5):824–836

Sinusas AJ (2010) Molecular imaging in nuclear cardiology: translating research concepts into clinical applications. Q J Nucl Med Mol Imaging 54(2):230–240

Speer MY et al (2009) Smooth muscle cells give rise to osteochondrogenic precursors and chondrocytes in calcifying arteries. Circ Res 104(6):733–741

St Hilaire C et al (2011) NT5E mutations and arterial calcifications. N Engl J Med 364(5):432–442

Stary HC et al (1994) A definition of initial, fatty streak, and intermediate lesions of atherosclerosis. A report from the committee on vascular lesions of the council on arteriosclerosis, American Heart Association. Circulation 89(5):2462–2478

Stary HC et al (1995) A definition of advanced types of atherosclerotic lesions and a histological classification of atherosclerosis. A report from the committee on vascular lesions of the council on arteriosclerosis, American Heart Association. Arterioscler Thromb Vasc Biol 15(9):1512–1531

Strauss HW, Grewal RK, Pandit-Taskar N (2004) Molecular imaging in nuclear cardiology. Semin Nucl Med 34(1):47–55

Tanaka A et al (2008) Morphology of exertion-triggered plaque rupture in patients with acute coronary syndrome: an optical coherence tomography study. Circulation 118(23):2368–2373

Tang D et al (2004) Effect of a lipid pool on stress/strain distributions in stenotic arteries: 3-D fluid-structure interactions (FSI) models. J Biomech Eng 126(3):363–370

Tang D et al (2005) Local maximal stress hypothesis and computational plaque vulnerability index for atherosclerotic plaque assessment. Ann Biomed Eng 33(12):1789–1801

Tarbell JM (2010) Shear stress and the endothelial transport barrier. Cardiovasc Res 87(2):320–330

Tawakol A et al (2006) In vivo 18F-fluorodeoxyglucose positron emission tomography imaging provides a noninvasive measure of carotid plaque inflammation in patients. J Am Coll Cardiol 48(9):1818–1824

Tonelli M et al (2005) Relation between serum phosphate level and cardiovascular event rate in people with coronary disease. Circulation 112(17):2627–2633

Tsimikas S, Shaw PX (2002) Non-invasive imaging of vulnerable plaques by molecular targeting of oxidized LDL with tagged oxidation-specific antibodies. J Cell Biochem Suppl 39:138–146

Urry DW (1971) Neutral sites for calcium ion binding to elastin and collagen: a charge neutralization theory for calcification and its relationship to atherosclerosis. Proc Natl Acad Sci U S A 68(4):810–814

Vengrenyuk Y et al (2006) A hypothesis for vulnerable plaque rupture due to stress-induced debonding around cellular microcalcifications in thin fibrous caps. Proc Natl Acad Sci U S A 103(40):14678–14683

Vengrenyuk Y, Cardoso L, Weinbaum S (2008) Micro-CT based analysis of a new paradigm for vulnerable plaque rupture: cellular microcalcifications in fibrous caps. Mol Cell Biomech 5(1):37–47

Vengrenyuk Y et al (2010) Computational stress analysis of atherosclerotic plaques in ApoE knockout mice. Ann Biomed Eng 38(3):738–747

Villa-Bellosta R, Sorribas V (2011) Calcium phosphate deposition with normal phosphate concentration. Role of pyrophosphate. Circ J 75(11):2705–2710

Villa-Bellosta R et al (2011) Extracellular pyrophosphate metabolism and calcification in vascular smooth muscle. Am J Physiol Heart Circ Physiol 301(1):H61–H68

Villa-Bellosta R et al (2013) Defective extracellular pyrophosphate metabolism promotes vascular calcification in a mouse model of Hutchinson-Gilford progeria

syndrome that is ameliorated on pyrophosphate treatment. Circulation 127(24):2442–2451
Virmani R et al (2000) Lessons from sudden coronary death: a comprehensive morphological classification scheme for atherosclerotic lesions. Arterioscler Thromb Vasc Biol 20(5):1262–1275
Virmani R et al (2003) Pathology of the thin-cap fibroatheroma: a type of vulnerable plaque. J Interv Cardiol 16(3):267–272
Virmani R et al (2007) The vulnerable atherosclerotic plaque: strategies for diagnosis and management. Blackwell, Malden, MA
Watson KE et al (1997) Active serum vitamin D levels are inversely correlated with coronary calcification. Circulation 96(6):1755–1760
Wenk JF (2011) Numerical modeling of stress in stenotic arteries with microcalcifications: a parameter sensitivity study. J Biomech Eng 133(1):014503
Yabushita H et al (2002) Characterization of human atherosclerosis by optical coherence tomography. Circulation 106(13):1640–1645
Yahagi K et al (2017) Pathology of human coronary and carotid artery atherosclerosis and vascular calcification in diabetes mellitus. Arterioscler Thromb Vasc Biol 37(2):191–204
Yang F et al (2003) Segmentation of wall and plaque in in vitro vascular MR images. Int J Cardiovasc Imaging 19(5):419–428
Yang H, Curinga G, Giachelli CM (2004) Elevated extracellular calcium levels induce smooth muscle cell matrix mineralization in vitro. Kidney Int 66(6): 2293–2299
Yao Y, Shahbazian A, Boström KI (2008) Proline and gamma-carboxylated glutamate residues in matrix Gla protein are critical for binding of bone morphogenetic protein-4. Circ Res 102(9):1065–1074
Yao Y et al (2010) Inhibition of bone morphogenetic proteins protects against atherosclerosis and vascular calcification. Circ Res 107(4):485–494
Yao Y et al (2013) A role for the endothelium in vascular calcification. Circ Res 113(5):495–504
Yao J et al (2015) Serine protease activation essential for endothelial-Mesenchymal transition in vascular calcification. Circ Res 117(9):758–769

Abdominal Aortic Aneurysm Pathomechanics: Current Understanding and Future Directions

Erica M. C. Kemmerling and Robert A. Peattie

Abstract

Abdominal aortic aneurysms (AAAs) are permanent, local expansions of the abdominal segment of the aorta that can potentially be fatal if progressing to rupture. AAAs are rarely found in patients under age 60, but are more common in older age groups, occurring in 2–3% of the whole population. Their rupture produces up to 14,000 deaths annually in the United States alone. Because aneurysmal rupture is a mechanical phenomenon, in recent years there has been a major effort among researchers to investigate the biologic and mechanical processes surrounding AAA progression and rupture. In addition to the basic science importance of understanding AAA pathophysiology, much of this research has been directed toward the development of accurate clinical criteria for assessing the risk of rupture on a patient-by-patient basis. This review first summarizes degenerative changes of the aorta wall associated with AAA pathogenesis. Current understanding of hemodynamics, transport, and wall mechanics in AAAs is then described, and open questions in aneurysm research are discussed along with potential directions in which further understanding could lead to improved clinical evaluation and management decision processes.

E. M. C. Kemmerling
Department of Mechanical Engineering, Tufts University, Medford, MA, USA

R. A. Peattie (✉)
Department of Surgery, Tufts Medical Center, Boston, MA, USA
e-mail: robert.peattie@tufts.edu

1 Introduction

Abdominal aortic aneurysms (AAAs) are degenerative, localized dilations of the abdominal aorta that can potentially be life-threatening if progressing to rupture (Fig. 1). AAAs have been estimated to occur in as much as 2–3% of the population (Ashton et al. 2002; Lederle et al. 2002), with approximately 150,000 new cases diagnosed each year (Karkos et al. 2000). The mortality rate on rupture is between 78% and 94% (Davis et al. 2013; Lederle 2009), and ruptured AAA is responsible for up to 14,000 deaths annually in the United States alone (National Center for Health Statistics 2018). Both open abdomen and endovascular surgical techniques are available for repair of unruptured AAAs. However, most patients are of advanced age and have other comorbid complications, making them

B. M. Fu, N. T. Wright (eds.), *Molecular, Cellular, and Tissue Engineering of the Vascular System*, Advances in Experimental Medicine and Biology 1097,
https://doi.org/10.1007/978-3-319-96445-4_8

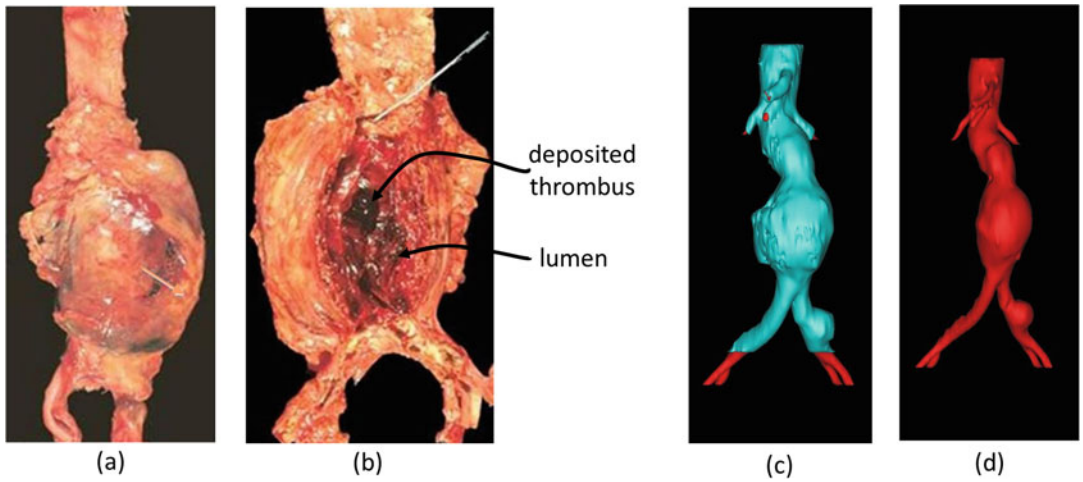

Fig. 1 Sample patient abdominal aortic aneurysm. (**a**) Whole aneurysm collected from a cadaver; (**b**) cadaver sample sectioned open to show lumen and thrombus; (**c**) segmented reconstruction of the lumen (red) and wall and thrombus (blue), obtained from CT imaging; (**d**) lumen only (red)

poor candidates for surgery. Further, surgical repair techniques are costly and are not without the potential for complications (Ghansah and Murphy 2004; van Marrewijk et al. 2005; Wu et al. 2018; Regnier et al. 2018; van Schaik et al. 2017). Thus there exists a major incentive for careful assessment of risk of rupture of specific individual patients to minimize the need for unnecessary or high-risk surgery.

The age distribution of AAA patients is predominantly skewed toward 60 and over. Among men aged 65–74 years, incidence has been reported to be 55 per 100,000 person-years, increasing to 112 per 100,000 person-years for men aged 75–85 years and 298 per 100,000 person-years for those older than 85 (Howard et al. 2015). Principal risk factors associated with the occurrence of AAA include advanced age, male gender, Caucasian race, a positive family history, and smoking. In contrast, clinically observable factors associated with expansion and rupture include large aneurysm diameter, rapid expansion, smoking, and hypertension (United States Census Bureau 2018). Interestingly, although there has been a general trend toward aging of the population in the United States for many years, in recent years the number of deaths from ruptured AAA has declined significantly, from 13,843 in 2005 (National Center for Health Statistics 2008) to 9,988 in 2015 (Karkos et al. 2000). In part this is due to improvements in diagnostic techniques combined with increased emphasis on screening for AAA in all patients over 50 at many medical centers. In addition, it has been suggested that decreased rates of smoking are contributing to reduced AAA mortality (Grøndal et al. 2015; Benson et al. 2016; Svensjö et al. 2011).

Decisions regarding elective surgical management of specific AAA patients are normally made balancing the risks of progression to rupture with the risks associated with performance of the surgery. Open abdomen repair is thought to be justified when maximum bulge diameter exceeds 5–5.5 cm or growth rate exceeds 3.5 mm/year, while endovascular repair can be recommended at lower bulge diameters due to its lower invasive disruption and complication rates (Chaikof et al. 2009; Moll et al. 2011; RESCAN Collaborators et al. 2013; Thompson et al. 2013). However, these criteria are most accurately thought of as rough guidelines rather than absolute standards. Postmortem examinations have shown that lesions smaller than 5 cm can rupture with appreciable frequency (Darling et al. 1977; Choksy et al. 1999; Hall et al. 2000), while as many as 60% of those larger than 5 cm do not rupture during the patient life span (Darling et al. 1977). In addition, analysis

of CT imaging comparing ruptured to unruptured AAAs has failed to demonstrate a statistically significant threshold size discriminating between the two groups (Ouriel et al. 1992). Thus there is no general agreement on whether aneurysmal diameter and growth rate alone are sufficient criteria for assessing the risk of rupture. Further, criteria related to bulge diameter and growth rate are correlative only and have no underlying basis with regard to the physical mechanism of rupture.

To address these limitations in the understanding of aneurysm growth and eventual failure, recent attention has focused on physical causes leading to rupture. From a physical perspective, AAA rupture is driven by mechanical stress within the vessel wall and becomes increasingly likely as peak stress magnitude exceeds the strength of the diseased wall to resist. As a result, an intensive effort to evaluate wall stress on a patient-specific basis has developed. Recent reviews include Vorp (2007), Humphrey and Taylor (2008), Martufi and Gasser (2013), Raut et al. (2013a), and Indrakusuma et al. (2016). In this chapter, degenerative changes of the aneurysm wall ultrastructure are described. Current understandings of AAA hemodynamics, transport, and wall mechanics are then summarized, along with the factors that mediate those issues. Finally, open questions in aneurysm research are discussed, and potential directions for improved clinical evaluation and management are suggested.

2 AAA Histopathology

The healthy adult aorta is approximately 12 cm in length on average, although its actual length in any individual depends on subject height. Its diameter tapers along its length, from 3.5 to 3.9 cm outer diameter at the aortic root to approximately 2.5 cm outer diameter in the abdomen. In both men and women, aging is associated with both increasing aortic diameter and a gradual loss of compliance, as a result of ultrastructural changes including an increase in collagen content and the gradual formation of intimal atheroma with calcium deposits.

The healthy abdominal aorta wall consists of three well-organized layers, the *tunica intima*, or inner layer; the *tunica media*, or middle layer; and the *adventitia*, or outer layer (Fig. 2a, b). Together, these provide a nearly uniform wall thickness of 0.2 cm. The intima consists of a single layer of endothelial cells supported by a subendothelial layer of loose connective tissue. It is separated from the media by an internal elastic lamina composed of fenestrated elastin fibers. The media, which is 0.5–1.0 mm thick, consists of a concentric series of 28–30 layers of helically arranged smooth muscle cells separated by layers of elastin fibers with reticular fibers, proteoglycans, and glycoproteins. The adventitia consists primarily of type I collagen fibers with lesser numbers of elastin fibers and scattered fibroblasts. In health, the wall consists on average of 45.5% collagen (60% type I and 22% type III), 30.1% elastin, and 22% smooth muscle by dry weight (Mescher 2016; Fisher and Llaurado 1966), although the aortic arch and thoracic aorta generally contain a higher percentage of elastin than the abdominal aorta (Dua and Dalman 2010). The lower elastin content and resulting decreased flexibility of the abdominal aorta is thought to relate to the far greater frequency of AAA occurrence compared with aneurysms of the aortic arch and thoracic aorta.

In contrast, patient aneurysmal walls lack the ultrastructural organization characteristic of the healthy aorta and can vary significantly between patients (Fig. 2c, d) (Pancheri et al. 2017; Holmes et al. 1995; Holzapfel and Ogden 2017; Hellenthal et al. 2009a, b; Rodella et al. 2016). A small number of wall samples retain a recognizable distribution of layers, with identifiable intima, media, and adventitia. However, in most AAA patient tissue samples, wall layers are largely disorganized, tortuous, and fragmented. The media and adventitia, to the extent they can be recognized, are densely invested with numerous fibroblasts along with extravasated red cells, granular and agranular leukocytes, and other inflammatory cell types. Many samples show regions of well-ordered tissue in some locations, but few are well organized throughout. Most contain regions of highly disorganized structure interspersed with regions of increased collagen or elastin concen-

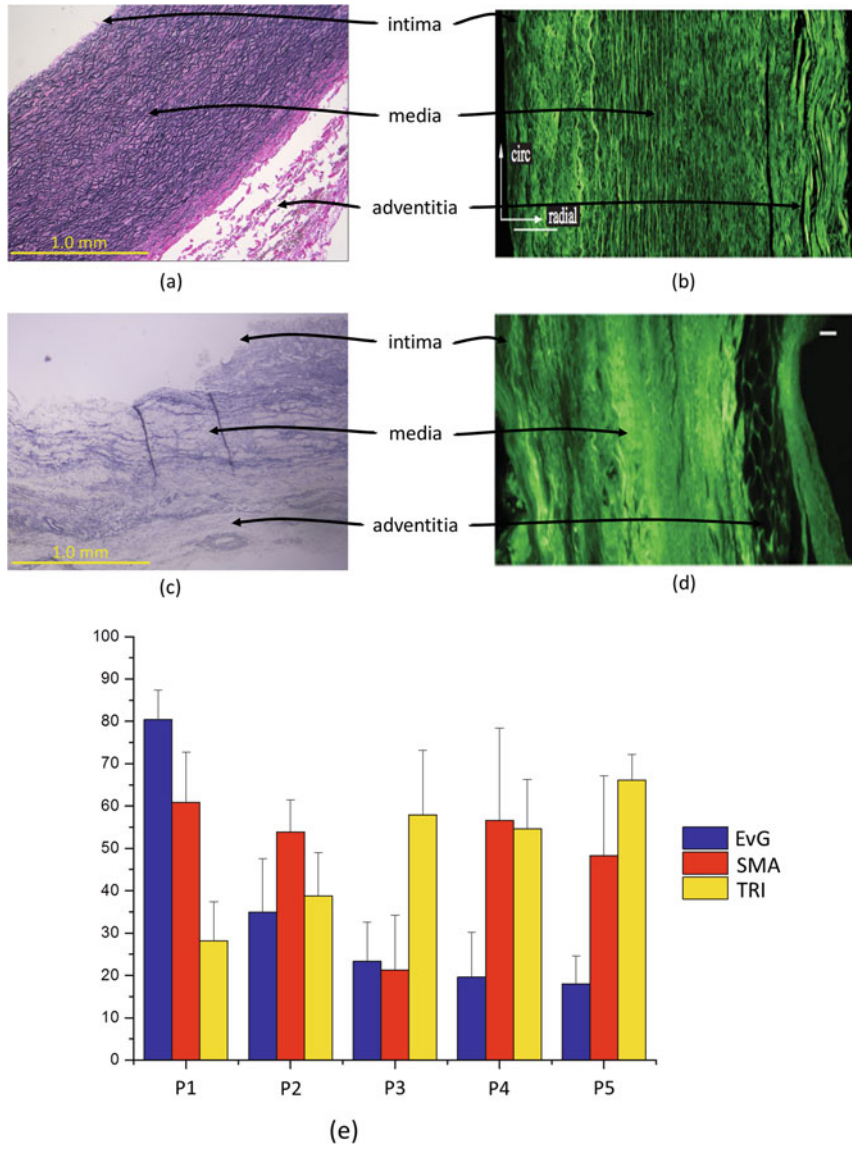

Fig. 2 Representative aorta wall ultrastructure. (**a**) Healthy aorta, stained with Elastica van Gieson to highlight elastin fibers (dark blue), showing the ordered structure of the media; (**b**) healthy aorta, imaged by second harmonic generation microscopy, showing the ordered distribution of collagen fibers; (**c**) aortic aneurysm, stained with Elastica van Gieson to highlight elastin fibers (dark blue), showing the disruption of distinctly recognizable media and adventitia and the loss of ordered media fibers; (**d**) aortic aneurysm, imaged by second harmonic generation microscopy, showing the disruption of media and adventitia and the loss of ordered collagen fibers**;** (**e**) fractional area of coverage for EvG (highlighting elastin fibers), anti-SMA (highlighting smooth muscle), or TRI (highlighting collagen fibers), for five representative patients. Images (b) and (d) used with permission of Dr. Gerhard Holzapfel

trations (Pancheri et al. 2017). In addition, most tissue samples show intramural empty spaces lined by large quantities of cell types not associated with healthy aorta wall tissue, presumably inflammatory cells. Significant loss of parietal structural architecture and disruption of smooth muscle is common (Fig. 2c, d). Further, the AAA wall also exhibits increased microvessel density compared to the healthy wall, which is thought to result from tissue hypoxia (Holmes et al. 1995). Finally, AAA walls often incorporate highly variable amounts of calcification and fat deposits (Holzapfel and Ogden 2017).

Quantitative histopathologic analysis has shown the extent to which the spatial distribution of structural proteins varies between patients (Fig. 2e) (Pancheri et al. 2017). Elastin coverage can vary from as little as 18% to as much as 80% of the wall, while collagen coverage can vary from 28% to 66%, and smooth muscle coverage can vary from 21% to 61%. In addition, the ratios of coverage for individual samples can also vary extensively. Some tissue samples show as much as threefold the coverage of elastin as collagen, indicating a widespread distribution of elastin fibers but only limited collagen. In contrast, other samples show limited elastin coverage but much wider distribution of collagen. Further, the areas in which these fibers appear can sum to values larger than 100%, indicating an extensive overlap of the elastin, collagen, and smooth muscle components within the wall.

While there is a general agreement on the structural protein content of the normal aorta, there has been an ongoing debate regarding the amounts of structural proteins in AAAs. It is generally agreed that elastogenesis is significantly attenuated (He and Roach 1994; Alexander 2004), which results in up to a 90% decrease in total elastin content (He and Roach 1994; Carmo et al. 2002; Cheheltani et al. 2017; Schmid et al. 2013; Dobrin et al. 1984; Vande Geest et al. 2006a). In contrast, changes to collagen mass and ground substance are not agreed upon. Increased collagen and ground matrix volumes were reported by He and Roach (He and Roach 1994) and Sobolewski et al. (Sobolewski et al. 1995). However, other authors have suggested total deposited collagen mass remains unchanged (McGee et al. 1991) or decreases (Vorp 2007; Choke et al. 2005). Moreover, regardless of changes in total collagen, evidence has accumulated that matrix metalloproteinase enzymes are significantly upregulated in the AAA wall (Alexander 2004; Lijnen 2001; Reeps et al. 2009). The most important among these are MMP-1, MMP-2, MMP-3, and MMP-9, which are responsible for degradation of collagen and elastin fibers and collagen fiber fragments. MMP-1, MMP-2, and MMP-3 are thought to be produced by resident cells within the wall, but MMP-9 is primarily synthesized by elicited inflammatory cells transported to the wall from the vasa vasorum. Their appearance, along with the presence of macrophages and B lymphocytes, indicates the presence of a strong inflammatory response in the diseased, expanding wall (Reeps et al. 2009).

In summary, it has been suggested that as the aneurysm wall expands, although total wall thickness remains approximately constant, the media, to the extent that it can be recognized, loses thickness and the adventitia widens (Freestone et al. 1995; Zarins et al. 1988). Genetic factors may contribute to this redistribution. In addition, as elastin is lost, mechanical load is transferred to collagen fibers. As a result, the adventitia is subject to stress-induced collagen turnover that increases reinforcement and thickening (Zarins et al. 1988). In the net, the combined effects of elastin loss and altered collagen and fibrillary cross-linking increase wall stiffness and decrease compliance and distensibility (Humphrey and Taylor 2008; Carmo et al. 2002; Sobolewski et al. 1995), reducing the ability of the wall to withstand systolic pressure and deformation pulses and predisposing it to risk of

rupture (Sobolewski et al. 1995; Humphrey 2002; Sakalihasan et al. 2005).

3 Mural Thrombus

Between 75% and 90% of AAAs present clinically with an irregular layer of deposited intraluminal thrombus (ILT) adhering to the wall inner surface (Choke et al. 2005; Swedenborg et al. 2004; Aslani 2005). Mural thrombus consists of a dense, three-dimensional network of fibrin strands in which red and white blood cells, platelets, cellular elements, proteins, and plasma are enmeshed. It shows three separate sublayers, designated *lumenal*, *medial*, and *abluminal*, each with its own distinct mechanical and histologic characteristics (Wang et al. 2001; Tong and Holzapfel 2015; Tong et al. 2011). The lumenal layer, which borders the AAA lumen and therefore is subjected to flow-induced stresses, has a relatively open, porous structure with thin fibrin strands. It exhibits anisotropic mechanical behavior, with a maximum tangential modulus of elasticity that varies from 189 ± 48 to 291 ± 69 kPa, depending on the patient and the orientation of load. The medial layer retains a porous structure, but its fibrin networks are composed of thicker bundles with condensed residue proteins. It is mechanically less stiff than the lumenal layer and shows an isotropic response to stress, with a maximum tangential modulus varying only from 137 ± 39 to 145 ± 47 kPa. The abluminal layer, which borders the AAA wall, is the least porous layer, with thick fibrin bundles. It has the largest fraction of condensed residue proteins and the lowest fraction of trapped erythrocytes. Mechanically it is also isotropic, with a maximum tangential modulus varying only from 102 ± 23 to 108 ± 31 kPa. Complicating these measurements, ILT material properties are often highly nonuniform even within one patient (Wang et al. 2001; Tong et al. 2011; O'Leary et al. 2014a; Gasser et al. 2008; Hinnen et al. 2007), and it has been shown that thrombi of male patients are significantly stiffer than those of female patients (Tong et al. 2013). In addition, detailed investigation of thrombus ultrastructure and two-dimensional mechanical properties has suggested that four distinct histologic phases can be distinguished and that regions of each phase can be found within each layer (Tong et al. 2011).

Both the causes of thrombogenesis and the role of thrombus in AAA progression are unclear. However, it has been suggested that thrombus deposition results from endothelial erosion produced by high shear stress bursts generated by strong turbulence in the lumenal flow (Peattie et al. 1996a, b). These bursts expose underlying collagen fibers, initiating a thrombotic cascade. Thrombus has the macroscopic protective effect of limiting endothelial loss while simultaneously reducing lumenal diameter, which delays onset of turbulence in the flow and reduces turbulence intensity. Further, the ability of ILT to sequester circulating leukocytes and platelets that produce proteases and growth factors and control local levels of plasmin leads to the activation of MMPs in the wall (Vorp et al. 2001; DiMartino and Vorp 2003). ILT also has been shown to be associated with thinning of the AAA wall, elicitation of inflammatory cells and apoptosis of smooth muscle cells within the wall, and degraded extracellular matrix (Kazi et al. 2003).

There is conflicting evidence regarding relationships between the distribution and thickness of ILT and the gross mechanical behavior of the AAA wall. Some studies have found that thrombus reduces peak wall stress (Inzoli et al. 1993; Mower et al. 1997; Wang et al. 2002). However, other authors suggest that ILT weakens the wall (DiMartino and Vorp 2003; Kazi et al. 2003; Adolph et al. 1997), increases AAA growth rate (Wolf et al. 1994), and increases likelihood of rupture (Satta et al. 1996; da Silva et al. 2000).

Most importantly, thrombus provides a diffusion barrier between the lumen and the wall and thereby directly reduces nutrient and respiratory gas transport to and from the inner regions of the wall. By blocking openings of the vasa vasorum to the lumen, it also indirectly compromises transport to the outer wall as well. In particular, oxygen transport is crucial for maintaining the viability and health of the aorta wall. As a result, it is surprising there has been so little research into thrombus-mediated limitations to mass transport

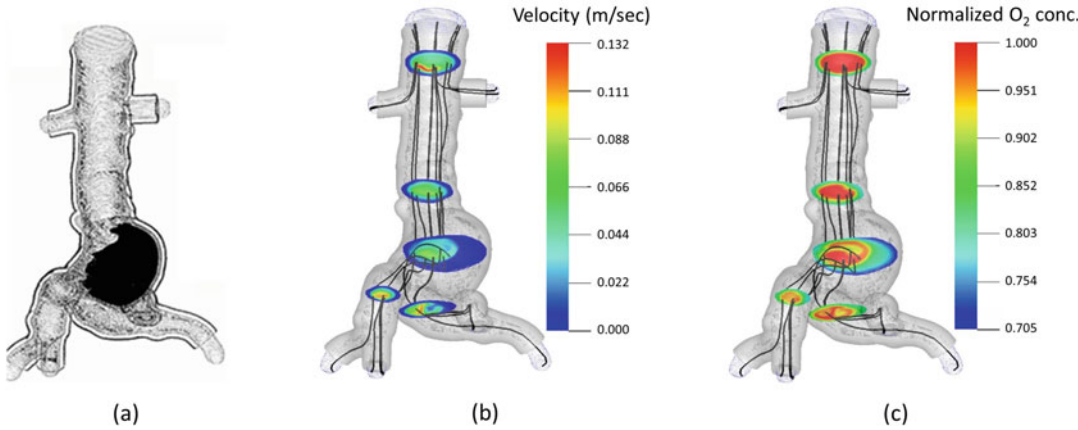

Fig. 3 Semitransparent isometric view of AAA model showing steady flow and O_2 transport simulations, Re = 686. (**a**) Wall (white), lumen (gray), and thrombus (black); (**b**) velocity contours and streamlines; (**c**) oxygen concentration contours and streamlines

in AAAs. Nevertheless, a small number of experimental and computational investigations of have been reported. Intraoperative oxygen partial pressure measurements performed on patients undergoing elective repair found O_2 tension in the wall of patients with thick thrombus layers was 18% of its value in the lumen, whereas in patients with little thrombus, it was 60% of lumenal value (DiMartino and Vorp 2003). The wall of patients with thick thrombus showed pronounced inflammation and increased angiogenic capillary vessels, both of which are markers of hypoxia. In turn, hypoxia caused a decrease in collagen synthesis and attracted macrophages to the wall endothelium (Vorp and Vande Geest 2005). Estimates of O_2 transport rates in idealized AAA models with varying thrombus thicknesses indicated transport decreased as thrombus thickness increased (Vorp et al. 1998a). Subsequent calculations in a model replicating the geometry of a specific patient found that O_2 supply from the lumen to the wall can be reduced by as much as 80% if thrombus thickness exceeds 5 mm (Sun et al. 2009).

These models do not address the effects of flow field turbulence, which significantly alters solute concentration distribution and transport rates. To address that limitation, flow fields and oxygen concentration distributions have been calculated in a patient-specific mathematical model containing separate lumen, thrombus, and vessel wall regions under steady turbulent flow conditions (Fig. 3). The flow had one inlet, the aorta immediately proximal to the renal arteries, and six outlets including renal and iliac branches. Oxygen partial pressure was taken as 90 mmHg at the inlet and 55 mmHg at the wall outer surface, both of which are typical values in vivo (Vorp et al. 1998a; Fung 1981; Ganong 1997). Appropriate forms of the Navier-Stokes and scalar transport equations were solved in all three model regions using commercial software (*PowerFLOW*, Dassault Systems Inc). Time-average velocity magnitude (Fig. 3b) and oxygen concentration (Fig. 3c) were greatest in a thrombus-free channel along the left side of the lumen. Oxygen partial pressure contours support the hypothesis that the presence of thrombus leads to wall oxygen starvation, since oxygen tension was significantly decreased in wall regions adjacent to a thick thrombus layer (Fig. 3c).

4 Hemodynamics

Flow field patterns are of central importance to the understanding of AAA pathophysiology and mechanics for two reasons. First, flow-induced forces on the AAA wall provide the loading

conditions that drive the macroscopic mechanical response of the wall and can lead to rupture. Second, it is well established that endothelial cell viability and mechanobiologic behavior can be modulated by altering the flow field and consequent microenvironment to which the cell is exposed (Dewey Jr et al. 1981; Davies et al. 1984). Since the inner surface of the aorta wall is lined with endothelial cells, evaluating lumenal hemodynamic patterns in detail is critical for understanding the pathophysiologic behavior of the AAA wall and predicting the evolution of its health.

4.1 Definitions

Aortic flow fields are often characterized with the following parameters:

1. Reynolds number (Re), the ratio of inertial forces to viscous forces in the flow, is defined as $\mathrm{Re} = {UL}/{\nu}$, where U is flow velocity, L is a characteristic length scale normally taken as the aorta diameter, and ν is the kinematic viscosity of the fluid.
2. Wall shear stress ($\overrightarrow{\mathrm{WSS}}$), the shear stress applied to the vessel wall inner surface, is defined as $\overrightarrow{\mathrm{WSS}} = \mu {\partial \overrightarrow{u}}/{\partial n}\Big|_{\mathrm{wall}}$, where $\overrightarrow{u}$ is the local velocity, n is the local direction normal to the vessel wall, and μ is the dynamic viscosity of the fluid.
3. Oscillatory shear index (OSI), a measure of the unidirectionality of the flow, is defined as

$$\mathrm{OSI} = 0.5 \times \left(1.0 - \frac{\left|\int_0^T \overrightarrow{\mathrm{WSS}} dt\right|}{\int_0^T \left|\overrightarrow{\mathrm{WSS}}\right| dt}\right)$$

where t is time and T is one period of the flow.

4.2 Features of Aneurysm Flows

Flow fields in abdominal aortic aneurysms have been shown to be highly patient-specific, with wide intrapatient variations in velocity, vorticity, wall shear stress, and turbulence intensity (Arzani and Shadden 2012, 2015; Arzani et al. 2014; O'Rourke and McCullough 2010) (Fig. 4). These parameters are highly dependent on details of the aneurysm shape. In addition, flow patterns upstream of the aneurysm can alter the flow within the aneurysmal bulge, particularly in cases where the patient's upstream aortic flow includes strong secondary flows perpendicular to the vessel's centerline (Hardman et al. 2013). Furthermore, the shape of arterial branches around the aneurysm and the characteristics of the flow through these branches can significantly influence flow features within the aneurysm itself (Taylor et al. 1998, 1999; Tang et al. 2006).

Nevertheless, several important flow features have been found in common in many patient-based AAA flow simulations and experimental investigations. The first is a transitional flow regime and resulting flow instability. Blood flow is generally laminar in small vessels and turbulent in large ones, and the transition occurs when the flow is between regimes. Although transition and turbulence are normally observed at Re $\approx$ 2000 in straight, rigid tubes, turbulence has been observed at far lower Reynolds numbers in AAAs both in vivo and in vitro (Bluth et al. 1990; Parashar et al. 2013; Khanafer et al. 2009), in some cases as low as Re $\approx$ 600 (Poelma et al. 2015). Even at these low values of Re, turbulence intensity can reach 80–100% (O'Rourke and McCullough 2010; Feller et al. 2001). Further, most of the flow is in the unstable transitional regime, and consequently, small perturbations can cause large changes in flow features. It has been shown theoretically that the bulged shape of an aneurysm promotes this behavior (Gopalakrishnan et al. 2014), and experiments and simulations have confirmed this (Peattie et al. 2004; Wilson et al. 2013). Recent work has suggested that some aneurysm flow instabilities have such a long timescale that they persist for multiple cardiac cycles, making the flow nonperiodic (Poelma et al. 2015).

A second common feature is separation, which occurs when the streamline closest to the

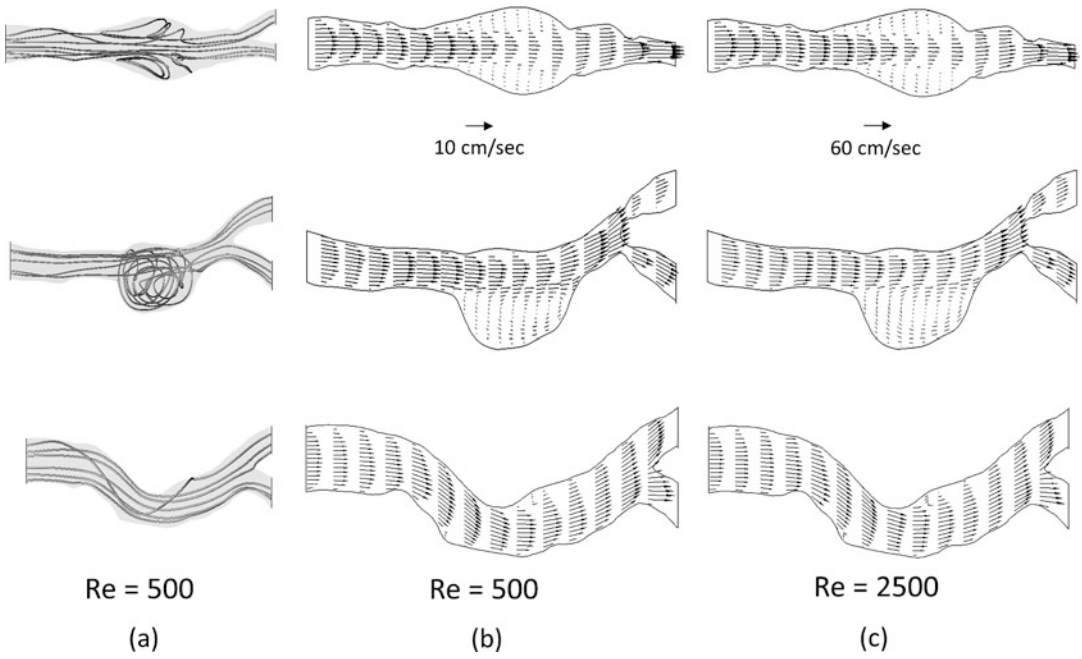

Fig. 4 Computational analysis of AAA velocity distribution in three representative patient-based models. (**a**) Stream lines calculated for laminar flow at Re = 500; (**b**) velocity distributions calculated for laminar flow at Re = 500; (**c**) velocity distributions calculated for turbulent flow at Re = 2500

vessel wall diverges away from the wall, creating a region of recirculating flow along the wall in the separated region. Many AAAs contain a jet of flow that separates from one wall, creating a large recirculation zone in the bulge (Fig. 4, top and middle rows) (O'Rourke and McCullough 2010; Feller et al. 2001). The separated region contains slow-moving flow that is poorly mixed with the faster-moving through-flow. It has been suggested that this type of separation region can lead to deposition of thrombus, particularly if OSI is also low (Peattie et al. 1996a, b; Wilson et al. 2013; O'Rourke et al. 2012; Arzani et al. 2013). However, there is also evidence that mixing between the separated region and the main jet is not negligible in many AAAs (Arzani and Shadden 2012).

A third feature observed in many AAA flows is vortex formation. Vortices have been observed to form at either the proximal (Khanafer et al. 2009) or distal (Gopalakrishnan et al. 2014) ends of the aneurysm bulge, and in both cases, to advect downstream once formed. These vortices usually form during systole but often persist through diastole (Arzani and Shadden 2012; Khanafer et al. 2009). The number of vortices, as well as their size and exact path, has been shown to be highly patient-specific (Arzani and Shadden 2012; O'Rourke and McCullough 2010). It has also been hypothesized that the presence of vortices is related to the deposition of ILT, although the causality of this relationship is unclear (Chen et al. 2014).

4.3 AAA Flow Fields, Quantitative Evaluations

Two main modalities have been used to study AAA flows: computational fluid dynamics (CFD) simulations (Fig. 4) and experiments (Figs. 5 and 6). There are far more published CFD studies of AAAs than experiments (e.g., Gopalakrishnan et al. 2014; Perktold 1987; Taylor and Yamaguchi 1994; Yu et al. 1999; Finol and Amon 2001; Finol et al. 2003; Callaghan et al. 2015; Rana et al. 2015; Neofytou et al. 2008; O'Rourke and McCullough 2008; Marrero et al. 2014; Lu

et al. 2016; Lozowy et al. 2017), in part because simulations are less expensive and less labor-intensive than experiments to initiate. The basic procedure for performing a CFD simulation on an aneurysm is as follows:

1. Generate the geometry, which can be an idealized shape or a patient-specific shape extracted from a medical image.
2. Discretize the geometry and perform a grid convergence test to ensure that the mesh is of high enough quality that characteristics of the mesh do not affect the solution.
3. Select models. AAA flows require a model for blood viscosity, a turbulence model, and a specification for flow coupling with non-flow factors such as wall deformation. Blood is shear thinning, but its non-Newtonian behavior is normally only apparent in arterioles and capillaries. Hence it is often assumed to be Newtonian in the aorta.
4. Select boundary conditions, specifying all inlet and outlet flow conditions.
5. Solve for the velocity and pressure distributions (e.g., Fig. 4).

Although CFD studies have generated significant insight into flow field properties, unfortunately they are not without drawbacks and have given rise to contradictory conclusions in some studies. For example, both high and low WSS have been correlated with aneurysm rupture (Xiang et al. 2014). In addition, it is well known that accurate solutions corresponding to in vivo flows can only be obtained when boundary conditions are correct (Figueroa et al. 2006). However, both inlet and outlet conditions are generally unknown for AAA flows in vivo. Finally, the choice of turbulence and fluid models can also lead to significant differences in solutions (Marrero et al. 2014).

AAA flow has also been studied experimentally, both in vivo with live patients and in vitro using phantoms emulating aneurysm geometries. The most common experimental techniques for studying AAA flow are:

1. Particle image velocimetry (PIV): Velocity measurements are acquired by tracking laser-illuminated particles within the flow. PIV is time-resolved and high resolution but requires an optically clear model (Fig. 5a) (Parashar et al. 2013; Chen et al. 2014; Yu et al. 1999; Bouillot et al. 2014; Deplano et al. 2013; Stamatopoulos et al. 2011, 2010).
2. Laser Doppler velocimetry (LVD): 3D velocity is measured at individual points in a flow by creating interference fringes between two laser beams and detecting single particles

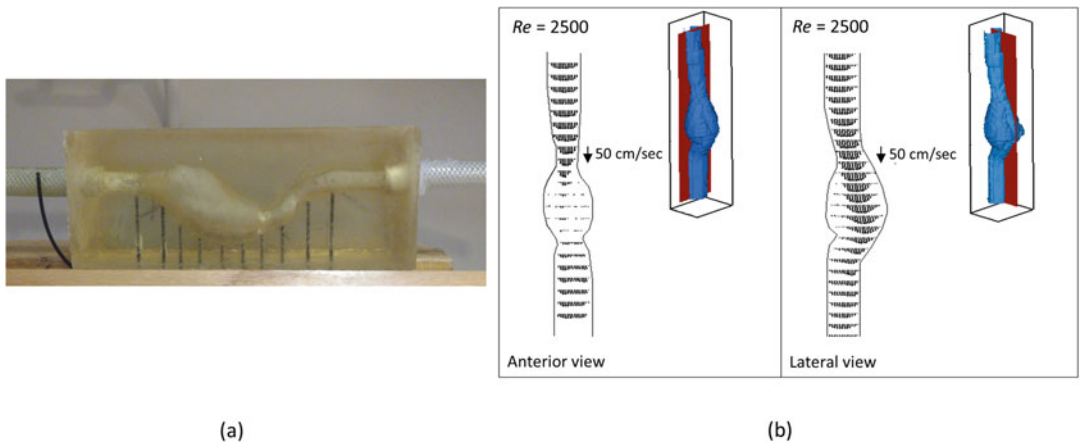

Fig. 5 Experimental measurement of AAA velocity distribution. (**a**) Representative patient-based phantom emulating lesion geometry. Black tubes represent wall pressure taps; (**b**) representative velocity distributions measured in this phantom by particle imaging velocimetry at Re = 2500. Insets show the plane in which these measurements were obtained

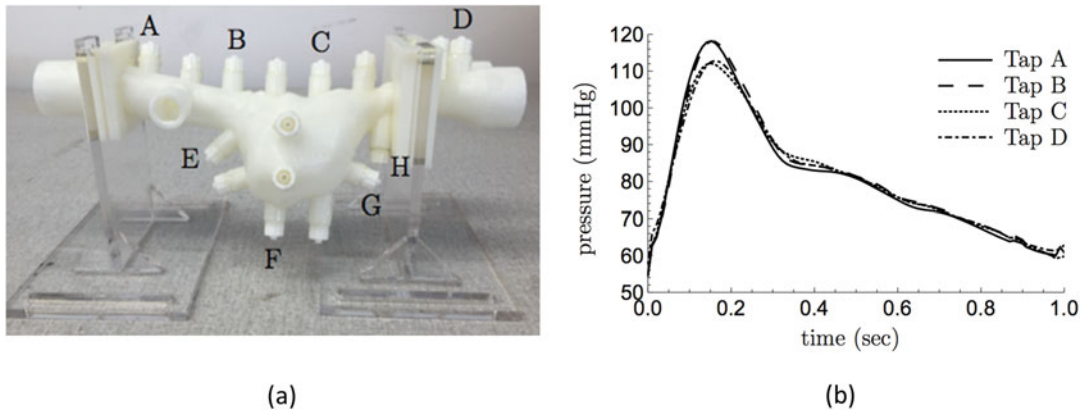

Fig. 6 (**a**) Patient-based AAA phantom, fabricated by 3D printing, showing wall pressure taps precast in the phantom; (**b**) pressure vs. time data measured in this phantom under pulsatile flow conditions

crossing the fringes. LVD is 3D and time-resolved but measures velocity only at discrete points (Peattie et al. 1996a, b; O'Rourke and McCullough 2010, 2008; Asbury et al. 1996; Chong and How 2004; Egelhoff et al. 1999).

3. Ultrasound Doppler velocimetry (UDV): An ultrasound transducer measures flow velocity by detecting the Doppler shift in sound waves scattered from moving blood. UDV is cheap and noninvasive and can be used on live patients because it does not require optical access to the flow. However, it has lower resolution and higher uncertainty than PIV (Peattie et al. 1996a, b; Asbury et al. 1996; Fraser et al. 2008).
4. Cardiovascular magnetic resonance (CMR): A medical magnetic resonance system measures 3D velocity by detecting accumulated phase of rotating atomic spins as they relax after an electromagnetic excitation pulse. CMR requires no optical access and is more accurate and higher resolution than UDV. However, data acquisition is slower and far more expensive than UDV (von Spiczak et al. 2015; Markl et al. 2004; Kung et al. 2011).
5. Pressure measurements: Transducers are connected to various points in a AAA phantom to measure pressure (Fig. 6). These measurements can be steady or time-resolved. Optical access is not required, but the measurements must be in vitro since in vivo measurements would require vessel punctures (Peattie et al. 2004; Anton et al. 2015).

In general experiments require fewer assumptions than computational simulations. For example, there is no need to select a turbulence model. However, they are usually significantly more expensive and time-consuming. In addition, the experimental challenges of establishing an in vitro pulsatile flow accurately simulating aortic conditions suggest the prudence of beginning experiments with simpler steady flow investigations (O'Rourke and McCullough 2010; Peattie et al. 2004; Anton et al. 2015).

5 Wall Mechanics

Predictions of the course of AAA growth, remodeling, and rupture depend critically on quantitative description of the deformation-related and failure-related material properties of the diseased vessel wall and on the resulting macroscale mechanical stress and strain distributions in the wall. Valid techniques for measuring these parameters noninvasively in vivo have generally not been developed yet. However, techniques for modeling wall stress on a patient-specific basis have evolved rapidly in the last 15 years.

5.1 Material Properties of Healthy and Aneurysmal Aortic Walls

Evaluation of biomechanical wall material characteristics is the first step in analysis of AAA wall mechanics for specific patients. Initial uniaxial tension tests on human abdominal aortic tissue samples showed the tissue maintains the characteristic J-shaped, stretch-associated stiffening behavior of healthy aortas (Rodella et al. 2016; Sumner et al. 1970). More recent biaxial testing emulating in vivo deformations during the cardiac cycle has confirmed that response but also established that unlike the healthy aorta, AAA tissue shows pronounced anisotropic behavior, with greater stiffness in the circumferential than the axial direction (Pancheri et al. 2017; Tong et al. 2011, 2013; Vande Geest et al. 2006b; O'Leary et al. 2014b; Polzer et al. 2013; Gasser et al. 2012). From a mechanical-structural point of view, this tissue anisotropy is the characteristic feature of AAAs. Further, aneurysmal wall anisotropy has been shown to change on a patient-to-patient basis and to be greater in diseased or older individuals than in samples from young healthy individuals (Vande Geest et al. 2006b; Holzapfel et al. 2004).

Equibiaxial tests at stress levels between 150 and 320 kPa have found maximum tangential moduli between 8 and 12 MPa in the circumferential direction and 6.0 and 8.5 MPa in the axial direction (Pancheri et al. 2017; Tong et al. 2011; Vande Geest et al. 2006b; O'Leary et al. 2014b). Moduli values have depended in part on the specific protocol and control method used in the individual tests and in part on the imposition of axial prestretch constraints emulating the in vivo aorta. In addition, intrapatient differences in the histology of the tissue samples are not small, and both calcifications and bulge wall thickness can measurably affect tissue mechanical behavior (Reeps et al. 2013). Further, increased thrombus age has been shown to be associated with greater measured tissue anisotropy (Tong et al. 2011).

Previous studies of relations between AAA mechanical properties and patient gender, age, and maximum bulge diameter have reported inconsistent findings. In some studies, tissue samples from male patients have been reported to have greater stiffness and tensile strength than samples from female patients (Tong et al. 2011; Vande Geest et al. 2006b; Reeps et al. 2013). However, in other studies no statistically significant difference in elastic mechanical properties based on gender has been found (Pancheri et al. 2017; O'Leary et al. 2014b). In addition, it is generally thought that the stiffness of the healthy aorta increases with age (Imura et al. 1986), which is attributed to a gradual loss of elastin and increase in the collagen content of the wall over time. However, no statistically significant change in the mechanical properties of AAA tissue samples has been found for patients over age 70 compared to those under 70 (Pancheri et al. 2017; O'Leary et al. 2014b). It has been suggested that the loss of ultrastructural organization associated with the AAA wall may offset age-related changes in the wall collagen and elastin content, preventing the development of age-driven trends in mechanical properties.

Attempts to measure tensile strength have been described by several authors (Vande Geest et al. 2006a, c; Di Martino et al. 2006; Raghavan et al. 2006). For example, Raghavan et al. reported failure tension of human AAA wall tissue strips harvested at autopsy to vary from 5.5 to 42.3 N/cm depending on the position within the wall from which the strip was harvested (Raghavan et al. 2006). More recently, failure tension of ex vivo tissue strips has been reported to show a positive correlation with collagen I, total collagen, and total proteoglycan content of the wall (Tanios et al. 2015). These extracellular matrix components were all reported to be increased in regions of elevated local stress, suggesting the AAA wall undergoes an adaptive remodeling response to maintain stability (Tanios et al. 2015). Failure tension has also been shown to correlate with patient medical history and blood chemistry (Reeps et al. 2013). Finally, the ex vivo wall strength of AAA tissue samples has been shown to fit a lognormal distribution (Polzer and Gasser 2015). This has permitted the development of a probabilistic approach to

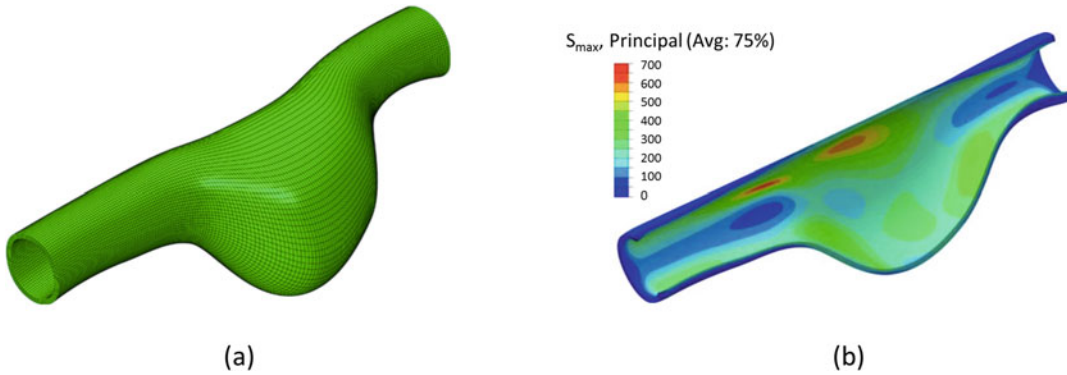

Fig. 7 (**a**) Finite element grid in a patient-based AAA model; (**b**) maximum principal stress distribution in this model calculated by finite element analysis with nonuniform flow-induced loading

rupture risk analysis based on the distributions of wall thickness and wall strength (Polzer and Gasser 2015).

5.2 Finite Element Analysis

Experimental measurements of vessel wall stresses in AAA are infeasible in a live patient, and synthetic vessels with realistic vessel wall material properties have not yet been fabricated. Consequently, the vast majority of work analyzing AAA wall stress and strain has involved finite element analysis (FEA, Fig. 7). There are many commercial software packages available for performing FEA (e.g., Ansys, Abaqus, Comsol), most of which allow customization of both the wall material model (e.g., linear vs. nonlinear elastic, isotropic vs. nonisotropic, etc.) and the numerical parameters characterizing the material. The procedure for performing FEA is similar to that for performing CFD, with the exception that a wall material model must be selected instead of a fluid model and the boundary conditions consist of prestretch constraints along with flow-induced loading and external interstitial pressure.

Both maximum von Mises stress (e.g., Inzoli et al. 1993; Mower et al. 1997; Wang et al. 2002; Raghavan et al. 2005) and maximum principal stress magnitude and position (e.g., Dorfmann et al. 2010) have been used as markers of wall stress development. Both have been found to be highly dependent on the specific shape and thrombus distribution of the patient lesion and the material behavior emulated in the calculation. Values in the range of 400–700 kPa are typical (Fig. 7b), with maximum stress dependent on the specific model details. Inclusion of collagen turnover in the analysis has been shown to reduce both maximum wall stress and spatial gradients of stress (Martufi and Gasser 2013), while incorporation of patient-specific, regionally varying wall thickness has been shown to increase maximum first principal stress magnitude 20–50% (Raut et al. 2013b).

The sophistication of wall stress analyses has advanced rapidly over the last 20 years. Results have been summarized and compared to healthy vessel studies in recent reviews (Humphrey and Holzapfel 2012), while the comparative effects of underlying assumptions have been discussed (Rodriguez et al. 2008), as have the effects of varying wall material properties (Schmid et al. 2013). In particular, early analyses were based on linearly elastic wall behavior (e.g., Stringfellow et al. 1987; Elger et al. 1996; Vorp et al. 1998b). Subsequent studies addressed first nonlinearly elastic behavior (e.g., Raghavan et al. 2005; Fillinger et al. 2002; Fillinger et al. 2003), then hyperelastic isotropic response (e.g., Wang et al. 2002; Doyle et al. 2009; Heng et al. 2008), and hyperelastic anisotropic models (e.g., Rodriguez et al. 2008). Recent studies have also uti-

lized patient-based geometries, nonuniform flow-induced loading, the presence of calcifications and ILT, and residual stresses (e.g., Dorfmann et al. 2010; Speelman et al. 2007; Maier et al. 2010 and the references in them). Unfortunately, there is not yet a general agreement on the effects that are necessary for a wall stress analysis to be sufficiently accurate for clinical application. Adding to this difficulty, it has been shown that FEA solutions are sensitive to geometry reconstruction details, mesh quality and size, pre-stress and zero pressure geometry, and solver settings such as convergence criteria and time step. Further, boundary conditions are difficult to measure in vivo and thus must be assumed in most FEA studies, so evaluating the validity of a particular FEA solution is challenging (Raut et al. 2013a). As a result, in spite of the wealth of knowledge accumulated through wall stress analyses to date, there remains a need for a consensus on the standards that would constitute a clinically usable model.

5.3 Fluid-Structure Interaction

Fluid-structure interaction (FSI) models couple CFD analysis of AAA flow fields and wall pressure and shear stress with FE analysis of the resulting wall strain and stress distributions. FSI models attempt to account for the interaction between flow and wall deformation. These models have the potential to accurately describe the link between flow and aneurysm wall stress, which has been shown to be significant. Unfortunately, in general, the number of assumptions that must be made to perform FSI is far greater than the number necessary to perform individual fluid or solid simulations. In addition to all the information needed to perform CFD and solid mechanics calculations on their own, FSI requires boundary and interface conditions coupling the fluid and structure motion. There is currently no agreement on the correct form of this coupling.

FSI studies have shown that including fluid-structure interaction in a wall stress calculation often yields results differing significantly from computations that ignore flow or vessel wall deformability. Flow field differences of up to 65% in velocity magnitude and 50% in WSS have been found between FSI and rigid-wall CFD. Smaller but still significant differences have been observed between FEA without flow and FSI calculations (Ene et al. 2014; Scotti and Finol 2007; Scotti et al. 2005). More details on FSI results are given by Raut et al. (2013a), who reviewed many FSI studies but found no agreement on "correct" material properties, types of coupling, or boundary conditions.

5.4 Growth Models

Advances in the understanding of AAA histopathology have enabled recent attempts to predict AAA growth rates based on mathematical modeling of elastin and collagen turnover within the wall. Collagen fibers are far stiffer than elastin fibers. However, in the healthy aorta, elastin supports most of the physiologic load imposed by flow in the lumen, since new collagen fibrils are deposited in a sinusoidal shape that does not carry load until stretched to straightness. Collagen itself is in a continual state of ongoing degradation and neodeposition in the wall, with a half-life between 3 and 90 days (Humphrey 1999). This process allows the wall to continuously remodel in response to changing mechanical and microenvironmental conditions. Although the loss of elastin associated with AAA expansion could alter the wall mechanical behavior, by itself it does not explain the large enlargement experienced by the wall, since collagen fiber families can carry flow-induced loads. Accordingly, aneurysmal bulge growth models must take into account turnover of both elastin and collagen fiber families.

Watton et al. (2004) modeled the aorta as a cylindrical, nonlinearly elastic membrane subject to a constrained axial prestretch and a constant internal systolic pressure. A constitutive relation incorporating relations between the wall stiffness and the concentration of elastin and collagen and shape of the collagen fibers was used to describe

the wall mechanical behavior. A prescribed, time-dependent, axisymmetric decay was imposed on elastin concentration, and physiologically realistic remodeling rates were applied to collagen turnover. Under these conditions, predicted bulge growth rates were comparable to those observed in vivo. Watton and Hill (2009) showed that by appropriate selection of remodeling parameters, the model predicted maximum bulge diameter to increase exponentially and the ratio of systolic to diastolic diameter to concomitantly decrease from 1.13 to 1.02. These predictions are consistent with physiological observations (Vardulaki et al. 1998; Lanne et al. 1992). More recently, Lin et al. used mixture theory to incorporate elastin and collagen fibers with anisotropic properties (Lin et al. 2018). An intermediate configuration from which the elastic stretch of collagen could be determined was defined through an evolving recruitment variable. In this approach, the aorta was taken to be a thick-walled tube subject to constant internal pressure and axial stretch. The model predicted a local increase of mass that was achieved via production of new material at a rate exceeding the removal of old material. The combined effects of loss of elastin, degradation of existing and deposition of new collagen, and fiber remodeling resulted in inhomogeneous mechanical properties and a physiologically realistic, continuous enlargement of the aneurysm bulge. Although the assumptions underlying these aneurysm growth models are not yet adequately realistic for clinical applicability, the models show promise for eventual use as noninvasive diagnostic tools if successfully developed.

6 Open Questions for Future Investigation

Although there has been significant progress in understanding aortic aneurysm progression, mechanics, and risk of rupture in the last two decades, many important problems remain unsolved. In particular,the following issues are important aspects of AAA pathology to which physical scientists can contribute essential information and understanding.

1. *Improving the accuracy of predictors of aneurysm growth and rupture*. It has been shown that aneurysm size is correlated with but is not always a sufficient predictor of rupture risk (Darling et al. 1977; Choksy et al. 1999; Hall et al. 2000; Ouriel et al. 1992). Alternative metrics for calculating growth risk and rupture potential evaluation that have been proposed include the presence of regions of high or low wall shear stress, fluid jets impinging on the vessel wall, high vessel wall mechanical stress, high thrombus deposition rate, and the presence of particular properties in the structure of the deposited thrombus. Unfortunately, none of these metrics have been vetted by more than a few studies, and there is no consensus on which would provide a clinically accurate primary diagnostic. Future work must compare many different factors in a large-scale longitudinal study to determine which ones have the strongest correlations with growth and rupture.
2. *Correlating AAA hemodynamics and wall stress analysis with patient anamnesis*. As described above, in recent years there has been extensive investigation of patient-based hemodynamic properties and wall stress development. However, to date there has been very little attempt to correlate these with patient clinical characteristics including age, gender, cigarette smoking history, atherosclerosis and other cardiac disease, hypertension, diabetes and other major disease, and injury history. Exploration of the relations between these characteristics and AAA mechanical behavior could provide significant insight into the state of health of the patient native aorta and subsequent AAA pathogenesis and progression.
3. *Using available tools to learn more about patient-specific aneurysms*. Since idealized models are not representative of the wide

variety of shapes, wall properties, and flow patterns found in patient AAAs, it is advantageous to have as much information as possible about individual patient lesions to predict patient prognosis. In particular, new methods of noninvasive diagnostic imaging allowing distinction between different wall and thrombus material properties would be particularly useful. The use of contrast agents must be minimized in these methods, since AAAs often develop in older patients at high risk of renal insufficiency, in whom use of contrast may be contraindicated. It would also be advantageous to develop AAA-specific image processing methods, such as segmentation techniques that can reliably distinguish vessel walls from thrombus deposits.

4. *Development of a reliable method for validation of aneurysm dynamics simulations*. As AAA fluid and solid mechanics models have grown increasingly more complex, it is hoped that hemodynamic and wall stress solutions derived from the models more closely approximate in vivo conditions. However, the accuracy of these solutions has not yet been verified by direct comparison with in vivo measurements. As a result, a general consensus regarding the assumptions needed for an accurate model has not yet emerged. This is an important difficulty, since the choice of assumptions can strongly affect the details of solutions. For example, in AAA CFD studies, both flow outlet conditions (Taylor 1966; Westerhof et al. 1969; Avolio 1980; Stergiopulos et al. 1992) and choice of turbulence model (O'Rourke and McCullough 2010; Steinman et al. 2013; Khanafer et al. 2007) have been shown to significantly impact solutions. Solid mechanics simulations require even more assumptions than CFD, since there is no universally accepted governing equation or material model for the AAA wall (Holzapfel and Ogden 2017). Accordingly, there is presently a major need for methodologies addressing the comparison of analytic and numerical model results with in vitro experimental measurements and for comparison of both with in vivo animal and patient studies.
5. *Reconciliation of conflicting studies*. A related question is how best to reconcile multiple studies that report contradictory conclusions. There are numerous high-quality, peer-reviewed scientific publications that present valid but conflicting evidence on the ways in which various factors affect AAA progression. For example, some studies suggest that thrombus accumulation decreases rupture potential (Inzoli et al. 1993; Mower et al. 1997; Wang et al. 2002), while others suggest it increases rupture potential (Kazi et al. 2003; Adolph et al. 1997; Wolf et al. 1994; Satta et al. 1996; da Silva et al. 2000). General rules about consistent links between biomechanical factors and aneurysm progression will be needed for mechanical studies to provide usable assistance for clinical AAA decisions and treatment. One potential approach to this problem may be through larger, long-term, multicenter studies in which enough patient-specific aneurysms can be evaluated together using different methods to generate statistically significant correlations between biomechanical factors and aneurysm pathophysiology (Xiang et al. 2014).
6. *Development of integrated growth models*. A large challenge will center on the development of comprehensive fluid-solid-biologic growth models (Humphrey and Taylor 2008; Humphrey and Holzapfel 2012) integrating all relevant information to predict AAA progression and rupture risk development. To be complete, such models will need to address not only hemodynamic and wall stress distributions but also a series of biologic effects in the wall resulting from the AAA mechanical environment. These effects have been summarized by other authors (Humphrey and Holzapfel 2012). In brief, they include matrix metalloproteinase activation and functionality, elastin and collagen fiber turnover, changes in smooth muscle cell density and phenotype, changes in fibroblast activity, and several other factors, as well as the complex set of interrelationships and

feedback patterns between all these factors and AAA biomechanics. The models will also need to take into consideration patient natural history and clinical parameters.

To summarize, then, although a great deal of information regarding AAA biomechanics has been generated to date, there remains a major need to utilize the knowledge basis surrounding AAA mechanobiology and pathophysiology to understand and predict lesion progression. The studies described herein have great potential to contribute to bringing personalized medicine to clinical aortic aneurysm management. Realizing that potential will require addressing the mechanical and biologic environments of the AAA and the relations between them. We hope this review indicates some possible directions that can be taken to contribute to this goal.

Acknowledgments The authors thank Dr. Gerhard Holzapfel for the use of images 2b and 2d, Mr. Sudharsan Madhavan for the assistance with the preparation of Fig. 3, and Mr. Erik Edgar for the assistance with the preparation of Figs. 4 and 5. This work was supported by National Science Foundation [grant numbers CMMI-1031366, CMMI-1352955].

Declaration of Conflicting Interests The authors declare that there is no conflict of interest.

References

Adolph R, Vorp DA, Steed DL, Webster MW, Kameneva MV, Watkins SC (1997) Cellular content and permeability of intraluminal thrombus in abdominal aortic aneurysm. J Vasc Surg 25:916–926

Alexander JJ (2004) The pathobiology of aortic aneurysms. J Surg Res 117:163–175

Anton R, Chen CY, Hung MY, Finol EA, Pekkan K (2015) Experimental and computational investigation of the patient-specific abdominal aortic aneurysm pressure field. Comput Methods Biomech Biomed Engin 18:981–992

Arzani A, Shadden SC (2012) Transport and mixing in patient specific abdominal aortic aneurysms with lagrangian coherent structures. Proceedings of the ASME Summer Bioengineering Conference; Parts A and B:9–10

Arzani A, Shadden SC (2015) Characterizations and correlations of wall shear stress in aneurysmal flow. J Biomech Eng 138:014503–014510

Arzani A, Suh GY, McConnell MV, Dalman RL, Shadden SC (2013) Progression of abdominal aortic aneurysm: effect of lagrangian transport and hemodynamic parameters. Proceedings of the ASME Summer Bioengineering Conference; Pt A:V01AT01A004

Arzani A, Suh GY, Dalman RL, Shadden SC (2014) A longitudinal comparison of hemodynamics and intraluminal thrombus deposition in abdominal aortic aneurysms. Am J Pysiol Heart Circ Physiol 307:H1786–H1795

Asbury CL, Ruberti JW, Bluth EI, Peattie RA (1996) Experimental investigation of steady flow in rigid models of abdominal aortic aneurysms. Ann Biomed Eng 23:29–39

Ashton HA, Buxton MJ, Day NE, Kim LG, Marteau TM, Scott RA, Thompson SG, Walker NM (2002) The multicentre aneurysm screening study (mass) into the effect of abdominal aortic aneurysm screening on mortality in men: a randomized control trial. Lancet 360:1531–1539

Aslani E (2005) Geometric and wall pressure characterization of patient abdominal aortic aneurysms. MS Thesis. Oregon State University, Corvallis, OR

Avolio AP (1980) Multi-branched model of the human arterial system. Med Biol Eng Comput 18: 709–718

Benson RA, Poole R, Murray S et al (2016) Screening results from a large United Kingdom abdominal aortic aneurysm screening center in the context of optimizing United Kingdom National Abdominal Aortic Aneurysm Screening Programme protocols. J Vasc Surg 63:301

Bluth EI, Murphey SM, Hollier LH, Sullivan MA (1990) Color flow doppler in the evaluation of aortic aneurysms. Int Angiol 9:8–10

Bouillot P, Brina O, Ouared R, Lovblad KO, Farhat M, Pereira VM (2014) Particle imaging velocimetry evaluation of intracranial stents in sidewall aneurysm: hemodynamic transition related to the stent design. PLoS One 9:e113762

Callaghan FM, Karkouri J, Broadhouse K, Evin M, Fletcher DF, Grieve SM (2015) Thoracic aortic aneurysm: 4D flow MRI and computational fluid dynamics model. Comput Methods Biomech Biomed Engin 18(Suppl 1):1894–1895

Carmo M, Colombo L, Bruno A, Corsi FRM, Roncoroni L et al (2002) Alteration of elastin, collagen and their cross-links in abdominal aortic aneurysms. Eur J Vasc Endovasc Surg 23:543–549

Chaikof EL, Brewster DC, Dalman RL, makaroun MS, Illig KA, Sicard GA, Timaran CH, Upchurch GR, Veith FJ (2009) The care of patients with an abdominal aortic aneurysm: the Society for Vascular Surgery practice guidelines. J Vasc Surg 50:S2–S49

Cheheltani R, Pichamuthu JE, Rao J, Weinbaum JS, Kiani MF, Vorp DA, Pleshko N (2017) Fourier transform infrared spectroscopic imaging-derived collagen content and maturity correlates with stress in the aortic wall of abdominal aortic aneurysm patients. Cardiovasc Eng Technol 8:70–80

Chen CY, Anton R, Hung MY, Menon P, Finol EA, Pekkan K (2014) Effects of intraluminal thrombus on patient-specific abdominal aortic aneurysm hemodynamics via stereoscopic particle image velocity and computational fluid dynamics modeling. J Biomech Eng 136:031001–031009

Choke E, Cockerill G, Wilson WRW, Sayed S, Dawson J, Loftus I, Thompson MM (2005) A review of biological factors implicated in abdominal aortic aneurysm rupture. Eur J Vasc Endovasc Surg 30:227–244

Choksy SA, Wilmink AB, Quick CR (1999) Ruptured abdominal aortic aneurysm in the Huntingdon district: a 10-year experience. Ann R Coll Surg Engl 81:27–31

Chong CK, How TV (2004) Flow patterns in an endovascular stent-graft for abdominal aortic aneurysm repair. J Biomech 37:89–97

Darling RC, Messina CR, Brewster DC, Ottinger LW (1977) Autopsy study of unoperated abdominal aortic aneurysms. The case for early resection. Circulation 56S:161–164

Davies PF, Dewey CF Jr, Bussolari SR, Gordon EJ, Gimbrone MA Jr (1984) Influence of hemodynamic forces on vascular endothelial function. In vitro studies of shear stress and pinocytosis in bovine aortic cells. J Clin Invest 73:1121–1129

Davis M, Harris M, Earnshaw JJ (2013) Implementation of the national health service abdominal aortic aneurysm screening program in England. J Vasc Surg 57:1440–1445

Deplano V, Meyer C, Guivier-Curien C, Bertrand E (2013) New insights into the understanding of flow dynamics in an in vitro model for abdominal aortic aneurysms. Med Eng Phys 35:800–809

Dewey CF Jr, Bussolari SR, Gimbrone MA Jr, Davies PF (1981) The dynamic response of vascular endothelial cells to fluid shear stress. J Biomech Eng 103:177–185

Di Martino ES, Bohra A, Vande Geest JP, Gupta N, Makaroun MS, Vorp DA (2006) Biomechanical properties of ruptured versus electively repaired abdominal aortic aneurysm wall tissue. J Vasc Surg 43:570–576; discussion 576

DiMartino ES, Vorp DA (2003) Effect of variation in intraluminal thrombus constitutive properties on abdominal aortic aneurysm wall stress. Ann Biomed Eng 31: 804–809

Dobrin PB, Baker WH, Gley WC (1984) Elastolytic and collagenolytic studies of arteries. Implications for the mechanical properties of aneurysms. Arch Surg 119:405–409

Dorfmann AL, Wilson C, Edgar ES, Peattie RA (2010) Evaluating patient-specific abdominal aortic aneurysm wall stress based on flow-induced loading. Biomech Model Mechanobiol 9:127–139

Doyle BJ, Grace PA, Kavanagh EG, Burke PE, Wallis F, Walsh MT, McGloughlin TM (2009) Improved assessment and treatment of abdominal aortic aneurysms: the use of 3D reconstructions as a surgical guidance tool in endovascular repair. Ir J Med Sci 178: 321–328

Dua MM, Dalman RL (2010) Hemodynamic influences on abdominal aortic aneurysm disease: application of biomechanics to aneurysm pathophysiology. Vasc Pharmacol 53(1–2):11–21

Egelhoff CJ, Budwig RS, Elger DF, Khraishi TA, Johansen KH (1999) Model studies of the flow in abdominal aortic aneurysms during resting and exercise conditions. J Biomech 32:1319–1329

Elger DF, Blackketter DM, Budwig RS, Johansen KH (1996) The influence of shape on the stresses in model abdominal aortic aneurysms. J Biomech Eng 118: 326–332

Ene F, Delassus P, Morris L (2014) The influence of computational assumptions on analysing abdominal aortic aneurysm haemodynamics. Proc Inst Mech Eng H 228:768–780

Feller KJ, Atkinson SJ, Peattie RA (2001) Quantification of flow stability in patient-based models of abdominal aortic aneurysms. ASME-BED 50:753

Figueroa CA, Vignon-Clementel IE, Jansen KE, Hughes TJR, Taylor CA (2006) A coupled momentum method for modeling blood flow in three-dimensional deformable arteries. Comput Methods Appl Mech Eng 195:5685–5706

Fillinger MF, Raghavan ML, Marra SP, Cronenwett JL, Kennedy FE (2002) In vivo analysis of mechanical wall stress and abdominal aortic aneurysm rupture risk. J Vasc Surg 36:589–597

Fillinger MF, Marra SP, Raghavan ML, Kennedy FE (2003) Prediction of rupture risk in abdominal aortic aneurysm during observation: wall stress versus diameter. J Vasc Surg 37:724–732

Finol EA, Amon CH (2001) Blood flow in abdominal aortic aneurysms: pulsatile flow hemodynamics. J Biomech Eng 123:474–484

Finol EA, Keyhani K, Amon CH (2003) The effect of asymmetry in abdominal aortic aneurysms under physiologically realistic pulsatile flow conditions. J Biomech Eng 125: 207–217

Fisher GM, Llaurado JG (1966) Collagen and elastin content in canine arteries selected from functionally different vascular beds. Circ Res 19: 394–399

Fraser KH, Meagher S, Blake JR, Easson WJ, Hoskins PR (2008) Characterization of an abdominal aortic velocity waveform in patients with abdominal aortic aneurysm. Ultrasound Med Biol 34:73–80

Freestone T, Turner RJ, Coady A, Higman DJ, Greenhalgh RM, Powell JT (1995) Inflammation and matrix metalloproteinases in the enlarging abdominal aortic aneurysm. Arterioscler Thromb Vasc Biol 15: 1145–1151

Fung Y-C (1981) Biomechanics: mechanical properties of living tissue. Springer-Verlag Inc., New York

Ganong WF (1997) Review of medical physiology, 19th edn. Appleton & Lange, Stamford, CT

Gasser TC, Gorgulu G, Folkesson M, Swedenborg J (2008) Failure properties of intraluminal thrombus in abdominal aortic aneurysm under static and pulsating mechanical loads. J Vasc Surg 48:179–188

Gasser TC, Gallinetti S, Xing X, Forsell C, Swedenborg J, Roy J (2012) Spatial orientation of collagen fibers in the abdominal aortic aneurysm's wall and its relation to wall mechanics. Acta Biomater 8: 3091–3103

Ghansah JN, Murphy JT (2004) Complications of major aortic and lower extremity vascular surgery. Semin Cardiothorac Vasc Anesth 8:335–361

Gopalakrishnan SS, Pier B, Biesheuvel A (2014) Dynamics of pulsatile flow through model abdominal aortic aneurysms. J Fluid Mech 758:150–179

Grøndal N, Søgaard R, Lindholt JS (2015) Baseline prevalence of abdominal aortic aneurysm, peripheral arterial disease and hypertension in men aged 65-74 years from a population screening study (VIVA trial). Br J Surg 102:902

Hall AJ, Busse EFG, McCarville DJ, Burgess JJ (2000) Aortic wall tension as a predictive factor for abdominal aortic aneurysm rupture: improving the selection of patients for abdominal aortic aneurysm repair. Ann Vasc Surg 14:152–157

Hardman D, Semple SI, Richards JMJ, Hoskins PR (2013) Comparison of patient-specific inlet boundary conditions in the numerical modelling of blood flow in abdominal aortic aneurysm disease. Int J Numer Method Biomed Eng 29:165–178

He CM, Roach MR (1994) The composition and mechanical properties of abdominal aortic aneurysms. J Vasc Surg 20:6–13

Hellenthal FA, Geenen IL, Teijink JA, Heeneman S, Schurink GW (2009a) Histological features of human abdominal aortic aneurysm are not related to clinical characteristics. Cardiovasc Pathol 18:286–293

Hellenthal FA, Buurman WA, Wodzig WK, Schurink GW (2009b) Biomarkers of AAA progression. Part 1:extracellular matrix degeneration. Nat Rev Cardiol 6:464–474

Heng MS, Fagan MJ, Collier JW, Desai G, McCollum PT, Chetter IC (2008) Peak wall stress measurement in elective and acute abdominal aortic aneurysms. J Vasc Surg 47:17–22

Hinnen JW, Rixen DJ, Koning OH, van Bockel JH, Hamming JF (2007) Development of fibrinous thrombus analogue for in-vitro abdominal aortic aneurysm studies. J Biomech 40:289–295

Holmes DR, Liao S, Parks WC, Thompson RW (1995) Medial neovascularization in abdominal aortic aneurysms: a histopathologic marker of aneurysmal degeneration with pathophysiologic implications. J Vasc Surg 21:761–771; discussion 771–762

Holzapfel GA, Ogden RW (eds) (2017) Biomechanics: trends in modeling and simulation. Springer-Verlag Inc, New York

Holzapfel GA, Sommer G, Regitnig P (2004) Anisotropic mechanical properties of tissue components in human atherosclerotic plaques. J Biomech Eng 126:657–665

Howard DP, Banerjee A, Fairhead JF et al (2015) Population-based study of incidence of acute abdominal aortic aneurysms with projected impact of screening strategy. J Am Heart Assoc 4:e001926

Humphrey JD (1999) Remodelling of a collagenous tissue at fixed lengths. J Biomech Eng 121:591–597

Humphrey JD (2002) Cardiovascular solid mechanics: cells, tissues, and organs. Springer-Verlag Inc, New York

Humphrey JD, Holzapfel GA (2012) Mechanics, mechanobiology, and modeling of human abdominal aorta and aneurysms. J Biomech 45:805–814

Humphrey JD, Taylor CA (2008) Intracranial and abdominal aortic aneurysms: similarities, differences, and need for a new class of computational models. Ann Rev Biomed Eng 10:221–246

Imura T, Yamamoto K, Kanamori K, Mikami T, Yasuda H (1986) Non-invasive ultrasonic measurement of the elastic properties of the human abdominal aorta. Cardiovasc Res 20:208–214

Indrakusuma R, Jalalzadeh H, Planken RN, Marquering HA, Legemate DA, Koelemay MJ, Balm R (2016) Biomechanical imaging markers as predictors of abdominal aortic aneurysm growth or rupture: a systematic review. Eur J Vasc Endovasc Surg 52: 475–486

Inzoli F, Boschetti F, Zappa M, Longo T, Fumero R (1993) Biomechanical factors in abdominal aortic aneurysm rupture. Eur J Vasc Surg 7:667–674

Karkos C, Mukhodpadhyay U, Papakostas I, Ghosh J, Thomson G, Hughes R (2000) Abdominal aortic aneurysm: the role of clinical examination and opportunistic detection. Eur J Vasc Endovasc Surg 19: 299

Kazi M, Thyberg J, Religa P, Roy J, Eriksson P, Hedin U, Swedenborg J (2003) Influence of intraluminal thrombus on structural and cellular composition of abdominal aortic aneurysm wall. J Vasc Surg 38: 1283–1292

Khanafer KM, Bull JL, Upchurch GR, Berguer R (2007) Turbulence significantly increases pressure and fluid shear stress in an aortic aneurysm model under resting and exercise flow conditions. Ann Vasc Surg 21:67–74

Khanafer KM, Bull JL, Berguer R (2009) Fluid-structure interaction of turbulent pulsatile flow within a flexible wall axisymmetric aortic aneurysm model. Eur J Mech B Fluids 28:88–102

Kung EO, Les AS, Medina F, Wicker RB, McConnell MV, Taylor CA (2011) In vitro validation of finite-element model of AAA hemodynamics incorporating realistic outlet boundary conditions. J Biomech Eng 133:041003–041011

Lanne T, Sonesson B, Bergqvist D, Bengtsson H, Gustafsson D (1992) Diameter and compliance in the male human abdominal aorta: influence of age and aortic aneurysm. Eur J Vasc Surg 6:178–184

Lederle FA (2009) The natural history of abdominal aortic aneurysm. Acta Chir Belg 109:7–12

Lederle FA, Johnson GR, Wilson SE, Ballard DJ, Jordan WD Jr, Blebea J, Littooy FN, Freischlag JA, Bandyk D, Rapp JH, Salam AA, Veterans Affairs Cooperative Study, I (2002) Rupture rate of large abdominal aortic aneurysms in patients refusing or unfit for elective repair. JAMA 287:2968–2972

Lijnen HR (2001) Plasmin and matrix metalloproteinases in vascular remodeling. Thromb Haemost 86:324–333

Lin WJ, Iafrati MD, Peattie RA, Dorfmann L (2018) Growth and remodeling with application to abdominal aortic aneurysms. J Eng Math 109. https://doi.org/10.1007/s10665-017-9915-9

Lozowy R, Kuhn D, Ducas A, Boyd A (2017) The relationship between pulsatile flow impingement and intraluminal thrombus deposition in abdominal aortic aneurysms. Cardiovasc Eng Tech 8:57–69

Lu YH, Mani K, Panigrahi B, Hsu WT, Chen CY (2016) Endoleak assessment using computational fluid dynamics and image processing methods in stented abdominal aortic aneurysm models. Comput Math Methods Med 2016:9

Maier A, Gee MW, Reeps C, Eckstein HH, Wall WA (2010) Impact of calcifications on patient-specific wall stress analysis of abdominal aortic aneurysms. Biomech Model Mechanobiol 9:511–521

Markl M, Draney MT, Hope MD, Levin JM, Chan FP, Alley MT, Pelc NJ, Herfkens RJ (2004) Time-resolved 3-dimensional velocity mapping in the thoracic aorta: visualization of 3-directional blood flow patterns in healthy volunteers and patients. J Comput Assist Tomogr 28:459–468

Marrero VL, Tichy JA, Sahni O, Jansen KE (2014) Numerical study of purely viscous non-newtonian flow in an abdominal aortic aneurysm. J Biomech Eng 136:101001–101010

van Marrewijk CJ, Leurs J, Vallabhaneni SR, Harris PL, Buth J, Laheij RJ (2005) Risk-adjusted outcome analysis of endovascular abdominal aortic aneurysm repair in a large population: how do stent-grafts compare? J Endovasc Ther 12:417–429

Martufi G, Gasser TC (2013) Review: the role of biomechanical modeling in the rupture risk assessment for abdominal aortic aneurysms. J Biomech Eng 135: 021010

McGee GS, Baxter BT, Shively VP, Chisholm R, McCarthy WJ, Flinn WR, Yao JST, Pearce WH (1991) Aneurysm or occlusive disease-factors determining the clinical course of atherosclerosis of the infrarenal aorta. Surgery 110:370–376

Mescher AM (2016) Junqueira's basic histology, text and atlas, 14th edn. McGraw-Hill Lange, New York

Moll FL, Powell JT, Fraedrich G, Verzini F, Haulon S, Waltham M, van Herwaarden JA, Holt PJE, van Keulen JW, Rantner B, Schlosser FJV, Setacci F, Ricco J-B (2011) Management of abdominal aortic aneurysms clinical practice guidelines of the European society for vascular surgery. Eur J Vasc Endovasc Surg 41:S1–S58

Mower WR, Quinones WJ, Gambhir SS (1997) Effect of intraluminal thrombus on abdominal aortic aneurysm wall stress. J Vasc Surg 26:602–608

National Center for Health Statistics (2008) www.cdc.gov/\penalty\z@nchs/\penalty\z@data/\penalty\z@nvsr/\penalty\z@nvsr56/\penalty\z@nvsr56_10.pdf

National Center for Health Statistics (2018) www.cdc.gov/\penalty\z@nchs/\penalty\z@deaths.htm

Neofytou P, Tsangaris S, Kyriakidis M (2008) Vascular wall flow-induced forces in a progressively enlarged aneurysm model. Comput Methods Biomech Biomed Engin 11:615–626

O'Leary SA, Kavanagh EG, Grace PA, McGloughlin TM, Doyle BJ (2014a) The biaxial mechanical behaviour of abdominal aortic aneurysm intraluminal thrombus: classification of morphology and the determination of layer and region specific properties. J Biomech 47:1430–1437

O'Leary SA, Healey DA, Kavanagh EG, Walsh MT, McGloughlin TM, Doyle BJ (2014b) The biaxial biomechanical behavior of abdominal aortic aneurysm tissue. Ann Biomed Eng 42:2440–2450

O'Rourke MJ, McCullough JP (2008) A comparison of the measured and predicted flowfliield in a patient-specific model of an abdominal aortic aneurysm. Proc Inst Mech Eng H 222:737–750

O'Rourke MJ, McCullough JP (2010) An investigation of the flow field within patient-specific models of an abdominal aortic aneurysm under steady inflow conditions. Proc Inst Mech Eng H 224:971–988

O'Rourke MJ, McCullough JP, Kelly S (2012) An investigation of the relationship between hemodynamics and thrombus deposition within patient-specific models of abdominal aortic aneurysm. Proc Inst Mech Eng H 226:548–564

Ouriel K, Green RM, Donayre C, Shortell CK, Elliott J, DeWeese A (1992) An evaluation of new methods of expressing aortic aneurysm size: relationship to rupture. J Vasc Surg 15:12–20

Pancheri FQ, Peattie RA, Reddy ND, Ahamed T, Lin W, Ouellette TD, Iafrati MD, Dorfmann AL (2017) Histology and biaxial mechanical behavior of abdominal aortic aneurysm tissue samples. J Biomech Eng 139:031002. https://doi.org/10.1115/1.4035261

Parashar A, Singh R, Panigrahi PK, Muralidhar K (2013) Chaotic flow in an aortic aneurysm. J Appl Phys 113:214909

Peattie RA, Asbury CL, Bluth EI, Ruberti JW (1996a) Steady flow in models of abdominal aortic aneurysms. Part I: investigation of the velocity patterns. J Ultrasound Med 15:679–688

Peattie RA, Asbury CL, Bluth EI, Riehle TJ (1996b) Steady flow in models of abdominal aortic aneurysms. Part II: wall stresses and their implications for *in vivo* thrombosis and rupture. J Ultrasound Med 15: 689–696

Peattie RA, Riehle TJ, Bluth EI (2004) Pulsatile flow in fusiform models of abdominal aortic aneurysms: flow

fields, velocity patterns and flow-induced wall stresses. J Biomech Eng 126:438–446
Perktold K (1987) On the paths of fluid particles in an axisymmetrical aneurysm. J Biomech 20:311–317
Poelma C, Watton PN, Ventikos Y (2015) Transitional flow in aneurysms and the computation of haemodynamic parameters. J R Soc Interface 12. https://doi.org/10.1098/rsif.2014.1394
Polzer S, Gasser TC (2015) Biomechanical rupture risk assessment of abdominal aortic aneurysms based on a novel probabilistic rupture risk index. J R Soc Interface 12:20150852
Polzer S, Gasser TC, Bursa J, Staffa R, Vlachovsky R, Man V, Skacel P (2013) Importance of material model in wall stress prediction in abdominal aortic aneurysms. Med Eng Phys 35:1282–1289
Raghavan ML, Fillinger MF, Marra SP, Naegelein BP, Kennedy FE (2005) Automated methodology for determination of stress distribution in human abdominal aortic aneurysm. J Biomech Eng 127:868–871
Raghavan ML, Kratzberg J, Castro de Tolosa EM, Hanaoka MM, Walker P, Da Silva ES (2006) Regional distribution of wall thickness and failure properties of human abdominal aortic aneurysms. J Biomech 39:3010–3016
Rana MS, Rubby MF, Hasan ABMT (2015) Study of physiological flow through an abdominal aortic aneurysm (AAA). Procedia Eng 105:885–892
Raut SS, Chandra S, Shum J, Finol EA (2013a) The role of geometric and biomechanical factors in abdominal aortic aneurysm rupture risk assessment. Ann Biomed Eng 41:1459–1477
Raut SS, Jana A, De Oliveira V, Muluk SC, Finol EA (2013b) The importance of patient-specific regionally varying wall thickness in abdominal aortic aneurysm biomechanics. J Biomech Eng 135:81010
Reeps C, Pelisek J, Seidi S, Schuster T, Zimmermann A, Kuehnl A, Eckstein HH (2009) Inflammatory infiltrates and neovessels are relevant sources of MMPs in abdominal aortic aneurysm wall. Pathobiology 76: 243–252
Reeps C, Maier A, Pelisek J, Heartl F, Grabher-Meier V, Wall WA, Essler M, Eckstein HH, Gee MW (2013) Measuring and modeling patient-specific distributions of material properties in abdominal aortic aneurysm wall. Biomech Model Mechanobiol 12: 717–733
Regnier P, Lareyre F, Hassen-Khodja R, Durand M, Touma J, Raffort J (2018) Sexual dysfunction after abdominal aortic aneurysm surgical repair: current knowledge and future directions. Eur J Vasc Endovasc Surg 55(2):267–280. https://doi.org/10.1016/j.ejvs.2017.11.028
RESCAN Collaborators, Brown MJ, Sweeting MJ et al (2013) Surveillance intervals for small abdominal aortic aneurysms: a meta-analysis. JAMA 309:806–813
Rodella LF, Rezzani R, Bonomini F, Peroni M, Cocchi MA, Hirtler L, Bonardelli S (2016) Abdominal aortic aneurysm and histological, clinical, radiological correlation. Acta Histochem 118:256–262
Rodriguez JF, Ruiz C, Doblaré M, Holzapfel GA (2008) Mechanical stresses in abdominal aortic aneurysms: influence of diameter, asymmetry, and material anisotropy. J Biomech Eng 130:021023
Sakalihasan N, Limet R, Defawe OD (2005) Abdominal aortic aneurysm. Lancet 365:1577–1589
Satta J, Laara E, Juvonen T (1996) Intraluminal thrombus predicts rupture of an abdominal aortic aneurysm. J Vasc Surg 23:737–739
van Schaik TG, Yeung KK, Verhagen HJ, de Bruin JL, van Sambeek MRHM, Balm R, Zeebregts CJ, van Herwaarden JA, Blankensteijn JD (2017) Long-term survival and secondary procedures after open or endovascular repair of abdominal aortic aneurysms. J Vasc Surg 66:1379–1389. https://doi.org/10.1016/j.jvs.2017.05.122
Schmid H, Grytsan A, Poshtan E, Watton PN, Itskov M (2013) Influence of differing material properties in media and adventitia on arterial adaptation–application to aneurysm formation and rupture. Comput Methods Biomech Biomed Engin 16:33–53
Scotti CM, Finol EA (2007) Compliant biomechanics of abdominal aortic aneurysms: a fluid-structure interaction study. Comput Struct 85: 1097–1113
Scotti CM, Shkolnik AD, Muluk SC, Finol EA (2005) Fluid-structure interaction in abdominal aortic aneurysms: effects of asymmetry and wall thickness. Biomed Eng Online 4:64
da Silva SE, Rodrigues AJ, Magalhães Castro de Tolosa E, Rodrigues CJ, Villas Boas do Prado G, Nakamoto JC (2000) Morphology and diameter of infrarenal aortic aneurysms: a prospective autopsy study. Cardiovasc Surg 8:526–532
Sobolewski K, Wolanska M, Bankowski E, Gacko M, Glowinski S (1995) Collagen, elastin and glycosaminoglycans in aortic aneurysms. Acta Biochim Pol 42: 301–308
Speelman L, Bohra A, Bosboom EMH, Schurink GWH, van de Vosse FN, Makaorun MS, Vorp DA (2007) Effects of wall calcifications in patient- specific wall stress analyses of abdominal aortic aneurysms. J Biomech Eng 129:105–109
von Spiczak J, Crelier G, Giese D, Kozerke S, Maintz D, Bunck AC (2015) Quantitative analysis of vortical blood flow in the thoracic aorta using 4D phase contrast MRI. PLoS One 10:e0139025
Stamatopoulos C, Papaharilaou Y, Mathioulakis DS, Katsamouris A (2010) Steady and unsteady flow within an axisymmetric tube dilatation. Exp Thermal Fluid Sci 34:915–927
Stamatopoulos C, Mathioulakis DS, Papaharilaou Y, Katsamouris A (2011) Experimental unsteady flow study in a patient-specific abdominal aortic aneurysm model. Exp Fluids 50:1695–1709
Steinman DA, Hoi Y, Fahy P et al (2013) Variability of computational fluid dynamics solutions for pressure and flow in a giant aneurysm: the ASME 2012 summer bioengineering conference CFD challenge. J Biomech Eng 135:021016–021013

Stergiopulos N, Young DF, Rogge TR (1992) Computer simulation of arterial flow with applications to arterial and aortic stenoses. J Biomech 25: 1477–1488

Stringfellow MM, Lawrence PF, Stringfellow RG (1987) The influence of aorta aneurysm geometry upon stress in the aneurysm wall. J Surg Res 42:425–433

Sumner DS, Hokanson DE, Strandness DE Jr (1970) Stress-strain characteristics and collagen-elastin content of abdominal aortic aneurysms. Surg Gynecol Obstet 130:459–466

Sun N, Leung JH, Wood NB, Hughes AD, Thom SA, Cheshire NJ, Xu XY (2009) Computational analysis of oxygen transport in a patient-specific model of abdominal aortic aneurysm with intraluminal thrombus. Br J Radiol 82(1):S18–S23

Svensjö S, Björck M, Gürtelschmid M et al (2011) Low prevalence of abdominal aortic aneurysm among 65-year-old Swedish men indicates a change in the epidemiology of the disease. Circulation 124:1118

Swedenborg J, Kazi M, Eriksson P, Hedin U (2004) Influence of the intraluminal thrombus in abdominal aortic aneurysms. Acta Chir Belg 104:606–608

Tang BT, Cheng CP, Draney MT, Wilson NM, Tsao PS, Herfkens RJ, Taylor CA (2006) Abdominal aortic hemodynamics in young healthy adults at rest and during lower limb exercise: quantification using image-based computer modeling. Am J Physiol Heart Circ Physiol 291:H668–H676

Tanios F, Gee MW, Pelisek J, Kehl S, Biehler J, Grabher-Meier V, Wall WA, Eckstein HH, Reeps C (2015) Interactions of biomechanics with extracellular matrix components in abdominal aortic aneurysm wall. Eur J Vasc Endovasc Surg 50:167–174

Taylor MG (1966) Wave transmission through an assembly of randomly branching elastic tubes. Biophys J 6:697–716

Taylor TW, Yamaguchi T (1994) Three-dimensional simulation of blood flow in an abdominal aortic aneurysm—steady and unsteady flow cases. J Biomech Eng 116:89–97

Taylor CA, Hughes TJR, Zarins CK (1998) Finite element modeling of three-dimensional pulsatile flow in the abdominal aorta: relevance to atherosclerosis. Ann Biomed Eng 26:975–987

Taylor CA, Hughes TJ, Zarins CK (1999) Effect of exercise on hemodynamic conditions in the abdominal aorta. J Vasc Surg 29:1077–1089

Thompson S, Brown L, Sweeting M, Bown M, Kim L, Glover M, Buxton M, Powell J (2013) Systematic review and meta-analysis of the growth and rupture rates of small abdominal aortic aneurysms: implications for surveillance intervals and their cost-effectiveness. Health Technol Assess 17:1–118

Tong J, Holzapfel GA (2015) Structure, mechanics and histology of intraluminal thrombi in abdominal aortic aneurysms. Ann Biomed Eng 43:1488–1501

Tong J, Cohnert T, Regitnig P, Holzapfel GA (2011) Effects of age on the elastic properties of the intraluminal thrombus and the thrombus-covered wall in abdominal aortic aneurysms: biaxial extension behavior and material modelling. Eur J Vasc Endovasc Surg 42: 207–219

Tong J, Schreifl AJ, Cohnert T, Holzapfel GA (2013) Gender differences in biomechanical properties, thrombus age, mass fraction, and clinical factors of abdominal aortic aneurysms. Eur J Vasc Endovasc Surg 45: 364–372

United States Census Bureau (2018) Percent Distribution of the Projected Population by Sex and Selected Age Groups for the United States: 2015 to 2060. www.census.gov/population/projections/data/national/2014/summarytables.html

Vande Geest JP, Wang DH, Wisniewski SR, Makaroun MS, Vorp DA (2006a) Towards a noninvasive method for determination of patient-specific wall strength distribution in abdominal aortic aneurysms. Ann Biomed Eng 34:1098–1106

Vande Geest JP, Sacks MS, Vorp DA (2006b) The effects of aneurysm on the biaxial mechanical behavior of human abdominal aorta. J Biomech 39: 1324–1334

Vande Geest JP, Dillavou ED, Di Martino ES, Oberdier M, Bohra A, Makaroun MS, Vorp DA (2006c) Gender-related differences in the tensile strength of abdominal aortic aneurysm. Ann N Y Acad Sci 1085: 400–402

Vardulaki KA, Prevost TC, Walker NM, Day NE, Wilmink ABM, Quick C, Ashton H, Scott R (1998) Growth rates and risk of rupture of abdominal aortic aneurysms. Br J Surg 85:1674–1680

Vorp DA (2007) Biomechanics of abdominal aortic aneurysm. J Biomech 40:1887–1902

Vorp DA, Vande Geest JP (2005) Biomechanical determinants of abdominal aortic aneurysm rupture. Arterioscler Thromb Vasc Biol 25:1558–1566

Vorp DA, Wang DH, Webster MW, Federspiel WJ (1998a) Effect of intraluminal thrombus thickness and bulge diameter on the oxygen diffusion in abdominal aortic aneurysm. J Biomech Eng 120:579–583

Vorp DA, Raghavan ML, Webster MW (1998b) Mechanical wall stress in abdominal aortic aneurysm: influence of diameter and asymmetry. J Vasc Surg 27: 632–639

Vorp DA, Lee PC, Wang DH, Makaroun MS, Nemoto EM, Ogawa S, Webster MW (2001) Association of intraluminal thrombus in abdominal aortic aneurysm with local hypoxia and wall weakening. J Vasc Surg 34:291–299

Wang DHJ, Makaroun M, Webster MW, Vorp DA (2001) Mechanical properties and microstructure of intraluminal thrombus from abdominal aortic aneurysm. J Biomech Eng 123:536–539

Wang DH, Makaroun MS, Webster MW, Vorp DA (2002) Effect of intraluminal thrombus on wall stress in patient-specific models of abdominal aortic aneurysm. J Vasc Surg 36:598–604

Watton PN, Hill NA (2009) Evolving mechanical properties of a model of abdominal aortic aneurysm. Biomech Model Mechanobiol 8:25–42

Watton PN, Heil M, Hill NA (2004) A mathematical model for the growth of the abdominal aortic aneurysm. Biomech Model Mechanobiol 3:98–113

Westerhof N, Bosman F, De Vries CJ, Noordergraaf A (1969) Analog studies of the human systemic arterial tree. J Biomech 2:121–143

Wilson JS, Virag L, Di Achille P, Karsaj I, Humphrey JD (2013) Biochemomechanics of intraluminal thrombus in abdominal aortic aneurysms. J Biomech Eng 135:021011

Wolf YG, Thomas WS, Brennan FJ, Goff WG, Sise MJ, Bernstein EF (1994) Computed tomography scanning findings associated with rapid expansion of abdominal aortic aneurysms. J Vasc Surg 20:529–535; discussion 535–528

Wu D, Price MD, Amarasekara HS, Green SY, Woodside SJ, Tullos A, Zhang Q, Coselli JS, LeMaireSA (2018) Unplanned readmissions after open thoracoabdominal aortic aneurysm repair. Ann Thorac Surg 105:228–234. https://doi.org/10.1016/j.athoracsur.2017.08.014

Xiang J, Tutino VM, Snyder KV, Meng H (2014) CFD: computational fluid dynamics or confounding factor dissemination? The role of hemodynamics in intracranial aneurysm rupture risk assessment. Am J Neuroradiol 35:1849–1857

Yu SCM, Chan WK, Ng BTH, Chua LP (1999) A numerical investigation on the steady and pulsatile flow characteristics in axi-symmetric abdominal aortic aneurysm models with some experimental evaluation. J Med Eng Technol 23:228–239

Zarins CK, Weisenberg E, Kolettis G, Stankunavicius R, Glagov S (1988) Differential enlargement of artery segments in response to enlarging atherosclerotic plaques. J Vasc Surg 7:386–394

Vascular Intervention: From Angioplasty to Bioresorbable Vascular Scaffold

Fengyi Du and Jiangbing Zhou

Abstract

Coronary artery disease (CAD) is the leading cause of mortality and morbidity worldwide. Clinically, CAD can be potentially managed through surgical artery bypass. However, due to the highly invasive nature, surgical intervention has been gradually replaced by percutaneous transluminal coronary angioplasty and recently by percutaneous coronary revascularization using metallic stents. However, the permanent presence of metallic scaffolds inevitably impairs arterial physiology and may induce a variety of adverse effects, such as inflammation, restenosis, thrombosis, and neoatherosclerosis. To address these limitations, revascularization using bioresorbable vascular scaffolds (BVSs) has emerged as the most promising approach. After angioplasty, BVSs provide temporarily mechanical support and are completely resorbed over defined time. This transient nature allows favorable arterial remodeling and avoids thrombosis and in-stent restenosis. However, the theoretical advantages of BVSs have yet to be demonstrated. In this chapter, we first review the evolution of nonsurgical vascular intervention approaches over the past few decades. Next, we discuss the current status of BVS development and propose potential approaches to addressing the limitations associated with the current BVSs.

1 Introduction

Blood vessels in peripheral organs consist of endothelial cells in the inner layer, vascular smooth muscle cells (SMCs) in the middle layer, and fibroblasts and matrix in the outer layer (Yancopoulos et al. 2000; Carmeliet 2003). In normal physiological conditions, blood vessels are responsible for transporting oxygen and nutrients throughout the body. These normal functions could be compromised in diseased conditions, which are often associated with endothelial cell dysfunction, inflammatory response, and proliferation and migration of SMCs toward the lumen (Ross 1999a; Libby et al. 2011; Owens et al. 2004). The aggregation of SMCs and immune cells, together with deposition of fat and cholesterol, leads to plaque building and vessel wall thickening. Over time, such chronic pathologic processes result in stenosis or vessel obstruction. Eventually, the

F. Du · J. Zhou (✉)
Departments of Neurosurgery and of Biomedical Engineering, Yale University, New Haven, CT, USA
e-mail: jiangbing.zhou@yale.edu

B. M. Fu, N. T. Wright (eds.), *Molecular, Cellular, and Tissue Engineering of the Vascular System*, Advances in Experimental Medicine and Biology 1097,
https://doi.org/10.1007/978-3-319-96445-4_9

lack of blood supply may induce significant tissue damage, leading to diseases, such as coronary artery disease (CAD), which remains as the leading cause of mortality and morbidity worldwide (Ross 1999b; Libby et al. 2011). Clinically, CAD could be potentially managed through pharmacological approaches. When the pharmacological approaches fail, vascular interventions, including surgical artery bypass or angioplasty, are needed. In this chapter, we will discuss vascular intervention approaches evolved over the past few decades, with emphasis on the emerging intervention approach involving the use of bioresorbable vascular scaffolds (BVSs).

2 Evolution of Mechanical Vascular Interventions

The first mechanical vascular intervention can be traced back to the 1970s, when percutaneous transluminal coronary angioplasty (PTCA), also called balloon angioplasty, was developed (Gruntzig 1978; Gruntzig et al. 1979) (Fig. 1). Clinically, a small guide wire is threaded across the blockage section in blood vessels. Accompanying with the wire, a pre-crimped balloon is delivered to the diseased location, where the balloon is inflated and expands the occluded coronary artery. After the procedure, the balloon is deflated and withdrawn. The introduction of PTCA revolutionized the clinical intervention of vascular diseases. However, it fails to provide long-term support to the diseased vessels and is associated with a high rate of restenosis (30–50%) (Kahn and Hartzler 1990).

To address this limitation, a small tubular wire mesh device, called bare metal stent (BMS), was invented. In clinical practice, BMS is delivered to the diseased vessel, where it provides permanent mechanical support to maintain vessel patency. Consequently, elastic recoil and constrictive remodeling are prevented. In 1994, the US Food and Drug Administration (FDA) approved the first BMS, Palmaz-Schatz balloon-expandable stent (Fischman et al. 1991; Schatz et al. 1991). The application of BMSs led to a dramatic reduction of restenosis. Unfortunately, the presence of bare metal often induces neointimal proliferation as a result of inflammatory response, leading to deposition of excess extracellular matrix proteins. This deposition ultimately causes re-obstruction of vessel lumen in 20–30% patients (Mani et al. 2007).

To reduce the risk of neointimal hyperplasia, a variety of drug-eluting stents (DESs), which carry immune-suppressant or cytotoxic agents, were developed in the late 1990s (Morice et al. 2002; Schofer et al. 2003). DESs not only provide mechanical support to maintain vessel patency but also release therapeutic agents, such as everolimus, sirolimus, zotarolimus, biolimus, tacrolimus, and paclitaxel, over 10–30 days in a controlled manner to prevent neointimal hyperplasia (Htay and Liu 2005). Encapsulation of therapeutic agents in DESs has been initially achieved through surface coating with permanent (also called non-erodible or durable) polymers, in which therapeutic molecules are loaded. Ini-

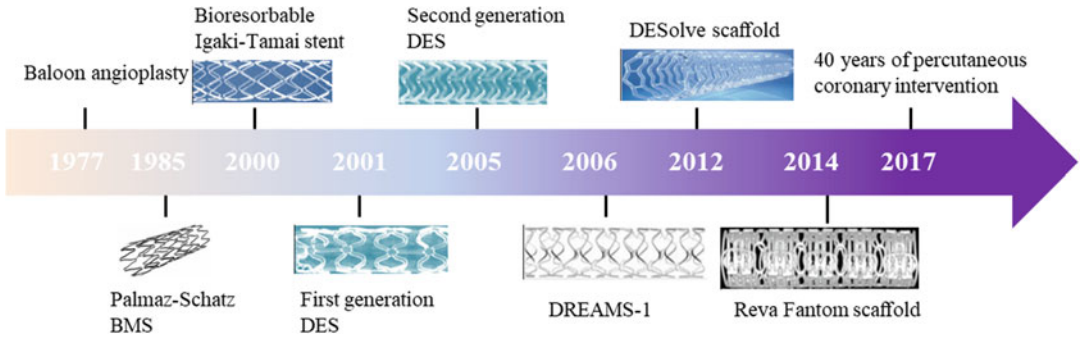

Fig. 1 Evolution of vascular intervention

tial clinical evidence showed that implantation of such devices significantly decreased the rate of restenosis, leading to 50–70% reduction in the need for repeat revascularization (Morice et al. 2002; Grube et al. 2003). However, clinical evidence also suggested that the presence of durable polymers increases in-stent thrombosis (Stettler et al. 2007). The rate of in-stent thrombosis in patients receiving DESs reached 0.36–0.6%, which is greater than that for patients receiving BMSs (Daemen et al. 2007; Wenaweser et al. 2008; Pinto Slottow et al. 2008). Apparently, the long-term presence of permanent polymers contributes to the adhesion and activation of leukocytes, which, in turn, leads to local chronic inflammation and hypersensitivity, and, eventually, increases the risk of in-stent thrombosis and restenosis (McFadden et al. 2004; Claessen et al. 2009). Learning from this lesson, the second-generation DESs were fabricated with biodegradable polymers loaded with safer therapeutic molecules. Clinical evidence showed that the second-generation DESs have improved safety and efficacy compared to the first-generation DESs (Fajadet et al. 2006; Wiemer et al. 2010).

Despite the promise, metallic DESs suffer from an inherited limitation due to the use of metal-based, nonbiodegradable backbones. After therapeutic molecules are released, the presence of metallic devices continuously presents pressure against the vessel wall, which often induces thrombosis and in-stent restenosis over time (Condado et al. 1997). To provide improved alternatives, recent efforts have been focusing on developing next-generation bioscaffolds using bioresorbable materials.

3 Bioresorbable Vascular Scaffold (BVS)

BVSs are small tubular wire mesh devices that are fabricated using bioresorbable materials. After angioplasty, BVSs provide mechanical support to diseased vessels for a period that is sufficient for vasculature self-healing and functional restoration (McFadden et al. 2004; Hofma et al. 2006). With time, BVSs are degraded and excreted from the body. To satisfy clinical applications, BVSs need to be designed to fulfill several criteria. First, during the implantation phase, BVSs should be capable of providing adequate radial strength and minimal acute recoil to restore vessel patency. Second, during the retention phase, BVSs should exhibit the biocompatibility and controlled drug release ability that are favorable for prevention of restenosis and thrombosis. Third, during the decomposition phase, BVSs should facilitate the revascularization via gradual disintegration of spatial structure. In addition, the degradation products must be nontoxic and can be safely eliminated from the body. To enable visualization, it is ideal that BVSs can be designed for noninvasively imaging by approaches that are routinely used in clinic, such as optical coherence tomography (OCT), computed tomography (CT), or magnetic resonance (MR) (de Ribamar Costa et al. 2016).

BVCs can be made of biodegradable polymers. The bioabsorbability of a given polymeric BVS is determined by the chemical structure and composition of the selected biomaterial as well as the strut design (Vert 2009; Onuma and Serruys 2011). The most often used polymer for BVC fabrication is poly-L-lactic acid (PLLA). BVSs consisting of PLLA are amorphous and semicrystalline by nature (Oberhauser et al. 2009). The crystalline feature makes the devices to be robust enough to provide mechanical support, while the amorphous property allows dispersing cargo therapeutics throughout the device, a feature that is favorable for controlled drug release. After implantation, PLLA undergoes hydrolytic degradation, resulting in production of lactic acid. Through the Krebs cycle, lactic acid is metabolized into pyruvate and then carbon dioxide and water, which are eventually excreted by the kidney (H_2O) and lung (CO_2) (Onuma and Serruys 2011; Boix 2003). PLLA with low molecular weight may induce inflammatory reactions, whereas PLLA with a molecular mass > 300 kDa is less immunoreactive (Lincoff et al. 1997). The duration of PLLA-based BVSs in the body depends on the crystallization degree of the polymer and varies from 2 to 4 years. In addition to

PLLA, several other biomaterials, such as poly-lactic acid (PLA; poly-D,L-lactic acid, PDLLA), poly(desaminotyrosyl-tyrosine ethyl ester) carbonate, and poly-anhydride ester (PAE), have also been explored (Ormiston et al. 2008; Grube 2009; Jabara 2009).

Bioabsorbable BVCs can also be fabricated using biodegradable metals, such as magnesium or magnesium alloy (Peuster et al. 2001; Moravej et al. 2010; Erbel et al. 2007). After implantation, magnesium element in BVSs undergoes anodic reaction, resulting in magnesium hydroxide, which is further converted to calcium phosphate with high water content. This conversion process may take over 1 year. The hydroxyapatite by-product eventually is eliminated by macrophages (Wittchow et al. 2013). In addition to magnesium, iron has also been explored for BVS fabrication (Peuster et al. 2006; Waksman et al. 2008).

The first BVS was designed and fabricated by Gammon and colleagues in the early 1980s (Gammon et al. 1991). Preclinical tests showed that implantation of this BVS did not induce obvious inflammatory response or thrombosis, and the endothelialization of stents took ~2 weeks. The first BVS made for human clinical trials is Igaki-Tamai stent, which was fabricated using PLLA monofilaments (molecular weight, 183 kDa) in a zigzag helical coil configuration (Tsuji et al. 2001). The zigzag configuration was designed to reduce vascular injury that could induce thrombus deposition and neointimal proliferation. Results from clinical trials found that Igaki-Tamai stents effectively reduced stenosis and caused less intimal hyperplasia than metallic stents (Tamai et al. 2017; Tamai 2004). The first drug-eluting BVS evaluated in clinical trials is Absorb BVS made by Abbott Vascular. Absorb BVS is fabricated using PLA and releases ~80% of cargo everolimus in the first 30 days and is fully bioabsorbed in ~18 months. Clinical results suggested that implantation of the Absorb BVSs induced minimal intrastent neointimal hyperplasia and a low stent area obstruction (Ormiston et al. 2008). In order to enable imaging, a radiopaque REVA scaffold was developed by Reva Medical Inc. using poly(desaminotyrosyl-tyrosine ethyl ester) carbonate, which made to clinical trials in 2007 (Grube 2009). The REVA scaffold utilizes a unique "slide and lock" geometry design that provides flexibility and strength. BVSs could be also fabricated to load and release more than one therapeutic molecule. IDEAL™ biodegradable stent, which was developed by Bioabsorbable Therapeutics using PAE, is designed to load with both sirolimus and salicylic acid to provide anti-inflammatory and antiproliferative effects. Unfortunately, the first-generation IDEAL™ stent failed to demonstrate the antiproliferative property in clinic (Jabara 2009). The first metallic BVS was fabricated by Biotronik (Berlin, Germany). Biotronik's first-generation metallic BVS is made using magnesium alloy WE43 and was shown to be effective and safe in human patients (Erbel et al. 2007). Biotronik's new-generation BVS is made with a modified composition of magnesium alloy with a PLA/drug coating layer and has shown considerable improvement in clinical efficacy (Kitabata et al. 2014) (31). Major BVSs that have been tested in clinic or are currently under clinical evaluation are described in Table 1.

To date, four BVSs, including Absorb, Desolve, ART Pure, and Magmaris, have received approval from the Conformité Européenne (CE) in Europe for clinical applications. Absorb, Desolve, and ART Pure are fabricated using PLLA, and Magmaris consisted of magnesium (Sotomi et al. 2017). Appearance and chemical/physical properties of these devices are illustrated in Fig. 2. Absorb BVS was also approved by the US FDA for clinical use in 2016.

4 Challenges and Prospective

Compared to metallic stents, BVSs potentially have several major advantages. First, the fully bioresorbable scaffolds provide greater potential for drug encapsulation and controlled drug release. Second, without metallic materials, BVSs are compatible with optical, CT, or MR imaging and, thus, have the flexibility to be engineered for clinical imaging. Third, due to the bioresorbability, BVSs are gradually eliminated in the body

Table 1 Currently available and upcoming BVSs

Classification	Scaffold	Manufacturer	Strut material	Eluted drug	Radiopacity	Resorption time (months)	Current status
Metallic	AMS-1	Biotronik	Mg alloy	None	None	<4	Discontinued
	DREAMS-1	Biotronik	Magnesium/PLGA	Paclitaxel	None	9	Clinical trials
	DREAMS-2	Biotronik	Magnesium/PLLA	Sirolimus	Metallic markers	9	Clinical trial to be commenced
	FADES	Zorion medical	Magnesium/PLGA	Unknown	Unknown	6–12	Preclinical test
	Unity BDS	QualiMed	Magnesium/PLLA	Sirolimus	Unknown	12	Preclinical test
Polymeric	Igaki-Tamai	Kyoto medical	PLLA	None	Gold markers	24–36	CE mark for peripheral use
	Absorb 1.0	Abbott vascular	PLLA	Everolimus	Platinum markers	18–24	Discontinued
	Absorb 1.1	Abbott vascular	PLLA	Everolimus	Platinum markers	24–48	CE mark
	DESolve	Elixir medical	PLLA	Novolimus	Metallic markers	12–24	CE mark
	DESolve Cx	Elixir medical	PLLA	Novolimus	Metallic markers	12–24	Clinical trials
	Fortitude	Amaranth	PLLA	None	None	3–6	Clinical trials
	APTITUDE	Amaranth	PLLA	Sirolimus	None	3–6	Clinical trials
	ART18AZ	ART	PDLLA	None	None	3–6	Clinical trials
	MeRes	Meril life	PLLA/PDLLA	Sirolimus	Platinum	24	Clinical trials
	Xinsorb	Huaan biotech	PLLA/PDLLA	Sirolimus	None	24–36	Clinical trials
	ON-ABS	OrbusNeich	PLLA/PDLLA	Sirolimus	None	Unknown	Preclinical test
	ReZolve	Reva medical	PTD-PC	Sirolimus	Radiopaque scaffold	4–6	Clinical trials
	Fantom	Reva medical	PTD-PC	Sirolimus	Iodine content	Unknown	Clinical trials

Note: *CE* Conformité Européenne, *PDLLA* poly-DL-lactic acid, *PLGA* poly lactic-co-glycolic acid, *PLLA* poly-L-lactic acid, *PTD-PC* poly-tyrosine-derived polycarbonate

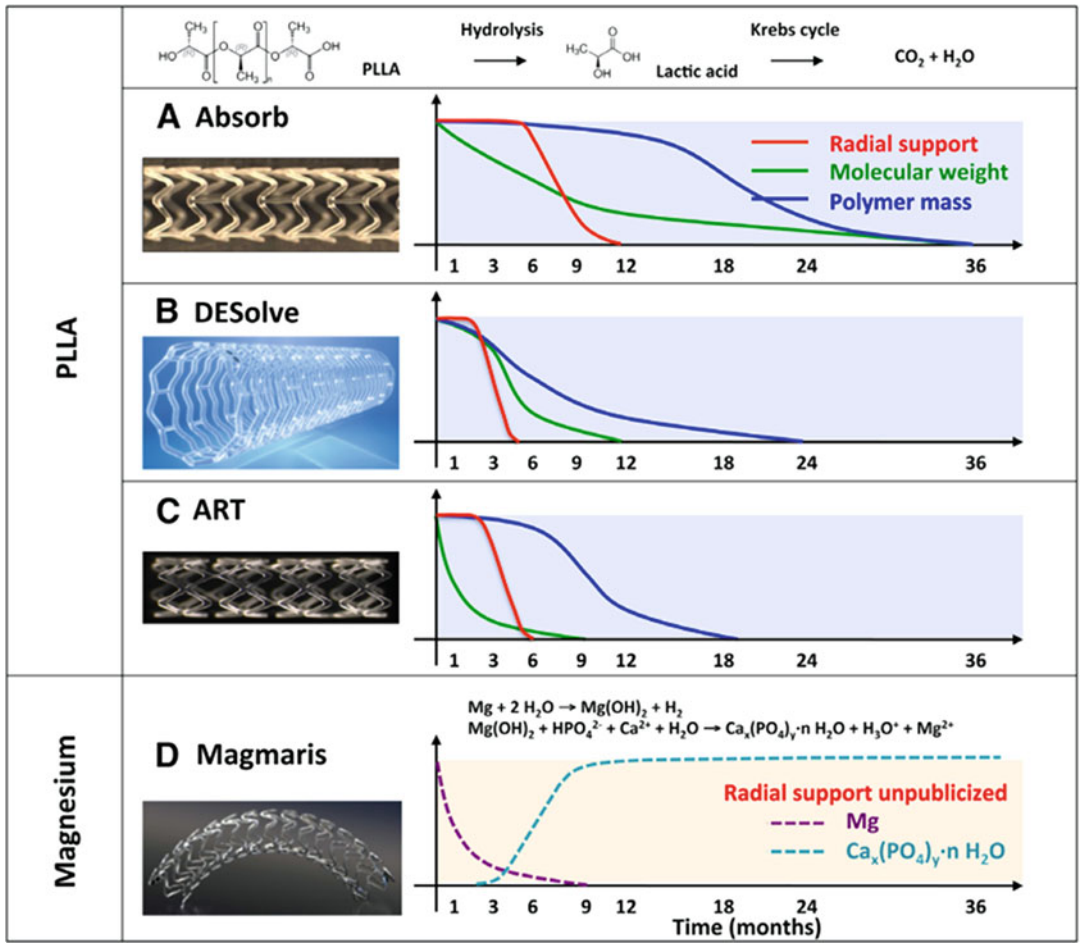

Fig. 2 Biodegradation process of CE-mark-approved bioresorbable scaffolds. Permission from reference Tamai et al. (2017)

over time, leaving no or minimal residual parts. This feature not only allows favorable arterial remodeling and future surgical revascularization but also avoids thrombosis and in-stent restenosis that are associated with metallic stents. However, the theoretical advantages of BVSs have yet to be demonstrated in clinic. Recently, results from the ABSORB III trial showed that, compared to Xience everolimus-eluting metallic stent, Absorb BVS has comparable efficacy but was associated with higher rates of thrombosis and target-lesion failure. Those observations, together with a higher price tag over the traditional metallic DES, led to the termination of Absorb BVS production in 2017, only 1 year after its approval by the US FDA. To fully fulfill the great promise of BVSs, many aspects to BVS design, fabrication, and functionalization need improvement.

1. Development of next-generation bioresorbable materials with enhanced mechanical properties and biocompatibility. Most existing BVSs are fabricated using polymeric materials. Compared to metals, the existing polymeric materials don't have comparable mechanical properties. To provide adequate radial strength and avoid acute recoil, the first-generation polymeric BVSs are fabricated in thickness of 150–200 μm with a crossing profile of 1.4–1.8 mm, which are significantly greater than those for metallic stents (~80 μm for thickness and ~1.0 mm

for crossing profile). In addition, compared to metallic stents, polymeric BVSs have less overexpanding capacity (Iqbal et al. 2014). These mechanical features not only cause a variety of delivery challenges, such as the need for very precise sizing and the difficulty in using in small or tortuous and noncompliant coronary vessels, but also induce many side effects, such as disruption of laminar blood flow and stimulation of thrombus formation (Tenekecioglu et al. 2016). The biocompatibility of polymeric materials may also need to be further improved. Polymeric materials that have been explored for BVS fabrication, including PLLA, PLA, polycarbonate, and PAE, are generally safe for clinical use. However, they may also induce side effects. In case that PLLA or PLA is used, degradation of BVSs results in production of a large amount of lactic acid, which may induce significant local acidosis and inflammation. To resolve all the problems discussed about, design and synthesis of novel polymers with enhanced mechanic properties and safety are warranted. Alternatively, BVCs may be fabricated using existing polymers but with incorporation of metallic or ceramic materials (Wang and Gale 2013; Wang 2011).

2. Improvement in BVC design and material processing techniques. Without changing materials, the radial strength of polymeric BVSs could be potentially enhanced through innovative design or material processing techniques (Sotomi et al. 2017). For example, a unique hybrid cell design with close cells at the edges and open cells along the length helps reduce the strut thickness and crossing profile of MeRes™ BVCs down to 100 μm and 1.2 mm. With improved processing techniques, such as annealing, stretch blow molding, spinning, and microbraiding, several new-generation BVCs with thinner struts have also been developed and are being tested in clinic (Abizaid 2016a; b; Seth 2016; Colombo 2016; Xu 2016). Early results from these trials have shown promise.
3. Functionalization of BVCs to promote vessel self-healing (Tesfamariam 2016). The current generation of BVCs was designed to carry immune-suppressants, such as sirolimus, and/or cytotoxic agents, such as paclitaxel. It has been shown that continuous release of those agents would delay or inhibit the formation of endothelial monolayer, which impedes the restoration of normal vascular physiological functions. Further improved BVCs could be potentially achieved by equipping BVSs with re-endothelialization agents.

5 Summary

Since the introduction of PTCA, vascular intervention approaches have seen several generations of evolvement. Among them, BVS represents the most exciting and promising one. However, the great promise of BVS has not been fulfilled. Continuous efforts are needed to address the major issues identified in clinical trials. It is anticipated that, with further improvement in material properties and device design, BVS will significantly enhance clinical management of vascular diseases.

References

Abizaid A (2016a) Desolve Nx, Cx and Amity: unique properties and results from 150 μm to 120 μm. Presented at TCT. November 1, 2016

Abizaid A (2016b) FANTOM II: six-month and nine-month clinical and angiographic results with a radiopaque desaminotyrosine polycarbonate-based sirolimus-eluting bioresorbable vascular scaffold in patients with coronary artery disease. Presented at TCT. November 1, 2016

Boix V (2003) Polylactic acid implants. A new smile for lipoatrophic faces? AIDS 17(17):2533–2535

Carmeliet P (2003) Blood vessels and nerves: common signals, pathways and diseases. Nat Rev Genet 4(9):710–720

Claessen BE, Beijk MA, Legrand V, Ruzyllo W, Manari A, Varenne O, Suttorp MJ, Tijssen JG, Miquel-Hebert K, Veldhof S, Henriques JP, Serruys PW, Piek JJ (2009) Two-year clinical, angiographic, and intravascular ultrasound follow-up of the XIENCE V everolimus-eluting stent in the treatment of patients with de novo native coronary artery lesions: the SPIRIT II trial. Circ Cardiovasc Interv 2(4):339–347

Colombo A (2016) FORTITUDE: Nine-month clinical, angiographic, and OCT results with an amorphous

PLLA-based sirolimus-eluting bioresorbable vascular scaffold in patients with coronary artery disease. Presented at TCT. November 1, 2016

Condado JA, Waksman R, Gurdiel O, Espinosa R, Gonzalez J, Burger B, Villoria G, Acquatella H, Crocker IR, Seung KB, Liprie SF (1997) Long-term angiographic and clinical outcome after percutaneous transluminal coronary angioplasty and intracoronary radiation therapy in humans. Circulation 96(3):727–732

Daemen J, Wenaweser P, Tsuchida K, Abrecht L, Vaina S, Morger C, Kukreja N, Juni P, Sianos G, Hellige G, van Domburg RT, Hess OM, Boersma E, Meier B, Windecker S, Serruys PW (2007) Early and late coronary stent thrombosis of sirolimus-eluting and paclitaxel-eluting stents in routine clinical practice: data from a large two-institutional cohort study. Lancet 369(9562):667–678

Erbel R, Di Mario C, Bartunek J, Bonnier J, de Bruyne B, Eberli FR, Erne P, Haude M, Heublein B, Horrigan M, Ilsley C, Bose D, Koolen J, Luscher TF, Weissman N, Waksman R, Investigators P-A (2007) Temporary scaffolding of coronary arteries with bioabsorbable magnesium stents: a prospective, non-randomised multicentre trial. Lancet 369:1869–1875

Fajadet J, Wijns W, Laarman GJ, Kuck KH, Ormiston J, Munzel T, Popma JJ, Fitzgerald PJ, Bonan R, Kuntz RE, Investigators EI (2006) Randomized, double-blind, multicenter study of the Endeavor zotarolimus-eluting phosphorylcholine-encapsulated stent for treatment of native coronary artery lesions: clinical and angiographic results of the ENDEAVOR II trial. Circulation 114(8):798–806

Fischman D, Savage M, Zalewski A, Goldberg S (1991) Overview of the Palmaz-Schatz stent. J Invasive Cardiol 3(2):75–84

Gammon RS, Chapman GD, Agrawal GM et al (1991) Mechanical features of the Duke biodegradable intravascular stent. JACC 17:235A

Grube E (2009) Bioabsorbable stent. The Boston scientific and REVA technology. EuroPCR, Barcelona, pp 19–22

Grube E, Silber S, Hauptmann KE, Mueller R, Buellesfeld L, Gerckens U, Russell ME (2003) TAXUS I: six- and twelve-month results from a randomized, double-blind trial on a slow-release paclitaxel-eluting stent for de novo coronary lesions. Circulation 107(1): 38–42

Gruntzig A (1978) Transluminal dilatation of coronary-artery stenosis. Lancet 1(8058):263

Gruntzig AR, Senning A, Siegenthaler WE (1979) Nonoperative dilatation of coronary-artery stenosis: percutaneous transluminal coronary angioplasty. N Engl J Med 301(2):61–68

Hofma SH, van der Giessen WJ, van Dalen BM et al (2006) Indication of long-term endothelial dysfunction after sirolimus-eluting stent implantation. Eur Heart J 27:166–170

Htay T, Liu MW (2005) Drug-eluting stent: a review and update. Vasc Health Risk Manag 1(4):263–276

Iqbal J, Onuma Y, Ormiston J, Abizaid A, Waksman R, Serruys P (2014) Bioresorbable scaffolds: rationale, current status, challenges, and future. Eur Heart J 35(12):765–776

Jabara R (2009) Poly-anhydride based on salicylic acid and adipic acid anhydride Barcelona, vol 25. EuroPCR, Spain

Kahn JK, Hartzler GO (1990) Frequency and causes of failure with contemporary balloon coronary angioplasty and implications for new technologies. Am J Cardiol 66(10):858–860

Kitabata H, Waksman R, Warnack B (2014) Bioresorbable metal scaffold for cardiovascular application: current knowledge and future perspectives. Cardiovasc Revasc Med 15(2):109–116

Libby P, Ridker PM, Hansson GK (2011) Progress and challenges in translating the biology of atherosclerosis. Nature 473:317–325

Lincoff AM, Furst JG, Ellis SG, Tuch RJ, Topol EJ (1997) Sustained local delivery of dexamethasone by a novel intravascular eluting stent to prevent restenosis in the porcine coronary injury model. J Am Coll Cardiol 29(4):808–816

Mani G, Feldman MD, Patel D, Agrawal CM (2007) Coronary stents: a materials perspective. Biomaterials 28(9):1689–1710

McFadden EP, Stabile E, Regar E, Cheneau E, Ong AT, Kinnaird T, Suddath WO, Weissman NJ, Torguson R, Kent KM, Pichard AD, Satler LF, Waksman R, Serruys PW (2004) Late thrombosis in drug-eluting coronary stents after discontinuation of antiplatelet therapy. Lancet 364(9444):1519–1521

Moravej M, Prima F, Fiset M et al (2010) Electroformed iron as new biomaterial for degradable stents: development process and structure–properties relationship. Acta Biomater 6:1726–1735

Morice MC, Serruys PW, Sousa JE, Fajadet J, Ban Hayashi E, Perin M, Colombo A, Schuler G, Barragan P, Guagliumi G, Molnar F, Falotico R, RAVEL Study Group. Randomized Study with the Sirolimus-Coated Bx Velocity Balloon-Expandable Stent in the Treatment of Patients with de Novo Native Coronary Artery Lesions (2002) A randomized comparison of a sirolimus-eluting stent with a standard stent for coronary revascularization. N Engl J Med 346(23): 1773–1780

Oberhauser JP, Hossainy S, Rapoza RJ (2009) Design principles and performance of bioresorbable polymeric vascular scaffolds. EuroIntervention 5(Suppl F): F15–F22

Onuma Y, Serruys PW (2011) Bioresorbable scaffold: the advent of a new era in percutaneous coronary and peripheral revascularization? Circulation 123: 779–797

Ormiston JA, Serruys PW, Regar E, Dudek D, Thuesen L, Webster MW, Onuma Y, Garcia-Garcia HM, McGreevy R, Veldhof S (2008) A bioabsorbable everolimus-eluting coronary stent system for patients with single de-novo coronary artery lesions (ABSORB): a prospective open-label trial. Lancet 371(9616):899–907

Owens GK, Kumar MS, Wamhoff BR (2004) Molecular regulation of vascular smooth muscle cell differentiation in development and disease. Physiol Rev 84: 767–801

Peuster M, Wohlsein P, Brügmann M et al (2001) A novel approach to temporary stenting: degradable cardiovascular stents produced from corrodible metal-results 6–18 months after implantation into New Zealand white rabbits. Heart 86:563–569

Peuster M, Hesse C, Schloo T, Fink C, Beerbaum P, von Schnakenburg C (2006) Long-term biocompatibility of a corrodible peripheral iron stent in the porcine descending aorta. Biomaterials 27(28):4955–4962

Pinto Slottow TL, Steinberg DH, Roy PK, Buch AN, Okabe T, Xue Z, Kaneshige K, Torguson R, Lindsay J, Pichard AD, Satler LF, Suddath WO, Kent KM, Waksman R (2008) Observations and outcomes of definite and probable drug-eluting stent thrombosis seen at a single hospital in a four-year period. Am J Cardiol 102(3):298–303

de Ribamar Costa J et al (2016) Initial results of the FANTOM 1 trial: a first-in-man evaluation of a novel, radiopaque sirolimus-eluting bioresorbable vascular scaffold. J Am Coll Cardiol 67:232–232

Ross R (1999a) Atherosclerosis-an inflammatory disease. N Engl J Med 340:115–126

Ross R (1999b) Mechanisms of disease—atherosclerosis—an inflammatory disease. New Engl J Med 340(2):115–126

Schatz RA, Baim DS, Leon M, Ellis SG, Goldberg S, Hirshfeld JW, Cleman MW, Cabin HS, Walker C, Stagg J et al (1991) Clinical experience with the Palmaz-Schatz coronary stent. Initial results of a multicenter study. Circulation 83(1):148–161

Schofer J, Schluter M, Gershlick AH, Wijns W, Garcia E, Schampaert E, Breithardt G, Investigators ES (2003) Sirolimus-eluting stents for treatment of patients with long atherosclerotic lesions in small coronary arteries: double-blind, randomised controlled trial (E-SIRIUS). Lancet 362(9390):1093–1099

Seth A (2016) MeRes100—design specifications and the 6-months MeRes-1 results. Presented at TCT. November 1, 2016

Sotomi Y, Onuma Y, Collet C, Tenekecioglu E, Virmani R, Kleiman NS, Serruys PW (2017) Bioresorbable scaffold: the emerging reality and future directions. Circ Res 120(8):1341–1352

Stettler C, Wandel S, Allemann S, Kastrati A, Morice MC, Schomig A, Pfisterer ME, Stone GW, Leon MB, de Lezo JS, Goy JJ, Park SJ, Sabate M, Suttorp MJ, Kelbaek H, Spaulding C, Menichelli M, Vermeersch P, Dirksen MT, Cervinka P, Petronio AS, Nordmann AJ, Diem P, Meier B, Zwahlen M, Reichenbach S, Trelle S, Windecker S, Juni P (2007) Outcomes associated with drug-eluting and bare-metal stents: a collaborative network meta-analysis. Lancet 370(9591):937–948

Tamai H (2004) Biodegradable stents four year follow-up. Presentation at TCT

Tamai H, Igaki K, Kyo E, Kosuga K, Kawashima A, Matsui S, Komori H, Tsuji T, Motohara S, Uehata H (2017) Initial and 6-month results of biodegradable poly-l-lactic acid coronary stents in humans. Circulation 102(4):399–404

Tenekecioglu E, Poon EK, Collet C, Thondapu V, Torii R, Bourantas CV, Zeng Y, Onuma Y, Ooi AS, Serruys PW, Barlis P (2016) The nidus for possible thrombus formation: insight from the microenvironment of bioresorbable vascular scaffold. JACC Cardiovasc Interv 9:2167–2168

Tesfamariam B (2016) Bioresorbable vascular scaffolds: biodegradation, drug delivery and vascular remodeling. Pharmacol Res 107:163–171

Tsuji T, Tamai H, Igaki K et al (2001) Biodegradable polymeric stent. Curr Interv Cardiol Rep 3: 10–17

Vert M (2009) Bioabsorbable polymers in medicine: an overview. EuroIntervention 5(suppl F):F9–F14

Waksman R, Pakala R, Baffour R, Seabron R, Hellinga D, Tio FO (2008) Short-term effects of biocorrodible iron stents in porcine coronary arteries. J Interv Cardiol 21(1):15–20

Wang Y (2011) Stent formed from bioerodible metal-bioceramic composite. US Patent Appl. No: 13/155936, Filed on 8 June 2011

Wang Y, Gale DC (2013) Methods of forming polymer-bioceramic composite medical devices with bioceramic particles. US Patent number 8,425,591, issued 23 April 2013

Wenaweser P, Daemen J, Zwahlen M, van Domburg R, Juni P, Vaina S, Hellige G, Tsuchida K, Morger C, Boersma E, Kukreja N, Meier B, Serruys PW, Windecker S (2008) Incidence and correlates of drug-eluting stent thrombosis in routine clinical practice. 4-year results from a large 2-institutional cohort study. J Am Coll Cardiol 52(14):1134–1140

Wiemer M, Serruys PW, Miquel-Hebert K, Neumann FJ, Piek JJ, Grube E, Haase J, Thuesen L, Hamm C (2010) Five-year long-term clinical follow-up of the XIENCE V everolimus eluting coronary stent system in the treatment of patients with de novo coronary artery lesions: the SPIRIT FIRST trial. Catheter Cardiovasc Interv 75(7):997–1003

Wittchow E, Adden N, Riedmüller J, Savard C, Waksman R, Braune M (2013) Bioresorbable drug-eluting magnesium-alloy scaffold: design and feasibility in a porcine coronary model. EuroIntervention 8:break 1441–1450

Xu B (2016) FIRESORB PLLA-based sirolimus-eluting scaffold: 6-month FUTURE-I results. Presented at TCT. November 1, 2016

Yancopoulos GD, Davis S, Gale NW, Rudge JS, Wiegand SJ, Holash J (2000) Vascular-specific growth factors and blood vessel formation. Nature 407(6801): 242–248

On the Physics Underlying Longitudinal Capillary Recruitment

Jacques M. Huyghe

Abstract

Numerous researchers have found that capillary vessel haematocrit depends on the vasodilatory state of the arterioles. At rest, vessel haematocrit is down to 15 %, suggesting a red blood cell velocity three times higher than the plasma velocity. This finding is analysed in the context of present understanding of propulsion of red blood cells (RBCs) and plasma by means of the arteriovenous pressure gradient. Interfacial forces between the red blood cells and the plasma are proposed as a rational explanation of the observed red blood cell velocities. While the arteriovenous pressure gradient across the capillaries propels the red blood cell and the plasma jointly, interfacial forces along the red blood cell membrane can propel RBCs at the cost of the plasma. Different options are explored for the physical origin of these interfacial forces and oxygen gradients are found to be the most probable source.

J. M. Huyghe (✉)
Bernal Institute, University of Limerick, Limerick, Ireland

Department of Mechanical Engineering, Eindhoven University of Technology, Eindhoven, The Netherlands
e-mail: jacques.huyghe@ul.ie

1 Introduction

Discharge haematocrit is defined as the volume of RBCs over total volume of a blood sample. Normal human discharge haematocrit values for males are 42%–54% and for females 38%–46 %. Because RBCs tend to flow in the centre of a lumen, the average speed of RBCs is higher than that of plasma. This means that if one takes a snapshot of a microcirculatory bed, the volume occupied by RBCs divided by the lumen volume on the snapshot yields a haematocrit value lower than the discharge haematocrit named above. This value, named vessel haematocrit, becomes lower as one moves to smaller and smaller vessels. This is known as the Fåhraeus effect (Martini et al. 1930; Fåhræus and Lindqvist 1931; Pries et al. 1986). In blood vessels with diameters less than 500 μm, the vessel hematocrit decreases with decreasing capillary diameter. If the average vessel heamatocrit in a blood compartment is H_v and the blood flowing through the compartment has a discharge haematocrit of H_d, then the ratio of the average velocity of the RBCs v_{RBC} over the average velocity of the plasma v_p is

$$\frac{v_{\mathrm{RBC}}}{v_p} = \frac{H_d}{H_v} \tag{1}$$

B. M. Fu, N. T. Wright (eds.), *Molecular, Cellular, and Tissue Engineering of the Vascular System*, Advances in Experimental Medicine and Biology 1097,
https://doi.org/10.1007/978-3-319-96445-4_10

The haemotocrit decreases up to the smallest vessels, the capillaries, meaning that nowhere in the circulation is the ratio $\frac{v_{RBC}}{v_p}$ higher than in the capillaries. This finding is surprising considering that the diameter of mammalian RBCs exceeds the diameter of capillaries by on average 25% (Snyder and Sheafor 1999). The capillary bed serves as a large surface area to allow blood tissue interchange of O_2 and other substances. RBCs deform into various shapes to accommodate this mismatch in size (Skalak and Branemark 1969), mostly the parachute shape. In addition, there is another dependency of the vessel haematocrit that pops up on the level of capillaries. Vessel haematocrit appears to depend on vasodilation of the feeding arterioles (Klitzman and Duling 1979; Sarelius and Duling 1982; Poole et al. 1997; Frisbee and Barclay 1998; Kindig and Poole 1998; Kindig et al. 2002; Copp et al. 2009). At rest, when arterioles are in vasoconstricted state, the vessel heamatocrit drops to 10–15 %. In vasodilated state it rises to 35–40 % (Fig. 1). This indicates that the largest ratio of RBC velocity over plasma velocity is observed when the arteriovenous pressure drop is at its lowest. Indeed, when the arterioles are constricted, most of the arteriovenous pressure drop is concentrated on the arterioles and not on the capillaries.

2 Capillary Recruitment

Some researchers link the varying value of capillary vessel haematocrit to the phenomenon of capillary recruitment (Poole et al. 2013). Capillary recruitment is concept that has been around for a hundred years. August and Marie Krogh applied O_2 diffusion theory from the lung to skeletal muscle. This changed the manner in which scientists viewed capillary bed structure and function. In a series of papers that led to his being awarded the 1920 Nobel Prize in Physiology or Medicine, Krogh (1919a,b) made the following proposals: (1) intramyocyte PO_2 decreases systematically with increasing distance from the nearest capillary; (2) in resting muscle, most capillaries do not support RBC flux and are constricted or collapsed (no RBCs or plasma in their lumen); and (3) to support the increased metabolic demands of contractions and reduce diffusion distances to intramyocyte mitochondria, more capillaries are "recruited" and hence support RBC flux. Since the time of Krogh, experimental techniques have improved dramatically, and the concept of capillary recruitment has been thoroughly reviewed. According to present insights, a small proportion of capillaries may

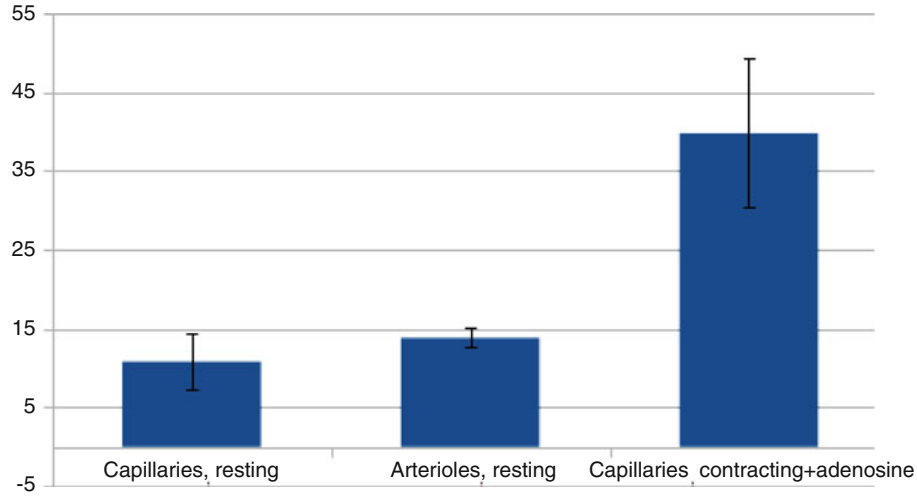

Fig. 1 Vessel haematocrit as measured in microvasculature by Klitzman and Duling (1979). Capillary haematocrit is in the resting muscle 10.9 ± 3.5 %. in contracting muscle superfused with 1 mM adenosine, capillary haematocrit jumps to 39.8 ± 9.5 %. Arteriolar haematocrit is 13.9 ± 1.2 % in resting muscle. None of the numerical models of RBC locomotion in capillaries can predict such major changes in capillary haematocrit

barely support plasma flow, whilst amongst others an order of magnitude difference in RBC flux, velocity and haematocrit is apparent, and RBC capillary path lengths vary substantially (Sarelius and Duling 1982; Poole et al. 1997; Kindig et al. 2002). Depending on the contractile activity of the muscle, the small arterioles may assume a greater (rest) or lesser role (exercise) in blood tissue O_2 flux (Carvalho and Pittman 2008; Poole et al. 2011). The appearance of more RBCs in capillary cross-sections from contracting muscle is to be expected based upon the demonstrated increase in capillary haematocrit as a function of contraction-induced elevation of capillary RBC flux and velocity from ~10 up towards 45% (Klitzman and Duling 1979; Klitzma et al. 1982; Kindig et al. 2002; Copp et al. 2009) (Fig. 1). Poole et al. (2013) introduce the concept of longitudinal recruitment, in which most capillaries support RBC flux at rest and, during contractions, capillary surface area is "recruited" along the length of previously flowing capillaries. This occurs, in part, by elevating capillary haematocrit and extending the length of the capillary available for blood myocyte exchange.

3 RBC Motion Modelling

Numerous models have been developed to describe the flow of RBCs in capillaries (Linderkamp and Meiselman 1982; Sharan and Popel 2001; Weinbaum et al. 2003; Han et al. 2006; Shi et al. 2012; Polwaththe-Gallage et al. 2015). Experimental studies of capillary flow have provided fertile ground for mathematical modelling of RBC motion in capillaries (Pries et al. 1996; Secomb 2003; Secomb et al. 2007; Pozrikidis 2010; Freund 2013). Both axisymmetric and non-axisymmetric problems have been considered. All of these models take the capillary pressure gradient as the only driving force. A mechano-electrochemical model considers a multicomponent mixture and incompressible fluid, an anionic porous deformable matrix and mobile ions as a model of the glycocalyx (Pozrikidis 2010). Alternatively an oncotic model of the glycocalyx has been developed by Pries et al. (1840b). Weinbaum and co-workers developed a poroelastic model of the glycocalyx able to predict an eightfold decrease in capillary resistance in a 6 μm diameter capillary with a 1 μm thick glycocalyx. This effect is likened to the low friction experienced by a skier while gliding over a layer of snow (Secomb 2003). Although this model does provide an explanation for the very low friction experienced by RBCs as they enter a capillary, it is unable to explain why the RBCs overtake the plasma so easily in capillaries in which they do not fit, and particularly when the pressure gradient is low. In fact, it can be easily understood that fluid-mechanical modelling of flow of a deformable RBC in a Newtonian fluid cannot simulate a vessel haematocrit lower than half the discharge haematocrit (Fig. 2). Nor can these models predict the large increase of capillary haematocrit as the arterioles dilate, termed "longitudinal recruitment" by Poole et al. (2013).

4 Bulk Versus Interfacial Forces

Hagen–Poiseuille's law (Fig. 3) has been widely used to quantify flow in a cylindrical tube subject to a pressure gradient (Poiseuille 1830, 1840a,b, 1841):

$$Q = -\frac{\pi D^4}{128\mu}\frac{\partial p}{\partial x} \tag{2}$$

in which D is the diameter of the tube, μ the dynamic viscosity of the fluid, p is the pressure, x is the coordinate along the axis of the tube and Q the fluid volumetric flow rate through the cross-section. The friction in a Poiseuille flow distributes over the whole liquid domain. This is why velocity gradients are present throughout the cross section of the tube leading to a parabolic velocity profile and hence fourth power dependence of the flux on the diameter of the tube. By contrast, electro-osmotic flow through the same tube is known to be a plug flow. Let us suppose that the inner walls of the tube have a negative charge. Electro-osmotic flow is the flow resulting from an electric potential gradient across the length of the tube (von Reuss 1809).

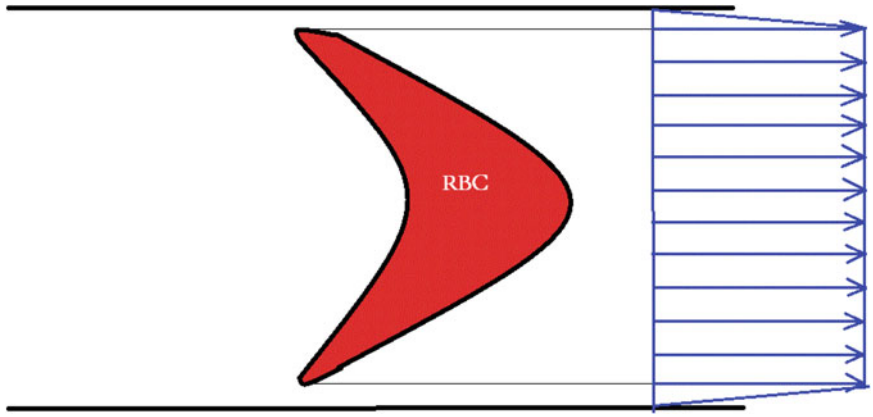

Fig. 2 An RBC moves through a capillary. As the RBC is close to the middle of the lumen, the RBC moves faster than the plasma. The slit between the RBC and the capillary glycocalyx is in the order of 100–200 nm, which is significantly smaller than the length of the slit (Vink and Duling 1996). The flow profile in a slit of this size is a linear velocity profile, starting from the glycolyx velocity to the RBC velocity. The resulting average plasma velocity is the order of half the RBC velocity. Substituting this result in Eq. (1) yields a vessel haematocrit of half the discharge haematocrit, independent of the pressure gradient, which is in conflict with experimental data

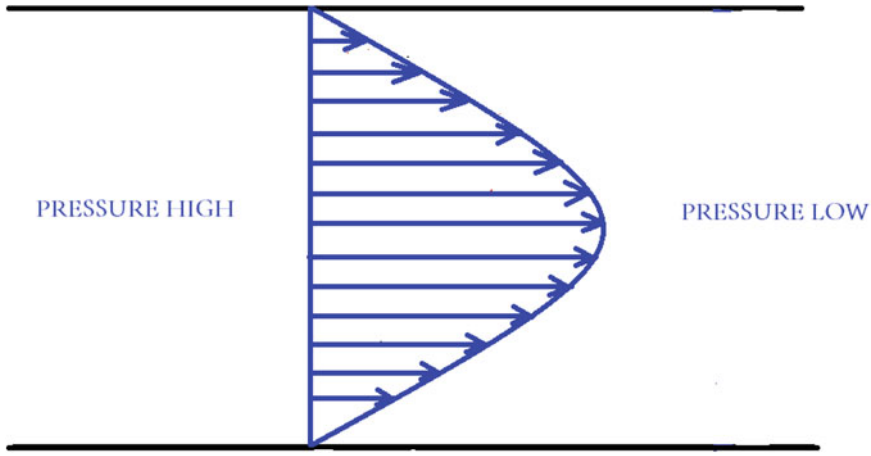

Fig. 3 The fluid in a tube is subject to a pressure gradient. If the fluid is newtonian, the velocity profile is parabolic and the flux is proportional to the fourth power of the diameter of the tube (Poiseuille 1840a,b, 1841)

Positive counter ions along the double layer of the inner lining of the tube move towards the negative electrode. The movement of the counterions is known as electrophoresis. The water in the tube is convected by the positive counter ions resulting in a flux of fluid towards the negative electrode. The movement of the fluid under an electric potential gradient is known as electro-osmosis. Because force generating onto the fluid originates at the interface between the fluid and the solid, electro-osmosis is known as an interfacial phenomenon. The gradient of velocity is concentrated in the thin double layer. The electro-osmotic flux through the tube is:

$$Q = -\frac{\pi D^2 \epsilon \epsilon_0 \zeta}{4\mu} \frac{\partial \xi}{\partial x} \tag{3}$$

in which ϵ_0 is the permittivity of the vacuum, ϵ is the relative permittivity of the fluid in the tube, ζ is the zeta potential associated with the double layer and ξ is the electric potential. Because

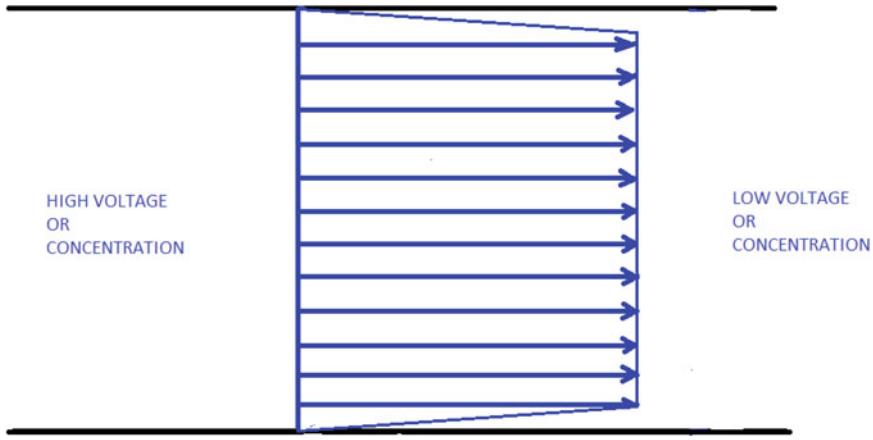

Fig. 4 The fluid in a tube is subject to a voltage gradient or a concentration gradient. The gradient induces a flow along the interfacial area between the fluid and the tube wall. The resultant flow profile is a plug flow. If the gradient is a voltage gradient, the resultant flux is an electro-osmotic flux. If the gradient is a concentration gradient, the resultant flux is a diffusio-osmotic flux

electro-osmotic flow is a plug flow, Q is proportional to the square of the diameter of the tube (Fig. 4). A consequence of the diameter square dependence of electro-osmotic flow is that the electro-osmotic permeability of a porous medium has a much weaker pore size dependence than hydraulic permeability has Casagrande (1949). Another example of an interfacial phenomenon is diffusio-osmosis. Diffusio-osmosis is defined as a plug flow developing in a tube under a gradient of an ionic or non-ionic concentration gradient. First discovered by Derjaguin et al. (1947, 1972), the phenomenon has attracted increasing attention in the last years in the context of microfluidics (Ebel et al. 1988; Anderson 1989; Keh and Weng 2001; Florea et al. 2014), self-propulsion of micro- and nano particles (Velegol et al. 2016; Shi et al. 2016). Typically, the diffusio-osmotic flux in a tube subject to a concentration gradient of a neutral solute (Anderson and Prieve 1991) is given by:

$$Q = -\frac{\pi D^2 kTLK}{4\mu}\frac{\partial c}{\partial x} \tag{4}$$

in which k is Boltzmann constant, T is the absolute temperature, L is a characteristic length of the wall-solute interaction, K is the Gibbs adsorption length and c is the concentration of the solute. It is obvious that because of the dependence of the Poiseuille flow on fourth power of the diameter, the pressure gradient is the dominant force in the larger vessels of the circulatory system. Interfacial forces cannot be significant anywhere else than in the smallest vessels. If at all interfacial forces play an important role in capillary flow, this role will be most significant when capillary pressure gradients are small. In other words, interfacial forces may be significant when the arterioles are constricted. This is exactly when capillary haematocrit is found to be surprisingly low (Fig. 1).

The archetype of a diffusio-osmotic propulsion of a particle is the Janus particle. Paxton (2004) developed rod-shaped particles, 370 nm in diameter and consisting of 1 μm long Pt and Au segments moving autonomously in aqueous hydrogen peroxide solutions by catalysing the formation of oxygen at the Pt end. In 2–3% hydrogen peroxide solution, these rods move predominantly along their axis in the direction of the Pt end at speeds of up to ten body lengths per second. Silica microspheres that are half-coated with platinum metal undergo self-propulsion in solutions of H_2O_2 (Ke et al. 2010). The beads are named after the roman god Janus who is depicted as having two faces. Microscopic observation of the particle motion, with segmentation of the image data,

demonstrates that the particles move, on average, with the platinum-coated region oriented opposite to the direction of motion, with the average speed increasing with increasing H_2O_2 concentration. The mechanism underlying the motion of the Janus particles is the spontaneous reaction of hydroxyperoxide into water plus oxygen:

$$2H_2O_2 \rightarrow 2H_2O + O_2 \tag{5}$$

The platinum serves as a catalyst, meaning that more oxygen is created along the platinum coated side (Paxton et al. 2006). The resulting oxygen gradients generate a diffusio-osmotic flow towards the platinum coated side, thus propelling the particle in the opposite direction (Ke et al. 2010). The flow of water towards the platinum is diffusio-osmosis, the resulting motion of the particle is diffusiophoresis. Typical velocities attained through this mechanism are in the range of tens of microns per second, pretty comparable to an RBC velocity in a capillary of a muscle at rest.

5 What Interfacial Forces May Be at Play in Capillary Flow?

Interfacial forces may be generated either by electrical potential gradient, ionic concentration gradients or neutral solute concentration gradients. Ionic concentrations within the plasma are tightly regulated and can therefore not be subject to gradients, nor is there any evidence of electric potential gradients within the capillaries. Numerous experiments have demonstrated steep gradients of oxygen right at the level of capillaries, and to a lesser extent in small arterioles. Hellums et al. (1977) studied the resistance to oxygen diffusion in capillaries and hypothesised the existence of erythrocyte associated transients within the plasma. Later studies demonstrated the transients of oxygen concentrations around RBCs first using Clarke electrodes (Ndubuizu and LaManna 2007; Lecoq et al. 2009), and recently using phosphorescence quenching methods (Lecoq et al. 2011). As a matter of fact, oxygen gradients have been measured by Lecoq et al. (2011) in rat brain capillaries as steep as 30 mmHgPO_2/μm. The energy pumped into the capillary flow by the arteriovenous pressure gradient is the volume times the pressure drop, which—if we take the pressure drop to be in the order of 1 kPa, and the cardiac output at rest 5 l/min—amounts to 1 kPa * 5 l/min = 5 J/min at capillary level. At rest, 10^{13} RBCs pass through capillaries in 1 min. All these blood cells carry about 750 g haemoglobin with them. Most (98%) of the oxygen in the blood is carried by the haemoglobin in the RBCs. The amount of oxygen carried by 5 l blood is about 1.4 g or 0.044 mole. Most of this oxygen is carried up to capillary entry where it is brought into close contact with tissue that is craving oxygen. The steep concentration gradient between the red blood cell and the tissue represents energy, just like the arteriovenous pressure gradient generated by the heart, has energy that can be exploited for locomotion. Oxygen gradients are most probably higher around RBCs at capillary entry than anywhere else in the body. The energy available from the gradients in oxygen at that level represents a multiple of the energy available from the arteriovenous pressure gradient. We can roughly evaluate a lower bound for this energy as $0.044 * R * T * \ln(c_{RBC}/c_{tissue})$, in which R is universal gas constant, T is absolute temperature, c_{RBC} the oxygen concentration in the RBC and c_{tissue} the concentration of oxygen in the tissue. If we take for $c_{tissue} = 26\,\mu M$ (Kiaer and Kristensen 1988), this energy amounts to hundreds of J per minute, which is two orders of magnitude larger than the energy associated with the arteriovenous pressure gradient. To the best of my knowledge, no researcher ever accounted for a possible transfer of power from oxygen gradients to RBC at systemic capillary entry. The core difference between propulsion by a pressure gradient and a diffusio-osmotic propulsion by an oxygen gradient, is that the oxygen gradient propels the RBC at the cost of the plasma, whereas the pressure gradient acts on the plasma while convecting the RBC along with it (Anderson 1989; Keh and Weng 2001; Ke et al. 2010; Sabass 2012). The oxygen gradient reduces therefore the vessel haematocrit. When arterioles are constricted, pressure gradients are low,

hence the diffusio-osmotic contribution draws the haematocrit levels down. When the arterioles are dilated, the pressure gradient is high and the diffusio-osmotic contribution of the oxygen gradient is comparatively negligible, hence the vessel haematocrit shoots up and longitudinal recruitment takes place.

6 Diffusio-osmotic Flow Between the RBC and the Glycocalyx

An RBC releases oxygen as it enters the metarterioles and capillaries. Because of this release, the RBC is surrounded by strong oxygen gradients (Lecoq et al. 2011). The Péclet number associated with the diffusion convection of oxygen

$$Pe = \frac{v_{\mathrm{RBC}} d_{\mathrm{RBC}}}{D} \tag{6}$$

is in the order of one. In Eq. (6), v_{RBC} is the velocity of the RBC, d_{RBC} is characteristic size of the RBC and D the diffusion coefficient of oxygen. Because Pe is in the order of one, the release of oxygen results in a modest trail of oxygen lagging behind the RBC. The size of this plume is enhanced by the parachute shape of the RBC as the oxygen release in the rear of the RBC is enclosed by the concave shape of the RBC membrane. The space between the RBC and the glycocalyx has been evaluated to be between 100–200 nm (Vink and Duling 1996). As a consequence of the plume of oxygen, one can reasonably expect that along the slit between glycocalyx and the RBC, there exists an oxygen gradient pointing to the rear of the RBC. Given the size of an RBC, the length and the width of the slit seems large compared to its thickness. Further we assume that the thickness L of the interfacial layer in which the solid surface interacts with the oxygen is small relative to the slit thickness. Derjaguin et al. (1961), Derjaguin and Dukhin (1971) obtained for the case in which the gradient is tangent to a solid/liquid interface and in which the potential energy $\phi(h)$ of the oxygen depends solely on its normal distance h from the interface:

$$v_{\mathrm{rel}} = -\frac{\partial c}{\partial x}\frac{kT}{\mu}\int_0^\infty h[e^{-\phi/kT} - 1]dh \tag{7}$$

in which v_{rel} is the interfacial velocity of the plasma relative to the solid surface bordering the interfacial area of thickness L, $\frac{\partial c}{\partial x}$ is the gradient in oxygen along the slit between the RBC and the glycocalyx and $\phi(h)$ is the potential describing the affinity of oxygen with the RBC membrane. The plasma velocity v_{rel} in the interfacial layer results in a slip velocity along the RBC membrane pointing to the rear of the RBC (Fig. 5). As a consequence, the oxygen saturated RBC is propelled by the oxygen gradients towards the front, i.e, towards low oxygen. That an RBC placed in a oxygen gradient should move can be understood by considering the case of attraction/repulsion between oxygen and RBC. Because of the gradient, there are more oxygen molecules interacting with the rear of the RBC compared to the front side, and hence the oxygenated RBC feels a pull toward lower oxygen concentration. Another way of looking at this motion is to consider the thermodynamic state of the RBC (Ruckenstein 1981): by moving toward higher concentration, the deoxygenated RBC can adsorb more oxygen, thereby lowering its surface energy, while by moving towards lower concentration, the oxygen-saturated RBC can release its oxygen more readily, thereby lowering its surface energy as well .

7 Conclusion

Present fluid–structure interaction models of RBC locomotion in capillary flow cannot explain the large change in haematocrit values between a muscle at rest and a stimulated muscle. This study presents a new hypothesis, aiming at explaining the discrepancy between model and experiment. A diffusio-osmotic velocity is hypothesised at the interface between the RBC and the plasma, generating a thrust that moves the RBC forward at the cost of the plasma. This diffusio-osmotic force is a sizable fraction of the force stemming from the pressure gradient at rest and negligible when the muscle is stimulated.

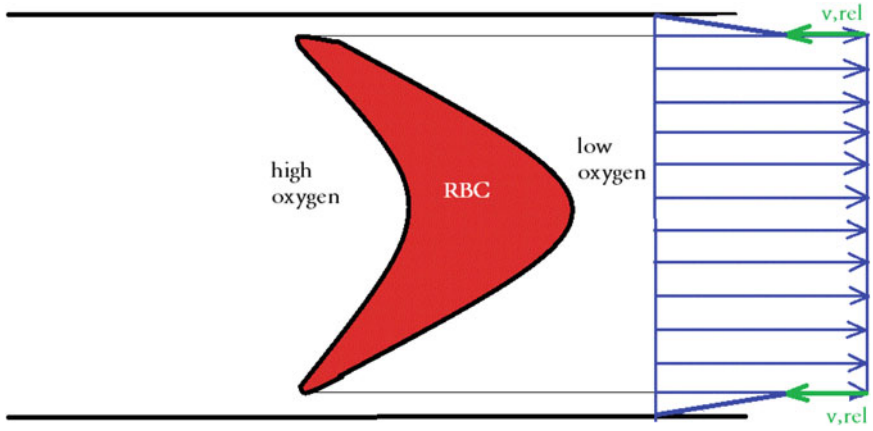

Fig. 5 A RBC moves into a capillary. As the RBC is close to the middle of the lumen, the RBC moves faster than the plasma. The RBC releases its oxygen to the surrounding tissue. Because of advection, the RBC leaves a plume of oxygen behind, resulting in a higher oxygen concentration behind the RBC than in front of the RBC. In the thin layer of oxygen-RBC interaction—typically a few nm in size—a diffusio-osmotic flow develops towards the high oxygen region. The flow profile in the slit of this size is a linear velocity profile, starting from the glycocalyx velocity to the RBC velocity minus the diffusio-osmotic velocity v_{rel}. The resulting average plasma velocity is lower than half the RBC velocity, if the diffusio-osmotic velocity is a sizeable fraction of the RBC velocity. This is only the case in a muscle at rest, and therefore explains the low haematocrit values measured in resting muscle. Longitudinal recruitment, i.e. increase in haematocrit values, occurs as soon as the pressure gradient becomes dominant in the stimulated muscle

The origin of the diffusio-osmosis is attributed to the steep oxygen gradients developing around the RBC at capillary entry.

Acknowledgements The author acknowledges support from the STW-foundation, the Technological Branch of the Netherlands Organisation of Scientific Research NWO, and the Ministery of Economic Affairs of the Netherlands, for project 12538, Interfacial aspects of Ionised Media. The author thanks Dr. Sami Musa (University of Limerick and Eindhoven University of Technology) and dr. Orest Shardt (University of Limerick) for enlightening discussions and for commenting the manuscript.

References

Anderson JL (1989) Colloid transport by interfacial forces. Annu Rev Fluid Mech 21:61

Anderson JL, Prieve DC (1991) Diffusiophoresis caused by gradients of strongly adsorbing solutes. Langmuir 7:403–406

Carvalho H, Pittman RN (2008) Longitudinal and radial gradients of PO2 in the hamster cheek pouch microcirculation. Microcirculation 15:215–224

Casagrande L (1949) Electroosmosis in soils. Géotechnique 1:159–177

Copp SW, Ferreira LF, Herspring KF, Musch TI, Poole DC (2009) The effects of aging on capillary hemodynamics in contracting rat spinotrapezius muscle. Microvasc Res 77:113–119

Derjaguin BV, Dukhin SS (1971) Application of thermodynamics of irreversible processes to the electrodiffusion theory of electrokinetic effects. Res Surface Forces 3:169

Derjaguin BV, Sidorenkov GP, Zubashchenkov EA, Kiseleva EV (1947) Kinetic phenomena in boundary films of liquids. Kolloidn Zh 9:335–347

Derjaguin BV, Dukhin SS, Korotkova AA (1961) Diffusiophoresis in electrolyte solutions and its role in the mechanism of film-formation from rubber latexes by the method of ionic deposition. Kolloidn Zh 23:53

Derjaguin BV, Dukhin SS, Koptelova MM (1972) Capillary osmosis through porous partitions and properties of boundary layers of solutions. J Colloid Interface Sci 38:584–595

Ebel JP, Anderson JL, Prieve DC (1988) Diffusiophoresis of latex particles in electrolyte gradients. Langmuir 4:396

Florea D, Musa S, Huyghe JM, Wyss HM (2014) Long-range repulsion of colloids driven by ion-exchange and diffusiophoresis. Proc Natl Acad Sci USA 111: 6554–6559

Fåhræus R, Lindqvist T (1931) The viscosity of the blood in narrow capillary tubes. Am J Physiol 96:562–568

Frisbee JC, Barclay JK (1998) Microvascular hematocrit and permeability-surface area product incontracting

canine skeletal muscle in situ. Microvasc Res 55: 153–164
Freund JB (2013) The flow of red blood cells through a narrow spleen-like slit. Phys Fluids 25:110007
Han Y, Weinbaum S, Spaan JAE, Vink H (2006) Large-deformation analysis of the elastic recoil of fibre layers in a brinkman medium with application to the endothelial glycocalyx. J Fluid Mech 554:217–235
Hellums JD (1977) The resistance to oxygen transport in the capillaries relative to that in the surrounding tissue. Microvasc Res 13:131–136
Ke H, Ye S, Carroll RL, Showalter K (2010) Motion analysis of self-propelled Pt-silica particles in hydrogen peroxide solutions. J Phys Chem A 114: 5462–5467
Keh HJ, Weng JC (2001) Diffusiophoresis of colloidal spheres in nonelectrolyte gradients at small but finite péclet numbers. Colloid Polymer Sci 279:305–311
Kiaer T, Kristensen KD (1988) Intracompartmental pressure, PO2, PCO2 and blood flow in the human skeletal muscle. Arch Orthop Trauma Surg 107:114–116
Kindig CA, Poole DC (1998) A comparison of the microcirculation in the rat spinotrapezius and diaphragm muscles. Microvasc Res 57:144–152
Kindig CA, Richardson TE, Poole DC (2002) Skeletal muscle capillary hemodynamics from rest to contractions: implications for oxygen transfer. J Appl Physiol 92:2513–2520
Klitzman B, Duling BR (1979) Microvascular hematocrit and red cell flow in resting and contracting striated muscle. Am J Physiol 237:H481–H490
Klitzman B, Damon DN, Gorczynski RJ, Duling BR (1982) Augmented tissue oxygen supply during striated muscle contraction in the hamster. relative contributions of capillary recruitment, functional dilation, and reduced tissue PO2. Circ Res 51:711–721
Krogh A (1919a) The number and distribution of capillaries in muscles with calculations of the oxygen pressure head necessary for supplying the tissue. J Physiol 52:409–415
Krogh A (1919b) The supply of oxygen to the tissue and the regulation of the capillary circulation. J Physiol 52:457–474
Lecoq J, Tiret P, Najac M, Shepherd GM, Greer CA, Charpak S (2009) Odor-evoked oxygen consumption by action potential and synaptic transmission in the olfactory bulb. J Neurosci 29:1424–1433
Lecoq J, Parpaleix A, Roussakis E, Ducros M, Houssen YG, Vinogradov SA, Charpak S (2011) Simultaneous two-photon imaging of oxygen and blood flow in deep cerebral vessels. Nat Med 17:893–899
Linderkamp O, Meiselman HJ (1982) Geometric, osmotic, and membrane mechanical properties of density-separated human red cells. Blood 59: 1121–1127
Martini P, Pierach A, Schreyer E (1930) Die Strömung des Blutes in engen Gefässen. eine Abweichung vom Poiseuille'schen Gesetz. Deutsches Archiv für klinische Medizin 169:212–222
Ndubuizu O, LaManna JC (2007) Brain tissue oxygen concentration measurements. Antioxid Redox Signal 9:1207–1219
Paxton WF, Kistler KC, Olmeda CC, Sen A, St. Angelo SK, Cao Y, Mallouk TE, Lammert PE, Crespi VH (2004) Catalytic nanomotors: autonomous movement of striped nanorod. J Am Chem Soc 126:13425–13431
Paxton WF, Sundararajan S, Mallouk TE, Sen A (2006) Minireview: chemical locomotion. Angew Chem 45:5420 –5429
Poiseuille JLM (1830) Recherches sur les causes du mouvement du sang dans les veines. J Physiol Exp Pathol 10:277–295
Poiseuille JLM (1840a) Recherches expérimentales sur ie mouvement des liquides dans les tubes de très petits diamètres; i. influence de la pression sur la quantité de liquide qui traverse les tubes de très petits diamètres. C R Acad Sci 11:961–67
Poiseuille JLM (1840b) Recherches expérimentales sur le mouvement des liquides dans les tubes de très petits diamètres; ii.influence de la longueur sur la quantité de liquide qui traverse les tubes de très petits diamètres; iii. influence du diamètre sur la quantité de liquide qui traverse les tubes de très petits diamètres. C R Acad Sci 11:1041–1048
Poiseuille JLM (1841) Recherches expérimentales sur le mouvement des liquides dans les tubes de très petits diamètres; iv. influence de la température sur la quantité de liquide qui traverse les tubes de très petits diamètres. C R Acad Sci 12:112–115
Polwaththe-Gallage HN, Saha SC, Sauret E, Flower RL, Gu Y (2015) Numerical inventigation of motion and deformation of a single red blood cell in a stenosed capillary. Int J Comput Methods 12:1540003
Poole DC, Musch TI, Kindig CA (1997) In vivo microvascular structural and functional consequences of muscle length changes. Am J Physiol 272:H2107–H2114
Poole DC, Copp SW, Hirai DM, Musch TI (2011) Dynamics of muscle microcirculatory and blood–myocyte O2 flux during contractions. Acta Physiol (Oxf) 202:293–310
Poole DC, Copp SW, Ferguson SK, Musch TI (2013) Skeletal muscle capillary function: contemporary observations and novel hypotheses. Exp Physiol 98:1645–1658
Pozrikidis C (2010) Computational hydrodynamics of capsules and biological cells. CRC Press, Boca Raton
Pries AR, Ley K, Gaehtgens P (1986) Generalization of the Fahraeus principle for microvessel networks. Am J Physiol 251(6):H1324–32
Pries AR, Secomb TW, Gaehtgens P (1996) Biophysical aspects of blood flow in the microvasculature. Cardiovasc Res 32:654–667
Ruckenstein E (1981) Can phoretic motion be treated as an interfacial tension gradient driven phenomena? J Colloid Interface Sci 77:83
Sabass BC (2012) Active, phoretic motion. Phd dissertation, University of Stuttgart, Department of Physics and Mathematics

Sarelius IH, Duling BR (1982) Direct measurement of microvessel hematocrit, red cell flux, velocity and transit time. Am J Physiol 243:H1018–1026

Sharan M, Popel AS (2001) A two-phase model for flow of blood in narrow tubes with increased effective viscosity near the wall. Biorheology 38: 415–428

Shi L, Pan T-W, Glowinski R (2012) Deformation of a single red blood cell in bounded poiseuille flows. Phys Rev E 85:016307

Shi N, Nery-Azevedo R, Abdel-Fattah AI, Squires TM (2016) Diffusiophoretic focusing of suspended colloids. Phys Rev Lett 117:258001

Skalak R, Branemark P-I (1969) Deformation of red blood cells in capillaries. Science 164(3880):717–719

Secomb TW (2003) Mechanics of RBCs and blood flow in narrow tubes. Chapman and Hall/CRC, Boca Raton

Secomb TW, Styp-Rekowska B, Pries AR (2007) Two-dimensional simulation of red bloodcell deformation and lateral migration in microvessels. Ann Biomed Eng 35:755–765

Snyder GK, Sheafor BA (1999) RBCs: centerpiece in the evolution of the vertebrate circulatory system. Am Zool 39:189–198

Velegol D, Garg A, Guha R, Kar A, Kumar M (2016) Origins of concentration gradients for diffusiophoresis. Soft Matter https://doi.org/10.1039/c6sm00052e

Vink H, Duling BR (1996) Identification of distinct luminal domains for macromolecules, erythrocytes and leucocytes within mammalian capillaries. Circ Res 79:581–589

von Reuss FF (1809) Notice sur un nouvel effet de l'électricité galvanique. Mémoires de la Société Impériale des Naturalistes de l'Université Impériale de Moscou 2:327

Weinbaum S, Zhang X, Han Y, Vink H, Cowin SC (2003) Mechanotransduction and flow across the endothelial glycocalyx. Proc Natl Acad Sci USA 100:7988–7995

Tumor Metastasis in the Microcirculation

Bingmei M. Fu

Abstract

Tumor cell metastasis through blood circulation is a complex process and is one of the great challenges in cancer research as metastatic spread is responsible for ~90% of cancer-related mortality. Tumor cell intravasation into, arrest and adhesion at, and extravasation from the microvessel walls are critical steps in metastatic spread. Understanding these steps may lead to new therapeutic concepts for tumor metastasis. Vascular endothelium forming the microvessel wall and the glycocalyx layer at its surface are the principal barriers to and regulators of the material exchange between circulating blood and body tissues. The cleft between adjacent endothelial cells is the principal pathway for water and solute transport through the microvessel wall in health. Recently, this cleft has been found to be the location for tumor cell adhesion and extravasation. The blood-flow-induced hydrodynamic factors such as shear rates and stresses, shear rate and stress gradients, as well as vorticities, especially at the branches and turns of microvasculatures, also play important roles in tumor cell arrest and adhesion. This chapter therefore reports the current advances from in vivo animal studies and in vitro culture cell studies to demonstrate how the endothelial integrity or microvascular permeability, hydrodynamic factors, microvascular geometry, cell adhesion molecules, and surrounding extracellular matrix affect critical steps of tumor metastasis in the microcirculation.

1 Introduction

Cancer is the second killer next to the heart disease worldwide (CDC 2015). The cause of death is usually organ failure caused by metastatic tumors that are derived from the primary tumor. Although the metastasis process is low efficiency, only 0.01% disseminated tumor cells would successfully survive and proliferate at new physiology environment (Weber 2007), this process responsible for >90% of cancer-related deaths (Gupta and Massague 2006). Recognized as the detachment and dissemination of the malignant tumor cells from the primary tumor and the development of secondary tumors at distant organs, tumor metastasis is a very complex multistep process; sequentially, it includes local invasion of tissue where tumor first starts, detachment from the primary tumor, intravasation, survival in the

B. M. Fu (✉)
Department of Biomedical Engineering, The City College of the City University of New York, New York, NY, USA
e-mail: fu@ccny.cuny.edu

B. M. Fu, N. T. Wright (eds.), *Molecular, Cellular, and Tissue Engineering of the Vascular System*, Advances in Experimental Medicine and Biology 1097,
https://doi.org/10.1007/978-3-319-96445-4_11

circulation and dissemination, arrest and adhesion, extravagation, proliferation, and angiogenesis (Chambers et al. 2002; Fidler 2011; Talmadge and Fidler 2010; Bacac and Stamenkovic 2008). Tumor metastasis can be through blood circulatory system or lymphatic system. The detached tumor cells can directly enter into the circulating blood and go to distant organs (Wyckoff et al. 2000), or they can enter the blood circulatory system indirectly via the lymphatic system (Chambers et al. 2002). The circulating tumor cells could spread from lymph nodes to distant organs via blood vessels associated with the nodes or by entering the venous system via the major lymphatic ducts (e.g., the thoracic duct) (Achen and Stacker 2008; Tobler and Detmar 2006). The preferential metastatic organs for breast cancers are the lungs, liver, brain, and bone (Kang et al. 2003; Minn et al. 2005; Berman et al. 2013). Tumor cells that initiate a metastatic colony must go through the following steps: (1) detach from the primary tumor colony, (2) invade the local host tissue, (3) penetrate into blood vessels or lymphatic vessels, (4) survive within the circulation, (5) arrest or adhere in the microvessels of distant organs, (6) extravasate from the blood stream, (7) adapt to the newly colonized milieu in new foreign environment, and (8) divide to form the new tumor (Bacac and Stamenkovic 2008; Nguyen et al. 2009).

At the microscopic levels, angiogenesis from the primary tumor, tumor cell intravasation through leaky angiogenic microvessels, arrest and adhesion in the microcirculation, interaction with the microvessel walls to increase microvascular permeability, extravasation to the secondary organ, and survival and proliferation in foreign organs are critical steps for tumor growth and metastasis (Fig. 1). Although various anti-angiogenic therapies have been postulated to inhibit tumor growth and intravasation since 1971, strategies targeting at tumor cell arrest and adhesion and targeting at microvessel integrity have not been well developed (Folkman 1971). In addition, while considerable progress has been made in understanding the mechanism

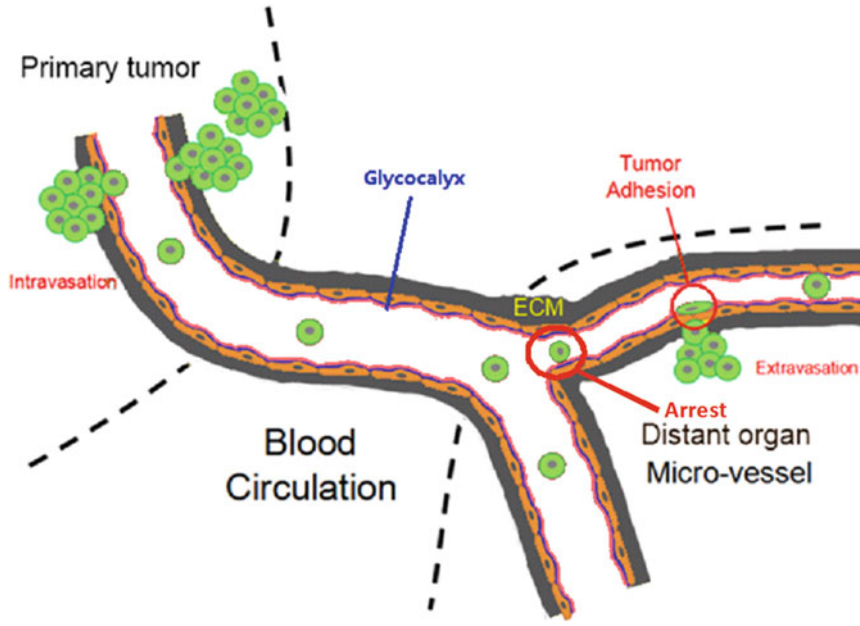

Fig. 1 Major steps for tumor metastasis in microvasculature. Tumor cells first get into the microcirculation near the primary tumor by intravasation across the microvessel wall. Then they arrest and adhere to the microvessel walls in a distant organ, where they degrade the microvessel wall integrity such as endothelial surface glycocalyx and junctions between adjacent endothelial cells forming the microvessel wall. Finally, they extravasate into the distant organ through the leaky microvessel wall (courtesy of Dr. Jie Fan)

of microvascular integrity compromise induced by tumor angiogenic factors, such as vascular endothelial growth factor (VEGF), our understanding of the microvascular integrity and its role in tumor metastasis is poor. Furthermore, previous studies suggested that mechanical factors might interact with the biochemical factors for tumor metastasis (Chambers et al. 2002), but how the localized hydrodynamic factors induced by the microcirculation affect tumor cell arrest, adhesion and accumulation have not been systematically studied. This chapter therefore reports the current advances from in vivo animal studies and in vitro culture cell studies to demonstrate how the endothelial integrity or microvascular permeability, hydrodynamic factors, microvascular geometry, cell adhesion molecules, and surrounding extracellular matrix affect critical steps of tumor metastasis in the microcirculation.

2 Microvascular Integrity and Tumor Metastasis

Microvascular bed is the primary location where water and nutrients are exchanged between circulating blood and body tissues. Microvessel walls consist mainly of endothelial cells. Under normal conditions, the cleft between endothelial cells (inter-endothelial cleft) is widely believed to be the principal pathway for water and hydrophilic solute (such as glucose, amino acids, vitamins, hormones) transport across the capillary wall (Michel and Curry 1999; Michel and Neal 1999). Electron, confocal, and multiphoton microscopy studies indicate that there are junctional strands with discontinuous leakages (Roberts and Palade 1995; Bundgaard 1984) and fiber matrix components, so-called endothelial surface glycocalyx (ESG) (Luft 1966; Adamson and Clough 1992; Salmon and Satchell 2012; Arkill et al. 2011; van den Berg et al. 2003; Reitsma et al. 2007; Ebong et al. 2011; Yen et al. 2012; Betteridge et al. 2017) at the endothelial surface. The transport of proteins or other macromolecules was thought to be through vesicle shuttle mechanisms (Michel and Curry 1999). Microvascular permeability is a quantitative measure of how permeable the microvessel wall is to all kinds of substances including water and solutes with a variety of sizes. Under healthy conditions, the microvessel wall maintains a normal permeability to water and small solutes for the material exchange during our body's metabolic processes. While in disease, the integrity of the vessel wall structure can be destroyed, and much larger particles such as proteins, leukocytes, and tumor cells can transfer through the wall. It is the transvascular pathways at the vessel wall and their structural barriers that determine and regulate the microvascular permeability. Therefore, one can quantify the microvascular permeability to determine the microvessel integrity.

2.1 Microvascular Permeability and Permeability Coefficients

The endothelial cells lining microvessel walls provide the rate-limiting barrier to extravasation of plasma components of all sizes from electrolytes to proteins. So far, there are three primary pathways observed in the wall of a continuous microvessel by using electron microscopy: intercellular clefts, transcellular pores, and vesicles. Microvessels of different types and in different tissues may have different primary transvascular pathways. Under different physiological and pathological conditions, the primary pathway can be changed for the same microvessel (Michel and Curry 1999). The cleft between adjacent endothelial cells is widely believed to be the principal pathway for water and hydrophilic solute transport through the microvessel wall under normal physiological conditions. The junction strands with discontinuous leakages in the cleft and ESG maintain the normal microvessel permeability to water and solutes. Changes in permeability are caused by the changes in these structural components. The molecular basis for the passage of molecules at the level of the breaks in tight junctions is more likely to be the localized absence of cell-cell contacts with corresponding loss of a closely regulated molecular sieve as suggested by Fu et al. (1994) and Michel and Curry (1999).

Thus the junction break-surface matrix model suggests independent mechanisms to regulate the permeability properties of the microvessel wall. The junction break size and frequency are likely to involve regulation of cell-cell attachment via occludins and other junction proteins including the cadherin-associated junctions (Fu et al. 1994, 2003, 2006; Fu and Shen 2004). On the other hand, the regulation of glycocalyx density and organization is likely to involve interaction of the molecules forming the cell surface with the cytoskeleton and with circulating plasma proteins. Some of the cellular mechanisms underlying these interactions are reviewed in Squire et al. (2001), Tarbell and Pahakis (2006), and Fu and Tarbell (2013). Under physiological and pathological conditions, microvessel permeability can be regulated acutely and chronically by mechanisms that are underway to be understood.

Serial section electron microscopy study on frog and rat mesenteric capillaries by Adamson et al. (2004) demonstrated that the junction strand was interrupted by infrequent breaks that, on average, were 150 nm long, spaced 2–4 μm apart along the strand, and accounted for up to 10% of the length of the strand under control conditions. At these breaks, the space between adjacent endothelial cells (average ~20 nm) was as wide as that in regions of the cleft between adjacent cells with no strands. The luminal surfaces of endothelial cells (ECs) lining vasculature are coated with a glycocalyx of membrane-bound macromolecules comprised of sulfated proteoglycans, hyaluronic acid, sialic acids, glycoproteins, and plasma proteins that adhere to this surface matrix (Tarbell and Pahakis 2006; Fu and Tarbell 2013). The thickness of this endothelial surface glycocalyx (ESG) was observed from less than 100 nm to ~1 μm on the microvessels in different tissues and species by using different preparations and observing methods (Luft 1966; Reitsma et al. 2007; Salmon et al. 2009; Salmon and Satchell 2012; Squire et al. 2001; van den Berg et al. 2003; van Hinsbergh and Nieuw Amerongen 2002; Vink and Duling 1996; Yen et al. 2012). Although the ESG thickness varies, its density and organization were hypothesized to be the same among different tissues and species because of its function as a molecular sieve to macromolecules such as serum albumin. The glycocalyx fiber radius is thus proposed to ~6 nm, and gap spacing between fibers is proposed to be ~8 nm (Squire et al. 2001). More details about the ESG are presented in Chaps. 1, 2, and 3.

Aforementioned ultrastructural study using electron microscopy and other methods shows that the microvessel wall behaves as a passive membrane for water and hydrophilic solute transport (Michel and Curry 1999). The membrane transport properties are often described by Kedem-Katchalsky equations derived from the theory of irreversible thermodynamics:

$$J_s = PRT\Delta C + \left(1 - \sigma_f\right) C J_v \qquad (1)$$

$$J_v = L_p \left(\Delta p - \sigma_d RT \Delta C\right) \qquad (2)$$

where J_s and J_v are the solute and total volumetric fluxes; ΔC and Δp are the concentration and pressure difference across the membrane. L_p, the hydraulic conductivity, describes the membrane permeability to water. P, the diffusive permeability, describes the permeability to solutes. σ_f is the solvent drag or ultrafiltration coefficient that describes the retardation of solutes due to membrane restriction, and σ_d, the reflection coefficient, describes the selectivity of membrane to solutes. In many transport processes, σ_f is equal to σ_d, and thus we often use σ, the reflection coefficient, to represent both of them. R is the universal gas constant and T is the absolute temperature.

2.2 Permeability Measurement

All of the permeability measurements have been interpreted in terms of L_p, P, and σ, which are measured experimentally on intact whole organisms (including human subjects), on perfused tissues and organs, on single perfused microvessels, and on monolayers of cultured microvascular endothelial cells. Different experimental preparations have their advantages and disadvantages. Although measurements made on the intact re-

gional circulation of an animal subject (usually using radioactive isotope-labeled tracers) suffer from uncertainties surrounding the exchange surface area of the microvessel wall and the values of the transvascular differences in pressure and concentration, they usually involve minimal interference with the microvessels themselves. These studies can provide valuable information concerning microvascular exchange under basal conditions. At the other end are measurements on single perfused vessels. The Landis technique has been used to measure the hydraulic conductivity L_p and reflection coefficient σ. Quantitative fluorescence microscope photometry and imaging microscopy are used to measure solute diffusive permeability P. Both of these techniques are described in detail in Michel and Curry (1999), Fu et al. (2003), and Cai et al. (2012). The surface area of the microvessel can be measured directly, as also can the difference in pressure and concentration across the vessel walls. The disadvantages of the single vessel preparation are (1) that they have direct interference with the vessels involved and (2) that they are usually restricted to a small number of convenient vessel types (e.g., mesenteric vessels on a two-dimensional translucent tissue). However, recent development of multiphoton microscopy enables the noninvasive determination of the cerebral microvascular solute permeability in rat brain (Shi et al. 2014).

Although the rapid growth of endothelial cell biology is largely a result of experiments on cultured endothelial cells in vitro (in dishes), there are limitations to the use of monolayers of cultured endothelial cells for gaining direct information about vascular permeability. In general, the in vitro permeability to albumin is 2–10 times larger than that from the in vivo (in live animals) measurement. Although the monolayers of cultured endothelial cells do not completely reflect the permeability characteristics of microvascular endothelium in vivo, they are the most accessible and convenient models for studying the molecular mechanisms by which the microvascular permeability is regulated. The techniques for measuring endothelial monolayer permeability to water and solutes were described in Lee et al. (2003), Cancel et al. (2007), Li et al. (2010), and Fan and Fu (2016).

2.3 Microvascular Hyperpermeability Increases Tumor Cell Adhesion

Microvascular hyperpermeability due to compromised microvessel wall integrity by inflammatory agents and cytokines is one factor that increases tumor cell adhesion to the microvessel endothelium. Vascular endothelial growth factors (VEGFs) are a family of cytokines that act to increase the delivery of nutrients to tissue by three distinct mechanisms: (a) endothelial cell growth, migration, and new blood vessel formation (angiogenesis); (b) increased blood flow (by vasodilatation); and (c) increased vascular permeability to water and solutes (Dvorak et al. 1995; Bates et al. 2001; Feng et al. 1999; Fu and Shen 2004). Combining in vivo permeability measurement and a mathematical model for the inter-endothelial transport, Fu and Shen (2003) predicted that acute effects of VEGF on microvascular integrity are widened gap opening of the inter-endothelial cleft and partial degradation of the ESG. Longer-term effects of VEGF include formation of gaps between adjacent endothelial cells in venular microvessels (Roberts and Palade 1995), vesiculovascuolar organelle pathways (Feng et al. 1999), transcellular pores, and fenestra (Dvorak et al. 1995; Drenckhahn and Ness 1997). Fu et al. (2006) also found that the VEGF-induced microvascular hyperpermeability can be abolished by enhancing intracellular levels of adenosine 3′,5′-cyclic monophosphate (cAMP), which strengthens the microvessel integrity by increasing the number of junction strands in the cleft between endothelial cells forming the microvessel wall.

Previous studies have found that many cancer cells express VEGF to a high degree (Lee et al. 2003), while the microvascular endothelium has abundant VEGF receptors including VEGFR2 (KDR/Flk-1) (Mukhopadhyay et al. 1998). VEGFR2 has been implicated in normal and pathological vascular endothelial cell biol-

ogy (Olsson et al. 2006). Recently, it has been shown that ectopic administration of VEGF enhances the adhesion and transmigration of human breast cancer MDA-MB-231 cells across a monolayer of human or mouse brain microvascular endothelial cells under a static condition in vitro (Lee et al. 2003; Fan et al. 2011; Fan and Fu 2016). In addition, VEGF enhances the adhesion of malignant MDA-MB-435 s cells and ErbB2-transformed mouse mammary carcinomas to intact rat mesenteric microvessels under flow in vivo (Shen et al. 2010).

2.4 Integrin Signaling, Cell Adhesion Molecules, and Tumor Metastasis

Although the non-specific trapping due to the friction between the tumor cells and the narrow part of microvasculature is found to be responsible for the initial tumor cell arrest (Gassmann et al. 2010; Glinskii et al. 2005; Kienast et al. 2010; Mook et al. 2003), the cell adhesion molecules are required for the adhesion in larger microvessels and transmigration (Brenner et al. 1995; Fan et al. 2011; Gassmann et al. 2010; Giancotti 2007; Giavazzi et al. 1993; Hood and Cheresh 2002; Lee et al. 2003; Liang et al. 2005; Shen et al. 2010; Schluter et al. 2006; Slattery et al. 2005; Steeg and Theodorescu 2008). The integrins are a family of signaling and cell adhesion receptors, which attach cells to the extracellular matrix (ECM) and in some cases to other cells, and cooperate with growth factor and cytokine receptors to regulate cell behavior. Signals elicited by integrins enable tumor cells to survive, proliferate, migrate independently of positional constrains (Guo and Giancotti 2004), and adhere (Fan et al. 2011). The α6β4 integrin is a laminin-5 receptor and was originally described as a "tumor-specific" protein, because of its apparent upregulation in multiple metastatic tumor types (Giancotti 2007). The β4 integrin is unique among integrins because the cytoplasmic portion of the β4 subunit is 1017 amino-acid-long and possesses distinctive adhesive and signaling functions (Giancotti 2007). Upon binding of the ectodomain of β4 to the basement membrane protein laminin-5, the cytoplasmic portion of β4 interacts with the keratin cytoskeleton to promote the assembly of hemidesmosomal adhesions (Litjens et al. 2006). In addition, β4 activates intracellular signaling autonomously as well as by associating with multiple receptor tyrosine kinases (RTKs), including the EGFR, ErbB2, Met, and Ron (Guo and Giancotti 2004; Moasser et al. 2001). Deletion of the β4 signaling domain delayed mammary tumor onset and inhibited primary tumor growth. The tumors arising in mutant mice were significantly more differentiated histologically as compared to control tumors. In addition, primary tumor cells expressing signaling-defective β4 displayed a reduced proliferative rate and invasive ability and underwent apoptosis when deprived of matrix adhesion. Finally, upon injection in the tail vein of nude mice, the mammary tumor cells expressing mutant β4 exhibited reduced ability to metastasize to the lung (Guo et al. 2006).

Recently, Fan et al. (2011) examined the adhesion of ErbB2-transformed mammary tumor cells to mouse brain microvascular endothelial monolayer. They found that integrin β4 signaling does not exert a direct effect on adhesion to the endothelium or the underlying basement membrane. Rather, it enhances ErbB2-dependent expression of VEGF by tumor cells. VEGF in turn partially disrupts the tight and adherens junctions that maintain the adhesion between endothelial cells, enabling tumor cells to intercalate between endothelial cells and extend projections reaching the underlying exposed basement membrane and enabling the adhesion between cell adhesion molecules (e.g., integrins) and ECM proteins (e.g., laminins).

In addition to blocking the cell adhesion molecules at the surface of tumor and endothelial cells or in the ECM, e.g., integrins, ICAM-1, P-selectin, junctional adhesion molecules, and laminins, Shen et al. (2010) measured cancer cell adhesion after pretreatment of tumor cells with the antibody blocking VEGF and pretreatment of the microvessel with VEGF receptor (KDR/Flk-1) inhibitor, SU1498. They found that anti-VEGF and SU1498 almost completely abolished the adhesion of malignant MDA-MB-435 s to

vascular endothelium in vivo. In an in vitro experiment, Fan et al. (2011) showed that although VEGF receptor inhibitor, SU1498 did not decrease the basal permeability of a microvascular endothelial monolayer, neither the tumor cell adhesion under the normal permeability conditions, it, however, abolished the microvascular hyperpermeability induced by VEGF as well as the increase in tumor cell adhesion.

2.5 Tumor Cell Adhesion and Transmigration Destroys Microvascular Integrity

Both in vitro and in vivo studies demonstrated that tumor cells prefer to adhere to and transmigrate from the endothelial junctions instead of cell bodies and VEGF or lipopolysaccharide (LPS, an inflammatory agent) increases the adhesion and transmigration (Fan et al. 2011; Fu et al. 2015; Fan and Fu 2016). Fan and Fu (2016) showed that 98% of the breast cancer MDA-MB-231 cells adhere at the endothelial junctions of bEnd3 (mouse brain microvascular endothelial cell) monolayer, of which, 63% at the tri-EC junctions. An in vivo study by Fu et al. (2015) also indicated that ~90% of cancer cell adhesion occurs at the junctions of ECs in the microvessels under normal physiological flows (Fig. 2). In addition to disrupt the tight and adherens junctions between adjacent endothelial cells in vitro (Fan et al. 2011) and in vivo (Fu et al. 2015), tumor cell adhesion and transmigration degrades endothelial surface glycocalyx (ESG) (Fan and Fu 2016; Cai et al. 2012). A recent study by Cai et al. (2012) showed that tumor cell MDA-MB-231 adhesion to microvessel walls increases microvessel permeability by degrading the ESG (Fig. 3). Degradation of ESG exposed more cell adhesion molecules at the endothelium and underneath basement membrane for the tumor cell adhesion.

In contrast, preservation of the ESG by a plasma glycoprotein orosomucoid by enhancing the charge and organization of the ESG decreases the microvessel permeability to albumin and reduces the tumor cell adhesion (Cai et al. 2012). Zhang et al. (2017) also showed that sphingosine-1-phosphate (S1P), a sphingolipid in plasma that plays a critical role in the cardiovascular and immune systems, preserves ESG of the microvessel wall and reduces tumor cell adhesion. Red blood cells (RBCs) are a major source of S1P in plasma, which acts continuously to maintain normal vascular permeability by protecting ESG (Zhang et al. 2016b). Alternatively, reinforcing endothelial junctions, e.g., by enhancing endothelial cAMP levels, can prevent microvessel permeability increase and reduce tumor cell adhesion (Fu et al. 2015) (Fig. 2).

3 Tumor Metastasis under Flow and in Microvasculature

In vitro static adhesion assays have been utilized to investigate tumor cell adhesion to endothelial cells (Earley and Plopper 2006; Lee et al. 2003) and to extracellular matrix (ECM) proteins (Guo et al. 2006). Tumor cell adhesion has also been investigated using flow chambers (Chotard-Ghodsnia et al. 2007; Giavazzi et al. 1993; Slattery et al. 2005) or artificial blood vessels (Brenner et al. 1995) to address flow effects. Direct injection of tumor cells into the circulation has enabled the observation of tumor cell metastasis in target organs after sacrificing the animals (Schluter et al. 2006), while intravital microscopy has been used to observe the interactions between circulating tumor cells and the microvasculature both in vivo and ex vivo (Gassmann et al. 2010; Glinskii et al. 2005; Guo et al. 2014; Kienast et al. 2010; Mook et al. 2003; Shen et al. 2010; Steinbauer et al. 2003; Yan et al. 2012).

3.1 Tumor Cell Adhesion in In Vitro Flow Chambers

Tumor cell extravasation is a dynamic process in which tumor cell adhesion to the vascular endothelium and transendothelial migration occur under flow conditions. Therefore, the geometry

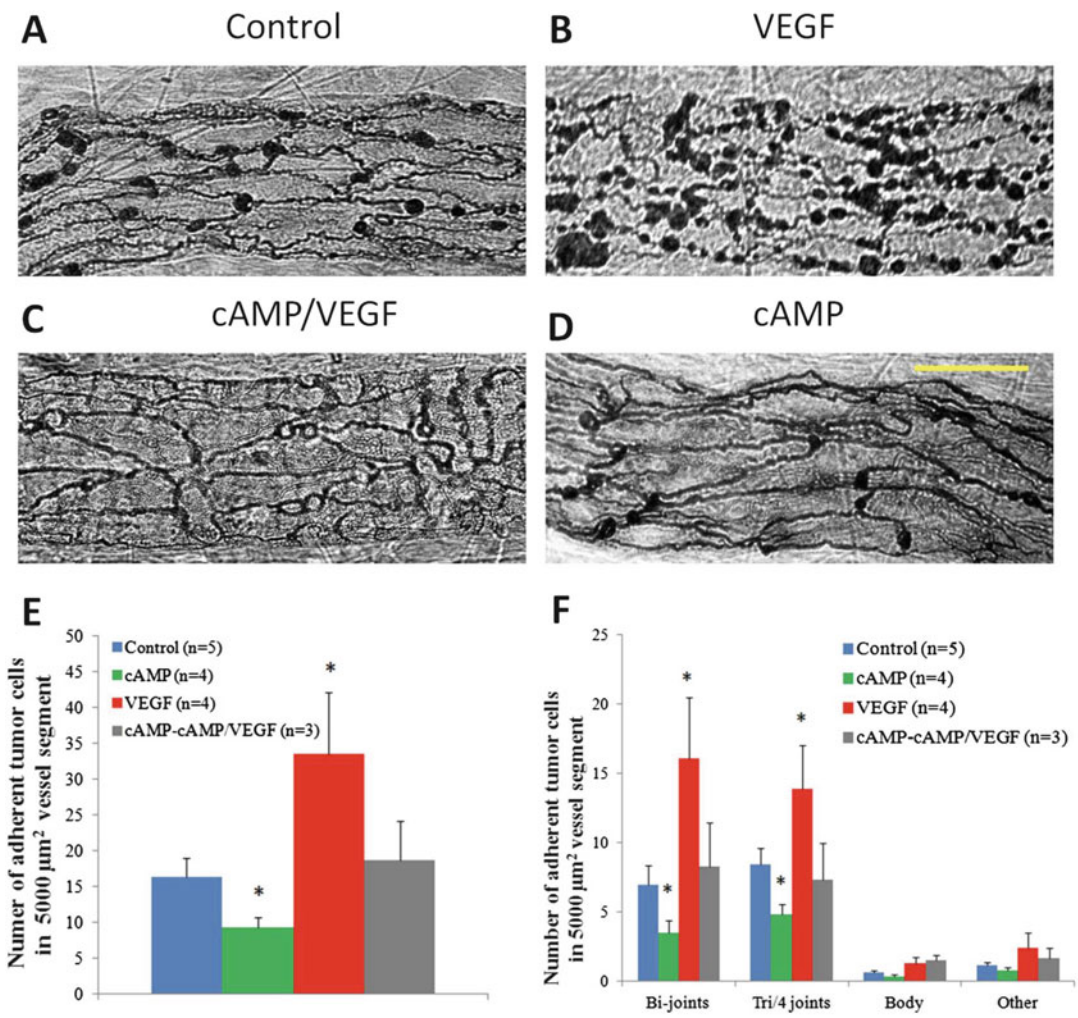

Fig. 2 In vivo MDA-MB-231 breast cancer cell adhesion to rat mesenteric microvessels under physiological flows. Tumor cells prefer to adhere to the junctions between endothelial cells forming the microvessel wall under control and various treatments scale bar = 30 μm. VEGF increases tumor cell adhesion, while cAMP decreases the adhesion. cAMP can also abolish the increased adhesion by VEGF (from Fu et al. 2015, with permission)

of microvasculature and the local hydrodynamic factors, along with the cell adhesion molecules at the tumor cell and endothelial cell should play a crucial role in tumor cell adhesion and extravasation. Tumor cells are exposed to flow while (a) circulating from the primary tumor, (b) arresting on downstream vascular endothelium, and (c) transmigrating into the secondary target organ. Investigations of the role of shear flow in tumor cell adhesion and extravasation should contribute to the understanding of the complex process of tumor metastasis. Tumor cell extravasation would normally occur in the microvasculature where shear forces are relatively low (like in postcapillary venules) although of sufficient magnitudes to activate cell surface receptors and alter vascular cell function. During tumor cell extravasation, there are significant changes in the structure and function of both tumor and endothelial cells. For example, a significant rearrangement of the cell cytoskeleton is required in both the tumor cells during migration (Lauffenburger and Horwitz 1996) and in the endothelial cells as the barrier function is altered (van Hinsbergh and

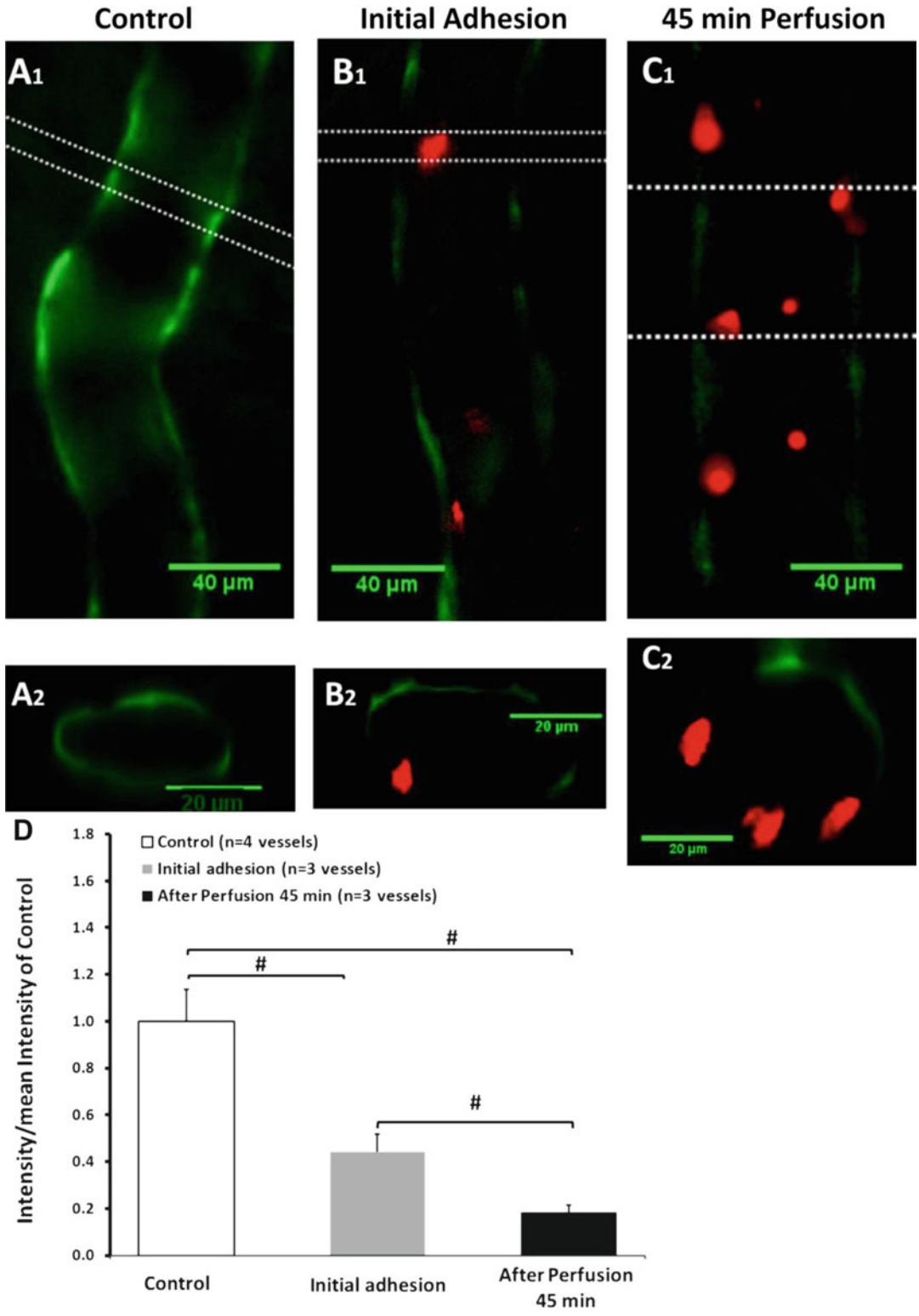

Fig. 3 Tumor cell adhesion degrades endothelial surface glycocalyx (ESG). FITC-anti-heparan sulfate-stained ESG (green) at a postcapillary venule under control (left column): midplane view (top) and cross-sectional view (bottom). Adhesion of cell tracker orange-labeled tumor cells (red) in a postcapillary venule at initial adhesion (mid-column) and after 45-min perfusion (right column) (from Cai et al. 2012, with permission)

Nieuw Amerongen 2002). The extravasation of tumor cells also induces endothelial cell remodeling (Kienast et al. 2010).

In an in vitro flow chamber study, Slattery et al. (2005) found that the shear rate, rather than the shear stress, plays a more significant role in PMN (polymorphonuclear neutrophils)-facilitated melanoma adhesion and extravasation. β2 integrins/ICAM-1 adhesion mechanisms were examined, and the results indicate LFA (lymphocyte function-associated)-1 and Mac-1 (CD11b/CD18) cooperate to mediate the PMN-EC (endothelial cell)-melanoma interactions under shear conditions. In addition, endogenously produced IL-8 contributes to PMN-facilitated melanoma arrest on the EC through the CXC chemokine receptors 1 and 2 (CXCR1 and CXCR2) on PMN (Liang et al. 2005; Slattery et al. 2005).

3.2 Effects of Hydrodynamic Factors on Tumor Metastasis

In addition to biochemical factors such as cell adhesion molecules (CAMs) and chemical/cytokines, circulating tumor cell adhesion in microvessel walls is affected by hydrodynamic factors, such as blood flow patterns, and flow-induced shear stresses and shear stress gradients (Bacac and Stamenkovic 2008; Wirtz and Searson 2012; Weiss 1992; Strell and Entschladen 2008; Mierke 2008). Numerous studies using in vivo and in vitro models have found that flow-induced hydrodynamic factors activate endothelial cells lining the blood vessel wall to generate reactive oxygen species, nitric oxide, and growth factors (Matsumoto et al. 2007; Bucci et al. 2005; Chiu et al. 2003; Zhang et al. 2016a, b). These substances can up- or downregulate the expression of endothelial CAMs and endothelial nitric oxide synthase (eNOS) depending on the strength of the mechanical factors, the flow patterns (e.g., laminar or turbulent), and the geometry of the vessel (e.g., straight or curved/branched) (Liu et al. 2008; Yan et al. 2010, 2012; Guo et al. 2014).

To investigate tumor cell adhesion in a well-controlled in vivo system, Shen et al. (2010) and Yan et al. (2012) used intravital video microscopy to measure the adhesion rate of malignant MDA-MB-435 s and 231 cells in straight and curved postcapillary venules on rat mesentery. A straight or curved microvessel was cannulated and perfused with tumor cells by a glass micropipette at a velocity of ∼1 mm/s, which is the mean normal blood flow velocity in this type of vessels. At less than 10 min after perfusion, there was a significant difference in cell adhesion to the straight and curved vessel walls. In 60 min, the averaged adhesion rate in the curved vessels was ∼1.5-fold of that in the straight vessels. In 51 curved segments, 45% of cell adhesion was initiated at the inner side, 25% at outer side, and 30% at both sides of the curved vessels. To investigate the mechanical mechanism by which tumor cells prefer adhering at curved sites, Yan et al. (2012) performed a computational study, in which the fluid dynamics was carried out by the lattice Boltzmann method (LBM), and the tumor cell dynamics was governed by the Newton's law of translation and rotation. The details of this multi-scale modeling are summarized in Chap. 12.

By injecting the tumor cells directly into the systemic circulation via carotid artery, Guo et al. (2014) found that MDA-MB-231 cancer cells prefer to adhere at the branched portion of the microvasculature rather than the non-branched portion. By numerical simulation, they also showed that there are higher shear rates/stresses and higher vorticities at the branching location where there are more arrested tumor cells (Fig. 4). Liu et al. (2008) demonstrated that thrombosis is also initiated at the curved portion of a vessel where there is a higher shear stress/rate and higher shear stress/rate gradient at the vessel wall. Furthermore, Shen et al. (2010) found that tumor cells adhered more in postcapillary venules under a normal blood flow velocity than under a reduced velocity. From these studies, it is likely that tumor cell adhesion sites are associated with localized hydrodynamic factors such as shear stresses and shear stress

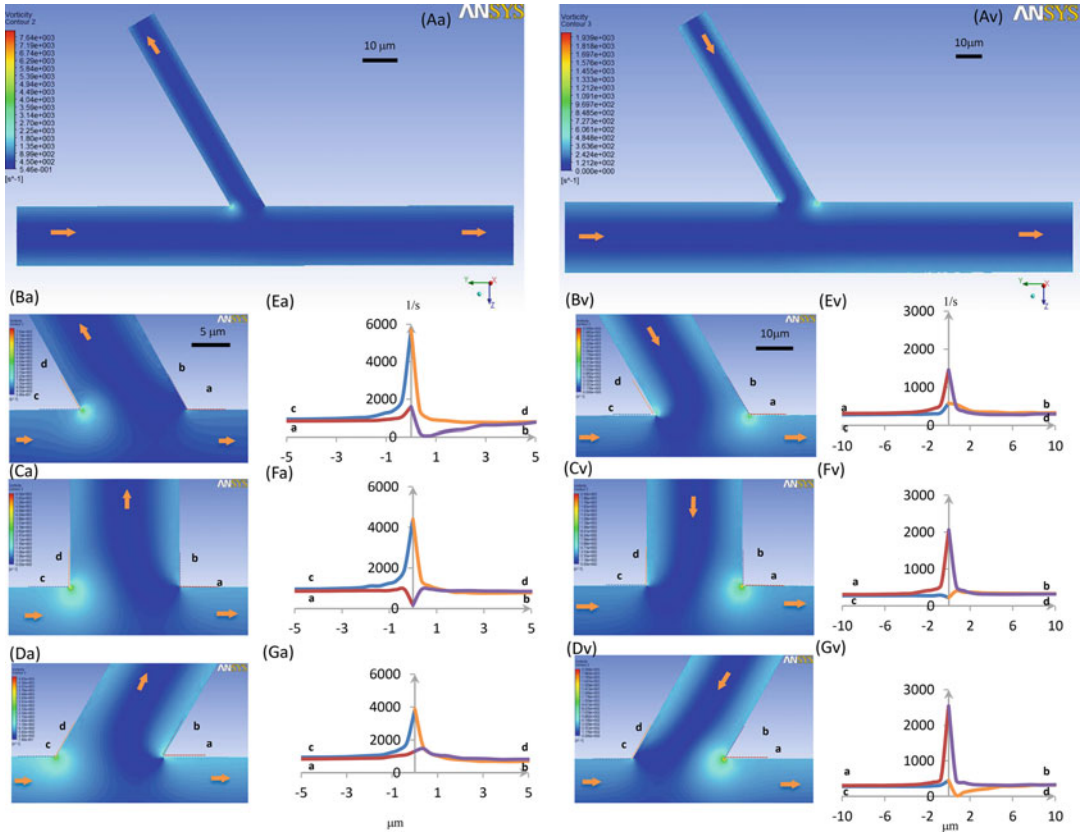

Fig. 4 Vorticity profiles in microvessels at intersections. Seven panels in the left column are arteriole-capillary intersections, and those in the right column are side branch vessel-postcapillary venule intersections. The top two Aa and Av are vorticity contour plots in the midplane of the vessels; Ba-Da and Bv-Dv are enlarged plots near the intersectional regions when branching angle θ is 60°, 90°, and 120°, respectively. Ea-Ga and Ev-Gv are detailed vorticity profiles at walls along dotted lines a–b (red) and c–d (blue) in Ba-Da and Bv-Dv. Arrows are flow directions in the microvessels. It was found that tumor cells prefer to arrest to the inner corners of the turns where there are higher vorticities (from Guo et al. 2014, with permission)

gradients. A recent study by Yen et al. (2015) showed that blood flow regulates nitric oxide (NO) production in rat mesenteric microvessels. The higher the flow velocity, the higher the endothelial NO production in postcapillary venules.

NO is the smallest signaling molecule that regulates a variety of important physiological functions (Forstermann and Sessa 2012). eNOS is responsible for most of the vascular NO production (Cooke et al. 1990). In cancer biology, NO can promote or inhibit tumor growth and metastasis, depending on its concentrations (Ridnour et al. 2006; Xu et al. 2002). Elevated NO and eNOS have been observed in cancer patients in malignancy states (Masri et al. 2005). Although high concentrations of NO are cytotoxic to the circulating tumor cells (Li et al. 1991; Mortensen et al. 2004; Pohl et al. 1991; Qiu et al. 2003; Wang et al. 2000), low levels of NO promote tumor cell arrest and adhesion (Scher 2007; Xu et al. 2002; Yudoh et al. 1997). NO at some optimal levels can inhibit cancer cell adhesion to cytokine-stimulated

endothelial cells (Lu et al. 2014; Xu et al. 2002), decrease tumor cell adhesion to naive and lipopolysaccharide (LPS)-treated postcapillary venules (Kong et al. 1996), and reduce invasion ability of cancer cells (Kielbik et al. 2014). Most recently, Zhang et al. (2016a, b) found that under normal physiological flow conditions, tumor cells prefer to adhere to the microvessel locations with a higher NO production such as curved portions. Inhibition of eNOS by NG-monomethyl-L-arginine (L-NMMA) attenuated the flow-induced NO production and reduced tumor cell adhesion. They also found that L-NMMA treatment for ~40 min reduced microvessel permeability to albumin. Therefore, their results suggest that inhibition of eNOS is a good approach to preventing tumor cell adhesion to intact microvessels under physiological flows.

In addition to the flow-induced hydrodynamic factors in the microvasculature, the mechanical properties such as rigidity of tumor cells determine their metastatic behaviors. Guck et al. (2005) and Koop et al. (1995) observed that tumor cells having a greater deformability are more invasive, malignant, and metastatic. Malignant (MCF-7) breast cells were found to have an apparent Young's modulus significantly lower (1.4–1.8 times) than that of their nonmalignant (MCF-10A) counterparts (Li et al. 2008). More recently, Swaminathan et al. (2011) found that

cancer cells with the highest migratory and invasive potential are five times less stiff than cells with the lowest migration and invasion potential. However, more rigid tumor cells may also be trapped in narrow capillaries. Most recently, Guo et al. (2014) injected fluorescently labeled human breast carcinoma cells or similarly sized rigid beads into the systemic circulation of a rat. Their arrest patterns in the microvasculature of mesentery were recorded and quantified. They found that ~93% of rigid beads were arrested either at arteriole-capillary intersections or in capillaries. Only ~3% were at the capillary-postcapillary venule intersections and in postcapillary venules. In contrast, most of the flexible tumor cells were either entrapped in capillaries or arrested at capillary or postcapillary venule-postcapillary venule intersections and in postcapillary venules. Forty-two percent of the flexible tumor cells were able to escape the capillary trapping.

4 Investigation of Tumor Metastasis by Using Microfluidic Systems

Although above summarized animal models for investigating tumor metastasis in the microcirculation have provided insightful information for the metastasis mechanism, it is necessary to explore the human tumor metastasis in microvessels formed by human endothelial cells. Therefore, the 2D transwell system and 2D and 3D single channel microfluidic system have been developed and used for decades by many researchers in investigating tumor cell and leukocyte adhesion, invasion, and transmigration under static and flow conditions (Cinamon and Alon 2003; Earley and Plopper 2006; Fan et al. 2011; Fan and Fu 2016; Lee et al. 2003; Shea et al. 2017; Slattery et al. 2005; Zhang et al. 2016a, b). Many recent microfluidic systems with complicated patterns have been developed to screen circulating tumor cells for diagnosis (Ferreira et al. 2016; Jiang et al. 2017; Khamenehfar and Li 2016; Khoo et al. 2018; Tadimety et al. 2017), to grow tumor cells with in and out flows for cancer drug screening (Chi et al. 2016; Dereli-Korkut et al. 2014) and to generate chemotaxis conditions for cancer cell migration (Liu et al. 2017; Um et al. 2017). Recently, an all-human 3D ex vivo hepatic microphysiological system was developed to mimic the stiffness of metastatic organ environment but without blood microvasculature (Clark et al. 2016). A 3D microfluidic system with simple blood microvasculature was developed but without real anatomical geometry (Kong et al. 2016). A sophisticated 3D microfluidic device (Fig. 5) with the generated microvasculature from human umbilical vein endothelial cells and human lung fibroblasts has been developed to quantify tumor cell intravasation and extravasation dynamics (Chen et al. 2013, 2017; Jeon et al. 2015; Zervantonakis et al. 2012).

The recently developed microfluidic systems recreated the tumor-vascular interface in 3D.

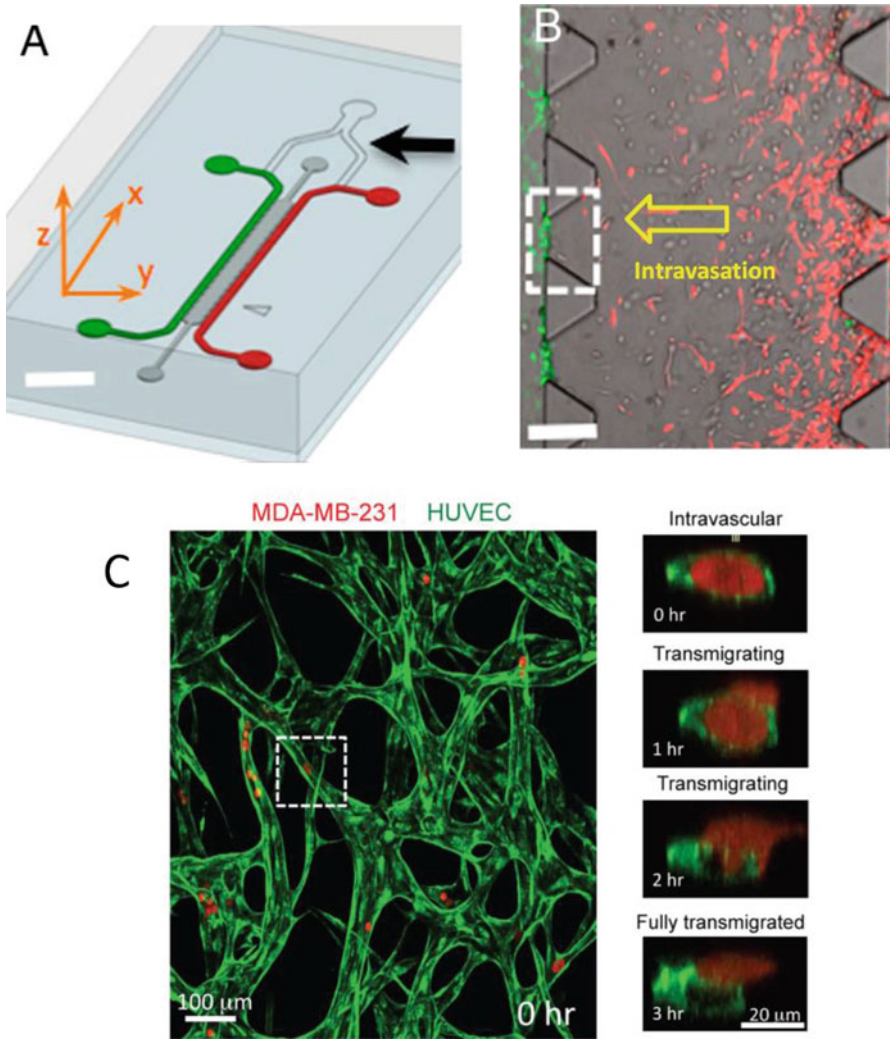

Fig. 5 Microfluidic tumor-vascular interface model. (**a**) Endothelial channel (green), tumor channel (red), and 3D extracellular matrix (ECM, dark gray) between the two channels. Channels are 500 μm wide, 20 mm in length, and 120 μm in height. Black arrow shows the y-junction. (Scale bar, 2 mm.) (**b**) Phase-contrast image showing the fibrosarcoma cells (HT1080, red) invading through the ECM (gray) toward the endothelium (microvascular endothelial cells, green). A single 3D ECM hydrogel matrix region is outlined with the white dashed square. (Scale bar, 300 μm.) (**c**) Confocal projection of a representative region of tumor (red) perfused microvascular network (green) at 20×. Representative cross-sectional views of a single transmigrating tumor cell (in dotted white box) and example of extravasation scoring (**a**, **b** from Zervantonakis et al. 2012 and **c** from Chen et al. 2017, with permission)

They not only enabled high-resolution, real-time imaging of tumor cell intravasation, arrest, adhesion, and extravasation and precise quantification of endothelial barrier function but also provided well-controlled tumor microenvironments mimicking various clinical conditions.

5 Summary and Future Study

Although transport across endothelium is a classical problem that has been investigated for more than several decades, the fundamental questions related to the structure-transport function of the microvessel wall and the interaction between the circulating cells and the cells forming the wall

still remain unclear. With the help from mathematical models for more accurate interpretations and predictions, new techniques involving transgenic animals with fluorescent protein-expressed endothelial cells and circulating blood and tumor cells, new fluorescent dyes for labeling the structural components of transvascular pathways, new developments in super-resolution optical microscopy and cryo-electron microscopy, and new developments in molecular biology and biochemistry will lead to more fascinating discoveries in this field.

One problem that has not been investigated thoroughly is the spatio-chemical organization and biomechanical properties of the endothelial surface glycocalyx, which is the barrier between circulating cells and endothelial cells forming the microvessel wall in addition to the molecular sieve. Newly developed super-resolution optical microscopy such as STORM (stochastic optical reconstruction microscopy) and STED (stimulated emission depletion) and AFM (atomic force microscopy) can be employed for this purpose. Another problem is to create transvascular models for cells such as leukocytes and cancer cells. The current multi-scale cell adhesion model can be revised to include the mechanical properties and morphological changes of adherent and endothelial cells in developing the cell transmigration models. The transvascular cell transport is crucial in many physiological and pathological processes including inflammatory response and tumor metastasis.

Acknowledgments This work was supported by the NSF CBET 0754158, NIH CA153325-01, CA137788-01, and 1UG3TR002151-01.

References

Achen MG, Stacker SA (2008) Molecular control of lymphatic metastasis. Ann N Y Acad Sci 1131:225–234

Adamson RH, Clough G (1992) Plasma proteins modify the endothelial cell glycocalyx of frog mesenteric microvessels. J Physiol 445:473–486

Adamson RH, Lenz JF, Zhang X, Adamson GN, Weinbaum S, Curry FE (2004) Oncotic pressures opposing filtration across non-fenestrated rat microvessels. J Physiol 557:889–907

Arkill KP, Knupp C, Michel CC, Neal CR, Qvortrup K, Rostgaard J, Squire JM (2011) Similar endothelial glycocalyx structures in microvessels from a range of mammalian tissues: evidence for a common filtering mechanism? Biophys J 101:1046–1056

Bacac M, Stamenkovic I (2008) Metastatic cancer cell. Annu Rev Pathol 3:221–247

Bates DO, Heald RI, Curry FE, Williams B (2001) Vascular endothelial growth factor increases Rana vascular permeability and compliance by different signalling pathways. J Physiol 533(Pt. 1):263–272

Berman AT, Thukral AD, Hwang WT, Solin LJ, Vapiwala N (2013) Incidence and patterns of distant metastases for patients with early-stage breast cancer after breast conservation treatment. Clin Breast Cancer 13:88–94

Betteridge KB, Arkill KP, Neal CR, Harper SJ, Foster RR, Satchell SC, Bates DO, Salmon AHJ (2017) Sialic acids regulate microvessel permeability, revealed by novel in vivo studies of endothelial glycocalyx structure and function. J Physiol 595(15):5015–5035

Brenner W, Langer P, Oesch F, Edgell CJ, Wieser RJ (1995) Tumor cell-endothelium adhesion in an artificial venule. Anal Biochem 225:213–219

Bucci M, Roviezzo F, Posadas I, Yu J, Parente L (2005) Endothelial nitric oxide synthase activation is critical for vascular leakage during acute inflammation in vivo. Proc Natl Acad Sci U S A 102:904–908

Bundgaard M (1984) The three-dimensional organization of tight junctions in a capillary endothelium revealed by serial-section electron microscopy. J Ultmstruct Res 88:1–17

Cai B, Fan J, Zeng M, Zhang L, Fu BM (2012) Adhesion of malignant mammary tumor cell MDA-MB-231 to microvessel wall increases microvascular permeability via degradation of endothelial surface glycocalyx. J of Appl Physiol 13(7):1141–1153

Cancel LM, Fitting A, Tarbell JM (2007) In vitro study of LDL transport under pressurized (convective) conditions. Am J Phys 293:H126–H132

CDC Report (2015) Number of deaths for leading causes of death

Chambers AF, Groom AC, MacDonald IC (2002) Dissemination and growth of cancer cells in metastatic sites. Nat Rev Cancer 2:563–572

Chen MB, Whisler JA, Jeon JS, Kamm RD (2013) Mechanisms of tumor cell extravasation in an in vitro microvascular network platform. Integr Biol (Camb) 5:1262–1271

Chen MB, Whisler JA, Fröse J, Yu C, Shin Y, Kamm RD (2017) On-chip human microvasculature assay for visualization and quantification of tumor cell extravasation dynamics. Nat Protoc 12(5):865–880

Chi CW, Rezwanuddin Ahmed AH, Dereli-Korkut Z, Wang S (2016) Microfluidic cell chips for high throughput drug screening. Bioanalysis 8(9):921–937

Chiu JJ, Chen LJ, Lee PL, Lee CI, Lo LW (2003) Shear stress inhibits adhesion molecule expression in vascular endothelial cells induced by coculture with smooth muscle cells. Blood 101:2667–2674

Chotard-Ghodsnia R, Haddad O, Leyrat A, Drochon A, Verdier C, Duperray A (2007) Morphological analysis of tumor cell/endothelial cell interactions under shear flow. J Biomech 40:335–344

Cinamon G, Alon R (2003) A real time in vitro assay for studying leukocyte transendothelial migration under physiological flow conditions. J Immunol Methods 273:53–62

Clark AM, Wheeler SE, Young CL, Stockdale L, Shepard Neiman J, Zhao W, Stolz DB, Venkataramanan R, Lauffenburger D, Griffith L, Wells A (2016) A liver microphysiological system of tumor cell dormancy and inflammatory responsiveness is affected by scaffold properties. Lab Chip 17(1):156–168

Cooke JP, Stamler J, Andon N, Davies PF, McKinley G (1990) Flow stimulates endothelial cells to release a nitrovasodilator that is potentiated by reduced thiol. Am J Phys 259:H804–H812

van den Berg BM, Vink H, Spaan JA (2003) The endothelial glycocalyx protects against myocardial edema. Circ Res 92:592–594

Dereli-Korkut Z, Akaydin D, Ahmed AHR, Jiang X, Wang S (2014) Three dimensional microfluidic cell arrays for ex vivo drug screening with mimicked vascular flow. Anal Chem 86(6):2997–3004

Drenckhahn D, Ness W (1997) The endothelial contractile cytoskeleton. In: Born GVR, Schwartz CJ (eds) Vascular endothelium: physiology, pathology and therapeutic opportunities. Schattauer, Stuttgart, Gennany, pp 1–15

Dvorak HF, Brown LF, Detmar M, Dvorak AM (1995) Vascular permeability factor/vascular endothelial growth factor, microvascular hyperpermeability, and angiogenesis. Am J Pathol 146:1029–1039

Earley S, Plopper GE (2006) Disruption of focal adhesion kinase slows transendothelial migration of AU-565 breast cancer cells. Biochem Biophys Res Commun 350:405–412

Ebong EE, Macaluso FP, Spray DC, Tarbell JM (2011) Imaging the endothelial glycocalyx in vitro by rapid freezing/freeze substitution transmission electron microscopy. Arterioscler Thromb Vasc Biol 31(8): 1908–1915

Fan J, Fu BM (2016) Quantification of malignant breast cancer cell MDA-MB-231 transmigration across brain and lung microvascular endothelium. Annals of Biomed Eng 44(7):2189–2201

Fan J, Cai B, Zeng M, Hao Y, Giancotti FG, Fu BM (2011) Integrin β4 signaling promotes mammary tumor cell adhesion to brain microvascular endothelium by inducing ErbB2-medicated secretion of VEGF. Ann of Biomed Eng 39(8):2223–2241

Feng D, Nagy JA, Payne K, Hammel I, Dvorak HF, Dvorak AM (1999) Pathways of macromolecular extravasation across microvascular endothelium in response to VPF/VEGF and other vasoactive mediators. Microcirculation 6(1):23–44

Ferreira MM, Ramani VC, Jeffrey SS (2016) Circulating tumor cell technologies. Mol Oncol 10(3):374–394

Fidler IJ (2011) The biology of cancer metastasis. Semin Cancer Biol 21:71

Folkman J (1971) Tumor angiogenesis: therapeutic implications. N Engl J Med 285:1182–1186

Forstermann U, Sessa WC (2012) Nitric oxide synthases: regulation and function. Eur Heart J 33:829–837

Fu BM, Shen S (2003) Structural mechanisms of vascular endothelial growth factor (VEGF) on microvessel permeability. Am J Phys 284(6):H2124–H2135

Fu BM, Shen S (2004) Acute VEGF effect on solution permeability of mammalian microvessels in vivo. Microvasc Res 68(1):51–62

Fu BM, Tarbell JM (2013) Mechano-sensing and transduction by endothelial surface glycocalyx: composition, structure, and function. Wiley Interdiscip Rev Syst Biol Med 5:381–390

Fu BM, Weinbaum S, Tsay RY, Curry FE (1994) A junction-orifice-fiber entrance layer model for capillary permeability: application to frog mesenteric capillaries. ASME J Biomech Eng 116:502–513

Fu BM, Chen B, Chen W (2003) An electrodiffusion model for effects of surface glycocalyx layer on microvessel solute permeability. Am J Phys 284: H1240–H1250

Fu BM, Shen S, Chen B (2006) Structural mechanisms in the abolishment of VEGF-induced microvascular hyperpermeability by cAMP. ASME J. Biomech. Eng. 128(3):313–328

Fu BM, Yang J, Shen S, Cai B, Fan J, Zhang L, Yen WY, Zeng M (2015) Reinforcing endothelial junctions prevents microvessel permeability increase and tumor cell adhesion in microvessels in vivo. Scientific Reports Oct 28

Gassmann P, Kang ML, Mees ST, Haier J (2010) In vivo tumor cell adhesion in the pulmonary microvasculature is exclusively mediated by tumor cell-endothelial cell interaction. BMC Cancer 10(177)

Giancotti FG (2007) Targeting integrin beta4 for cancer and anti-angiogenic therapy. Trends Pharmacol Sci 28:506–511

Giavazzi R, Foppolo M, Dossi R, Remuzzi A (1993) Rolling and adhesion of human tumor cells on vascular endothelium under physiological flow conditions. J Clin Invest 92:3038–3044

Glinskii OV, Huxley VH, Glinsky GV, Pienta KJ, Raz A, Glinsky VV (2005) Mechanical entrapment is insufficient and intercellular adhesion is essential for metastatic cell arrest in distant organs. Neoplasia 7(5):522–527

Guck J, Schinkinger S, Lincoln B, Wottawah F, Ebert S, Romeyke M, Lenz D, Erickson HM, Ananthakrishnan R, Mitchell D, Kas J, Ulvick S, Bilby C (2005) Optical deformability as an inherent cell marker for testing malignant transformation and metastatic competence. Biophys J 88(5):3689–3698

Guo W, Giancotti FG (2004) Integrin signalling during tumour progression. Nat Rev Mol Cell Biol 5:816–826

Guo W, Pylayeva Y, Pepe A, Yoshioka T, Muller WJ, Inghirami G, Giancotti FG (2006) Beta 4 integrin amplifies ErbB2 signaling to promote mammary tumorigenesis. Cell 126:489–502

Guo P, Cai B, Lei M, Liu Y, Fu BM (2014) Differential arrest and adhesion of tumor cells and microbeads in the microvasculature. Biomech Model Mechanobiol 13:537–550

Gupta GP, Massague J (2006) Cancer metastasis: building a framework. Cell 127:679–695

van Hinsbergh VW, Nieuw Amerongen GP (2002) Intracellular signalling involved in modulating human endothelial barrier function. J Anat 200:549–560

Hood JD, Cheresh DA (2002) Role of integrins in cell invasion and migration. Nat Rev Cancer 2:91–100

Jeon JS, Bersini S, Gilardi M, Dubini G, Charest JL, Moretti M, Kamm RD (2015) Human 3D vascularized organotypic microfluidic assays to study breast cancer cell extravasation. Proc Natl Acad Sci U S A 112(1):214–219

Jiang X, Wong KHK, Khankhel AH, Zeinali M, Reategui E, Phillips MJ, Luo X, Aceto N, Fachin F, Hoang AN, Kim W, Jensen AE, Sequist LV, Maheswaran S, Haber DA, Stott SL, Toner M (2017) Microfluidic isolation of platelet-covered circulating tumor cells. Lab Chip 17(20):3498–3503

Kang Y, Siegel PM, Shu W, Drobnjak M, Kakonen SM (2003) A multigenic program mediating breast cancer metastasis to bone. Cancer Cell 3:537–549

Khamenehfar A, Li PC (2016) Microfluidic devices for circulating tumor cells isolation and subsequent analysis. Curr Pharm Biotechnol 17(9):810–821

Khoo BL, Grenci G, Lim YB, Lee SC, Han J, Lim CT (2018) Expansion of patient-derived circulating tumor cells from liquid biopsies using a CTC microfluidic culture device. Nat Protoc 13(1):34–58

Kielbik M, Szulc I, Brzezinska M, Bednarska K, Przygodzka P (2014) Nitric oxide donors reduce the invasion ability of ovarian cancer cells in vitro. Anti-Cancer Drugs 25:1141–1151

Kienast Y, von Baumgarten L, Fuhrmann M, Klinkert WE, Goldbrunner R, Herms J, Winkle F (2010) Real-time imaging reveals the single steps of brain metastasis formation. Nature Med 16(1):116–122

Kong L, Dunn GD, Keefer LK, Korthuis RJ (1996) Nitric oxide reduces tumor cell adhesion to isolated rat postcapillary venules. Clin Exp Metastasis 14: 335–343

Kong J, Luo Y, Jin D, An F, Zhang W, Liu L, Li J, Fang S, Li X, Yang X, Lin B, Liu T (2016) A novel microfluidic model can mimic organ-specific metastasis of circulating tumor cells. Oncotarget 7(48):78421–78432

Koop S, MacDonald IC, Luzzi K, Schmidt EE, Morris VL, Grattan M, Khokha R, Chambers AF, Groom AC (1995) Fate of melanoma cells entering the microcirculation: over 80% survive and extravasate. Cancer Res 55(12):2520–2523

Lauffenburger DA, Horwitz AF (1996) Cell migration: a physically integrated molecular process. Cell 84: 359–369

Lee TH, Avraham HK, Jiang S, Avraham S (2003) Vascular endothelial growth factor modulates the transendothelial migration of MDA-MB-231 breast cancer cells through regulation of brain microvascular endothelial cell permeability. J Biol Chem 278: 5277–5284

Li LM, Kilbourn RG, Adams J, Fidler IJ (1991) Role of nitric oxide in lysis of tumor cells by cytokine-activated endothelial cells. Cancer Res 51:2531–2535

Li QS, Lee GY, Ong CN, Lim CT (2008) AFM indentation study of breast cancer cells. Biochem Biophys Res Commun 374(4):13–609

Li G, Simon M, Shi Z, Cancel L, Tarbell JM, Morrison B, Fu BM (2010) Permeability of endothelial and astrocyte cocultures: in vitro blood-brain barrier models for drug delivery. Ann of Biomed Eng 38(8):2499–2511

Liang S, Slattery MJ, Dong C (2005) Shear stress and shear rate differentially affect the multi-step process of leukocyte-facilitated melanoma adhesion. Exp Cell Res 310(2):282–292

Litjens SH, de Pereda JM, Sonnenberg A (2006) Current insights into the formation and breakdown of hemidesmosomes. Trends Cell Biol 16:376–383

Liu Q, Mirc D, Fu BM (2008) Mechanical mechanisms of thrombosis in intact bent microvessels of rat mesentery. J Biomech 41:2726–2734

Liu Z, Han X, Zhou Q, Chen R, Fruge S, Jo MC, Ma Y, Li Z, Yokoi K, Qin L (2017) Integrated microfluidic system for gene silencing and cell migration. Adv Biosyst 1(6)

Lu Y, Yu T, Liang H, Wang J, Xie J (2014) Nitric oxide inhibits hetero-adhesion of cancer cells to endothelial cells: restraining circulating tumor cells from initiating metastatic cascade. Sci Rep 4:4344

Luft JH (1966) Fine structures of capillary and endocapillary layer as revealed by ruthenium red. Fed Proc 25(6):1773–1783

Masri FA, Comhair SA, Koeck T, Xu W, Janocha A (2005) Abnormalities in nitric oxide and its derivatives in lung cancer. Am J Respir Crit Care Med 172:597–605

Matsumoto K, Nishi K, Kikuchi M, Kadowaki D, Tokutomi Y (2007) Alpha1-acid glycoprotein suppresses rat acute inflammatory paw edema through the inhibition of neutrophils activation and prostaglandin E2 generation. Biol Pharm Bull 30:1226–1230

Michel CC, Curry FE (1999) Microvascular permeability. Physiol Reviews 79(3):703–761

Michel CC, Neal CR (1999) Openings through endothelial cells associated with increased microvascular permeability. Microcirculation 6(1):45–62

Mierke CT (2008) Role of the endothelium during tumor cell metastasis: is the endothelium a barrier or a promoter for cell invasion and metastasis. J Biophys 2008:183516

Minn AJ, Kang Y, Serganova I, Gupta GP, Giri DD et al (2005) Distinct organ-specific metastatic potential of individual breast cancer cells and primary tumors. J Clin Invest 115:44–55

Moasser MM, Basso A, Averbuch SD, Rosen N (2001) The tyrosine kinase inhibitor ZD1839 (“Iressa”) inhibits HER2-driven signaling and suppresses the growth of HER2-overexpressing tumor cells. Cancer Res 61:7184–7188

Mook ORF, Marle J, Vreeling-Sindelarova H, Jongens R, Frederiks WM, Noorden CJK (2003) Visualisation of early events in tumor formation of eGFP-transfected rat colon cancer cells in liver. Hepatology 38:295–304

Mortensen K, Christensen IJ, Nielsen HJ, Hansen U, Larsson LI (2004) High expression of endothelial cell nitric oxide synthase in peritumoral microvessels predicts increased disease-free survival in colorectal cancer. Cancer Lett 216:109–114

Mukhopadhyay D, Nagy JA, Manseau EJ, Dvorak HF (1998) Vascular permeability factor/vascular endothelial growth factor-mediated signaling in mouse mesentery vascular endothelium. Cancer Res 58(6): 1278–1284

Nguyen DX, Bos PD, Massague J (2009) Metastasis: from dissemination to organ-specific colonization. Nat Rev Cancer 9:274–284

Olsson AK, Dimberg A, Kreuger J, Claesson-Welsh L (2006) VEGF receptor signalling—in control of vascular function. Nat Rev Mol Cell Biol 7(5):359–371

Pohl U, Herlan K, Huang A, Bassenge E (1991) EDRF-mediated shear-induced dilation opposes myogenic vasoconstriction in small rabbit arteries. Am J Physiol 261:H2016–2023

Qiu H, Orr FW, Jensen D, Wang HH, McIntosh AR et al (2003) Arrest of B16 melanoma cells in the mouse pulmonary microcirculation induces endothelial nitric oxide synthase-dependent nitric oxide release that is cytotoxic to the tumor cells. Am J Pathol 162:403–412

Reitsma S, Slaaf DW, Vink H, van Zandvoort MA, oude Egbrink MG (2007) The endothelial glycocalyx: composition, functions, and visualization. Pflug Arch: Eur J Physiol 454:345–359

Ridnour LA, Thomas DD, Donzelli S, Espey MG, Roberts DD (2006) The biphasic nature of nitric oxide responses in tumor biology. Antioxid Redox Signal 8:1329–1337

Roberts WG, Palade GE (1995) Increased microvascular permeability and endothelial enestration induced by vascular endothelial growth factor. J Cell Sci 108:2369–2379

Salmon AH, Satchell SC (2012) Endothelial glycocalyx dysfunction in disease: albuminuria and increased microvascular permeability. J Pathol 226(4):562–574

Salmon AH, Neal CR, Sage LM, Glass CA, Harper SJ, Bates DO (2009) Angiopoietin-1 alters microvascular permeability coefficients in vivo via modification of endothelial glycocalyx. Cardiovasc Res 83(1):24–33

Scher RL (2007) Role of nitric oxide in the development of distant metastasis from squamous cell carcinoma. Laryngoscope 117:199–209

Schluter K, Gassmann P, Enns A, Korb T, Hemping-Bovenkerk A, Holzen J, Haier J (2006) Organ-specific metastatic tumor cell adhesion and extravasation of colon carcinoma cells with different metastatic potential. Am J Pathol 169:1064–1073

Shea DJ, Li YW, Stebe KJ, Konstantopoulos K (2017) E-selectin-mediated rolling facilitates pancreatic cancer cell adhesion to hyaluronic acid. FASEB J 31(11):5078–5086

Shen S, Fan J, Cai B, Lv Y, Zeng M, Hao Y, Giancotti F, Fu BM (2010) Vascular endothelial growth factor enhances mammary cancer cell adhesion to endothelium *in vivo*. J of Exp Physiology 95:369–379

Shi L, Zeng M, Sun Y, Fu BM (2014) Quantification of blood-brain barrier solute permeability and brain transport by multiphoton microscopy. J Biomech Eng 136:031005

Slattery MJ, Liang S, Dong C (2005) Distinct role of hydrodynamic shear in leukocyte-facilitated tumor cell extravasation. Am J Phys 288:C831–C839

Squire JM, Chew M, Nneji G, Neal C, Barry J, Michel CC (2001) Quasi-periodic substructure in the microvessel endothelial glycocalyx: a possible explanation for molecular filtering? J Struct Biol 136:239–255

Steeg PS, Theodorescu D (2008) Metastasis: a therapeutic target for cancer. Nat Clin Pract Oncol 5(4):206–219

Steinbauer M, Guba M, Cernaianu G, Köhl G, Cetto M, Kunz-Schugart LA, Gcissler EK, Falk W, Jauch KW (2003) GFP-transfected tumor cells are useful in examining early metastasis in vivo, but immune reaction precludes long-term development studies in immunocompetent mice. Clin Exp Metastasis 20: 135–141

Strell C, Entschladen F (2008) Extravasation of leukocytes in comparison to tumor cells. Cell Commun Signal 6:10

Swaminathan V, Mythreye K, O'Brien ET, Berchuck A, Blobe GC, Superfine R (2011) Mechanical stiffness grades metastatic potential in patient tumor cells and in cancer cell lines. Cancer Res 71(15):5075–5080

Tadimety A, Syed A, Nie Y, Long CR, Kready KM, Zhang JX (2017) Liquid biopsy on chip: a paradigm shift towards the understanding of cancer metastasis. Integr Biol (Camb) 23 9(1):22–49

Talmadge JE, Fidler IJ (2010) AACR centennial series: the biology of cancer metastasis: historical perspective. Cancer Res 70:5649–5669

Tarbell JM, Pahakis MY (2006) Mechanotransduction and the glycocalyx. J Intern Med 259:339–350

Tobler NE, Detmar M (2006) Tumor and lymph node lymphangiogenesis–impact on cancer metastasis. J Leukoc Biol 80:691–696

Um E, Oh JM, Granick S, Cho YK (2017) Cell migration in microengineered tumor environments. Lab Chip 17(24):4171–4185

Vink H, Duling BR (1996) Identification of distinct luminal domains for macromolecules, erythrocytes, and leukocytes within mammalian capillaries. Circ Res 79:581–589

Wang HH, McIntosh AR, Hasinoff BB, Rector ES, Ahmed N et al (2000) B16 melanoma cell arrest in the mouse liver induces nitric oxide release and sinusoidal cytotoxicity: a natural hepatic defense against metastasis. Cancer Res 60:5862–5869

Weber GF (2007) Molecular mechanisms of cancer. Springer, Netherlands

Weiss L (1992) Comments on hematogenous metastatic patterns in humans as revealed by autopsy. Clin Exp Metastasis 10:191–199

Wirtz DKK, Searson PC (2012) The physics of cancer: the role of physical interactions and mechanical forces in metastasis. Nat Rev Cancer 11:512

Wyckoff JB, Jones JG, Condeelis JS, Segall JE (2000) A critical step in metastasis: in vivo analysis of intravasation at the primary tumor. Cancer Res 60:2504–2511

Xu W, Liu LZ, Loizidou M, Ahmed M, Charles IG (2002) The role of nitric oxide in cancer. Cell Res 12:311–320

Yan WW, Liu Y, Fu BM (2010) Effects of curvature and cell-cell interaction on cell adhesion in microvessels. Biomech Model Mechanobiol 9:629–640

Yan WW, Cai B, Liu Y, Fu BM (2012) Effects of wall shear stress and its gradient on tumor cell adhesion in curved microvessels. Biomech Model Mechanobiol 11(5):641–653. https://doi.org/10.1007/s10237-011-0339-6

Yen WY, Cai B, Zeng M, Tarbell JM, Fu BM (2012) Quantification of the endothelial surface glycocalyx on rat and mouse blood vessels. Microvasc Res

Yen WY, Cai B, Yang J, Zhang L, Zeng M, Tarbell JM, Fu BM (2015) Endothelial surface glycocalyx can regulate flow-induced endothelial NO production in microvessels in vivo. PLoS One 10(1):e0117133

Yudoh K, Matsui H, Tsuji H (1997) Nitric oxide induced by tumor cells activates tumor cell adhesion to endothelial cells and permeability of the endothelium in vitro. Clin Exp Metastasis 15:557–567

Zervantonakis IK, Hughes-Alford SK, Charest JL, Condeelis JS, Gertler FB, Kamm RD (2012) Three-dimensional microfluidic model for tumor cell intravasation and endothelial barrier function. Proc Natl Acad Sci U S A 109(34):13515–13520

Zhang L, Zeng M, Fu BM (2016a) Inhibition of endothelial nitric oxide synthase decreases breast cancer cell MDA-MB-231 adhesion to intact microvessels under physiological flows. Am J Physiol Heart Circ Physiol 310(11):H1735–H1747

Zhang L, Fan J, Zeng M, Curry F-RE, John MT, Fu BM (2016b) Sphingosine-1-phosphate (S1P) maintains normal microvascular permeability by preserving endothelial surface glycocalyx (ESG) in intact microvessels. Microcirculation 23(4):301–310

Zhang L, Zeng M, Fu BM (2017) Sphingosine-1-phosphate reduces adhesion of malignant mammary tumor cells MDA-MB-231 to microvessel walls by protecting endothelialsurface glycocalyx. Cell Mol Biol (Noisy-le-Grand) 63(4):16–22

Modeling Cell Adhesion and Extravasation in Microvascular System

L. L. Xiao, W. W. Yan, Y. Liu, S. Chen, and B. M. Fu

Abstract

The blood flow behaviors in the microvessels determine the transport modes and further affect the metastasis of circulating tumor cells (CTCs). Much biochemical and biological efforts have been made on CTC metastasis; however, precise experimental measurement and accurate theoretical prediction on its mechanical mechanism are limited. To complement these, numerical modeling of a CTC extravasation from the blood circulation, including the steps of adhesion and transmigration, is discussed in this chapter. The results demonstrate that CTCs prefer to adhere at the positive curvature of curved microvessels, which is attributed to the positive wall shear stress/gradient. Then, the effects of particulate nature of blood on CTC adhesion are investigated and are found to be significant in the microvessels. Furthermore, the presence of red blood cell (RBC) aggregates is also found to promote the CTC adhesion by providing an additional wall-directed force. Finally, a single cell passing through a narrow slit, mimicking CTC transmigration, was examined under the effects of cell deformability. It showed that the cell shape and surface area increase play a more important role than the cell elasticity in cell transit across the narrow slit.

L. L. Xiao
College of Automotive Engineering, Shanghai University of Engineering Science, Shanghai, China

W. W. Yan
College of Metrology and Measurement Engineering, China Jiliang University, Hangzhou, China

Y. Liu (✉)
Department of Mechanical Engineering, The Hong Kong Polytechnic University, Kowloon, Hong Kong, China
e-mail: yang.liu@polyu.edu.hk

S. Chen
School of Aerospace Engineering and Applied Mechanics, Tongji University, Shanghai, China

B. M. Fu
Department of Biomedical Engineering, The City College of the City University of New York, New York, NY, USA

1 Introduction

Metastasis contributes to as much as 90% cancer-associated deaths and is mainly mediated by the circulating tumor cells (CTCs) in the blood circulation. Cancer cells initially group together to form a primary tumor. To metastasize, a cancer cell detaching from the primary tumor invades the surrounding tissue, enters the blood circulatory or lymphatic system, which delivers it to a distant location, and finally establishes itself in the new metastatic site. Blood stream

B. M. Fu, N. T. Wright (eds.), *Molecular, Cellular, and Tissue Engineering of the Vascular System*, Advances in Experimental Medicine and Biology 1097,
https://doi.org/10.1007/978-3-319-96445-4_12

provides the common way for the CTC transport. Although various types of cancer cells can be found in the blood of patients, the cancer cells exhibit metastatic inefficiency (Weiss 1982) as most of them are trapped and rapidly and lethally damaged in the microvasculature while subjecting to body's defense system, collisions with blood cells, and hemodynamic shear forces. As a result, fewer than 1 in 10, 000 cancer cells can survive, and the concentration of cancer cells in the blood of patients is as low as in the order of one in a million leukocytes (Maheswaran and Haber 2010) or one in a billion blood cells (Yu et al. 2011). To leave away from the microvascular system, the CTCs must adhere to the vessel walls of distant organs and eventually penetrate the vascular wall to form secondary tumors. The precise behaviors and mechanisms by which tumor cell extravasates across the blood vessel remain poorly understood.

The adhesion of cells to surface under flow condition as a principal step in the cancer metastasis has attracted much attention in the past few decades. A major conceptual development is the recognition that cellular adhesions are often mediated via a surprisingly small number of receptor-ligand bonds (Zhu et al. 2000), where the receptors are located on the surface of endothelial cells lining the vessel wall and ligands are distributed on the membrane of the CTCs. Considerable progress has been made in identifying molecules involved in adhesion. For leukocyte emigration, adhesion molecules of the selectin family (as ligands) mediate the initial rolling of cells on the endothelium, whereas firm adhesion is mediated by interactions between integrin receptors and immunoglobulin superfamily cell adhesion molecules (Springer 1994). Despite that a similar mechanism is expected for CTCs, that is not the true case. Dong et al. (2005) suggested that neutrophils (PMNs) could possibly form a bridge and bind to both the melanoma cell and endothelial cell monolayer through the bonds formed between the adhesion molecules. Melanoma extravasation is enhanced significantly by adding PMNs. To explain this mechanism, Behr et al. (2015) proposed a local numerical model to characterize the biochemical interactions between circulating melanoma tumor cells and adherent PMN, which is feasible to predict the adhesion outcomes for many realizations of the cells and flow condition at a reasonable speed. The interactions between ligands on CTCs and endothelial cell bound surface receptors are largely dependent on receptor-ligand distances at nanoscale, which are controlled by the glycocalyx coated on the surface of CTCs and endothelial cells (Mitchell and King 2014). The presence of the thick glycocalyx expressed on ECs may prevent the adhesion of CTCs under normal physiological conditions, but changes in fluid shear stress may induce shedding of the glycocalyx, which can increase the availability of adhesion receptors and then promote CTC adhesion. After firmly adhered to the vascular endothelium, tumor cells may produce biological factors that optimally tune EC contractility to promote tumor cell extravasation from the blood vessel wall (Stroka and Konstantopoulos 2014). By using confocal microscopy (Fan and Fu 2015), the transmigration of malignant breast tumor cell through the endothelial monolayers has been observed. It is shown that more than 95% of tumor cells cross the endothelial monolayer through the junctions between adjacent endothelial cells and only a few percent through the cell bodies. Tumor cells undergo dramatic shape changes, driven by a significant rearrangement of the cell cytoskeleton (Sugihara-Seki and Fu 2005; Wirtz et al. 2011). Invasive cancer cells can decrease the endothelial barrier function through regulating the biomechanical properties of endothelial cells (Mierke 2011, 2012). In addition, it is found that metastatic cancer cells are softer than their normal or benign counterparts, which may facilitate squeezing through confine spaces much smaller than the size of the cell body (Cross et al. 2007; Suresh 2007).

The CTCs are exposed to complicated vascular microenvironment once in the circulation. For the blood flow in microcirculation, the length scale is usually about several to several hundreds of micrometers, on which level a homogeneous continuum description is not adequate due to the significant particulate nature of the blood flow. The discrete nature of the blood in mi-

crovasculature makes it clear that the behaviors of individual cells play a key role in the fluid dynamics and rheology of the blood and transport of CTCs within microvasculature. For example, the deformability of RBCs and their propensity to reversibly aggregate coupled with complex structure of the microvasculature may lead to nonuniform hematocrit and heterogeneous viscosity (Fung 1993; Pries et al. 1992; Reinke et al. 1987) and further determine the route of CTCs (Haier and Nicolson 2001; Koumoutsakos et al. 2013; Wirtz et al. 2011). However, it is difficult to predict tumor cell behaviors, and it is hard to experimentally measure the multiscale blood flows including CTCs and the interactions between CTCs and blood cells or vascular endothelium. Along with the advances in computer technology and algorithms for multi-physics and multiscale simulation, some numerical models of flowing blood systems have been established to explicitly solve the blood flows ranging from cellular to organ scales, which can be found in the recent reviews (Freund 2014; Gompper and Fedosov 2016; Imai et al. 2016; Ju et al. 2015; Kunz et al. 2015).

The cells and surrounding fluid can be modeled using continuum-based methods or mesoscopic methods. For solving fluid flow, the traditional approach is the discretization of incompressible Navier-Stokes equations on a mesh that constitutes the flow domain, such as Eulerian finite-difference and finite volume methods, which is complemented by the semi-Lagrangian lattice Boltzmann method. Owing to the fact that the Reynolds numbers of blood flow in microcirculation are much less than one, the inertia effect can be neglected, and boundary element/integral method can be introduced by virtue of the linearity of the Stokes flow equations and the availability of Green's functions (Freund 2014). In addition, particle-based methods based on Newton's law have been developed in the past few decades, in which the fluid domain is discretized using Lagrangian moving particles whose ensemble behavior statistically returns the appropriate dynamics of the system. For the modeling of cells, as their deformability plays a key role for the hemodynamics, two representative models characterize cell deformation: one is a shell-based membrane model based on a continuum description, which has been developed by Pozrikidis (2001), including the elastic tensions and bending moments; and another employs a spring-based membrane network model describing the microstructure details at spectrin molecular level (Li et al. 2005).

The treatment of coupling of deformable cells and fluid flow has always been a major challenge associated with the modeling of blood flow. Pozrikidis (2003) and Zhao et al. (2010) combined the shell-based cell model with boundary element/integral methods to investigate the deformation of RBCs in the flow, wherein a series of quasi-steady-state equations based on appropriate Green's functions are integrated over the individual cell and vessel wall surfaces to compute the flow. Despite their accuracy for solving cellular flows, they are limited to Stokes problems of very low Reynolds number, which is applicable for capillaries, venules, and arterioles. As powerful alternatives including inertia effects, mesh-based methods coupled with the discrete spring-based network model have emerged, accompanied by the immersed boundary method (IBM). As a classical fluid-structure interaction approach, IBM has been widely applied to solve the interactions between CTCs, RBCs, or WBCs and plasma flow combined with finite volume method, finite element method, and lattice Boltzmann method. The Lagrangian nodes for the membrane are described to be moving on fixed Eulerian grids for the fluid, and the physical quantities are transferred between them by using an interpolation function. Rejniak (2012) employed immersed boundary-finite-difference method to investigate the transport of an individual CTC with considering the interactions of CTCs and endothelial wall. Unlike the finite-difference methods, LBM is endowed with the stochastic nature, which is significant for the cellular flow at mesoscale. The fluid is represented by the fictitious particles which conform to a set of kinetic and collision rules on a discrete lattice mesh, while the cell membrane is discretized into a set of computational nodes

as an immersed boundary. IB-LBM as the most common method has been used to investigate leukocyte or tumor cell margination (Sun and Munn 2006; Takeishi et al. 2014, 2015), RBC aggregation (Vahidkhah and Fatouraee 2012; Zhang et al. 2008), and cell adhesion (Takeishi et al. 2016; Yan et al. 2012, 2010). It is simple to deal with complex geometries and can be easily implemented in a parallel computing environment. But when treating the irregular boundaries, refined meshes are required to confine the particle movement, which incurs high computational cost. Particle-based methods become attractive because different types of particles are employed to identify different components of the computational domain, which enables the interactions between fluid and cell membrane easier to deal with and can provide sufficient accuracy at an affordable computational cost. In this chapter, we mainly focus on dissipative particle dynamic (DPD) method and the spring-based network membrane model. Most of the applications of DPD on simulations of RBCs or WBCs have been conducted by Karniadakis' group, from the deformation of a single RBC (Fedosov et al. 2010a; Pivkin and Karniadakis 2008) to blood rheology (Fedosov et al. 2010b; Li et al. 2012) and WBC margination (Fedosov and Gompper 2014), which provides important guidance for the numerical studies of CTC metastasis.

2 Mathematical Models for Cell Adhesion

The mathematical modeling of cell adhesion provides a powerful tool to quantify experimental observations and to integrate them into a unified sequence of cell adhesion events. These models not only help to test the hypotheses suggested by experimental observations but also to gain insights about the mechanisms of cell adhesion. The extensive studies on biophysical experiments of cell adhesion have led to the development of various mathematical models. The construction and application of these models have demonstrated that it is possible to analyze certain cellular processes by highly quantitative approaches (Zhu 2000). Many mathematical models have been proposed to describe different important events in cell adhesion. Hammer and Apte (1992) firstly proposed a mathematical model to simulate the interaction of a single cell with a ligand-coated surface under flow conditions. This model can simulate the effect of many parameters on adhesion, such as the number of receptors on microvilli tips, the density of ligands, the rates of reaction between receptors and ligands, the stiffness of the resulting receptor-ligand springs, the response of springs to strain, and the magnitude of bulk hydrodynamic stresses. The model can successfully recreate the entire range of expected and observed adhesive phenomena, from completely unencumbered motion, to rolling, to transient attachment, to firm adhesion. Moreover, this model can generate meaningful statistical measures of adhesion, including the mean and variance in velocity, rate constants for cell attachment and detachment, and the frequency of adhesion. King and Hammer (2001) used the completed double-layer boundary integral equation method to study the adhesive interactions between multiple rigid particles and a planar boundary in a viscous fluid. The simulation results revealed a mechanism for the capture of free-stream cells once an initial cell has adhered to provide a nucleation site. Wang et al. (2006) developed a population balance model for cell aggregation and adhesion process in a nonuniform shear flow. They carried out Monte Carlo simulation based on the model for the heterotypic cell-cell collision and adhesion to a substrate under dynamic shear forces. Shao and Xu (2007) numerically studied the adhesion between a microvillus-bearing cell and a ligand-coated substrate by adopting Monte Carlo method. They found that most of the adhesion was mediated by a single bond if the total adhesion frequency was less than 20%.

Mathematical models of cell adhesion relate the forward and reverse reaction rates for receptor-ligand bonds. These laws about the reaction rates for cell adhesion have been defined as "adhesive dynamic models", which can be used to couple the effect of receptor-ligand bonds on cell adhesion. Figure 1 shows the

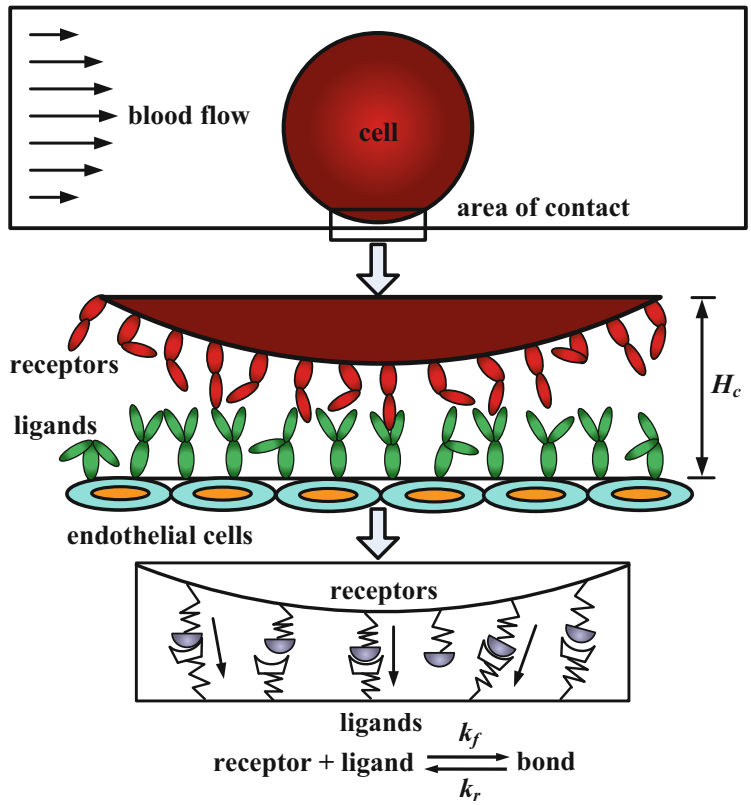

Fig. 1 The schematic view of adhesive dynamic model for cell adhesion

schematic view of adhesive dynamic model for cell adhesion. In this model, the cell adhesion molecules on the surface of circulating cell are defined as receptors, and these on the surface of endothelial cells are defined as ligands. Once the distance between the receptor and the ligand is smaller than the critical length Hc, it has the chance to form receptor-ligand bonds. Interactions between receptors and ligands are realized by the ideal adhesive springs, and the spring forces are calculated via the compression or expansion of these springs. This dynamic process relates the bond association and dissociation rate of adhesive dynamic models. The following are the two typical cell dynamic models.

2.1 Bell's Model

Bell's model (Bell 1978) was validated to be a good approximation for different states of cell adhesion in the straight microvessels, such as free movement, rolling, landing, and firm adhesion (Caputo and Hammer 2005). In the model, the association rate of the bond is 84 s^{-1}, which is a reasonable value that extensive simulations have shown can properly recreate experimental values for velocity and dynamics of rolling in the straight microvessels (Chang et al. 2000). As to the dissociation rate of the bond, Bell (1978) adopted the kinetic theory of the strength of solids and proposed a constitutive relation between dissociation rate and force. Therefore, the bond association rate k_f and bond dissociation rate k_r are

$$k_f = 84\ s^{-1} \text{ and } k_r = k_r^0 \exp\left(\frac{\gamma f}{k_b T}\right) \quad (1)$$

where k_b is the Boltzmann constant, T is the absolute temperature, k_r^0 is the unstressed dissociation rate, γ is the reactive compliance that describes the degree to which force facilitates bond breakage, and both k_r^0 and γ are the functional properties of adhesion molecules. f is the

spring force of each bond which can be obtained according to the Hooke's law: $f = \sigma(\chi - \lambda)$, where σ is the spring constant, χ is the distance between the end points of receptor and ligand, and λ is the equilibrium bond length.

2.2 Dembo et al.'s Model

Dembo et al. (1988) modeled a piece of membrane with immobile discrete bonds and allowed the membrane to detach. They did this by letting the applied tension exceed the bond stress. This model can be used to predict the critical membrane tension required for detachment and the resulting peeling velocities of the membrane. The main contribution of this model is the expression for the rate constants as a function of distance between the membranes. Dembo et al. (1988) demonstrated the reasonable, thermodynamically consistent rate expressions relating the bond association rate k_f and bond dissociation rate k_r to χ as

$$k_f = k_f^0 \exp\left(-\frac{\sigma_{ts}(\chi-\lambda)^2}{2k_bT}\right) \text{ and } k_r = k_r^0 \exp\left(-\frac{(\sigma-\sigma_{ts})(\chi-\lambda)^2}{2k_bT}\right) \quad (2)$$

where k_f^0 and k_r^0 are the reaction rate constants when the spring is at its equilibrium length and σ and σ_{ts} are the spring constant and "transition state" spring constant, respectively.

Once the forward association rate and reverse dissociation rate of the bond are known, the appropriate expressions for the probability of formation and breakage of the bond tethers in a time step dt can be obtained by (Chang and Hammer 1996; Yan et al. 2016)

$$P_f = 1 - \exp\left(-k_f \cdot dt\right) \text{ and } P_r = 1 - \exp\left(-k_r \cdot dt\right) \quad (3)$$

where P_f is the probability of forming a bond and P_r is the probability of breaking a bond in a time interval dt.

3 CTC Adhesion Under the Blood Flow in a Curved Microvessel

It has been found that the CTCs are more likely adherent to the curved microvessels than the straight ones (Liu et al. 2008; Yan et al. 2012). At the curved sites, there are rather complicated distributions of wall shear stress. The wall shear stress or its variation may activate receptor-ligand bond formation, which appears to render these sites to be prone to catch cells. Based on the experimental observation, Yan et al. (2012) revised Bell's model by integrating the effect of wall shear stress and its gradient on CTC adhesion, respectively. The models are:

Case 1: The bond association/dissociation rates are related to shear stress:

$$k_f = k_f^n \cdot \left(\frac{\tau}{\tau_0}\right)^{k_1} \text{ and } k_r = k_r^n \cdot \left(\frac{\tau}{\tau_0}\right)^{k_2} \quad (4)$$

Case 2: The bond association/dissociation rates are related to shear stress gradients:

$$k_f = k_f^n \cdot \exp\left(k_3 \frac{d\tau}{dl}\right) \text{ and } k_r = k_r^n \cdot \exp\left(-k_4 \frac{d\tau}{dl}\right) \quad (5)$$

where k_f^n and k_f^n are the normal bond association/dissociation rates that calculated from Eqs. (1) and (3). τ and τ_0 are the wall shear stresses along the curved portion of a vessel and along the straight portion, respectively, and $d\tau/dl$ is the wall shear stress gradient along the curved portion. k_1, k_2 and k_3, k_4 are coefficients that represent the sensitivity of wall shear stress and its gradient to bond association/dissociation rates, respectively.

Case 3: Use the same model as case 2. Only the jumps or drops in the wall shear stress gradient can trigger the change of bond association/dissociation rates. Once triggered, the association/dissociation rates will keep the maximum/minimum value until the next wall shear stress gradient jump or drop occurs.

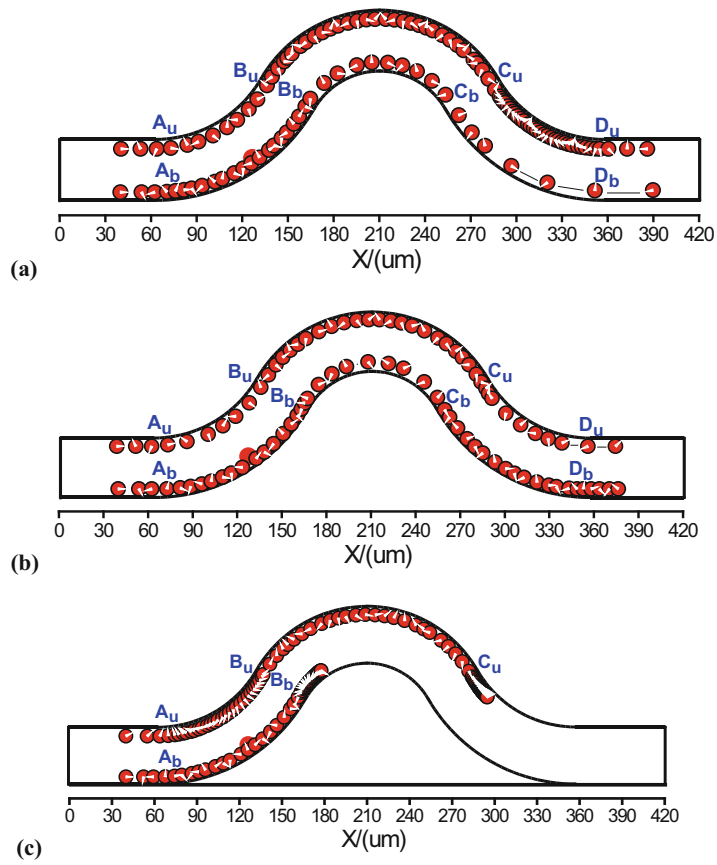

Fig. 2 The CTC trajectory for these three cases: (**a**) case 1, (**b**) case 2, (**c**) case 3. Here, A_u, B_u, C_u, D_u and A_b, B_b, C_b, D_b represent the conjunctions of positive and negative curvature segments along the upper and bottom walls, respectively

The numerical simulations on CTC adhesion with three modified adhesive dynamic models have been executed. Since the curvature would affect the trajectory of the cell (Yan et al. 2010), a curved microvessel with both positive and negative curvature is designed, where A_u, B_u, C_u, D_u and A_b, B_b, C_b, D_b are the conjunctions of positive and negative curvature segments, respectively. To assure the CTC would roll over the conjunctions, the cell is released near either the upper or the bottom wall at the entrance. Figure 2 shows the CTC trajectory for these three cases where the denser trajectory means slower motion and the coarse trajectory indicates faster motion. For case 1, the denser trajectory occurs at [A_b, B_b] and [B_u, C_u] due to the centrifugal effect. In addition, the highly denser trajectory occurs between C_u and D_u, indicating that there is a stronger CTC adhesion in the positive curvature where the local wall shear stress significantly increases. The coarser trajectory happens between C_b and D_b, indicating a faster cell motion there due to the decrease in k_f and increase in k_r, both of which result from the drop of wall shear stress there. For case 2, the denser trajectory occurs near the conjunction B_b and C_u, indicating a slower cell motion there due to the stronger adhesive effect caused by the large jump in the wall shear stress gradient there. The coarser trajectory exists in the positive curvature at [B_b, C_b], [A_u, B_u], and [C_u, D_u], indicating a faster cell motion not due to the adhesive effect but due to the centrifugal effect. For case 3, when the CTC approaches to the conjunctions B_b and C_u, the cell moves slower and slower, represented by a black band in the cell trajectory. Generally, the positive wall shear stress/gradient jump would enhance CTC adhesion, while the negative wall shear stress/gradient jump would weaken CTC adhesion. The wall shear stress/gradient, over a

threshold, has significant contribution to CTC adhesion by activating or inactivating adhesion molecules. These results elucidated why the CTC adhesion prefers to occur at the positive curvature of curved microvessels with very low Reynolds number (in the order of 10^{-2}) laminar flow.

4 CTC Adhesion Under the Blood Flow of RBC Suspensions

To characterize the deformation of cells, cell membrane is discretized into a collection of particles connected by elastic springs. A spring-based network model endowed with in-plane and bending energy as well as constraint of surface area and volume has been introduced by Boey et al. (1998) to describe RBC initially. A systematic coarse-grained procedure was introduced by Pivkin and Karniadakis (2008) to reduce the number of degrees of freedom dramatically in the RBC model. This coarse-grained model was further improved by Fedosov et al. (2010a), yielding accurate mechanical response. The RBC aggregation is described by the intercellular interaction, which is characterized by a Morse potential function proposed by Liu and Liu (2006). We have employed this model to investigate the deformation and motion of two RBCs in a stenosed microvessel (Xiao et al. 2016b). Adhesion of CTCs to the vessel wall is modeled by the probabilistic model developed by Hammer and Apte (1992), which is based on Dembo et al.'s model. If the distance between a receptor and a free ligand is less than the reactive distance, a new bond randomly forms, while a pre-existing bond is statistically ruptured within the rupture distance. Receptor-ligand bonds are modeled as individual Hookean springs. Details of these models and related parameters have been described in a recent study (Xiao et al. 2017).

Although the process of cell adhesion to the vessel wall has been numerically investigated, the blood was treated as a homogeneous Newtonian fluid for simplicity, and the simulation system is limited to two-dimensional (Rejniak 2012; Yan et al. 2012, 2010). In microvessels, the RBCs, as the main constituents of blood, are comparable to the vessel in size, contributing to the particulate nature and heterogeneous viscosity of the blood. The tendency of RBCs flowing to the vessel center pushes leukocytes toward the endothelium, leading to the process of margination and initiating attachment to the endothelium. Evidence has been provided that tumor cell margination resembles leukocyte margination (Bendas and Borsig 2012). Therefore, explicit modeling of RBCs along with CTCs is required. The adhesion of CTCs also largely depends on the other blood hydrodynamic conditions, which are closely associated with the vascular structure, RBC aggregation, and flow rate.

Microvascular system is a complex network of microvessels connected by a set of short bifurcated segments. The blood flow patterns at microvessel branches determine the transport process and adhesion of CTCs. When there exists a large difference in the size of the daughter branches or the daughter branches of equal diameter have different flow velocities, the distribution of RBCs and plasma may not be uniform at these sites, indicating that the daughter branches may receive various levels of hematocrit (Yen and Fung 1978), named as phase separation. Such effect would affect the locomotion strategies of CTCs in blood stream, which is crucial for cell adhesion. In larger vessels, CTCs are assumed to switch from floating with the blood cells to margination and then to initial attachment to the endothelial wall, to rolling on it, to arrest. Fedosov and Gompper (2014) showed that in the vessel with diameter of 20 μm, leukocyte tends to move toward the vessel wall at regions of intermediate hematocrits, $Ht = 0.2$–0.4. It has been also found that the white blood cell (WBC) rolling speed increases with RBC concentration because it is affected by RBC-WBC collision frequency and blunting of the velocity profile (Sun and Munn 2005). In addition, the WBC adhesion increases at the hematocrit ranging from 10 to 30% (Abbitt and Nash 2003). But if the size of blood vessels is smaller than that of WBCs or CTCs, such as capillaries, cell arrest would occur without cell rolling due to size restriction (Chen et al. 2013). Takeishi et al. (2016) found that the

cell travels by bullet motion in capillaries, which allows it to firmly adhere to the wall even under weak receptor-ligand interaction force.

To investigate the effect of vessel size coupled with hematocrit, the flow of the CTC in different microvessels of various diameters ranging from 10 to 20 μm at different levels of hematocrit was simulated. A separation distance δ is introduced to trace the radial position of the CTC delivered by the blood flow, which is defined by the closest distance between the CTC membrane and the vessel wall surface. Figure 3a illustrates the probability of separation distance computed over a time period of 0.9 s. Here, $\delta \leq 0.1$ μm indicates that the CTC attaches to the vessel wall since the association length is set to 0.1 μm. From the bar chart, it can be seen that for $D = 10$ μm, the initial adherent CTC nearly attaches to the vessel wall, which is independent on the hematocrit. This is due to the fact that the CTC has a stronger confinement. That is why the tumor cell extravasation is expected in the microvessels with a diameter less than the cell diameter. For $D = 15$ μm, with the decrease in the hematocrit, the probability of CTC detachment from the vessel improves. At lower hematocrit ($Ht = 0.1$, 0.2), the rolling tumor cell might be pulled off the vessel by the intercellular interactions. However, at $Ht = 0.3$, the CTC maintains to roll along the wall. Due to the particulate nature of blood, the CTC has a lower collision frequency with red blood cells and subjects to a weaker wall-directed force at lower hematocrits. However, at $Ht = 0.3$, a stronger wall-directed force inhibits detachment of CTC from the vessel wall. For $D = 20$ μm, the initial adherent CTC is more likely to detach from the vessel at higher hematocrit. The initial adherent CTC can be found to detach from the vessel for all cases during rolling along the wall. But at higher hematocrit, the CTC cannot arrive at the vessel again during this simulation time period. Under the low shear flow rate, the weak tendency of RBC flowing toward the center of a microvessel inhibits the margination of CTC. Instead, the effect of particulate nature is so pronounced that RBCs in the blood flow are distributed separately and the number of RBCs near the wall is larger compared to the lower hematocrits, leading to an enhanced lift force. Therefore, the CTC nearly cannot reach the vessel wall at high hematocrit ($Ht = 0.3$), while at a low concentration of RBCs ($Ht = 0.1$), the detached CTC can easily reapproach the vessel wall under the pushing force exerted by the RBCs.

The margination and firm adhesion of WBCs to the endothelium also attributes to the ability of RBC aggregates because of an enhanced probability of contact between leukocytes and the vessel wall (Abbitt and Nash 2003; Munn and Dupin 2008; Pearson and Lipowsky 2000; Sun and Munn 2006). Then the effects of RBC aggregates on the adhesion of the CTC under different flow rates in the microvessel ($D = 20$ μm) were investigated. Firstly, for the case without RBC aggregation, by comparing the variation of the number of receptor-ligand bonds over the time period of around 0.8 s at different flow rates, Fig. 3b shows that at high flow rate ($\gamma = 17.72\ s^{-1}$), the initial adherent CTC detaches from the wall quickly due to the increasing lift force. But after a short time, the RBCs flowing toward the vessel center expel the CTC from the RBC core and further initiate the adhesion of the CTC to the vessel wall, as shown in Fig. 3f. In addition, the number of formed bonds is more than that at low flow rate due to the large deformation resulting from the large shear force, as plotted in Fig. 3c. The CTC maintains its original spherical shape at low flow rate.

The main effect of RBC aggregation is that the time of CTC contact to the vessel extends and the presence of RBC aggregation provides an additional wall-directed force to compress the adherent CTC (as shown in Fig. 3e, g), leading to an increasing number of receptor-ligand bonds. At low flow rate ($\gamma = 2.2\ s^{-1}$), the RBC aggregates enable the CTC to stably roll along the surface of the vessel wall with a certain number of bonds. Nevertheless, the weak deformation inhibits the formation of firmed adhesion. However, the large deformation induced by the high flow rate increases the CTC contact area; thus the number of bonds increases considerably, which can be seen at $t = 0.4$ s for the case of RBC aggregation in Fig. 3b. If the adhesive force is largerthan the

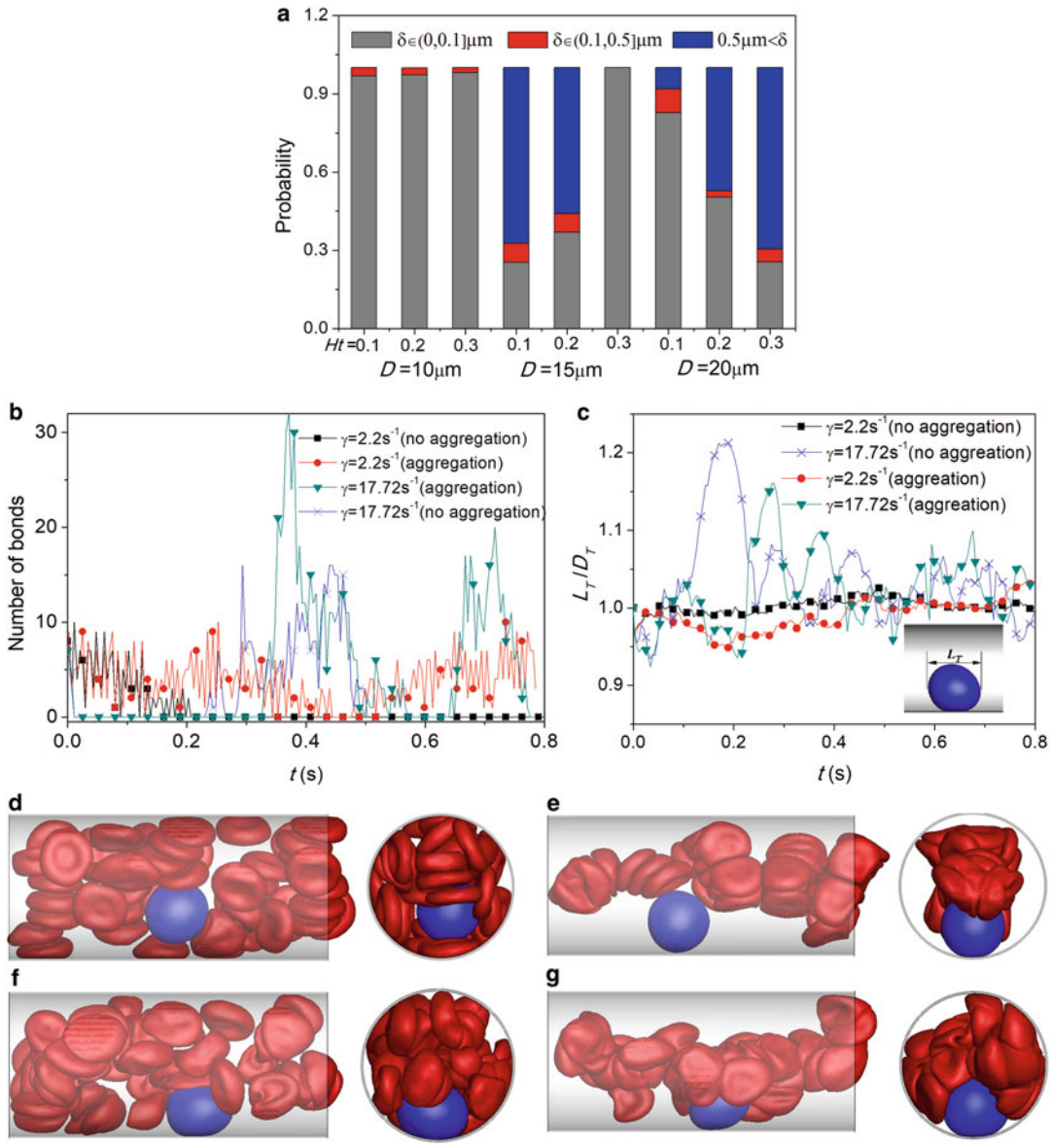

Fig. 3 Probability of the separation distance between the CTC membrane and wall surface for different tubes at $Ht = 0.1$, 0.2, and 0.3 (**a**); variation of number of receptor-ligand bonds (**b**) and the deformation of CTC along the flow direction (**c**) for the cases of RBC aggregation and non-aggregation at different flow rates for $D = 20$ μm, where L_T refers to the length of the CTC along the flow direction and D_T defines the diameter of the CTC; and snapshots of the flow of a CTC and RBCs for the cases of (**d**) $\gamma = 2.2$ s^{-1}, without RBC aggregation; (**e**) $\gamma = 2.2$ s^{-1}, with RBC aggregation; (**f**) $\gamma = 17.72$ s^{-1}, without RBC aggregation; (**g**) $\gamma = 17.72$ s^{-1}, with RBC aggregation

hydrodynamic viscous force exerted on the CTC, firm adhesion may be formed.

In addition to the vessel size and the RBC concentration as well as its behaviors, the microvascular geometry as well as CTC clusters provide other important factors in tumor cell metastasis. In vivo experiments showed that tumor cells as well as blood cells prefer to aggregate near the bend in a curved microvessel (Liu et al. 2008) and the bifurcations in microvasculature serve

the major sites of tumor cell adhesion (Guo et al. 2014; Zhang et al. 2016). King et al. (2015) experimentally investigated the circulating tumor cell dynamics in the microvasculature and showed that the rolling velocity of cancer cells increases with the number of cells or aggregates. CTC clusters were found to be capable of transiting through 5- to 10-μm-diameter blood vessels with greater metastatic potential than singlets, which inspires the strategies of interfering with cell-cell adhesion by chemical or enzymatic agents to reduce the probability of metastasis (Au et al. 2016; Hong et al. 2016).

5 CTC Transmigration Through the Blood Vessel Wall

To understand how CTCs undergo large elastic deformation during penetrating the vascular wall, it is necessary to analyze this process from the mechanical point of view. Few studies have investigated the mechanical process of the adherent tumor cells physically penetrating the vascular wall. But the passage of cell through a narrow channel, slit, or small pore has attracted much attention since the 1980s. Freund (2013) numerically investigated the flow of red blood cells (RBCs) through a narrow slit and observed that the cells infold in the slit due to high velocity or high cytosol viscosity, which might provide a mechanism for jamming. Omori et al. (2014) revealed that the transit time increases nonlinearly with the viscosity ratio when RBCs pass through a thin micropore. Wu and Feng (2013) explored malaria-infected RBCs transit through microchannel in terms of the cell deformability. Li et al. (2014) and Quinn et al. (2011) simulated a single RBC flowing through a narrow cuboid channel using dissipative particle dynamics and found that the cell deformation and transit time depend on cross-sectional geometry and cell size. These studies on RBC passage through a confined geometry provide important insights into a tumor cell's journey through the interendothelial cleft. As for the studies on tumor cell transmigration, cell deformation in microfluidic device offers effective measurement means to quantify the mechanical properties of cell in vitro (Chaw et al. 2007; Leong et al. 2011). It is found that the surface area of cancer cells increases by more than threefold during the cell deformation through 10 μm microgap (Chaw et al. 2007). Moreover, high-resolution time-lapse microscopy was employed to investigate the dynamic nature of tumor cell extravasation in an in vitro microvascular network platform. The findings showed that the tumor cell extrudes firstly through the formation of a small opening (1–2 μm) between endothelial cells and the opening grows to form a pore 8–10 μm in diameter to allow for nuclear transmigration (Chen et al. 2013). Finally, the numerical study on the circulating tumor cells passing through a 3D microfiltering channel shed lights on the importance of channel geometry on deformability-based cancer cell separation (Zhang et al. 2014).

Based on the numerical findings on the passage of RBCs through a constricted environment and experimental studies in tumor cell transmigration, it is necessary to furtherly examine the detailed mechanical process of tumor cell extravasation. The narrow slit between endothelial cells that line the microvessel wall is the principal pathway for tumor cell extravasation to the surrounding tissue (Fan and Fu 2015). To understand this crucial step for tumor hematogenous metastasis, an individual cell passing through a narrow slit is numerically investigated. As the elasticity affects greatly the cell deformability, cells with different values of Young's modulus squeezing into the slit of 6 μm width are compared, and it was found that reducing the elasticity modulus by ten times can double the protrusion length (the distance between the cell front end and the entry of the slit), but still doesn't enable the cell to pass the narrow slit (Xiao et al. 2016a).

As another determinant of the static deformability of the cells, the cell surface-to-volume ratio was also considered. Cancer cells exhibit various kinds of shapes, including round, oval, elongated, and clusters (Park et al. 2014). The shape transformation from sphere to flat ellipsoid largely increases the surface-to-volume ratio. In this section, spherical and ellipsoidal cell with the same volume and mechanical properties passing

through the narrow slit are compared in terms of the deformation. The effects of initial orientation of ellipsoidal cell on its transit through the slit are investigated. In order to characterize the cell deformation, the expression of local strain has been introduced in the previous study (Chen et al. 2013). Based on this definition, the average deformation γ_i for the membrane particle i is expressed as follows:

$$\gamma_i = \sqrt{\frac{\sum_{j=1}^{N_i} \left(\frac{l_{ij}}{l_{ij,0}} - 1\right)^2}{N_i}} \tag{6}$$

where N_i represents the number of springs which is connected by particle i and l_{ij} and $l_{ij,0}$ are the instantaneous and spontaneous lengths of springs, respectively. The local deformation contour for each membrane particle is plotted in Fig. 4.

When the spherical cell protrudes the slit, its forefront suffers large deformation, but the rear end doesn't nearly deform. The middle part of the cell located in the slit retains to be stretched with local γ reaching 80% after blockage, as shown in Fig. 4a. But for an ellipsoidal cell, the deformation depends on its initial orientation. When its seminor axis is parallel to y axis at initial time, the cell can pass through the slit easily, which can be seen in Fig. 4b, as the length of seminor axis is comparable to the slit. When the cell enters the slit, its front end is stretched initially. With the increase in protrusion length, the extruded part of cell expands, and the middle part maintains to be stretched, while the rear end almost keeps its original shape. After exiting from the slit, the forefront of the cell is stretched largely, while the rear end is compressed. But if the cell rotates 90° around z or x axis at initial time, the size of cell is nearly double the slit width. Therefore, the cell should compress itself when traversing the narrow slit, which produces large deformation. As its centroid reaches the center of the slit, the extruded part expands largely and local γ can attain 70%, while the exposed part has not been squeezed into the slit shrinks and even some wrinkles appear on the membrane, as can be seen in Fig. 4c, d. When the cell exits from the slit, it enfolds within the slit. After passing through the slit, the expanding part gradually shrinks, and the shrinking one expands slowly. In fact, before transmigrating through the slit between two endothelial cells, a tumor cell has to adhere to the endothelium. Then the adherent spherical cell would spread out into a flat shape before extravasation (Albelda et al. 1994; Dewitt and Hallett 2007; Stoletov et al. 2010; Zhu et al. 2000). This shape change enables tumor cells to transmigrate through a much narrower slit.

6 Summary

As one critical step in cancer metastasis, CTC adhesion prefers to occur at the curved microvessels. To explore this mechanical mechanism, a numerical study based on a modified adhesive dynamic model was proposed, and it can be found that the positive shear stresses/gradients promote cell adhesion by activating cell adhesion molecules.

Then the particulate effects of blood on the adhesion of CTC in microvessels were examined. When the vessel size is comparable to the CTC diameter, the probability of CTC adhesion is independent on the hematocrit. With the increase in vessel size, an enhanced adhesion occurs at higher hematocrit due to the growing wall-directed force. In a larger microvessel, an increased lift force induced by collision of the high concentration of RBCs facilitates CTC detachment from the vessel wall. In the aggregating RBC suspensions, an enhanced CTC adhesion can be found because an additional wall-directed force enforced by the RBC aggregates further compresses the CTC and enables the CTC to stably roll along the vessel wall.

As for the CTC transmigration across the endothelium, the deformability of the CTC has significant contribution to this event. Particularly, the cell shape and surface area increase are the more important determinant factors of cell deformability compared to the cell elasticity when the cell passes through the narrow slit.

Acknowledgments Supports given by HKRGC PolyU 5202/13E, PolyU G-YBG9 and G-UACM, National Nat-

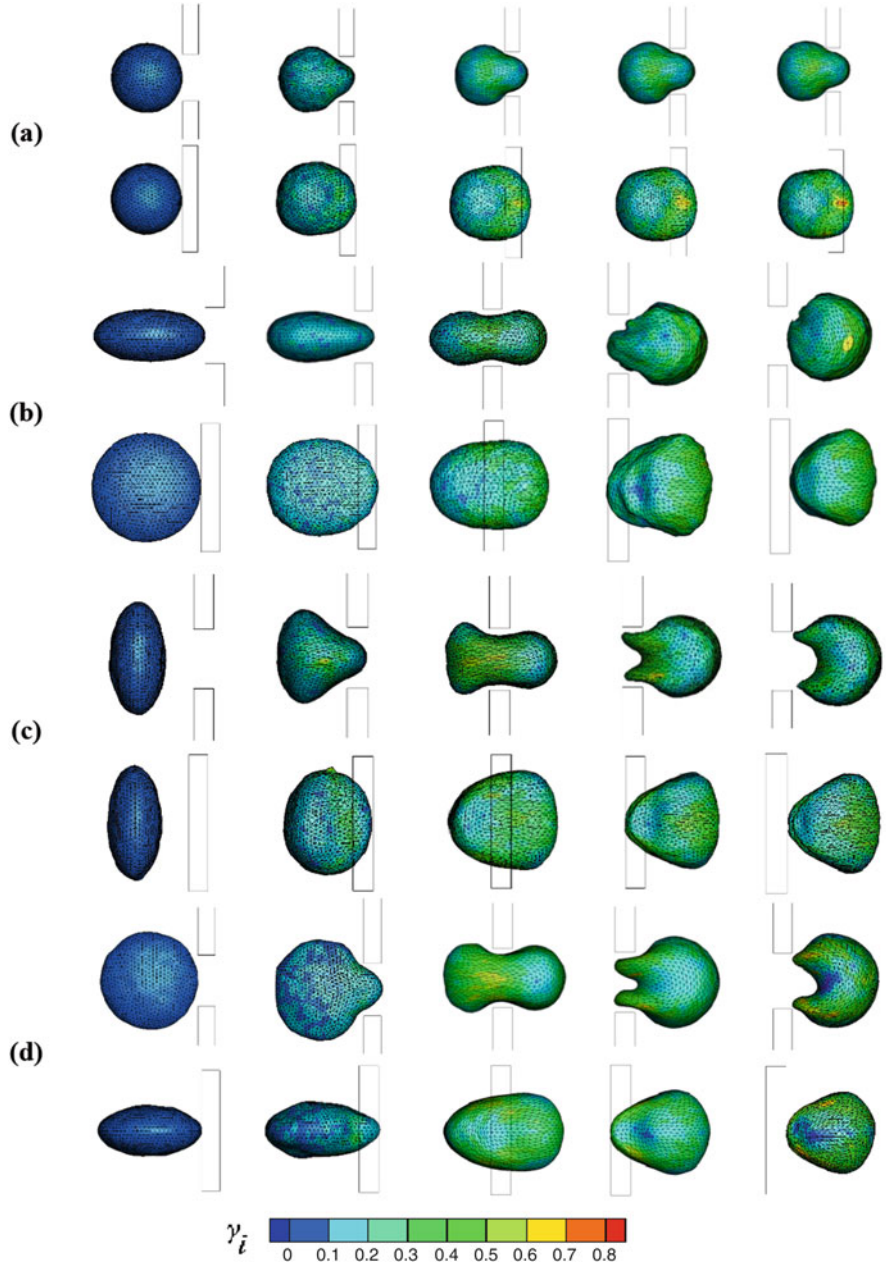

Fig. 4 Snapshots of the cell deformation for different relaxed shapes through the narrow slit from the front view (the upper row) and the top view (the lower row) separately. A/V is 0.667 μm^{-1} in (**a**), 0.730 μm^{-1} in (**b**, **c**) and (**d**). (**b**, **c**) and (**d**) represent that the seminor axis of the cell is parallel to y, x, and z axis, respectively

ural Science Foundation of China (Grant No. 51276130), and NIH SC1 CA153325-01 are gratefully acknowledged.

References

Abbitt KB, Nash GB (2003) Rheological properties of the blood influencing selectin-mediated adhesion of flowing leukocytes. Am J Physiol Heart Circ Physiol 285:H229–H240

Albelda SM, Smith CW, Ward PA (1994) Adhesion molecules and inflammatory injury. FASEB J 8: 504–512

Au SH et al (2016) Clusters of circulating tumor cells traverse capillary-sized vessels. Proc Natl Acad Sci U S A 113:4947–4952. https://doi.org/10.1073/pnas.1524448113

Behr J, Gaskin B, Fu C, Dong C, Kunz R (2015) Localized modeling of biochemical and flow interactions during cancer cell adhesion. PLoS One 10:e0136926. https://doi.org/10.1371/journal.pone.0136926

Bell GI (1978) Models for the specific adhesion of cells to cells. Science 200:618–627

Bendas G, Borsig L (2012) Cancer cell adhesion and metastasis: selectins, integrins, and the inhibitory potential of heparins. Int J Cell Biol 2012:676731. https://doi.org/10.1155/2012/676731

Boey SK, Boal DH, Discher DE (1998) Simulations of the erythrocyte cytoskeleton at large deformation. I. Microscopic models. Biophys J 75:1573–1583

Caputo KE, Hammer DA (2005) Effect of microvillus deformability on leukocyte adhesion explored using adhesive dynamics simulations. Biophys J 89:187–200. https://doi.org/10.1529/biophysj.104.054171

Chang KC, Hammer DA (1996) Influence of direction and type of applied force on the detachment of macromolecularly-bound particles from surfaces. Langmuir 12:2271–2282. https://doi.org/10.1021/La950690y

Chang KC, Tees DFJ, Hammer DA (2000) The state diagram for cell adhesion under flow: leukocyte rolling and firm adhesion. Proc Natl Acad Sci U S A 97:11262–11267. https://doi.org/10.1073/pnas.200240897

Chaw KC, Manimaran M, Tay EH, Swaminathan S (2007) Multi-step microfluidic device for studying cancer metastasis. Lab Chip 7:1041–1047

Chen MB, Whisler JA, Jeon JS, Kamm RD (2013) Mechanisms of tumor cell extravasation in an in vitro microvascular network platform. Integr Biol 5:1262–1271

Cross SE, Jin YS, Rao J, Gimzewski JK (2007) Nanomechanical analysis of cells from cancer patients. Nat Nanotechnol 2:780–783

Dembo M, Torney DC, Saxman K, Hammer D (1988) The reaction-limited kinetics of membrane-to-surface adhesion and detachment. Proc R Soc Lond B Biol Sci 234:55–83. https://doi.org/10.1098/rspb.1988.0038

Dewitt S, Hallett M (2007) Leukocyte membrane "expansion": a central mechanism for leukocyte extravasation. J Leukoc Biol 81:1160–1164

Dong C, Slattery MJ, Liang S, Peng HH (2005) Melanoma cell extravasation under flow conditions is modulated by leukocytes and endogenously produced interleukin 8. Molecular Cell Biomech 2:145–159

Fan J, Fu BM (2015) Quantification of malignant breast cancer cell MDA-MB-231 transmigration across brain and lung microvascular endothelium. Ann Biomed Eng 44(7):2189–2201. https://doi.org/10.1007/s10439-015-1517-y

Fedosov DA, Gompper G (2014) White blood cell margination in microcirculation. Soft Matter 10: 2961–2970

Fedosov DA, Caswell B, Karniadakis GE (2010a) Systematic coarse-graining of spectrin-level red blood cell models. Comput Methods Appl Mech Eng 199: 1937–1948

Fedosov DA, Caswell B, Popel AS, Karniadakis GE (2010b) Blood flow and cell-free layer in microvessels. Microcirculation 17:615–628

Freund JB (2013) The flow of red blood cells through a narrow spleen-like slit. Phys Fluids 25:110807

Freund JB (2014) Numerical simulation of flowing blood cells. Annu Rev Fluid Mech 46:67. https://doi.org/10.1146/annurev-fluid-010313-141349

Fung YC (1993) Biomechanics: mechanical properties of living tissues, 2nd edn. Springer-Verlag, New York

Gompper G, Fedosov DA (2016) Modeling microcirculatory blood flow: current state and future perspectives. WIREs Syst Biol Med 8:157–168. https://doi.org/10.1002/wsbm.1326

Guo P, Cai B, Lei M, Liu Y, Fu BMM (2014) Differential arrest and adhesion of tumor cells and microbeads in the microvasculature. Biomech Model Mechanobiol 13:537–550. https://doi.org/10.1007/s10237-013-0515-y

Haier J, Nicolson GL (2001) Tumor cell adhesion under hydrodynamic conditions of fluid flow. APMIS 109:241–262. https://doi.org/10.1034/j.1600-0463.2001.d01-118.x

Hammer DA, Apte SM (1992) Simulation of cell rolling and adhesion on surfaces in shear-flow - general results and analysis of selectin-mediated neutrophil adhesion. Biophys J 63:35–57

Hong YP, Fang F, Zhang Q (2016) Circulating tumor cell clusters: what we know and what we expect (review). Int J Oncol 49:2206–2216

Imai Y, Omori T, Shimogonya Y, Yamaguchi T, Ishikawa T (2016) Numerical methods for simulating blood flow at macro, micro, and multi scales. J Biomech 49:2221–2228. https://doi.org/10.1016/j.jbiomech.2015.11.047

Ju M, Ye SS, Namgung B, Cho S, Low HT, Leo HL, Kim S (2015) A review of numerical methods for red blood cell flow simulation. Comput Methods Biomech Biomed Engin 18:130–140. https://doi.org/10.1080/10255842.2013.783574

King MR, Hammer DA (2001) Multiparticle adhesive dynamics: hydrodynamic recruitment of rolling leukocytes. Proc Natl Acad Sci USA 98:14919–14924. https://doi.org/10.1073/pnas.261272498

King MR et al (2015) A physical sciences network characterization of circulating tumor cell aggregate transport. Am J Physiol Cell Physiol 308:C792–C802. https://doi.org/10.1152/ajpcell.00346.2014

Koumoutsakos P, Pivkin I, Milde F (2013) The fluid mechanics of cancer and its therapy. Annu Rev Fluid Mech 45(45):325–355. https://doi.org/10.1146/annurev-fluid-120710-101102

Kunz RF, Gaskin BJ, Li Q, Davanloo-Tajbakhsh S, Dong C (2015) Multi-scale biological and physical modelling of the tumour micro-environment. Drug Discov Today Dis Model 16:7–15. https://doi.org/10.1016/j.ddmod.2015.03.001

Leong FY, Li QS, Lim CT, Chiam KH (2011) Modeling cell entry into a micro-channel. Biomech Model Mechanobiol 10:755–766

Li J, Dao M, Lim CT, Suresh S (2005) Spectrin-level modeling of the cytoskeleton and optical tweezers stretching of the erythrocyte. Biophys J 88:3707–3719. https://doi.org/10.1529/biophysj.104.047332

Li XJ, Popel AS, Karniadakis GE (2012) Blood-plasma separation in Y-shaped bifurcating microfluidic channels: a dissipative particle dynamics simulation study. Phys Biol 9:026010

Li X, Peng Z, Lei H, Dao M, Karniadakis GE (2014) Probing red blood cell mechanics, rheology and dynamics with a two-component multi-scale model. Philos Transact A Math Phys Eng Sci 372:20130389. https://doi.org/10.1098/rsta.2013.0389

Liu YL, Liu WK (2006) Rheology of red blood cell aggregation by computer simulation. J Comput Phys 220:139–154. https://doi.org/10.1016/j.jcp.2006.05.010

Liu Q, Mirc D, Fu BM (2008) Mechanical mechanisms of thrombosis in intact bent microvessels of rat mesentery. J Biomech 41:2726–2734

Maheswaran S, Haber DA (2010) Circulating tumor cells: a window into cancer biology and metastasis. Curr Opin Genet Dev 20:96–99. https://doi.org/10.1016/j.gde.2009.12.002

Mierke CT (2011) Cancer cells regulate biomechanical properties of human microvascular endothelial cells. J Biol Chem 286:40025–40037

Mierke CT (2012) Endothelial cell's biomechanical properties are regulated by invasive cancer cells. Mol BioSyst 8:1639–1649

Mitchell MJ, King MR (2014) Physical biology in cancer. 3. The role of cell glycocalyx in vascular transport of circulating tumor cells. Am J Phys Cell Phys 306:C89–C97. https://doi.org/10.1152/ajpcell.00285.2013

Munn LL, Dupin MM (2008) Blood cell interactions and segregation in flow. Ann Biomed Eng 36:534–544

Omori T, Hosaka H, Imai Y, Yamaguchi T, Ishikawa T (2014) Numerical analysis of a red blood cell flowing through a thin micropore. Phys Rev E 89:013008

Park S, Ang RR, Duffy SP, Bazov J, Chi KN, Black PC, Ma HS (2014) Morphological differences between circulating tumor cells from prostate cancer patients and cultured prostate cancer cells. PLoS One 9:e85264

Pearson MJ, Lipowsky HH (2000) Influence of erythrocyte aggregation on leukocyte margination in postcapillary venules of rat mesentery. Am J Physiol Heart Circ Physiol 279:H1460–H1471

Pivkin IV, Karniadakis GE (2008) Accurate coarse-grained modeling of red blood cells. Phys Rev Lett 101:118105

Pozrikidis C (2001) Effect of membrane bending stiffness on the deformation of capsules in simple shear flow. J Fluid Mech 440:269–291

Pozrikidis C (2003) Numerical simulation of the flow-induced deformation of red blood cells. Ann Biomed Eng 31:1194–1205. https://doi.org/10.1114/1.1617985

Pries AR, Neuhaus D, Gaehtgens P (1992) Blood-viscosity in tube flow - dependence on diameter and hematocrit. Am J Phys 263:H1770–H1778

Quinn DJ, Pivkin I, Wong SY, Chiam KH, Dao M, Karniadakis GE, Suresh S (2011) Combined simulation and experimental study of large deformation of red blood cells in microfluidic systems. Ann Biomed Eng 39:1041–1050

Reinke W, Gaehtgens P, Johnson PC (1987) Blood-viscosity in small tubes - effect of shear rate, aggregation, and sedimentation. Am J Phys 253:H540–H547

Rejniak KA (2012) Investigating dynamical deformations of tumor cells in circulation: predictions from a theoretical model. Front Oncol 2:111. https://doi.org/10.3389/fonc.2012.00111

Shao JY, Xu G (2007) The adhesion between a microvillus-bearing cell and a ligand-coated substrate: a Monte Carlo study. Ann Biomed Eng 35:397–407. https://doi.org/10.1007/s10439-006-9221-6

Springer TA (1994) Traffic signals for lymphocyte recirculation and leukocyte emigration - the multistep paradigm. Cell 76:301–314. https://doi.org/10.1016/0092-8674(94)90337-9

Stoletov K, Kato H, Zardouzian E, Kelber J, Yang J, Shattil S, Klemke R (2010) Visualizing extravasation dynamics of metastatic tumor cells. J Cell Sci 123:2332–2341

Stroka KM, Konstantopoulos K (2014) Physical biology in cancer. 4. Physical cues guide tumor cell adhesion and migration. Am J Physiol Cell Physiol 306:C98–C109. https://doi.org/10.1152/ajpcell.00289.2013

Sugihara-Seki M, Fu BMM (2005) Blood flow and permeability in microvessels. Fluid Dyn Res 37:82–132

Sun CH, Munn LL (2005) Particulate nature of blood determines macroscopic rheology: a 2-D lattice Boltzmann analysis. Biophys J 88:1635–1645

Sun C, Munn LL (2006) Influence of erythrocyte aggregation on leukocyte margination in postcapillary expansions: a lattice Boltzmann analysis. Physica A 362:191–196. https://doi.org/10.1016/j.physa.2005.09.027

Suresh S (2007) Biomechanics and biophysics of cancer cells. Acta Biomater 3:413–438

Takeishi N, Imai Y, Nakaaki K, Yamaguchi T, Ishikawa T (2014) Leukocyte margination at arteriole shear rate. Physiol Rep 2:e12037. https://doi.org/10.14814/phy2.12037

Takeishi N, Imai Y, Yamaguchi T, Ishikawa T (2015) Flow of a circulating tumor cell and red blood cells in microvessels. Phys Rev E 92:063011

Takeishi N, Imai Y, Ishida S, Omori T, Kamm RD, Ishikawa T (2016) Cell adhesion during bullet motion in capillaries. Am J Physiol Heart Circ Physiol 311:H395–H403

Vahidkhah K, Fatouraee N (2012) Numerical simulation of red blood cell behavior in a stenosed arteriole using the immersed boundary-lattice Boltzmann method. Int J Numer Methods Biomed Eng 28:239–256. https://doi.org/10.1002/cnm.1463

Wang JK, Slattery MJ, Hoskins MH, Liang SL, Dong C, Du Q (2006) Monte Carlo simulation of heterotypic cell aggregation in nonlinear shear flow. Math Biosci Eng 3:683–696

Weiss L (1982) Metastatic inefficiency. Pathol Res Pract 176:86–86

Wirtz D, Konstantopoulos K, Searson PC (2011) The physics of cancer: the role of physical interactions and mechanical forces in metastasis. Nat Rev Cancer 11:512–522. https://doi.org/10.1038/nrc3080

Wu TH, Feng JJ (2013) Simulation of malaria-infected red blood cells in microfluidic channels: passage and blockage. Biomicrofluidics 7:044115

Xiao LL, Liu Y, Chen S, Fu BM (2016a) Numerical simulation of a single cell passing through a narrow slit. Biomech Model Mechanobiol 15:1655–1667

Xiao LL, Liu Y, Chen S, Fu BM (2016b) Simulation of deformation and aggregation of two red blood cells in a stenosed microvessel by dissipative particle dynamics. Cell Biochem Biophys 74:513–525. https://doi.org/10.1007/s12013-016-0765-2

Xiao LL, Liu Y, Chen S, Fu BM (2017) Effects of flowing RBCs on adhesion of a circulating tumor cell in microvessels. Biomech Model Mechanobiol 16:597–610. https://doi.org/10.1007/s10237-016-0839-5

Yan WW, Liu Y, Fu BM (2010) Effects of curvature and cell-cell interaction on cell adhesion in microvessels. Biomech Model Mechanobiol 9:629–640. https://doi.org/10.1007/s10237-010-0202-1

Yan WW, Cai B, Liu Y, Fu BM (2012) Effects of wall shear stress and its gradient on tumor cell adhesion in curved microvessels. Biomech Model Mechanobiol 11:641–653. https://doi.org/10.1007/s10237-011-0339-6

Yan WW, Liu Y, Fu BM (2016) LBM simulations on the influence of endothelial SGL structure on cell adhesion in the micro-vessels. Comp Math Appl https://doi.org/10.1016/j.camwa.2016.07.005

Yen RT, Fung YC (1978) Effect of velocity distribution on red-cell distribution in capillary blood-vessels. Am J Phys 235:H251–H257

Yu M, Stott S, Toner M, Maheswaran S, Haber DA (2011) Circulating tumor cells: approaches to isolation and characterization. J Cell Biol 192:373–382. https://doi.org/10.1083/jcb.201010021

Zhang J, Johnson PC, Popel AS (2008) Red blood cell aggregation and dissociation in shear flows simulated by lattice Boltzmann method. J Biomech 41:47–55. https://doi.org/10.1016/j.jbiomech.2007.07.020

Zhang ZF, Xu J, Hong B, Chen XL (2014) The effects of 3D channel geometry on CTC passing pressure - towards deformability-based cancer cell separation. Lab Chip 14:2576–2584

Zhang L, Zeng M, Fu BM (2016) Inhibition of endothelial nitric oxide synthase decreases breast cancer cell MDA-MB-231 adhesion to intact microvessels under physiological flows. Am J Phys Heart Circ Phys 310(11):H1735–H1747. https://doi.org/10.1152/ajpheart.00109.2016

Zhao H, Isfahani AHG, Olson LN, Freund JB (2010) A spectral boundary integral method for flowing blood cells. J Comput Phys 229:3726–3744. https://doi.org/10.1016/j.jcp.2010.01.024

Zhu C (2000) Kinetics and mechanics of cell adhesion. J Biomech 33:23–33. https://doi.org/10.1016/S0021-9290(99)00163-3

Zhu C, Bao G, Wang N (2000) Cell mechanics: mechanical response, cell adhesion, and molecular deformation. Annu Rev Biomed Eng 2:189–226. https://doi.org/10.1146/annurev.bioeng.2.1.189

Transport Across the Blood-Brain Barrier

Bingmei M. Fu

Abstract

The blood-brain barrier (BBB) is a dynamic barrier essential for maintaining the microenvironment of the brain. Although the special anatomical features of the BBB determine its protective role for the central nervous system (CNS) from blood-borne neurotoxins, however, the BBB extremely limits the therapeutic efficacy of drugs into the CNS, which greatly hinders the treatment of major brain diseases. This chapter summarized the unique structures of the BBB; described a variety of in vivo and in vitro experimental methods for determining the transport properties of the BBB and the permeability of the BBB to water, ions, and solutes including nutrients, therapeutic agents, and drug carriers; and presented recently developed mathematical models which quantitatively correlate the anatomical structures of the BBB with its barrier functions. Recent findings for modulation of the BBB permeability by chemical and physical stimuli were described. Finally, drug delivery strategies through specific trans-BBB routes were discussed.

B. M. Fu (✉)
Department of Biomedical Engineering, The City College of the City University of New York, New York, NY, USA
e-mail: fu@ccny.cuny.edu

1 Introduction

The most complicated and amazing organ in our body is the brain. It contains ~100 billion neurons and ~1 trillion glial cells (supporting cells in the brain including astrocytes, oligodendrocytes, microglia, and ependymal cells). Along with a tremendous amount of blood vessels, these cells and surrounding extracellular matrix form a highly complex, though well-organized, 3-D interconnecting arrays. In order to perform its highly complicated tasks, the brain needs a substantial amount of energy to maintain electrical gradients across neuronal membranes and consequently requires a sufficient supply of oxygen and nutrients. Although it only accounts for ~2% of the body weight, the brain uses ~20% of the blood supply. The blood is delivered through a complex network of blood vessels that runs >650 km and passes a surface area of ~20 m^2. The mean distance between adjacent capillaries is ~40 μm, which allows almost instantaneous equilibration in the brain tissue surrounding the microvessels for small solutes such as glucose, amino acids, vitamins, oxygen, etc. However, unlike peripheral microvessels in other organs where there is a relatively free small solute exchange between the blood and tissue, the microvessels in the brain (cerebral microvessels) constrain the movement of molecules be-

B. M. Fu, N. T. Wright (eds.), *Molecular, Cellular, and Tissue Engineering of the Vascular System*, Advances in Experimental Medicine and Biology 1097,
https://doi.org/10.1007/978-3-319-96445-4_13

tween blood and the brain tissue (Abbott 1992; Pardridge 1998). This characteristic provides a natural defense against toxins circulating in the blood, which, on the other hand, prevents the delivery of therapeutic agents to the brain.

The vascular barrier system in the brain consists of the blood-brain barrier (BBB) and the blood-cerebrospinal fluid (CSF) barriers. The blood-brain barrier (BBB) is the name for the wall of the cerebral microvessels in the brain parenchyma. At the surface of the brain parenchyma, microvessels running in the pia mater are called pial microvessels, which are often used as in vivo models for studying the BBB permeability. Due to its unique structure that will be discussed in the next section, the BBB maintains very low permeability to water and solutes. In the middle of the brain parenchyma, there are ventricular cavities (ventricles) filled with cerebrospinal fluid (CSF) secreted by the epithelial cells of choroid plexus (Brown et al. 2004a, b; Engelhardt and Coisne 2011). The choroid plexus is a highly vascular tissue with leaky, fenestrated capillaries covered with ependymal epithelium, which has relatively tight junctions. The multicell layer between the blood and the CSF in the choroid plexuses is called the blood-CSF barrier. Since the area of the BBB is about 1000 times that of the blood-CSF barrier, it is more important to circumvent the impermeability of the BBB for delivering drugs to the brain (Pardridge 2007). The total surface area of the BBB constitutes by far the largest interface for blood-brain exchange, which is between 12 and 18 m^2 for the average human adult (Nag and Begley 2005). Unlike these two tight blood barriers, the interface between the CSF and brain tissue along the ependymal surface of the ventricles and that between pia mater and brain tissue, so called the brain-CSF barriers, is rather leaky, implying a possible route for drug delivery to the brain. The CSF is formed by the choroid plexuses of the ventricles, passes the ventricles to the subarachnoid space over the pia mater, and is finally absorbed to the venules in the dura mater through arachnoid microvilli and arachnoid granulations (Redzic and Segal 2004). Recent studies (reviewed in Bakker Erik et al. 2016; Brinker et al. 2014) revealed that the process of CSF absorption is far more complicated than the previous view, due to the discovery of brain lymphatic system (Aspelund et al. 2015; Louveau et al. 2015; Greenwood 2017) and perivascular and paravascular clearance mechanisms (Carare et al. 2008; Iliff et al. 2013).

2 The Blood-Brain Barrier

The blood-brain barrier (BBB) is a unique dynamic regulatory interface between the cerebral circulation and the brain tissue, and it is essential for maintaining the microenvironment within the brain. No other body organ so absolutely depends on a constant internal microenvironment as does the brain. In the brain, the extracellular concentrations of amino acids and ions such as Na^+, K^+, and Ca^{2+} must be retained in very narrow ranges. If the brain is exposed to big chemical variations for these molecules, neurons would not function properly because some amino acids serve as neurotransmitters and certain ions modify the threshold for neuronal firing. The BBB also protects the central nervous system (CNS) from blood-borne neuroactive solutes, such as glutamate, glycine, norepinephrine, epinephrine, and peptide hormones (Smith 2000), which can increase with physiological changes (e.g., diet and stress) and pathological changes (e.g., injury and diseases). In addition, the BBB plays a key role in facilitating the brain uptake of essential nutrients like glucose, hormones, and vitamins and larger molecules like insulin, leptin, and iron transferring to sustain brain growth and metabolism (Zhang and Pardridge 2001).

The term "blood-brain barrier" was coined by Lewandowsky in 1900 while he demonstrated that neurotoxic agents affected brain function only when directly injected into the brain but not when injected into the systemic circulation (Lewandowsky 1900). Nevertheless, the first experimental observation of this vascular barrier between the cerebral circulation and the CNS should date back to the 1880s, when Paul Ehrlich discovered that certain water-soluble dyes, like

trypan blue, after injected into the systemic circulation, were rapidly taken by all organs except the brain and spinal cord (Ehrlich 1885). Ehrlich interpreted these observations as a lack of the affinity of the CNS for the dyes. However, subsequent experiments performed by Edwin Goldmann, an associate of Ehrlich, demonstrated that the same dyes, when injected directly into the CNS, stained all types of cells in the brain tissue but not any other tissues in the rest of the body (Goldmann 1913). It took additional 70 years until this barrier was firstly localized to cerebral microvascular endothelial cells by electron microscopic studies performed by Reese and Karnovsky (1967). Although the concept of the BBB has continued to be refined over the past several decades, the recent understanding of the basic structure of the BBB is built on the general framework established by their studies in the late 1960s; more specifically, the BBB exists primarily as a selective transport barrier at the level of cerebral capillary endothelium.

The anatomical structure of the blood-brain barrier (BBB) is sketched in Fig. 1. The circumference of the BBB lumen is surrounded by endothelial cells, the opposing plasmalemma membranes of which are connected by tight junctions. At the luminal surface of the endothelial cell, there is a rather uniform fluffy glycocalyx layer (Ueno et al. 2004; Haeren et al. 2016; Yoon et al. 2017). This mucopolysaccharide structure is highly hydrated in electrolytic solution and contains large numbers of solid-bound fixed negative charges due to the polyanionic nature of its constituents abundant in glycoproteins, acidic oligosaccharides, terminal sialic acids, proteoglycan, and glycosaminoglycans aggregates. Pericytes attach to the abluminal membrane of the endothelium at irregular intervals. In a peripheral microvessel, there is a loose and irregular basal lamina (or basement membrane) surrounding the pericytes. In contrast, in the BBB, pericytes and endothelial cells are ensheathed by a very uniform basement membrane of 20–100 nm thickness (Farkas and Luiten 2001), which is composed of collagen type IV, heparan sulfate proteoglycans, laminin, fibronectin, and other extracellular matrix proteins (Bakker Erik et al. 2016). The basal lamina is contiguous with the plasma membranes of astrocyte end feet that wrap almost the entire abluminal surface of the endothelium (Pardridge 1998).

In addition to the anatomical structures, the BBB differs from the peripheral microvessels in the following aspects. The mitochondrial content of the endothelial cells forming the BBB is greater than that of such cells in all non-neural tissues. It is suggested that this larger metabolic work capacity may be used to maintain the unique structural characteristics of the BBB and/or by metabolic pumps that may require energy to maintain the differences in composition of the cerebral circulation and the brain tissue (Oldendorf et al. 1977). The BBB has high electrical resistance, much less fenestration, and more intensive junctions, which are responsible for restricting paracellular passage of water and polar solutes from the peripheral circulation entering into the CNS (Butt et al. 1990; Hawkins and Davis 2005). Between adjacent endothelial membranes, there are junctional complexes which include adherens junctions (AJs), tight junctions (TJs), and possibly gap junctions (Simard et al. 2003). The structure of the junction complexes between endothelial cells is shown in Fig. 2 (Kim et al. 2006; Abbott et al. 2010). Both AJs and TJs act to restrict paracellular transport across the endothelium, while gap junctions mediate intercellular communication. AJs are ubiquitous in the vasculature, and their primary component is vascular endothelial (VE)-cadherin. They basically mediate the adhesion of endothelial cells to each other and contact inhibition during vascular growth and remodeling. Although disruption of AJs at the BBB can lead to increased permeability, TJ is the major junction that confers the low paracellular permeability and high electrical resistance (Romero et al. 2003). The tight junction complex includes two classes of transmembrane molecules: occludins and claudins. These transmembrane proteins from adjacent endothelia cells interact with each other and form seals in the spaces between adjacent endothelial cells. The cytoplasmic tails of the transmembrane proteins are linked to the

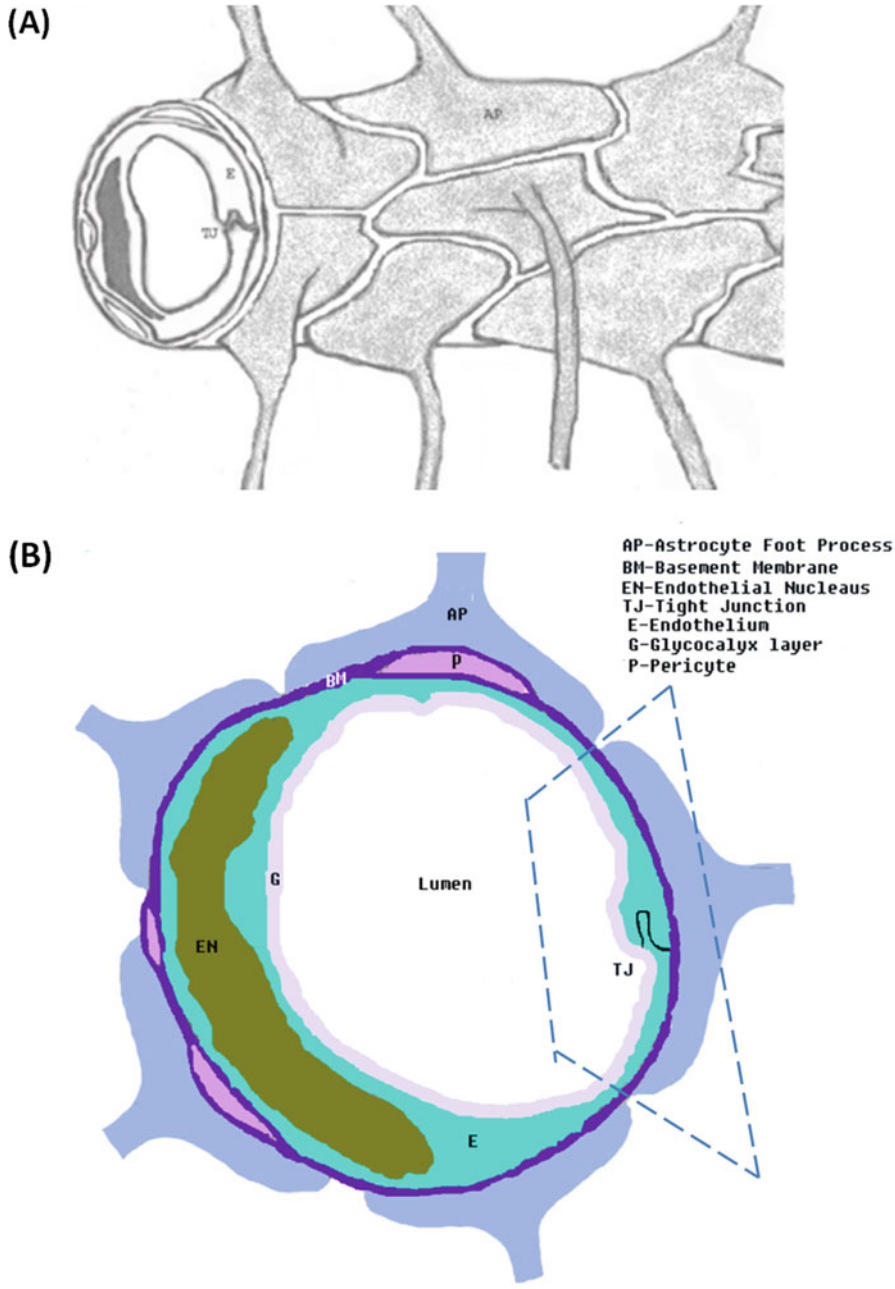

Fig. 1 Schematic of the three-dimensional view (**a**) and cross-sectional view (**b**) of the blood-brain barrier (BBB) or cerebral microvessel (the microvessel in the brain) wall. In addition to other structures as in a peripheral microvessel, the BBB is wrapped by astrocyte foot processes (AP). BM, basement membrane (or basal lamina); E, endothelial cell; EN, nucleus of endothelial cell; P, pericytes; G, surface glycocalyx layer; TJ, tight junction. Modified from (Li et al. 2010a, b)

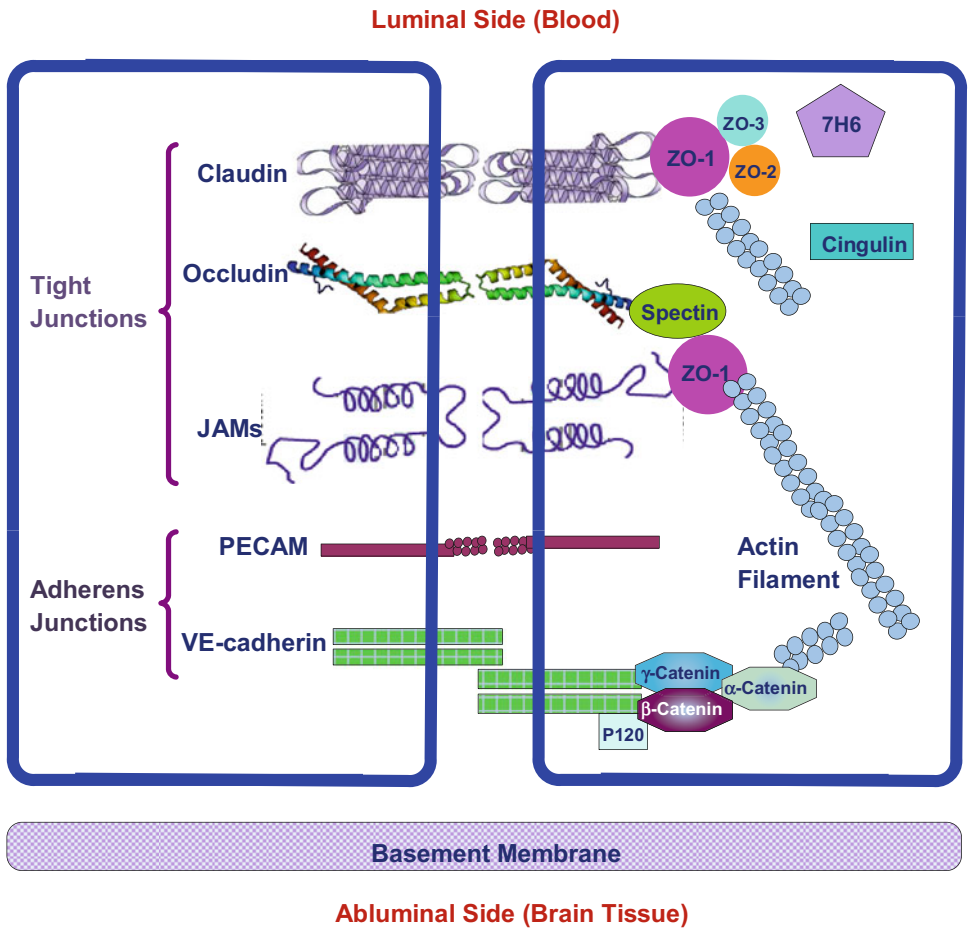

Fig. 2 Schematic of junctional complex in the paracellular pathway of the BBB. Modified from (Abbott et al. 2010)

actin cytoskeleton via a number of accessory proteins such as members of the zonula occludens family, ZO-1, ZO-2, and ZO-3.

A number of grafting and cell culture studies have suggested that the ability of cerebral endothelial cells to form the BBB is not intrinsic to these cells, but the cellular milieu of the brain somehow induces the barrier property into the blood vessels. It is believed that all components of the BBB are essential for maintaining functionality and stability of the BBB. Pericytes seem to play a key role in angiogenesis, structural integrity, and maturation of cerebral microvessels (Ballabh et al. 2004). The extracellular matrix of the basal lamina appears to serve as an anchor for the endothelial layer via interaction of laminin and other matrix proteins with endothelial integrin receptors (Moody 2006). It was suggested that astrocytes are critical in the development and/or maintenance of unique features of the BBB. Additionally, astrocytes may act as messengers to or in conjunction with neurons in the moment-to-moment regulation of the BBB permeability (Ballabh et al. 2004).

3 Transport Pathways Across the Blood-Brain Barrier

The BBB endothelial cells differ from those in peripheral microvessels by more intensive tight junctions, sparse pinocytic vesicular transport, and much less fenestrations. The transport of substances from the capillary blood into the

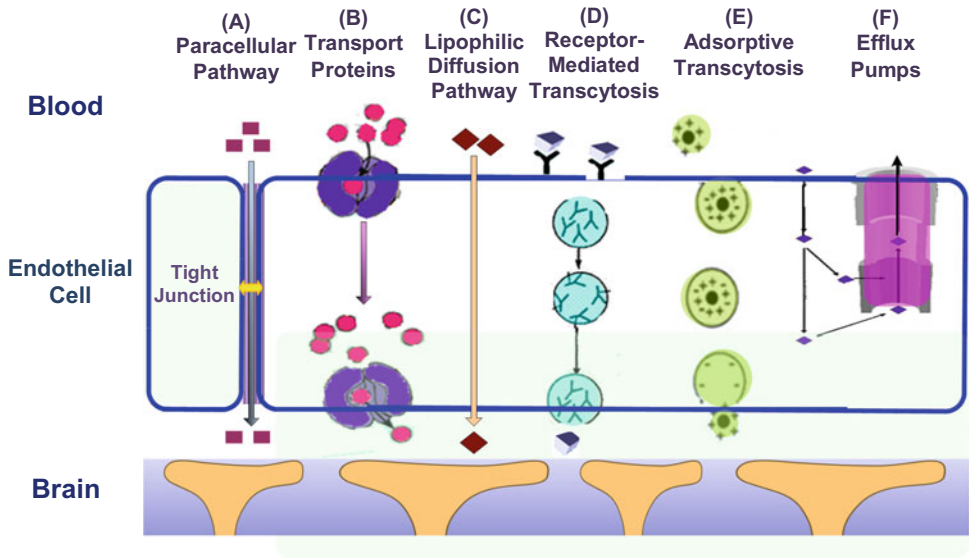

Fig. 3 Transport pathways across the brain endothelial cell. Modified from (Neuwelt 2004)

brain tissue depends on the molecular size, lipid solubility, binding to specific transporters, and electrical charge (Moody 2006). Figure 3 summarizes the transport routes across the BBB (Neuwelt 2004). Compared to the peripheral microvessel wall, the additional structure of the BBB and tighter endothelial junctions greatly restrict hydrophilic molecules transport through the gaps between the cells, i.e., the paracellular pathway of the BBB, route A in Fig. 3. In contrast, small hydrophobic molecules such as O_2 and CO_2 diffuse freely across plasma membranes following their concentration gradients, i.e., the transcellular lipophilic diffusion pathway, route C in Fig. 3. The BBB permeability to most molecules can be estimated on the basis of their octanol/water partition coefficients (Sawchuk and Elmquist 2000). For example, diphenhydramine (Benadryl), which has a high partition coefficient, can easily cross the BBB, whereas water-soluble loratadine (Claritin) is not able to penetrate the BBB and has little effect on the CNS (Kay 2000).

However, the octanol/water partition coefficients do not completely reflect BBB permeability to solutes. Some solutes with low partition coefficients that easily enter into the CNS generally cross the BBB by active or facilitated transport mechanisms, which rely on ion channels, specific transporters, energy-dependent pumps, and a limited amount of receptor-mediated transcytosis. Glucose, amino acids, and small intermediate metabolites, for example, are ushered into brain tissue via facilitated transport mediated by specific transport proteins (route B in Fig. 3), whereas larger molecules, such as insulin, transferrin, low-density lipoprotein, and other plasma proteins, are carried across the BBB via receptor-mediated (route D) or adsorptive transcytosis (route E). Some small molecules with high octanol/water partition coefficients are observed to poorly penetrate the BBB. Recent studies suggested that these molecules are actively pumped back into blood by efflux systems (route F in Fig. 3). These efflux systems greatly limit drug delivery across the BBB. For instance, P-glycoprotein (P-gp), which is a member of the adenosine triphosphate-binding cassette family of exporters, has been demonstrated to be a potent energy-dependent transporter. P-gp contributes greatly to the efflux of xenobiotics from the brain to the blood and has increasingly been recognized as having a protective role and being responsible for impeding the delivery of therapeutic agents (Schuetz et al. 1996). The

organic anion transporters and glutathione-dependent multidrug resistance-associated proteins (MRPs) also contribute to the efflux of organic anions from the CNS, and many drugs with the BBB permeabilities that are lower than predicted are the substrates for these efflux proteins (Pardridge 1998; Abbott et al. 2010; Neuwelt 2004; Begley 2007). While the brain endothelium is the major barrier interface, the transport activity of the surrounding pericytes (Shimizu 2008), basement membrane, and astrocyte foot processes (Fig. 1) (Wolburg-Buchholz et al. 2009) also contributes to the BBB barrier function under physiological conditions and may act as a substitute defense if the primary barrier at the endothelium is compromised (Li et al. 2010a, b).

4 Quantification of Transport Across the Blood-Brain Barrier

4.1 Permeability of the Blood-Brain Barrier

The same as a peripheral microvessel, the wall of the BBB can be viewed as a membrane. The membrane transport properties are often described by Kedem-Katchalsky equations derived from the theory of irreversible thermodynamics (Curry 1983):

$$J_s = PRT\Delta C + (1 - \sigma_f) C J_v$$

$$J_v = L_p (\Delta p - \sigma_d RT \Delta C)$$

where J_s and J_v are the solute and volumetric fluxes and ΔC and Δp are the concentration and pressure difference across the membrane. L_p, the hydraulic conductivity, describes the membrane permeability to water. P, the diffusive permeability, describes the permeability to solutes. σ_f is the solvent drag or ultrafiltration coefficient that describes the retardation of solutes due to membrane restriction, and σ_d, the reflection coefficient, describes the selectivity of a membrane to solutes. In many transport processes, σ_f is equal to σ_d, and thus we often use σ, the reflection coefficient, to represent both of them. These three coefficients can be determined experimentally and theoretically. In addition to these quantitative coefficients, there are other less quantitative permeability indicators for the BBB, e.g., brain uptake index (BUI) and brain efflux index (BEI) (Pardridge 1998). In the following sections, in vivo and in vitro experiments for determining permeability of the BBB are introduced, as well as the mathematical models.

4.2 Determination of the Blood-Brain Barrier Permeability In Vivo and Ex Vivo

Several in vivo and ex vivo rat models have been used for the study of the transport across the BBB, including pharmacokinetic methods (Cornford et al. 1992; Zlokovic et al. 1986), intracerebral microdialysis (de Lange et al. 1999; Zhang et al. 2017), positron emission tomography (PET) (Elsinga et al. 2004), magnetic resonance imaging (MRI) (Wang et al. 2007), the intravital microscopy study (Gaber et al. 2004), occluding single microvessel measurement (Easton and Fraser 1994), and single microvessel fluorescence imaging method (Yuan et al. 2009; Shi et al. 2014a, b, c).

Pharmacokinetic methods are used to evaluate the delivery of a molecule from the systemic circulation into the brain, in which the amount of solute delivered to the brain can be expressed by percentage of injected dose delivered per gram of the brain. Generally, a small volume of buffered Ringer's solution containing the radiolabeled compound of interest and a radiolabeled diffusible reference compound as an internal standard (such as ^{3}H-water) is injected into the common carotid artery, or the internal carotid artery, or the venule depending on different techniques. Then, the animal is sacrificed 5–15 s after injection, and the brain tissue and the injection solution are analyzed to calculate the brain uptake index (BUI), which is the ratio of radiolabeled test compound/^{3}H reference in

the brain, divided by the ratio of radiolabeled test compound/^{3}H reference in the injection mixture. Another permeability indicator, brain efflux index (BEI), can also be determined using this method: BEI = (amount of test compound injected into the brain – amount of test compound remaining in the brain)/amount of test compound injected into the brain. The assumptions of these models are (1) the reference compound is freely diffusible across the BBB; (2) the drug does not back-diffuse from the brain to the blood; and (3) no metabolism of the compounds occurs before decapitation. The advantage of these pharmacokinetic methods is fast, and many compounds can be assessed in a short time, which is ideal in the high-throughput setting. The major disadvantages are (1) brain extraction only occurs over a limited time, making it difficult to accurately determine the brain uptake index and (2) the driving force for the transport is unknown.

Intracerebral microdialysis involves direct sampling of brain interstitial fluid by a dialysis fiber implanted into the brain parenchyma. The concentration of compound that has permeated into the brain following oral, intravenous, or subcutaneous administration can be monitored over time within the same animal. Any drug that enters the brain interstitial fluid will permeate into the physiological solution within the probe, and the solution may be subsequently assayed by an appropriate technique. The major advantage of this technique is that it provides pharmacokinetic profiles of drugs in the brain without killing animals at different time points. One limitation of this technique is that it greatly relies on and limited by the sensitivity of the assay technique (de Lange et al. 1999), since the solute concentrations may be extremely low in the dialysate. Another major disadvantage is that insertion of the probe can result in chronic BBB disruption.

More recently, various imaging techniques, including positron emission tomography (PET) and magnetic resonance imaging (MRI), have been used to determine BBB permeability in humans. PET is a noninvasive tracer technique used to quantify the BBB extravasation. Magnetic resonance imaging (MRI) is also a noninvasive technique, but it is more qualitative than quantitative. The major disadvantages for these techniques include their inherent costs, labor intensity, relatively low resolution (100 μm to 1 mm per pixel), and inability to differentiate between parent compound and metabolites (Yuan et al. 2009; Nicolazzo et al. 2006).

All of the abovementioned methods only measure certain indexes of relative permeability for the drug uptake to the brain since they cannot determine the driving force for the efflux. Because it is hard to measure the BBB permeability in brain parenchyma, the microvessels in pia dura at the surface of the brain are often used in in vivo BBB permeability study. Although pial microvessels do not have the entire ensheathment of astrocytes as those cerebral microvessels in the parenchyma, the pial and cerebral microvessels appear to have many morphophysiological properties in common. These include ultrastructural characteristics, permeability of cell junctions to electron-dense tracers, trans-endothelium electrical resistance, and molecular properties of endothelium. For these reasons, pial microvessels are often used in the BBB permeability studies (Allt and Lawrenson 1997).

Gaber et al. (2004) suggested a method to measure clearance or leakage of drug out of the pial microvessels rather than "true" permeability of the microvessels to solute. Again, this method cannot determine the driving force, the concentration difference of the test solute across the BBB. The occluding single microvessel measurement is done directly on one single exposed pial microvessel after the frontal craniotomy removing a small section of the skull and the dura mater (Easton and Fraser 1994). This method has well-controlled conditions including known concentration difference across the microvessel wall. However, recent study suggests that the exposed rat pial microvessels become leaky to both small and large molecules within 20–60 min following the craniotomy and the permeability of the exposed microvessels rises sharply after 160 min (Easton et al. 1997).

To quantify the permeability of intact rat pial microvessels and overcome the abovementioned disadvantages, Yuan et al. (2009) developed a

noninvasive method, without exposing the cortex, to measure the solute permeability (P) of postcapillary venules on rat pia mater to various-sized solutes. The pial microvessels were observed by a high numerical aperture objective lens through a section of frontoparietal bones thinned with a micro-grinder (revised surgical method from Easton et al. 1997). P was measured on individual pial venular microvessels with the perfused fluorescence tracer solution through the carotid artery by using highly sensitive quantitative fluorescence microscope imaging method. Their results indicate that the solute permeability of rat pial microvessels is about an order of magnitude lower than that of rat mesenteric microvessels, from 1/11 for a small solute, sodium fluorescein, to 1/6 for a large solute, albumin or dextran 70 k. The permeability of rat mesenteric microvessels to these solutes was measured by Fu and Shen (2004). Recently, by employing multiphoton microscopy with longer wavelength lasers for the deeper penetration, the solute permeability of cerebral microvessels in the rat parenchyma was quantified as well as the solute brain tissue diffusion coefficient (Shi et al. 2014a, b, c). Their method is shown in Fig. 4. They found that the BBB permeability to solutes of molecular weight ranging from 4 kDa to 160 kDa, in the cerebral microvessels of rat brain parenchyma 100–250μm below the pia mater, is not significantly different from that of rat pial microvessels for the same-sized solutes except for the small solute, sodium fluorescein (molecular weight 376 kDa) (Yuan et al. 2009). They also found that the ratios

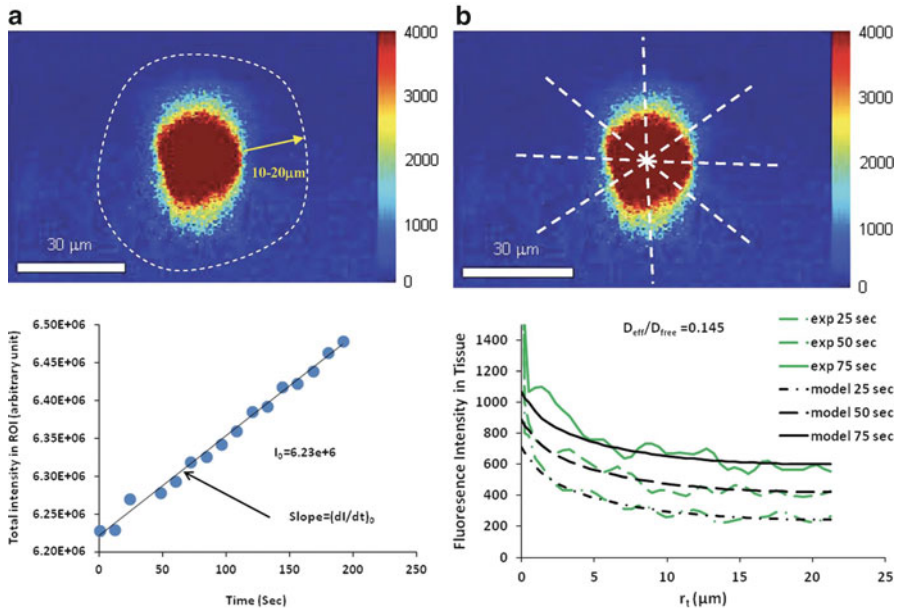

Fig. 4 Quantitative multiphoton fluorescence microscopy for the measurement of the BBB solute permeability (**a**) and brain tissue diffusion coefficient (**b**) for a rat cerebral microvessel ~200 μm below the pia mater. The images were collected during the in vivo experiments, and the fluorescence intensity was analyzed off-line. When the fluorescence-labeled test solute was injected into the carotid artery, the cerebral microvessel lumen is filled with fluorescent solute, producing I_0 in the dashed line enclosed area (ROI) in the left figure of (**a**). With continued perfusion, the measured fluorescence intensity increased indicating further transport of the solute out of the microvessel and into the surrounding tissue. The initial solute flux into the tissue was measured from the slope $(dI/dt)_0$ of the intensity vs. time line, right figure in (**a**). The solute permeability P was calculated as $P = 1/I_0 \times (dI/dt)_0 \times r/2$. Here r is the microvessel radius. (**b**) The averaged intensity of the eight dashed lines on the right figure was plotted as a temporal function of the distance from the vessel edge (r_t). Matching these lines (green) with the predictions (black) from a mathematical model for unsteady diffusion of a solute (right figure in (**b**)) can give the solute brain tissue diffusion coefficient D_{eff}. D_{free} shown here is the solute diffusion coefficient in a free solution. Redrawn from (Shi et al. 2014a, b, c)

of the effective brain tissue diffusion coefficient to the free one are 0.46, 0.19, 0.12, 0.12, 0.11, and 0.11, correspondingly, for sodium fluorescein; dextran 4 k, 20 k, 40 k, and 70 k; and IgG (molecular weight ~160 kDa).

4.3 In Vitro Blood-Brain Barrier Models

The development of in vitro models for the BBB has enabled the study of transport phenomena at the molecular and cellular levels. The aim of such in vitro BBB models is to functionally resemble as many as possible the unique characteristics of the BBB. Compared with in vivo animal models, the in vitro models are relatively accessible, flexible, reproducible, and abundantly available. Previous investigations showed that the permeability of the in vitro BBB models to various compounds such as sucrose, retinoic acid, retinol, haloperidol, caffeine, and mannitol was comparable to the permeability data obtained from in vivo models (Franke et al. 1999). Recent studies showed that the solute permeability of the in vitro BBB model generated from the cultured bEnd3 (mouse brain microvascular endothelial cell line) or cocultured together with primary astrocytes (Gaillard and de Boer 2000; Brown et al. 2007; Li et al. 2010a, b) is comparable to that of the cerebral microvessels from in vivo studies for the similar-sized solutes except for the small solutes of molecular weight less than 10 kDa (Li et al. 2010a, b; Yuan et al. 2009; Shi et al. 2014a, b, c; Fan and Fu 2016). The in vitro BBB model also showed good expression of essential junction proteins, claudin-5, occludin, ZO-1, and VE-cadherin, while the primary astrocytes used in the coculture expressed GFAP (glial fibrillary acidic protein, a specific protein of astrocytes) (Brown et al. 2007; Li et al. 2010a, b). But the hydraulic conductivity of this in vitro BBB model (Li et al. 2010a, b) is two orders of magnitude higher than that from the in vivo study (Fraser et al. 1990), while trans-endothelial electrical resistance (TEER) is two orders of magnitude lower (Crone and Olesen 1982).

To characterize the transport properties of in vitro BBB models, the solute permeability of the in vitro BBB was determined by measuring the flux of the selected tracer. The most commonly used cell culture substrate consists of a porous membrane support submerged in the culture medium (Transwell apparatus). The Transwell system is characterized by a horizontal side-by-side or vertical diffusion system. During the experiment, the flux of tracers into the abluminal compartment of the Transwell system is recorded as a function of the time, and the solute permeability is calculated from the slope of the flux. The tracers used in the transport experiments are labeled by a fluorescent dye or isotope whose intensity can be measured quantitatively (Li et al. 2010a, b). Another index, trans-endothelial electrical resistance (TEER), or the ionic conductance of the monolayer, is also a measurement of the "tightness" of the in vitro BBB models (Crone and Olesen 1982; Li et al. 2010a, b).

So far, two major types of in vitro BBB models have been developed: endothelial cell monolayer and coculture of endothelial cells with glial cells (the non-nerve cells in the brain). The cells for these models are basically obtained from primary/sub-passaged or immortalized cell cultures. The origins of the cells are also very diverse: human, primate, bovine, porcine, rodent, and murine species.

The brain capillary endothelial cells (BCEC) have been used to establish tissue culture systems ever since the technique of culturing highly purified populations of microvascular cells became available in the early 1980s. The first endothelial monolayers were established using BCEC grown on culture dishes, microcarriers (e.g., dextran beads), and various kinds of filters, including nylon mesh and polycarbonate. These cultured BCEC keep their endothelial phenotypes and provide a simple model for the study of the permeability of the BBB. For instance, they express angiotensin-converting enzyme, von Willebrand factor, and internalized acetylated low-density lipoprotein. However, they were reported to lose many BBB-specific features they possessed in vivo. For instance, they are

lack of specific brain endothelial markers γ-glutamyl transpeptidase, marker enzyme alkaline phosphatase (Meyer et al. 1990), and glucose transporter system (Hemmila and Drewes 1993). Moreover, the permeability of the BCEC monolayer to sucrose was reported to be from 10^{-4} to 10^{-5} cm/s compared with 10^{-6} cm/s in vivo. The TEER for endothelial monolayer was also found to be pretty low, from 20 to 1400 Ω cm^2, compared with more than 2000 Ω cm^2 in vivo. So the BCEC monolayer alone is not a well-characterized model for the BBB. The major reason for this may be the lack of in situ environment and brain-derived signals.

In human body, the BBB are almost completely ensheathed by surrounding tissue, mostly astrocyte foot processes. Experimental results from electron microscopic techniques show that astrocytes do have significant effects on the formation of the unique BBB phenotype of brain endothelial cells (Abbot 2002; Haseloff et al. 2005). They induce formation of the tight junctions between endothelial cells and increase paracellular integrity of the BBB. To better mimic the in vivo BBB, a model with coculture of BCEC and astrocyte was developed. This coculture model was characterized on the basis of specific cell-type properties and specific BBB properties by electron microscopic evaluation and immunohistochemistry methods (Gaillard and de Boer 2000). The results showed that BCEC displayed (1) characteristic endothelial cell morphology, (2) expression of endothelial cell markers (i.e., CD51, CD62P, CD71, and cadherin 5), (3) tight junction formation between the cells, and (4) expression of typical barrier marker γ-glutamyl transpeptidase (γ-GTP) and P-glycoprotein (Pgp) and transferrin receptor. Astrocytes displayed characteristic astrocyte morphology and expressed glial fibrillary acidic protein (GFAP). Transmission electron microscopy showed evidence of tight junction formation between the endothelial cells and few pinocytic vesicles. A 15-fold increase in γ-glutamyl transpeptidase activity was measured in the endothelial cells cocultured with astrocytes (Demeuse et al. 2002). The permeability of the coculture system to several tracers was reported to be lower than the endothelial monolayer. These results indicate that the coculture system is a better model to study the transport across the BBB.

Primary brain capillary endothelial cells have the closest resemblance to the BBB phenotype in vivo and exhibit excellent characteristics of the BBB at early passages (Nicolazzo et al. 2006). They, however, have inherent disadvantages such as being extremely time-consuming and costly to generate, being easily contaminated by other neurovascular unit cells, losing their BBB characteristics over passages, and requiring high technical skills for extraction from brain tissue (Deli et al. 2005; Brown et al. 2007). An immortalized mouse brain endothelial cell line, bEnd3, has recently been under investigation for in vitro BBB models because of its numerous advantages over primary cell culture: the ability to maintain BBB characteristics over many passages, easy growth and low cost, formation of functional barriers, and amenability to numerous molecular interventions (Brown et al. 2007; Soga et al. 2001; Yoder 2002; Yuan et al. 2010a, b; Tyagi et al. 2009). Previous RT-PCR analysis showed that bEnd3 cells express the tight junction proteins ZO-1, ZO-2, occludin, and claudin-5 and junctional adhesion molecules (Brown et al. 2007; Li et al. 2010a, b; Omidi et al. 2003). They also maintained functionality of the sodium- and insulin-dependent stereospecific facilitative transporter GLUT-1 and the P-glycoprotein efflux mechanism (Omidi et al. 2003), formed fairly tight barriers to radiolabeled sucrose, and responded like primary cultures to disrupting stimuli (Brown et al. 2007).

To characterize the transport properties of in vitro BBB models, Malina et al. (2009) (Bowman et al. 1983; Thompson et al. 1994; Salvetti et al. 2002; Karyekar et al. 2003; Hamm et al. 2004; Kemper et al. 2004; Boveri et al. 2005; Kraus et al. 2008; Poller et al. 2008) measured the diffusive permeability of endothelial cell monolayer and coculture of endothelial cells with astrocytes to fluorescence- or isotope-labeled tracers, e.g., sucrose, inulin, and mannitol. Sahagun et al. (1990) reported the ratio between abluminal concentration and luminal concentration of different-sized dextrans (4 k, l0 k, 20 k, 40 k, 70 k,

and 150 k) across mouse brain endothelial cells. Gaillard and de Boer (2000) measured the permeability of sodium fluorescein and FITC-labeled dextran 4 k across a coculture of calf brain capillary endothelial cells with rat astrocytes. Many investigators have measured the trans-endothelial electrical resistance (TEER) of brain endothelial monolayers and cocultures as an indicator of ion permeability (Santaguida et al. 2006; de Vries et al. 1996; Cucullo et al. 2002; Zhang et al. 2006).

To seek for in vitro BBB models that are more accessible than animals for investigating drug transport across the BBB, Li et al. (2010a, b) characterized the junction protein expression and quantified the TER and permeability to water (L_p) and solutes (P) of four in vitro BBB models: bEnd3 monoculture, bEnd3 coculture with astrocytes, coculture with two BM substitutes (collagen type I and IV mixture), and Matrigel. Collagen type IV network is the basic framework of native BM (Engvall 1995; Miosge 2001), and Matrigel is a soluble and sterile extract of BM derived from the EHS tumor, which has been widely used as a reconstituted BM in studying cell morphogenesis, differentiation, and growth (Kleinman and Martin 2005). Their results show that L_p and P of the endothelial monoculture and coculture models are not different from each other. Compared with in vivo permeability data from rat pial microvessels, P of the endothelial monoculture and coculture models are not significantly different from in vivo data for dextran 70 k, but they are 2–4 times higher for small solutes TAMRA and dextran 10 k. This suggests that the endothelial monoculture and all of the coculture models are fairly good models for studying the transport of relatively large solutes (drugs or drug carriers) across the BBB.

4.4 Transport Models for the Paracellular Pathway of the Blood-Brain Barrier

Transport across the BBB include both paracellular and transcellular pathways (Pardridge 2005). While large molecules cross the BBB through transcellular pathways, water and small hydrophilic solutes cross the BBB through the paracellular pathway (Hawkins and Davis 2005). The paracellular pathway of the BBB is formed by the endothelial surface glycocalyx, the tight junction openings, the BM filled with extracellular matrix, and the openings between adjacent astrocyte foot processes (Fig. 1b). In addition to the endothelial tight junctions, the BM and the astrocyte foot processes provide a significant resistance to water and solute transport across the BBB.

The breakdown of the BBB and increased permeability are widely observed in many brain diseases such as stroke, traumatic head injury, brain edema, Alzheimer's disease, AIDS, brain cancer, meningitis, and hypertension (Beaumont et al. 2000; Dietrich et al. 1994; Fukuda et al. 1995; Baldwin et al. 1996; Cernak et al. 2004; Montagne et al. 2017; Setiadi et al. 2017). Although numerous biochemical factors are found to be responsible for the breakdown of the BBB in disease, the quantitative understanding of how these factors affect the structural components of the BBB to induce BBB leakage is poor. On the other hand, to design therapeutic drugs with better transport properties across the BBB relies greatly on this understanding. Therefore, it is important to investigate how the structural components in the paracellular pathway of the BBB affect its permeability to water and solutes through mathematical modeling.

Extended from a previous three-dimensional model for studying the transport across the peripheral microvessel wall with endothelium only (Fu et al. 1994; Fu and Chen 2003; Fu and Shen 2004), Li et al. (2010a, b) developed a new model for the transport across the BBB, which included the BM and wrapping astrocyte foot processes. The simplified model geometry is shown in Fig. 5. This is the enlarged view for the part near tight junction shown in Fig. 1b. At the luminal side, there is an endothelial surface glycocalyx layer (SGL) with a thickness of L_f from 100 to 400 nm under normal physiological conditions (Squire et al. 2001; Arkill et al. 2011, 2012; Schulze and Firth 1992). Between adjacent endothelial cells, there is an inter-endothelial cleft with a length of L ~500 nm and a width of

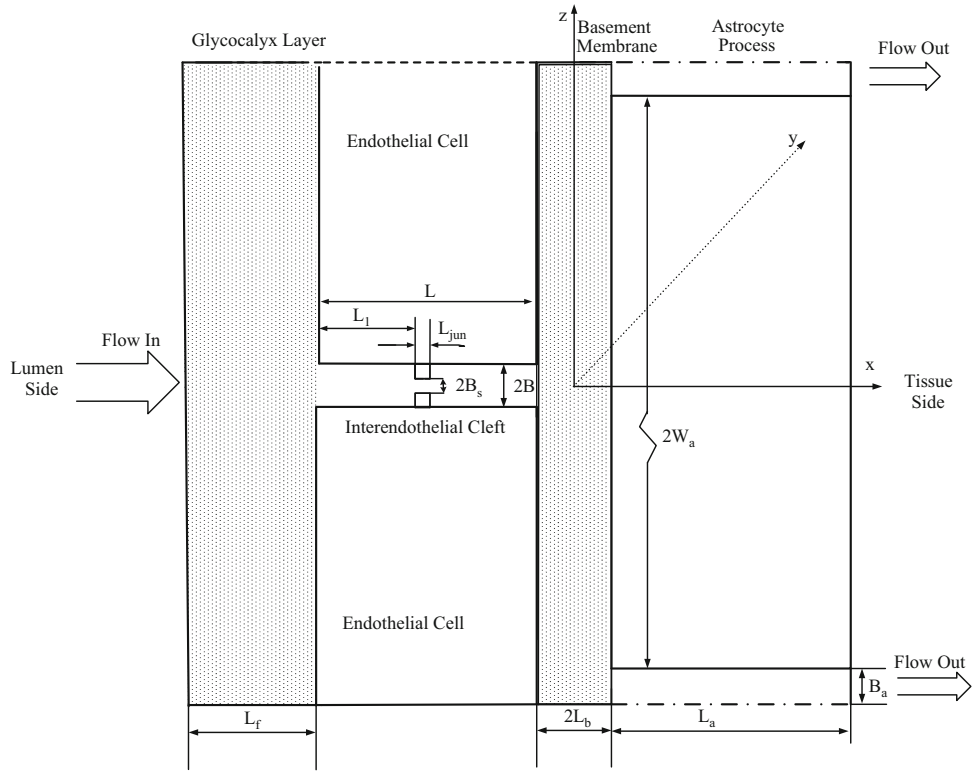

Fig. 5 Model geometry for the paracellular pathway of the BBB (not in scale) showing the dashed line enclosed region in Fig. 1b. The thickness of the endothelial surface glycocalyx layer is L_f. The inter-endothelial cleft has a length of L and a width of $2B$. The length of the tight junction strand in the inter-endothelial cleft is L_{jun}. The width of the small continuous slit in the junction strand is $2B_s$. The distance between the junction strand and luminal front of the cleft is L_1. The width of the basement membrane is $2L_b$ and the length of the astrocyte foot processes is $2W_a$. The cleft between astrocyte foot processes has a length of L_a and a width of $2B_a$. The surface glycocalyx layer and the endothelial cells are defined as the endothelium only while the BBB is defined to include the endothelium, the basement membrane, and the astrocytes. Redrawn from Li et al. (2010b)

2B ∼20 nm (Schulze and Firth 1992; Adamson et al. 2004). In the inter-endothelial cleft, there is a L_{jun} (∼10 nm) thick junction strand with a continuous slit-like opening of width $2B_s$, which varies depending on the location of the cerebral microvessels (from ∼1 to 10 nm). The distance between the junction strand and luminal front of the cleft is L_1. At the tissue side of the cleft, a BM separates the endothelium and the astrocyte foot processes. The thickness of the BM is $2L_b$ (20–40 nm), and the length of the astrocyte foot processes is $2W_a$ (∼5000 nm). Between adjacent astrocyte foot processes, there is a cleft with length L_a (∼1000 nm) and width $2B_a$ (20–2000 nm). The anatomic parameters for the BBB structural components were obtained from the electron microscopy studies in the literature.

Unlike the peripheral microvessel wall, the endothelium of the BBB has negligible large discontinuous breaks in the junction strand of the inter-endothelial cleft, and the small slit in the junction strand is assumed continuous (Hawkins and Davis 2005). As a result, the cross-sectional BBB geometry is the same along the axial direction (y direction in Fig. 5), and thus the model could be simplified to 2-D (in x, z plane). It could be further simplified to a unidirectional flow in each region due to very narrow clefts and the BM. In addition, the curvatures of the BM and the endothelium can be neglected because their widths are much smaller than the diameter of the microvessel. The fluid flow in the cleft regions of the BBB was approximated by the Poiseuille

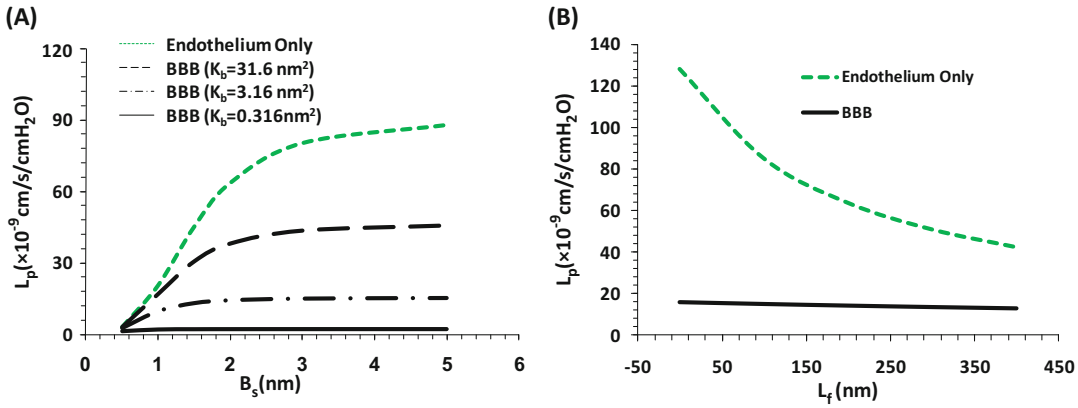

Fig. 6 Model predictions for hydraulic conductivity L_p (**a**) as a function of B_s, the half width of the small slit in the junction strand under two cases: when considering transport across the endothelium only (endothelium only, green line) and when considering transport across the entire BBB (BBB). In the BBB case, three different fiber densities were considered for the basement membrane: the same as the fiber density in the surface glycocalyx layer ($K_b = 3.16$ nm^2, the dash-dot-dash line), ten times lower ($K_b = 31.6$ nm^2, the dashed line) and higher ($K_b = 0.316$ nm^2, the solid line); (**b**) as a function of the surface glycocalyx layer thickness L_s. Redrawn from (Li et al. 2010a, b)

flow while those in the endothelial SGL and BM by the Darcy and Brinkman flows, respectively. Diffusion equations in each region were solved for the solute transport. After solving for the pressure, water velocity, and solute concentration profiles, the hydraulic conductivity L_p and solute permeability P can be calculated.

Figure 6a shows the model predictions for L_p as a function of tight junction opening B_s when the BM has different fiber densities. K_b is Darcy permeability in the BM. When the fiber density in the BM is the same as that in the SGL, $K_b = 3.16$ cm^2. The green line in Fig. 6a shows the case of peripheral microvessels with only endothelium. When B_s increases from 0.5 to 2 nm, L_p will increase by ~20-fold. In contrast, when the endothelium is wrapped by the BM and the astrocytes as for the BBB, increase in B_s from 0.5 to 2 nm only induces fivefold increase in L_p when the fiber density in the BM is the same as that in the SGL (dash-dot-dash line). If the fiber density in the BM is ten times of that in the SGL, the increase is only 1.6-fold in L_p (solid line), while if the fiber density in the BM is 1/10 of that in the SGL, the increase is 12-fold in L_p (dashed line). Even at a large B_s of5 nm, when the BM is filled with the same density fibers as in the SGL, the BBB permeability is only 17% of that of endothelium only. This percentage can be as low as 2% if the fiber density in the BM is ten times of that in the SGL. Figure 6b shows the model predictions for L_p as a function of the endothelial SGL thickness L_f. The green line is for the case of endothelium only while the solid line for that of the BBB. We can see the decrease in L_f from 400 to 0 nm increases L_p by threefold in the case of endothelium only, while in the case of the BBB, the increase is only 25% in L_p with the protection of the BM and the astrocytes. Similar results are predicted for the solute permeability (Li et al. 2010a, b). These results indicate that the BM and astrocytes of the BBB provide a great protection to the CNS under both physiological and pathological conditions. However, on the other hand, these unique structures also impede the drug delivery to the brain through the BBB. Most recently, an electro-diffusion model for the blood-brain barrier to the charged molecules was developed to take into consideration of the effect of charges in the SGL and BM on the solute transport across the BBB (Li and Fu 2011).

5 Modulation of the Blood-Brain Barrier Permeability by Chemical and Physical Stimulations

5.1 Modulation of the BBB Permeability by Chemical Stimuli

During cerebrovascular and neurological diseases, the BBB is compromised, and its permeability can be increased by various types of stimuli including cytokines, inflammatory mediators, metabolites of arachidonic acid, excitatory amino acids, nitric oxide, and bacterial infection. Among cytokines is vascular endothelial growth factor (VEGF), which is upregulated in many brain diseases (Ohlin et al. 2011; Suidan et al. 2010). By using submicron resolution multiphoton fluorescence microscopy with a longer penetration depth into brain parenchyma of rats, Shi et al. (2014b) quantified the temporal VEGF effects on the BBB permeability to various-sized molecules. They found that exposure to 1 nM VEGF transiently increased the BBB permeability to 2.2, 10.5, 9.8, and 12.8 times their control values, for sodium fluorescein, dextran 20 k and 70 k, and IgG, respectively, within 30 s, and all returned to control in 2 min.

Previous studies have shown that elevated intracellular 3,5-cyclic monophosphate (cAMP) levels enhance endothelial junction barriers and thus reduce permeability in peripheral microvessels (Adamson et al. 1998; Fu et al. 2006; Fukuhara et al. 2005; Mehta and Malik 2006; Moore et al. 1998; Sayner 2011) and in cultured BBB models (Balyasnikova et al. 2000; Rubin et al. 1991; Wolburg et al. 1994). Studies on intact microvessels also showed that elevation of cAMP levels abolished the increase in the hydraulic conductivity stimulated by adenosine triphosphate (ATP) in frog and hamster mesenteric microvessels (He and Curry 1993) as well as in the solute permeability induced by VEGF in the same type of microvessels of frogs and rats (Fu et al. 2006, 2015). Administration of a cAMP analogue abolished VEGF-induced rat mesenteric microvessel hyperpermeability (Fu et al. 2015). Employing multiphoton microscopy, Shi et al. (2014b) demonstrated that after 20 min pretreatment of 2 mM cAMP analogue, 8-bromo-cAMP, the initial increase by 1 nM VEGF was completely abolished in the BBB permeability to all solutes. The response pattern of the BBB permeability to VEGF and cAMP and the ratios of the peak to control values for rat cerebral microvessels are similar to those for rat mesenteric (peripheral) microvessels, except the ratios are higher in permeability of cerebral microvessels for the intermediate and large solutes. Their results imply a new approach for delivering large therapeutic agents to the brain.

5.2 Modulation of the BBB Permeability by Physical Stimuli

Among the numerous strategies to deliver therapeutic drugs into the central nervous system, the focused ultrasound (FUS) sonication combined with microbubbles (MBs) has been shown to be effective in transiently disrupting the BBB for noninvasive drug delivery (Hynynen et al. 2006; Chen et al. 2013; Yang et al. 2011; Curley et al. 2017). At appropriate acoustic power density (or pressure), burst repetition rate, duty cycle, and sonication duration and in the presence of MBs with proper materials, sizes, and concentrations, FUS can achieve noninvasive, selective and localized disruption of BBB without visible damage to the brain tissue (Konofagou 2012; Deng 2010). FUS-induced BBB disruption has been widely assessed by using magnetic resonance imaging (MRI) or post-FUS histological examination (Yang et al. 2011: Chu et al. 2013; Park et al. 2010). Indirect MRI collects the images of brain slices in the presence of a MRI contrast agent such as gadolinium to access the BBB disruption in different locations of the brain. Alternatively, post-FUS histological examination relates the BBB disruption to the amount of Evans blue extravasation in the brain tissue after the dye is intravenously injected into

the blood circulation before or after sonication. However, the submillimeter spatial resolution of the MRI studies and the postmortem histological examinations only assess the relatively large leakage of the BBB, and these methods are restricted to the exploration of a region that is much larger than a single microvessel with its surrounding tissue. Therefore the BBB disruption assessed by the MRI and histological examination is more qualitative rather than quantitative. To overcome aforementioned limitations, two-photon microscopy was employed to quantitatively access the enhanced permeability of the cerebral vasculature after FUS (Nhan et al. 2013). In addition to micrometer spatial resolution, two-photon microscopy offers the advantage of deep tissue penetration, which is essential for the BBB permeability measurement. By employing the two-photon microscopy, Shi et al. (2014c) quantified the BBB permeability to dextran 155 k with similar molecular weight to an antibody by applying different doses of FUS in the presence of MBs with an optimal size and concentration. After ~5 min by applying the FUS on the thinned skull in the presence of MBs for 1 min, TRITC-dextran 155 k in 1% BSA mammalian Ringer's solution was injected into the cerebral circulation via the ipsilateral carotid artery by a syringe pump. Simultaneously, the temporal images were collected from the brain parenchyma ~100–200 μm below the pia mater. At the optimal dose, permeability increased by ~14-fold after 5 min post-FUS, and permeability returned to the control level after 25 min. FUS without MBs or MBs injected without FUS did not change the permeability. Their method provides an accurate in vivo assessment for the transient BBB permeability change under the treatment of FUS. The optimal FUS dose found for the reversible BBB permeability increase without BBB disruption is reliable and can be applied to future clinical trials.

Transcranial direct current stimulation (tDCS) is a noninvasive electrical stimulation technique investigated for a broad range of medical and performance indications. Most recently, Shin et al. (2016) found that after 1 mA tDCS treatment for 20 min, the permeability of rat cerebral microvessels 100–200μm below pia mater to sodium fluorescein (molecular weight 376 kDa) and dextran 20 k and 70k increased to about 8-fold, 35-fold, and 35-fold of their respective control values, 10 min post-tDCS treatment, correspondingly. All of the increased BBB permeability returns to the control in 20 min posttreatment. Their method provides another noninvasive approach for delivering therapeutic agents to the brain through the BBB.

6 Drug Delivery Through the Blood-Brain Barrier

A large number of people in the world are now suffering from CNS diseases. The total number of patients with CNS diseases is reported to be larger than that with cardiovascular diseases (Pardridge 2007). While the BBB serves as a natural defense that safeguards the brain against the invasion of various circulating toxins and infected cells, it also provides a significant impediment toward the delivery of diagnostic and therapeutic agents to the brain via the systemic route. Various methods such as intracerebral implantation, microdialysis, convection-enhanced distribution (CED), osmotic shock, and chemical modification of the BBB have been developed for delivering drugs into the brain. However, the applications of these methods are limited, and they can only partially keep with the demands of modern therapies. For instance, the efficiency of intracerebral implantation, microdialysis, and CED methods is low since their major transport mechanisms are diffusion and convection of interstitial fluid. The penetration distances of drugs delivered by the first two methods are reported to be less than 1 mm with simple diffusion (Mak et al. 1995). CED has been shown in laboratory experiments to deliver high-molecular-weight proteins 2 cm from the injection site in the brain parenchyma after 2 h of continuous infusion (Bobo et al. 1994). However, the success of CED relies on precise placement of the catheters and other infusion parameters for delivery into the correct location in the brain parenchyma. For effective treatment of the CNS

diseases, therapeutic agents have to reach the specific regions of the brain at an adequate amount. As discussed earlier, due to the abundance and the largest contact area of the BBB for blood-brain exchange, it is more reasonable to develop strategies for drug delivery through the BBB.

The above session for the modulation of the BBB permeability by chemical and physical stimuli discusses potential noninvasive methods for drug delivery through the BBB. Novel nanomaterials-based nanocarriers have also been developed for drug delivery across the BBB (Tsou et al. 2017). More specifically, as shown in Fig. 3, we can directly deliver therapeutic agents through paracellular pathway (route A), through lipophilic diffusion pathway (route C), or through transporters at the BBB by closely mimicking their substrates (route B) or mounting the drugs on the ligands of the specific receptors expressed at the BBB (e.g., low-density lipoprotein receptor-related protein) for transcytosis (Trojan horse approach or receptor-mediated transcytosis, RMT, route D), as well as using cationized proteins, peptides, and nanoparticle carriers for adsorptive-mediated transcytosis (AMT, route E). The following summarizes the delivery strategies through these routes, respectively.

6.1 Delivery Through Paracellular Pathway (Route A)

To increase the hydrophilic drug delivery from the blood to the brain tissue, we can transiently open the barriers in the paracellular pathway of the BBB, e.g., the cleft opening ($2B$ in Fig. 5), the tight junction opening ($2B_s$), and the BM width ($2L_b$), or degrade the fiber matrix in the endothelial surface glycocalyx and in the BM. Osmotic shock by intracarotid administration of a hyperosmotic mannitol causes endothelial cells to shrink and increase $2B$, $2B_s$, and $2L_b$. Subsequent administration of drugs can increase their concentrations in the brain to a therapeutic level (Kroll and Neuwelt 1998; Doolittle et al. 2002). Physical means such as application of electric and magnetic fields can increase the drug brain uptake. Focused ultrasound, guided by MRI, combined with microbubbles injected into the blood stream has been shown to disrupt the BBB and increase the distribution of Herceptin in brain tissue by 50% in mice (Hynynen et al. 2001, 2006; Kinoshita 2006). Application of inflammatory agents such as bradykinin analogue can open the tight junction of the BBB and increase the drug transport to the brain (Dean et al. 1999; Borlongan and Emerich 2003). However, these approaches are relatively costly and non-patient friendly. They may also enhance tumor dissemination after BBB disruption and damage the neurons by allowing the passage of unwanted blood components into the brain (Gabathuler 2010).

6.2 Delivery Through Lipophilic Diffusion Pathway (Route C)

Some molecules, e.g., alcohol, nicotine, and benzodiazepine, can freely enter the brain through route C in Fig. 3. Their ability to passively (diffusion by concentration differences across the cell membrane) cross the BBB depends on the molecular weight, charge (low hydrogen-bonding capabilities), and lipophilicity (Lipinski 2000). Therefore, if we can modify the drugs through medicinal chemistry, e.g., reduce the relative number of polar groups, or incorporate them with a lipid carrier, we can enhance their brain uptake (Shashoua and Hesse 1996). Modification of antioxidants with pyrrolopyrimidines increases their ability to access target cells in the CNS (Sawada et al. 1999). Covalently attaching 1-methyl-1,4-dihydronicotinate to a hydroxymethyl group can enhance the delivery of ganciclovir (Cytovene, an antiviral medication) to the brain (Bodor et al. 1981; Brewster et al. 1994). However, the modification which helps for the drug delivery to the brain often results in loss of the therapeutic function of a drug. In addition, increase of lipophilicity of a drug can result in making it a substrate for the efflux pump P-glycoprotein (route F in Fig. 3) (Gabathuler 2010).

6.3 Delivery Through Transporter-Mediated Pathway (Route B)

The brain requires tremendous amount of essential substances for survival and function, e.g., glucose, insulin, hormones, low-density lipoprotein (LDL), etc. These nutrients and substances are transported into the brain, not by paracellular or lipophilic diffusion pathway as described earlier but by specific transporters or receptors at the BBB. Drugs can be modified to take advantages of the native BBB nutrient transporter systems or by being conjugated to ligands that recognize receptors expressed at the BBB for the receptor-mediated transcytosis. This physiological approach is by far recognized as the most likely successful drug delivery method to the brain.

Peptides and small molecules may use specific transporters expressed on the luminal and basolateral sides of the endothelial cells to cross into the brain. So far, at least eight different nutrient transporters have been identified to transport a group of nutrients with similar structures. Drugs can be modified to closely mimic the endogenous carrier substrates of these transporters and be transported through the specific transporter-mediated transcytosis. Dopamine can be used to treat Parkinson's disease, but itself is non-brain penetrant. Instead, dopamine's metabolic precursor, L-Dopa, if delivered by a neutral amino acid carrier through its transporter at the BBB, shows a clear clinical benefit on patients with Parkinson's disease (Pardridge 2017). To use a BBB transporter for drug delivery, several important factors must be considered: the kinetics and structural binding requirements of the transporter, therapeutic compound manipulation so that the compound binds but also remains active in vivo, and actual transport of the compound into the brain instead of just binding to the transporter (Gabathuler 2010).

6.4 Delivery Through Receptor-Mediated Pathway (Route D)

Instead of by transporters, larger essential molecules are delivered into the brain by specific receptors highly expressed at the endothelial cells of the BBB. The receptor-mediated transcytosis (RMT) includes three steps: receptor-medicated endocytosis of the molecule at the luminal side of the endothelium (blood side), transport through the endothelial cytoplasm, and exocytosis of the molecule at the abluminal side of the endothelium (brain side). Although the exact mechanisms of RMT have not been well understood, drug delivery targeting three receptors (the insulin receptor, the transferrin receptor, and the LDL receptor) has been developed since the start of this century (Pardridge 2017). More and more receptors have been targeted for the drug delivery since then (Gabathuler 2010). This physiological approach is often called molecular Trojan horse since the therapeutic compounds are conjugated to the specific ligands or the antibodies, which can be recognized and delivered through transcytosis by the specific matching receptors at the endothelial cell membrane. In addition to molecular Trojan horses, drugs can be packaged to liposomes and other nanoparticles coated with targeting molecules such as antibodies to the specific receptors to improve the drug-loading capacity.

Although the Trojan horses for the BBB drug delivery are very promising in delivering large peptides and recombinant proteins such as neurotrophins, enzymes, and monoclonal antibodies (Pardridge 2007), the traffic is limited by the number and carrying capacity of the receptors, as well as by the number of drug molecules that can attach to each antibody (Miller 2002). In addition, Gosk et al. (2004) showed that using anti-transferrin mAb for drug delivery through the systemic administration,although the total amount of

the drug in the brain is high, most of it stays associated with brain microvessel endothelial cells instead of in the brain parenchyma. Due to the high affinity of the antibodies, it is a challenge to dissociate from their specific receptors. Furthermore, widespread distribution of the receptors on peripheral organs would limit the specific delivery to the brain, and on the other hand, may induce additional toxicity.

6.5 Delivery Through Adsorptive-Mediated Pathway (Route E)

Adsorptive-mediated transcytosis (AMT) involves endocytosis and exocytosis of charged substances by the endothelial cells of the BBB. Its mechanism is different from that of the RMT, which needs specific matching receptors and ligands. Kumagai et al. (1987) observed that polycationic proteins such as protamine could not only bind to the endothelial cell surface but also penetrate the BBB. Mixing protamine, poly-L-lysine, or other cationic molecules with proteins (e.g., albumin) largely increased the BBB permeability to these proteins. These findings can be explained by AMT triggered by electrostatic interactions between the positively charged proteins and negatively charged membrane regions at the brain endothelium. At normal physiological pH, the luminal surface of the cerebral endothelium and the surrounding BM (see Fig. 1b) carry negative charge (Ueno et al. 2004; Lawrenson et al. 1997) and provide the necessary environment for delivering positively charged drugs and drug carriers. Recently, a quantitative in vivo animal study by Yuan et al. (2010a, b) found that the charge density of the endothelial surface glycocalyx and that of the BM in rat pial microvessels is ~30 mEq/L. In another in vitro cell culture study, Yuan et al. (2010a, b) found the similar charge density on the surface of a cell monolayer of bEnd3, an immortalized mouse cerebral microvessel endothelial cell line.

To efficiently deliver a therapeutic protein or peptide across the BBB, the simplest way is to cationize the protein or peptide by amidation of its carboxylic acid groups, as well as glutamic and aspartic acid side chain groups with positively charged amines (Hervé et al. 2008). The degree of cationization of a protein or peptide may be critical for its pharmacokinetic fate. Cationization enhances the delivery while induces potential toxicity and immunogenicity of these proteins. PEGylation of cationized molecules can minimize the immunogenicity of these molecules. Positively charged cell-penetrating peptides (CPPs) are often used as the drug carriers for the brain delivery. Commonly used CPPs are penetratin, transportan, Syn-B, and Tat (Hervé et al. 2008). Brain uptake of enkephalin analogue dalargin was enhanced several hundred folds after carried by the CPPs (Rousselle et al. 2003). Decoration of CPPs on the surface of liposome- and biopolymer-based nanoparticles containing drugs has shown to promote their uptake by the brain and entrance to the cytoplasm of neurons (Liu et al. 2008). The drawbacks through AMT are lack of tissue selectivity although the BBB may contain higher concentrations of negative charges than other tissues and possible disruption of the BBB and binding of polycationic substances to the negatively charged plasma proteins and other anionic sites resulting in toxicity (Lockman et al. 2004).

Acknowledgment The author would like to thank the funding support from the National Institutes of Health RO1NS101362-01 and U54CA132378-09.

References

Abbott NJ (1992) Comparative physiology of the blood-brain barrier. In: Physiology and pharmacology of the blood-brain barrier. Springer, Heidelberg

Abbott NJ (2002) Astrocyte-endothelial interactions and blood-brain barrier permeability. J Anat 200(6):629

Abbott NJ, Patabendige AK, Dolman DE, Yusof SR, Begley DJ (2010) Structure and function of the blood-brain barrier. Neuorbiol Dis 37:13

Adamson RH, Liu B, Fry GN, Rubin LL, Curry FE (1998) Microvascular permeability and number of tight junctions are modulated by cAMP. Am J Phys 274(6 Pt 2):H1885–H1894

Adamson RH, Lenz JE, Zhang X, Adamson GN, Weinbaum S, Curry FE (2004) Oncotic pressures oppos-

ing filtration across non-fenestrated rat microvessels. J Physiol Lond 557:889
Allt G, Lawrenson JG (1997) Is the pial microvessel a good model for blood-brain barrier studies? Brain Res Rev 24:67
Arkill KP, Knupp C, Michel CC, Neal CR, Qvortrup K, Rostgaard J, Squire JM (2011) Similar endothelial glycocalyx structures in microvessels from a range of mammalian tissues: evidence for a common filtering mechanism? Biophys J 101(5):1046–1056
Arkill KP, Neal CR, Mantell JM, Michel CC, Qvortrup K, Rostgaard J, Bates DO, Knupp C, Squire JM (2012) 3D reconstruction of the glycocalyx structure in mammalian capillaries using electron tomography. Microcirculation 19(4):343–351
Aspelund A, Antila S, Proulx ST, Karlsen TV, Karaman S, Detmar M, Wiig H, Alitalo K (2015) A dural lymphatic vascular system that drains brain interstitial fluid and macromolecules. J Exp Med 212(7):991. https://doi.org/10.1084/jem.20142290
Bakker Erik NTP, Bacskai BJ, Arbel-Ornath M, Aldea R, Bedussi B, Morris AWJ, Weller RO, Carare RO (2016) Lymphatic clearance of the brain: perivascular, paravascular and significance for neurodegenerative diseases. Cell Mol Neurobiol 36:181–194
Baldwin SA, Fugaccia I, Brown DR, Brown LV, Scheff SW (1996) Blood-brain barrier breach following cortical contusion in the rat. J Neurosurg 85(3):476
Ballabh P, Braun A, Nedergaard M (2004) The blood-brain barrier: an overview: structure, regulation, and clinical implications. Neurobiol Dis 16:1
Balyasnikova IV, Pelligrino DA, Greenwood J, Adamson P, Dragon S, Raza H, Galea E (2000) Cyclic adenosine monophosphate regulates the expression of the intercellular adhesion molecule and the inducible nitric oxide synthase in brain endothelial cells. J Cereb Blood Flow Metab 20(4):688–699
Beaumont A, Marmarou A, Hayasaki K, Barzo P, Fatouros P, Corwin F, Marmarou C, Dunbar J (2000) The permissive nature of blood brain barrier (BBB) opening in edema formation following traumatic brain injury. Acta Neurochir Suppl 76:125
Begley DJ (2007) Structure and function of the blood-brain barrier. In: Enhancement in drug delivery. CRC Press, Boca Raton, p 575
Bobo RH, Laske DW, Akbasak A, Morrison PF, Dedrick RL, Oldfield EH (1994) Convection-enhanced delivery of macromolecules in the brain. Proc Natl Acad Sci U S A 91(6):2076
Bodor N, Farag HH, Brewster ME (1981) Site-specific, sustained release of drugs to the brain. Science 214(4527):1370
Borlongan CV, Emerich DF (2003) Facilitation of drug entry into the CNS via transient permeation of blood brain barrier: laboratory and preliminary clinical evidence from bradykinin receptor agonist, Cereport. Brain Res Bull 60(3):297
Boveri M, Berezowski V, Price A, Slupek S, Lenfant AM, Benaud C, Hartung T, Cecchelli R, Prieto P, Dehouck MP (2005) Induction of blood-brain barrier properties in cultured brain capillary endothelial cells: comparison between primary glial cells and C6 cell line. Glia 51(3):187
Bowman PD, Ennis SR, Rarey KE, Betz AL, Goldstein GW (1983) Brain microvessel endothelial cells in tissue culture: a model for study of blood-brain barrier permeability. Ann Neurol 14(4):396
Brewster ME, Raghavan K, Pop E, Bodor N (1994) Enhanced delivery of ganciclovir to the brain through the use of redox targeting. Antimicrob Agents Chemother 38(4):817
Brinker T, Stopa E, Morrison J, Klinge P (2014) A new look at cerebrospinal fluid circulation. Fluids Barriers CNS 11:10
Brown PD, Davies SL, Speake T, Millar ID (2004a) Molecular mechanisms of cerebrospinal fluid production. Neuroscience 129:957
Brown RC, Egleton RD, Davis TP (2004b) Mannitol opening of the blood–brain barrier: regional variation in the permeability of sucrose, but not 86Rb+ or albumin. Brain Res 1014(1–2):221–227
Brown RC, Morris AP, O'Neil RG (2007) Tight junction protein expression and barrier properties of immortalized mouse brain microvessel endothelial cells. Brain Res 1130(1):17
Butt AM, Jones HC, Abbott NJ (1990) Electrical resistance across the blood-brain barrier in anaesthetized rats: a developmental study. J Physiol 429:47
Carare R, Bernardes-Silva M, Newman T, Page A, Nicoll J, Perry V, Weller R (2008) Solutes, but not cells, drain from the brain parenchyma along basement membranes of capillaries and arteries: significance for cerebral amyloid angiopathy and neuroimmunology. Neuropathol Appl Neurobiol 34(2):131–144
Cernak I, Vink R, Zapple DN, Cruz MI, Ahmed F, Chang T, Fricke ST, Faden AI (2004) The pathobiology of moderate diffuse traumatic brain injury as identified using a new experimental model of injury in rats. Neurobiol Dis 17(1):29
Chen CC, Sheeran PS, Wu SY, Olumolade OO, Dayton PA, Konofagou EE (2013) Targeted drug delivery with focused ultrasound-induced blood–brain barrier opening using acoustically-activated nanodroplets. J Control Release 172(3):795–804
Chu PC, Chai WY, Hsieh HY et al (2013) Pharmacodynamic analysis of magnetic resonance imaging-monitored focused ultrasound-induced blood–brain barrier opening for drug delivery to brain tumors. Biomed Res Int 2013:627496
Cornford EM, Young D, Paxton JW, Sofia RD (1992) Blood-brain barrier penetration of felbamate. Epilepsia 33:944
Crone C, Olesen SP (1982) Electrical resistance of brain microvascular endothelium. Brain Res 241(1):49–55
Cucullo L, McAllister MS, Kight K, Krizanac-Bengez L, Marroni M, Mayberg MR, Stanness KA, Janigro D (2002) A new dynamic in vitro model for the multidimensional study of astrocyte-endothelial cell interactions at the blood-brain barrier. Brain Res 951(2):243

Curley CT, Sheybani ND, Bullock TN, Price RJ (2017) Focused ultrasound immunotherapy for central nervous system pathologies: challenges and opportunities. Theranostics 7(15):3608–3623

Curry FE (1983) Mechanics and thermodynamics of transcapillary exchange. In: Handbook of physiology. The cardiovascular system. The American Physiology Society, Bethesda

Dean RL, Emerich DF, Hasler BP, Bartus RT (1999) Cereport (RMP-7) increases carboplatin levels in brain tumors after pretreatment with dexamethasone. Neuro-Oncology 1(4):268

Deli MA, Abraham CS, Kataoka Y, Niwa M (2005) Permeability studies on in vitro blood-brain barrier models: physiology, pathology, and pharmacology. Cell Mol Neurobiol 25(1):59

Demeuse P, Kerkhofs A, Struys-Ponsar C, Knoops B, Remacle C, de Aguilar PV (2002) Compartmentalized coculture of rat brain endothelial cells and astrocytes: a syngenic model to study the blood-brain barrier. J Neurosci Methods 121(1):21

Deng CX (2010) Targeted drug delivery across the blood–brainbarrierusing ultrasound technique. Ther Deliv 1(6):819–848

Dietrich WD, Alonso O, Halley M (1994) Early microvascular and neuronal consequences of traumatic brain injury: a light and electron microscopic study in rats. J Neurotrauma 11(3):289

Doolittle ND, Abrey LE, Ferrari N, Hall WA, Laws ER, McLendon RE, Muldoon LL, Peereboom D, Peterson DR, Reynolds CP, Senter P, Neuwelt EA (2002) Targeted delivery in primary and metastatic brain tumors: summary report of the seventh annual meeting of the blood-brain barrier disruption consortium. Clin Cancer Res 8(6):1702

Easton AS, Fraser PA (1994) Variable restriction of albumin diffusion across inflamed cerebral microvessels of the anaesthetized rat. J Physiol 475:147

Easton AS, Sarker MH, Fraser PA (1997) Two components of blood-brain barrier disruption in the rat. J Physiol 503(3):613

Ehrlich P (1885) Das sauerstufbudurfnis des organismus. Hireschwald, Berlin

Elsinga PH, Hendrikse NH, Bart J, Vaalburg W, van Waarde A (2004) PET studies on P-glycoprotein function in the blood-brain barrier: how it affects uptake and binding of drugs within the CNS. Curr Pharm Des 10:1493

Engelhardt B, Coisne C (2011) Fluids and barriers of the CNS establish immune privilege by confining immune surveillance to a two-walled castle moat surrounding the CNS castle. Fluids Barriers CNS 8(4):10–1186

Engvall E (1995) Structure and function of basement membranes. Int J Dev Biol 39(5):781

Fan J, Fu BM (2016) Quantification of malignant breast cancer cell MDA-MB-231 transmigration across brain and lung microvascular endothelium. Ann Biomed Eng 44(7):2189–2201

Farkas E, Luiten PG (2001) Cerebral microvascular pathology in aging and Alzheimer's disease. Prog Neurobiol 64(6):575

Franke H, Galla HJ, Beuckmann CT (1999) An improved low-permeability in vitro-model of the blood-brain barrier: transport studies on retinoids, sucrose, haloperidol, caffeine and mannitol. Brain Res 818(1):65

Fraser PA, Dallas AD, Davies S (1990) Measurement of filtration coefficient in single cerebral microvessels of the frog. J Physiol 423:343–361

Fu BM, Chen B (2003) A model for the structural mechanisms in the regulation of microvessel permeability by junction strands. ASME J Biomech Eng 125:620

Fu BM, Shen S (2004) Acute VEGF effect on solute permeability of mammalian microvessels in vivo. Microvasc Res 68:51

Fu BM, Tsay R, Curry FE, Weinbaum S (1994) A junction-orifice-entrance layer model for capillary permeability: application to frog mesenteric capillaries. ASME J Biomech Eng 116:502

Fu BM, Shen S, Chen B (2006) Structural mechanisms in the abolishment of VEGF-induced microvascular hyperpermeability by cAMP. J Biomech Eng 128(3):317–328

Fu BM, Yang J, Cai B, Fan J, Zhang L, Zeng M (2015) Reinforcing endothelial junctions prevents microvessel permeability increase and tumor cell adhesion in microvessels in vivo. Sci Rep 5:15697

Fukuda K, Tanno H, Okimura Y, Nakamura M, Yamaura A (1995) The blood-brain barrier disruption to circulating proteins in the early period after fluid percussion brain injury in rats. J Neurotrauma 12(3):315

Fukuhara S, Sakurai A, Sano H, Yamagishi A, Somekawa S, Takakura N, Saito Y, Kangawa K, Mochizuki N (2005) Cyclic AMP potentiates vascular endothelial cadherin-mediated cell-cell contact to enhance endothelial barrier function through an Epac-Rap1 signaling pathway. Mol Cell Biol 25(1):136–146

Gabathuler R (2010) Approaches to transport therapeutic drugs across the blood-brain barrier to treat brain diseases. Neurobiol Dis 37(1):48

Gaber MW, Yuan H, Killmar JT, Naimark MD, Kiani MF, Merchant TE (2004) An intravital microscopy study of radiation-induced changes in permeability and leukocyte-endothelial cell interactions in the microvessels of the rat pia mater and cremaster muscle. Brain Res Protocol 13:1

Gaillard PJ, de Boer AG (2000) Relationship between permeability status of the blood-brain barrier and in vitro permeability coefficient of a drug. Eur J Pharm Sci 12(2):95

Goldmann E (1913) Vitalfarbung am zentralnervensystem. Abhandl Kongil preuss Akad Wiss, vol 1, pp. 1

Gosk S, Vermehren C, Storm G, Moos T (2004) Targeting anti-transferrin receptor antibody (OX26) and OX26-conjugated liposomes to brain capillary endothelial cells using in situ perfusion. J Cereb Blood Flow Metab 24(11):1193

Greenwood J, Hammarlund-Udenaes M, Jones HC, Stitt AW, Vandenbrouke RE, Romero IA, Campbell M, Fricker G, Brodin B, Manninga H, Gaillard PJ, Schwaninger M, Webster C, Wicher KB, Khrestchatisky M (2017) Current research into brain barriers and the delivery of therapeutics for neurological diseases: a report on CNS barrier congress London, UK, 2017. Fluids Barriers CNS 14(1):31

Haeren RH, van de Ven SE, van Zandvoort MA, Vink H, van Overbeeke JJ, Hoogland G, Rijkers K (2016) Assessment and imaging of the cerebrovascular glycocalyx. Curr Neurovasc Res 13(3):249–260

Hamm S, Dehouck B, Kraus J, Wolburg-Buchholz K, Wolburg H, Risau W, Cecchelli R, Engelhardt B, Dehouck MP (2004) Astrocyte mediated modulation of blood-brain barrier permeability does not correlate with a loss of tight junction proteins from the cellular contacts. Cell Tissue Res 315(2):157

Haseloff RF, Blasig IE, Bauer HC, Bauer H (2005) In search of the astrocytic factor(s) modulating blood-brain barrier functions in brain capillary endothelial cells in vitro. Cell Mol Neurobiol 25(1):25

Hawkins BT, Davis TP (2005) The blood-brain barrier/neurovascular unit in health and disease. Pharmacol Rev 57:173

He P, Curry FE (1993) Differential actions of cAMP on endothelial [Ca2+]i and permeability in microvessels exposed to ATP. Am J Phys 265(3 Pt 2): H1019–H1023

Hemmila JM, Drewes LR (1993) Glucose transporter (GLUT1) expression by canine brain microvessel endothelial cells in culture: an immunocytochemical study. Adv Exp Med Biol 331:13

Hervé F, Ghinea N, Scherrmann JM (2008) CNS delivery via adsorptive transcytosis. AAPS J 10(3):455

Hynynen K, McDannold N, Vykhodtseva N, Jolesz FA (2001) Noninvasive MR imaging-guided focal opening of the blood-brain barrier in rabbits. Radiology 220(3):640

Hynynen K, McDannold N, Vykhodtseva N, Raymond S, Weissleder R, Jolesz FA, Sheikov N (2006) Focal disruption of the blood-brain barrier due to 260-kHz ultrasound bursts: a method for molecular imaging and targeted drug delivery. J Neurosurg 105(3):445

Iliff JJ, Wang M, Zeppenfeld DM, Venkataraman A, Plog BA, Liao Y, Deane R, Nedergaard M (2013) Cerebral arterial pulsation drives paravascular CSF-interstitial fluid exchange in the murine brain. J Neurosci 33(46):18190–18199

Karyekar CS, Fasano A, Raje S, Lu RL, Dowling TC, Eddington ND (2003) Zonula occludens toxin increases the permeability of molecular weight markers and chemotherapeutic agents across the bovine brain microvessel endothelial cells. J Pharm Sci 92(2):414

Kay GG (2000) The effects of antihistamines on cognition and performance. J Allergy Clin Immunol 105:S622

Kemper EM, Boogerd W, Thuis I, Beijnen JH, van Tellingen O (2004) Modulation of the blood-brain barrier in oncology: therapeutic opportunities for the treatment of brain tumours? Cancer Treat Rev 30(5):415

Kim JH, Park JA, Lee SW, Kim WJ, Yu YS, Kim KW (2006) Blood-neural barrier: intercellular communication at glio-vascular interface. J Biochem Mol Biol 39(4):339

Kinoshita M (2006) Targeted drug delivery to the brain using focused ultrasound. Top Magn Reson Imaging 17(3):209

Kleinman HK, Martin GR (2005) Matrigel: basement membrane matrix with biological activity. Semin Cancer Biol 15(5):378

Konofagou EE (2012) Optimization of the ultrasound-induced blood–brain barrier opening. Theranostics 2(12):1223–1237

Kraus J, Voigt K, Schuller AM, Scholz M, Kim KS, Schilling M, Schabitz WR, Oschmann P, Engelhardt B (2008) Interferon-beta stabilizes barrier characteristics of the blood-brain barrier in four different species in vitro. Mult Scler 14(6):843

Kroll RA, Neuwelt EA (1998) Outwitting the blood-brain barrier for therapeutic purposes: osmotic opening and other means. Neurosurgery 42(5):1083

Kumagai AK, Eisenberg JB, Pardridge WM (1987) Absorptive-mediated endocytosis of cationized albumin and a beta-endorphin-cationized albumin chimeric peptide by isolated brain capillaries.Model system of blood-brain barrier transport. J Biol Chem 262(31):15214

de Lange EC, de Boer BA, Breimer DD (1999) Microdialysis for pharmacokinetic analysis of drug transport to the brain. Adv Drug Deliv Rev 36:211

Lawrenson JG, Reid AR, Allt G (1997) Molecular characteristics of pial microvessels of the rat optic nerve. Can pial microvessels be used as a model for the blood-brain barrier? Cell Tissue Res 288:259–265

Lewandowsky M (1900) Zur lehre von der cerebrospinalflussigkeit. Z Klin Med 40:480

Li G, Fu BM (2011) An electro-diffusion model for the blood-brain barrier permeability to charged molecule. ASME J Biomech Eng 133(2):0210

Li G, Simon M, Shi Z, Cancel L, Tarbell JM, Morrison B, Fu BM (2010a) Permeability of endothelial and astrocyte cocultures: in vitro blood-brain barrier models for drug delivery. Ann Biomed Eng 38(8):2499

Li G, Yuan W, Fu BM (2010b) A model for water and solute transport across the blood-brain barrier. J Biomech 43(11):2133

Lipinski CA (2000) Drug-like properties and the causes of poor solubility and poor permeability. J Pharmacol Toxicol Methods 44(1):235

Liu L, Guo K, Lu J, Venkatraman SS, Luo D, Ng KC, Ling EA, Moochhala S, Yang YY (2008) Biologically active core/shell nanoparticles self-assembled from cholesterol-terminated PEG-TAT for drug delivery across the blood-brain barrier. Biomaterials 29(10):1509

Lockman PR, Koziara JM, Mumper RJ, Allen DD (2004) Nanoparticle surface charges alter blood-brain barrier integrity and permeability. J Drug Target 12(9–10):635

Louveau A, Smirnov I, Keyes TJ, Eccles JD, Rouhani SJ, Peske JD, Derecki NC, Castle D, Mandell JW, Lee

KS (2015) Structural and functional features of central nervous system lymphatic vessels. Nature 523:337–341. https://doi.org/10.1038/nature14432
Mak M, Fung L, Strasser JF, Saltzman WM (1995) Distribution of drugs following controlled delivery to the brain interstitium. J Neuro-Oncol 26(2):91
Malina KC, Cooper I, Teichberg VI (2009) Closing the gap between the in-vivo and in-vitro blood-brain barrier tightness. Brain Res 1284:12
Mehta D, Malik AB (2006) Signaling mechanisms regulating endothelial permeability. Physiol Rev 86(1):279–367
Meyer J, Mischeck U, Veyhl M, Henzel K, Galla HJ (1990) Blood-brain barrier characteristic enzymatic properties in cultured brain capillary endothelial cells. Brain Res 514(2):305
Miller G (2002) Drug targeting. Breaking down barriers. Science 297(5584):1116
Miosge N (2001) The ultrastructural composition of basement membranes in vivo. Histol Histopathol 16(4):1239
Montagne A, Zhao Z, Zlokovic BV (2017) Alzheimer's disease: a matter of blood-brain barrier dysfunction? J Exp Med 214(11):3151–3169
Moody DM (2006) The blood-brain barrier and blood-cerebral spinal fluid barrier. Semin Cardiothorac Vasc Anesth 10(2):128
Moore TM, Chetham PM, Kelly JJ, Stevens T (1998) Signal transduction and regulation of lung endothelial cell permeability. Interaction between calcium and cAMP. Am J Phys 275(2 Pt 1):L203–L222
Nag S, Begley DJ (2005) Blood-brain barrier, exchange of metabolites and gases. In: Pathology and genetics. Cerebrovascular diseases. ISN Neuropath. Press, Basel
Neuwelt EA (2004) Mechanisms of disease: the blood-brain barrier. Neurosurgery 54(1):131
Nhan T, Burgess A, Cho EE, Stefanovic B, Lilge L, Hynynen K (2013) Drug delivery to the brain by focused ultrasound induced blood–brain barrier disruption: quantitative evaluation of enhanced permeability of cerebral vasculature using two-photon microscopy. J Control Release 172(1):274–280
Nicolazzo JA, Charman SA, Charman WN (2006) Methods to assess drug permeability across the blood-brain barrier. J Pharm Pharmacol 58:281
Ohlin KE, Francardo V, Lindgren HS, Sillivan SE, O'Sullivan SS, Luksik AS, Vassoler FM, Lees AJ, Konradi C, Cenci MA (2011) Vascular endothelial growth factor is upregulated by L-dopa in the parkinsonian brain: implications for the development of dyskinesia. Brain 134(Pt 8):2339–2357
Oldendorf WH, Cornford ME, Brown WJ (1977) The large apparent work capability of the blood-brain barrier: a study of the mitochondrial content of capillary endothelial cells in brain and other tissues of the rat. Ann Neurol 1:409
Omidi Y, Campbell L, Barar J, Connell D, Akhtar S, Gumbleton M (2003) Evaluation of the immortalised mouse brain capillary endothelial cell line, bEnd3, as an in vitro blood-brain barrier model for drug uptake and transport studies. Brain Res 990(1–2):95
Pardridge WM (1998) CNS drug design based on principles of blood-brain barrier transport. J Neurochem 70:1781
Pardridge WM (2005) Molecular biology of the blood-brain barrier. Mol Biotechnol 30(1):57
Pardridge WM (2007) Drug targeting to the brain. Pharm Res 24:1733
Pardridge WM (2017) Delivery of biologics across the blood-brain barrier with molecular trojan horse technology. BioDrugs 31(6):503–519
Park J, Fan Z, Kumon RE, El-Sayed ME, Deng CX (2010) Modulation of intracellular Ca2+ concentration in brain microvascular endothelial cells in vitro by acoustic cavitation. Ultrasound Med Biol 36(7):1176–1187
Poller B, Gutmann H, Krahenbuhl S, Weksler B, Romero I, Couraud PO, Tuffin G, Drewe J, Huwyler J (2008) The human brain endothelial cell line hCMEC/D3 as a human blood-brain barrier model for drug transport studies. J Neurochem 107(5):1358
Redzic ZB, Segal MB (2004) The structure of the choroid plexus and the physiology of the choroid plexus epithelium. Adv Drug Deliv Rev 56:1695
Reese TS, Karnovsky MJ (1967) Fine structural localization of a blood-brain barrier to exogenous peroxidase. J Cell Biol 34(1):207
Romero IA, Radewicz K, Jubin E, Michel CC, Greenwood J, Couraud PO, Adamson P (2003) Changes in cytoskeletal and tight junctional proteins correlate with decreased permeability induced by dexamethasone in cultured rat brain endothelial cells. Neurosci Lett 344(2):112
Rousselle C, Clair P, Smirnova M, Kolesnikov Y, Pasternak GW, Gac-Breton S, Rees AR, Scherrmann JM, Temsamani J (2003) Improved brain uptake and pharmacological activity of dalargin using a peptide-vector-mediated strategy. J Pharmacol Exp Ther 306(1):371
Rubin LL, Hall DE, Porter S, Barbu K, Cannon C, Horner HC, Janatpour M, Liaw CW, Manning K, Morales J, Tanner LI, Tomaselli KJ, Bard F (1991) A cell-culture model of the blood-brain-barrier. J Cell Biol 115(6):1725–1735
Sahagun G, Moore SA, Hart MN (1990) Permeability of neutral vs. anionic dextrans in cultured brain microvascular endothelium. Am J Phys 259(1 Pt 2):H162
Salvetti F, Cecchetti P, Janigro D, Lucacchini A, Benzi L, Martini C (2002) Insulin permeability across an in vitro dynamic model of endothelium. Pharm Res 19(4):445
Santaguida S, Janigro D, Hossain M, Oby E, Rapp E, Cucullo L (2006) Side by side comparison between dynamic versus static models of blood-brain barrier in vitro: a permeability study. Brain Res 1109:1
Sawada GA, Williams LR, Lutzke BS, Raub TJ (1999) Novel, highly lipophilic antioxidants readily diffuse across the blood-brain barrier and access intracellular sites. J Pharmacol Exp Ther 288(3):1327

Sawchuk RJ, Elmquist WF (2000) Microdialysis in the study of drug transporters in the CNS. Adv Drug Deliv Rev 45:295

Sayner SL (2011) Emerging themes of cAMP regulation of the pulmonary endothelial barrier. Am J Physiol Lung Cell Mol Physiol 300(5):L667–L678

Schuetz EG, Schinkel AH, Relling MV, Schuetz JD (1996) P-glycoprotein: a major determinant of rifampicin-inducible expression of cytochrome P4503A in mice and humans. Proc Natl Acad Sci U S A 93:4001

Schulze C, Firth JA (1992) Interendothelial junctions during blood-brain-barrier development in the rat - morphological-changes at the level of individual tight junctional contacts. Dev Brain Res 69(1):85

Setiadi A, Korim WS, Elsaafien K, Yao ST (2017) The role of the blood-brain barrier in hypertension. Exp Physiol 103(3):337–342

Shashoua VE, Hesse GW (1996) N-docosahexaenoyl, 3 hydroxytyramine: a dopaminergic compound that penetrates the blood-brain barrier and suppresses appetite. Life Sci 58(16):1347

Shi L, Zeng M, Sun Y, Fu BM (2014a) Quantification of blood-brain barrier solute permeability and brain transport by multiphoton microscopy. J Biomech Eng 136(3):031005

Shi L, Zeng M, Fu BM (2014b) Temporal effects of vascular endothelial growth factor and 3,5-cyclic monophosphate on blood-brain barrier solute permeability in vivo. J Neurosci Res 92(12):1678–1689

Shi L, Palacio-Mancheno P, Badami J, Shin DW, Zeng M, Cardoso L, Tu R, Fu BM (2014c) Quantification of transient increase of the blood-brain barrier permeability to macromolecules by optimized focused ultrasound combined with microbubbles. Int J Nanomedicine 18(9):4437–4448

Shimizu S (2008) A novel approach to the diagnosis and management of meralgia paresthetica. Neurosurgery 63(4):E820

DW Shin, N Khadka, J Fan, M Bikson, BM Fu (2016) Transcranial direct current stimulation transiently increases the blood-brain barrier solute permeability in vivo SPIE Medical Imaging Conference, Feb. 27-March 3, 2016, San Diego, CA, USA

Simard M, Arcuino G, Takano T, Liu QS, Nedergaard M (2003) Signaling at the gliovascular interface. J Neurosci 23(27):9254

Smith QR (2000) Transport of glutamate and other amino acids at the blood-brain barrier. J Nutr 130:1016

Soga N, Connolly JO, Chellaiah M, Kawamura J, Hruska KA (2001) Rac regulates vascular endothelial growth factor stimulated motility. Cell Commun Adhes 8(1):1

Squire JM, Chew M, Nneji G, Neal C, Barry J, Michel CC (2001) Quasi-periodic substructure in the microvessel endothelial glycocalyx: a possible explanation for molecular filtering? J Struct Biol 136(3):239

Suidan GL, Dickerson JW, Chen Y, McDole JR, Tripathi P, Pirko I, Seroogy KB, Johnson AJ (2010 Jan 15) CD8 T cell-initiated vascular endothelial growth factor expression promotes central nervous system vascular permeability under neuroinflammatory conditions. J Immunol 184(2):1031–1040

Thompson SE, Cavitt J, Audus KL (1994) Leucine-enkephalin effects on paracellular and transcellular permeation pathways across brain microvessel endothelial-cell monolayers. J Cardiovasc Pharmacol 24(5):818

Tsou YH, Zhang XQ, Zhu H, Syed S, Xu X (2017) Drug delivery to the brain across the blood-brain barrier using nanomaterials. Small

Tyagi N, Moshal KS, Sen U, Vacek TP, Kumar M, Hughes WM Jr, Kundu S, Tyagi SC (2009) H2S protects against methionine-induced oxidative stress in brain endothelial cells. Antioxid Redox Signal 11(1):25

Ueno M, Sakamoto H, Liao YJ, Onodera M, Huang CL, Miyanaka H, Nakagawa T (2004) Blood-brain barrier disruption in the hypothalamus of young adult spontaneously hypertensive rats. Histochem Cell Biol 122(2):131

de Vries HE, BlomRoosemalen MCM, van Oosten M, de Boer AG, van Berkel TJ, Breimer DD, Kuiper J (1996) The influence of cytokines on the integrity of the blood-brain barrier in vitro. J Neuroimmunol 64(1):37

Wang R, Ashwal S, Tone B, Tian HR, Badaut J, Rasmussen A, Obenaus A (2007) Albumin reduces blood-brain barrier permeability but does not alter infarct size in a rat model of neonatal stroke. Pediatr Res 62:261

Wolburg H, Neuhaus J, Kniesel U, Krauss B, Schmid EM, Ocalan M, Farrell C, Risau W (1994) Modulation of tight junction structure in blood-brain barrier endothelial cells. Effects of tissue culture, second messengers and cocultured astrocytes. J Cell Sci 107(Pt 5):1347–1357

Wolburg-Buchholz K, Mack AF, Steiner E, Pfeiffer F, Engelhardt B, Wolburg H (2009) Loss of astrocyte polarity marks blood-brain barrier impairment during experimental autoimmune encephalomyelitis. Acta Neuropathol 18(2):219

Yang FY, Lin YS, Kang KH, Chao TK (2011) Reversible blood–brain barrier disruption by repeated transcranial focused ultrasound allows enhanced extravasation. J Control Release 150(1):111–116

Yoder EJ (2002) Modifications in astrocyte morphology and calcium signaling induced by a brain capillary endothelial cell line. Glia 38(2):137

Yoon JH, Lee ES, Jeong Y (2017) In vivo imaging of the cerebral endothelial glycocalyx in mice. J Vasc Res 54(2):59–67. https://doi.org/10.1159/000457799 Epub 2017 Apr 1

Yuan W, Lv Y, Zeng M, Fu BM (2009) Non-invasive measurement of solute permeability in cerebral microvessels of the rat. Microvasc Res 77:166

Yuan W, Li G, Fu BM (2010a) Effect of surface charge of immortalized mouse cerebral endothelial cell monolayer on transport of charged solutes. Ann Biomed Eng 38(4):1463

Yuan W, Li G, Zeng M, Fu BM (2010b) Modulation of the blood-brain barrier permeability by plasma glycoprotein orosomucoid. Microvasc Res 80(1):148–157

Zhang Y, Pardridge WM (2001) Rapid transferrin efflux from brain to blood across the blood-brain barrier. J Neurochem 76:1597

Zhang Y, Li CS, Ye YY, Johnson K, Poe J, Johnson S, Bobrowski W, Garrido R, Madhu C (2006) Porcine brain microvessel endothelial cells as an in vitro model to predict in vivo blood-brain barrier permeability. Drug Metab Dispos 34(11):1935

Zhang Q, Fu BM, Zhang ZJ (2017) Borneol, a novel agent that improves central nervous system drug delivery by enhancing blood-brain barrier permeability. Drug Deliv 24(1):1037–1044

Zlokovic BV, Begley DJ, Djuricic BM, Mitrovic DM (1986) Measurement of solute transport across the blood-brain barrier in the perfused Guinea pig brain: method and application to N-methyl-alpha-aminoisobutyric acid. J Neurochem 46:1444

Blood-Brain Barrier Integrity and Clearance of Amyloid-β from the BBB

Irsalan Cockerill, Joy-Anne Oliver, Huaxi Xu, Bingmei M. Fu, and Donghui Zhu

Abstract

Alzheimer's disease, a type of dementia, affects memory, behavior, and cognitive processes in affected individuals. It is one of the prominent diseases, accounting for 60–80% of dementia cases and affecting a significant population of persons over the age of 65 years. While rare, Alzheimer's disease (AD) may affect the younger population as well. With such a widespread number of persons affected with AD, scientists have undertaken the initiative to develop a cure for this devastating disease; however, it has been deemed quite challenging. A dysfunctional blood-brain barrier, with impaired ability to clear amyloid-β from the brain, has been directly linked to the development of Alzheimer's disease. The blood-brain barrier restricts the flow of many substances into and out of the brain and serves as a selective and protective barrier to the brain. A proper functioning blood-brain barrier contributes to the maintenance and integrity of the brain. In turn, different systems and mechanisms within the blood-brain barrier are set in place to facilitate mediated passage of materials and substances between the brain and the bloodstream. In relation to AD, the mediation of amyloid-β clearance is of great importance in maintaining the blood-brain barrier's integrity.

1 Introduction

Performing ordinary activities such as eating, drinking, or exercising can affect the blood composition in innumerable ways, including shifts in salt levels to increases or decreases in the lipid or amino acid content in the blood. Blood travels throughout the body via the circulatory system, and through this system the blood transports oxygen, carbon dioxide, and nutrients into and out of the various tissues of the body. Metabolites that are toxic to the brain can even be present in the bloodstream; however these "toxic" metabolites

Irsalan Cockerill and Joy-Anne Oliver are contributed equally to this work.

I. Cockerill · J.-A. Oliver · D. Zhu (✉)
Department of Biomedical Engineering, University of North Texas, Denton, TX, USA
e-mail: Donghui.Zhu@unt.edu

H. Xu
Fujian Provincial Key Laboratory of Neurodegenerative Disease and Aging Research, Institute of Neuroscience, College of Medicine, Xiamen University, Fujian Sheng, China

Degenerative Diseases Program, Sanford Burnham Prebys Medical Discovery Institute, La Jolla, CA, USA

B. M. Fu
Department of Biomedical Engineering, The City College of the City University of New York, New York, NY, USA

B. M. Fu, N. T. Wright (eds.), *Molecular, Cellular, and Tissue Engineering of the Vascular System*, Advances in Experimental Medicine and Biology 1097,
https://doi.org/10.1007/978-3-319-96445-4_14

may be beneficial to the body. The blood-brain barrier (BBB) blocks the streaming of harmful materials present in the bloodstream from entering the central nervous system (CNS) and maintains brain homeostasis by regulating the movement of compounds across the endothelium of cerebral capillaries (Kreutzer et al. 2011). It acts as a defense mechanism, consisting of the endothelial cells lining the blood vessels in the brain that are "glued" together very tightly by structures known as tight and adherens junctions and other structures that combine to facilitate the functioning of the BBB. For decades, scientists have focused on ways to penetrate the BBB in designing many drug delivery methods and techniques in the prevention and treatment of neuro diseases such as Alzheimer's and dementia.

The function of the brain and the study of the BBB serve as a vital integral to the investigation of brain diseases such as Alzheimer's disease and dementia. Scientists spend a great deal of time focusing on the vital aspects that make up the BBB structure and how these characteristics contribute to its specific functions. They have also developed a central concept to understanding the factors that contribute to the degradation of brain functioning and the cause of Alzheimer's disease. Additionally, they have used these concepts in designing appropriate drug delivery techniques in combating this devastating disease.

2 Blood-Brain Barrier Structure and Function

Neurons present in the CNS are between 8 and 20 μm from the capillaries and require a constant supply of oxygen and nutrients (Tajes et al. 2014). Nutrients and oxygen leave the blood to enter the brain through the endothelial layer that lines the blood vessels of the blood-brain barrier. The endothelial cells of the BBB consist of numerous transport systems that enable necessary materials required for proper brain functioning but do not easily cross the barrier (Fig. 1). Studies have shown that small molecules of sizes less than ~800 Da can cross the BBB easily because they are small enough to pass through tight junctions. However, molecules larger than ~800 Da

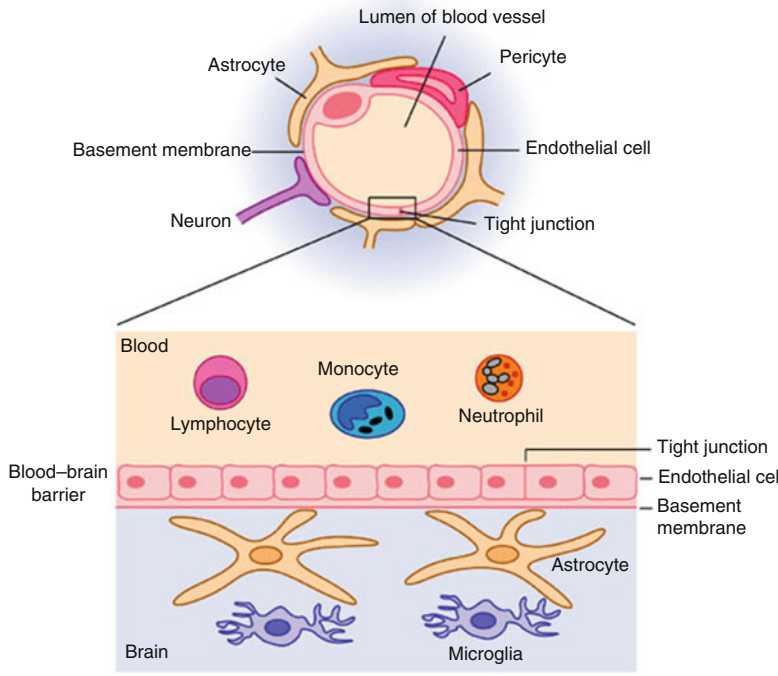

The blood–brain barrier (BBB)

Fig. 1 Structure of the blood-brain barrier including its components. The BBB is not a rigid structure but a dynamic interface with a range of interrelated functions, resulting from the presence of extremely effective tight junctions, trans endothelial transport systems, enzymes, and regulation of leukocyte permeation, which thereby generate the physical, transport, enzymatic, and immune regulatory functions of the BBB (Joan Abbott and Friedman 2013). There are three cellular elements of the brain microvasculature that compose the BBB—endothelial cells, astrocyte endfeet, and pericytes (Aarts and Arundine 2003)

have difficulty crossing the BBB (Tajes et al. 2014).

Restrictive permeability is key for the ideal functioning of the BBB. The main function of the endothelium is to block the passage of unwanted materials and toxins from entering the brain. The presence of tight and adherens junctions between the endothelial cells forming the BBB allows for the cells to be packed together in such a way that there is almost no space between them. The presence of the BBB ensures high specificity of nutrients reaching the neurons in the CNS despite the surrounding environmental influences of the harmful substances in the body.

The endothelium allows for rapid-free diffusion or gaseous exchange of small particles such as oxygen from the blood into the brain and carbon dioxide from the brain into the blood (Zhao et al. 2015a). Hydrophilic molecules such as glucose cannot pass through the endothelium as easily as oxygen and carbon dioxide do and require receptors and channels to facilitate their transport into and out of the brain (Zhao et al. 2015a).

The general components of the BBB are quite similar in morphology of the peripheral cells; however, there are notable modifications that are specific to maintaining ideal functioning and homeostasis of the BBB. For it to be maintained, the endothelial cells of the BBB consist of the following notable difference from peripheral cells:

- *The presence of intercellular tight junctions and the absence of fenestration*. The BBB is primarily composed of a considerable number of endothelial cells. The significance of the endothelial cells is to act as a barrier, preventing the passage of various materials into and out of the brain. Fenestration refers to the presence of pores in the capillaries that allow the passage of large molecular weight materials. Fenestrated capillaries are found in the intestinal mucosa, renal glomeruli, pancreas, endocrine gland, and other tissues of the body. Because the BBB focuses on preventing the free passage of materials into the brain, fenestration is not present.
- *The low level of non-specific transcytosis (pinocytosis) and paracellular diffusion of hydrophilic compounds*. Non-specific transcytosis involves the movement of various macromolecules across the interior of the cells through vesicles that are captured from outside the cell. Unlike other endothelial cells of the body, the absence of the high quantity of non-specific transcytosis benefits the BBB by facilitating the selectiveness to the materials that enter the brain tissue. Paracellular transport refers to the transfer of substances across the epithelium through the intercellular space between the cells. Tight and adherens junctions make up the intercellular spaces and cause limited space to be present between the cells of the endothelium. Because of this, the passage of hydrophilic or water-loving materials is not possible as long as the BBB is fully functioning.
- *The presence of a large number of mitochondria in endothelial cells*. Mitochondria in the endothelial cells forming the BBB provide energy in the form of ATP through respiration and regulate cellular metabolism and gene expression. They play a crucial role in maintaining the integrity of the BBB through the miR-34a-mediated mechanism. MicroRNA 34a, also referred to as miR-34a, is a microRNA that the human body encodes using the miR-34A gene. The miR-34a participates in post-transcription regulation of gene expression by affecting the stability and translation of mRNAs during gene expression. When a specific miRNA binds to its target on a messenger RNA (mRNA), it can inhibit the expression of that mRNA. MicroRNAs are referred to as master regulators of gene expression and are known to regulate up to 30% of the protein coding genes in the human genome. One single miRNA can bind to a target and regulate more than 100 different transcripts. With such ability, the presence of mitochondria in the endothelial cells of the BBB is crucial for the regulation of the integrity of the barrier through its role on gene expression.

- *The polarized expression of membrane receptors and transporters.* These are responsible for the active transport of blood-borne nutrients to the brain or the efflux of potentially toxic compounds from the cerebral to the vascular compartment. Nutrients and other materials enter and exit through the endothelial cells of the BBB via transport systems. The diffusion of substances into the brain can be divided into two processes: paracellular (substances travel between cells) and transcellular (substances travel across cells). Substances that move paracellular are limited as they are subjected to tight junctions. However, substances that move transcellular primarily travel via active transport. Apart from the paracellular diffusion (sucrose) and the transcellular diffusion (ethanol) mechanisms that occur at the BBB, other types of transcellular transport mechanisms include ion channels, e.g., K^+ gated, ion-symport channels (e.g., $Na^+/K^+/Cl^-$ cotransporter), ion-antiporter channels (e.g., Na^+/H^+ exchange), facilitated diffusion (e.g., glucose via GLUT-1), active efflux pumps (e.g., P-glycoprotein), active-antiporter transport (e.g. Na^+/K^+ ATPase), and receptor-mediated endocytosis (e.g., transferrin and insulin). The two main efflux transporters in the BBB are multidrug resistance gene (MDR1) and breast cancer resistance protein (BCRP). They are both expressed on the apical membrane of the endothelium, pumping substances from the cell into the bloodstream, and function by preventing xenobiotics from crossing the BBB.

2.1 Tight Junctions

Tight junctions are located in the apical section of the paracellular pathway between adjacent endothelial cells. Tight junctions primarily form a seal to avoid paracellular diffusion of solutes into the brain. Additionally, they regulate the lateral diffusion of nutrients and other particles between the apical and basolateral plasma membrane domains that maintain the plasma membrane and lipid polarity. Tight junction functions are enhanced by the presence of astrocytes and pericytes. Their presence in the BBB shares similar characteristics to those of epithelial tight junctions but is a specific difference that allows BBB tight junctions to fulfill their functions. These BBB tight junctions are sensitive to ambient factors (Wolburg 2000). Tight junctions consist of a number of proteins, primarily claudins, occludins, and junctional adhesion molecules JAMs that directly contribute to maintaining their viability. Other proteins that contribute to the structure and functioning of tight junctions include PDF motif MAGUK (ZO-1, 2 and 3), non-PDF motif cingulin, 7H6 ZONAB, Rab13, PK C heterotrimeric G protein, and catenin (120 and p100) (Wolburg 2000).

2.2 Adherens Junctions

Adherens junction is the junction present in the BBB whose cytoplasmic face is linked to the actin cytoskeleton. They are responsible for keeping contiguous cells together and therefore assist in maintaining the structure of tight junctions. Adherens junctions are present in the endothelial cells of the BBB and are primarily comprised of transmembrane glycoproteins of the cadherin armadillo superfamily. The transmembrane glycoproteins mainly consist of vascular endothelium cadherin also known as VE-cadherins that have the ability to form homotypic adhesive complexes with adjacent cells in the presence of Ca^{2+}. The Armadillo superfamily acts as an anchor through cytoplasmic plaque that links the glycoproteins to the cytoskeleton.

2.3 Astrocytes

Astrocytes are star-shaped glial cells that connect neurons directly to the endothelial cells of the BBB. They play a very important role in the BBB by providing structural support of the endothelial cells and reinforcing the BBB function by the endothelial cells. Specific contribution of astrocytes to the BBB is not as prominent as those of tight junctions and endothelial cells (Weiss et al. 2009).

2.4 Pericytes

Pericytes engulf the basal membrane that surrounds the endothelial cells of the BBB. They contribute to the regulation of endothelium proliferation, angiogenesis, and inflammatory process. Pericytes also regulate specific gene expression in the endothelial cells and deter polarization of astrocyte endfeet surrounding CNS blood vessels.

2.5 Transport Across the BBB

Nutrients, ions, and other molecules travel across the BBB through two general mechanisms (Fig. 2):

2.5.1 Paracellular Transport

Movement of particles is between the endothelial cells, through the junctional complex. The paracellular pathway is described as a passive transport process involving the movement of hydrophilic molecules across the barrier, depending on their electrochemical, hydrostatic, and osmotic gradient. Tight junctions primarily mediate paracellular transport, and the movement of particles is dependent on solute concentration. The contractility and adhesive forces of the endothelial cytoskeleton control the permeability of the junction complex of the tight junctions through which paracellular transport occurs (Tajes et al. 2014). The dynamic equilibrium between both forces accounts for this type of transport through the BBB. However, although this is one of the primary transport mechanisms, it plays a minor role in developing brain-targeted drugs in the treatment of many brain-related diseases such as dementia and Alzheimer's.

2.5.2 Transcellular Transport

It refers to the movement of nutrients, ions, or particles across the endothelial cells of the BBB that may or may not require energy. Through transcellular pathway, particles move across the luminal and abluminal membrane of the capillary

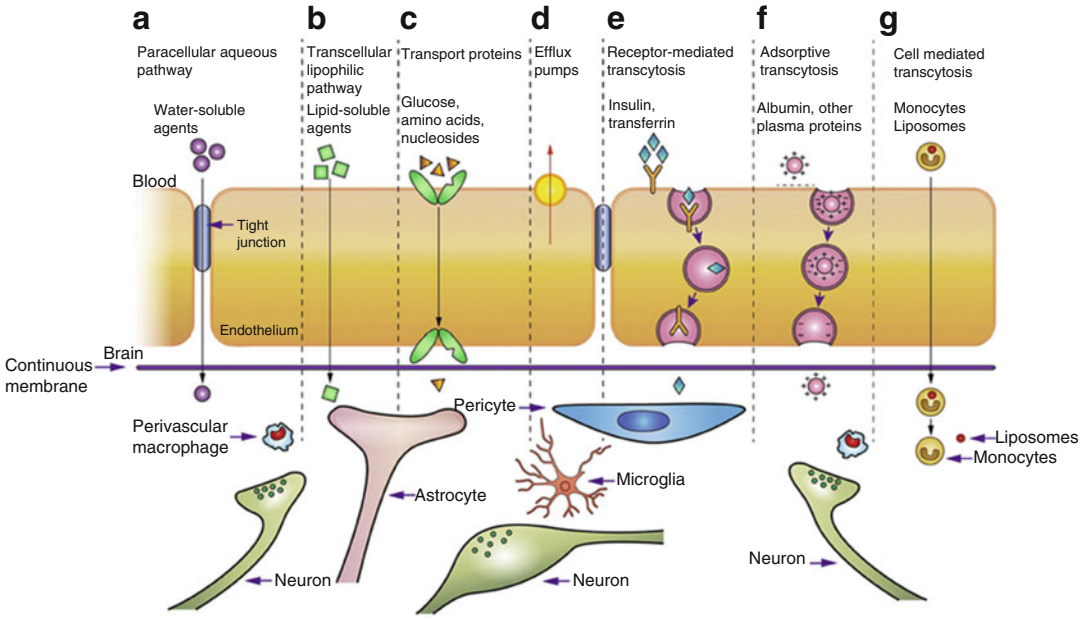

Fig. 2 Transport pathways across the blood-brain barrier. (**a**) Paracellular pathway for water-soluble agents, (**b**) transcellular pathway for lipid-soluble molecules, (**c**) carrier-mediated pathway, (**d**) efflux transport system, (**e**) receptor-mediated transcytosis pathway, (**f**) absorptive transcytosis pathway, and (**g**) cell-mediated pathway (Liu 2012)

endothelium via mechanisms such as receptor-mediated transcytosis, efflux transport systems, endocytosis of positively charged molecules, and carrier-mediated transport (Tajes et al. 2014).

2.5.3 Receptor-Mediated Transcytosis

A form of active transport that is temperature dependent and is the primary transport mechanism used by the brain's endothelial cells. High-molecular-mass proteins, such as insulin, and low-density proteins and lipoproteins such as leptin, transferrin, and insulin-like growth factor (IGF) require this type of transport. Receptor-mediated transcytosis requires a two-step process: (1) the formation of an endocytic vesicle where the receptor-ligand recognition facilitates the formation of coated pits. These pits become endocytic vesicles and engulf the ligand. (2) Endosomal fusion dissociates the receptor from the ligand, and the contents are released via exocytosis. Some of the vesicles fuse with lysosomes and lose the content due to factors such as low pH and enzyme-mediated hydrolysis and, therefore, never make it across the BBB and into the CNS. This pathway is safe and effective in CNS drug delivery because of its specificity and lack of size and lipophilicity dependence (Tajes et al. 2014).

2.5.4 Efflux Transport System

This mechanism actively transports particles via ATP and concentration dependence and is responsible for the removal of materials out of the CNS, into the systemic circulation, therefore eliminating the buildup of compounds that would have entered through the BBB via different pathways. The prototypic efflux transporter is known as the glycoprotein P (gp-P), present on the luminal membrane of the endothelial cells, and it is present in high concentrations within the capillaries of the brain to maintain the brain's vitality. The gp-P is a member of the class of multidrug resistance receptors, well known for being an ATP-dependent remover of anticancer drugs, antibiotics, immune system suppressors, or ionic channel modulators. There are additional efflux transporter systems that do not use the same mechanism as gp-P as they do not have the ability to hydrolyze ATP, a critical ability of the ATP-binding cassette (ABC) transporter family. The other systems include monocarboxylate transporters (MCTs) and organic anion transporters/organic anion transporter polypeptides (OAT/OATPs) (Tajes et al. 2014). However, these systems are unable to transport materials against their concentration gradient and therefore participate in bidirectional transport of materials via ion or substrate gradients based on the material concentration on both sides of the barrier.

2.5.5 Charged Compound Interaction

This transport mechanism occurs when positively charged compounds interact with negatively charged compounds of the endothelial cell membrane to facilitate absorptive-mediated endocytosis to occur at the BBB. This pathway is mainly used by scientists to increase the delivery of conjugated drugs across the BBB during drug delivery into the CNS (Tajes et al. 2014).

2.5.6 Carrier-Mediated Pathway

A form of saturable transport that mediates the exchange of particles between the systemic circulation and the brain's parenchyma. This process can be ATP dependent or ATP independent. The protein carriers that participate in this pathway are located in the luminal and abluminal membrane and are usually polarized. Within the BBB, there are numerous carrier systems that promote the selectiveness of substrates and other molecules that travel through the barrier. Glucose, for instance, is supplied through the GLUT-1 transporter by concentration gradient through passive transport (Tajes et al. 2014). Passive transport is defined as the movement of molecules such as ions and nutrients across cell membranes without the need of ATP. Other compounds such as amino acid require different carriers depending on their physiochemical properties.

3 Alzheimer's Disease and Amyloid-β

Alzheimer's disease is a central nervous system (CNS) disease, caused by the dysfunction of the blood-brain barrier (BBB). Alzheimer's disease, being the most common type of dementia, affects over 36 million individuals worldwide and is quite prevalent in persons of age 65 years and older. Symptoms of Alzheimer's begin from memory loss and cognitive impairment and can progress in severity as time progresses. Depending on how severe the disease is, individuals have to be institutionalized and may soon die. If left untreated, the occurrence of Alzheimer's disease can become widespread where it can become a threat to the worldwide healthcare system.

Amyloid-β is a protein constituent that is considered the hallmark of Alzheimer's disease. Individuals with this disease are known to have clumps of deposited Aβ within the brain tissue that form plaques and contribute to nerve cell death. The presence of Aβ in the brain tissue causes the destruction of synapses from an early stage prior to its accumulation and further damage. Synapses are referred to as contact points where nerve cells relay signals to one another. Amyloid-β originates as a solitary molecule and favors the formation of small clusters that are soluble and able to travel freely into the brain. The accumulation of clusters leads to the plaque formation which becomes deposited throughout the brain tissue. However, these cluster forms are capable of binding strongly to a receptor on the nerve cells that set into motion a cascade of events that erodes the synapses with other nerve cells. Therefore, scientists have developed a hypothesis—*the amyloid cascade hypothesis* states that amyloid-β (Aβ) decomposition in the CNS initiates a cascade of molecular events that cause neurodegeneration, leading to Alzheimer's disease onset and progression.

The presence of synapses between nerve cells contributes to memory storage, planning, thought processes, and emotions. Once synapses degradation begins to occur, persons experience loss of these attributes—the symptoms of Alzheimer's disease. The presence of a protein receptor, paired immunoglobulin-like receptor B also known as PirB, present on the nerve cells on the brains of mice, binds strongly with Aβ. The PirB in the brain reduces plasticity in the nervous system and weakens synapses. When Aβ binds to PirB, it breaks down cofilin activity—a protein that breaks down actin, a building block protein that maintains the structure of the synapses—and revs up the synapses degradation. The main receptors for amyloid-beta peptide (Aβ) transport across the blood-brain barrier (BBB) from the brain to the blood and the blood to the brain are low-density lipoprotein receptor-related protein-1s (LRP1) and receptor for advanced glycation end products (RAGE), respectively (Deane et al. 2009). Because the BBB plays a vital role in maintaining CNS homeostasis, its dysfunction results in the onset of Alzheimer's and many other brain diseases.

4 Amyloid-β Clearance Mechanisms from the Brain

Insufficient amyloid-β (Aβ) clearance is a hallmark in the pathogenesis and progress of Alzheimer's disease (AD). Neurons predominantly secrete Aβ into the interstitial fluid (ISF) upon amyloid precursor protein (APP) hydrolysis. Several clearance mechanisms exist which include low-density lipoprotein receptor-related protein 1 (LRP1)-mediated transport, cerebral parenchymal cells, and choroid plexus secretion and cerebrospinal spinal (CSF) production, while heavy metals may impair clearance. Understanding the biochemical pathways at work can further advance our knowledge of the disease and lead to the development of effective therapies.

4.1 LRP1-Mediated Clearance of Aβ

LRP1 is a member of the low-density lipoprotein receptor family which includes LRP1B, megalin/LRP2, very-LDLR (VLDLR) apolipopro-

tein E receptor 2 (ApoER2)/LRP8, sortilin-related receptor (SorLA/LR11), LRP5, and LRP6 (Kanekiyo and Bu 2014). LRP1 has been widely studied for its implication in AD. It is a receptor for more than 40 different ligands and participates in Aβ metabolism by binding directly or indirectly to Aβ. LRP1 is ubiquitously expressed all throughout the body and highly concentrated in the liver, lung, and brain (Kanekiyo and Bu 2014). It plays an integral part in brain hemostasis. APP undergoes processing via α, β, and γ secretase; the latter two confer a more amyloidogenic pathology, whereas α-secretase produces soluble sAPPα. The transmembrane APP undergoes cleavage of its N-terminal domain by β-secretase followed by C-terminal cleavage by γ-secretase, producing Aβ which is a small protein of 39–43 amino acids long; $Aβ_{40}$ and $Aβ_{42}$ have an intrinsic tendency to self-assemble into SDS-stable oligomers which form insoluble β-pleated sheet structures termed amyloid fibrils (Bhattacharjee et al. 2014). β, followed by γ-secretase processing, results in exocytosis of Aβ in neurons, and LRP1 mediates uptake of Aβ in brain parenchyma (by microglia, neurons, and astrocytes). As a major endothelial surface receptor, LRP1 mediates clearance of Aβ across the BBB. Cell membrane-bound LRP1, concentrated on the abluminal endothelial side, assists with transcytosis. Phosphatidylinositol binding clathrin assembly (PICLAM) protein is encoded by the PICLAM gene and is involved in internalization and endocytosis of membrane receptors. It is abundantly expressed in the brain capillary endothelium and has been shown to affect Aβ metabolism and transport through the BBB (Zhao et al. 2015b). In a detailed study conducted by our group, the precise mechanism of PICLAM-mediated Aβ migration from the brain to the blood was discovered. *Picalm*$^{+/-}$ heterozygous mice were generated for the study and displayed significant retention of $Aβ_{40}$ and $Aβ_{42}$ by 38 and 36% following intracerebral administration of Aβ, respectively (Zhao et al. 2015b). Upon Aβ binding to LRP1, phosphatidylinositol binding clathrin assembly protein (PICLAM) binds to the YXXXL intracellular domain tail of LRP1, triggering a conformational structural change and driving the clearance of brain Aβ transcytosis to systemic circulation (Zhao et al. 2015b). Clathrin heavy chain (CHC) and clathrin adapter protein α-adaptin (AP-2) were also found to be essential for proper internalization of Aβ, a mechanism confirmed by siRNA knockdown of PICALM, CHC, and AP-2. *Picalm* deficiency diminished $Aβ_{40}$ and $Aβ_{42}$ efflux across BBB by 41 and 61%, respectively, a finding that was further validated by lower plasma levels of 48% Aβ40 and 65% $Aβ_{42}$ compared to *Picalm*$^{+/+}$ controls (Zhao et al. 2015b). During this process, Aβ is directed away from Rab 7, a GTPase that directs late endosomes to lysosomes resulting in ligand degradation, and ushered toward Rab 5 and Rab 11, GTPases responsible for recycling endosomes and transcytosis and exocytosis of ligands (Zhao et al. 2015b). Peak co-localization between PICALM and Rab5 was higher than that of PICALM and Rab11, suggesting transfer of endocytotic vesicles from Rab5 to Rab11 is a rate-limiting step (Zhao et al. 2015b). In the liver, soluble-LRP1 (sLRP1) is synthesized and secreted into the peripheral circulation where it sequesters recently emigrated Aβ across the BBB, leading to clearance from the kidneys. Coimmunoprecipitation of sLRP1-bound Aβ in neurologically normal humans has indicated that circulating sLRP1 can sequester 70–90% of plasma Aβ (Ramanathan et al. 2015). This precise mechanism creates an "Aβ sink" where systemic concentration of Aβ is kept low enough, thus driving Aβ transcytosis across the BBB. The precise mechanism is detailed in Fig. 3.

4.2 Brain Parenchymal-Mediated Clearance of Aβ

Brain parenchyma cells represent an alternate pathway for clearance of Aβ (Fig. 4). In neurons, APP undergoes processing where it is secreted into ISF. From there, neighboring neurons can uptake Aβ in a LRP1-mediated endocytosis fashion. It can be further degraded in the lysosome. Disturbances in lysosome functionality have been implicated in intraneuronal Aβ

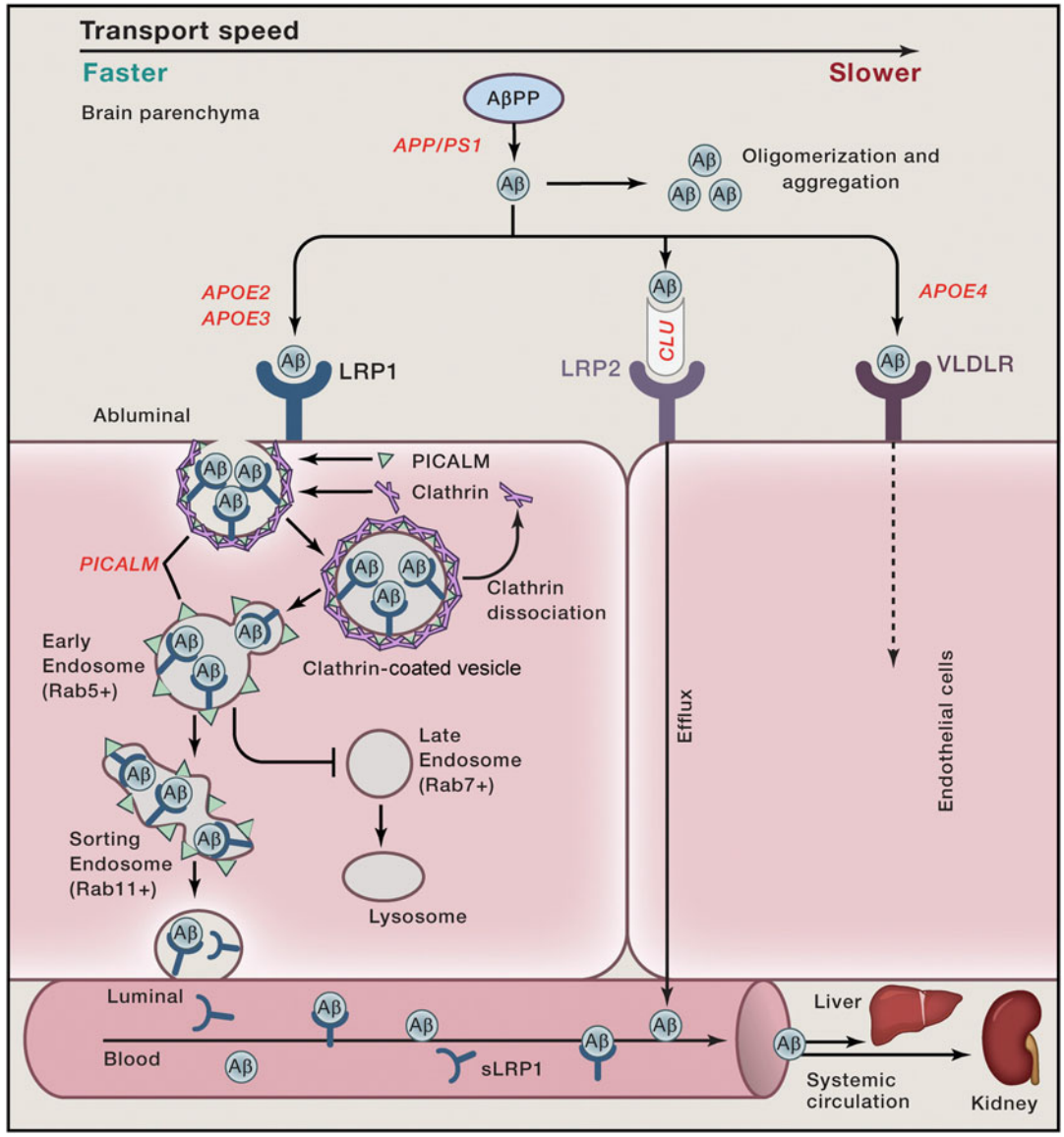

Fig. 3 APP undergoes processing by α secretase, generating sAPPα, while β and γ secretase sequentially produce Aβ. Binding of Aβ to APOE2, APOE3, or APOE34 dictate transport speed through BBB. APOE2 and APOE3-AB result in PICALM-mediated transcytosis via Rab 5 and Rab 11 through BBB. sLRP1 is directed toward the liver and kidneys for systemic clearance. Slower Aβ clearance is controlled by APOE4 γ-secretase processing, resulting in Aβ oligomerization and limited clearance via VLDLR. Courtesy of Zhao et al. 2015a

aggregation and deposition. LRP1 knockdown mice display higher concentrations of ISF Aβ, exhibiting exacerbated AD pathology.

Microglia represent another clearance mechanism of Aβ. Soluble Aβ (sAβ) is taken up in a macropinocytosis manner and transported to lysosomes, whereas large Aβ fibrils are taken up by multicomponent cell surface receptors. Phagocytosis of apoptotic cells via LPR1 has also been demonstrated, suggesting an alternate pathway of Aβ clearance for microglia. Interestingly, inhibition of LRP1 via antagonists such as lactoferrin, α2macroglobulin (α2M), and RAP results is diminished Aβ uptake (Kanekiyo

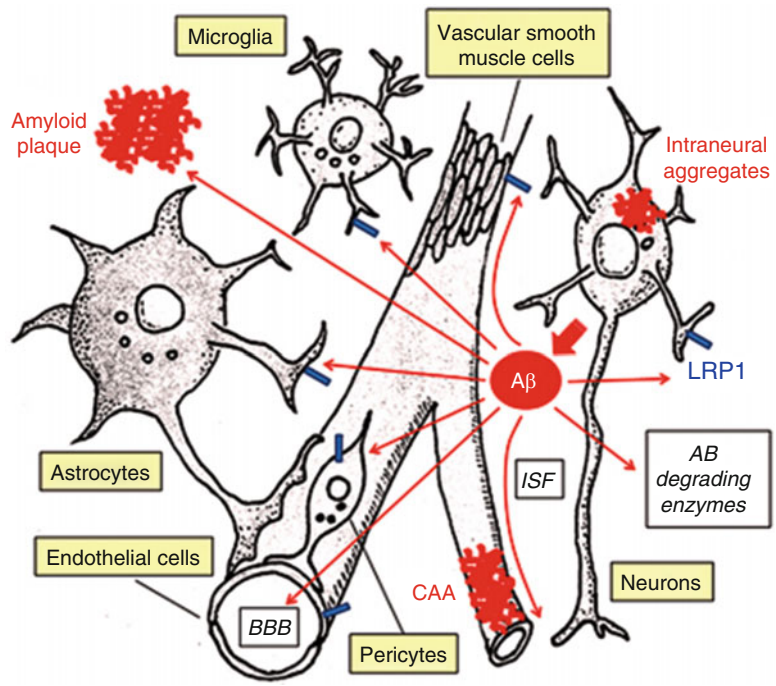

Fig. 4 Neuronal secretion of Aβ can be cleared through several mechanisms. Aβ can be assimilated by microglia, astrocytes, pericytes, endothelial cells, or transported across BBB. Aβ may also be enzymatically processed by insulin-degrading enzyme (IDE) or neprilysin. Failure in Aβ clearance may result in amyloid plaques, synaptic dysfunction, and neuronal loss. Adopted from Kanekiyo and Bu 2014

and Bu 2014). Interestingly, in a human BBB model performed by Bernas, microglia initiate blood-derived monocyte recruitment through secretion of RANTES, otherwise known as "regulated on action," normal T cell expressed and secreted, a chemotactic cytokine (Zhagi et al. 2009). Emigrating monocytes are attracted to neuritic plaques where they intrude into neurons, harvesting Aβ. Subsequently, monocyte-derived macrophages become swollen and attempt to emigrate through the BBB. Compared to controls, AD macrophages acquire a swollen phenotype and upregulate apoptotic pathways, namely, caspases-6, 7, and 8 (Zhagi et al. 2009). Through engorgement of Aβ and apoptosis, migrating macrophages burst spilling fibrillar Aβ into the vessel wall (Zhagi et al. 2009), known as cerebral amyloid angiopathy, CAA. Apparently, decreased phagocytosis of Aβ results from downregulation of β-1,4-mannosyl-glycoprotein 4-β-N-acetylglucosaminyltransferase (MGAT-3), an enzyme important in phagocytosis of Aβ. Increased vessel angiopathy activates inflammatory pathways, resulting in increased ROS, oxidative stress, and chemokines, further exacerbating the disease. Aβ deposition within cerebral vessels also results in loss and degeneration of pericyte and smooth muscle cells. Mice defective in pericytes express higher levels of intercellular adhesion molecule 1 (ICAM-1) in the brain endothelium, and larger numbers of $Gr1^{+}$ leukocytes infiltrate into the brain parenchyma (Zenaro et al. 2016), demonstrating the importance of pericytes in regulating the immune response.

Pericytes are located on the abluminal side of the BBB and cover approximately 25% of their circumference. Pericytes express LRP1 and adenosine triphosphate-binding cassette transporter B1 (ABCB1) which have both been shown to play roles in Aβ clearance. As part of the neurovascular unit (NVU), pericytes are critical for the development and stability of the BBB and regulate blood flow through capillaries through controlling cellular contraction/relaxation (Zenaro et al. 2016). Additionally, endothelial secreted platelet-derived growth factor BB (PDGF-BB) binds to basement membrane heparan sulfate proteoglycan, initiating pericyte proliferation, migration, and recruitment (Zhao et al. 2015b). Transgenic null mice have demonstrated PDGF-

BB that is imperative for CNS microvessels as complete loss leads to rupture, microaneurisms, and embryonic lethality. Aβ deposition has been shown to increase PDGRβ shedding from pericytes, demonstrating yet another degenerative effect of the amyloid cascade. A major biochemical pathway at work involved APOE; APOE binds to LRP1 on localized pericytes, activating and/or suppressing the proinflammatory cyclophilin A, an isozyme involved in cis-trans isomerization of proline imidic peptide bonds, nuclear factor kB (CypA-NFkB) pathway; the APOE4 variant causes activation of this pathway, while APOE3 translates into suppression (Zhao et al. 2015b). Secretion of APOE occurs at the level of the astrocyte.

Astrocytes cover up to 90% of brain microvessels and rely on bidirectional feedback from pericytes in maintaining BBB integrity. Their presence in the NVU is essential in maintaining tight junctions of the BBB. Astrocytes close to plaques express LRPs and can internalize Aβ in an APOE-dependent manner. Some studies have shown intra-astrocytic Aβ to induce dysfunction, while others have shown that Aβ can be degraded. Speculation surrounds the idea that astrocytes may traffic Aβ close to endfeet where abluminal endothelial cells and pericytes may eliminate AB via ABCB1/LRP1 (ElAli and Rivest 2013). They express relatively low levels of ABCB1 and elevated levels of ABCA1, a known factor in APOE lipidation (ElAli and Rivest 2013), resulting in reduced Aβ aggregation. As such, astrocytes contribute to Aβ clearance in making Aβ more diffusible through the BBB. Aquaporin-4 (AQP4) is abundant in astrocyte processes adjacent to cerebral microvessels, and its expression is key in uptake and degradation of Aβ (Zenaro et al. 2016). The reallocation of AQP4 from astrocyte end processes to non-endfeet has been observed in several models of AD, suggesting increased depolarization and communicational interference with pericytes (Zenaro et al. 2016). Additionally, astrocytes mediate neuroinflammation through active secretion of cytokines and chemokines, establishing a link between the NVU and immunoregulatory processes. Given this information, astrocytes mediate several aspects of Aβ clearance and may reduce and/or contribute to AD pathology.

4.3 Choroid Plexus Removal of Aβ

The choroid plexus (CP) is a network of capillaries and cuboidal epithelial cells lining the four ventricles of the brain. As a lining of the ventricular system, the epithelial cells produce cerebrospinal fluid (CSF) and actively filter blood and plasma. Therefore, they serve as a secondary barrier, the blood-CSF barrier, paralleling that of the BBB. Fluid is filtered into and out of the CSF. Indeed, many of the tight junction proteins, zonula occludens (ZO-1), and Aβ clearance proteins are present, RAGE, LRP1, and gp-P (Gonzalez-Marrero et al. 2015). Choroid plexus maintains proper integrity, pressure, and composition of CSF through secretion of ions, nutrients, metabolic precursors, and proteins (Lun et al. 2016). Two proteins, transthyretin (TTR) and aquaporin-1 (AQP-1), are often used as benchmarks to gauge the health of CP. AQ1 is a transmembrane protein of the CP involved in transporting water from blood to CSF, while TTR is a transport protein involved in binding thyroxine and retinol-binding protein bound to retinol. TTR has also been found to bind Aβ and thus prohibiting the formation of Aβ fibrils. As such, TTR is an important indicator in the pathogenesis of AD.

Gonzalez-Marrero et al. investigated the effects of triple transgenic (3xTg-AD)-induced mice, harboring presenilin 1 (PS1/M146 V), APPSwe, and tauP301L on CP; these animal models mimic the critical hallmarks of AD as presenilin 1 mutants mimic overproduction of $A\beta_{42}$ through interaction with γ-secretase, APPSwe accelerates Aβ production because it is a transgene coding for a 695 amino acid isoform of Aβ, and tauP301L results are tau hyperphosphorylation. 3xTg-AD mice display behavior alterations, cognitive deficits, and accelerated Aβ plaques and NFT starting from 12 months (Gonzalez-Marrero et al. 2015). Their

results indicate 3xTg-AD mice exhibit age-related pathology at 16 months similar to AD (Gonzalez-Marrero et al. 2015). Additionally, they found more than twofold increases in $A\beta_{42}$ in the stroma and altered cellular distribution patterns as compared to non-Tg mice; 3xTg-AD showed uniform $A\beta_{42}$ throughout the CP, while controls displayed apical $A\beta_{42.}$ CP can receive up to 5–10 times more blood flow than other brain regions, and thus maintaining hemostasis and vascular perfusion is pertinent in assessing proper removal of Aβ. Further analysis revealed ~twofold higher collagen IV deposition around CP and blood vessel basement membranes (Gonzalez-Marrero et al. 2015). Collagen IV deposition increased BM thickness and is suggestive of altered BBB integrity. According to Fick's diffusion theory, a major factor affecting diffusion across biological membranes is membrane thickness (Gonzalez-Marrero et al. 2015). Consequently, reduced permeability, oxygenation, plasma ultrafiltration, and CSF formation become less efficient, consistent with most models of AD pathology (Gonzalez-Marrero et al. 2015). TTR and AQP-1 staining also revealed >threefold and 31% lower expression in 3xTg-AD as compared to controls, respectively. Increases in cellular and stroma $A\beta_{42}$ indicate impaired Aβ metabolism and clearance. AD patients show elevated levels of Aβ in plasma due to compromised binding to sLRP1. Elevated systemic levels of Aβ can reenter the brain and CP via RAGE-mediated transport; indeed, this study also found elevated cytoplasmic RAGE expression in CP, suggesting increases in Aβ upregulate RAGE (Gonzalez-Marrero et al. 2015).

4.4 Heavy Metal Toxicity

Heavy metal accumulation and toxicity appear to be major variables in the pathogenesis of Alzheimer's disease and disrupt clearance mechanisms of Aβ. Aluminum (Al) is one of the most abundant elements in the biosphere, and its industrial production and environmental prevalence makes it one of the most neurotoxic elements we are exposed to daily. Al's contribution to AD is based on at least seven independent-derived observations:

1. Al strongly promotes Aβ aggregation and accumulation, known as amyloid cascade.
2. In vitro and in vivo analyses display marked increases in pro-inflammatory transcription factor NF-kB.
3. mRNA and miRNA expression induced by Al is strikingly similar to that of AD.
4. Dietary consumption of Al induces lipid peroxidation, oxidative stress, apoptosis, and gene expression deficits.
5. Many deficits observed in AD are recapitulates in Al-treated cellular or animal models.
6. Numerous worldwide epidemiological studies correlate Al in drinking water as hydrated Al potassium sulfate, $KAl(SO_4)_2{\cdot}12H_2O$, to AD.
7. A significant number of pharmaceutical treatments rely on antioxidant and iron/aluminum chelation therapy (Bhattacharjee et al. 2013).

In fact, the scientific literature is replete with studies showing neurotoxic effects of Al.

The only oxidation state of aluminum is Al^{3+}, and it has a small ionic radius (50 pm) relative to zinc (Zn^{2+}; 74 pm), calcium (Ca^{2+}; 99 pm), and sodium (Na^{+}; 95 pm) which makes it a very effective cross-linker of proteins. Al-induced conformational changes have been demonstrated using circular dichroism (CD) spectroscopy (Kawahara and Kato-Negishi 2011; Exley et al. 1993). Within the amino acid sequence of Aβ, arginine (Arg^5), tyrosine (Tyr^{10}), and histidine (His^{13}) demonstrate metal-binding properties. This makes this particular amino acid sequence particularly susceptible to cross-linking. Studies have demonstrated that polymerization of Aβ occurs in the presence of Al and treatment with deferoxamine (DFO) results in dissolving of the network (Kawahara and Kato-Negishi 2011).

Al also affects iron (Fe) homeostasis as it has comparable properties. Binding of Al to ferritin, transferrin, iron regulatory protein (IRP), and/or iron-responsive elements (IRE) has profound implications in the production of free radicals via the increase in Fe concentrations. IRP is a cytoso-

lic protein which functions as a posttranscriptional switch for Fe homeostasis, binding to 5′ and 3′ untranslated regions of mRNA containing IREs. As a negative regulator, it inhibits the production of ferritin in Fe-depleted cells by blocking ferritin mRNA from translation within the ribosome. Conversely, the lack of IRP binding to mRNA untranslated regions results in endonuclease cleavage of the construct. Al has the ability to disrupt all pathways in iron homeostasis because, as mentioned previously, it can bind all relevant proteins in this pathway. Importantly, APP and ferritin contain an IRE within their mRNA, and Al has been shown to increase APP production in experimental animal models (Kawahara and Kato-Negishi 2011).

Several studies have exhibited increased Al deposition in the brain of AD patients, especially in areas of hippocampal formation and occipital lobes. Al >2.00 μg/g dry wt is considered pathologically concerning, while >3.00 μg/g dry wt is considered pathologically significant and thus will contribute to exacerbation of AD pathology, earlier onset, and more aggressive etiology (Mirza et al. 2017). In a recent study of 12 humans, 7 females and 5 males, autopsy-confirmed familial AD diagnosed patients, postmortem tissue samples were obtained from occipital, frontal, parietal, and temporal lobes. The samples were analyzesd for Al content using validated lumogallion and fluorescence microscopy. Eleven of 12 individuals had at least one tissue sample with a pathologically significant (>3.00 μg/g dry wt) content of Al (Mirza et al. 2017). The brains of nine individuals displayed Al content >5.00 μg/g dry wt, while five of these had at least one sample upward of >10.00 μg/g dry wt (Mirza et al. 2017). Furthermore, Al appears to show a differential deposition in arteries that supply the brain and CNS (Bhattacharjee et al. 2013). A postmortem, case-controlled study of AD patients unveiled a concentration gradient of Al while dissecting the celiac, femoral, aorta, vertebral, common carotid, internal carotid, basilar, middle cerebral, and posterior cerebral arteries (PCA). The PCA had a ninefold increase in Al, amounting to 54.2 μg/g dry wt (Bhattacharjee et al. 2013). The PCA provides major blood supply to the hippocampus, suggesting a possible correlation between increased Al affinity for the PCA and hippocampal dysfunction. The concentration gradient of Al may be related to its increased affinity for phosphates covalently linked to lipids lining the cerebral vasculature.

5 BBB Dysfunction and Impaired BBB Clearance

The BBB provides a physical separation of blood from components of the brain. However, dysfunction of the barrier is highly implicated in numerous neurodegenerative diseases, including autism, Parkinson's disease, dementia, multiple sclerosis, HIV-1 encephalitis, severe hypertension, AD, etc. (Haorah et al. 2007). Increasingly elevated levels of reactive oxygen species (ROS), impaired insulin resistance, and elevated cholesterol esters play important roles in BBB dysfunction.

5.1 ROS Exacerbate Alzheimer's Disease

ROS are natural byproducts of cellular metabolism. They are generated in response to mitochondria's production of adenosine triphosphate (ATP). During this process, hydrogen ions are pumped across the inner mitochondrial membrane. Lastly, oxygen is reduced to form water. This process inevitably produces small amounts of superoxide ($\cdot O_2^-$) which can react with water to form hydroperoxyl (HO_2) and hydroxide (OH). Subsequently, ROS can lead to lipid peroxidation, damage to local tissues and DNA, activation of apoptosis, and recruitment of immune cells to the site of inflammation. Therefore, they play a leading role in nearly all aspects of neurodegenerative diseases. They may act alone or in response to other factors and represent complex interactions of cellular metabolism in conjunction with their environment. Matrix metalloproteinases (MMPs) have been shown to be upregulated in response

to ROS. Specifically, ROS-mediated activation of MMP2 and MMP9 has demonstrated degradation of basement membrane proteins and subsequent loss of BBB integrity. Additionally, ROS-induced phosphorylation of tight junction proteins (claudin-5, occludin, ZO-1) via upregulation of protein tyrosine kinase (PTK) (with diminished protein tyrosine phosphatase) triggers leaky BBB. Furthermore, loss of BBB stability leads to infiltration of leukocytes and exacerbated brain inflammation. Fibrinogen, albumin, thrombin, hemoglobin, and immunoglobulins have been discovered in postmortem studies of AD and amyotrophic lateral sclerosis (ALS), exemplifying the pathological consequences of BBB disruption (Fig. 5).

5.2 Insulin Resistance and Its Role in Vascular Hemostasis

Vascular pathologies are believed to contribute significantly to the spectrum of neurodegenerative diseases, including dementia, mild cognitive impairment, AD, etc. Until recognition of the significance of neuritic plaques and neurofibrillary tangles (NFTs), vascular dysfunction was the prevailing view surrounding cognitive deficits in AD (Mullins et al. 2017). Insulin signaling has profound consequences on vascular hemostasis, BBB functionality, and AD exacerbation. Insulin can be produced de novo in the brain, but the general consensus is that insulin's actions are primarily pancreas-derived. Its vasodilation properties couple PI3K signaling to increased generation of nitric oxide (NO) in endothelial cells, a potent vasodilator. NO diffuses freely into nearby smooth muscle cells resulting in production of cyclic guanosine monophosphate (cGMP) and thus regulating vasoconstriction. Furthermore, NO inhibits platelet aggregation, monocyte adhesion, and thrombosis, all of which damage the vessel wall (Mullins et al. 2017). Microvascular disruption leads to production of ROS and potentiates overexpression of receptor for advanced glycation end products (RAGE), the endothelial receptor responsible for plasma Aβ transcytosis from the blood to the brain (Mullins et al. 2017).

Binding of insulin to brain endothelium elicits autophosphorylation of insulin receptor substrate-1 (IRS-1) and activation of several pathways, including PI3K/Akt, leading to membrane localization of glucose transporters (GLUTs), primarily GLUT 1 and GLUT 3 in the brain, and mediation of glycogen synthase kinase-3β (GSK-3β)-regulated hyperphosphorylation of tau proteins, a trademark of neurofibrillary tangles in AD (Mullins et al. 2017). A detailed analysis by Talbot et al. uncovered significant downregulation of insulin pathway IR → IRS-1 → PI3K and greatly reduced signaling in response to IGF-1 in the IGF-1R → IRS-2 → PI3K pathway of AD patients without diabetes relative to normal controls (2012). They found that IRS-1 and IRS-2 activation is primarily separate around physiologically relevant concentrations (∼1 nM) and responds to insulin and IGF-1, respectively, but this response can crosstalk under conditions of hyperinsulinemia (∼10 nM) or excessive IGF-1 (∼10 nM) (Talbot et al. 2012). Additionally, modest downregulation occurred at the level of IR, while major reductions occurred downstream: 90% for IRS-1 phosphotyrosine, pY, (IRS-1 pY), 89% for Akt1 pS, 76% for GSK-3β pY^{216}, 83% for GSK-3β pS^{9}, 74% for mTOR pS^{2448}, and 90% for ERK2 pT^{185}/pY^{187} (Talbot et al. 2012). Their analysis indicated this extensive downregulation must occur, not from IR inhibition but from bottom-up effects (Talbot et al. 2012). Consistently, they found excessive phosphorylation of IRS-1 at critical serine sites, S312, S616, and/or S636, resulting in suppression of IRS-1. Phosphorylation at these sites was also significantly correlated with basal activation of GSK-3, inhibitor of kappa B kinase (IKK), JNK, mTOR, and PKCζ/λ. IR-sensitizing drugs appear to ameliorate this inhibition and improve Aβ pathology (Talbot et al. 2012). In contrast to Chia et al., Talbot found overall suppression of GSK-3, refuting the hypothesis of GSK-3-mediated hyperphosphorylation of Tau protein; these conflicting results warrant more research. In conclusion, excessive phosphorylation of IRS-1 pS^{616} had the largest and most negative effects

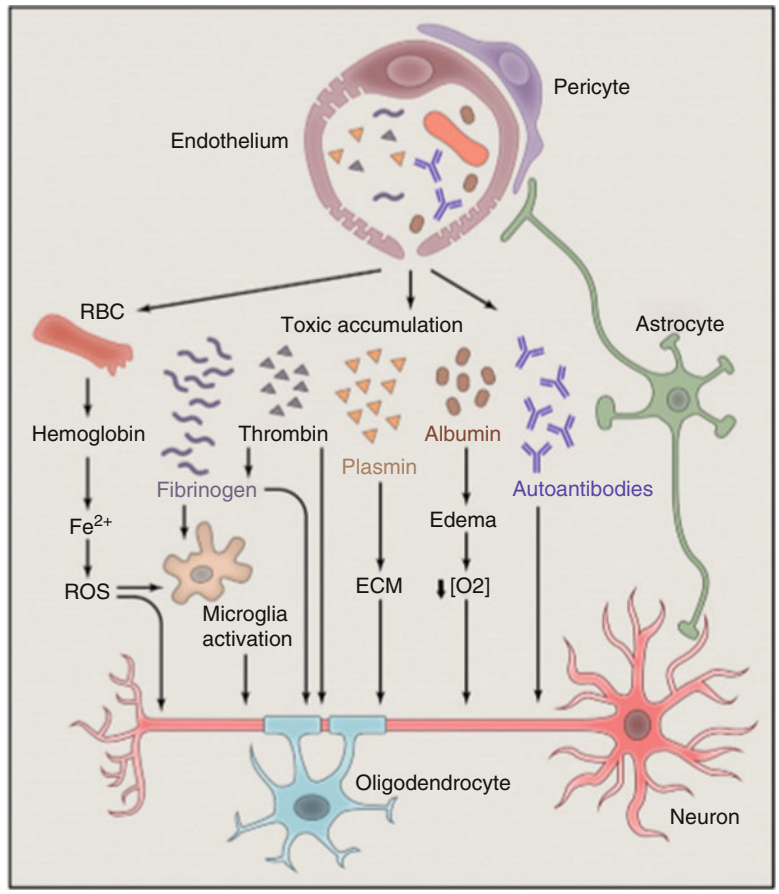

Fig. 5 Effects of disrupted BBB and leakage of toxic blood components into the cerebrum Dysfunctional pericyte-endothelial and astrocyte-endothelial signaling results in localized breakdown of the BBB. As BBB becomes leaky, proteins from the blood escape into local tissues, triggering inflammation. Fe^{2+} derived from red blood cells acts as a pro-oxidant and producer of ROS. Fibrinogen triggers activation of microglial cells, promoting neuroinflammation and demyelination. Additionally, fibrinogen, thrombin, and plasmin activate cleavage of extracellular matrix proteins and detachment of neurons, leading to cell death. Albumin results in hypoperfusion, hypoxia, and localized edema. Production of autoantibodies against neuron components such as myelin is possible via loss of immune privilege. Courtesy of Zhao et al. 2015b

on episodic memory score and appears to be a major factor in cognitive decline associated with AD (Talbot et al. 2012).

5.3 Cholesterol Effects on AD

Hypercholesterolemia and defective lipid metabolism have a strong link to AD. Grimm's work established a pertinent link between high cholesterol, activation of β and γ-secretase, and pathogenesis of AD (2008). They found inhibition of cholesterol through administering lovastatin, an inhibitor of HGM-CoA reductase, and extraction of cholesterol by methyl-β-cyclodextrin treatment reduces β and γ-secretase activities (Grimm et al. 2008), thereby reducing the intracellular concentrations of $Aβ_{40}$ and $Aβ_{42}$. Production of cholesterol begins with the addition of two molecules of acetyl-CoA to form acetoacetyl-CoA. Another reaction of acetoacetyl-CoA with acetyl-CoA produces 3-hydroxy-3-methylglutaryl-CoA (HMG-CoA), whereby HMG-CoA reductase

acts to form mevalonate. In fact, statins exert their cholesterol-lowering effects through inhibition of this enzyme, which is the rate-limiting step in the process. Through more than 20 enzymatic steps, cholesterol is produced. Cholesterol is used by every cell in the body where it is concentrated in lipid rafts within the cell membrane. It increases membrane packing by interacting with membrane phospholipids and, in doing so, maintains cell fluidity. Cholesterol also serves as a precursor for vitamin D, bile acids, and the biosynthesis of steroid hormones, including testosterone and estrogen. The brain houses approximately 25% total cholesterol and is predominantly found in the non-esterified form (Gamba et al. 2015). Because cholesterol and lipoproteins are unable to cross the BBB, neurons rely on astrocyte de novo synthesis and secretion of APOE-cholesterol complexes. Of note, 24-hydroxycholesterol (24-OH), an oxidation product of cholesterol, is secreted by the neuron and combines with nuclear liver X receptor (LXR), and they are secreted to neighboring astrocytes, where they facilitate transcription and production of APOE; APOE is the brain's principal cholesterol transport system (Gamba et al. 2015). In essence, neurons secrete 24-OH-LXR to astrocytes where it promotes production of APOE, and then astrocytes secrete the newly produced APOE-cholesterol complexes back to the neuron (Gamba et al. 2015).

APOE is an apolipoprotein in that its primary function is to transport lipids, fat, and cholesterol throughout lymphatic and circulatory systems. It is found on the surface of chylomicrons and intermediate density lipoproteins (IDLs). APOE is synthesized peripherally in the liver and by macrophages but also by astrocytes within the central nervous system.

Implications of APOE polymorphisms in AD are believed to be related to cholesterol transport. APOE has been shown to colocalize with cholesterol and Aβ fibrils in senile plaques. Of interest, the APOE4, but not APOE2 and APOE3 variant, may confer increased susceptibility to late-onset AD, synergizes with Aβ toxicity, and is more susceptible to cleavage than APOE3 (Gamba et al. 2015). In part, it is because of indirect activation of the proinflammatory CypA-NFkB matrix metalloproteinase 9 (MMP-9) pathway, which leads to breakdown of BBB through destruction of basement membrane and tight junctions (Gamba et al. 2015). As mentioned previously (Fig. 5), destruction of the BBB tight junctions can lead compromised blood flow and hypoxic conditions, accumulation of blood proteins and leukocytes, and further potentiate the inflammatory condition of the brain. According to the vascular two-hit hypothesis, an initial vascular insult to the brain (*hit 1*) elicited by hypoxia, hypoperfusion, or a disrupted BBB proceeds observed amyloid pathology in AD (Gamba et al. 2015). Accumulated Aβ (*hit 2*), predominantly an effect of faulty Aβ clearance in late-onset AD, now triggers a pathological cascade of neuronal injury, cognitive decline, and AD dementia (Gamba et al. 2015).

Several oxysterols have been implicated in Alzheimer's disease. Because oxysterols can cross the BBB, more than 20 different metabolites have been associated with AD, but two cholesterol oxidation products are highly implicated. 24-OH is produced almost exclusively in the brain by the enzyme cholesterol 24-hydroxylase (CYP46A1), and 27-hydroxy cholesterol (27-OH), to a lesser extent, is produced by the enzyme cholesterol 27-hydroxylase (CYP27A1). 27-OH is subsequently converted into 7α-hydroxy-3-oxo-4-cholestenoic acid (7-OH-4-C) by the enzyme CYP7B where it exits the brain via the BBB and gets excreted following processing by the liver. However, 27-OH can flow from systemic circulation to the brain, serving as a potential link between intracerebral and extracerebral pools of cholesterol, and may contribute to hypercholesterolemia in the brain (Gamba et al. 2015). 24-OH is the primary cholesterol metabolite of the brain and has been shown to promote brain protection through its efflux and inhibition of Aβ production. During early stages of the disease, higher levels of 24-OH have been found in the CSF and peripheral circulation as compared to healthy controls (Gamba et al. 2015). However, late stages of AD exemplify lower plasma levels of 24-OH,

suggesting decreased oxidation of cholesterol by the enzyme CYP46A1, loss of neurons and ongoing demyelinization, and/or reduced transport through the BBB (Gamba et al. 2015).

6 Conclusion

After more than 100 years since the first description, AD now affects about 30 million people worldwide. Age is a significant biological risk factor. While we are gaining knowledge of underlying genetic predispositions, molecular mechanisms, and potential etiologies of this complex disease, there is still much we do not know. Genetic predispositions contribute to approximately 1–10% of familial AD cases, while environmental factors appear to have the biggest impact. The two common hallmarks of AD, Aβ plaques and Tau NFTs, may be the result of upstream events, or they may be at the center of AD pathogenesis. With that being said, Aβ appears to have detrimental effects on many aspects of the disease, including loss of synaptic plasticity, neuronal death, compromised BBB integrity, increased expression of RAGE and implicated clearance by LRP1, increased leukocyte extravasation across inflamed endothelium, and elevated levels of oxidative stress leading to ROS and continuous neuroinflammation. Several clearance mechanisms exist involving enhanced metabolism and proteolytic cleavage of Aβ or clearance from the cortex to systemic circulation. As complications of BBB integrity arise from activation of MMP-2 and MMP-9, ROS, cholesterol metabolism, and impaired insulin signaling, amplified Aβ deposits in and around microvessels, known as cerebral amyloid angiopathy (CAA), become evident. As Aβ fibrils accumulate, neural and ISF accumulation results in a cascade of significant brain degeneration and atrophy of hippocampal and cortical structures.

As late-onset AD accounts for ~90% of cases, environmental effects and epigenetics are at the core of AD. As heavy metals, specifically Al, are known as neurotoxins implicated in neurodegenerative diseases, this calls into question their increasing presence in our environment. Al is present everywhere in the biosphere and yet has no biological role. Several studies have found increased deposition of Al in occipital, frontal, temporal, and parietal lobes of early- and late-onset AD. In fact, one study suggested it is the deposition of Al which leads to earlier onset and more aggressive etiology of AD (Mirza et al. 2017). Interestingly and importantly, Al deposition has been found in cerebral blood vessels supplying critical structures of the brain, including a ninefold increase in the PCA which immediately supplies blood to the hippocampus, a major area of the temporal lobe affected in AD. Alterations in endothelium have profound consequences on downstream blood flow, typically resulting in hypoxic conditions to the tissue. This may explain the substantial damages inflicted on the hippocampus.

Another confounding factor in AD is the increasing prevalence of insulin resistance. This may explain why diabetics are at much higher risk of developing AD. The rate of insulin transport across the BBB is slowed by obesity and aging. Additionally, high circulating levels of free fatty acids in the bloodstream promotes IR. As seen here, hyperphosphorylation of IRS-1 leads to diminished insulin signaling. This effect can be seen as downregulated GLUT receptors and aberrant endothelial NO responses. A disruption in endothelial-mediated NO signaling has grave consequences for cerebral blood flow. The parenchyma relies on adequate blood flow for oxygenation, enzymatic and cellular function, and retrieval of important nutrients, and without it, cells can undergo apoptosis or take on an inflammatory state. Adequate blood flow is also imperative for clearance of Aβ. Impaired perfusion combined with the neurotoxic effects of Al, Al deposition in the PCA, and augmented collagen thickening of the basement membrane create an environment for BBB dysfunction and pose significant challenges in clearance in Aβ. For this reason, AD is largely believed to be a vascular disease.

Atherosclerotic plaques have been observed in a significant number of clinical studies which led to initial hypotheses of AD being a vascular disease. As cholesterol is a primary component of

vascular plaques, it should come as no surprise that cholesterol is heavily implicated in AD. In fact, statins have shown some benefit in experimental studies. In senile plaques, APOE binds and colocalizes with cholesterol. The APOE ϵ4 variant is considered a substantial risk factor in AD. Given the presence of oxysterol metabolism within the brain, their transport to and from the brain, and implications in AD, further studies are warranted to decipher the exact role they play in the disease.

References

Aarts MM, Arundine M (2003) Novel concepts in excitotoxic neurodegeneration after stroke. Expert Rev Mol Med 5:1–22

Bhattacharjee S, Zhao Y, Hill JM, Culicchia F, Kruck TP, Percy ME et al (2013) Selective accumulation of aluminum in cerebral arteries in Alzheimer's disease (AD). J Inorg Biochem 126:35–37

Bhattacharjee S, Zhao Y, Hill JM, Percy ME, Lukiw WJ (2014) Aluminum and its potential contribution to Alzheimer's disease (AD). Front Aging Neurosci 6:1–3

Deane R, Bell RD, Sagare A, Zlokovic BV (2009, March) Clearance of Amyloid-β Peptide Across the Blood-Brain Barrier: Implication for Therapies in Alzheimer's Disease. CNS Neurol Disord Drug Targets 8:16–30

ElAli A, Rivest S (2013) The role of ABCB1 and ABCA1 in beta-amyloid clearance at the neurovascular unit in Alzheimer's disease. Frontierd in Aging Neuroscience; 1-6

Exley C, Price NC, Kelly SM, Birchall JD (1993) An interation of B-amyloid with aluminum in vitro. FEBS Lett 324:293–295

Gamba P, Testa G, Gargiulo S, Staurenghi E, Poli G, Leonarduzzi G (2015) Oxidized cholesterol as the criving force behind the development of Alzheimer's disease. Front Aging Neurosci 7:1–21

Gonzalez-Marrero I, Gimenez-Llort L, Johanson CE, Carmona-Calero EM, Castaneyra-Ruiz L, Brito-Armas JM et al (2015) Choroid plexus dysfunction impairs beta-amyloid clearance in a triple transgenic model of Alzheimer's disease. Front Cell Neurosci 9:1–10

Grimm MO, Grimm HS, Tomic I, Beyreuther K, Hartmann T, Bergmann C (2008) Independent Inhibition of Alzheimer's Disease β- and γ-Secretase Cleavage by Lowered Cholesterol Levels. J Biol Chem 283: 11302–11311

Haorah J, Ramirez SH, Schall K, Smith D, Pandya RP (2007) Oxidative stress activates protein tyrosine kinsase and matrix metalloproteinases leading to blood-brain barrier dysfunction. J Neurochem 101:566–576

Joan Abbott N, Friedman A (2013) Overview and introduction: The blood–brain barrier in health and disease. Epilepsia 53:1–6

Kanekiyo T, Bu G (2014) The low-density lipoprotein receptor-related protein 1 and amyloid-β clearance in Alzheimer's disease. Front Aging Neurosci 6:1–12

Kawahara M, Kato-Negishi M (2011) Link between Aluminum and the Pathogenesis of Alzheimer's Disease: The Integration of the Aluminum and Amyloid Cascade Hypothesis. Int J Alzheimers Dis 2011:1–17

Kreutzer JS, DeLuca J, Caplan B (2011) Blood brain barrier. In: Tran N (ed) Encyclopedia of clinical neuropsychology. Springer, New York, p 426

Liu YC (2012) Modern methods for delivery of drugs across the blood–brain barrier. Adv Drug Deliv Rev 64:640–665

Lun MP, Monuki ES, Lehtinen MK (2016) Development and functions of the choroid plexus-cerebrospinal fluid system. Nat Reviews 16:445–457

Mirza A, King A, Troakes C, Exley C (2017) Aluminum in brain tissue in familial Alzheimer's disease. J Trace Elem Med Biol 40:30–36

Mullins RJ, Diehl TC, Chia CW, Kapogiannis D (2017) Insulin resistance as a link between amyloid-beta and tau pathologies in Alzheimer's disease. Front Aging Neurosci 9:1–16

Ramanathan A, Nelson AR, Sagare AP, Zlokovic BV (2015) Impaired vascular-mediated clearance of brain amyloid beta in Alzheimer's disease: the role, regulation and restoration of LRP1. Front Aging Neurosci 7:1–12

Tajes M, Ramos-Fernandez E, Weng-Jiang X, Bosch-Morato M, Guivernau B, Eraso-Pichot A et al (2014) The blood-brain barrier: Structure, function and therapeutic approaches. Mol Membr Biol 31:152–167

Talbot K, Wang H-Y, Kazi H, Han L-Y, Bakshi KP, Stucky A et al (2012) Demonstrated brain insulin resistance in Alzheimer's disease patients is associated with IGF-1 resistance, IRS-1 dysregulation, and cognitive decline. J Clin Invest 122:1316–1338

Weiss N, Miller F, Cazaubon S (2009) The blood-brain barrier in brain homeostasis and neurological diseases. Biochim Biophys Acta 1788:843–852

Wolburg UK (2000) Tight junctions of the blood–brain barrier. Cell Mol Neurobiol 20:57–76

Zenaro E, Piacentino G, Constantin G (2016) The blood-brain barrier in Alzheimer's disease. Neuobiol Dis 107:1–16

Zhagi J, Goldenson B, Inayathullah M, Lossinsky AS, Masoumi A, Avagyan H et al (2009) Alzheimer disease macrophages shuttle amyloid-beta from neurons to vessels, contributing to amyloid angiopathy. Acta Neuropathol 117:111–124

Zhao Z, Nelson AR, Betsholtz C, Zlokovic BV (2015a) Establishment and dysfunction of the blood-brain barrier. Cell 163:1064–1078

Zhao Z, Sagare AP, Ma Q, Halliday MR, Kong P, Kisler K et al (2015b) Central role for PICLAM in amyloid-β blood-brain barrier transcytosis and clearance. Nat Neurosci 18:978–987

Mathematical Models of Cell Response Following Heating

Neil T. Wright

Abstract

The cells of the cardiovascular system can experience temperature excesses of a few degrees during a diseased state or of tens of degrees during a thermal therapy treatment. These raised temperatures may be acute or of long duration. The multiple cell lines that compose each tissue then react, in approximate order of increasing thermal insult, by expressing heat shock proteins, undergoing apoptosis, or suffering necrosis. Mathematical models of the response of cells could aid in planning and designing thermal therapies. The multi-factor nature of the cell response makes it challenging to develop such models. The models most used clinically are mathematically simple and based on the response of representative tissues. The model that might provide the most fundamental understanding of the biochemical response of cells requires many parameters, some of which are difficult to measure. None of the semi-empirical models that provide improved prediction of cell fate have been widely accepted to plan therapies. There remain great opportunities for developing mathematical models cell response.

N. T. Wright (✉)
Department of Mechanical Engineering, Michigan State University, East Lansing, MI, USA
e-mail: ntwright@msu.edu

1 Introduction

The cells and tissues of the cardiovascular system may be subjected to supraphysiological temperatures during thermal therapies such as high intensity focused ultrasound (HIFU) for cardiac ablation (Bessiere et al. 2016), transmyocardial laser revascularization (Briones et al. 2015; Okada et al. 2011), and radio frequency ablation (Langberg et al. 1992). These high temperature therapies are typically designed to denature proteins, ablate tissues, or kill cells. Cells may also exhibit a protective response—mammalian cells have been shown to express heat shock proteins (HSPs) even at fibril temperatures of 38–41 °C (Bettaieb and Averill-Bates 2015; Evans et al. 2015; Taylor and Starnes 2003). These chaperone proteins can protect cells from further heat shock as well as other stresses, such as ischemia-reperfusion injury (Benjamin and McMillan 1998). HSPs have also been cited

B. M. Fu, N. T. Wright (eds.), *Molecular, Cellular, and Tissue Engineering of the Vascular System*, Advances in Experimental Medicine and Biology 1097,
https://doi.org/10.1007/978-3-319-96445-4_15

as protecting against atrial myolysis and atrial fibrillation (Brundel et al. 2006a,b). So heating can either destroy cells or protect them from further stressors, depending on factors in the cell environment, especially temperature level and duration of treatment.

Significant advances have been made in terms of modeling the growth and remodeling of cardiovascular tissues in response to changes in the mechanical environment (Lee et al. 2016). Still, much remains to be understood for comprehensive biochemomechanical models that account for the response of cells and tissues (Humphrey and Rajagopal 2002; Humphrey 2008). Even for isolated acellular collagenous tissues, the uniaxial response to load and heating may yield a simple model (Chen et al. 1998), while the biaxial response may be considerably more challenging (Harris and Humphrey 2004). Inclusion of cells further challenges the development of comprehensive models. Endothelial cells, smooth muscle cells, and some fibroblasts compose much of arteries and veins. That more than 50% of the cells in heart tissue are fibroblasts (Xin et al. 2013) is testament to the significant activity required to maintain the extracellular matrix.

Mathematical modeling of the response of cells to heating can aid in the design of treatment strategies, as well as in the understanding of underlying mechanisms of cellular behavior. A number of mathematical models to predict cell death after heating have been developed and have been the subject of previous reviews (e.g., He and Bischof 2003; Pearce 2013; Wright 2013). Most of these models have been based on the response of cells in culture, which has the benefits of isolating the response of specific cell lines in well-controlled environments. Most of the cell death data used to develop these models have ignored the mode of cell death, whether by necrosis, apoptosis, or some other pathway. As a result, most of these models consider the overall cell survival outcome rather than specific biochemical pathways. There are, of course, models of apoptosis developed by detailed consideration of the caspase pathways (Fussenegger et al. 2000; Eißing et al. 2007). These models may involve too many parameters for general use in modeling cell death following hyperthermia (Pearce 2013). Furthermore, the data upon which most models have been developed are for monocultures of cells cultured on gels. Cells respond to heating differently when cultured in a monolayer rather than in suspension (Laszlo 1992), when culture on a gel as opposed to being cultured between gel layers (Song et al. 2014), and when grown in co-cultures (Mayrhauser et al. 2011a,b; Hesami et al. 2008). More studies are needed to understand better conditions like those in vivo.

Two commonly used measures to evaluate tissue responses in vivo are the Henriques damage integral and equivalent heating at 43 °C CEM_{43}. The Henriques damage integral (Henriques 1947) is often used to evaluate burn injury. It was established using in vivo measurements of the response of porcine and human skin to well-quantified temperature boundary conditions. Thus, it expresses the overall response of tissue. It has often been used to model cells or as a baseline for comparison to other models. Equivalent heating at 43 °C (Sapareto et al. 1978) is used to evaluate thermal therapies, especially those used as adjuvants to chemo- or radio-therapy. It was based on the cologenic analysis of survival of Chinese hamster ovary (CHO) cells in culture. Both of these models rely on first-order kinetics with an Arrhenius dependence on temperature. Thus, they may over-predict the treatment response for short treatment times (Pearce 2013). These models are for comparison of treatments, especially given the challenges associated with maintaining uniform and constant temperatures in vivo.

This review examines the response of cells to heating and some of the mathematical models of cell death. Section 2 reviews results for thermotolerance with special attention to the temperature of the heat shock, its duration, and when the greatest expression of HSPs occurs after the heat shock has ended. It also summarizes the heat shock temperature and duration associated with different modes of cell death. Section 3 discusses the Arrhenius-based models that are often used for dosing thermal therapies or modeling the extent of thermal burns. This section then explores some of the semi-empirical models used to describe cell survival following heating. Lastly,

it considers the utility of the apparent enthalpy-entropy compensation that has been measured in cell death and denaturation of structural proteins.

2 Cell Response to Heating

In the grossest sense, cells respond to heating at mildly supraphysiological temperatures, perhaps even a degree or two warmer than 39 °C, by developing thermotolerance. At somewhat hotter temperatures, they tend to undergo apoptosis. And at still hotter temperatures, they undergo necrosis. Samali et al., for example, measured thermotolerance in Jurkat cells kept at up to 42 °C, apoptosis for cells at 44 °C, and necrosis at 46 °C (Samali et al. 1999). Similar results have been measured in HeLa cells (Bettaieb and Averill-Bates 2008). Many factors other than temperature level alone determine the cell fate. Moreover, there may be a continuum of cell death modes from apoptosis to necrosis (Raffray and Cohen 1997; Syntichaki and Tavernarakis 2002). The Nomenclature Committee on Cell Death (NCCD) suggests that biochemical rather than morphological metrics should be used to characterize cell death, given the variety of morphologically identified cell death modes and the improvements to biochemical assays (Galluzzi et al. 2012). They note that from a practical sense it is difficult to distinguish between a reversible perturbation to hemostasis and an irreversible path to cell death (Galluzzi et al. 2015). In clinical applications, pathologists are encouraged to diagnose cell death using morphological characterizations as either necrosis, apoptosis, or apoptosis/single cell necrosis (Elmore et al. 2016).

In cell culture studies, clonogenic assays provide a definitive measure of cell survival, although the mode of death of the non-surviving cells is left unanswered. Results from cell culture studies form the basis for many of the mathematical models of cell survival. Figure 1 shows typical cell survival curves, here for Chinese hamster ovary (CHO) cells that have been heated at temperatures from 41.5 to 46.5 °C (Dewey et al. 1977). In addition to temperature level, the duration of heating is important in determining the response. At temperatures of less than 42.5 °C, for these cells and experimental conditions, cell survival declines with increased heating time, but appears to develop a plateau. This plateau suggests development of themotolerance (Lee and Dewey, 1987). For treatment temperatures of 43 °C and greater, there is no apparent plateau at longer heating times. For the warmer temperatures, each 1 °C increase in treatment temperature halves the time required to reach $S = 10^{-3}$, where S is the fraction of cells surviving. The upper dashed line in Fig. 1 shows

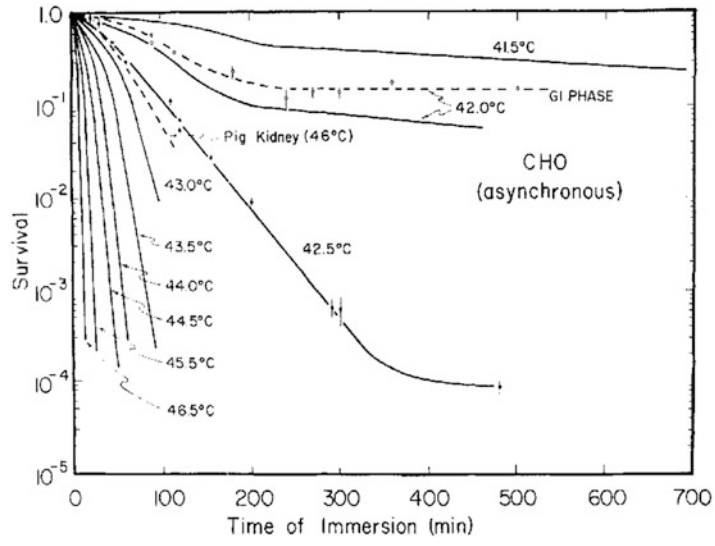

Fig. 1 An example cell survival curve following heating of Chinese hamster ovary (CHO) cells from 41.5 °C to 46.5 °C (Dewey et al., 1977). Dewey et al. included porcine kidney cells heated at 46 °C to illustrate that the kinetics response differs for various cell lines. Note: the solid and dashed curves shown are not representative of a mathematical model

that the response of CHO cells in the G1 phase is somewhat less sensitive to heating at 42 °C than are asynchronous CHO cells. As may also seen in the figure, the lower dashed line shows that pig kidney cells heated at 46 °C respond in a similar fashion to the CHO cells, albeit with a slower response rate than the CHO cells at the same temperature.

2.1 Thermotolerance

Thermotolerance in mammalian cells is a function of temperature level and duration of heating. It is usually associated with the expression of HSPs (Peper et al., 1998), often HSP70 and HSP27, while other members of the HSP family may be expressed, especially due to other stresses (Gabai and Sherman, 2002; Kampinga, 1993; Rylander et al., 2005; Sriram Rodriguez-Fernandez, 2012). The expression of HSPs following heat shock depends on the duration and temperature level of the heating. HSP is normally bound to heat shock transcription factor HSF-1 (Kampinga, 2006). After heat shock, HSP preferentially binds to the newly denatured proteins, which frees HSF-1 to start gene transcription. After the heat shock has ended, expression of HSPs is a non-monotonic function of time with peak expression occurring several hours later. The delay period may be optimized for maximum expression (Kampinga, 2006; Peper et al., 1998; Wang et al., 2003; Rylander et al., 2006) and might be altered by chemical (pharmaceutical) treatments of the cells (Lee and Dewey, 1987). After peak express, HSP expression decays, often to the level prior to heat treatment.

A number of studies have measured thermotolerance in a number of cell lines. Table 1 lists some of the parameters for several of these studies. Heat shock temperatures T_{hs} range from 41.5 to 60 °C, with durations ranging from one minute to several hours. Most of the studies found that $40 \leq T_{hs} \leq 45$ °C was most effective in HSP expression. Of the studies listed here, thermotolerance was determined by HSP concentration, with the exception of Spiro et al. (1982) who measured the clonogenicity of CHO cells.

Spiro et al. (1982) demonstrated that thermotolerance of CHO cells can be developed using either relatively long times (6–14 h) at relatively cool temperatures (42 °C) or acutely with times less than 1 h at hotter temperatures (45.5 °C). Protection from subsequent thermal injury appeared identical. Importantly, thermal tolerance developed even with fractionated acute or fractionated chronic heat treatments. Li et al. (1982) measured thermotolerance and corresponding expression of HSPs in Chinese hamster ovary HA-1 fibroblast cells following 20 min at 45 °C. Landry et al. (1982) measured thermal tolerance and HSP induction following 30 min at 43 °C.

Bettaieb and Averill-Bates (2015) measured thermotolerance and HSP72 expression in HeLa cells following exposure at 40 °C for 3 h. Samali et al. (1999) measured HSP72 expression in Jurkat cells heated for 1 h at 40 °C, but measured greater production of HSP72 at 42 °C for 1 h.

Wang et al. (2008) used cultured bovine aortic endothelial cells transfected with green fluorescent protein to examine the kinetics of HSP70 production. Based on earlier studies (Wang et al., 2003), they heated the cells at 42 °C for 1–2 h. They measured fluorescence for up to 20 h after heating and observed that HSP70 had a bimodal expression with peaks at 3 h and 12 h after the heat shock. The HSP70 translocated from the cytoplasm to the nucleus during the period 6–16 h after the heat shock. Zou et al. (2003) measured HSP expression in COS-7 cells (fibroblast-like from monkey kidney) in culture after 1 h heating at 42 °C and then 24 h at 37 °C.

The local environment alters the response to heating of a given cell line, that is, whether they are grown in suspension or in monolayers (Laszlo, 1992). More recently, Song et al. (2014) compared the thermotolerance and survival responses to heating of a human prostate cancer cell line (PC3 cells) cultured in a 3D gel to the response in a 2D culture. Treatment temperatures ranged from 37 to 57 °C and lasted up to 2 h. HSP70 increased in 3D cultures as compared to 2D cultures that were heated at 45 °C, but had the same expression when the heat treatment

Table 1 Summary of some of the heat shock response parameters for several cell lines

Cell line	T_{hs} (°C)	t_{hs} (h)	t_{peak} (h)	Tolerance metric	Ref.
CHO—10B2	41.5, 42, 45.5	6, 10, 14		Cell survival	Spiro et al. (1982)
Chinese hamster HA-1	45	0.33	8	HSP59, HSP72, HSP87	Li et al. (1982)
Primary rat					
Hepatic epithelial	43	0.5	8–32	HSP27, HSP70, HSP89, HSP107	Landry et al. (1982)
Rat hepatoma H35	42	2	12	HSP25, HSP70	Wang et al. (2009)
HeLa	44	0.25	4	HSP27, HSP60, HSP70, HSC70, HSP90	Stege et al. (1995)
HeLa	40	3		Peak not measured	Bettaieb and Averill-Bates (2015)
Jurkat	40, 42	1	6	HSP27, HSP72	Samali et al. (1999)
Bovine endothelial	42	0.5 to 5	3 & 14	HSP70	Wang et al. (2003)
RWPE-1	44–60	0.0167–0.5	1–10	HSP27, HSP60, HSP70	Rylander et al. (2010)
PC3	44–60	0.0167–0.5	1–10	HSP27, HSP60 HSP70	Rylander et al. (2010)

HSP expression, except where noted. T_{hs} is the temperature of the heat shock, t_{hs} is the duration of the heat shock, and t_{peak} is the time after the heat shock has ended, at this there is peak expression of the HSPs

was 44 °C. This suggests the challenging nature of understanding and modeling the heat shock response.

Several models of thermotolerance have been developed. Peper et al. developed a framework to model HSP70 synthesis and compared its predictions with results for rat hepatoma cells (Peper et al., 1998). The model was organized as five computational blocks and the equations were solved using the Simulink extension of Matlab. The first block models the denaturation of proteins in the cells, to which HSP then binds preferentially, thus freeing heat shock transcription factors (HSF) to which the HSP had been bound. The second block simulates the binding of HSF with heat shock sequence elements (HSE), activating the heat shock genes. The third block models the interaction of HSF with HSE to start the synthesis of HSP70-mRNA. The fourth block models the synthesis of HSP70-mRNA. Finally, the fifth block models the synthesis and subsequent decay of HSP70 itself. Values for the 24 parameters in the model were either taken from published results or, in a few cases, based on limiting results of the model. Their computed values of HSP70 synthesis following a 0.5 h heat shock at 42 °C compared well with measurements in Reuber H35 hepatoma cells. Each showed a peak in total HSP70 synthesis at about 4 h after heat shock

Rybiński et al. (2013) developed a model to examine hyperthermia as an adjuvant to chemotherapy, such as in the case of hyperthermia combined with a proteasome-inhibitor. Two models were developed: a deterministic model composed of 12 ordinary differential equations and a continuous-time Markov chain probabilistic model. The overall results of the two models were similar, albeit with significant scatter in the probabilistic model. Scheff et al. developed a model of the dynamic heat shock response in HeLa cells in vitro. The model added previously simplified analyses to include temperature-dependent transcription, translation, and HSF oligomerization. The authors used data mining to compile in vitro heat shock responses of HeLa cells allowing semiquantitaive demonstration of molecular mechanisms. Their model results agreed well with measurements of total HSP for a 15 min heat shock, for which peak

was at about 10 h following heat shock (Stege et al., 1995).

Rylander et al. (2005, 2007, 2010) incorporated a mathematically simpler model of HSP expression as part of a mathematical model developed for design and planning of laser therapies. Assuming that the rate of production of HSPs could be modeled as the product of a temperature and time dependent rate function $f(t, T)$ and the instantaneous concentration of the HSP $H(t, T)$, the model could be expressed as

$$H(t, T) = A\mathrm{e}^{(\alpha t - \beta t^{\gamma})} \tag{1}$$

where α, β, and γ are temperature-dependent parameters determined for each cell line, with $\gamma > 1$ and A is a temperature-dependent constant. Values given by the model agreed well with measurements for normal and malignant human prostate lines. While not addressing the underlying reactions of HSP production, it provides a more expedient model of HSP production for potential use in clinical predictions of laser therapies.

2.2 Cell Death

Much of the quantitative understanding about cell death following heat shock comes from early studies that used clonogenic assays (Dewey et al., 1977; Sapareto et al., 1978; Jung, 1986; Mackey and Dewey, 1988; Westra and Dewey, 1971). Figure 1 is an example of survival curves for CHO cells following heat shock at temperatures of 41.5 to 46.5 °C. These curves illustrate the role of heat shock duration, as well as the change in response that occurs for heat shock at about 43 °C. Clonogenic assays provide a definitive fraction of the cells that survive, but are independent of the mode of cell death, be it necrosis, apoptosis, or some other mode.

Necrosis and apoptosis have been the two most commonly studied modes of cell death following heat shock. The end state of necrosis is cell membrane rupture. Cells undergoing necrosis are often identified by cell staining, such as with propidium iodide (PI) and flow cytometry (Feng et al., 2008). Apoptosis is characterized by the cell breaking into smaller bodies that contain the still functional organelles. Apoptotic cells are identified using different assays, such as the TUNEL assay (Gorczyca et al., 1992). The mode of cell death has been measured to change with temperature level (Laszlo, 1992; Bettaieb and Averill-Bates, 2015; Glory and Averill-Bates, 2016; Bettaieb and Averill-Bates, 2008). For example, Bettaieb and Averill-Bates measured development of thermotolerance in HeLa cells heated at 40 °C for up to 3 h, while apoptosis occurred when cells were heated at from 42 to 43 °C for up to 3 h and necrosis occurred at temperatures hotter than 45 °C (Bettaieb and Averill-Bates, 2008). The change in response with increasing temperature agrees with other results, such as Jurkat cells that were apoptotic for a temperature of 44 °C and necrotic for heating at 46 °C (Samali et al., 1999), each for 1 h. HSP27 and HSP72 were not expressed for temperatures greater than 42 °C. Heating cells can also cause oxidative stress (Bettaieb and Averill-Bates, 2008) and endoplasmic reticulum (ER) stress (Bettaieb and Averill-Bates, 2015). Bettaieb and Averill-Bates also found that thermotolerance by HSP72 expression provided protection from both ER stress and apoptosis due to ER stress. Santos-Marques, conversely, found that cell death signaling is expressed more quickly than thermotolerance develops during continuous heating of hepatocytes at 41 °C (Santos-Marques et al., 2006).

Cell culture studies provide great insight into many aspects of cell survival. The response may be changed by many factors. Purschke et al. (2010) proposed the term active thermal bystander effect (ATBE) to refer to cells that experience DNA damage and apoptosis, even though they do not themselves experience a lethal heat shock and have no contact with cells that have experienced heat shock. Measurements of human fibroblasts in culture demonstrated this signaling phenomenon. Milleron and Bratton (2006) measured apoptosis in Jukat cells due to heat shock without the usual caspase activating complexes being expressed. Heat shock was induced by 2 h heating at 45 °C. Neither caspase-8 nor caspase-

2 was measured, leading the authors to propose that an apical protease replaces the usual initiator caspases.

3 Models of Cell Survival Following Hyperthermia

Three types of cell survival (or death) models have received the most attention and have been the subject of previous reviews (e.g., Pearce 2013; Wright 2013; He and Bischof 2003). The first type of model stems from studies of tissue damage during accidental burns or hyperthermia treatments in oncology. The two most prevalent are the Henriques damage integral (Henriques, 1947) and the equivalent heating at 43 °C (CEM_{43}) (Sapareto et al., 1978). These have been most used clinically to provide a guide for determining thermal dose in tissues that may experience time-varying and non-uniform temperature fields. Their development acknowledges that tissues comprise heterogeneous populations of cells within a complex extracellular environment and that with the different cells responding at different rates, an overall response may be expected. The models tend to be mathematically simple to facilitate making clinical decisions. While the models were developed using tissues, they have been applied to cell survival.

The second group are semi-empirical models that are based on hypothetical mechanisms, rather than detailed biochemical signaling or pathways of cell death. The models have between two and five parameters; having few parameters facilitates parameter estimation from cell survival experiments. These models have been applied predominantly to in vitro studies.

The third group of models of cell survival are based on biochemical pathways, such as those associated with apoptosis. These mechanistic models of caspase activation often comprise numerous equations and tens of parameters (Fussenegger et al., 2000). Obtaining accurate values for the required parameters makes these models challenging to evaluate. Pearce (2013, 2015) evaluated a reduced model of apoptosis developed by Eißing et al. (2004, 2007) for possible use as a model of heat shock response. The reduced model assigns all activity of initiator caspases to the caspase 8 response and the executioner caspases to caspase 9. Pearce notes that although they may be too complex for clinical use, these mechanistic models could offer insight into the mechanisms of cell death following heat shock. Würstle et al. (2014) suggest that "bottom-up" biochemical models when coupled with tissue level models might someday provide diagnostic insight.

3.1 Models Based on Tissue Response

The Henriques model of thermal injury has been used since the late 1940s (Henriques, 1947). It was developed as part of a series of experimental studies of thermal burn injuries (Henriques and Moritz, 1947; Moritz, 1947; Moritz and Henriques, 1947). The model is based on the Arrhenius model of chemical kinetics and may be written as

$$\Omega = \int_{t_0}^{t} A e^{-E_a/RT(t)} dt \tag{2}$$

where Ω is the damage parameter, t is time, A is the frequency factor, E_a is the activation energy, R is the ideal gas constant, and $T(t)$ is the time-varying absolute temperature. Based on measurements on porcine and human skin, Henriques and Moritz report values of $A = 3.1 \times 10^{98}\,\mathrm{s}^{-1}$ and $E_a = 6.27 \times 10^{8}\,\mathrm{J\,kmol}^{-1}$. Henriques suggested that $\Omega = 0.53$ corresponds to a first degree burn (onset of erythema) and $\Omega = 1.0$ to a second degree burn (partial thickness burn). Later, Takata et al. suggested, based on examination of laser interactions with tissue, that $\Omega = 10^4$ signifies a 3rd degree (full thickness) burn (Takata et al., 1977).[1] Diller and Pearce (1999) note that values of Ω greater than 10 have "little significance"

[1] Many papers mistakenly credit Henriques and Moritz for suggesting that 3rd degree burns correspond to $\Omega = 10^4$. Henriques (1947) lists only $\Omega = 0.53$ and $\Omega = 1.0$. $\Omega = 10^4$ is beyond their measured responses (Moritz and Henriques, 1947; Moritz, 1947).

because of the significant changes to the tissue that occur during the burn process. To illustrate this, they used the relationship that $\ln(\Omega) = c(t)/c_0$, where $c(t)$ is the current concentration of native proteins and c_0 is the original concentration (Pearce and Thomsen, 1995). Then, $\Omega = 10$ results in less than 0.0045% of the native state proteins remaining. Han and Pearce measured damage to heart muscle and found $A = 3.5 \times 10^{22}$ s^{-1} and $E_a = 1.64 \times 10^5$ J kmol^{-1}.

Perhaps more often used to plan clinical treatments of hyperthermia is the concept of equivalent heating at 43 °C (CEM_{43}) (Sapareto and Dewey, 1984). This is based on the observation that for temperatures greater than 43 °C, each degree increase in temperature doubles the rate of cell death. Cooler than 43 °C and there is a fourfold decrease in reaction rate per degree of cooling. Typically, there is distribution of temperatures in the treated tissue and CEM_{43} seeks to relate the therapeutic effects to those temperatures to that which would be expected to occur at the common temperature of 43 °C (Dewey et al., 1977), chosen because of the break in the change in reaction rate. Hahn presented a development of CEM_{43} (Hahn et al., 1982). For equal damage at different temperatures $T_1 \neq T_2$, $\Omega_1(T_1) = \Omega_2(T_2)$, Eq. (2) can be evaluated as

$$t_2 e^{-E_a/RT_2} = t_1 e^{-E_a/RT_1} \tag{3}$$

for constant temperature conditions. Then,

$$t_2/t_1 = e^{-(E_a/R)/(\Delta T/T_1T_2)} \tag{4}$$

where $\Delta T = T_2 - T_1$. If T_1 is 320 K (43 °C) and T_2 is the treatment temperature, a treatment time of t_2 is required to obtain the same result as would occur for a treatment duration t_1 at 43 °C, that is $t_2 = CEM_{43}$. Rewriting this with the new notation gives, for $T_2 > 43$ °C,

$$CEM_{43} = t_2 0.47^{\Delta T} \approx t_2 0.5^{\Delta T} \tag{5}$$

for $E_a = 141$ kcal mol^{-1} and $T_1T_2 = 313 \times 314$ s^2. An implication is that the treatment rate doubles for each increase of 1 °C for $T_2 > 43$ °C. An apparent change in the activation energy[2] occurs at 43 °C, leading to its choice for CEM_{43}. It might also be noted that the change in activation energy results in the rate slowing to one quarter for each 1 °C cooling for $T_2 < 43$ °C. A detailed review of Pearce (2013) examines the origins in chemical kinetics and applicability of CEM_{43} and Henriques damage integral Ω.

3.2 Semi-empirical Models of Cell Response

The earliest of the semi-empirical models is the one based on first-order chemical kinetics, which may be written as

$$\frac{dN(t)}{dt} = -k_1(T)N(t), \tag{6}$$

where $N(t)$ is the time dependent number of cells, $k_1(T)$ is the temperature-dependent rate parameter for the first-order model, and t is the duration of the heat treatment for the cells. The rate parameter can be related to temperature using the Arrhenius relation, $k_1 = A \exp[E_a/(RT)]$, where A is the frequency factor, E_a is the activation energy, R is the gas constant, and T is the absolute temperature. This relation sometimes leads to this being call the Arrhenius model. For a temperature jump condition, where the cells are suddenly heated at an elevated, but constant, temperature for a duration t, Eq. (6) may be integrated to get

$$S = \frac{N(t)}{N_0} = e^{-k_1 t}, \tag{7}$$

where N_0 is the original number of cells and S is the fraction of cells surviving after heating. The temperature and time dependence are assumed and will not be written explicitly for the remainder. Thus, $S = 1$ for no heat treatment (i.e., $t = 0$) and decreases to a limiting value of $S = 0$ as $t \to \infty$.

[2] More precisely, this is the activation enthalpy (Dewey et al., 1977), which is nearly equal to the activation energy for condensed systems (Laidler, 1987).

Pearce (2015) has observed that the Arrhenius model overestimates cell death at temperatures between 43 and 55 °C early after heat shock, but can capture the behavior of the exponential range of cell survival curves (Bauer and Henle, 1979). This behavior is illustrated in Panel (a) of Fig. 2. Significantly, the first-order Arrhenius model fails to capture the prominent shoulder region that exists in plots of cell death histories after heating. Moreover, if $\Omega = \ln(N/N_0)$, then Eqs. (6) and (2) are equivalent for constant temperature heating (Pearce and Thomsen, 1995).

To capture the response of the shoulder region and improve the Arrhenius (first-order) model while retaining the advantage of its simplicity, Pearce (2015) proposed adding a temperature-dependent time delay to the Arrhenius model. This time delay accounts for the initial cellular responses, which may require time for the initiator and executioner caspase pathways that occur in apoptosis, for example, to happen. The time delay t_d may be written as

$$t_d = b - mT \tag{8}$$

where b and m are empirically determined constants specific to each cell types. Note that for the correlation, T is written in terms of °C but that the model would hold in principle using T in kelvins, with only changes to the values of the intercept b. Pearce notes that the time-delay model may sacrifice some accuracy in the early part of the response, even though it provides improved accuracy during the later part of the treatment when prediction of cell death is most crucial in clinical practice. He demonstrated its utility using data from PC3 cells (Feng et al., 2008), AT1 cells (He et al., 2000), and CHO cells (Sapareto et al., 1978). The cell death assays were propidium iodide (PI) staining for the PC3 and AT1 cells, calcein leakage for the AT1 cells, and clonogenicity for the AT1 and CHO cells. The parameters b and m were functions of the cell line and the assay used for cell death. The values of A and E_a for Eq. (2) changed little from those found using Eq. (2) without t_d, except for calcein leakage. Here, using a different data set for CHO cells than did Pearce, Fig. 2, panel (d) illustrates the significantly improved agreement of the first-order model, Eq. (7) when using the time delay.

Johnson and Pavelec (1972) proposed a model by assuming that n_J independent molecular events are required for cell death. Each of these events was assumed to be a first-order reaction with a temperature-dependent rate parameter k_J. Then, the fraction of cells surviving after heating can be calculated using

$$S = 1 - (1 - e^{-k_J t})^{n_J}, \tag{9}$$

The rate parameter was assumed to be related to temperature via transition rate theory such that

$$k_J = \frac{\kappa_B T}{h} \exp\left(\frac{\Delta S_a}{R}\right) \exp\left(-\frac{\Delta H_a}{RT}\right) \tag{10}$$

with ΔS_a is the activation entropy, ΔH_a is the activation enthalpy, κ_B is Boltzmann's constant, and h is Planck's constant. Measurements for V strain Chinese hamster lung tissue cells subject to heating at specified steady temperatures of 41 to 46 °C suggested that H_a was similar to that measured during the denaturation of some proteins. Inspired by models of cell survival following exposure to ionizing radiation, Dewey et al. (1977) suggested a similar equation

$$S = 1 - (1 - e^{-t/t_D})^{n_D} \tag{11}$$

where t_D is the characteristic time of cell damage, which would be proportional to the inverse of a typical rate parameter $k(T)$. Hahn et al. (1982) proposed a model, which Lepock (2003) wrote as

$$S = 1 - [1 - (1 - k_H)^t]^{n_H}, \tag{12}$$

where the temperature dependence of k_H is defined using rate theory in a similar fashion to Eq. (10). Taking a Taylor series expansion of Eqs. (9) and (12) and evaluating for small t shows that Eqs. (9) and (12) are equivalent to a first

order, suggesting that Eqs. (9), (11), and (12) would behave similarly.

These models provide good predictions of the cell survival, as is illustrated in panel (b) of Fig. 2. The number of "lethal events" each of these models suggests for cell death varies from 2 to 100. Dewey et al. suggested that 100 events are required for cell death of CHO cells heated at 43 °C that is $n_D = 100$. Wright (2013) estimated $1.65 \leq n_J \leq 9.42$ for PC3 data of Feng et al. (2008), while for CHO survival data (Westra and Dewey, 1971), he found $17.5 \leq n_J \leq 55$. Lepock cites values of $1 \leq n_H \leq 30$.

Roti and Henle (1980) proposed a model inspired by one developed by Kellerer and Rossi (1971) for ionizing radiation dosimetry. Roti and Henle wrote

$$S = e^{-(a+bt)t}, \tag{13}$$

where a and b are experimentally determined parameters. Parameters a and b each have an Arrhenius-type relationship with temperature and have the same value of E_a. The AIC showed that the model is better suited to lower temperature hyperthermia, but its predictions are worse than the other models as treatment temperatures rise (Wright, 2013).

Two of the cell survival models examined in Wright (2013) used statistical arguments in their formulation. Jung (1986) developed a model by assuming that temperature-dependent random events produce nonlethal lesions at a rate p. One of these lesions becomes lethal in a second set of random events with rate c. The combined effect can predict the cell survival as

$$S = \exp\left\{\frac{p}{c}\left[1 - ct - e^{-ct}\right]\right\}. \tag{14}$$

While a cell was postulated to remain viable with many of the irreversibly formed nonlethal lesions, a single lethal lesion results in death of a cell.

Another statistical model postulated a temperature-dependent parameter ϵ that is normally distributed within a population of cells (Mackey and Roti, 1992). For a unit variance, the parameter ϵ may be calculated as

$$f(\epsilon) = \frac{1}{\sqrt{2\pi}} \exp[-(\epsilon - \bar{\epsilon})^2/2], \tag{15}$$

where

$$\bar{\epsilon} = \bar{\epsilon}_f(1 - e^{-k_M * t}) + \bar{\epsilon}_0 e^{-k_M * t}, \tag{16}$$

where $\bar{\epsilon}_0$ is an assumed mean initial value for the cell population, $\bar{\epsilon}_f$ represents the mean final value of $\bar{\epsilon}$, and k_M is a temperature-independent constant for each cell line. The initial mean $\bar{\epsilon}_0$ can be assumed to equal zero. A cell is assumed to be clonogenically viable while its value of ϵ is greater than a minimum value $\epsilon_{\min}$. The survival function is then

$$S = \frac{1}{\sqrt{2\pi}} \int_{\epsilon_{\min}}^{\infty} \exp[-(\epsilon - \bar{\epsilon}_f[1 - e^{-k_m t}])^2/2] d\epsilon, \tag{17}$$

which Wright (2013) integrated to

$$S = \frac{1}{2}\mathrm{erfc}\left[\frac{-(\epsilon_{\min} - \bar{\epsilon}_f[1 - e^{-k_m * t}])}{\sqrt{2}}\right]. \tag{18}$$

Mackey and Roti Roti took $\epsilon_{\min} = -3$ giving an asymptote of $S \approx 1$ at $t = 0$. The value of $\bar{\epsilon}_f$ changes with different temperatures.

Feng et al. (2008) developed a three-parameter model based on statistical thermodynamics. Two populations of cells are assumed (one living and the other dead) and the most probable distribution of these two populations is predicted. The model can be written as

$$S = \frac{1}{1 + e^{(\gamma/T + \alpha t + \beta)}} \tag{19}$$

where α, β, and γ are constants that depend on the cells line and treatment temperature. Feng et al. demonstrated the utility of this model over the treatment range of 44–58 °C based on two prostate cell lines: prostate cancer cells (PC3) and healthy prostate cells (RWPE-1). Figure 2, panel (c) illustrates the quality of the fit of this model for CHO cells.

O'Neill et al. (2011) proposed a three-state model that captured the shoulder region with a cell state of vulnerable cells V that is intermediate between undamaged S cells and the dead ones D. Unlike Jung (1986), the vulnerable cells are assumed to be able to return to the undamaged state. Written in terms of the normalized populations of cells S, V, and D, the model is

$$\frac{dS}{dt} = -k_f S + k_b V \tag{20}$$

$$\frac{dD}{dt} = k_f V \tag{21}$$

$$V = 1 - S - D \tag{22}$$

where k_f is the forward reaction parameter, assumed to be equal for both the transition from S to V and the transition from V to D, and k_b is a backward reaction parameter for the healing process of V to S. To account for the small rate of damage at 37 °C and assuming that the damaged cells may alter the rate of further damage, k_f is defined as

$$k_f = \overline{k_f} e^{t/t_k}(1 - S). \tag{23}$$

where $\overline{k_f}$ and t_k are fitting parameters, along with k_b. The ratio of relative temperatures (i.e., in °C) t and t_k is unusual in thermodynamics. Because the system is non-linear with the dependence of k_f on S, a numerical solution was sought.

Most of the models had been compared with the first-order chemical kinetics model (Eq. (7)), for which they each do better. To compare them with one another, Wright (2013) used the Akaike information criterion (AIC) Akaiki (1974) and data for PC3 cells (Feng et al., 2008) and CHO cells (Westra and Dewey, 1971). The AIC compares the quality of fit of a model to data, but includes a penalty term for the number of parameters in a model. The models of Jung, Johnson and Pavelec, and Feng et al. provided the best fits overall. The delay-time model of Pearce (2015) was unavailable at the time of comparison.

3.3 Enthalpy-Entropy Compensation

The apparent relationship between E_a and $\ln A$ in the Arrhenius equation, or equivalently,[3] H_a and S_a in transition state theory, is an area of continued enquiry. The concept of enthalpy-entropy compensation is that $\ln A$ is proportional to E_a, which is to say that there is only one independent parameter. In the context of heating damage to proteins and cells, He and Bischof (2003), Qin et al. (2014) have written

$$\ln A = 0.38 E_a - 9.36 \tag{24}$$

for a wide range of proteins, cells, and tissues from a wide range of studies. Wright (2003) had written a similar equation for a more limited group of cells and proteins. Miles and Ghelashvili (1999) modeled denaturation of collagen I using the concept of a "polymer-in-a-box" (Doi and Edwards, 1986) to explain the apparent proportionality of H_a and S_a. While some (Freed, 2011) have provided arguments from statistical mechanics in favor of compensation, others (Sharp, 2001) have shown from statistical thermodynamics to suggest that the apparent relationship between the two parameters may depend on the typically small perturbations in temperature that are common in biology. Similarly, Barrie (2012) suggested that uncertainties in data may lead to "apparent compensation effect." These arguments are supported by an analysis of the scaled sensitivity coefficients χ_i (Harrington and Wright, 2005) that gives the relation

$$\frac{\chi_{S_a}}{\chi_{H_a}} = -\frac{T S_a}{H_a}, \tag{25}$$

which varies by 3% for $T \in (313, 323)$ K. When scaled sensitivity coefficients of two parameters are correlated, as is the case for linearly dependent variations, then only one of the two parameters can be estimated using the experiment (Beck and Arnold, 1977) for which the coefficients are determined. Despite, questions regarding its theoretical basis, the empirically

[3] For condensed systems, $E_a \approx H_a$ and $\ln A \sim S_a$.

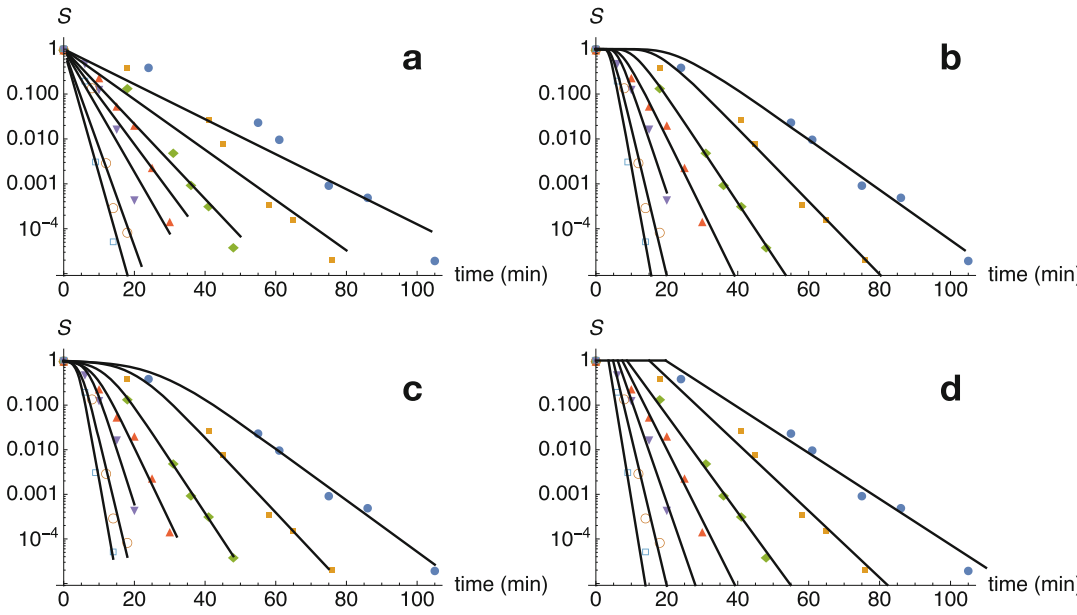

Fig. 2 Illustrative model fits of CHO cell survival from Westra and Dewey (1971) heated to 43.5 °C (filled circles), 44 °C (filled squares), 44.5 °C (diamonds), 45 °C (triangles), 45.5 °C (inverted triangles), 46 °C (open circles), and 46.5 °C (open squares). Panel (**a**) shows the first-order model fit using the Arrhenius model of k as a function of temperature. Panel (**b**) is the model fit of Johnson and Pavelec (1972). Panel (**c**) is the model fit of Feng et al. (2008). Panel (**d**) is the temperature-dependent time-delay model fit of Pearce (2015)

based compensation equations could provide useful information in modeling thermal damage over the limited range of temperatures typical of hyperthermia.

4 Conclusions

Heating cells can produce positive effects, such as thermotolerance, or negative effects, cell death. Thermotolerance, typically the result of the expression of HSPs, can then protect from further heating, but also help cells survive other stresses, such as ischemia-reperfusion injury. Heating at higher temperatures or for longer times typically kills cells. This may be intended, as a treatment, or accidental, as a burn. Certainly, cells that have not been subject to higher temperatures may still perish from the ATBE (Purschke et al., 2010).

Mathematical models of cellular responses to heat shock can aid in understanding of the mechanisms of cell survival and thermotolerance. They can help with the design and planning of thermal therapies with in vivo temperatures that typically vary with both in space and time. The models that are currently the most useful in clinical practice are based on the integrated response of the population of various cells and the ECM. The models that might provide the most fundamental understanding of thermotolerance and cell survival require many parameters, some of which are difficult to measure. Models that combine expressions of HSPs with those of potential cell death (Rylander et al., 2010) may someday prove the most useful in planning treatments, but still require incorporating more of the fundamental biochemical mechanisms.

Acknowledgements The author thanks Prof. John Pearce for his insightful comments regarding modeling of cell death.

References

Akaiki H (1974) A new look at the statistical model identification. IEEE Trans Autom Control 19:716–723

Barrie PJ (2012) The mathematical origins of the kinetic compensation effect: 1. the effect of random experimental errors. Phys Chem Chem Phys 14:318–326

Bauer KD, Henle KJ (1979) Arrhenius analysis of heat survival curves from normal and thermotolerant cho cells. Radiat Res 78:251–263

Beck J, Arnold K (1977) Parameter estimation in engineering and science. Wiley, New York

Benjamin IJ, McMillan DR (1998) Stress (heat shock) proteins: molecular chaperones in cardiovascular biology and disease. Circ Res 83:117–132

Bessiere F, N'Djin WA, Colas EC, Chavrier F, Greillier P, Chapelon, JY, Chevalier P, Lafon C (2016) Ultrasound-guided transesophageal high-intensity focused ultrasound cardiac ablation in a beating heart: a pilot feasibility study in pigs. Ultrasound Med Biol 42(8): 1848–1861

Bettaieb A, Averill-Bates DA (2008) Thermotolerance induced at a fever temperature of 40 °C protects cells against hyperthermia-induced apoptosis mediated by death receptor signaling. Biochem Cell Biol 86: 521–538

Bettaieb A, Averill-Bates DA (2015) Thermotolerance induced at a mild temperature of 40 °C alleviates heat shock-induced ER stress and apoptosis in HeLa cells. Biochim Biophys Acta 1853:52–62

Briones E, Lacalle JR, Marin-Leon I, Rueda JR (2015) Transmyocardial laser revascularization versus medical therapy for refractory angina. Cochrane Database Syst Rev 2:CD003712

Brundel BJ, Henning RH, Ke L, van Gelder IC, Crijns HJ, Kampinga HH (2006a) Heat shock protein upregulation protects against pacing-induced myolysis in HL-1 atrial myocytes and in human atrial fibrillation. J Mol Cell Cardiol 41:555–562

Brundel BJ, Shiroshita-Takeshita A, Qi X, Yeh YH, Chartier D, van Gelder IC, Henning RH, Kampinga HH, Nattel S (2006b) Induction of heat shock response protects the heart against atrial fibrillation. Circ Res 99:1394–1402

Chen SS, Wright NT, Humphrey JD (1998) Phenomenological evolution equations for heat-induced shrinkage of a collagenous tissue. IEEE Trans Biomed Eng 45:1234 –1240

Dewey W, Hopwood L, Sapareto S, Gerweck L (1977) Cellular responses to combinations of hyperthermia and radiation. Radiology 123:463–479

Diller K, Pearce J (1999) Issues in modeling thermal alterations in tissues. Ann N Y Acad Sci 888:153–164

Doi M, Edwards SF (1986) The theory of polymer dynamics. Oxford University Press, Oxford

Eißing TE, Conzelmann H, Gilles ED, Allgöwer F, Bullinger E, Scheurich P (2004) Bistability analyses of a caspase activation model for receptor-induced apoptosis. J Biol Chem 279:36892–36897

Eißing TE, Waldherr S, Allgöwer F, Scheurich P, Bullinger E (2007) Steady state and (bi-) stability evaluation of simple protease signalling networks. BioSyst 90:591–601

Elmore SA, Dixon D, Hailey JR, Harada T, Herbert RA, Maronpot, RR, Nolte T, Rehg JE, Rittinghausen S, Rosol TJ, Satoh H, Vidal JD, Willard-Mack CL, Creasy DM (2016) Recommendations from the INHAND apoptosis/necrosis working group. Toxicol Pathol 44:173–188

Evans SS, Repasky EA (2015) Fisher DT: fever and the thermal regulation of immunity: the immune system feels the heat. Nat Rev Immunol 15(6): 335–349

Feng Y, Oden JT, Rylander MN (2008) A two-state cell damage model under hyperthermic conditions: theory and in vitro experiments. J Biomech Eng 130: 041016–1–10

Freed KF (2011) Entropy-enthalpy compensation in chemical reactions and adsorption: an exactly solvable model. J Phys Chem B 115:1689–1692

Fussenegger M, Bailey JE, Varner J (2000) A mathematical model of caspase function in apoptosis. Nat Biotechnol 18:768–774

Gabai VL, Sherman MY (2002) Molecular biology of thermoregulation. J Appl Physiol 92:1743–1748

Galluzzi L, Vitale I, Abrams J, Alnemri E, Baehrecke E, Blagosklonny, M, Dawson T, Dawson V, El-Deiry W, Fulda S, Gottli E, Green D, Hengartner M, Kepp O, Knight R, Kumar S, Lipton S, Lu X, Madeo, F, Malorni W, Mehlen P, Nunez G, Peter M, Piacentini M, Rubinsztein D, Shi Y, Simon HU, Vandenabeele P, White E, Yuan J, Zhivotovsky B, Melino G, Kroemer G (2012) Molecular definitions of cell death subroutines: recommendations of the nomenclature committee on cell death 2012. Cell Death Differ 19:107–120

Galluzzi L, Pedro JBS., Vitale I, Aaronson S, Abrams J, Adam D, Alnemri E, Altucci L, Andrews D, Annicchiarico-Petruzzelli M, Baehrecke E, Bazan N, Bertrand M, Bianchi K, Blagosklonny M, Blomgren K, Borner C, Bredesen D, Brenner C, Campanella M, Candi, E, Cecconi F, Chan F, Chandel N, Cheng E, Chipuk J, Cidlowski J, Ciechanover A, Dawson T, Dawson V, Laurenzi VD, Maria RD, Debatin KM, Daniele ND, Dixit V, Dynlacht B, El-Deiry W, Fimia G, Flavell R, Fulda S, Garrido C, Gougeon ML, Green D, Gronemeyer H, Hajnoczky G, Hardwick J, Hengartner M, Ichijo H, Joseph B, Jost P, Kaufmann T, Kepp O, Klionsky D, Knight R, Kumar S, Lemasters J, Levine B, Linkermann A, Lipton S, Lockshin, R., López-Otín C, Lugli E, Madeo F, Malorni W, Marine JC, Martin S, Martinou JC, Medema J, Meier P, Melino S, Mizushima N, Moll U, Muñoz-Pinedo C, Nuñez G, Oberst, A, Panaretakis T, Penninger J, Peter M, Piacentini M, Pinton P, Prehn J, Puthalakath H, Rabinovich G, Ravichandran K, Rizzuto R, Rodrigues C, Rubinsztein D, Rudel T, Shi Y, Simon HU, Stockwell B, Szabadkai G, Tait S, Tang H, Tavernarakis N, Tsujimoto Y, Berghe TV, Vandenabeele P, Villunger A, Wagner E, Walczak H, White E, Wood W, Yuan J, Zakeri Z, Zhivotovsky B, Melino G, Kroemer G (2015) Essential versus ac-

cessory aspects of cell death: recommendations of the NCCD 2015. Cell Death Differ 22:58–73
Glory A, Averill-Bates DA (2016) The antioxidant transcription factor Nrf2 contributes to the protective effect of mild thermotolerance (40 °C) against heat shock-induced apoptosis. Free Radic Biol Med 99:485–497
Gorczyca W, Bruno S, Darzynkiewicz R, Gong J, Darzynkiewicz Z (1992) DNA strand breaks occurring during apoptosis: their early in situ detection by terminal deoxynucleotidyl transferase and nick translation assays and prevention by serine protease inhibitors. Int J Oncol 1:639–648
Hahn GM (1982) Hyperthermia and cancer. Plenum Press, New York
Harrington PL, Wright NT (2005) Sensitivity analysis of Arrhenius parameters for denaturation of collagen. In: Proceedings of 2005 ASME summer bioengineering conference
Harris JL, Humphrey JD (2004) Kinetics of thermal damage to a collagenous membrane under biaxial isotonic loading. IEEE Trans Biomed Eng 51(2):371–379
He X, Bischof JC (2003) Quantification of temperature and injury response in thermal therapy and cryosurgery. Crit Rev Biomed Eng 31(5):355–422
He X, Bhowmick S, Bischof J (2000) Supraphysiological thermal injury in dunning at-1 prostate tumor cells. J Biomech Eng 122:51–59
Henriques Jr FC (1947) Studies of thermal injury V. The predictability and the significance of thermally induced rate processes leading to irreversible epidermal injury. Arch Pathol 43:489–502
Henriques Jr FC, Moritz AR (1947) Studies of thermal injury. I. The conduction of heat to and through skin and the temperatures attained therein. Am J Pathol 23:531–549
Hesami S, Mohammadi M, Rezaee MA, Jalili A, Rahmani MR (2017) The effects of hyperthermia on the immunomodulatory properties of human umbilical cord vein mesenchymal stem cells (MSCs). Int J Hyperth 33(7):705–712. http://dx.doi.org/10.1080/02656736.2017.1309576. PMID: 28540823
Humphrey JD (2008) Vascular adaptation and mechanical homeostasis at tissue, cellular, and sub-cellular levels. Cell Biochem Biophys 50:53–78
Humphrey JD, Rajagopal R (2002) A constrained mixture model for growth and remodeling of soft tissues. Math Models Methods Appl Sci 12(3):407–430
Johnson HA, Pavelec M (1972) Thermal injury due to normal body temperature. Am J Pathol 66:557–564
Jung H (1986) A generalized concept for cell killing by heat. Rad Res 106:56–72
Kampinga HH (1993) Thermotolerance in mammalian cells. J Cell Sci 104:11–17
Kampinga HH (2006) Cell biological effects of hyperthermia alone or combined with radiation or drugs: A short introduction to newcomers in the field. Int J Hyperth 22:191–196
Kellerer A, Rossi H (1971) RBE and the primary mechanics of radiation action. Rad Res 47:15–34
Laidler KJ (1987) Chemical kinetics. Harper & Row, New York
Landry J, Chrétien P, Bernier D, Nicole LM, Marceau N, Tanguay RM (1982) Thermotolerance and heat shock proteins induced by hyperthermia in rat liver cells. Int J Radiat Oncol Biol Phys 8:59–62
Langberg JJ, Calkins H, El-Atassi R, Broganelli M, Leon A, Kalbfleisch S, Morady F (1992) Temperature monitoring during radiofrequency catheter ablation of accessory pathways. Circulation 86(5): 1469–1474
Laszlo A (1992) The effects of hyperthermia on mammalian cell structure and function. Cell Prolif 25:59–87
Lee L, Kassab G, Guccione J (2016) Mathematical modeling of cardiac growth and remodeling. Wiley Interdiscip Rev Syst Biol Med 8(3):211–226
Lee YJ, Dewey WC (1987) Induction of heat shock proteins in Chinese hamster ovary cells and development of thermotolerance by concentrations of puromycin. J Cell Physiol 132:1–11
Lepock J (2003) Cellular effects of hyperthermia: relevance to the minimum dose for thermal damage. Int J Hyperth 19(3):252–266
Li GC, Petersen NS, Mitchell HK (1982) Induced thermal tolerance and heat shock protein synthesis in Chinese hamster ovary cells. Int J Radiat Oncol Biol Phys 8:63–67
Mackey MA, Dewey WC (1988) Time-temperature analyses of cell killing of synchronous G1 and S phase Chinese hamster cells *in vitro*. Radiat Res 113:318–333
Mackey MA, Roti Roti JL (1992) A model of heat-induced clonogenic cell death. J Theor Biol 156(1):133–146
Mayrhauser U, Stiegler P, Stadlbauer V, Koestenbauer S, Leber B, Konrad K, Iberer F, Portucaller RH, Tscheiliessnigg K (2011a) Effect of hyperthermia on liver cell lines: important findings for thermal therapy in hepatocellular carcinoma. Anticancer Res 31:1583–1588
Mayrhauser U, Stiegler P, Stadlbauer V, Koestenbauer S, Leber B, Konrad K, Iberer F, Tscheiliessnigg K (2011b) Cell to cell interactions influence sensitivity of liver cell lines during hyperthermia. Anticancer Res 31:3713–3718
Miles CA, Ghelashvili M (1999) Polymer-in-a-box mechanism for the thermal stabilization of collagen molecules in fibers. Biophys J 76:3243–3252
Milleron RS, Bratton SB (2006) Heat shock induces apoptosis independently of any known initiator caspase-activating complex. J Biol Chem 281(25):16991–17000
Moritz AR (1947) Studies of thermal injury. III. The pathology and pathogenesis of cutaneous burns, an experimental study. Am J Pathol 23:915–941
Moritz AR, Henriques Jr FC (1947) Studies of thermal injury. II. The relative importance of time and surface temperature in the causation of cutaneous burns. Am J Pathol 23:695–720

Okada M, Yoshida M, Tsuji Y, Horii H (2011) Clinical application of laser treatment for cardiovascular surgery. Laser Ther 20(3):217–232

O'Neill DP, Peng T, Stiegler P, Mayrhauser U, Koestenbauer S, Tscheiliessnigg K, Payne SJ (2011) A three-state mathematical model of hyperthermic cell death. Ann Biomed Eng 39(1):570–579

Pearce JA (2013) Comparative analysis of mathematical models of cell death and thermal damage processes. Int J Hyperth 29(4):1464–5157

Pearce JA (2015) Improving accuracy in Arrhenius models of cell death: adding a temperature-dependent time delay. J Biomech Eng 137:121006

Pearce JA, Thomsen S (1995) Rate process analysis of thermal damage. In: Welch AJ, van Germert MJC (eds) Optical and thermal response of laser-irradiated tissue. Plenum, New York, pp 561–606

Peper A, Grimbergent CA, Spaan JAE, Souren JEM, Wijk RV (1998) A mathematical model of the HSP70 regulation in the cell. J Mol Biol 14:97–124

Purschke M, Laubach HJ, Anderson RR, Manstein D (2010) Thermal injury causes dna damage and lethality in unheated surrounding cells: active thermal bystander effect. J Invest Dermatol 130:86–92

Qin Z, Balasubramanian SK, Wolkers WF, Pearce JA, Bischof JC (2014) Correlated parameter fit of Arrhenius model for thermal denaturation of proteins and cells. Ann Biomed Eng 42:2392–2404

Raffray M, Cohen GM (1997) Apoptosis and necrosis in toxicology: a continuum or distinct models of cell death. Pharmacol Ther 75(3):153–177

Roti JL, Henle KJ (1980) Comparison of two mathematical models for describing heat-induced cell killing. Rad Res 81:374–383

Rybiński M, Szymańska Z, Lasota S, Gambin A (2013) Modelling the efficacy of hyperthermia treatment. J R Soc Interface 10(88). http://dx.doi.org/10.1098/rsif.2013.0527. http://rsif.royalsocietypublishing.org/content/10/88/20130527

Rylander MN, Feng Y, Bass J, Diller KR (2005) Thermally induced injury and heat-shock protein expression in cells and tissues. Ann N Y Acad Sci 1066:222–242

Rylander MN, Feng Y, Zhang Y, Bass J, Stafford RJ, Volgin A, Hazle JD, Diller KR (2006) Optimizing heat shock protein expression induced by prostate cancer laser therapy through predictive computational models. J Biomed Opt 11:11–11–16. http://dx.doi.org/10.1117/1.2241310

Rylander MN, Feng Y, Bass J, Diller KR (2007) Heat shock protein expression and injury optimization for laser therapy design. Lasers in Surgery and Medicine 39:731–746

Rylander MN, Feng Y, Zimmermann K, Diller KR (2010) Measurement and mathematical modeling of thermally induced injury and heat shock protein expression kinetics in normal and cancerous prostate cells. Int J Hyperth 26(8):748–764

Samali A, Holmberg CI, Sistonen L, Orreniusa S (1999) Thermotolerance and cell death are distinct cellular responses to stress: dependence on heat shock proteins. FEBS Lett 461:306–310

Santos-Marques MJ, Carvalho F, Sousa C, Remião F, Vitorino R, Amado F, Ferreira R, Duarte JA, de Lourdes Bastos M (2006) Cytotoxicity and cell signalling induced by continuous mild hyperthermia in freshly isolated mouse hepatocytes. Toxicology 224(3):210–218. https://doi.org/10.1016/j.tox.2006.04.028. http://www.sciencedirect.com/science/article/pii/S0300483X06002344

Sapareto SA, Dewey WC (1984) Thermal dose determination in cancer therapy. Int J Radiat Oncol Biol Phys 10:787–800

Sapareto SA, Hopwood LE, Dewey WC, Raju MR, Gray JW (1978) Effects of hyperthermia on survival and progression of Chinese hamster ovary cells. Cancer Res 38:393–400

Sharp K (2001) Entropy–enthalpy compensation: fact or artifact? Protein Sci 10:661–667

Song AS, Najjar AM, Diller KR (2014) Thermally induced apoptosis, necrosis, and heat shock protein expression in three-dimensional culture. J Biomech Eng 136(071006-1)

Spiro IJ, Sapareto SA, Raaphorst GP, Dewey WC (1982) The effect of chronic and acute heat conditioning on the development of thermal tolerance. Int J Radiat Oncol Biol Phys 8:53–58

Sriram K, Rodriguez-Fernandez M, III FD (2012) A detailed modular analysis of heat-shock protein dynamics under acute and chronic stress and its implication in anxiety disorders. PLoS ONE 7(8):e42958

Stege GJJ., Brunstinc JF, Kampinga HH, Konings AWT (1995) Thermotolerance and nuclear protein aggregation: protection against initial damage or better recovery. J Cell Physiol 164:579–586

Syntichaki P, Tavernarakis N (2002) Death by necrosis. EMBO reports 3(7):604–609. http://dx.doi.org/10.1093/embo-reports/kvf138

Takata AN, Zaneveld L, Richter W (1977) Laser-induced thermal damage of skin. Final report SAM-TR-77-38, USAF School of aerospace medicine, Warminster, PA

Taylor RP, Starnes JW (2003) Age, cell signalling and cardioprotection. Acta Physiol Scand 178:107–116

Wang S, Diller KR, Aggarwal SJ (2003) Kinetics study of endogenous heat shock protein 70 expression. J Biomech Eng 125:794–797

Wang S, Xie W, Rylander MN, Tucker PW, Aggarwal S, Diller KR (2008) HSP70 kinetics study by continuous observation of HSP-GFP fusion protein expression on a perfusion heating stage. Biotechnol Bioeng 99:146–154

Wang S, Chen PC, Berthiaume F, Toner M, Jayaraman A, Yarmush ML (2009) Dynamic effect of heat shock pretreatment on apoptotic responses to TNF-α in liver cells. J Biomech Eng 131:071003

Westra A, Dewey WC (1971) Variation in sensitivity to heat shock during the cell cycle of Chinese hamster cells *in vitro*. Int J Rad Bio 19:467–477

Wright NT (2003) On a relationship between the Arrhenius parameters from thermal damage studies. J Biomech Eng 125:300–304

Wright NT (2013) Comparison of models of post-hyperthermia cell survival. J Biomech Eng 135:051001

Würstle M, Zink E, Prehn J, Rehm M (2014) From computational modelling of the intrinsic apoptosis pathway to a systems-based analysis of chemotherapy resistance: achievements, perspectives and challenges in systems medicine. Cell Death Dis 5:e1258. https://doi.org/10.1038/cddis.2014.36

Xin M, Olson EN, Bassel-Duby R (2013) Mending broken hearts: cardiac development as a basis for adult heart regeneration and repair. Nat Rev Mol Cell Biol 14: 529–541

Zou Y, Zhu W, Sakamoto M, Qin Y, Akazawa H, Toko H, Mizukami M, Takeda N, Minamino T, Takano H, Nagai T, Nakai A, Komuro I (2003) Heat shock transcription factor 1 protects cardiomyocytes from ischemia/reperfusion injury. Circulation 108: 3024–3030

Hypothermia Used in Medical Applications for Brain and Spinal Cord Injury Patients

Liang Zhu

Abstract

Despite more than 80 years of animal experiments and clinical practice, efficacy of hypothermia in improving treatment outcomes in patients suffering from cell and tissue damage caused by ischemia is still ongoing. This review will first describe the history of utilizing cooling in medical treatment, followed by chemical and biochemical mechanisms of cooling that can lead to neuroprotection often observed in animal studies and some clinical studies. The next sections will be focused on current cooling approaches/devices, as well as cooling parameters recommended by researchers and clinicians. Animal and clinical studies of implementing hypothermia to spinal cord and brain tissue injury patients are presented next. This section will review the latest outcomes of hypothermia in treating patients suffering from traumatic brain injury (TBI), spinal cord injury (SCI), stroke, cardiopulmonary surgery, and cardiac arrest, followed by a summary of available evidence regarding both demonstrated neuroprotection and potential risks of hypothermia. Contributions from bioengineers to the field of hypothermia in medical treatment will be discussed in the last section of this review. Overall, an accumulating body of clinical evidence along with several decades of animal research and mathematical simulations has documented that the efficacy of hypothermia is dependent on achieving a reduced temperature in the target tissue before or soon after the injury-precipitating event. Mild hypothermia with temperature reduction of several degrees Celsius is as effective as modest or deep hypothermia in providing therapeutic benefit without introducing collateral/systemic complications. It is widely demonstrated that the rewarming rate must be controlled to be lower than 0.5 °C/h to avoid mismatch between local blood perfusion and metabolism. In the past several decades, many different cooling methods and devices have been designed, tested, and used in medical treatments with mixed results. Accurately designing treatment protocols to achieve specific cooling outcomes requires collaboration among engineers, researchers, and clinicians. Although this problem is quite challenging, it presents a major opportunity for bioengineers to create methods and devices that quicklyand

L. Zhu (✉)
Department of Mechanical Engineering, University of Maryland Baltimore County, Baltimore, MD, USA
e-mail: zliang@umbc.edu

B. M. Fu, N. T. Wright (eds.), *Molecular, Cellular, and Tissue Engineering of the Vascular System*, Advances in Experimental Medicine and Biology 1097,
https://doi.org/10.1007/978-3-319-96445-4_16

safely produce hypothermia in targeted tissue regions without interfering with routine medical treatment.

1 History of Cooling as a Treatment Tool in Medicine

Unlike heating, which has been used since ancient times as an infection prevention method for treating wounds, the medical benefits of cooling were not well understood and implemented until the recent centuries. It has been documented that cooling was used to minimize bleeding and to fight fevers. During Napoleon's war against Russia in the nineteenth century, it was an observation by physicians that the soldiers left in snow had an improved survival rate than those given a warm blanket and/or placed close to a fire. They also observed that fast thawing frostbite extremities directly over open fires expedited tissue destruction. Those lessons learned in the early wars were implemented in the medical practice of the twentieth century, which included development of various devices that actively removed heat from the body with a great level of temperature control. One pioneer in this field is Dr. Temple Fay, who hypothesized that tumor cell multiplication and progression could be inhibited by cooling, since it was rare to see tumors developing in the body extremities. He later tested this hypothesis in cancer patients. He also implemented cooling for pain relief. In the 1940s, Dr. Fay published the first case study of using hypothermia for cerebral injury patients (Fay 1945). Along a similar timeline, industrial development of refrigeration systems began in the 1930s, which assisted medical professionals with better implementation and control of cooling methods to patients than previous passive techniques, such as whole-body immersion into cold water or ice baths.

Human tissue requires a constant supply of oxygen-rich blood. Among all tissues, heart and brain tissues in the head and spinal regions are most valuable to ischemia. Unlike liver or muscle tissues, a shortage of oxygen delivery to the brain would immediately impair neuronal functions since the brain does not have a storage for glucose. It is well documented that brain tissue cannot recover after only 5 min of normothermic (37 °C) brain ischemia, but this duration increases to more than 45 min when the brain tissue temperature is lowered to 10 °C (Wass et al. 1995). Therefore, induced hypothermia has been studied as a means to protect the brain from ischemia since the 1940s (Kabat 1940; Fay 1945; Miller 1949; Bigelow et al. 1950; Lazorthes and Campan 1958; Sedzimir 1959; Vandam and Burnap 1959a, b; Drake and Jory 1962). Another application is in open-heart and open-neck surgeries when surgeons need to repair malformation in those regions. Surgeons could work efficiently if they operate on a bloodless field and minimize the risk of hemorrhage. In the 1950s and 1960s, cardiopulmonary bypass in conjunction with induced hypothermia was usually employed to provide cardiac surgeons sufficient time for many neuro-procedures while avoiding permanent brain/heart/spinal cord damage. Another field was in cerebral resuscitation, where cerebral hypothermia was introduced to cardiac arrest patients in order to maximize the ability of the brain tissue to survive anoxic no-flow states. In the 1970s, numerous animal experiments and clinical studies showed the benefits of hypothermia in prolonging tolerance of brain tissue to ischemia. Hypothermia contributed significantly to reduced mortality associated with previously inoperable cardiac and cerebral pathologies. However, most of the neuroprotective effects of lowering body temperature have been more evident in animal experiments than in patients.

Early studies commonly used deep states of hypothermia with temperatures $\leq$30 °C. For example, Dr. Fay's initial experiment lowered the body temperature of the patient to 27 °C. Deep hypothermia introduced detrimental systemic complications, such as pneumonia, ventricular fibrillation, and acidosis, which are especially fatal to elderly and fragile patients. In the 1970s and 1980s, research in hypothermia to enhance brain tissue recovery after ischemic

attack became dormant. This may be due to advancements in medicine to identify alternative and less risky treatment methods. In addition, thermal management difficulties made it hard to demonstrate benefits of deep hypothermia on neuroprotection. In the 1980s, researchers began to reinvestigate the idea of mild hypothermia since it can be relatively easy to control cooling extent and implement cooling methods. Extensive experimental studies on canine, swine, and rodent models have been conducted to evaluate efficacies of different cooling methods, temperature reductions, hypothermia durations, cooling initiation relative to the ischemic event, and rewarming rates on tissue recovery from ischemia. The neuroprotective mechanisms of hyperthermia have become increasingly better understood in the past three decades due to those animal experiments. Unfortunately, supporting data in human subjects are still limited, especially for randomized multicenter clinical trials (Clifton et al. 2001, 2011). In clinical studies, hypothermia therapy seems more successful in open-heart and open-neck surgery than in traumatic head injury. This is not unexpected, because cooling initiation after traumatic head injury is usually implemented several hours following the event, which may be too late to maximize the benefits conferred by hypothermia. However, these challenges can create opportunity for future investigations to develop more effective and well-controlled approaches for treating tissue ischemia. It is anticipated that hypothermia will be proven as an effective method to limit and eliminate injury and death associated with ischemic injury and benefit a vast patient population.

2 Biological and Chemical Reactions to Injury and Neuroprotective Mechanisms Associated with Cooling

Tissue ischemia can be the result of ischemic stroke, cardiovascular and respiratory disorders, and external physical trauma. If the initial damage is limited, the tissue may be able to recover. If the injury is extensive, secondary tissue damage occurs, which includes intracranial hypertension (brain swelling), hemorrhage, hypoxia, and edema. It is well known that brain oxygen stores become exhausted within 15 s and brain energy stores become exhausted within 5 min after global ischemia (Wass et al. 1995). Energy loss in tissue results in depolarization of cell membranes. A series of biochemical reactions and cascades initiated by the trauma will then follow. Those cascade events evolve gradually and may last several days after the initial trauma. The increase in extracellular K^+, energy depletion, disruption of the blood-brain barrier, free radical and glutamate release, excitotoxicity, and inflammation are typical consequences of those cascade events. The loss of selective neurons following global or local brain ischemia may lead to permanent neurologic deficit and even death. Thus, secondary injury can be more fatal to patients than the initial injury, and it is not uncommon to hear news reports on deaths occurring several hours or several days after the initial trauma.

Originally, researchers suggested that cooling may decrease blood perfusion in the injured region, similar to cold-induced halting of bleeding. Brain oxygen consumption can decrease by approximately 5–7% for every degree Celsius decrease in tissue temperature. Thus, a reduction in the energy expenditures of cerebral metabolic rates of glucose and oxygen was observed in deep hypothermia implementations. Later, people started to question this mechanism due to the observed benefits associated with mild hypothermia of lowering tissue temperature by only 1 or 2 °C. In the past several centuries, many researchers began to suggest that cooling may play an important role in deterring deleterious biochemical actions in secondary tissue injury triggered by the initial trauma. It has been demonstrated that hypothermia may modify a wide range of cell necrosis mechanisms (Marion et al. 1996; Maier et al. 2002; Yenari et al. 2000). Cooling retards progression of the ischemic cascade and pathological neuroexcitation. In brain tissue hypothermia, cooling may

attenuate the opening of the blood-brain barrier, reduce glutamate release, inhibit inflammation, and slow down free radical generation and release. It may also impair glutamate-mediated calcium influx or directly inhibit calcium-mediated effects on calcium/calmodulin kinase. As a result, hypothermia preserves high-energy phosphates that may facilitate the maintenance of membrane integrity during ischemia, limit edema formation, lower intracranial pressure, and interrupt necrosis and apoptosis (Xu et al. 2002). All of the mechanisms lead to prolonged cell survival and can improve outcomes after reperfusion and rewarming.

3 Cooling Parameters Affecting the Protective Outcomes of Hypothermia

Numerous controlled animal experiments have demonstrated the benefit of initiation of cooling before the brain injury to confer significant neuroprotective outcomes. The general consensus is to initiate brain hypothermia as early as possible following an ischemia-precipitating event, although some studies have shown neuroprotective effects even when the treatment was delayed by up to 6 h (Colbourne and Corbett 1995). Brain injury mechanisms typically progress rapidly within 3–6 h after the initial injury. Hypothermia can reduce the initial inflammatory response after head trauma and minimize or prevent secondary brain injury. It is well accepted that for animal models, there is a 1–2 h treatment window after which the benefits of hypothermia are strongly diminished. However, it is difficult to correlate animal data directly to humans. Unfortunately, it is still a challenge to shorten the time between the injury and induction of hypothermia. Usually, the process of transporting the patient to the hospital is unproductive for this objective. A portable sensor attached to the patient that alerts the medical center of the impending case can minimize delay of treatment. Further, simple cooling approaches that can be implemented by the emergency medical service (EMS) personnel in the ambulance have been suggested to achieve this goal.

Precooling is an option only for circumstances under which the onset of tissue injury is foreseen. It is a clinical option for open-heart and open-neck surgical procedures. Experimental data from a rat model demonstrated the greatest benefits of neuroprotection when hypothermia was induced during global ischemia (Dietrich et al. 1993). Additionally, initiation of hypothermia before the injury completely prevented secondary brain damage in gerbils (Welsh et al. 1990).

Because tissue temperature has profound effects on local metabolism and cellular activities, it is expected that different depths of hypothermia have varying effects on the clinical outcome of minimizing secondary tissue injury. Hypothermia can be categorized as deep or severe (less than <28 °C), moderate (28–32 °C), and mild (32–35 °C) (Kirkpatrick et al. 1999). The traditional view that colder is better (Michenfelder 1988) has been questioned in the past decades (Tisherman et al. 1999). As brain temperature decreases, great systemic toxicity is observed, and the adverse effects outweigh the neuroprotection mechanisms associated with therapeutic hypothermia (Chambers 1999). Deep hypothermia is associated with arrhythmias (Mouritzen and Anderson 1966), cardiac complications (Frank et al. 1993), coagulopathies (Rohrer and Natale 1992), and pulmonary infections (Bohn et al. 1986). In addition, severe or moderate cooling usually requires sedation and mechanical ventilation. Therefore, deep cooling approaches are limited to facilities that have intensive care units and situations that medically justify the collateral complications. On the other hand, there are numerous studies in recent years suggesting that the preferred cooling temperature for neuroprotection is between 32 and 35 °C (Colbourne and Corbett 1995; Gunn and Gunn 1998). Many studies have shown improved neurological outcomes using mild hypothermia, compared with either the deep cooling group or the normothermia group. Additional studies are needed to determine which targeted temperature is most associated with the beneficial effects of hypothermia in patients suffering from specific injury.

Secondary effects of brain injury, including edema and elevated pressure, are known to persist several days after focal cerebral ischemia (Dirnagl et al. 1999). Therefore, prolonging brain hypothermia therapy may benefit those patients. Experimental studies have tested whether a long cooling duration is safe for patients. A duration of 24 h was proposed initially, and it was later extended to 48 h by Bernard and Rosalion (2008), Clifton et al. (1993), McIntyre et al. (2003), and Shiozaki et al. (1993). A review by Peterson et al. (2008) documents profound neuroprotective benefits observed in patients who underwent more than 48 h of hypothermia. Although prolonged cooling can maximize clinical neurological benefits, it may also increase systemic complications associated with cooling, which may be more severe in patients with compromised health. The optimal duration of treatment remains unknown for clinical applications, especially when other confounding factors are involved. Closely monitoring patients during hypothermia therapy should be an important planning consideration.

The importance of controlling the rewarming rate in the brain tissue from a state of hypothermia has been widely documented. Rapid rewarming may result in a dangerous rebound of intracranial pressure elevation and cerebral perfusion pressure reduction; the importance of gradual rewarming has been emphasized in multiple clinical studies (Shiozaki et al. 1993). Previous theoretical analysis (Diao et al. 2003) of simulated passive (and uncontrolled) rewarming by removal of a head-cooling device yields an average calculated rate of approximately 3 °C/h. Animal experiments conducted on rats (Diao and Zhu 2006) suggest that a fast rewarming rate might result in a mismatch between local blood perfusion and metabolism. As suggested in a study (Thoresen and Wyatt 1997), the rewarming rate in tissue should be conducted slowly at 0.25–0.5 °C/h. In some clinical trials, rewarming from hypothermia was conducted with a feedback control system over 18 h. It is critical to develop a thermoregulating system that allows not only fast cooling but also an adjustable and controlled rewarming rate.

4 Currently Used Cooling Approaches/Devices

The ability to cool deeply embedded interior tissues, such as the brain and spinal cord, is limited by considerations of the second law of thermodynamics. Unlike the heating process, which can be dissipative, cooling requires that a negative temperature gradient be applied across the interstitial transport medium. If conduction is used to drive the heat transfer process, the magnitude of cooling that can be produced is directly proportional to the gradient established across the medium and the thermal conductivity of the medium. Alternatively, under normothermic conditions, high blood perfusion rates in tissue regions can be used as the primary mechanism to remove heat from the body core and redistribute it to the surface area. This mechanism is dependent on the level of blood perfusion through the cutaneous circulation in conjunction with conduction through the skin and cooling on the surface. Unfortunately, a high blood perfusion rate in the brain or spinal cord acts to continuously rewarm the tissue, thus inhibiting cooling penetration from a cold front and limiting temperature reduction in those regions. A different option for cooling is by convection, which involves introducing a chilled perfusate solution directly into the circulatory system. However, this approach is highly invasive and has its inherent risks. Both approaches have been adopted for inducing tissue hypothermia, but heat removal by conduction through the overlying tissue has limited efficacy due to the poor thermal conductivity of the body tissue. Both approaches have been implemented in reducing tissue temperature either via systemic (whole-body) or selective (local) cooling. In general, the faster the achieved cooling, the more invasive the involved procedures.

Most of the clinical studies to date have examined systemic (whole-body) hypothermia. Either the whole-body mass or the blood in circula-

tion is cooled using this approach. The major methodological drawback of this approach is the inherently slow cooling rate (~0.5 °C/h) due to the large volume of the human body to be cooled and the increase in thermal resistance due to arteriovenous shunt vasoconstriction (Marion et al. 1997; Schwab et al. 1998a, b; Krieger et al. 2001). Among all methods, skin surface cooling is the most studied in hypothermia. Various techniques have been used to cool the skin, including convective air circulation, cooling blankets or jackets, water mattresses, ice packs, and alcohol or ice-water bathing. Surface cooling is an easy approach and does not require sophisticated equipment. The side effects include shivering and vasoconstriction. Full-body immersion into cold water makes it difficult to attach monitoring sensors to patients (Olsen et al. 2003). Also, vasoconstriction induced by skin surface cooling greatly increases the thermal resistance of the skin, further hindering heat transfer from the body core to the surface.

Direct cooling of the blood in circulation is an attractive technique because it bypasses the thermal resistance of superficial tissue layers. Intravascular catheters have been proposed as a method to induce a fast cooling rate (Georgiadia et al. 2001; Dixon et al. 2002; Doufas et al. 2002; Inderbitzen et al. 2002; Dae et al. 2003; Mack et al. 2003; Holzer et al. 2005). This method uses a covered cooling catheter that is inserted into the femoral vein and advanced to the inferior vena cava via abdominal X-ray guidance. Coolant is pumped into the catheter to achieve fast heat removal from the venous blood and with a cooling capacity of up to 150 W. Since its introduction to clinical trials, intravascular catheters have been tested in both brain and spinal cord injury patients, and their safety and effectiveness have been well documented. The drawback of this approach is the invasive nature of the surgical procedures involved, which can vary depending on the skill of the surgeon. Therefore, its clinical use has been limited to special hospitals, and it is not a technology available to personnel with limited training and resources (Georgiadia et al. 2001).

Chilled saline has been suggested as a preferred resuscitation fluid for patients with neurological and neurosurgical injuries (Polderman et al. 2005; Kollmar et al. 2009). It is inexpensive, easy to store, and frequently utilized as hydration fluid in hospitalized patients. This method of inducing hypothermia was tested in a swine model (Vanden Hoek et al. 2004). For a high intravenous infusion rate of 120 mL/min, a core cooling rate was measured at up to 18 °C/h. In a clinical study (Virkkunen et al. 2004), Ringer's solution was infused at a rate of 100 mL/min to patients after resuscitation from nontraumatic cardiac arrest, and no serious adverse hemodynamic complications occurred. This approach is found to be very effective in achieving fast cooling. Intravenous coolants administered in an on-demand, temperature-guided, and supervised setting seem to be a reasonable approach for core cooling that avoids potentially unsafe use of extended fluid volumes and infusion time periods. However, it is questionable whether the patients can tolerate such a large infusion rate of fluid, especially in some patients with compromised kidney functions.

In sports medicine, controlling temperature elevation in the body may be related to athletic performance (Enomoto et al. 1996; Grahn et al. 1998, 2005, 2008). One technology uses an applied negative pressure on glabrous skin of the hand to mechanically distend arteriovenous anastomoses, thereby greatly increasing the cutaneous blood perfusion. By diverting a significant fraction of the cardiac output to the skin, where there can be effective heat transfer with the environment, it is possible to use the circulatory system as a convective conduit for thermal energy between the body surface and the thermal core, including the brain. In initial studies with humans, it has been possible to achieve cooling rates of core temperature of 10 °C/h and higher, which would be adequate for hypothermia induction in cases of TBI. One concern raised by neurosurgeons is the adverse effect of decreased blood pressure, which can be dangerous to patients with compromised health. However, this approach may still have potential to decrease

body temperature and induce hypothermia at targeted brain or spinal cord regions without interference with simultaneous treatments at those targeted locations.

Localized cooling has been utilized in the past decades for patients suffering from tissue injury. It is the brain or spinal tissue that requires temperature reduction, not the entire body mass. Therefore, local cooling has been utilized in the past when the targeted tissue region becomes accessible in order to implement the cooling devices. Following spinal cord injury, the injured region is often exposed to allow surgical decompression. Hypothermia to the injured spinal cord region can be easily introduced using epidural heat exchanger or infusion of cold saline solution to the subarachnoid space. It has been reported that incorporating a cooling device into a routine neurocritical care device for monitoring interstitial pressure and/or draining ventricular fluid allows direct cooling of the injured intraparenchymal brain region (Zhu and Rosengart 2008). Cooling the dura surface directly was also proposed when the brain hemisphere is exposed. Selective brain cooling by targeting temperature reduction in the brain tissue alone has been well studied in the past. Feasible approaches include head surface cooling relying on cooling penetration from the scalp to the brain tissue, neck collar or interstitial cooling device targeting arterial blood supplied to the brain tissue, intracarotid flushing, and cooling in the ventricular space. Cooling on the head and neck surface requires 1 or 2 h to reach steady state with a penetration depth limited to the superficial regions of the brain cortex (Wang et al. 2004; Eginton 2007; Poli et al. 2013). An interstitial cooling device placed directly on the surface of the common carotid artery was proposed and tested (Wang and Zhu 2007, Wang et al. 2008, Wei et al. 2008). The approach might be too invasive for stroke patients, but it may be suitable for open-neck surgery when the carotid artery has already been exposed. Similar to the intravascular cooling catheter, intracarotid flushing advances a cooling catheter to the carotid artery in order to induce rapid cooling (4 °C temperature reduction in cerebral cortex within 10 min) (Ding et al. 2004). An endovascular cooling catheter may sound very invasive, but the rationale of implementing it was based on frequent clinical use of endovascular recanalization during some brain injury situations or cardiopulmonary bypass surgeries requiring circulatory arrest (Bachet and Guilmet 2002; Choi et al. 2006). One clinical trial was conducted to infuse cold saline (4–17 °C) at a rate of 33 mL/min (Choi et al. 2010). Similar to intravenous flushing, administration of a large volume of fluid may cause systemic volume overload and hemodilution (Esposito et al. 2014). The measured temperature reduction at the jugular venous bulb was lower than 1 °C after 10 min, which is smaller than theoretical predictions. The authors argued that the jugular venous bulb temperature does not correlate well with the deep brain temperature. Nasopharyngeal cooling takes advantage of the dense blood vessels in the nasal cavity, and cooling in the cavity may penetrate into the nearby brain regions (Esposito et al. 2014). Ventilation of cold air into the nasal cavity may not be very effective due to small thermal capacity of air. On the other hand, inserting a cooling catheter with coolant (RhinoChill™) seems effective in reducing the temperature of that region. Results from clinical trials on implementing the nasopharyngeal cooling were not very encouraging due to very small temperature drops and concerns on increasing blood pressure in patients (Andrews et al. 2005; Harris et al. 2007; Abou-Chebl et al. 2011; Covaciu et al. 2011; Poli et al. 2013; Springborg et al. 2013). Another approach is to cool the cerebrospinal fluid (CSF) in order to reduce the temperature of the brain. One way of implementation is to insert a cooling catheter into the lateral ventricles of the brain while maintaining normal body temperature. This method has been tested in sheep, and it reduced the brain temperature to 34.5 °C after 3 h (Moomiaie et al. 2012). A clinical study was performed to test ventricular infusion on O_2 supply to the brain region, and a brain temperature drop was observed. A mathematical simulation was performed to explore the possibility of cooling the CSF on the

back of the torso, resulting in cooling of the brain (Smith and Zhu 2010b).

5 Applications with Evaluation of Clinical Outcomes of Tissue Hypothermia

5.1 Traumatic Brain Injury

Traumatic brain injury (TBI) is a nondegenerative, noncongenital insult to the brain tissue due to externally inflicted trauma (McIntyre et al. 2003). The major consequences of head injury include skull fractures, intracranial hemorrhages, elevated intracranial pressure, and cerebral contusion. Unlike stroke, which is often associated with the elderly, TBI affects a predominantly young population, as TBIs occur mostly as a result of motor vehicle accidents. Neuroprotective outcomes in clinical trials that treated head injury using hypothermia are not consistent. There is marked heterogeneity among available clinical studies (Shaefi et al. 2016).

The lack of conclusive results of improved neurologic functions in TBI patients has deterred clinicians from implementing cooling as a standard treatment. In 1994, a multicenter, randomized, and prospective phase III study of systemic hypothermia in severe brain injury that involved seven medical centers in the United States (Clifton et al. 2001) was initiated based on the promise of decades of somewhat sporadic experiments and anecdotal positive clinical outcomes for hypothermia used to treat TBI in addition to a previously extensive phase II clinical trial (Clifton et al. 1993). This study enrolled 392 patients, ages 16–65, who suffered a coma from brain injury in the absence of other major traumas. A control group received standard management with a nominal core temperature of 37 °C. The treatment group received the same management protocol at a target temperature of 33 °C. There was a large variation in the cooling induction time due to many individual circumstances. The cooling process began at 4.1 ± 1.2 h post-injury via surface cooling technology and completed by 8.3 ± 3.0 h. Hypothermia was maintained for 48 h and was followed by slow rewarming distributed over 18 h. Some of the patients were already hypothermic (≤35 °C) owing to independent circumstances on admission to the hospital and were retained in a treatment subgroup. Overall, very minimal difference was observed between the treatment and control groups (Clifton et al. 2001), with the exception of significantly better outcomes from the subgroup of individuals already hypothermic at admission (Clifton et al. 2002). Although the results of this study were discouraging, they directly led to an enhanced appreciation for the need of achieving a hypothermic state quickly following a TBI in order for the therapy to be effective (Marion et al. 1997; Markgraf et al. 2001). Thus, the stage was set for current developments in the application of hypothermia for TBI. Unfortunately, a recent large clinical trial by the Clifton group in 2011 found no significant difference in outcomes between hypothermia and normothermia TBI patients even though targeted temperature reduction was achieved within 5 h, hypothermia was maintained for a long duration of 48 h, and rewarming was very gradual at 0.25 °C/h (Clifton et al. 2011). This clinical trial only suggested a possible benefit of hypothermia to patients with surgically resectable lesions (Clifton et al. 2011). Another randomized large clinical trial on severe TBI children in 2008 showed that hypothermia does not improve outcomes of those children and may also contribute to higher mortality in the participants of the cooling group (Hutchison et al. 2008). The results are disappointing since the trial enrolled a large patient group of 225 children and focused on early initiation of cooling (6.3 ± 2.3 h after injury) and slow rewarming (0.5 °C/h). Similarly, two recent clinical trials in Japan and Europe also failed to identify neurological benefits of hypothermia in treating TBI patients (Andrews et al. 2015; Maekawa et al. 2015).

In the meantime, several clinical studies (Shiozaki et al. 1993; Marion et al. 1997; Metz et al. 1996) tested hypothermia therapy in patients with severe head injury and achieved improved outcomes compared to normothermia groups. Hypothermia benefits were evident in patients with a coma score of 5–6 at months 3 and 6 (Marion

et al. 1997). It is reported that more than 62% of patients in the hypothermia group achieved good outcomes versus 39% in the control group. Jiang et al. (2000) evaluated the long-term benefits of hypothermia in patients with severe traumatic head injury. It was found that mortality decreased by 40% and the rate of favorable outcome increased by 70% in the hypothermia group 1 year after the head injury. One of the common benefits identified in the above studies was a marked reduction of the intracranial pressure in the hypothermia group after days of treatment. A recent study (Puccio et al. 2009) explored the use of cooling to counteract fever typically following TBI. Fever may exacerbate secondary injury severity after the initial injury by inducing excitotoxicity, free radical production, blood-brain barrier breakdown, cytoskeletal proteolysis, and inhibition of protein kinases. It has been found that higher fever was associated with higher risk of death in stroke and TBI patients (Saxena et al. 2015). In the Puccio study (Puccio et al. 2009), hypothermia reduced the fever burden in those patients, which may have potentially attenuated secondary injury. It was recommended that cooling should be maintained at least until after the intracranial pressure returns to the normal range (Shiozaki et al. 1993; Jiang et al. 2000). Some researchers (Safar and Kochanek 2001) attributed the failure to demonstrate the benefits by hypothermia to the delay of cooling initiation, which is often more than 4 h after the injury in clinical treatments (Clifton et al. 2001). A clinical trial by Gal et al. (2002) showed that more than 87% of patients achieved good neurological outcome in the hypothermia group, suggesting certain methodological discrepancies in the Clifton study. A clinical trial of hypothermia on traumatic head injury (Qiu et al. 2005) showed improved extradural pressure and reduced mortality from 51% in the control group (43 patients) to 26% in the hypothermia group (also 43 patients). Another clinical study by the same group (Liu et al. 2006) documented improved neurological outcomes in TBI patients 2 years after the hypothermia treatment, including complications that were manageable. A review by Peterson et al. (2008) of hypothermia-related neuroprotection on TBI patients identifies a cooling duration longer than 48 h as a favorable factor; however, it cautions the risk of pneumonia. The results also suggest favorable effects of hypothermia on the patients in trials having long-term follow-up periods of 1 or 2 years. There was one recent clinical trial conducted in China (Zhao et al. 2011) that attributed improved neurological outcomes in TBI patients by cooling to a reduction in blood glucose and lactate levels.

A retrospective and cross-sectional meta-analysis by Li and Yang (2014) concluded that moderate hypothermia benefitted TBI patients by resulting in better neurological outcomes, and reduced death rate is shown, although the data were not statistically significant. Overall, there is a lack of well-controlled, large clinical trials that provide convincing evidence of the benefits and safety of brain hypothermia as a treatment for traumatic head injury patients. A recent review (Saxena et al. 2015) suggested conducting clinical trials using mild hypothermia when the brain temperature is reduced by 1–2 °C in order to minimize systemic complications of hypothermia with targeted temperatures as low as 33 °C. The 4th edition of the Guidelines for the Management of Severe Traumatic Brain Injury, issued by the Brain Trauma Foundation in 2017, cautions on implementing mild hypothermia for patients with TBI while emphasizing adequate pharmacologic intervention as the 1st priority (Carney et al. 2017).

5.2 Brain Ischemic Injury from Stroke

The Guidelines on Acute Stroke Treatment by the American Stroke Association identify hypothermia after stroke as a promising field of research but state that well-established clinical trials are needed before endorsement. A review by Van Der Worp et al. (2007) concludes that hypothermia improved outcomes of animals suffering from ischemic stroke by more than 30%. This result is especially true in well-controlled animal stroke models (Barone et al. 1997). It is relatively easier to have reproducible models of

transient global brain ischemia via occlusion of the distal middle cerebral and ipsilateral common carotid arteries than that of focal brain ischemia, for which it is more difficult to define experimental conditions. Computerized images of cerebral infarct volume and edema are commonly used to evaluate ischemic damage to the brain tissue. If the animals are kept alive after the injury, cognitive evaluation is conducted to assess the long-term protective outcome of cooling. The efficacy of hypothermia is better with a lower target temperature (Kurasako et al. 2003) and/or when it is initiated before or during the onset of ischemia. A study by Kurasako et al. (2003) on a spontaneously hypertensive rat model demonstrated a strong, linear, temperature-dependent reduction in infarct volume and edema progression in transient focal ischemia. Neuroprotection by hypothermia is more prominent in lower-temperature (28 °C and 30 °C) groups. More improvements are found in temporary models rather than in permanent ischemic models (Marion et al. 1997; Morikawa et al. 1992).

There are limited clinical trials to test the efficacy and safety of various hypothermia approaches for acute ischemic stroke patients. Overall, it has been demonstrated that more robust, randomized clinical trials with large patient enrollments are needed to provide conclusive evidence for the benefits of hypothermia in stroke patients. Clinical studies by Schwab et al. (1998a, b, 2001) showed that more than half of the patients survived severe stroke after up to 72 h of hypothermia at 33 °C. Most of the 38% mortality rate of the stroke patients occurred during the rewarming process, which suggests an important role of gradual rewarming after hypothermia. Although the clinical studies were not conducted using a control group, the observed 38% mortality rate is much lower than a typical death rate of 70% in severe stroke patients (Hacke et al. 1996; Berrouschot et al. 1998). A small clinical trial by Kammersgaard et al. (2000) using mild hypothermia (35 °C) in 17 patients also showed marked improvement of mortality rate of 12% compared to 23% in controls. Unlike the Schwab studies that were associated with many serious systemic complications, including thrombocytopenia, bradycardia, and pneumonia, the only reported side effect in the Kammersgaard trial was shivering, which was treated by pethidine. Kasner et al. (2002) conducted a clinical trial with mild hypothermia induced by acetaminophen administration in an attempt to achieve brain cooling rapidly. The results were inconclusive because acetaminophen produced only a very mild state of hypothermia of <36.5 °C, bringing into question its clinical efficacy. A randomized trial of hypothermia in infants with hypoxic-ischemic encephalopathy showed reduced risk of death or disability (Shankaran et al. 2005). However, neuroprotection from hypothermia was not obvious in additional two clinical studies (Krieger et al. 2001; de Georgia et al. 2004), even though the results favored hypothermia.

Endovascular cooling of blood has been investigated by various research groups as an effective cooling method to induce a fast cooling rate varying from 0.9 to 6.9 °C/h. Rather than cooling the entire body, this approach targets blood in circulation via a cooling catheter inserted into the femoral vein and advanced to the inferior vena cava. Several clinical trials in the early 2000s suggested safety and effectiveness of the fast endovascular approach on brain ischemic patients (de Georgia et al. 2004; Hemmen et al. 2010). One side effect noticed was shivering, but it can be managed by combining other medications and treatment. The Hemmen study enrolled 59 ischemic stroke patients and randomly assigned participants to a control group or a hypothermia group that used endovascular cooling to lower the body temperature to 33 °C. Based on the 90-day follow-up outcome, no statistically significant difference in mortality was reported (Hemmen et al. 2010). A smaller clinical trial published in 2006 with only 25 patients focused on evaluating the effect of hypothermia on patients with malignant supratentorial cerebral ischemia (Els et al. 2006). Again, an endovascular cooling catheter was utilized to quickly reduce body temperature to 35 °C. The 6-month follow-up outcome in the hypothermia group was better than that in the normothermia group and had similar side effects or complications (Els et al. 2006). The

most recent clinical trial implemented mild hypothermia for 48 h using endovascular cooling in acute ischemic stroke patients. Based on the data measured in a larger participant group of 75 patients, it showed less cerebral edema, lower incidence of hemorrhagic transformation, and better outcomes in the cooling group than that of the normothermia group (Hong et al. 2014). The neurological outcome was measured using a modified Rankin Scale (mRS) score 3 months after the treatment, and more than half of the patients in the cooling group scored as "good," while only 22% of the patients in the control group scored as "good."

5.3 Cardiac Arrest

Clinical trials using hypothermia treatment after cardiac arrest yield strong evidence to support beneficial effects of cooling to patients. A recent review by Schenone et al. (2016) analyzed 149 papers and later evaluated 24 papers related to clinical trials that implemented systemic hypothermia in cardiac arrest patients. Among them, 11 studies with randomized controlled trials and observational cohort studies compared results between hypothermia and normothermia groups. Most of the reports demonstrated increased odds of survival with good neurological outcomes when hypothermia was implemented to out-of-hospital cardiac arrest patients.

Two early randomized clinical trials published in 2002 enrolled a total of 352 adult comatose survivors after out-of-hospital cardiac arrest (OHCA) (Bernard et al. 2002; Holzer et al. 2002). A targeted core body temperature of approximately 33 °C was achieved in the hypothermia group, and the normothermia group had body temperatures higher than 37 °C, with or without fever control. Results at the 6-month follow-up showed that the percentage of patients with favorable neurological outcomes increased from approximately 30% in the normothermia group to approximately 50% in the hypothermia group. Further, the 6-month mortality rate was much lower in the cooling group than in the control group. In Lauren et al. (2005), they performed a randomized clinical study on a small patient group (61 cardiac arrest patients) to evaluate effects of high-volume hemofiltration with or without hypothermia on decreasing mortality rate. Compared to the control group, high-volume hemofiltration improved the overall prognosis after resuscitation from OHCA. The effect of hypothermia alone was not evaluated directly, but the results suggest that hypothermia if applied early might lower the mortality rate within several weeks after the treatment (Lauren et al. 2005). In a retrospective study, the effects of external cooling implemented to cardiac arrest patients (55 hypothermia vs. 54 normothermia) were evaluated (Oddo et al. 2006). They found that the patients in the cooling group had a much lower mortality rate with better neurological outcomes than that of the normothermia group. Therapeutic hypothermia was found particularly beneficial in patients with a short duration of cardiac arrest. Similarly, in another retrospective study (Belliard et al. 2007), external cooling using ice packs resulted in significantly higher survival rates than that of the normothermia group. They also commented that the cooling method was easy to implement without observing significant complications. In another retrospective study of 75 patients, targeted reduction of body temperature to 33 °C was achieved using either external or endovascular cooling (Ferreira et al. 2009). They found that hypothermia significantly increased the survival rate from 42% in the control group to 67% in the cooling group, and the percentage of patients with favorable neurological outcomes jumped from 19 to 51% in the cooling group. Interestingly, although there was no statistically significant difference in the survival rates of both cooling methods, the percentage of patients with favorable neurological outcomes in the endovascular subgroup was higher than that of the external cooling subgroup (62 vs. 40%). The authors observed a much shorter duration to reach targeted body temperature reduction using endovascular cooling. Effects of cooling were also evaluated in another retrospective study published in 2011, by

comparing patients treated with a conservative approach with patients treated with active cooling (Petrovic et al. 2011). Hypothermia was found to decrease patient mortality rate from 81% in the normothermia group to 44% in the cooling group of cardiac arrest patients. Despite the above-reported positive effect of hypothermia on patient outcome and survival, a randomized large-scale clinical trial published recently by Nielsen et al. (2013) raised many questions on the benefits of hypothermia on cardiac patients. This study included more than 900 out-of-hospital cardiac arrest patients, and it showed no significant difference between patients in the cooling group and in the normothermia group when evaluating the survival rate and neurological outcomes at the 180-day follow-up. Overall, reports on the beneficial effects of hypothermia on the outcomes of cardiac arrest patients were frequently observed in the past 15 years, unlike outcomes when treating TBI or stroke patients.

Previous studies have also examined whether targeted temperature reduction matters. Unfortunately, most of the studies have not shown a significant difference when implementing a specific temperature over another during hypothermia. A recent review article suggested that in some of the clinical trials involving cardiac arrest patients, a delay in cooling initiation or a delay in reaching the targeted temperature increased risk of death and/or poor neurological outcomes (Fukuda 2016). Related to initiation of cooling, some studies have been performed to evaluate the efficacy of initiating hypothermia before the patient arrives at the hospital or before return of spontaneous circulation. In small clinical trials, the results from prehospital cooling and cooling before return of spontaneous circulation are encouraging due to data demonstrating improved survival rates and neurological outcomes. However, results from large randomized clinical trials are currently in progress and have not yet provided conclusive evidence of the benefits of cooling. Some studies suggested that fever control alone may be sufficient in resulting in improved neurological outcomes (Nielsen et al. 2013).

5.4 Brain Ischemic Injury During Surgery

In TBI, ischemic stroke, or cardiac arrest, it is difficult to implement hypothermia before the injury occurs. Previous well-controlled animal experiments have shown the importance of initiating cooling before the injury to confer the benefits of hypothermia in neuroprotection (Welsh et al. 1990; Dietrich et al. 1993). Cardiopulmonary surgery would make precooling possible. It is well known that brain injury is a common postsurgical observation after cardiopulmonary surgery (Miller 1993; Roach et al. 1996). It is believed that neurological dysfunction results from regional or global brain ischemia as a consequence of hypoperfusion due to circulatory arrest and formation of emboli (Nussmeier 2002).

Early animal studies (Gillinov et al. 1993; Zeiner et al. 1996a, b) have been performed to assess the improved neurological outcomes associated with hypothermia. It has been found that profound brain hypothermia significantly improved the neuro-deficit score of 48.3 in the control group to 19.2 in the cooling group (0 = normal and 100 = brain dead). Improved neurological outcome was also shown in a dog model of cardiac arrest (Sterz et al. 1991). In a study by Moyer et al. (1992), spontaneous cerebral hypothermia of 33 °C decreased focal infarction volume in a rat brain by 75%. A recent animal study performed on dogs also showed a 70% survival rate following surgery of mitral valve plasty after more than 90 min of cardiopulmonary bypass using profound hypothermia (20 °C).

Numerous experimental studies have shown that brain hypothermia enhances the brain's tolerance to ischemia during cardiopulmonary surgery and thereby improves neurological outcomes. Hypothermic circulatory arrest temporarily suspends blood flow under very cold body temperatures. When the tissue is cooled to allow blood circulation to stop, cellular activity becomes low without introducing significant damage to the patient. This also allows sufficient time for the surgeon to repair under a bloodless field in open-heart and open-neck surgery. It is

very rare to see published results of randomized clinical trials that compare patient outcomes in a hypothermia group with that of a normothermia group, since therapeutic hypothermia has been implemented as a standard therapy in the international resuscitation guidelines since the 1970s. Most of the current research is focused on evaluating the effects of the degree of hypothermia and various reperfusion techniques. One recent survey suggested that most clinical practices utilize deep hypothermia with the body temperature reduced to 20 °C or lower (Gutsche et al. 2014), allowing at least 30 min of time for cardiac repairment. Mild brain hypothermia was reported to minimize cerebral impairment in 1500 patients undergoing pulmonary endarterectomy (Jamieson et al. 2003). The protective effect of hypothermia was also evident in patients undergoing carotid endarterectomy (Kouchoukos et al. 1994), wherein there were no early postoperative strokes or reversible ischemic neurologic deficits following the surgery. An FDA-approved cooling system known as ChillerPad™ and ChillerStrip™ system (Seacoast Technologies, Inc., Portsmouth, NH) was employed in a clinical trial of aneurysm repair; hypothermia markedly reduced vasogenic edema and protected the blood-brain barrier (Wagner and Zuccarello 2005). One recent clinical study reported no significant difference in patient mortality between implementations of either profound hypothermia (∼15 °C) or deep hypothermia (∼20 °C). The authors suggested that deep hypothermia is a safe approach that is easy to implement without certain complications associated with profound hypothermia (Gong et al. 2016). Another clinical study focused on hypothermia at 31 °C in bypass surgery also demonstrated similar mortality rates to that of deep or profound hypothermia (Guo et al. 2014). Currently, the most recent studies in this field are evaluation of whether moderate hypothermia is equally effective as profound hypothermia in providing tissue protection. In addition, this research helps elucidate how to increase the bypass duration and allow surgeons a longer time to operate in complicated surgical procedures.

5.5 Spinal Cord Injury

The nervous system includes the brain, spinal cord, and a complex network of neurons. Like the brain, the spinal cord is covered by the meninges and contains both gray matter and white matter. Also similar to the brain tissue, the spinal cord is subjected to severe damage after injury, and hypothermia may provide neuroprotection after acute spinal cord injury.

Each year, more than 12,000 new cases of spinal cord injury are reported in the United States, and it affects all ages. Only 1% of those patients were discharged neurologically normal, and most patients suffered from either complete quadriplegia or paraplegia that required significant medical costs following their discharge from the hospital. It is a great challenge to develop new treatment options to preserve spinal cord tissue, thus facilitating recovery of some motor functions controlled by the spinal cord (Steeves et al. 2011).

There have been many animal studies conducted to evaluate the efficacy of spinal cord cooling under well-controlled injury settings. Animal models including rats and pigs have been proven valuable not only in isolating various factors in spinal cord injury but also understanding various molecular pathways involved in the injury (Strauch et al. 2004; Yoshitake et al. 2004; Ha and Kim 2008; Morino et al. 2008; Purdy et al. 2013; Grulova et al. 2013). Animal models have also been used to test various local and systemic cooling approaches or devices. Typically, spinal cord injury is induced by contusion with weight impact, compression of the spinal cord, distraction via stretching the spinal cord, dislocation by lateral displacement of the vertebra, or transection that severs the cord (Cheriyan et al. 2014). In a rat model, hypothermia of 32–33 °C was introduced to the spinal cord 30 min after the injury for a duration of 4 h, and the results were encouraging by showing improvement in locomotor deficits and reducing the area of damage (Yu et al. 2000). In one study using TUNEL (terminal deoxynucleotidyl transferase (TdT) dUTP nick-end labeling) stain as an index of cell damage

on rats with spinal cord contusion injuries, the authors observed marked decrease in TUNEL in the hypothermia group of 32 °C in the evaluation at both the 72-h and 7-day follow-ups as compared to that of the control and sham groups (Shibuya et al. 2004). In another contusion model, modest hypothermia of 4 h also resulted in significant increases in white matter and gray matter volumes and preservation of neurons when compared with normothermic controls. The rats in the cooling group also had a faster rate of recovery in open-field locomotor ability and improved forelimb strength (Lo Jr et al. 2009). Hypothermia was shown to significantly improve the behavioral and histologic outcomes in rats that underwent compression injury (Batchelor et al. 2010; Maybhate et al. 2012). In one recent study, beneficial effects of hypothermia on survival of neural stem cells in a transplantation for recovery from SCI were demonstrated when compared with control groups (Wang and Pearse 2015). Overall the benefits of deep or moderate hypothermia on spinal cord injury have been well documented by many animal studies in controlled experimental settings.

In clinical settings, cooling initiation to spinal cord injury patients may not be introduced as early as that of well-controlled animal experiments. This is largely due to the transportation of patients to trauma centers and time required to obtain a patient's consent to include hypothermia as an experimental treatment option. Therefore, results from clinical studies vary on neuroprotection and function recovery due to hypothermia. Early studies in the 1970s typically used an ice pack or cold saline infusion to the injured spinal cord for several hours. Unfortunately, those studies are often associated with small sample sizes and lack of control groups (Selker 1971; Tator 1972; Negrin Jr 1973; Meacham and McPherson 1973; Bricolo et al. 1976). The most recent clinical study using local cooling via an extradural saddle device on 20 SCI patients suggested an improved ASIA (American Spinal Injury Association) grade (Hansebout and Hansebout 2014). Although there was no control group of patients in normothermic conditions, the authors state that the outcomes due to cooling were better than that of traditional treatments (Hansebout and Hansebout 2014).

In recent years, systemic hypothermia for spinal cord injury has attracted a lot of attention due to development of an endovascular catheter that induces fast cooling and can quickly reach targeted temperature reduction. Unlike local cooling when laminectomy may be needed before cooling can be applied, systemic hypothermia can be implemented immediately after injury by cooling the blood using ice-cold saline or endovascular cooling catheters. Several clinical studies on implementing systemic cooling to SCI patients are encouraging. Some of them were carried out to evaluate safety of implementing the device within a small group of patients (Cappuccino et al. 2010; Tripathy and Whitehead 2011). Initial results by Levi et al. (2009, 2010) show improved patients' AIS (ASIA Impairment Scale) grades with normal complications, and their follow-up study demonstrated favorable outcomes in those patients. A recent clinical trial by the same group enrolled more than 35 acute SCI patients (Dididze et al. 2013). At the 10-month follow-up evaluation, more than 43% of the patients improved at least one ISNCSCI (International Standards for Neurological Classification of Spinal Cord Injury) grade despite the relatively late cooling initiation of approximately 6 h after injury (Dididze et al. 2013). Currently there are no randomized large multicenter clinical trials to test systemic hypothermia on spinal cord injury patients. Although robust experimental and limited clinical studies have demonstrated that hypothermia is beneficial for acute SCI patients, further studies are critical in providing convincing evidence of the efficacy of hypothermia on the recovery of a devastating injury with very poor outcomes.

6 Engineering Contributions in Brain Hypothermia

6.1 Development of Cooling Devices

The major contribution of engineering in therapeutic brain hypothermia is the design of reliable and safe devices that achieve target cooling rates and temperatures. New technologies are typically evaluated for thermal efficacy and safety in small and large animal models to determine their suitability for testing in humans. During the design, patient safety is a prime consideration, and potential issues include leakage of coolant, induced freezing damage to tissue, physical trauma, etc. Sterilizability, size minimization consistent with thermal performance requirements, and physical packaging are typical design considerations during the development of the device. Another important thing often neglected by engineers is how the cooling device may interfere with normal medical treatments.

In general, there are two categories of device designs that are used clinically for therapeutic hypothermia: skin surface and endovascular cooling. More than six companies (Medivance, MTRE, Seabrook, Cincinnati Sub-Zero, Birchbrook, and Garnar) manufacture surface cooling devices, such as cooling blankets, garments, helmets, and pads. This category of devices is based on noninvasive methods and has been most broadly applied in clinical trials to date. An alternative approach is presented by AVAcore™ in which an applied negative pressure to glabrous skin in conjunction with cooling is used to enhance blood perfusion through arteriovenous anastomoses, thereby increasing convective energy transport with the body core. This technique has the potential for providing much faster cooling rates. There are three companies (Radiant Medical, Innercool Therapies, and Alsius) that have developed endovascular catheters for cooling human blood as it flows past the device that is inserted into a large vessel. Endovascular cooling is superior in providing a fast cooling rate. However, its major drawbacks are increased risk of blood clotting, invasive surgical insertion procedures, and complications associated with whole-body cooling. Other approaches, such as intracarotid cooling and interstitial cooling in the neck, are in their infant stages and have yet to be tested in large animal models and clinical studies.

6.2 Mathematical Simulations of Cooling and Rewarming Processes

In the past three decades, clinicians have realized the importance of closely monitoring brain temperature during hypothermia. Even a small reduction in brain temperature can improve neurological outcomes of patients suffering from brain injury. Temperature variation within normothermic brain tissue is usually very small. However, especially during therapeutic hypothermia, temperature gradients can develop not only between the brain and core but also within regions of the brain (Busto et al. 1987; Mellergard et al. 1990; Stone et al. 1995; Wass and Lanier 1996; Schwab et al. 1997, 1998a, b). Information on internal temperature gradients is difficult to obtain clinically by measurement with temperature probes owing to the risk of inducing additional tissue damage. Current noninvasive temperature measurements such as magnetic resonance imaging (± 2 °C) lack the desired resolution to monitor small temperature variations in the brain region. Therefore, analytical methods for understanding the transient and spatial temperature distribution in brain tissue during hypothermia therapy are clinically valuable.

Quantitative thermal modeling aids in identification of an optimal treatment protocol, and appropriate constitutive input data creates a potential for designing personalized therapeutic regimens. Theoretical modeling provides clinicians with powerful tools to improve the ability to deliver safe and effective therapy. Most importantly, thermal modeling permits the identification and evaluation of critical monitoring sites to assess the cooling extent and to assure patient safety.

Most of the current theoretical thermal models in brain hypothermia implement the Pennes bioheat equation (Pennes 1948) that simplifies the thermal contribution of local blood vessels as a simple heat source term added to the traditional heat conduction equation (Zhu and Diao 2001; Diao et al. 2003; Dennis et al. 2003; Ley and Bayazitoglu 2003, 2004; Janssen et al. 2005; Wang and Zhu 2007; Neimark et al. 2008; Zhu and Rosengart 2008; Zhu et al. 2009). With the advancement in computational resources, researchers have the capability to simulate the 3D temperature field of the head and neck and to consider multiple large blood vessels individually in the model. When point-to-point temperature nonuniformities are important, a model that incorporates perfusion through the vasculature is necessary to accurately predict the tissue temperature field. However, complex vascular geometry may prompt a researcher to model only selected large blood vessels individually and neglect the others. There were several attempts in the past to model large blood vessels, including the carotid arteries and jugular veins in the neck, during brain hypothermia (Zhu 2000; Bommadevera and Zhu 2002; Eginton 2007; Wang and Zhu 2007). In those studies, temperature decay along the large arteries was used to evaluate whether various techniques could induce sufficient cooling to the arterial blood that supplies the brain. Owing to the complicated vascular structure, it is difficult to model effects of individual blood vessels in the brain region. Van Leeuwen et al. (Van Leeuwen et al. 2000) predicted temperature contours based on detailed vasculature in the brain and found that they agree very well with those predicted by the Pennes model. This may be mainly due to the large rate and diffuse pattern of blood perfusion in the brain tissue, for which the Pennes bioheat equation is a preferred approach. Advanced computational methods also allow researchers to model the head with a more realistic geometry than a simple hemispherical structure. The head geometry is usually based on magnetic resonance images (MRIs), which can be imported into grid-generating algorithms and then interfaced with numerical software for temperature simulation (Van Leeuwen et al. 2000; Dennis et al. 2003; Ley and Bayazitoglu 2003). However, the results obtained from the more complicated head models to date are very similar to those predicted by a simple, layered head geometry.

Most of the mathematical simulations are aimed at providing detailed temperature contours in a targeted tissue region, as well as predicting how long it takes to establish a steady state. These help determine a cooling rate at specific locations. Those simulation results are essential in evaluating the thermal feasibility of these cooling methods. Early studies simulated a temperature field inside the brain hemisphere with cooling on the scalp by a helmet (Van Leeuwen et al. 2000; Zhu and Diao 2001; Diao et al. 2003). It has been shown that cooling penetration from the scalp to the brain tissue is only limited to less than 8 mm unless the brain region is ischemic. Therefore, cooling in the brain white matter is not feasible. Later mathematical simulations were carried out based on image scan-generated realistic head models due to advancement in computational resources in the 2000s (Dennis et al. 2003; Janssen et al. 2005; Ley and Bayazitoglu 2003, 2004). Interstitial cooling on the common carotid artery was simulated to demonstrate the importance of the length of the cooling device to achieve desirable temperature reduction in the brain (Wang and Zhu 2007; Wang et al. 2008). It has been shown that cooling is limited when the blood flow rate of the common carotid artery is high. The neck collar has been proposed to cool the brain tissue during the summer time. Although it may provide cold sensation to the neck tissue, simulation of the temperature field in the neck and head region suggests that less than 0.3 °C of blood temperature reduction would be achieved using a cold neck collar (Eginton 2007). Cooling on the torso of patients suffering spinal cord injury was proposed as a noninvasive approach to cool the spinal cord and CSF. Since CSF in the spinal cord is connected with that in the head, simulations were performed to predict temperature reduction in the spinal cord tissue and possible hypothermia in the brain tissue, from the pulsation of the cooled CSF (Smith and Zhu 2010a, b).

Theoretical models were developed before the implementation of endovascular infusion of cold saline into the common carotid artery. All the computational models simulate infusion of cold saline with an infusion rate varying from 7.5 to 50 mL/min (Konstas et al. 2007; Neimark et al. 2007a, b, 2008, 2013; Slotboom et al. 2004, Slotboom 2007). It has demonstrated a very fast temperature drop of the brain to 34 °C within 10 min. Those simulation predictions can be viewed as the upper limit of temperature reduction since they fail to address thermal resistance of the catheter as well as loss of cooling to the surrounding regions. Similarly, simulations were performed to determine the effects of intravenous infusion of saline in chilled or ice slurry on fever control in brain injury patients. The proposed approach would result in a maximal cooling rate of 0.45 °C/h when infusing an ice slurry saline at a maximal rate of 450 mL/h (Rosengart et al. 2009, Zhu et al. 2009).

Most importantly, mathematical simulation has also been used to extrapolate experimental measurements of cooling extent to a wide variety of situations. One example is during the early stages of designing and implementing an intraparenchymal cooling device (Zhu and Rosengart 2008). The cooling device consists of a 2.5-cm long, dual-lumen stainless steel shaft with cold water circulating from a slurry ice bath to the device. The diameter of the device is approximately 2.7 mm. Experiments to measure temperature on the cooling device surface and a brain location 6.4 mm from the probe surface were performed on a primate animal model with the cooling device inserted into the parenchymal region. Once validated with the animal experiment, the theoretical model was used to predict the performance of the cooling device in a human brain. The results were also extrapolated to show cooling penetration in ischemic brain regions, where the local blood perfusion rate is much lower than that of a healthy brain. An approximate relationship was established as the cooling penetration depth is inversely proportional to the square root of the local blood perfusion rate of the brain tissue. The relationship suggests that the cooling penetration depth doubles when the local blood perfusion rate decreases to 25% of its normal level.

One of the major challenges in mathematic simulation of cooling and rewarming processes is assessment of local blood perfusion variations in response to cooling. In most mathematical simulations, blood perfusion is usually considered as a constant during cooling or is considered to be decreasing as a function of the local tissue temperature following the Q_{10} law (Bering 1961; Hoffman et al. 1982). The predicted temperature distribution in the brain is in agreement with the observed temperature field during steady state. However, there is a large discrepancy between theoretical and experimental data on how long it takes to establish a steady state during cooling and rewarming.

In an experimental study performed on a rat model during head surface cooling, thermocouples were inserted into the brain to monitor the temperature reduction and recovery (Diao and Zhu 2006). The measured characteristic time to establish a steady state varied from 5 min to longer than 40 min, whereas the mathematical simulation predicted a much smaller characteristic time (less than 5 min). This is due to the small size of the rat head and constant blood flow rate during the simulation. These results imply that the change of the blood perfusion rate in tissue contributes significantly to the characteristic transient time constant. A similar conclusion can be drawn from other animal models (Zhu and Rosengart 2008) and alternative cooling approaches (Wang et al. 2008).

The Q_{10} law represents a linear relationship between $1/T$, where T is tissue temperature, and log $CMRO_2$ (the cerebral metabolic rate of oxygen consumption). This law states that the metabolic rate decreases by a factor of Q_{10} with each 10 °C reduction in temperature. Q_{10} is a parameter, which has been reported (Hoffman et al. 1982) to vary between 2 and 4.4 based on correlations with experimental measurements. Based on a Q_{10} value of 2, it has been calculated that hypothermia decreases cerebral metabolic rate by an average value of 7% for the first 1 °C reduction in temperature, whereas metabolic rate is reduced to one half of the normal value when

the temperature reduction is by 10 °C. During normal conditions, cerebral blood flow (CBF) may follow the same pattern as that of cerebral metabolism due to their direct coupling. Several temperature simulations have incorporated the Q_{10} law (Dennis et al. 2003; Diao et al. 2003; Janssen et al. 2005; Zhu and Rosengart 2008). Because the local blood perfusion keeps decreasing with the temperature during cooling, the temperature field from the cold surface can penetrate more readily into the deep brain region, which, in turn, would further trigger perfusion reduction. If the temperature dependence of perfusion progresses during cooling, the result would be an extended time to reach a steady state.

During cerebral ischemia or head injury, not only the Q_{10} value may change but also CBF may be decoupled from metabolism. A number of studies have examined the variation of CBF during systemic hypothermia. Using the radioactive microsphere technique, Busija and Leffler (Busija and Leffler 1987) measured CBF in anesthetized newborn pigs. They concluded that systemic hypothermia reduced CBF secondary to the depression of cerebral metabolic rate. Verhaegen et al. (Verhaegen et al. 1993) measured the cortical blood flow in anesthetized rats using a laser Doppler flowmeter (LDF) and found that CBF was reduced during moderate hypothermia. Okubo et al. (Okubo et al. 2001) examined the effect of systemic cooling on cerebral metabolism and regional CBF variation in newborn piglets. They measured the regional CBF with colored microspheres and demonstrated that a reduction of cerebral cortex temperature resulted in a decrease in the blood flow in all brain regions. Unlike many experimental studies on CBF response during systemic cooling, there have been only few studies on the effect of selective brain cooling on CBF, and the various results are inconsistent. Laptook et al. (2001) examined the differences of CBF in newborn swine during selective brain cooling versus whole-body cooling and illustrated that the global CBF was reduced during both whole-body cooling and selective brain cooling. Ibayashi et al. (2000) demonstrated that the regional CBF decreased when selective brain cooling was implemented on rats. However, a previous study (Kuluz et al. 1993) using the LDF technique showed that the cortical CBF in normal, lightly anesthetized rats increased during selective brain cooling. In a study, the blood flow rate of the common carotid artery was measured continuously using an LDF applied in an in vivo setting to study the transient behavior of temperature and blood flow responses during selective brain cooling and rewarming using a cooling helmet (Diao and Zhu 2006). Very similar transient profiles of brain temperature and blood flow rate of the common carotid artery, as characterized by their characteristic time constants, were observed in rats (Diao and Zhu 2006). Nonetheless, more rigorous experimental verification is needed to establish the correlation between the CBF and blood flow rate of the common carotid artery. The accuracy of mathematical simulations can continue to be questionable unless the simulations can be verified with experimental data that simultaneously monitors the local blood perfusion rate during cooling and rewarming.

7 Concluding Remarks

Hypothermia's efficacy in improving treatment outcomes in patients suffering from cell and tissue damage caused by ischemia is still ongoing despite more than 80 years of animal experiments and clinical practice. This method can be applied to a wide variety of conditions, including spinal cord injury, traumatic brain injury, stroke, cardiopulmonary surgery, and cardiac arrest. Overall, an accumulating body of clinical evidence along with several decades of animal research and mathematical simulations has documented that the efficacy of hypothermia is dependent on achieving a reduced temperature in the target tissue before or soon following the injury-precipitating event. Mild hypothermia with a several degrees Celsius temperature reduction is as effective as modest or deep hypothermia in resulting in therapeutic benefits without introducing collateral/systemic complications. It is widely documented that rewarming rate must be controlled to be lower

than 0.5 °C/h in order to avoid mismatch between local blood perfusion and metabolism. In the past several decades, many different cooling methods and devices have been designed, tested, and used in medical treatments with mixed results. Accurately and predictably designing treatment protocols to achieve specific cooling outcomes requires collaboration among engineers, researchers, and clinicians. Although the problem is quite challenging, it presents a major opportunity for bioengineers to design new methods and devices that can quickly and safely produce hypothermia in targeted tissue regions without interfering with routine medical treatment.

References

Abou-Chebl A, Sung G, Barbut D, Torbey M (2011) Local brain temperature reduction through intrnasal cooling with the RhinoChill device: preliminary safety data in brain-injured patients. Stroke 42:2164–2169

Andrews PJ, Harris B, Murray GD (2005) Randomized controlled trial of effects of the airflow through the upper respiratory tract of intubated brain-injured patients on brain temperature and selective brain cooling. Br J Anaesth 94:330–335

Andrews PJ, Sinclair HL, Rodriguez A, Harris BA, Battison CG, Rhodes JK et al (2015) Hypothermia for intracranial hypertension after traumatic brain injury. N Engl J Med 373:2403–2412

Bachet J, Guilmet D (2002) Brain protection during surgery of the aortic arch. J Card Surg 17(2):115–124

Barone FC, Feuerstein GZ, White RF (1997) Brain cooling during transient focal ischemia provides complete neuroprotection. Neurosci Biobehav Rev 21:31–44

Batchelor PE, Kerr NF, Gatt AM, Aleksoska E, Cox SF, Ghasem-Zadeh A, Wills TE, Howells DW (2010) Hypothermia prior to decompression: buying time for treatment of acute spinal cord injury. J Neurotrauma 27:1357–1368

Belliard G, Catez E, Charron C et al (2007) Efficacy of therapeutic hypothermia after out-of-hospital cardiac arrest due to ventricular fibrillation. Resuscitation 75:252–259

Bernard SA, Gray TW, Buist MD, Jones BM, Silverster W et al (2002) Treatment of comatose survivors of out-of-hospital cardiac arrest with induced hypothermia. N Engl J Med 346:557–563

Bernard S, Rosalion A (2008) Therapeutic hypothermia induced during cardiopulmonary resuscitation using large-volume, ice-cold intravenous fluid. Resuscitation 76:311–313

Bering E (1961) Effect of body temperature change on cerebral oxygen consumption of the intact monkey. Am J Phys 200:417–419

Berrouschot J, Sterker M, Bettin S, Koster J, Schneider D (1998) Mortality of space-occupying ("malignant") middle cerebral artery infarction under conservative intensive care. Intensive Care Med 24:620–623

Bigelow WG, Callaghan JC, Hopps VA (1950) General hypothermia for experimental intracardiac surgery: use of artificial pacemaker for cardiac standstill and cardiac rewarming in general hypothermia. Ann Surg 132:531–543

Bohn DJ, Biggar WD, Smith CR, Conn AW, Baker GA (1986) Influence of hypothermia, barbiturate therapy, and intracranial pressure monitoring on morbidity and mortality after near-drowning. Crit Care Med 14:529–534

Bommadevera M, Zhu L (2002) Temperature difference between the body core and the arterial blood supplied to the brain during hyperthermia or hypothermia in humans. Biomech Model Mechanobiol 1(2):137–149

Bricolo A, Ore GD, da Pian R, Faccioli F (1976) Local cooling in spinal cord injury. Surg Neurol 6:101–106

Busija DW, Leffler CW (1987) Hypothermia reduces cerebral metabolic rate and cerebral blood flow in newborn pigs. Am J Phys 253:H869–H873

Busto R, Dietrich WD, Globus MY-T, Valdes I, Scheinberg P, Ginsberg MD (1987) Small differences in intraischemic brain temperature critically determine the extent of ischemic neuronal injury. J Cereb Blood Flow Metab 7:729–738

Cappuccino A, Bisson LJ, Carpenter B, Marzo J, Dietrich WD, Cappuccino H (2010) The use of systemic hypothermia for the treatment of an acute cervical spinal cord injury in a professional football player. Spine 35:E57–E62

Chambers S (1999) Induced hypothermia for head injury. Nurs Crit Care 4:112–116

Carney N, Totten AM, O'Reilley C, Ullman JS, Havryluk GW Bell MJ et al (2017) Guidelines for the management of severe traumatic brain injury, 4th edition. Neurosurgery 80(1):6–15

Cheriyan T, Yoshihara H, Maier SP II, Ryan DJ, Weinreb JH, Errico TJ (2014) Neuroprotective effect of prophylactic intrathecal methylprednisolone in spinal cord injury in rat model. Spine J 14(11):S86–S87

Choi JH, Bateman BT, Mangla S, Marshall RS, Probhakaran S, Chong J et al (2006) Endovascular recanalization therapy in acute ischemic stroke. Stroke 37:419–424

Choi JH, Marshall RS, Neimark MA, Konstas AA, Lin E, Chiang YT et al (2010) Selective brain cooling with endovascular intracarotid infusion of cold saline: a pilot feasibility study. Am J Neuroradiol 31:928–934

Clifton GL, Allen S, Barrodale P, Plenger P, Berry J et al (1993) A phase II study of moderate hypothermia in severe brain injury. J Neurotrauma 10:263–271

Clifton GL, Miller ER, Choi SC, Levin HS, McCauley S et al (2001) Lack of effect of induction of hypothermia after acute brain injury. N Engl J Med 344:556–563

Clifton GL, Miller ER, Choi SC, Levin HS, McCauley S et al (2002) Hypothermia on admission in patients with severe brain injury. J Neurotrauma 19:293–301

Clifton GL, Valadka A, al ZD (2011) Very early hypothermia induction in patients with severe brain injury (the National Acute Brain Injury Study: hypothermia II): a randomised trial. Lancet Neurol 10(2):131–139

Colbourne F, Corbett D (1995) Delayed postischemic hypothermia: a six month survival study using behavioral and histological assessments of neuroprotection. J Neurosci 15:7250–7260

Covaciu L, Weis J, Bengtsson C, Allers M, Lunderquist A, Ahistrom H et al (2011) Brain temperature in volunteers subjected to intranasal cooling. Intensive Care Med 37:1277–1284

Dae MW, Gao DW, Ursell PC, Stillson CA, Sessler DI (2003) Safety and efficacy of endovascular cooling and rewarming for induction and reversal of hypothermia in human-sized pigs. Stroke 34:734–738

de Georgia MA, Krieger DW, Abou-Chebl A, Devlin TG, Jauss M et al (2004) Cooling for acute ischemic brain damage (COOL AID) a feasibility trial of endovascular cooling. Neurology 63:312–317

Dennis BH, Eberhart RC, Dulikravich GS, Radons SW (2003) Finite element simulation of cooling of realistic 3-D human head and neck. J Biomech Eng 125: 832–840

Dididze M, Green BA, Dietrich WD, Vanni S, Wang MY, Levi AD (2013) Systemic hypothermia in acute cervical spinal cord injury: a case-controlled study. Spinal Cord 51:395–400

Diao C, Zhu L, Wang H (2003) Cooling and rewarming for brain ischemia or injury: theoretical analysis. Ann Biomed Eng 31:346–353

Diao C, Zhu L (2006) Temperature distribution and blood flow response in rat brain during selective brain cooling. Med Phys 33:2565–2573

Dixon SR, Whitbourn RJ, Dae MW, Grube E, Sherman W et al (2002) Induction of mild systemic hypothermia with endovascular cooling during primary percutaneous coronary intervention for acute myocardial infarction. J Am Coll Cardiol 40:1928–1934

Dietrich WD, Prado R, Halley M, Watson BD (1993) Microvascular and neuronal consequences of common carotid artery thrombosis and platelet embolization in rats. J Neuropathol Exp Neurol 52(4):351–360

Ding Y, Li J, Luan X, Lai Q, McAllister JP et al (2004) Local saline infusion into ischemic territory induces regional brain cooling and neuroprotection in rats with transient middle cerebral artery occlusion. Neurosurgery 54:956–965

Dirnagl U, Iadecola C, Moskowitz MA (1999) Pathobiology of ischemia stroke: an integrated view. Trends Neurosci 22:391–397

Doufas AG, Akca O, Barry A, Petrusca DA, Suleman M et al (2002) Initial experience with a novel heat-exchanging catheter in neurosurgical patients. Anesth Analg 95:1752–1756

Drake CG, Jory TA (1962) Hypothermia in the treatment of critical head injury. Can Med Assoc J 87:887–891

Eginton ML (2007) Evaluation of the effectiveness of a commercial cooling collar in reducing body temperature during heat stress: theoretical modeling of body temperature distribution. Master's thesis. University of Maryland, Baltimore County

Els T, Oehm E, Voigt S, Klisch J, Hetzel A, Kassubek J (2006) Safety and therapeutical benefit of hemicraniectomy combined with mild hypothermia in comparison with hemicraniectomy alone in patients with malignant ischemic stroke. Cerebrovasc Dis 21:79–85

Enomoto S, Hindman BJ, Dexter F, Smith T, Cutkomp J (1996) Rapid rewarming causes an increase in the cerebral metabolic rate for oxygen that is temporarily unmatched by cerebral blood flow. Anesthesiology 84:1392–1400

Esposito E, Ebner M, Ziemann U, Poli S (2014) In cold blood: intraarteral cold infusions for selective brain cooling in stroke. J Cereb Blood Flow Metab 34: 743–752

Fay T (1945) Observations on generalized refrigeration in cases of severe cerebral trauma. Assoc Res Nerv Ment Dis Proc 4:611–619

Ferreira I, Schutte M, Oosterloo E et al (2009) Therapeutic hypothermia improves outcome after out-of-hospital cardiac arrest. Neth Heart J 17:378–384

Frank SM, Beattie C, Christopherson R et al (1993) Unintentional hypothermia is associated with postoperative myocardial ischemia. Anesthesiology 78:468–476

Fukuda T (2016) Targeted temperature management for adult out-of-hospital cardiac arrest: current concepts and clinical applications. J Intensive Care 4(1–8):30

Gal R, Cundrle I, Zimova I, Smrcka M (2002) Mild hypothermia therapy for patients with severe brain injury. Clin Neurol Neurosurg 104:318–321

Georgiadia D, Schwarz S, Kollmar R, Schwab S (2001) Endovascular cooling for moderate hypothermia in patients with acute stroke: first results of a novel approach. Stroke 32:2550–2553

Gillinov AM, Bator JM, Zehr KJ, Redmond JM, Burch RM et al (1993) Neutrophil adhesion molecule expression during cardiopulmonary bypass with bubble and membrane oxygenators. Ann Thorac Surg 56(4): 847–853

Gong M, Ma W-G, Guan X-L, Wang L-F, Li J-C, Lan F, Sun L-Z, Zhang H-J (2016) Moderate hypothermic circulatory arrest in total arch repair for acute type a aortic dissection: clinical safety and efficacy. J Thorac Dis 8(5):925–933

Grahn DA, Brock-Utne JG, Watenpaugh DE, Heller HC (1998) Recovery from mild hypothermia can be accelerated by mechanically distending blood vessels in the hand. J Appl Physiol 85:1643–1648

Grahn DA, Cao VH, Heller HC (2005) Heat extraction through the palm of one hand improves aerobic exercise endurance in a hot environment. J Appl Physiol 99:972–978

Grahn D, Murray JLS, Watenpaugh DE, Heller HC (2008) Cooling via one hand improves physical performance in heat-sensitive individuals with Multiple Sclerosis: A preliminary study. BMC Neurol 8:14

Grulova I, Slovinska L, Nagyova M, Cizek M, Cizkova D (2013) The effect of hypothermia on sensory-motor function and tissue sparing after spinal cord injury. Spine J 13:1881–1891

Gunn AJ, Gunn TR (1998) The "pharmacology" of neuronal rescue with cerebral hypothermia. Early Hum Dev 53:19–35

Guo J, Wang Y, Zhu J, Cao J, Chen Z, Li Z, Qian X (2014) Right axillary and femoral artery perfusion with mild hypothermia for aortic arch replacement. J Cardiothorac Surg 9(1–6):94

Gutsche JT, Feinman J, Silvay G, Patel PA, Ghadimi K, Landoni G, Yue Y, augoustides JGT (2014) Practice variations in the conduct of hypothermic circulatory arrest for adult aortic arch repair: focus on an emerging European paradigm. Heart Lung Vessel 6(1):43–51

Ha KY, Kim YH (2008) Neuroprotective effect of moderate epidural hypothermia after spinal cord injury in rats. Spine 33:2059–2065

Hacke W, Schwab S, Horn M, Spranger M, De Georgia M, von Kummer R (1996) "Malignant" middle cerebral artery territory infarction: clinical course and prognostic signs. Arch Neurol 53:309–315

Hansebout RR, Hansebout CR (2014) Local cooling for traumatic spinal cord injury: outcomes in 20 patients and review of the literature. J Neurosurg Spine 20(5):550–561

Harris BA, Andrews PJ, Murray GD (2007) Enhanced upper respiratory tract airflow and head fanning reduce brain temperature in brain-injured, mechanically ventilated patients: a randomized, crossover, factorial trial. Br J Anaesth 98:93–99

Hemmen TM, Raman R, Guluma KZ, Meyer BC, Gomes JA, Cruz-Flores S et al (2010) Intravenous thrombolysis plus hypothermia for acute treatment of ischemic stroke(ICTuS-L): flinal results. Stroke 41:2265–2270

Hoffman W, Miletich DJ, Albrecht R (1982) Differential cerebral hypothermia. Cryobiology 19:392–401

Holzer M, Cerchiari E, Martens P, Roine R, Sterz F et al (2002) Mild therapeutic hypothermia to improve the neurologic outcome after cardiac arrest. N Engl J Med 346:549–556

Holzer M, Behringer W, Janata A, Bayegan K, Schima H et al (2005) Extracorporeal venovenous cooling for induction of mild hypothermia in human-sized swine. Crit Care Med 33:1346–1350

Hong JM, Lee JS, Song JH, Jeong HS, Choi HA et al (2014) Therapeutic hypothermia after recanalization in patients with acute ischemic stroke. Stroke 45:134–140

Hutchison JS, Ward RE, Lacroix J, Hébert PC, Barnes MA, Bohn DJ, Dirks PB, Doucette S, Fergusson D, Gottesman R, Joffe AR, Kirpalani HM, Meyer PG, Morris KP, Moher D, Singh RN, Skippen PW, for the Hypothermia Pediatric Head Injury Trial Investigators and the Canadian Critical Care Trials Group (2008) Hypothermia therapy after traumatic brain injury in children. N Engl J Med 358:2447–2456

Ibayashi S, Kakano K, Ooboshi H, Kitazono T (2000) Effect of selective brain hypothermia on regional cerebral blood flow and tissue metabolism using brain thermo-regulator in spontaneously hypertensive rats. Neurochem Res 25:369–375

Inderbitzen B, Yon S, Lasheras J, Dobak J, Perl J, Steinberg GK (2002) Safety and performance of a novel intravascular catheter for inducing and reversal of hypothermia in a porcine model. Neurosurgery 50: 364–370

Jamieson SW, Kapelanski DP, Sakakibara N, Manecke GR, Thistlethwaite PA et al (2003) Coronary endarterectomy: experience and lessons learned in 1500 cases. Ann Thorac Surg 76(5):1457–1462

Janssen FEM, van Leeuwen GMJ, van Steenhoven AA (2005) Modeling of temperature and perfusion during scalp cooling. Phys Med Biol 50(17): 4065–4073

Jiang JY, Yu MK, Zhu C (2000) Effect of long-term mild hypothermia therapy in patients with severe traumatic brain injury: 1-year follow-up review of 87 cases. J Neurosurg 93:546–549

Kabat H (1940) The greater resistance of very young animals to arrest of the brain circulation. Am J Phys 122:588–599

Kammersgaard LP, Rasmussen BH, Jorgensen HS, Reith J, Weber U, Olsen TS (2000) Feasibility and safety of inducing modest hypothermia in awake patients with acute stroke through surface cooling: a case-control study. Stroke 31:2251–2256

Kasner SE, Wein T, Piryawat P, Villar-Cordove CE, Chalela JA et al (2002) Acetaminophen for altering body temperature in acute stroke: a randomized clinical trial. Editorial comment: a randomized clinical trial. Stroke 33:130–135

Kirkpatrick AW, Chun R, Brown R, Simons RK (1999) Hypothermia and the trauma patient. Can J Surg 42:333–343

Tisherman SA, Rodriguez A, Safar P (1999) Therapeutic hypothermia in traumatology. Surg Clin North Am 79:1269–1289

Kollmar R, Schellinger PD, Steigleder T, Kohrmann M, Schwab S (2009) Ice-cold saline for the induction of mild hypothermia in patients with acute ischemic stroke: a pilot study. Stroke 40:1907–1909

Konstas AA, Neimark MA, Laine AF, Pile-Spellman J (2007) A theoretical model of selective cooling using intracarotid cold saline infusion in the human brain. J Appl Physiol 102:1329–1340

Kouchoukos NT, Daily BB, Wareing TH, Murphy SF (1994) Hypothermic circulatory arrest for cerebral protection during combined carotid and cardiac surgery in patients with bilateral carotid artery disease. Ann Surg 219(6):699–705

Krieger DW, De Georgia MA, Abou-Chebl A, Andrefsky JC, Sila CA et al (2001) Cooling for acute ischemic brain damage (COOL AID): an open pilot study of induced hypothermia in acute ischemic stroke. Stroke 32:1841–1854

Kuluz JW, Prado R, Chang J, Ginsberg MD, Schleien CL, Busto R (1993) Selective brain cooling increases cortical cerebral blood flow in rats. Am J Phys 265:H824–H827

Kurasako T, Zhan L, Pulsinelli WA, Nowak TS (2003) Transient cooling during early reperfusion attenuates delayed edema and infarct progression in the spontaneously hypertensive rat. Distribution and time course of regional brain temperature change in a model of postischemic hypothermic protection. J Cereb Blood Flow Metab 27:1919–1930

Laptook AR, Shalak L, Corbett RJT (2001) Differences in brain temperature and cerebral blood flow during selective head vs whole-body cooling. Pediatrics 108(5):1103–1110

Lauren I, Adrie C, vinsonneau C et al (2005) High-volume hemofiltration after out-of-hospital cardiac arrest: a randomized study. J Am Coll Cardiol 46:432–437

Lazorthes G, Campan L (1958) Hypothermia in the treatment of craniocerebral traumatism. J Neurosurg 15:162–167

Levi AD, Green BA, Wang MY, Dietrich WD, Brindle T, Vanni S et al (2009) Clinical application of modest intravascular hypothermia after spinal cord injury. J Neurotrauma 26:407–415

Levi AD, Casella G, Green BA, Dietrich WD, Vanni S, Jagid J et al (2010) Clinical outcomes using modest intrvascular hypothermia after acute cervical spinal cord injury. Neurosurgey 66:670–677

Ley O, Bayazitoglu Y (2003) Effect of physiology on the temperature distribution of a layered head with external convection. Int J Heat Mass Transf 46(17): 3233–3241

Ley O, Bayazitoglu Y (2004) Temperature distribution in a realistic human head during selective and whole body cooling and during circulatory arrest. Proc. IMECE, IMECE2004–60733, Nov. 13–19. Anaheim, California

Li P, Yang C (2014) Moderate hypothermia treatment in adult patients with severe traumatic brain injury: a meta-analysis. Brain Inj 28:1036–1041

Liu WG, Qiu WS, Zhang Y, Wang WM, Lu F, Yang XF (2006) Effects of selective brain cooling in patients with severe traumatic brain injury: a preliminary study. J Int Med Res 34(1):58–64

Lo TP Jr, Cho KS, Garg MS, Lynch MP, Marcillo AE, Koivisto DL, Stagg M, Abril RM, Patel S, Dietrich WD (2009) Systemic hypothermia improves histological and functional outcome after cervical spinal cord contusion in rats. J Comp Neurol 514:433–448

Mack WJ, Huang J, Winfree C, Kim G, Oppermann M et al (2003) Ultrarapid, convection-enhanced intravascular hypothermia: a feasibility study in nonhuman primate stroke. Stroke 34:1994–1999

Maekawa T, Yamashita S, Nagao S, Hayashi N, Ohashi Y, Brain-Hypothermia Study Group (2015) Prolonged mild therapeutic hypothermia versus fever control with tight hemodynamic monitoring and slow rewarming in patients with severe traumatic brain injury: a randomized controlled trial. J Neurotrauma 32:422–429

Markgraf CG, Clifton GL, Moody MR (2001) Treatment window for hypothermia in brain injury. J Neurosurg 95:979–983

Maier CM, Sun GH, Cheng D, Yenari MA, Chan PH, Steinberg GK (2002) Effects of mild hypothermia on superoxide anion production, superoxide dismutase expression, and activity following transient focal cerebral ischemia. Neurobiol Dis 11:28–42

Marion DW, Leonov Y, Ginsberg M, Katz LM, Kochanek PM et al (1996) Resuscitative hypothermia. Crit Care Med 24(suppl):S81–S89

Marion DW, Penrod LE, Kelsey SF, Obrist WD, Kochanek PM et al (1997) Treatment of traumatic brain injury with moderate hypothermia. N Engl J Med 336:540–546

Maybhate A, Hu C, Bazley FA, Yu Q, Thakor NV, Kerr CL All AH (2012) Potential long-term benefits of acute hypothermia after spinal cord injury: assessments with somatosensory-evoked potentials. Crit Care Med 40:573–579

McIntyre LA, Fergusson DA, Hebert PC, Moher D, Hutchison JS (2003) Prolonged therapeutic hypothermia after traumatic brain injury in adults: a systematic review. JAMA 289:2992–2999

Meacham WF, McPherson WF (1973) Local hypothermia in the treatment of acute injuries of the spinal cord. South Med J 66:95–97

Metz C, Holzschuh M, Bein T, Woertgen C, Frey A et al (1996) Moderate hypothermia in patients with severe head injury: cerebral and extracerebral effects. J Neurosurg 85:533–541

Mellergard P, Nordstrom C, Christensson M (1990) A method for monitoring intracerebral temperature in neurosurgical patients. Neurosurgery 27:654–657

Michenfelder J (1988) Protecting the brain. In: Michenfelder J (ed) Anesthesia and the brain. Clinical, functional, metabolic and vascular correlates, 1st edn. Churchill Livingstone, USA, pp 181–193

Miller JA (1949) Factors in neonatal resistance to anoxia. I. Temperature and survival of newborn Guinea pigs under anoxia. Science 110:113–114

Miller JH (1993) Partial replacement of an infected arterial graft by a new prosthetic polytetrafluoroethylene segment: a new therapeutic option. J Vasc Surg 17(3):546–558

Moomiaie RM, Gould G, Solomon D, Simmons J, Kim J, Botta D et al (2012) Novel intracranial brain cooling catheter to mitigate brain injuries. J Neurointerv Surg 4:130–133

Morino T, Ogata T, Takeba J, Yamamoto H (2008) Microglia inhibition is a target of mild hypothermic treatment after the spinal cord injury. Spinal Cord 46: 425–431

Morikawa E, Ginsberg MD, Dietrich WD, Duncan RC, Kraydieh S et al (1992) The significance of brain temperature in focal cerebral ischemia: histopathological consequences of middle cerebral artery occlusion in the rat. J Cereb Blood Flow Metab 12(3):380–389

Mouritzen CV, Anderson MN (1966) Mechanisms of ventricular fibrillation during hypothermia: relative change in myocardial refractory period and conduction velocity. J Thorac Cardiovasc Surg 51:579–584

Moyer DJ, Welsh FA, Zager EL (1992) Spontaneous cerebral hypothermia diminishes focal infarction in rat brain. Stroke 23(12):1812–1816

Negrin J Jr (1973) Spinal cord hypothermia in the neurosurgical management of the acute and chronic posttraumatic paraplegic patient. Paraplegia 10:336–343

Neimark MA, Konstas AA, Choi JH, Laine AF, Pile-Spellman J (2007a) Local control of temperature in a theoretical human model of selective brain cooling. Conf Proc IEEE Eng Med Biol Soc 2007:6349–6352

Neimark MA, Konstas AA, Laine AF, Pile-Spellman J (2007b) Integration of jugular venous return and circle of Willis in a theoretical human model of selective brain cooling. J Appl Physiol 103:1837–1847

Neimark MA, Konstas A, Choi JH, Laine AF, Pile-Spellman J (2008) Brain cooling maintenance with cooling cap following induction with intracarotid cold saline infusion: a quantitative model. J Theor Biol 253(2):333–344

Neimark MA, Konstas AA, Lee L, Laine AF, Pile-Spellman J, Choi J (2013) Brain temperature changes during selective cooling with endovascular intracarotid Intraarterial cold saline infusion: simulation using human data fitted with an integrated mathematical model. J Neurointerv Sur 5:165–171

Nielsen N, Wetterslev J, Cronberg T, Erlinge D, Gasche Y, Hassager C, Horn J, Hovdenes J, Kjaergaard J, Kuiper M, Pellis T, Stammet P, Wanscher M, Wise MP, Aneman A, Al-Subaie N, Boesgaard S, Bro-Jeppesen J, Brunetti I, Bugge JF, Hingston CD, Juffermans NP, Koopmans M, Kober L, Langorgen J, Lilja G, Moller JE, Rundgren M, Rylander C, Smid O, Werer C, Winkel P, Friberg H, Investigators TTMT (2013) Targeted temperature management at 33 degrees C versus 36 degrees C after cardiac arrest. N Engl J Med 369:2197–2206

Nussmeier NA (2002) A review of risk factors for adverse neurologic outcome after cardiac surgery. J Extra Corpor Technol 34:4–10

Oddo M, Schaller MD, Feihl F, Ribordy V, Liaudet I (2006) From evidence to clinical practice: effective implementation of thrapeutic hypothermia to improve patient outcome after cardiac arrest. Crit Care 34: 1865–1873

Okubo K, Itoh S, Isobe K, Kusaka T, Nagano K et al (2001) Cerebral metabolism and regional blood flow during moderate systemic cooling in newborn piglets. Pediatr Int 43:496–501

Olsen TS, Weber UJ, Kammersgaard LP (2003) Therapeutic hypothermia for acute stroke. Lancet Neurol 2: 410–416

Pennes HH (1948) Analysis of tissue and arterial blood temperatures in the resting human forearm. J Appl Physiol 1:93–122

Peterson K, Carson S, Carney N (2008) Hypothermia treatment for traumatic brain injury: a systematic review and meta-analysis. J Neurotrauma 25:62–71

Petrovic M, Panic G, Jovelic A et al (2011) Therapeutic hypothermia and neurological outcom after cardiac arrest. Vojnosanit Pregl 68:495–499

Polderman KH, Rijnsburger ER, Peerdeman SM, Birbes AR (2005) Induction of hypothermia in patients with various types of neurologic injury with use of large volumes of ice-cold intrvenous fluid. Crit Care Med 33:2744–2751

Poli S, Purrucker J, Priglinger M, Diedler J, Sykora M, Popp E et al (2013) Induction of cooling with a passive head and neck cooling device: effects on brain temperature after stroke. Stroke 44:708–713

Puccio AM, Fischer MR, Jankowitz BT, Yonas H, Darby JM, Okonkwo DO (2009) Induced normothermia attenuates intracranial hypertension and reduces fever burden after severe rraumatic brain injury. Neurocrit Care 11(1):82–87

Purdy PD, Novakovic RL, Giles BP, Miller SL, Riegel MS (2013) Spinal cord hypothermia without systemic hypothermia. Am J Neuroradiol 34(1):252–256

Qiu W, Liu W, Shen H, Wang W, Zhang Z et al (2005) Therapeutic effect of mild hypothermia on severe traumatic head injury. Chin J Traumatol 8:27–32

Roach GW, Kanchuger M, Mangano CM, Newman M, Nussmeier N et al (1996) Adverse cerebral outcomes after coronary bypass surgery. Multicenter study of Perioperative Ischemia Research Group and the Ischemia Research and Education Foundation investigators. N Engl J Med 335:1857–1863

Rohrer MJ, Natale AM (1992) Effect of hypothermia on the coagulation cascade. Crit Care Med 20: 1402–1405

Rosengart AJ, Zhu L, Schappeler T, Goldenberg FD (2009) Fever control in hospitalized stroke patients using simple intravenous fluid regimens – a theoretical evaluation. J Clin Neurosci 16(1):51–55

Safar P, Kochanek PM (2001) Comments on "lack of effect of induction of hypothermia after acute brain injury". N Engl J Med 345:66

Saxena M, Young P, Pilcher D, Bailey M, Harrison D, Bellomo R et al (2015) Early temperature and mortality in critically ill patients with acute neurological diseases: trauma and stroke differ from infection. Intensive Care Med 41:823–832

Schenone AL, Cohen A, Patarroyo G, Harper L, Wang X, Shishehbor MH, Menon V, Duggal A (2016) Therapeutic hypothermia after cardiac arrest: a systematic review/meta-analysis exploring the impact of expanded criteria and targeted temperature. Resuscitation 108:102–110

Schwab S, Spranger M, Aschoff A, Steiner T, Hacke W (1997) Brain temperature monitoring and modulation in patients with severe MCA infarction. Neurology 48:762–767

Schwab S, Schwarz S, Aschoff A, Keller E, Hacke W (1998a) Moderate hypothermia and brain temperature in patients with severe middle cerebral artery infarction. Acta Neurochir 71(suppl):131–134

Schwab S, Schwarz S, Spranger M, Keller E, Bertram M, Hacke W (1998b) Moderate hypothermia in the treatment of patients with severe middle cerebral artery infarction. Stroke 29:2461–2466

Schwab S, Georgiadis D, Berrouschot J, Schellinger PD, Graffagnino C, Mayer SA (2001) Feasibility and safety of moderate hypothermia after massive hemispheric infarction. Stroke 32(9):2033–2035

Sedzimir CB (1959) Therapeutic hypothermia in cases of head injury. J Neurosurg 16:407–414
Selker RG (1971) Icewater irrigation of the spinal cord. Surg Forum 22:411–413
Shaefi S, Mittel AM, Hyam JA, Boone MD, Chn CC, Kasper EM (2016) Hypothermia for severe traumatic brain injury in adults: recent lessons from randomized controlled trials. Surg Neurol Int 103(1–11):7
Shankaran S, Laptook AR, Ehrenkranz RA, Tyson JE, McDonald SA et al (2005) Whole-body hypothermia for neonates with hypoxic–ischemic encephalopathy. N Engl J Med 353:1574–1584
Shibuya S, Miyamoto O, Janjua NA, Itano T, Mori S, Norimatsu H (2004) Post-traumatic moderate systemic hypothermia reduces TUNEL positive cells following spinal cord injury in rat. Spinal Cord 42:29–34
Shiozaki T, Sugimoto H, Taneda M, Yoshida H, Iwai A et al (1993) Effect of mild hypothermia on uncontrollable intracranial hypertension after severe head injury. J Neurosurg 79:363–368
Slotboom J, Kiefer C, Brekenfeld C, Ozdoba C, Remonda L, Nedeltchev K et al (2004) Locally induced hypothermia for treatment of acute ischaemic stroke: a physical feasibility study. Neuroradiology 46:923–934
Slotboom J (2007) Localized therapeutic hypothermia in the brain for the treatment of ischemic stroke. J Appl Physiol 102:1303–1304
Smith K, Zhu L (2010a) Theoretical evaluation of a simple cooling pad in inducing hypothermia in spinal cord following traumatic injury. Med Biol Eng Comput 48(2):167–175
Smith K, Zhu L (2010b) Brain hypothermia induced by cooled spinal fluid using a cooling pad: theoretical analyses. Med Biol Eng Comput 48(8): 783–789
Springborg JB, Springborg KK, Romner B (2013) First clinical experience with intranasal cooling for hyperthermia in brain-injured patients. Neurocrit Care 18:400–405
Steeves JD, Kramer K, Fawcett JW, Cragg J, Lammertse DP, Blight AR, Marion RJ, Ditunno JF Jr, Coleman WP, Geisler FH, Guest J, Jones L, Burns S, Schubert M, van Hedel HJ, Curt AEMSCI Study Group (2011) Extent of spontaneous motor recovery after traumatic cervical sensorimotor complete spinal cord injury. Spinal Cord 49:257–265
Sterz F, Safar P, Tisherman S, Radovsky A, Kuboyama K, Oku K (1991) Mild hypothermic cardiopulmonary resuscitation improves outcome after prolonged cardiac arrest in dogs. Crit Care Med 19(3):379–389
Stone JG, Young WL, Smith CR, Solomon RA, Wald A et al (1995) Do standard monitoring sites reflect true brain temperature when profound hypothermia is rapidly induced and reversed? Anesthesiology 82: 344–351
Strauch JT, Lauten A, Spielvogel D, Rinke S, Zhang N, Weisz D, Bodian CA, Griepp RB (2004) Mild hypothermia protects the spinal cord from ischemic injury in a chronic porcine model. Eur J Cardiothorac Surg 25:708–715
Tator CH (1972) Acute spinal cord injury: a review of recnet studies of treatment and pathophysiology. Can Med Assoc J 107:143–145
Thoresen M, Wyatt J (1997) Keeping a cool head, posthypoxic hypothermia—an old idea revisited. Acta Paediatr 86:1029–1033
Tripathy S, Whitehead CF (2011) Endovascular cooling for severe hyperthermia in cervical spine injury. Neurocrit Care 15:525–528
Vandam DV, Burnap TK (1959a) Hypothermia (part 1). N Engl J Med 261:546–553
Vandam DV, Burnap TK (1959b) Hypothermia (part 2). N Engl J Med 261:595–603
Vanden Hoek TL, Kasza KE, Beiser DG, Abella BS, Franklin JE et al (2004) Induced hypothermia by central venous infusion: saline ice slurry vs chilled saline. Crit Care Med 32:S425–S431
Van Der Worp HB, Sena ES, Donnan GA, Howells DW, Macleod MR (2007) Hypothermia in animal models of acute ischemic stroke: a systematic review and meta-analysis. Brain 130:3063–3074
Van Leeuwen GMJ, Hand J, Lagendijk JW, Azzopardi V, Edwards AD (2000) Numerical modeling of temperature distributions within the neonatal head. Pediatr Res 48:351–356
Verhaegen MJJ, Todd MM, Hindman BJ, Warner DS (1993) Cerebral autoregulation during moderate hypothermia in rats. Stroke 24:407–414
Virkkunen I, Yli-Hankala A, Silfvast T (2004) Induction of therapeutic hypothermia after cardiac arrest in prehospital patients using ice-cold Ringer's solution: a pilot study. Resuscitation 62(3):299–302
Wagner KR, Zuccarello M (2005) Local brain hypothermia for neuroprotection in stroke treatment and aneurysm repair. Neurol Res 27:238–245
Wang H, Olivero W, Lanzino G, Elkins W, Rose J, Honings D et al (2004) Rapid and selective cerebral hypothermia achieved using a cooling helmet. J Neurosurg 100:272–277
Wang J, Pearse DD (2015) Therapeutic hypothermia in spinal cord injury: the status of its use and open questions. Int J Mol Sci 16:16848–16879
Wang Y, Zhu L (2007) Selective brain hypothermia induced by an interstitial cooling device in human neck: theoretical analyses. Eur J Appl Physiol 101(1):31–40
Wang Y, Zhu L, Rosengart AJ (2008) Targeted brain hypothermia induced by an interstitial cooling device in the rat neck: experimental study and model validation. Int J Heat Mass Transfer 51:5662–5670
Wass CT, Lanier WL, Hofer RE, Scheithauer BW, Andrews AG (1995) Temperature changes of $\geq 1°C$ alter functional neurologic outcome and histopathology in a canine model of complete cerebral ischemia. Anesthesiology 83:325—335
Wass CT, Lanier WL (1996) Hypothermia-associated protection from ischemic brain injury: implications for patient management. Int Anesthesiol Clin 34(4):95–111
Wei G, Hartings JA, Tortella FC, Lu XM (2008) Extraluminal cooling of bilateral common carotid arteries

as a method to achieve selective brain cooling for neuroprotection. J Neurotrauma 25:549–560

Welsh FA, Sims RE, Harris VA (1990) Mild hypothermia prevents ischemic injury in gerbil hippocampus. J Cereb Blood Flow Metab 10:557–563

Xu L, Yenari MA, Steinberg GK, Giffard RG (2002) Mild hypothermia reduces apoptosis of mouse neurons in vitro early in the cascade. J Cereb Blood Flow Metab 22:21–28

Yenari MA, Onley D, Hedehus M, deCrespigny A, Sun GH et al (2000) Diffusion- and perfusion-weighted magnetic resonance imaging of focal cerebral ischemia and cortical spreading depression under conditions of mild hypothermia. Brain Res 885:208–219

Yoshitake A, Mori A, Shimizu H, Ueda T, Kabei N, Hachiya T, Okano H, Yozu R (2004) Use of an epidural cooling catheter with a closed countercurrent lumen to protect against ischemic spinal cord injury in pigs. J Thorac Cardiovasc Surg 134:1220–1226

Yu CG, Jimenez O, Marcillo AE, Weider B, Bangerter K, Dietrich WD, Castro S, Yezierski RP, (2000) Beneficial effects of modest systemic hypothermia on locomotor function and histopathological damage following contusion-induced spinal cord injury in rats. J Neurosurg 93:85–93

Zeiner A, Muellner M, Frossard M, Janata K, Behringer W et al (1996a) Mild therapeutic hypothermia to improve neurological outcome after cardiac arrest—a pilot study. Circulation 94:I9–I10

Zeiner A, Mullner M, Sterz F, Frossard M, Laggner A (1996b) Mild resuscitative therapeutic hypothermia after cardiac arrest and its influence on hemodynamic parameters. Crit Care Med 24:A115

Zhao QJ, Zhang XG, Wang LX (2011) Mild hypothermia therapy reduces blood glucose and lactate and improves neurologic outcomes in patients with severe traumatic brain injury. J Crit Care 26:311–315

Zhu L (2000) Theoretical evaluation of contributions of both radial heat conduction and countercurrent heat exchange in selective brain cooling in humans. Ann Biomed Eng 28:269–277

Zhu L, Diao C (2001) Theoretical simulation of temperature distribution in the brain during mild hypothermia treatment for brain injury. Med Biol Eng Comput 39:681–687

Zhu L, Rosengart AJ (2008) Cooling penetration into normal and injured brain via intraparenchymal brain cooling probe: theoretical analyses. Heat Trans Eng 29(3):284–294

Zhu L, Schappeler T, Cordero-Tumangday C, Rosengart AJ (2009) Thermal interactions between blood and tissue: development of a theoretical approach in predicting body temperature during blood cooling/rewarming. Adv Numer Heat Transfer 3:197–219

Biomechanical Changes of Tympanic Membrane to Blast Waves

Rong Z. Gan

Abstract

Eardrum or tympanic membrane (TM) is a multilayer soft tissue membrane located at the end of the ear canal to receive sound pressure and transport the sound into the middle ear and cochlea. Rupture of the TM is one of the most frequent injuries of the ear after blast exposure in military service members. The TM mechanical property changes induced by blast waves also affect progressive hearing loss in veterans. This chapter describes the biomechanical measurements and modeling of blast wave transduction through the ear and the TM mechanical property changes after blast exposure. The human TM rupture thresholds were determined with a relationship to blast wave direction. It is found that the sensitivity of TM stress change with respect to the pressure reaching on TM surface characterizes the mechanical damage of the TM in relation to blast waves. Mechanical properties of the human TM after exposure to blasts were measured using acoustic loading and laser Doppler vibrometry with the inverse problem-solving method. The complex modulus of the TM exposed to blast waves had significant reduction compared to normal tissue. The SEM images of post-blast TM showed obvious microstructural changes from the normal TM which indicate the tissue damage caused by blast exposures. This chapter provides important data on human TM damage and mechanical changes induced by blast overpressure waves.

1 Introduction

The eardrum or tympanic membrane is a soft tissue membrane separating the ear canal from the middle ear. The tympanic membrane (TM) plays an important role in transmission of sound pressure from the environment into mechanical vibration of the ossicular chain in the middle ear, which is transported into the inner ear or cochlea and then to the brain for hearing. Exposure to high-intensity sound or blast overpressure waves causes injuries to auditory system and results in acute hearing loss in military service members and the long-term hearing disabilities in veterans (Cave et al. 2007; Dougherty et al. 2013). The primary blast injury to the ear is induced by direct effect of blast overpressure waves upon the TM and middle ear ossicular chain. Rupture of the

R. Z. Gan (✉)
Biomedical Engineering Laboratory, School of Aerospace and Mechanical Engineering, University of Oklahoma, Norman, OK, USA
e-mail: rgan@ou.edu

B. M. Fu, N. T. Wright (eds.), *Molecular, Cellular, and Tissue Engineering of the Vascular System*, Advances in Experimental Medicine and Biology 1097,
https://doi.org/10.1007/978-3-319-96445-4_17

TM is one of the most frequent injuries of the ear and has been investigated in animals and humans with wide variability (Cho et al. 2013; Fausti et al. 2009).

The TM perforation induces the reduction of energy transfer efficiency and has been measured in human temporal bones (Voss et al. 2007; Gan et al. 2009), animals (Bigelow et al. 1996; Santa Maria et al. 2007), and clinical studies (Ahmad and Ramani 1979; Mehta et al. 2006). Gan et al. (2007, 2009) used a three-dimensional finite element (FE) model of the human ear including the external ear canal, middle ear, and uncoiled cochlea with two straight fluid channels separated by the basilar membrane to predict the perforation-induced change of middle ear function for sound transmission. The acoustic-structure-fluid coupled FE analysis was employed in the model to evaluate a complex combination of two sound conduction routes: the mechanical route through the ossicular chain and the acoustic route through the air in the middle ear cavity. Perforations created in the FE model were also produced in human cadaver ears or temporal bones to verify the FE model results by Gan et al. (2009). A good agreement between the model and experimental data indicated that the TM perforation mainly affects the middle ear transfer function at low frequencies for normal sound.

Blast overpressure is a high-intensity disturbance in the ambient air pressure that creates high-intensity sound (impulse) over 170 dB SPL. In addition to TM perforation or rupture, any damage induced by blast waves to the TM tissue would affect its mechanical properties and alter the normal performance of the TM for sound transmission. There are two basic types of experimental data which are used to assess the extent and nature of blast-induced damage to the TM: mechanical property changes and microstructural variations of the TM (Engles et al. 2017; Liang et al. 2017).

A recent study on chinchilla blast model by Gan et al. (2016) reported the relationships between the TM rupture threshold, the TM damage pattern, and the overpressure waveforms. The results demonstrated that the TM rupture threshold was closely related to overpressure waveforms at the entrance of the ear canal. The waveforms recorded under the shielded case had almost equal positive-negative pressure phases, while the waveforms recorded in the open field had the positive pressure only. The TM rupture threshold measured in the shielded case was much lower than that in the open field. These findings in animal blast model brought further research requests on identifying human TM damage after blast exposure and the TM rupture threshold in relation to blast overpressure level and wave direction.

The first part of this chapter reports our current study on measuring blast wave transmission through the human ear and the relationship between the TM damage and the incident blast wave direction. In addition to experimental tests in human cadaver ears, a 3D FE model of the human ear for blast simulation based on the model published by Gan et al. (2004, 2007) was developed to modeling blast overpressure transduction through the ear (Leckness 2016). The mechanisms of TM injury in relation to blast wave direction were investigated using this model. The study was completed in the Biomedical Engineering Laboratory at the University of Oklahoma, and the results were presented at the 2016 Military Health System Research Symposium (MHSRS).

The second part of this chapter reports the changes of TM tissue mechanical properties after multiple blast exposures of human cadaver ears based on our recent study by Engles et al. (2017). Microstructural variations of the TM were detected by scanning electron microscopy (SEM) images, which provide an insight into the structural aspects of the injury on the surface of the TM. Changes of the structure and mechanical properties of the TM directly affect sound transmission and result in conductive hearing loss. We have also measured the changes of TM mechanical properties in chinchilla blast model using a micro-fringe protection method, but the results are not included in this chapter. The readers can find the information from the current publication by Liang et al. (2017).

2 Part I. Human TM Rupture in Relation to Blast Overpressure Direction

2.1 Experimental Setup, Procedure, and Results from Blast Tests

A "head block" attached with human cadaver ear or temporal bone and mounted with two pressure sensors was developed in our lab to measure the transfer functions of the ear canal and middle ear in response to blast overpressure. Three pressure sensors are simultaneously monitoring the blast pressure at the entrance of the ear canal (P0), near the TM in the canal (P1), and behind the TM in the middle ear (P2). The P0 sensor (Model 102B16, PCB Piezotronics, Depew, NY) was placed at 1 cm lateral to the ear canal opening with the sensing surface facing the blast. The P1 and P2 sensors (Model 105C02, PCB Piezotronics) were placed at 3 mm from the TM and inside the middle ear cavity through the Eustachian tube, respectively.

The "head block" was exposed to open-field blast inside an anechoic test chamber in our lab along three directions, the vertical, horizontal, and front, with respect to the head as shown in Fig. 1. A well-controlled compressed air (nitrogen)—driven blast apparatus located inside the test chamber—was used to create a blast overpressure wave (Gan et al. 2016; Hawa and Gan 2014). Polycarbonate film (McMaster-Carr, Atlanta, GA) of varying thickness (0.13–1.0 mm) was employed to generate blast overpressure of at least 30 psi (207 kPa or 200 dB SPL). The overpressure level was controlled by changing the thickness of the film or the distance from the blast reference plane. By increasing the blast peak pressure P0, the TM was finally ruptured, and all three pressure waveforms (P0, P1, and P2) were recorded simultaneously at each pressure level.

The pressure sensor signal was measured by cDAQ 7194 and A/D converter 9215 (National Instruments Inc., Austin, TX) with the sampling rate of 100 k/s (10 μs dwell time). The LabVIEW software package (NI Inc.) was used for data acquisition and analysis. The waveform of each blast test was saved in a PC for further analysis.

A total of 41 fresh human temporal bones (TBs) were used in this study for testing of three wave directions: from the top of the head (the vertical setup), from the lateral to the ear (the horizontal setup), and from the front of the face (the front setup). The schematic of the setup along these three directions is shown in Fig. 1a. Figure 1b displays the head block with a right cadaver ear exposed to the vertical wave direction. The P0 pressure sensor was fixed near the ear canal entrance. All the TBs were obtained from the Life Legacy Foundation, a certified human tissue supply source for military research. The study protocol was approved by the US Army Medical

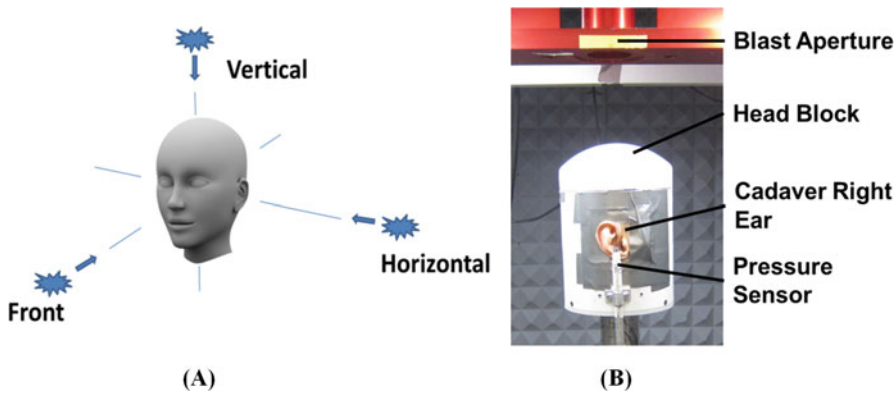

Fig. 1 (**a**) Schematic of three blast wave directions with respect to the head. (**b**) The picture of experimental setup with the head block along the vertical wave direction inside the test chamber

Research and Materiel Command (USAMRMC) Office of Research Protections (ORP).

It usually took 3–4 iterations of blast tests to reach the TM rupture threshold defined as the peak pressure before the TM rupture. That means if the TM ruptured after the third blast, the threshold was the peak pressure level of the second blast. The initial blast pressure level was selected based on the system calibration using different films and changing the distance between the sensor surface and the blast reference plane. The number of blast tests also varied with individual TBs due to the variation among the human samples and setups. To confirm the TM damage, an otoscopic examination of the ear was performed first, and further verification was done using wideband tympanometry to determine whether the TM was ruptured (Gan et al. 2016). When the TM was found without rupture, the next blast test was conducted with an increase of the overpressure level. The testing stopped when the TM was ruptured.

Figure 2a shows typical overpressure waveforms of P0 (black), P1 (red), and P2 (green) recorded from three cadaver ears in the vertical, horizontal, and front tests (before the TM rupture). The pressure waves are displayed in 2 ms of time duration, and the positive overpressure is followed by negative pressure. As shown in Fig. 2a, the peak P0 level was around 50 kPa or 7.5 psi or 188 dB SPL for all three tests. The P1 peak pressure shows a substantial increase compared to the P0 pressure in all wave direction tests. The results demonstrate the effect of the ear canal on enhancing the impulse pressure level near the TM in the canal.

The otoscopic photographs displayed in Fig. 2b illustrate the TM damages observed at the vertical (V), horizontal (H), and front (F) tests with the peak P0 pressure levels of 191, 186, and 189 dB SPL (or 11, 6, and 8 psi), respectively. There is no consistent TM rupture pattern observed from the experiments at different wave directions. However, the damage along the

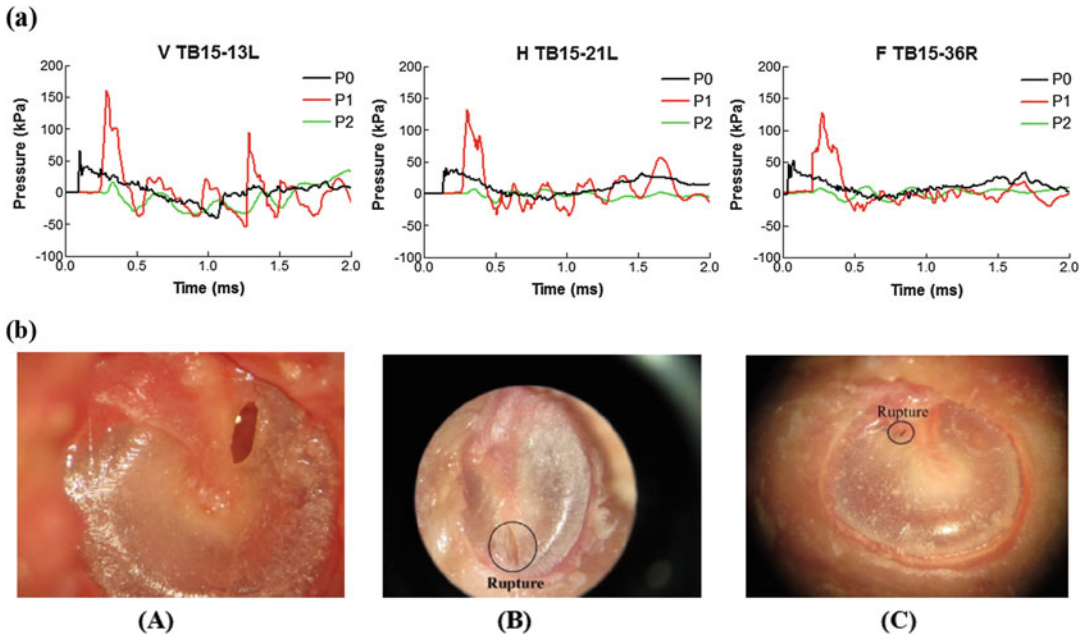

Fig. 2 (**a**) Overpressure waveforms of P0 (black), P1 (red), and P2 (green) recorded from three cadaver ears or temporal bones under the vertical (left), horizontal (medium), and front (right) tests. (**b**) Otoscopic pictures of human TMs ruptured after blast exposure. (**A**) Vertical test, left ear, TM ruptured in the superior-posterior region; (**B**) horizontal test, left ear, TM ruptured in the inferior side; (**C**) front test, right ear, TM ruptured in the superior-posterior region

TM-radial fiber direction is commonly observed from the experiments. Another area is near the manubrium or inferior side of the TM along the radial direction.

Table 1 lists the mean and standard deviation (SD) of P0, P1, and P2 ratio of P1/P0 and the TM rupture P0 and P1 thresholds obtained from all tests along three blast wave directions: V, H, and F. The P1 rupture threshold was determined by multiplying the P1/P0 ratio and the P0 rupture threshold for each direction. The results in Table 1 show that the P0 rupture threshold for the V and F directions are comparable and that the P0 threshold in H-direction is significantly lower than the other two directions. Conversely, the P1/P0 ratio in H direction is well above the others. It is also observed from Table 1 that the P1 rupture threshold (the pressure that is directly responsible for TM damage) is similar for the V and H directions, at 20.2 and 20.1 psi, respectively. Interestingly, the results indicate that the F direction requires less pressure as measured at P1 to rupture the TM.

The recorded waveforms (P0 and P1) from blast tests in TBs are impulse pressure profiles (short duration and nonperiodic). The impulse pressure energy spectra analysis on recorded waveforms in the time domain was conducted in MATLAB to determine the signal energy distribution over the frequencies (ten octave frequency bands) under three blast wave directions. First, the recorded pressure waveforms were converted to pressure distributions over the frequencies of 20–20 kHz by using FFT spectral analysis. Next, following the methods of impulse signal energy distribution theory reported by Hamernik et al. (1991), Hamernik and Keng (1991), Hamernik and Qiu (2001), and Gan et al. (2016), the total sound exposure was divided by the standard characteristic impedance of the air ρc as impulse energy flux (energy per unit area) and expressed as

$$E^* = \frac{1}{\rho c}\int_0^T p^2(t)dt, \quad \left[\mathrm{J/m^2}\right] \tag{1}$$

where $p(t)$ is the instantaneous value of acoustic pressure in Pa or N/m^2, dt is the time increment for scanning of acoustic pressure in seconds, and $\rho c = 406$ mks rayls to produce a quantity with units of energy flux (i.e., J/m^2). Both ρ and c are pressure-dependent in the shock front. The duration of $T = 6$ ms was used for calculation in the present study.

Eight octave band-pass filters with center frequencies at 125 Hz, 250 Hz, 500 Hz, 1 kHz, 2 kHz, 4 kHz, 8 kHz, and 16 kHz were designed. A low-pass filter L125 and a high-pass filter H16k were also designed to catch signals at frequencies lower than 125 Hz and higher than 16 kHz. The filtered signals were then generated, and the sound energy in each band was calculated as the distribution of pressure energy flux over ten bands. Instead of directly comparing the energy flux values in the three wave directions, the energy in each band was normalized with respect to the total sound energy in that band.

The comparison of impulse energy flux (energy per unit area in unit J/m^2) distributed in ten frequency bands from below 125 Hz to over 16 kHz obtained from waveforms recorded in three wave direction tests demonstrates that (1) P0 pressure-induced energy is mainly distributed at frequencies below 1 kHz and there is a large peak for V direction at 500 Hz; (2) P1 pressure-induced energy is distributed at frequencies up to 4 kHz; and (3) blast waves at F and H directions result in relatively large energy flux of both P0 and P1 at frequencies below 125 Hz. This energy analysis suggests that P1 pressure waveform should be considered as a primary factor for blast-induced TM damage because P1 energy distributions on octave bands are similar for all three wave directions and concentrated from 500 Hz to 4 kHz.

2.2 Finite Element Modeling Prediction

The 3D FE model of the human ear developed by Gan et al. (2004, 2007) for sound transmission and being used for TM perforation studies (Gan et al. 2009) was modified to simulate the blast wave transmission through the ear as shown in Fig. 3a. The FE model consisted of the ear

Table 1 Mean and SD of peak pressure values of P0, P1, and P2, ratio of P1/P0, and the TM rupture P0 and P1 thresholds

Blast wave direction	TB sample	P0 (psi)	P1 (psi)	P2 (psi)	P1/P0	Threshold P0 (psi)	Threshold P1 (psi)
Vertical	Mean ± SD($N = 13$)	8.9 ± 1.8	19.3 ± 3.3	2.3 ± 1.6	2.2 ± 0.5	9.2 ± 1.7	20.2 ± 2.2
Horizontal	Mean ± SD($N = 14$)	6.4 ± 2.1	19.0 ± 6.1	2.2 ± 1.4	3.0 ± 0.7	6.7 ± 1.2	20.1 ± 1.9
Front	Mean ± SD($N = 14$)	9.8 ± 2.0	16.3 ± 3.3	2.1 ± 0.7	1.7 ± 0.4	9.8 ± 2.1	16.7 ± 2.5

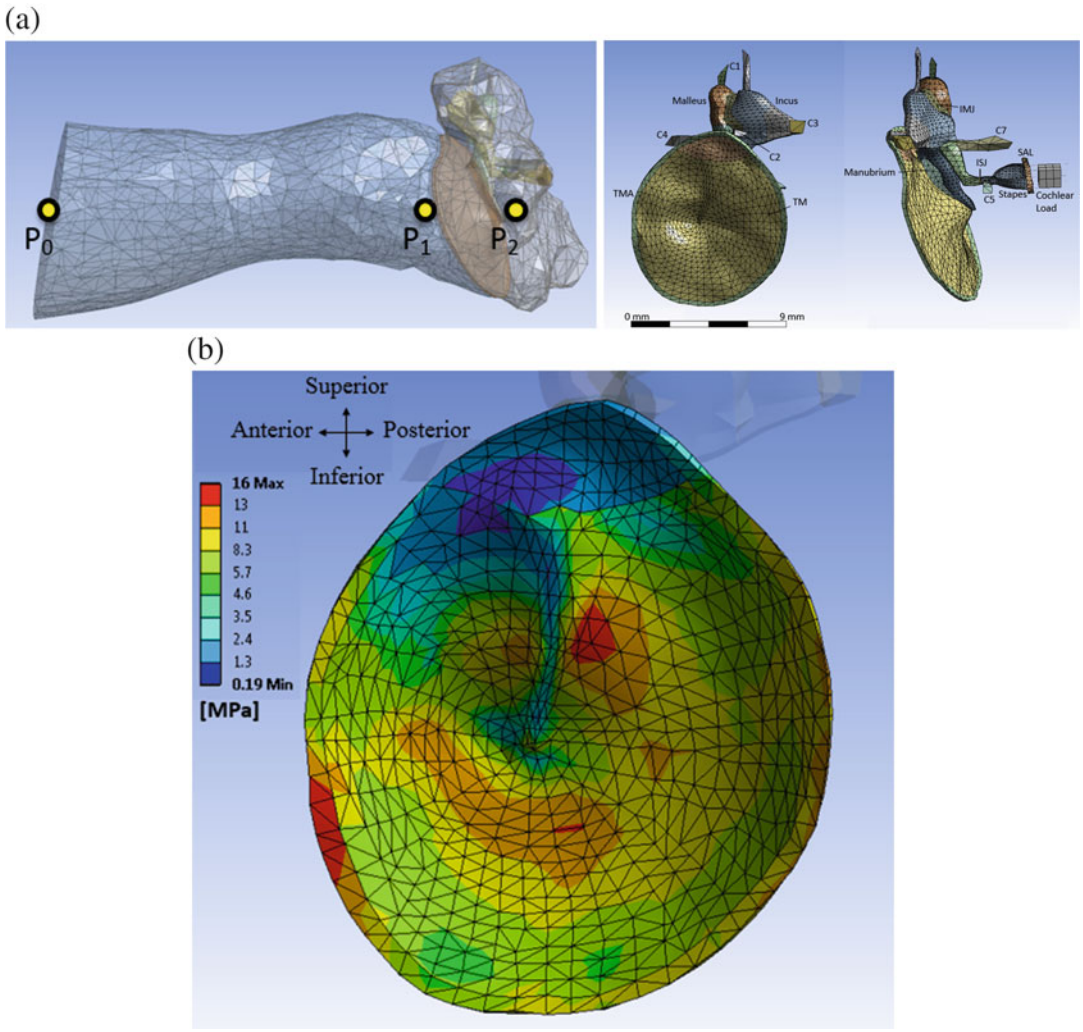

Fig. 3 (**a**) (Left) FE model of the human ear comprised of the ear canal, TM, middle ear ossicles, and middle ear cavity. The locations for pressure monitoring points are designated as P0, P1, and P2. (Right) Structural mesh of the model, showing the TM, TMA, middle ear ossicles, IMJ, ISJ, suspensory ligaments/muscle tendons (all Cs and SAL), and cochlear load. (**b**) FE model-derived distribution of the equivalent (von Mises) stress in the TM when the maximum stress was reached under the vertical wave direction

canal, TM, TM annulus (TMA), three ossicles connected by two joints (incudomalleolar joint (IMJ) and incudostapedial joint (ISJ)), middle ear suspensory ligaments/muscle tendons (Cs), stapedial annual ligament (SAL), and middle ear cavity. The cochlea was not included in this initial model for blast simulation, but the cochlear load was applied on the stapes footplate by a mass block-dashpot system with the cochlear input impedance of 20 GΩ (Gan et al. 2004).

This FE model of the human ear was regenerated in ANSYS Workbench (ANSYS Inc., Canonsburg, PA) where Fluent and ANSYS Mechanical coupled with fluid-structure interaction analyses were employed to compute blast overpressure transduction from the environment to the TM and middle ear (Leckness 2016). Briefly, the viscoelastic material properties were assigned to soft tissues in the middle ear including the TM, TMA, IMJ, ISJ, and SAL. The experimentally recorded P0 waveforms from the head block with cadaver TBs were applied onto the boundary at the entrance of the ear canal, and the pressure waveforms P1 and P2 were then calculated and compared with those measured from the experiments. The FE model was then employed to investigate the mechanisms of TM injury under recorded P1 profiles from the vertical, horizontal, and front directions. P1 overpressure waveforms recorded from multiple iterations of blast tests in 14 temporal bones (4 from the vertical direction and 5 from the horizontal and front directions) were applied to the surface of the TM in the FE model, and the maximum stress distributions were calculated. Note that the detailed description and validation of the FE model of the human ear are not included in this paper, which can be found from Leckness (2016).

The equivalent (von Mises) stress was used as a measure of the stress state of the TM. The average maximum stresses induced by the P1 rupture threshold waveforms were 16.2 ± 3.00 MPa, 16.3 ± 2.44 MPa, and 14.3 ± 2.53 MPa for the vertical, horizontal, and front directions, respectively. The average maximum stresses induced by the P1 waveforms that caused visible TM damage were 20.3 ± 1.18 MPa, 18.8 ± 1.99 MPa, and 15.5 ± 3.46 MPa for the vertical, horizontal, and front directions, respectively. An example of TM stress distribution at the time of maximum stress due to an applied P1 waveform of 134 kPa peak pressure in the vertical wave direction is displayed in Fig. 3b. As shown in this figure, the maximum stress reached 16 MPa, and the regions of the highest stress were along the anterior portion of the TMA, the posterior to the center of the manubrium, and the inferior to the bottom of the manubrium. These locations may indicate potential sites for TM rupture.

2.3 Mechanisms of TM Rupture in Relation to Blast Wave Direction

The P1 threshold for TM damage should more accurately represent the pressure applied to the TM than the P0 threshold. The experimental results shown in Table 1 indicate that P1 threshold in F direction is lower than V and H directions, or in other words, the blast wave from the front of the face (F direction) is easier to cause TM rupture than other blast wave directions. *Why does the F direction result in a lower P1 threshold for TM damage?* To answer this question and understand the mechanism behind the experimental findings, the FE model of the human ear was used to compute the distributions of the stress in the TM and derive the sensitivity of TM stress with respect to P1 pressure increase as the TM stress gradient with respect to P1, $d\sigma/dP_1$. The stress gradient was calculated based on experimental P1 waveforms of pre-threshold up to the rupture level, usually 2–4 pressure waveforms per cadaver ear or temporal bone. Fourteen cadaver ears (four from the V direction and five from the H and F directions) were selected for calculation. As an example, Fig. 4a–c shows a series of P1 pressure waveforms over 0.5 ms duration from three temporal bone experiments in V, H, and F direction tests, respectively. The P1 waveforms were used to calculate $d\sigma/dP_1$ in V, H, and F directions using the model.

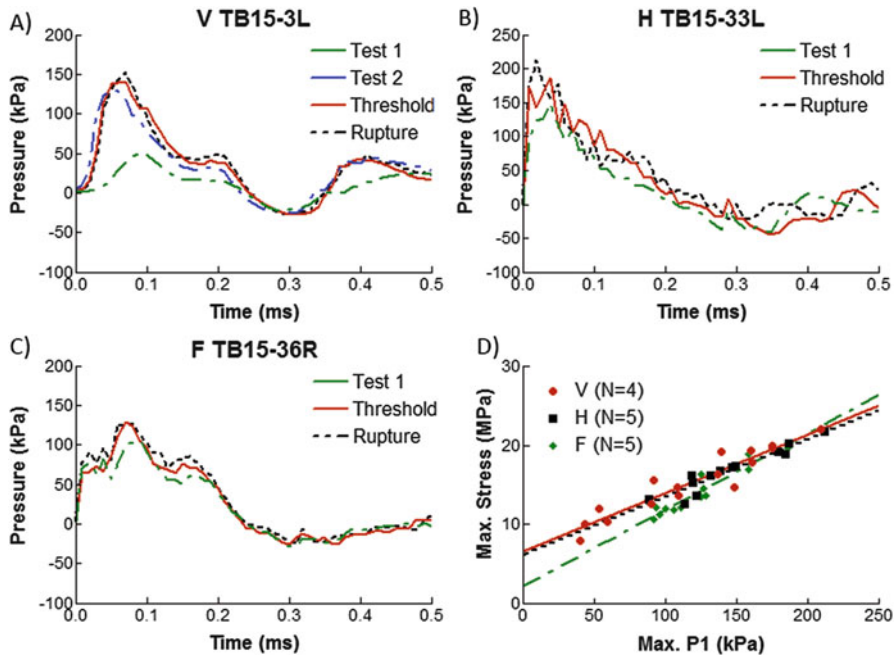

Fig. 4 (**a**–**c**) represent the P1 pressure waveforms with incremental peak pressure level from initial test 1 to TM rupture recorded from a temporal bone sample TB15-3L in V direction test, from sample TB15-33L in H direction test, and from sample TB15-36R in F direction test, respectively. (**d**) Plots of FE model-derived maximum stress in the TM vs. P1 peak pressure obtained from V direction ($N = 4$), H direction ($N = 5$), and F direction ($N = 5$)

All the data points of the maximum stress in the TM vs. the maximum (peak) P1 pressure obtained along the V, H, and F blast direction tests were plotted in Fig. 4d. Statistical correlation was then applied to determine the best-fit line for the data points at each direction. Figure 4d shows the comparison of the slope (i.e., stress gradient) $d\sigma/dP_1$ at three directions. The mean value of stress gradient was calculated as 74.1, 73.0, and 96.7 for V, H, and F direction, respectively. This indicates that the change of maximum stress in the TM with respect to P1 peak pressure in F direction is higher than the other two directions. The high sensitivity of TM stress with respect to the P1 pressure in F direction may characterize mechanical damage of the TM induced by blast. The average maximum stress was lowest for the front direction, as was the average P1 rupture threshold; this suggests that neither the stress level nor P1 level alone determines TM failure but that TM failure is best predicted by the rate change of stress with respect to maximum P1 pressure reaching the TM.

3 Part II. TM Tissue Mechanical Property Changes After Exposure to Blast Waves

3.1 Summary of TM Mechanical Property Measurements

The TM or eardrum is a multilayer membrane including the epidermal, collagen fibrous, and mucosal layers from the lateral to the medial side. The collagen fibers provide primarily the mechanical stiffness of the TM. It consists of a matrix of ground substance embedding approximately 22-μm-thick collagen fiber layer aligned primarily along the radial direction emanating from the umbo and approximately 15-μm-thick collagen fiber layer along the circumferential direction (Lim 1995). A major part of the TM is the

pars tensa, which is within tympanic annulus ring located at the boundary; the malleus manubrium bone is attached in the central portion at the medial side. The small dimensions of the TM (about 70 μm thick and 9 mm in diameter) make it difficult to measure the mechanical properties. Numerous investigations of the mechanical behavior of human TMs have been performed at static or low strain rates (von Békésy 1960; Dirckx and Decraemer 2001; Fay et al. 2005; Cheng et al. 2007; Huang et al. 2007; Daphalapurkara et al. 2009).

The static properties of the human TM were first reported by von Békésy (1960) as 20 MPa from a bending test on a rectangular cadaver TM strip. Further investigations into mechanical properties of human TM have been performed at quasi-static or low-frequency range (Cheng et al. 2007; De Greef et al. 2014; Fay et al. 2005; Huang et al. 2007). However, the TM works under the auditory frequency range of 20–20,000 Hz, and the dynamic properties of the TM need to be measured over the auditory frequency range. Kirikae (1960) determined Young's modulus in the circumferential direction to be 40 MPa at 890 Hz. Zhang and Gan (2010) reported an investigation on dynamic properties of human TM using acoustic stimulation and laser Doppler vibrometry (LDV) measurement. Utilizing various techniques, the dynamic properties of the human TM in the auditory frequency range have been further characterized (Luo et al. 2009; Zhang and Gan 2012). Nevertheless, there are only a few investigations providing accurate mechanical data for the damaged TM after exposure to blast overpressure (Luo et al. 2015; Gan et al. 2016; Engles et al. 2017).

A better understanding of dynamic properties of the human TM exposed to blast waves is of considerable interest for assessment of blast-induced damage of the auditory system as well as for hearing protection devices. Luo et al. (2015) used a highly sensitive miniature split Hopkinson tension bar (SHTB) to measure the mechanical properties of the TM at high strain rates and derive Young's modulus changes of the TM after multiple blast exposures. The SHTB provided a uniaxial tensile test for TM strip specimens in the time domain. The tensile strain of the TM specimens in SHTB tests was typically 10–30%. Due to the sensitivity of the TM's stiffness characteristics to strain rates, the results from SHTB test can be utilized to characterize the failure behavior and nonlinear stress-strain curve of the TM in relation to impact loading. However, from the view of TM transmitting sound vibration, mechanical property changes of the TM induced by blast waves should be quantified in response to sound stimulation.

Despite the progress made in understanding the change of mechanical properties induced by blast exposure, accurate measurement of the mechanical properties of damaged TM is still needed as addressed (Engles et al. 2017). First, due to the nonlinear stiffness characteristics of the TM, the mechanical properties vary with strain. It is necessary to determine how mechanical stiffness of the TM decreases when the TM is exposed to repeated blast exposures. Second, the residual stiffness of damaged TM reflects the severity of injury to the TM, and the property data gives us an insight into the mechanical state of the TM immediately after exposure. Third, the material properties can be used to validate the biomechanical modeling of TM perforation induced by blast exposure. Thus, the knowledge about residual TM stiffness after blast exposure may assist emergency medical personnel in the evaluation and treatment of blast-injured TM, avoiding further auditory injury.

3.2 Dynamic Properties of Human TM After Blast Exposure

A study on dynamic properties of human TM after exposure to blast waves by using acoustic loading and laser Doppler vibrometry measurement with an inverse problem-solving method to determine the complex modulus of the TM specimen was recently completed in our lab (Engles et al. 2017). The TM specimens were prepared from human temporal bones following exposures to blast overpressure using the established methodologies described in Sections I–

A and shown in Fig. 1b. It usually took three iterations of blasts to reach the TM rupture. The peak pressure before the TM rupture defined as the TM rupture threshold ranged from 7.6 to 9.0 psi (52.4–62.1 kPa) from ten human cadaver ears or temporal bones. The TM specimen for mechanical test was the rectangular strip with approximate dimensions of 6 × 2 mm cut from either the posterior or anterior site of the pars tensa with the tympanic annulus attached. The specimen was then mounted to the material testing system (MTS).

The experimental setup with LDV to measure dynamic properties of the TM specimen can be found in Fig. 3 of Engles et al. (2017). Briefly, the sound was delivered from a speaker through a 1-mm-diameter sound delivery tube at 2 mm away from the center of the lateral side of the specimen. A dynamic signal analyzer (DSA) (PSA, HP 35670A, CA) coupled to a power amplifier (B&K 2718, Norcross, GA) was used to generate a pure tone sound of 90 dB SPL over the frequency range of 200–8000 Hz. To monitor the input sound pressure level, a probe microphone (ER-7C, Etymotic Research, IL) was attached to the sound delivery tube at 1 mm from the TM surface. Specimen vibrations were measured with the LDV (HLV-1000, Polytech PI, Austin, CA) while focusing the beam at the reflective tape. The vibration velocity of the specimen was acquired by the DSA and recorded on a PC for further analysis.

Dynamic testing of each specimen was simulated in a FE model in ANSYS using acoustic-structure coupled analysis. To mimic the vibration of the TM specimen in response to sound stimuli in an open field, a FE model including the solid structure of the specimen and a spherical area of air surrounding the TM was built. To facilitate acoustic pressure coupled to the TM surface, the surface of acoustic elements (air) in contact with the TM solid structure was defined as a fluid-structure interface. The standard linear solid model or Weichert model was used to describe the viscoelastic behavior of the TM (O'Connor et al. 2008; Zhang and Gan 2010). The relaxation modulus of the TM can be expressed as

$$E(t) = E_0 + E_1 \exp\left(-\frac{t}{\tau_1}\right) \tag{2}$$

where E_0 is the relaxed elastic modulus at $t = \infty$, $E_0 + E_1$ is the initial elastic modulus at $t = 0$, and τ_1 is the relaxation time. The relaxation modulus in the time domain can be converted to the complex modulus in the frequency domain. The complex modulus E^* is expressed as

$$E^*(\omega) = E'(\omega) + iE''(\omega) \tag{3}$$

where $E'(\omega)$ is the storage modulus, $E''(\omega)$ is the loss modulus, and ω is the angular frequency. Further, $E'(\omega)$ and $E''(\omega)$ can be expressed as

$$E'(\omega) = E_0 + \frac{E_1 \tau_1^2 \omega^2}{1 + \tau_1^2 \omega^2} \tag{4}$$

$$E''(\omega) = \frac{E_1 \tau_1 \omega}{1 + \tau_1^2 \omega^2} \tag{5}$$

The loss factor $\eta(\omega)$ can be expressed as

$$\eta(\omega) = \tan(\delta) = \frac{E''(\omega)}{E'(\omega)} \tag{6}$$

where δ is the phase angle.

An iterative FE simulation of the dynamic test was performed to find material constants that achieve the best match between the modeling results and actual measurements. A short description of the process was given by Engles et al. (2017). An example of the experimental results of the amplitude-frequency curve from two TM samples (47 L and 41 L) compared with the FE model-derived curves was shown in Fig. 6 of their paper. The three parameters E_0, E_1, and τ_1 for each specimen were determined through the FE model, and the experimental curves were represented by the resonance frequency f_n and the amplification ratio R (ratio between the amplitude at the resonance frequency and the amplitude at the lowest frequency measured).

To determine the effect of blast waves on mechanical properties of the TM, the complex modulus for post-blast TMs was plotted against normal TMs published by Zhang and Gan (2010)

using acoustic stimulation and LDV in Fig. 5. The blast exposure caused the storage modulus to become significantly reduced across the frequency range. Similarly, the loss modulus for post-blast TMs was also much lower than the normal TMs. The decrease of loss modulus was significant (Student's t test, $p < 0.0065$). These data reveal that the blast overpressure causes a frequency-dependent stiffness reduction of the TM. Loss factor is the ratio between the loss modulus and storage modulus. The post-blast TMs had a lower loss factor at frequencies below 2 kHz and a larger loss factor at frequencies over 2 kHz compared to the normal TMs. As shown in Fig. 5, the blast resulted in a flat storage modulus curve in the high-frequency range. This is one of the reasons that caused the larger loss factor in the post-blast TMs at high frequencies.

An additional insight from this study is the data clearly show that retained complex modulus of the TM after blast exposure was reduced more than 50%. The TM rupture caused by blast exposure includes perforation of the TM and reduction of complex modulus in the remaining part of the TM. The TM perforation and alteration in mechanical properties can contribute to a conductive hearing loss. The effect of TM perforations on sound transmission through the middle ear was investigated in temporal bone models by Gan et al. (2009). Their results indicated that TM perforations caused more than 20 dB reduction in the TM and stapes footplate displacements at frequencies below 1 kHz.

3.3 Microstructural Changes in Post-Blast TM

TM is a complex trilaminar membrane. Its middle layer, the lamina propria, has a composite structure consisting of radially and circumferentially oriented collagen fibers embedded in the ground substance (Lim 1995). To evaluate the microstructural changes of the TM after expo-

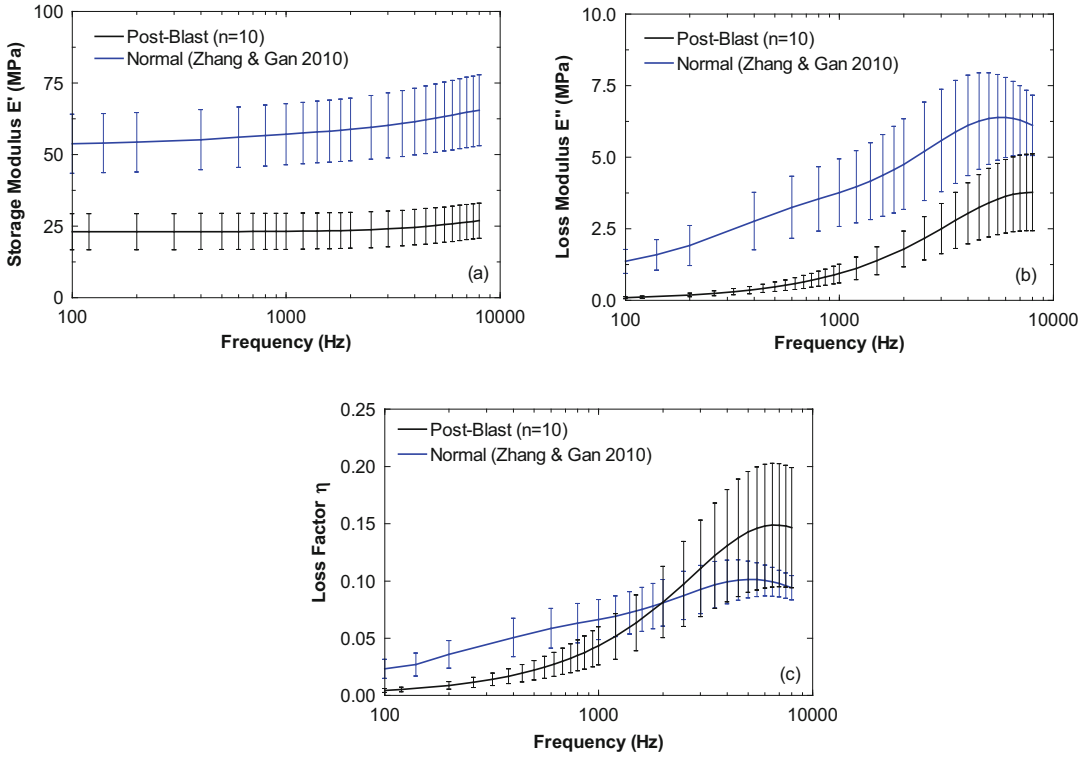

Fig. 5 Comparison of complex modulus between blast-exposed and normal TMs over the frequency range of 100–8000 Hz. (**a**) Storage modulus, (**b**) loss modulus, and (**c**) loss factor

sure to blast, the SEM images were obtained for both pre- and post-blast human TMs and examined with electron microscopes (NEON 40 EsB, Zeiss, Oberkochen, Germany; JSM-840, JEOL Ltd., Tokyo, Japan) in the Samuel Roberts Noble Microscopy Laboratory at the University of Oklahoma.

Figure 6 shows the SEM image obtained from a post-blast TM (left panel) and a normal TM (right panel). The images were viewed from the lateral side and focused on areas where the epithelial layer separated from the TM during SEM preparation. The effect of blast waves on the fiber bundles can be observed from Fig. 6 as shown by the radial orientation of the post-blast TM tears, which was a result of the circumferential fiber fractures. The normal TM shows a generally smoother appearance, reflecting the normal state of the TM. The SEM images suggested that the TM damage along the radial direction may be more severe than that along the circumferential direction after blast exposure.

In a study performed by Luo et al. (2015), the results indicated that Young's modulus is higher in the radial direction than in the circumferential direction and the fracture strength in the radial direction is also higher than that in the circumferential direction under the condition of the same strain rate. When the TM is exposed to blast waves, it is more probable that the circumferential fibers, which have a lower fracture strength, would break before the radial fibers. Figure 6 demonstrates that the post-blast TM tears were oriented in the radial direction, indicating the microstructure changes caused by blast exposures. However, it is difficult to quantify the extent of microstructure damage of TM by using SEM images. The weakened mechanical properties are the reflection of microstructure damage, but it is not applicable to build a direct relation between microstructure damage of TM and changes of macro-mechanical properties at the present stage.

4 Conclusions

1. The relationship between the TM damage threshold and blast overpressure wave direction has been investigated in human cadaver ears and the FE model of the human ear. The "head block" attached with the temporal bone was exposed to open-field blast inside the test chamber at three incident wave directions, vertical, horizontal, and front, with respect to the head. Results demonstrate that blast overpressure P0 at the ear canal entrance induced the highest peak pressure P1 near the TM in the canal, which determines the TM injury. The P1 pressure differences in vertical, horizontal, and front tests reflect the variations of energy flux distribution over frequencies, peak P1/P0 ratio, and TM rupture threshold. FE modeling results indicate that P1 threshold for TM rupture in front direction is the lowest because of the highest TM stress change rate with respect to P1 pressure increase, $\delta\sigma/\delta p_1$, compared with the vertical and horizontal directions.
2. The dynamic properties of post-blast TMs were measured on ten human cadaver TM

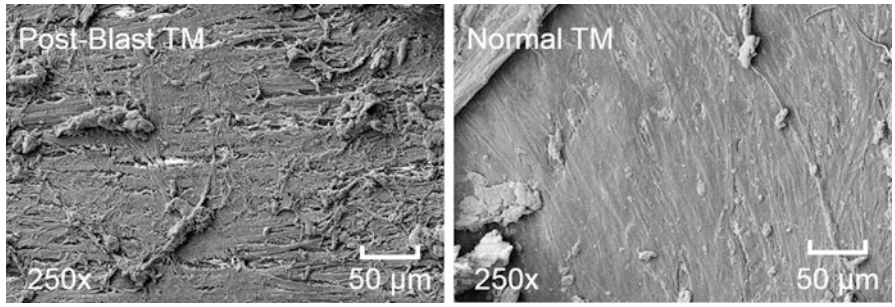

Fig. 6 SEM images of the TM surface. The left image shows the damage of the post-blast TM. The right panel shows the SEM image of the normal TM surface

samples following the blast. Acoustic stimulation was used as a driving force to induce vibrations of the TM over a frequency range of 200–8000 Hz, and LDV was used to measure the sample vibrations. The inverse problem-solving method with the FE modeling of each TM specimen test was used to determine the complex modulus. Results include the storage modulus and the loss modulus over the frequency range of 100–8000 Hz obtained from all TM specimens. The mean storage modulus was ranging from 23.1 to 26.9 MPa at frequencies from 100 to 8000 Hz. The mean loss modulus was from 0.10 to 3.78 MPa at frequencies of 100–8000 Hz. Compared to the mechanical properties of normal TMs determined previously using the same method, the storage and loss modulus of the TMs exposed to blast waves had significant reduction. The SEM images of post-blast TMs compared with normal TMs showed obvious microstructural changes which indicate the tissue damage caused by the multiple blast exposures. This study provides important data on the human TM mechanical changes after exposure to blast overpressure waves.

Acknowledgments This work was supported by the US Army Medical Research and Materiel Command (USAMRMC) Grant W81XWH-14-1-0228. The author would like to thank Kegan Leckness, MS; Don Nakmali, MS; Warren Engles, MS; Xiao D. Ji, PhD; and Xuelin Wang, PhD, for their work involved in the projects reported in this chapter.

References

Ahmad SW, Ramani GV (1979) Hearing loss in perforations of the tympanic membrane. J Laryngol Otol 93:1091–1098

von Békésy G (1960) Experiments in hearing. McGraw Hill, New York

Bigelow DC, Swanson PB, Saunders JM (1996) The effect of tympanic membrane perforation size on umbo velocity in the rat. Laryngoscope 106:71–76

Cave KM, Cornish EM, Chandler DW (2007) Blast injury of the ear: clinical update from the global war on rerror. Mil Med 172:726–730

Cheng T, Dai C, Gan RZ (2007) Viscoelastic properties of human tympanic membrane. Ann Biomed Eng 35:305–314

Cho S-I, Gao SS, Xia A, Wang R, Salles FT, Raphael PD, Abaya H, Wachtel J, Baek J, Jacobs D, Rasband MN, Oghalai JS (2013) Mechanisms of hearing loss after blast injury to the ear. PLoS One 8(7):e67618

Daphalapurkara NP, Dai C, Gan RZ, Lu H (2009) Characterization of the linearly viscoelastic behavior of human tympanic membrane by nanoindentation. J Mech Behav Biomed Mater 2(1):82–92

De Greef D, Aernouts J, Aerts J, Cheng JT, Horwitz R, Rosowski JJ, Dirckx JJJ (2014) Viscoelastic properties of the human tympanic membrane studied with stroboscopic holography and finite element modeling. Hear Res 312:69–80

Dirckx JJ, Decraemer WF (2001) Effect of middle ear components on eardrum quasi-static deformation. Hear Res 157:124–137

Dougherty AL, MacGregor AJ, Han PP, Viirre E, Heltemes KJ, Galarneau MR (2013) Blast-related ear injuries among U.S. military personnel. JRehabil Res Dev 50:893–904

Engles WG, Wang X, Gan RZ (2017) Dynamic properties of human tympanic membrane after exposure to blast waves. Ann Biomed Eng 45(10):2383–2394. https://doi.org/10.1007/s10439-017-1870-0

Fausti SA, Wilmington DJ, Gallun FJ, Myers PJ, Henry JA (2009) Auditory and vestibular dysfunction associated with blast-related traumatic brain injury. J Rehabil Res Dev 46(6):797–810

Fay J, Puria S, Decraemer WF, Steele C (2005) Three approaches for estimating the elastic modulus of the tympanic membrane. J Biomech 38:1807–1815

Gan RZ, Feng B, Sun Q (2004) Three-dimensional finite element modeling of human ear for sound transmission. Ann Biomed Eng 32(6):847–859

Gan RZ, Reeves BP, Wang X (2007) Modeling of sound transmission from ear canal to cochlea. Ann Biomed Eng 35(12):2180–2195

Gan RZ, Cheng T, Dai C, Yang F, Wood MW (2009) Finite element modeling of sound transmission with perforations of tympanic membrane. J Acoust Soc Am 126:243–253

Gan RZ, Nakmali D, Ji X, Leckness K, Yokell Z (2016) Mechanical damage of tympanic membrane in relation to impulse pressure waveform - A study in chinchillas. Hear Res 340:25–34

Hamernik RP, Keng D (1991) Impulse noise: some definitions, physical acoustics and other considerations. J Acoust Soc Am 90:189–196

Hamernik RP, Qiu W (2001) Energy-independent factors influencing noise-induced hearing loss in the chinchilla model. J Acoust Soc Am 110:3163–3168

Hamernik RP, Ahroon WA, Hsueh KD (1991) The energy spectrum of an impulse: Its relation to hearing loss. J Acoust Soc Am 90:197–204

Hawa T, Gan RZ (2014) Pressure distribution in a simplified human ear model for the high intensity sound transmission. J Fluids Eng 136:111108-1–111108-6

Huang G, Daphalapurkar NP, Gan RZ, Lu H (2007) A method for measuring linearly viscoelastic properties

of human tympanic membrane using nanoindentation. J Biomech Eng 130:014501

Kirikae I (1960) The structure and function of the middle ear. University Press, Tokyo

Leckness K (2016) Novel finite element method to predict blast wave transmission through human ear. MS Thesis. University of Oklahoma, Oklahoma

Liang J, Yokell Z, Nakmali D, Gan RZ, Lu H (2017) The effect of blast overpressure on the mechanical properties of a chinchilla tympanic membrane. Hear Res 354:48–55

Lim DJ (1995) Structure and function of tympanic membrane: A review. Acta Otorhinolaryngolog Belg 49:101–115

Luo H, Dai C, Gan RZ, Lu H (2009) Measurement of young's modulus of human tympanic membrane at high strain rates. J Biomech Eng 131: 064501–064501

Luo H, Jiang S, Nakmali D, Gan RZ, Lu H (2015) Mechanical properties of a human eardrum at high strain rates after exposure to blast waves. J Dyn Behav Mater 2:59–73

Mehta RP, Rosowski JJ, Voss SE, O'Neil E, Merchant SN (2006) Determinants of hearing loss in perforations of the tympanic membrane. Otol Neurotol 27:136–143

O'Connor KN, Tam M, Blevins NH, Puria S (2008) Tympanic membrane collagen fibers: a key to high-frequency sound conduction. Laryngoscope 118:483–490

Santa Maria PL, Atlas MD, Ghassemifar R (2007) Chronic tympanic membrane perforation: a better animal model is needed. Wound Repair Regen 15:450–458

Voss SE, Rosowski JJ, Merchant SN, Peake WT (2007) Non-ossicular signal transmission in human middle ears: experimental assessment of the 'acoustic route' with perforated tympanic membranes. J Acoust Soc Am 122(4):2135–2153

Zhang X, Gan RZ (2010) Dynamic properties of human tympanic membrane – experimental measurement and modelling analysis. IJECB 1:252–270

Zhang X, Gan RZ (2012) Dynamic properties of human tympanic membrane based on frequency-temperature superposition. Ann Biomed Eng 41:205–214